2010

Geological analysis and hydrodynamic modeling of tropical cyclone influence: northeastern Gulf of Mexico inner shelf

Amy Lynn Spaziani
Louisiana State University and Agricultural and Mechanical College

GEOLOGICAL ANALYSIS AND HYDRODYNAMIC MODELING OF TROPICAL CYCLONE INFLUENCE: NORTHEASTERN GULF OF MEXICO INNER SHELF

A Thesis

Submitted to the Graduate Faculty of the
Louisiana State University and
Agricultural and Mechanical College
in partial fulfillment of the
requirements for the degree of
Master of Science

in

The Department of Oceanography and Coastal Sciences

by
Amy Spaziani
B.A., State University of New York at Geneseo, 2004
May 2010

For my grandmother, “Gig”, who always told me I could do anything.

ACKNOWLEDGEMENTS

This research was funded by the Department of Environmental Protection of the State of Florida, and data was provided through Taylor Engineering, Alpine Ocean Seismic Inc., Sonographics Inc. and Morgan and Eklund, Inc. I also thank Dr. Prasad Thoppil, NRL, Stennis Space Center, for providing the HYCOM model data. The Gulf Coast Association of Geological Societies (GCAGS) provided additional funding through the student grant program. The Danish Hydraulic Institute (DHI) Water and Environment provided the numerical model program. I thank my adviser, Dr. Gregory W. Stone, and my graduate committee – Drs. Harry Roberts, Philip Bart, and Baozhu Liu – for their support and guidance. In addition to my committee, Dr. Felix Jose has been a tremendous source of support, help, encouragement, and direction in my time as a graduate student, and I am extremely grateful to him.

Several people were instrumental in the collection and processing of data for this research. I thank the WAVCIS Laboratory at LSU: Drs. Baozhu Liu, Felix Jose, Daijiro Kobashi, Yixin Luo, and Yuliang Chen for their assistance in the processing the granulometry data, and Floyd De Mers from the Coastal Studies Institute Field Support Group at LSU, for assistance with the cores. I thank Dr. Daijiro Kobashi for providing me with the routine to compute resuspension intensity. I also thank the Earth Scan Laboratory at LSU: Dr. Nan Walker, Dr. Eurico D'Sa, Alaric Haag, Joe Calvasina, and Chet Pilley for their assistance in obtaining satellite images. I am extremely grateful to my officemates, Seyed Mostafa Siadatmousavi and Yuliang Chen, and Jenny Lentz for their patience and guidance in teaching new computer programs, such as ArcGIS.

The completion of this research would not have been possible without the support and discussion from several individuals, both colleagues and friends. To name a few, I thank Dr. Julie Dean Rosati, U.S. Army Corps of Engineers; Dr. Walter Guidroz, BP, America; Mr. Chuck Dill, Alpine Ocean Seismic, Inc.; Dr. Mark Byrnes, Applied Coastal; Dr. Joao Rego, Delft Institute; and several fellow students at LSU: Seyed Mostafa Siadatmousavi, Kyle Metz, Mohammadnabi Alladadi, Clint Edrington, Brenda Babin, and Stephanie Welch.

Last, but certainly not least, I thank my parents, David and Barbara, and my friends and family, for their unwavering belief in me and loving support. I extend a special thank you to all who did not give up hope that I would indeed finish.

TABLE OF CONTENTS

LIST OF TABLES

LIST OF FIGURES

ABSTRACT

The need to characterize offshore resources as borrow areas for beach restoration has initiated interest of the impact of storms to the inner continental shelf. While numerous studies have investigated the response of coastal systems to major storms, very little is known about the geological response of inner shelves to frequent and intense storms.

This approach integrated a geological study with modeling of hydrodynamics during recent storms, in order to relate trends in the geological signature to physical forcing mechanisms during storms. First, waves and hydrodynamic conditions were modeled during two major recent storms that made landfall in the northeastern Gulf of Mexico. Results of the models were used in calculations of bottom shear stress and potential for resuspension of sediments. These results were further corroborated with satellite images of suspended particles. Second, vibracores, seismic and bathymetry data were collected to characterize the geologic history and recent changes to the geology of the inner shelf. These data were analyzed through physical interpretations, granulometric and radiocarbon analyses, and erosion/accretion calculations.

The results indicate that storms have the potential to have a tremendous impact on the continental shelf, and can resuspend sediments in depths of 80 m or more, and last for several hours to a few days. A substantial offshore movement and downwelling component is also evident, with implications for a southwest moving geostrophic flow. The results of the geological analysis indicate that the stratigraphy of the inner shelf is a derivative of the last glacial to interglacial changes in sea level, with a highly modified Holocene reworked section. These modifications include winnowed sediments that coarsen to the inner shelf seafloor, the

maintenance and migration of shelf shoals, and the development of numerous shelf ridges and troughs.

These modifications are the direct result of frequent and intense hurricanes impacting the northeastern Gulf of Mexico. The modifications observed can be directly correlated to different phases of a storm's impact on the shelf. From this, a conceptual model was developed that summarizes these modifications and the phases from which they formed. This study provides a framework and fundamental understanding of inner shelf characteristics and the impact of storm-related hydrodynamics on erosion and deposition, in addition to providing insight on sand resources on the inner shelf.

CHAPTER 1. INTRODUCTION

1.1 Motivation and Scientific Significance

Given its location (Fig. 1.1) and importance to the United States in terms of industrial, economic, ecological, and recreational resources, the Gulf of Mexico has been the subject of a significant number of geological studies. Research conducted along the northeast Gulf of Mexico (GoM), has become of particular interest in the past two decades with the rapid increase in population and influx of tourists traveling to the Florida and Alabama coasts, as well as the recent increase in hurricane activity and intensity (Muller and Stone, 2001) (see Fig. 1.2). A keen understanding of the sediment transport dynamics and wave climate during storms is important for any future coastal planning or development involving dredging, beach re-nourishment, or coastal development and management; especially for the State of Florida and its coastal counties (Byrnes et al., 1999; Donoghue et al., 2003; Byrnes et al., 2008). In addition, knowledge of modern depositional environments facilitates recognition of similar systems in the geologic record, which is especially useful in the identification of those containing economic mineral deposits or petroleum resources (Palacas et al., 1972; McBride et al., 2004).

Sediment transport is of particular interest in the northeastern GoM due to concern regarding coastal erosion, which has been exacerbated with the landfall of recent hurricane/tropical cyclones. The long-term stability of the heavily developed Florida coast has been threatened by the storm-induced sand depletion of the beach/backshore. Hence an understanding of the wave transformation and sediment transport associated with different meteorological and oceanographic (metocean) conditions along the inner shelf of this coast could be important when deciding mitigation strategies. Limited information on sediment transport

processes and the impact of storms on the continental shelf exists for the northeastern GoM, however, with most studies having been conducted along the Louisiana-Texas coast (Snedden et al., 1988; Guidroz et al., 2007; Dellapenna et al., 2008).

Sedimentology and bottom stratigraphy are critical to any study of shelf sediment transport and the GoM sedimentation patterns are very complex. Most geological studies in the GoM have focused on the Mississippi Delta and offshore Louisiana, the northwestern GoM, and the Apalachicola Delta, in Florida (see Fisk et al., 1954; Schnable and Goodell, 1968; Kindinger, 1988; Donoghue, 1992; Sydow and Roberts, 1994; Roberts, 1997; Anderson and Bart, 1999; Rodriguez et al., 1999; Flocks et al., 2006). Research and detailed geology of the northeastern GoM are comparatively scarcer and less documented, particularly off the central Florida Panhandle. Most research has focused on the coastal bays (Palacas, 1968; Isphording and Isphording, 1991; Bentley et al., 2000), sand sheet sediments (Doyle and Sparks, 1980; McBride et al., 2004), or the Apalachicola Delta and embayment (Schnable and Goodell, 1968; Donoghue, 1992; Anderson and Bart, 1999; McKeown et al., 2004). Recent data suggests that the offshore region is considerably complex, and that the sand sheet sediments are of economic importance for beach restoration. Therefore, a study of the bottom stratigraphy and geological history of this area is important to the scientific community, as well as for developing viable beach nourishment projects for the adjacent coast. The tectonic stability of the region coupled with limited input of riverine sediment in the modern system in the northeastern GoM, create an excellent natural laboratory for the study of longer term phenomena, such as sea level changes, and shorter term events, such as the impact of storms. Few studies have linked the geology of the region, in terms of stratigraphy, geomorphology, and sedimentology, to the physical processes that force

sediment transport and erosion, especially during major storm events. Therefore, the scientific, industrial, economic, and political communities drive the motivation behind this research.

1.2 Statement of Research Problem, Hypothesis and Objectives

It is proposed as a hypothesis for this thesis research that the frequent storminess encountered in the GoM has a significant impact on the redistribution of bottom sediments on the inner shelf. The geologic record of the inner shelf may or may not reflect this impact given a number of factors, specifically the rate of sea level rise, the nature of offshore sediments and stratigraphic relationships, the frequency and intensity of storms, their ability to generate wave heights large enough to initiate and suspend sediments, and the nature of currents carrying sediments in suspension.

As previously stated, this study involves two components: the first is a study of sediment transport trends modeled during two hurricane case studies that entered the northeastern GoM. The second is the geological history of the late Quaternary sediments and stratigraphy on the inner shelf. Recent data from offshore Choctawhatchee Bay, Florida, in the northeastern GoM (Fig. 1.1), indicates that the sedimentology and stratigraphy of this region does not conform to all characteristics and properties of a normal marine transgression. It is proposed that the decrease in rate of sea level rise in the past 3,000-5,000 yrs (Coleman and Smith, 1964; Tornqvist et al., 2004) has allowed modern hydrodynamics and sedimentation processes to reconfigure and control the sedimentation and stratigraphy of the shelf; hence the stratigraphy of this region is a product of both sea level rise and marine transgression, as well as modern hydrodynamic processes of a storm dominated coast. This study addresses these factors, both geologic and hydrodynamic, which control the stratigraphy and sedimentation during the late Quaternary.

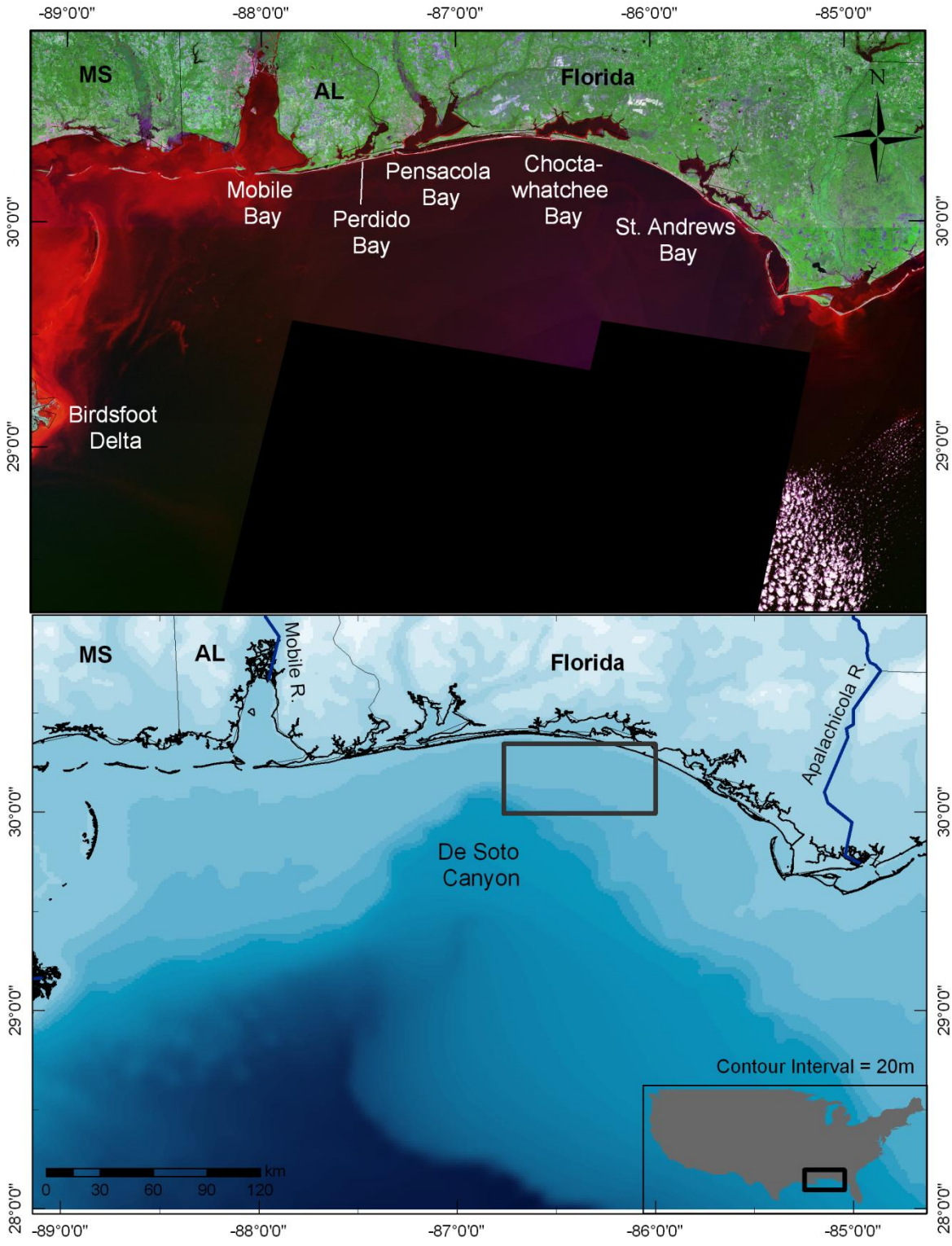

Figure 1.1. Location of the study area in the northeastern GoM: top, satellite image with coastal features annotated; bottom, digital elevation model with major rivers and submarine features annotated. The dark gray box indicates the approximate extent of the proposed study area. Satellite imagery from www.zulu.gov; coastal bathymetry from Arnante (2009).

Figure 1.2. Coasts of the Florida Panhandle. Top photos, development (left) and tourism. Bottom left photo, destroyed road on Santa Rosa Island due to Tropical Storm Arlene. Bottom right photo, beach restoration after Hurricane Ivan. Bottom two photos courtesy of B. Liu.

Incorporating these two elements, this research seeks to answer the following questions regarding sediment dynamics on the inner shelf and in the sediment record:

1. To what extent do major storms play a role on the sedimentology of the inner shelf?
2. Can storm signatures (i.e. deposits, trends, sediment patterns, both spatial and temporal) be observed in surface and near-surface sedimentology?
3. What is the nature of sediment transport during storm events on the inner shelf offshore of the Florida Panhandle?

Specific objectives of this study will address the following:

1. Hydrodynamics during large storms, specifically during tropical storms and hurricanes,
2. The effect the wave and current regimes on shelf sediments during storms,
3. Sediment dispersal pathways,
4. Depositional environments and evolution during the late Quaternary,
5. Patterns of erosion and deposition on the shelf, and
6. A conceptual model for shelf development during a storm-dominated highstand.

1.3 Study Area and Present-Day System

According to the definition by Wright (1995), the inner shelf describes the region immediately seaward of the surf zone where waves frequently agitate the seabed. The inner shelf generally ranges in depth from 5 to 30 m of water and extends approximately 10 km offshore. The GoM is a passive margin and an isolated sea (Bryant et al., 1991). The GoM shelves and their modern morphology have been primarily controlled by sea level fluctuations during the Pleistocene (Coleman et al., 1986). The northeastern GoM in particular, is experiencing a somewhat stable highstand, and is very similar to the Atlantic eastern U.S. Coast, especially in terms of sediment deficiency (Wright, 1995). It is considered an autochthonous shelf, as much of its sediments are derived from reworking of older sediment, as opposed to sediments being actively deposited from riverine input.

The study area for this thesis is the inner continental shelf off Choctawhatchee Bay, Florida, on the central Florida Panhandle in the northeastern GoM (Fig. 1.1). The study area encompasses the nearshore and inner to mid shelf area from approximately the 10 m isobath down to the 30 m isobath, just beyond the flanks of a large submerged shoal on the inner shelf. The area is encompassed by the coordinates 86°W to 87°W longitude and 30°N to 30.5°N

latitude. Cape San Blas and the Apalachicola Embayment (Apalachicola) are to the east of the study area, while to the west, offshore, is the head of the De Soto Canyon and farther west, the bird's foot delta of the Mississippi River. The beach/onshore region of the proposed study area is characterized by Pleistocene headlands (Grayton Beach), white quartz sand beaches (Mirimar Beach, Fort Walton Beach) and a barrier island (Santa Rosa Island) (Fig. 1.2). Large bays characterize the coast of the northeastern GoM, including St. Andrews Bay, Choctawhatchee Bay (landward of the study area), Pensacola Bay, Perdido Bay, and Mobile Bay (Fig. 1.1). At the mouth of Choctawhatchee Bay, sediment from the bay is forming an ebb tide delta.

Several rivers flow into the northeastern GoM but are predominately third and fourth order rivers (Winker, 1991) compared to the rest of the GoM. The Mobile River to the west and the Apalachicola to the east, bound the northeastern GoM region with larger, secondary rivers. Very little sediment is transported to the Gulf via these rivers. The majority is retained in the bays along the coast (Boone, 1973). The Choctawhatchee River is the major river flowing into Choctawhatchee Bay (Fig. 1.1). The region experiences a humid climate, with prevailing winds from the southeast during most of the year. These winds are the controlling factor on general wave direction (southeast to northwest) and longshore transport (east to west) (Fig. 1.1). The region is micro-tidal (H_0 = <0.75 m) with deviations of more than 0.6 m (2 ft), primarily due to wind setup (Stone, 1991). The coast is moderate to low-energy during fair-weather conditions (Tanner, 1960). The northeastern GoM is also storm-dominated, due to the inundation of frequent cold front storms, tropical storms, and hurricanes (Stone, 1991; Muller and Stone, 2001).

Only recently has the transport of sediment between the coastal zone and the inner shelf been examined along this region, with most of the focus placed on the coastal region and barriers

(Stone et al., 2007). Net transport in the area is westward, dominated by longshore transport, from eroding headlands of Pleistocene bluffs along Grayton Beach, thereby providing nourishment for Santa Rosa Island (Stone et al., 1992; Stone and Stapor, 1996). A cell of longshore transport has been delineated in the study area that begins just east of Choctawhatchee Bay and ends at the western terminus of Santa Rosa Island. A (small) southern transport component also transports some sediments offshore to the inner shelf (Stone and Stapor, 1996). However, some onshore transport of sediment during the Late Holocene has been recognized (Stone and Stapor, 1996). Sediment sources in this area include erosion from the Pleistocene headlands on Grayton Beach and Mirimar Beach, cannibalism of Santa Rosa Island, particularly on Pensacola Beach, and resuspension on the inner shelf (Stone, 1991).

1.4 Factors Controlling Continental Shelf Geology

Continental shelf geology is controlled by a number of factors, including geological, physical, and biological influences. The inner shelf is particularly sensitive to these processes. Continental shelves are considered geologically ephemeral features in that they do not exist during glacial lowstands or long periods of highstand where shorelines prograde to the shelf break (Nittrouer and Wright, 1994). Therefore sea level change, eustasy, hydro-isostasy, and glacial isostasy are all key geologic processes that affect continental shelves. Tectonism, passive versus active margin, subsidence, uplift, growth faults, and basement subsidence are structural factors that can affect the geology of shelves as well. The shelf geometry plays a role as well, and can isolate a shallow sea (epicontinental) or open it to the deep ocean (pericontinental). The width, depth, steepness, and landward and seaward boundaries (i.e. coast and shelf break) all play a key role in the geology of the shelf. Riverine input, sedimentation, source regions and

composition, compaction rates, carbonate production, progradation of river deltas play a role in the geology, as does particle shape, size, and composition of material that is deposited.

Other factors that are important in shaping the geology of shelves are physical in nature, particularly where and when they influence the bottom boundary layer. The inner shelf is friction dominated, where the surface and bottom boundary layers overlap (Wright, 1995). The wave climate and regime, that is the orbital asymmetry of the waves, wave heights, wave directions, are important to influencing the shelf through sediment suspension and transport. Currents and geostrophic flow, internal waves, infragravity waves, buoyant plumes, and upwelling and downwelling regimes are also important for sediment transport (Nittrouer and Wright, 1994). Storms, weather and climate affect these physical oceanic processes, which in turn influences the shelf. The frequency of such events causing erosion, transport, and deposition, and the depth of the mixing and erosion also affect shelf stratification.

Other influences are biological and anthropogenic. Biological mixing occurs as organisms burrow seafloor sediments. Many storm layers are often obliterated, or at least highly modified, in the geologic record due to bioturbation. However organisms can contribute to the sedimentation of the seafloor, adding organic oozes or carbonate skeletons. In recent decades, humans have significantly impacted the shelf, by activities such as dredging sediments for beach restoration or the construction of drilling platforms and pipelines and removal of sub-bottom fluids.

1.5 Conceptual Framework

Based on the discussion above, it is, therefore, important to evaluate modern sediment transport trends and potential on the inner shelf during storms, which is the topic of Chapter 2 in thesis. In this chapter, modeled wave heights and calculated sheer stresses on the inner shelf are

interpreted as an indicator of the ability of storm waves to re-suspend sediments. Satellite imagery is compared with model results to qualitatively assess the transport direction of the sediment that is in resuspension. This chapter initiates this thesis research by examining the wave climate, flow direction, and potential for resuspension during and after tropical cyclones.

It is also necessary to understand the sub-bottom stratigraphy that has evolved since the last glacial lowstand, to properly assess any possible storm signature. In Chapter 3, a discussion and in-depth analysis and interpretation of the geological record of the late Quaternary are provided. Results from vibracores, seismic data, grain size analysis and radiocarbon dates are used to interpret the depositional environment and history of sedimentation off Choctawhatchee Bay, and used to ground truth the models applied in Chapter 2. The chapter concludes by integrating these interpretations with the results of other stratigraphic and sedimentological studies in this region.

Chapter 4 presents a synthesis of the results and evaluation of the initial research question. A conceptual model is proposed that describes shelf development as a function of storm forcing. Recommendations for future research are presented based on this study and those of others. The fifth chapter summarizes the major conclusions of this research.

CHAPTER 2. NUMERICAL MODELING OF TROPICAL CYCLONE HYDRODYNAMICS AND SEDIMENT

2.1 Introduction

The recent increase in the frequency and strength of tropical cyclones along the northeastern GoM has raised considerable concern and interest in monitoring the storm-induced sediment transport, erosion and deposition of material in the northern Gulf (Isphording and Imsand, 1991; Davis, 1997; Keen et al., 2004; Hapke and Christiano, 2007; Byrnes et al., 2008; Dellapenna et al., 2008; Department of Environmental Protection, 2008). Landfall of frequent and often destructive storms coupled with the substantial increase in coastal development and tourism along the Florida Panhandle, have provoked an increasing interest in issues involving sediment resuspension and transport both onshore and off, due to the interest in sand mining from offshore shoals for replenishing severely eroding beaches. It is therefore necessary to understand the hydrodynamics associated with these high energy events and their effects on shelf sediments.

The northeastern GoM is micro-tidal (<2 m tidal range), however, a moderate-energy wind and wave environment exists during fair-weather conditions (Tanner, 1960). Cold fronts from the northwest, frequent the area at a rate of approximately 30 – 40 per year, generally occurring from October to March or early April (Moeller et al., 1993). Tropical cyclones (hurricanes and tropical storms) frequent the region as well (Muller and Stone, 2001) creating a storm-dominated coast, particularly during the winter and late summer seasons.

2.1.1 Tropical Cyclone History

Return periods of tropical cyclones in the northern GoM are among the highest in the Gulf and Atlantic coasts combined (Muller and Stone, 2001). In addition, recent studies have

shown an increase in storm intensity and frequency in the past decade. Return rates for tropical cyclones are estimated to be once every three years, while return rates for catastrophic hurricanes (category three or higher on the Saffir-Simpson Hurricane Scale) are once every 35 years along the western Florida Panhandle (Keim et al., 2007). Figure 2.1 illustrates the return rate of tropical storms, hurricanes and catastrophic hurricanes (category 3 or higher on the Saffir-Simpson hurricane classification scale).

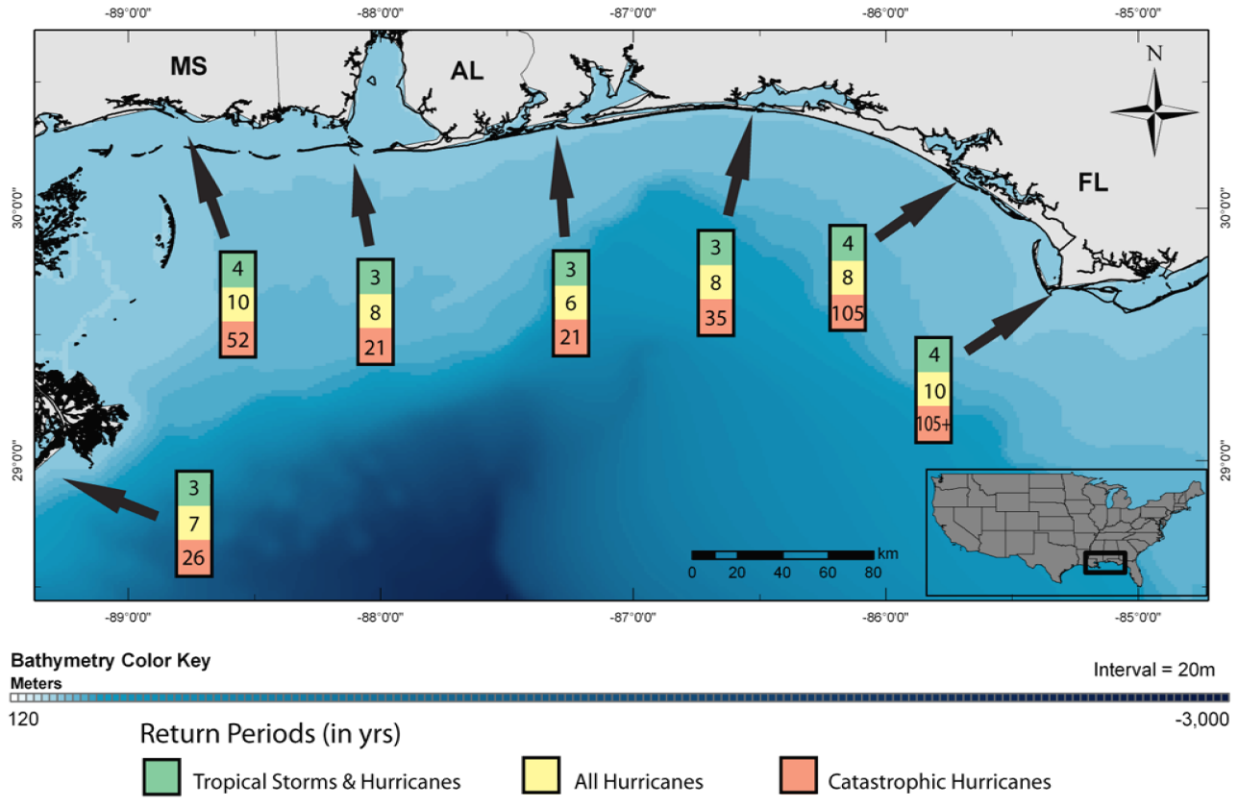

Figure 2.1. Average return periods (in years) for tropical storms and hurricanes, tropical hurricanes (category 1-5) and catastrophic hurricanes (category 3-5) of the northeastern GoM. Locations for averages from west to east: Boothville, LA; Gulfport, MS; Dauphin Island, AL; Pensacola Beach, FL; Destin, FL; Panama City Beach, FL; Apalachicola, FL. Modified from Keim, et al. (2007); bathymetry from Divins and Metzger (2008).

In the past decade alone, ten storms have impacted the northeastern GoM, from Mississippi to Apalachicola, FL. Three of these storms were category 3 or higher: Ivan (2004), Dennis (2005) and Katrina (2005). Other major storms to have impacted the region include

Florence (1953), Camille (1969), Eloise (1975), Frederic (1979), Elena (1985), and Opal (1995) (NOAA Coastal Services Center). For this study, two recent major hurricanes have been chosen that made landfall on the northeastern Gulf coast very near to the area of interest (Fig. 2.2): hurricanes Ivan and Dennis. These hurricanes were chosen as case studies for understanding the effect of storms on the shelf due to their intensity, proximity to the study area, and availability of data. Both hurricanes were category three at landfall; however they differed greatly in size, extent, and history.

Hurricane Ivan was a classic long-lived hurricane that originated off the west coast of Africa on 31 August 2004. Before making landfall on the northern Gulf Coast, Hurricane Ivan reached category 5 status three times, making it the only category 5 hurricane of the 2004 Atlantic hurricane season. It made landfall at approximately 06:50 UTC on 16 September 2004 just west of Gulf Shores, Alabama as a large category 3 hurricane, approximately 100 km from western Florida (Fig. 2.2). At this point, the eye diameter of the hurricane was approximate 74 – 93 km (40 – 50 n mi), resulting in the strongest winds occurring over western the Florida Panhandle and Alabama border. The storm surge recorded was highest along the coast, from Destin, Florida to Mobile Bay/Baldwin County, Alabama, ranging from 3.0 – 4.6 m (10 – 15 ft). Ivan was unique and memorable in that upon landfall, the hurricane continued northeast becoming extra-tropical in the northern Atlantic, made a clockwise circle and came back through the GoM again as a tropical storm, making final landfall on the western Louisiana coast (Fig. 2.2) (Stewart, 2004).

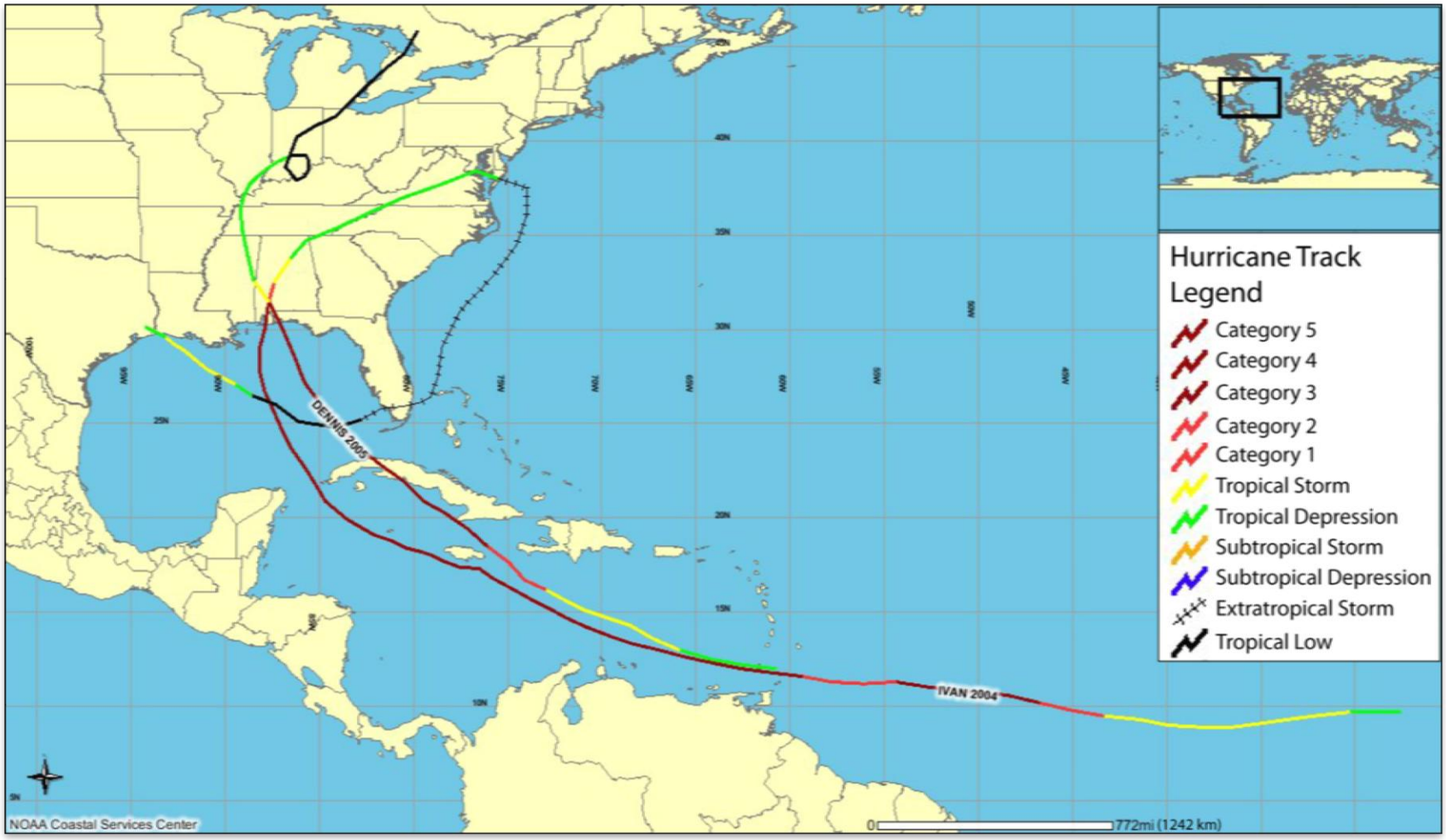

Figure 2. 2. Track positions and intensities of hurricanes Ivan and Dennis through the Atlantic Basin and GOM. Created with NOAA Coastal Services Center query storm tracks feature (http://csc-s-maps-q.csc.noaa.gov/hurricanes/index.jsp).

Hurricane Dennis was an unusually strong summer hurricane that originated off the west coast of Africa on 29 June 2005. It reached category 4 status twice, and crossed Cuba and the GoM, but dropped to a category 3 status just prior to landfall at approximately 19:30 UTC 10 July 2005. Landfall occurred within the study area, on Santa Rosa Island, Florida, between Navarre Beach and Gulf Breeze (Fig. 2.2). Post-landfall, Dennis weakened rapidly as it moved north-northwest. Dennis was a much smaller storm in size than Ivan, with hurricane-force winds extending over only a small portion of the western Florida Panhandle; however tropical storm force winds extended over most of the northeastern GoM (Fig. 2.3). The highest storm surges were recorded around Apalachicola, Florida, on the order of 1.8 to 2.7 m (6-9 ft) (Beven, 2005).

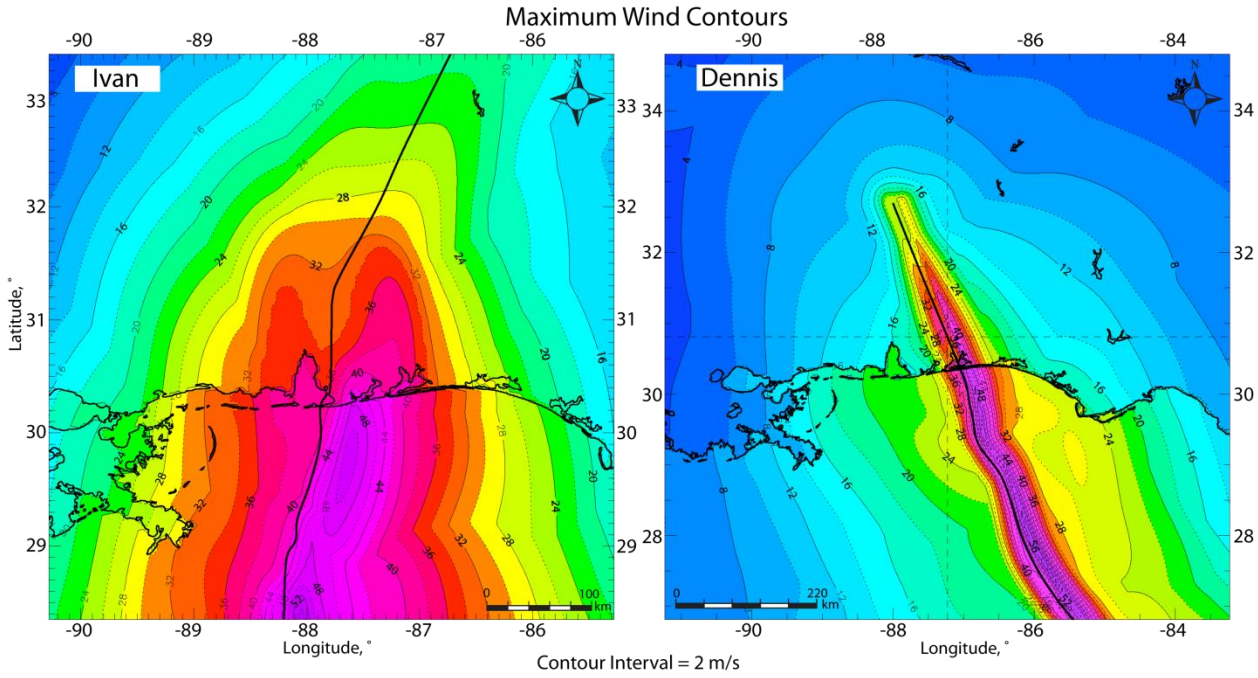

Figure 2.3. Wind fields for hurricanes Ivan (left) and Dennis (right). Contours (lines and colors) represent maximum wind speed in m/s and have an interval of 2 m/s. Data from AOML (http://www.aoml.noaa.gov/hrd/data_sub/wind.html).

Hurricane Cindy made landfall as a tropical storm near the study area within a few weeks of Hurricane Dennis at 09:00 UTC 6 July 2005 (Stewart, 2006). Cindy made landfall southwest of Waveland, Mississippi, to the west, over 150 km from the Florida Panhandle. Because of the

significantly weaker wind and wave fields during tropical storms, the initial purpose of this study was not to analyze tropical storm hydrodynamics. However, given the convenience of this tropical storm making landfall in the northeastern GoM, close to the landfall of a hurricane chosen for the case study, the wave model for Dennis was extended to compute the wave climate during landfall of Cindy. Therefore, a limited discussion will be given to a third case study as well, that of tropical storms.

2.1.2 Erosion and Deposition due to Storm Impacts

It is well established that barrier islands and beaches suffer greatly from erosion during storms (Stone et al., 1985; Basillie, 1987; Davis, 1997; Keen and Stone, 2000; Stone et al., 2004). In particular, barrier island breaching and overwash plays an important role in the redistribution of sediments during storms (Stone et al., 2004). Stone et al. (2007) found that eroded material from barrier island beaches is deposited in the lagoon or the bay behind the barrier. They discussed barrier overwash as a mechanism for retaining barrier island volume, and for post-Hurricane Ivan, 90 % of Santa Rosa Island sediments in Florida could be accounted for in a study of beach profiles pre- and post- storm. Although a considerable amount of sediment was lost in the overwash platform and dune, this material was found to be redeposited on the bay beach and nearshore behind the island, where an increase in sediment volume was observed. The study also concluded that smaller storms such as cold fronts generate high frequency steep waves that erode material from the subaerial portion of the barrier, especially along the bay side, thereby transporting it back on the island. Other studies support this idea of barrier island overwash and sedimentation to the back-barrier lagoon or sound as well (Hayes, 1966; Bentley et al., 2000; Liu and Fearn, 2000; Bentley et al., 2002; Stone et al., 2004; Stone, 2006).

Some studies suggest that when barrier islands are breached, channels in the barriers allow for transport of sediment back to the nearshore and inner neritic zone during the return/ebb flow of storm surge (Hayes, 1966, 1967; Kahn and Roberts, 1982). It is also suggested that sand may be transported to the shelf from coastal sources (Curray, 1960; Mazzullo and Bates, 1985). Siringan and Anderson (1994) observed channels on the Texas shoreface but concluded that strong, along-shelf currents on the east Texas shelf prohibited the development of storm deposits on the open shelf. However, these currents may have been the mechanisms for transport of sand that formed storm beds on the central Texas coast (Siringan and Anderson, 1994). Many studies suggest that the dominant sediment transport during storms is offshore, with deposition on the inner shelf (Snedden et al., 1988; Nittrouer and Wright, 1994), however, disagreement lies in how far offshore sediment is transported, indicating material could be deposited on the inner to mid-shelf or worked off the shelf entirely, especially the fine-grained material.

Fine grained material is readily resuspended in the bays along the coast as well, and can be expunged into the open water during return flow of storm surge (Isphording and Imsand, 1991). Isphording and Isphording (1991) estimated that several million tons of sediment leave the bays with each event. In Apalachicola Bay, 80 million tons of sediment were removed after hurricanes Elena and Fredric, and in Mobile Bay, 290 million tons of sediment were removed and transported primarily offshore, due to these storms.

Extreme wave heights during hurricanes are large enough to resuspend sediment on at least the inner shelf, and possibly greater depths depending on the size and speed of the hurricane (Keen and Allen, 2000; Keen and Glenn, 2002; Teague et al., 2006; Dellapenna et al., 2008; Spaziani et al., 2009). Large enough waves, depending on the water depth, produce bottom shear stresses sufficient to resuspend sediment on the seabed while currents mix the sediment up into

the water column and transport it along and across the shelf (Wright, 1995; Wiberg, 2000). Along the Texas coast, pits and linear scour features have been observed offshore and at the toe of the beach after Hurricane Claudette (Dellapenna et al., 2008). Bottom scour was calculated for post-Hurricane Ivan, that resulted in seafloor modification off Mobile Bay, Alabama in 60 – 90 m water depth (Teague et al., 2006). The presence of megaripples on the inner shelf off Panama City, Florida suggest a regional isobath-following flow post-hurricanes (Fleischer et al., 1996).

The mechanisms for the formation and preservation of storm-related features and/or beds on the shelf are not well understood, especially in consideration of the previous studies of the direction of transport of material during and post storm. Wiberg (2000) states that it is very hard to preserve storm beds, unless storms are in concert with extreme flooding from rivers, such as the study from the Eel River, and low bioturbation ensues, similar to what one might see in low oxygen conditions. Stratification of vertical distribution of stresses in water column limit depth of which sediment can be resuspended to about 10 cm at depths of 50 m or greater indicating that little erosion would occur and little deposition of an event layer, unless sediment is being introduced from the coast or bays. Bioturbation of the top 10 cm would obliterate any sediment resuspended in a storm (Wiberg, 2000). However, Hayes (1966, 1967) postulates that in storm-dominated systems, the rock record may be comprised primarily of severe storm beds and reworked deposits, as smaller storm deposits and features are ephemeral.

While fair-weather transport dynamics have been well-documented for the study area (e.g. Stone and Stapor, 1996), the disagreement of these studies demonstrates that transport and deposition, and to some extent resuspension, is not well understood during high-energy storm events. The scientific question evolves when one study can account for erosion on the inner

shelf while other studies focus on "event layers". Many studies also only consider transported sediment from suspended sediment (i.e. Wiberg, 2000), however, bedload and sheet flow transport can have a significant impact on erosion and deposition (Li et al., 1997). This study investigates hurricane-induced sediment resuspension and transport using a third-generation spectral wave model, a coupled hydrodynamic and wave model, and satellite imagery, for hurricanes Ivan and Dennis' impact on the northeastern GoM. The purpose of this research is to gain a better understanding of the role of major storms and their associated hydrodynamic influence on resuspension, dispersion and deposition of sediments on the inner shelf. Specific objectives include 1) assessment of the wave climate on the inner shelf during tropical cyclones, 2) prediction of sediment resuspension potential due to waves, 3) evaluation of suspended sediments, both temporal and spatial on the shelf, and 4) identification of sediment dispersal pathways and sediment sinks during the approaching and post-landfall phases of tropical cyclones.

2.2 Methods

2.2.1 Satellite Imagery

Few studies have attempted to couple resuspension and satellite imagery (e.g. Stumpf and Pennock, 1989). A fine spatial resolution of the sensor and frequent revisit intervals of the satellite are important to capture short-term events such as sediment resuspension during and post storm phases. Terra and Aqua (launched in 1999 and 2002, respectively), both carry the Moderate-resolution Imaging Spectroradiometer (MODIS) instrument, and provide a revisit time of 1-2 times per day which is crucial for capturing effects of short-term phenomena, i.e. storms on the coast and shelf. Miller et al. (2005) provides an overview of the advantages of using MODIS imagery to examine suspended sediments. The spatial capacity of MODIS varies, but at

a resolution of 250 m, band 1, the red channel, and band 2, near infrared (NIR), provide the higher definition required to observe suspended material along the coast and inner shelf. A common method for the detection of suspended sediments in coastal waters is to relate reflectance of sediments in suspension in a vertical water column to the reflectance measured in the red portion (ca. 600-700 nm) of the visible spectrum (Stumpf and Pennock, 1989). In coastal and inland waters scattering from suspended sediments frequently dominates this reflectance spectrum, compared to pure water and phytoplankton absorption (Miller et al., 2005). Suspended sediments are easily observed by reflectance data due to their contrast with highly absorptive ocean water (Robinson, 2004). In general, approximately 90 percent of the signal is reflected back to the satellite at the first attenuation length (Reza, 2008). Shorter wavelengths (i.e. green and blue) penetrate deeper than those of red or infrared (Liu et al., 2003). Reza (2008) suggests that in clear water, the depth of reflectances could be up to 40 m for the shorter wavelengths, while longer ones may penetrate several meters or more. In the northeastern GoM, reflections of the seafloor bottom can be seen on clear, calm days (Walker, N., personal communication). However, both the presence of suspended sediments and increased turbidity will significantly lower the penetration depth of light and therefore reduce the first attenuation length significantly, restricting satellite observations of suspended sediments during high energy events, such as storms, to the surface waters only.

The MODIS images, both Aqua and Terra, when available, processed to Level 1b (Rayleigh scattering correction applied) were downloaded from the NASA Earth Observing System (EOS) via the Earth Scan Laboratory at Louisiana State University (LSU). Five, nearly cloud-free and sun glint-free images were chosen for Ivan (Appendix A). For Dennis, two images were chosen, 11 July 2005 at 18:32 UTC and 12 July 2005 at 19:17 UTC, but were of

much lesser quality. All images and band widths, with time and date of satellite pass are located in Appendix A. The geo-positional accuracy of each image was assessed by overlaying a coastal vector onto each image and adjusting the coordinates manually, where needed. An atmospheric correction to reduce scattering from aerosols was applied to the red channel images using the clear water pixel assumption. Briefly, the reflectance of clear water should be zero, or near zero in the NIR channel due to negligible values of water-leaving radiance and any reflectance in clear water (black in NIR) is due to aerosol scattering, referred to as the black pixel assumption (Siegel et al., 2000). Using this theory, the lowest value of reflectance (from deeper water) was obtained from NIR images from each day and subtracted from the entire corresponding red channel image. Reflectance values were then extracted in a 250 m resolution grid over the study area. Data were later eliminated over land and along the coast to reduce noise from high reflectance values over land. The red, blue and green channels were also combined using the program TVIS, in the Earth Scan Laboratory at LSU, to create a true color image for each day. True color images can reveal significant indications of suspended material during or after storms (Stone et al., 2005), as well as providing a time series of imagery and suspension events. These images were crucial in choosing the time range over which the models were run. Images during tropical storms and cold fronts were examined, but not chosen due to the lack of noticeable material in suspension on the shelf.

In addition to MODIS images, three SeaWiFS (Sea-viewing Wide Field-of-view Sensor, 1 km resolution) level 2 images were also obtained from Dr. Eurico D'Sa at LSU, to analyze specific concentrations of suspended particulate matter. Because SeaWiFS has a spatial resolution of 1 km, MODIS images are more useful in determining coastal changes over a small area. However, a MODIS algorithm was not available for conversion of the material in the

image to volumetric concentrations, thus SeaWiFS imagery was used to attempt to quantify the amount of sediment in suspension. A land and cloud mask was applied to these images from wavelengths dominated by inorganic material. A simple algorithm (D'Sa et al., 2007) was used to map reflectance in mg/l from the 670 nm and 555 nm wavelengths.

2.2.2 Wave Model

The spectral wave (SW) model, MIKE 21, was utilized to examine the wave fields on the inner shelf during hurricanes Ivan and Dennis. The commercially available model was developed by DHI^{TM} Water and Environment based on flexible mesh. Details on the model physics and parameterization can be obtained from Sorensen et al. (2004). The MIKE 21 SW model has been successfully implemented for the GoM and Louisiana coast (Jose et al., 2007). In particular, Kobashi (2009) and Kobashi et al. (2009)used this model to examine wave heights during fair-weather, cold front storms and hurricanes over Ship Shoal in southwestern Louisiana to assess the impact for sand removal. Freeman (2010) applied modeling techniques using the computed wave heights and simulated flow from MIKE 21/3 coupled hydrodynamic model (also used in this research) to evaluate change to a coastal lake bed in southern Louisiana. Finkle et al. (2005) used MIKE 21 to assess the wave transformation over the continental shelf off southeast Florida and evaluate submarine geomorphic changes.

Several variables (input) were used for the model, including wind speed, bathymetry (water depth), wave boundary conditions, and sediment size (for bottom friction). The majority of waves are generated by stress induced from wind blowing over the water. Therefore, wind velocity is one of the most important variables to the wave model. Wind velocity was derived from re-analyzed surface wind data from NOAA's Atlantic Oceanographic and Meteorological Laboratory (AOML, 2006) (Fig. 2.3). The surface wind analysis is based on measurements

made in-flight (hurricane hunters), as well as input from any available surface weather observations, such as buoys, coastal platforms, and satellite data. The high resolution (~6 km) AOML data set was blended with NOAA's North American Regional Reanalysis (NARR, 2007) data set (~32 km resolution) to develop the gridded input wind data.

Hurricane-induced wave fields for the entire GoM, during hurricanes Ivan and Dennis were generated using this module of MIKE 21 (Fig. 2.4). Wave boundary conditions for a high resolution coastal grid were extracted from the regional model for the study area, to account for long period waves, according to the method established by Jensen, et al. (2007). The reduction in size of the model area allowed for greater enhancement of the mesh grid (Fig. 2.4). The grid contained 7,162 nodes and 14,023 triangular elements. The resolution in the coastal model ranged from 0.5 km along the shore and inner shelf to 4.5 km along the mid to outer shelf. Bathymetry was obtained from NOAA's National Geophysical Data Center (Divins and Metzger, 2008). Figure 2.5 presents sediment size distribution used as input for the model. Bottom friction was based on mean grain size of sediment that was compiled from core tops of vibracores samples processed at the Coastal Studies Institute at LSU (see Chapter 3, section 3.2 and Appendix G) and integrated with sediment data downloaded from usSEABED (Reid et al., 2006). Careful examination of these data led to the removal of a value of 0.02 m offshore of Panama City, FL, for sediment input and subsequent calculations with mean grain diameter (D) as a variable. The model data were validated with in-field measured data downloaded from five National Data Buoy Center (NDBC, 2008) buoys (Fig. 2.6, for locations).

2.2.3 Resuspension Calculations

To assess how wave conditions can affect the bottom and initiate sediment movement, a series of calculations were implemented. The first step was to calculate bottom boundary layer

parameters for non-cohesive sediments (i.e. sand). Bottom shear velocity (u_{*W}) and shear stress (τ_W) due to waves were estimated using linear wave theory from Madsen (1976):

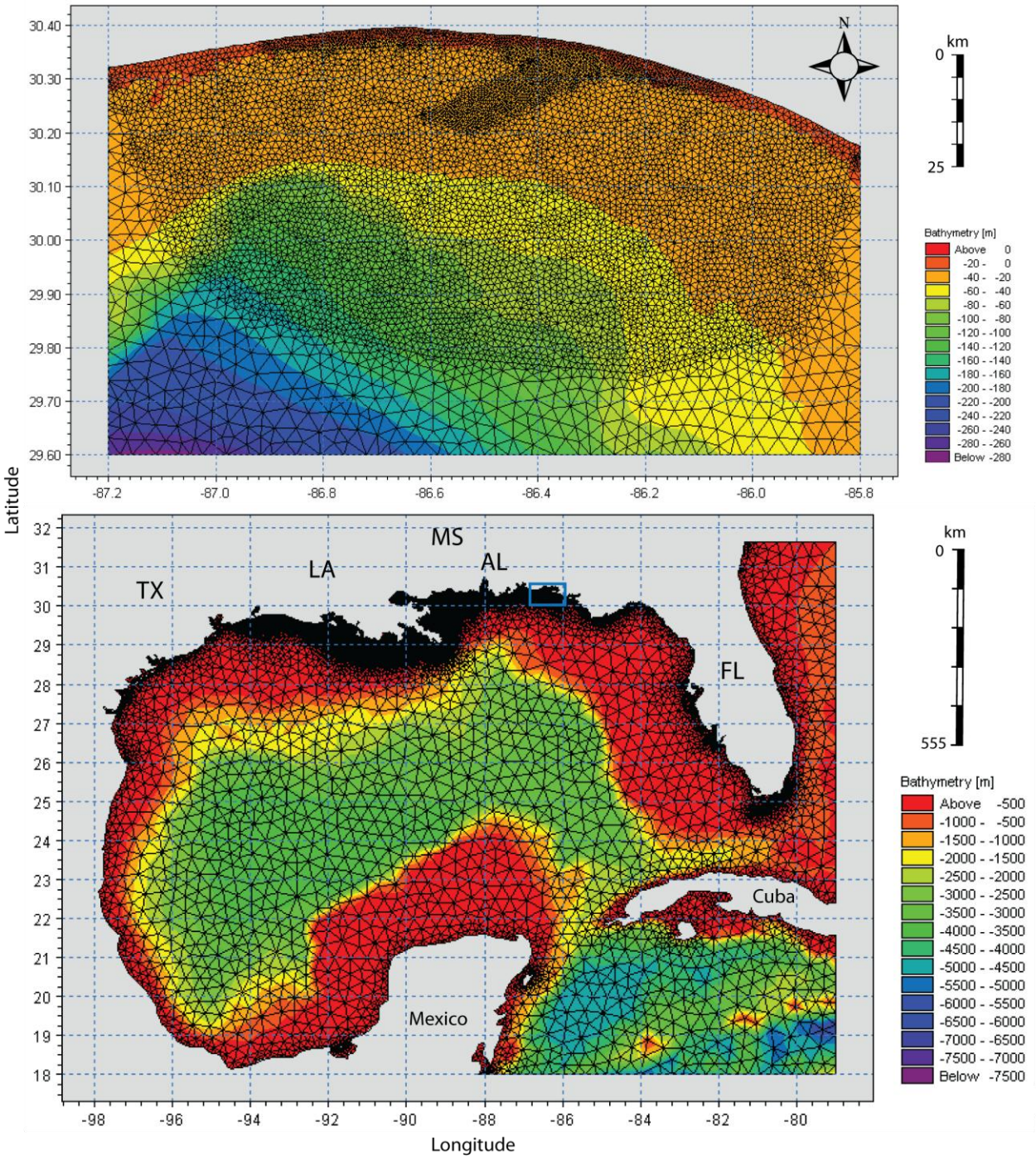

Figure 2.4. Local computational mesh grid and elements used for wave simulations. Top, nested coastal model mesh and bathymetry; bottom, regional GoM model mesh and bathymetry for boundary conditions (modified from Jose, et al., 2007). The blue square in the bottom map indicates the extent of the top map and the subsequent figures from model output.

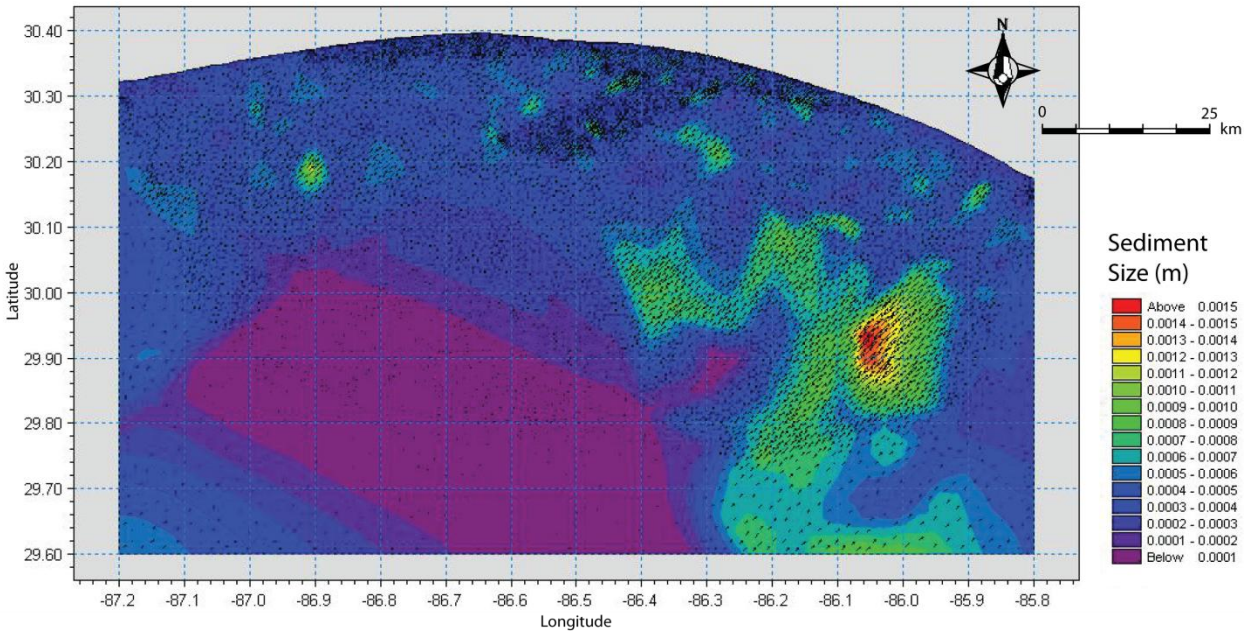

Figure 2.5. Sediment sample distribution used for bottom friction input for the wave model, compiled from grain size analysis (this study, Chapter 3), and usSEABED data. High density data near the coast and on the inner shelf indicates locations of samples taken for this study.

$$u_{*w} = \sqrt{\frac{\tau_w}{\rho_f}} \tag{1}$$

where H_S is significant wave height in m (from wave model). Linear wave theory was used over higher orders because the area of interest was primarily deep water during fair weather conditions. The wave number (k) for equations 1 and 2 was estimated by the dispersion relation:

$$\left(\frac{2\pi}{T_P}\right)^2 = gk\tanh(kh) \tag{4}$$

where g is gravitational acceleration (9.8 m/s^2).

From these calculations, an index of the potential for resuspension was developed by a simple subtraction, hereafter referred to as the resuspension intensity or RI (Pepper et al., 1999; Kobashi et al., 2007; Kobashi, 2009). Since the sediment entrainment threshold occurs at the

critical shear stress and velocity, dependent primarily on grain size (Woodroffe, 2003), the potential for resuspension of sediment can be estimated by subtracting the critical shear stress (τ_{cr}) from the calculated wave shear stress from equation 2:

$$RI = \tau_W - \tau_{cr} \quad (5)$$

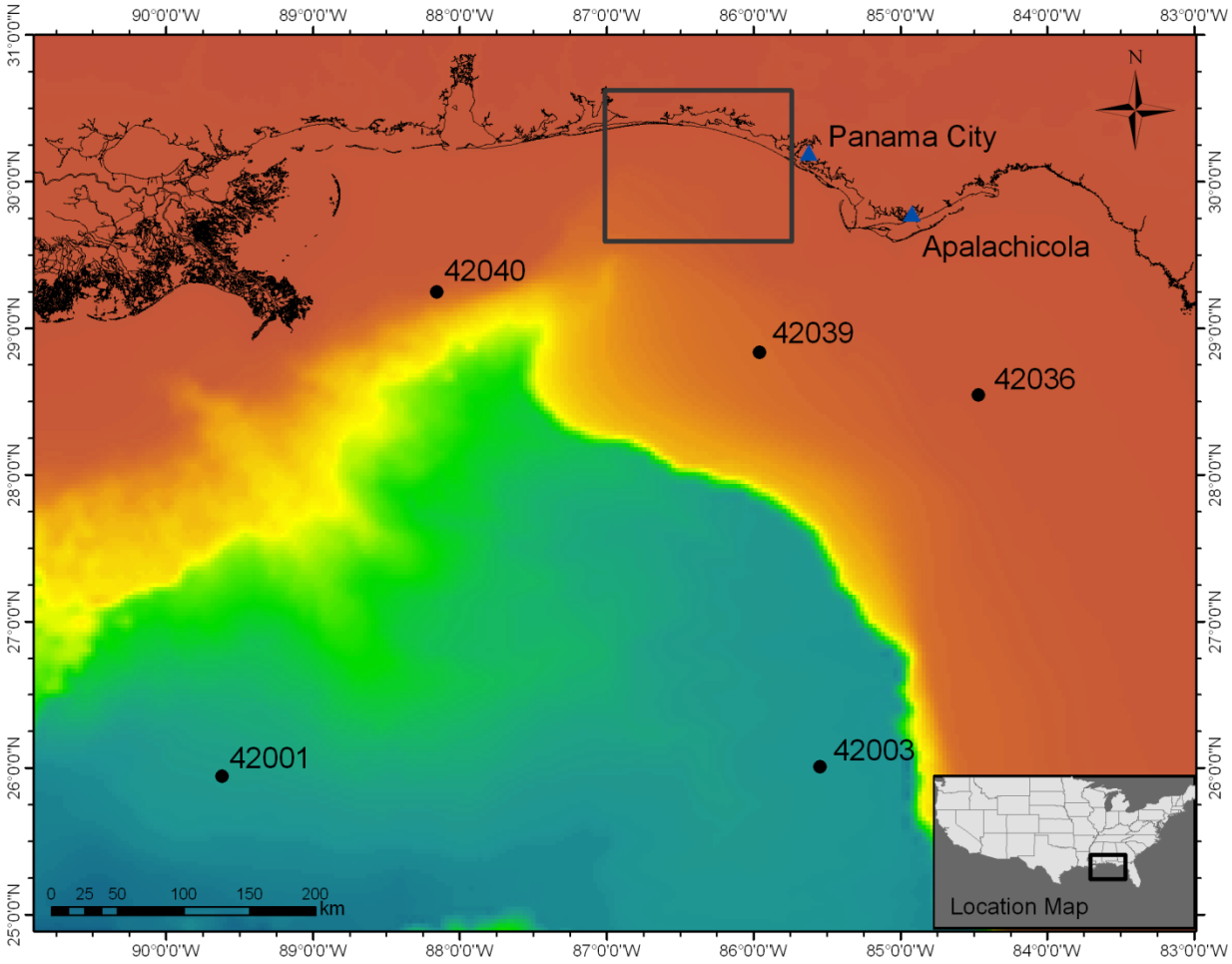

Figure 2.6. NDBC buoy locations and tidal gauges used for the validation of wave model (NDBC buoys, black circles) and hydrodynamic model (NOAA tide gauge stations, blue triangles). Study area highlighted by dark gray box. Bathymetry data from Arnante and Eakins (2009).

The critical shear stress was estimated based on a modified Yalin's parameter ($\sqrt{\Xi}$), derived in Miller et al. (1977) and Li et al. (1997). The advantage of the Yalin parameter (Yalin,

1977), as opposed to Shield's threshold curve, is that it can be calculated from known fluid and grain parameters, and threshold θ_{cr} can be determined directly:

$$\sqrt{\Xi} = \left[\frac{\rho_s - \rho_f \quad gD^3}{\rho_f \nu^2} \right]^{0.5} \tag{6}$$

where ρ_s is the sediment density (2650 kg/m^3 for quartz sand) and D is the sediment diameter (m). Using the method illustrated by Li et al. (1997), the following equations were used based on Yalin's parameter for sediment grain sizes in the study area:

$$\log \theta_{cr} = 0.04(\log \sqrt{\Xi})^2 - 0.356 \log \sqrt{\Xi} - 0.977 \quad \sqrt{\Xi} < 100 \tag{7a}$$

$$\log \theta_{cr} = 0.132 \log \sqrt{\Xi} - 1.804 \quad 100 < \sqrt{\Xi} < 3000 \tag{7b}$$

The parameter $\log\theta_{cr}$ represents Shields' threshold criterion. These equations were derived from a graphical comparison of Shields' threshold criterion versus Yalin's parameter in Miller (1977). This curve was replicated with the data from this study, using both equations, 7a and 7b, from Li et al. (1997), and then using only equation 7a (Fig. 2.7). The curve for this study was smoother and better replicated that of Miller's if equation 7b was not used. Careful examination of the data in Miller's plot showed a lack of data points where the Yalin parameter was between 100 and 120, perhaps suggesting the curve derived by Li et al. (1997) was slighly low. In addition, only 20 percent of samples from the study area fell under the qualifications for equation 7b (where the Yalin parameter was between 100 and 120 for mean grain sizes in the study area), which could also justify excluding this equation.

2.2.4 Coupled Hydrodynamic Model, MIKE 21/3 FM

To simulate three dimensional currents and flow patterns on the shelf, a coupled wave and hydrodynamic model was implemented for Hurricane Ivan, MIKE 21/3 FM (flexible mesh),

since sediment transport is mainly determined by wave conditions and associated with wave-induced currents (Nielsen, 1992). This was run separately from the previous wave model so that the wave model could be run on a smaller scale (see Fig. 2.4). This approach uses the MIKE 21 SW wave model coupled with a three dimensional flow model, MIKE 3 flow model. Like the wave model, the approach for the hydrodynamic flow model is based on an unstructured flexible mesh in the horizontal plane, but the vertical domain utilizes structured mesh in the 3D model. Setup and parameterization of the model followed instructions outlined by DHI (2007) and Jensen et al. (2007). The model equations are based on numerical solution of the three dimensional incompressible Reynolds averaged Navier-Stokes equations subject to the assumptions of Boussinesq and hydrostatic pressure and are explained in greater detail by DHI (2006).

Input for the wave model was identical to that of the initial run. However, for the coupled model, the domain was extended to incorporate a larger region of the northeastern GoM, so that validation could be made using sea surface heights from tidal gauges at Panama City and Apalachicola (Fig. 2.6). Accommodating the entire shelf and deeper water also allows for better interpretation of currents at greater depths for the simulation. Higher resolution bathymetry (15 seconds) was incorporated along the coast and shelf of Choctawhatchee Bay, FL, while one minute resolution was used further offshore. A new mesh grid was created to accommodate the larger domain. The new mesh contained 13,714 nodes and 27,234 elements, with a resolution of 0.9 to 2.0 km over the entire shelf, and 5.0 to 6.5 km over deep water (Fig. 2.8).

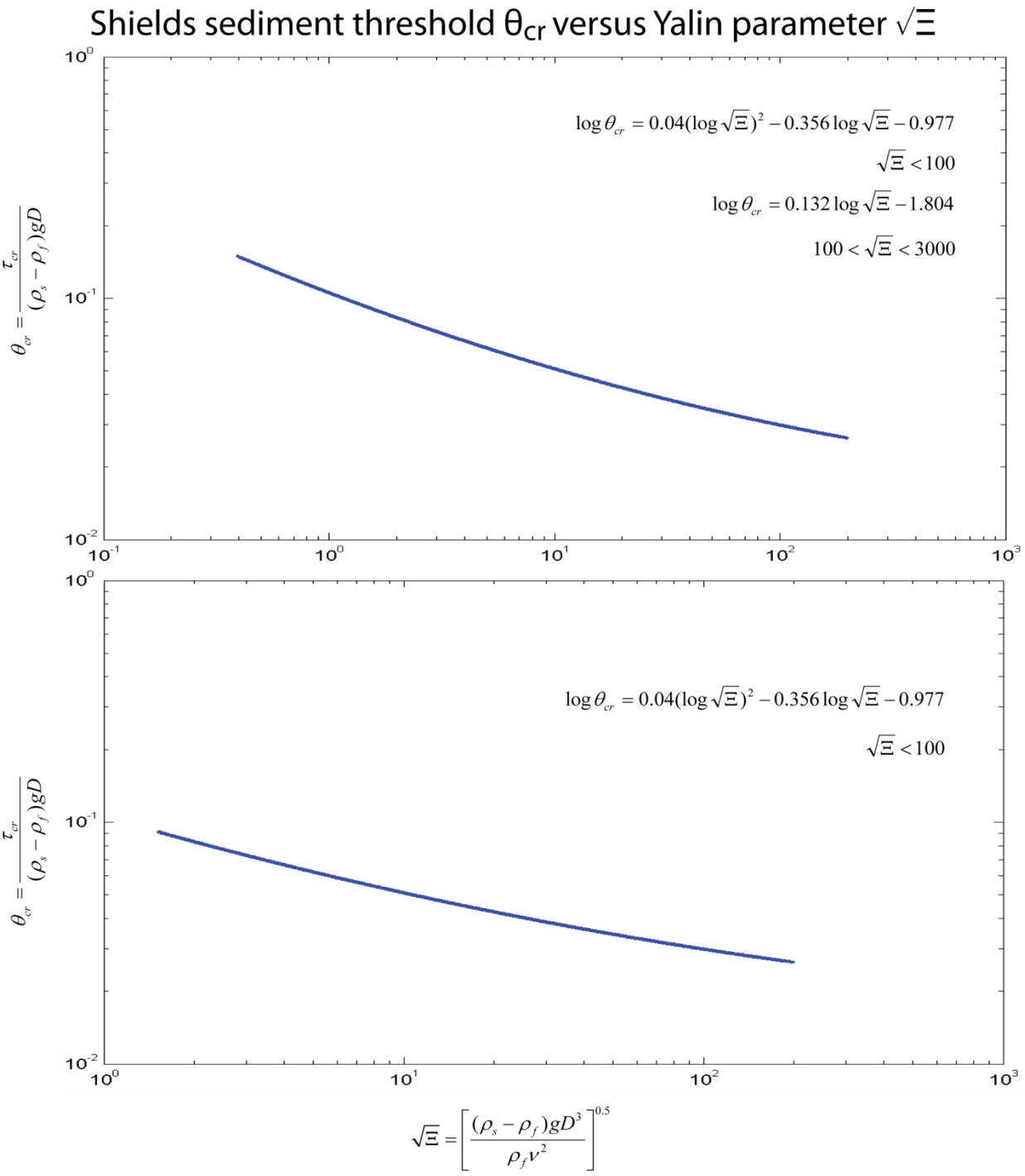

Figure 2.7. Replicated Miller's curve (1977) using grain size data compiled for this study to calculate Shields critical threshold versus Yalin's parameter. Top, both equations (7a and 7b) were used as extracted by Li et al. (1997) and bottom, using only the first equation of Miller's curve (for $\sqrt{\Xi}$ <100). The smaller slope of the bottom graph more accurately reproduces Miller's curve.

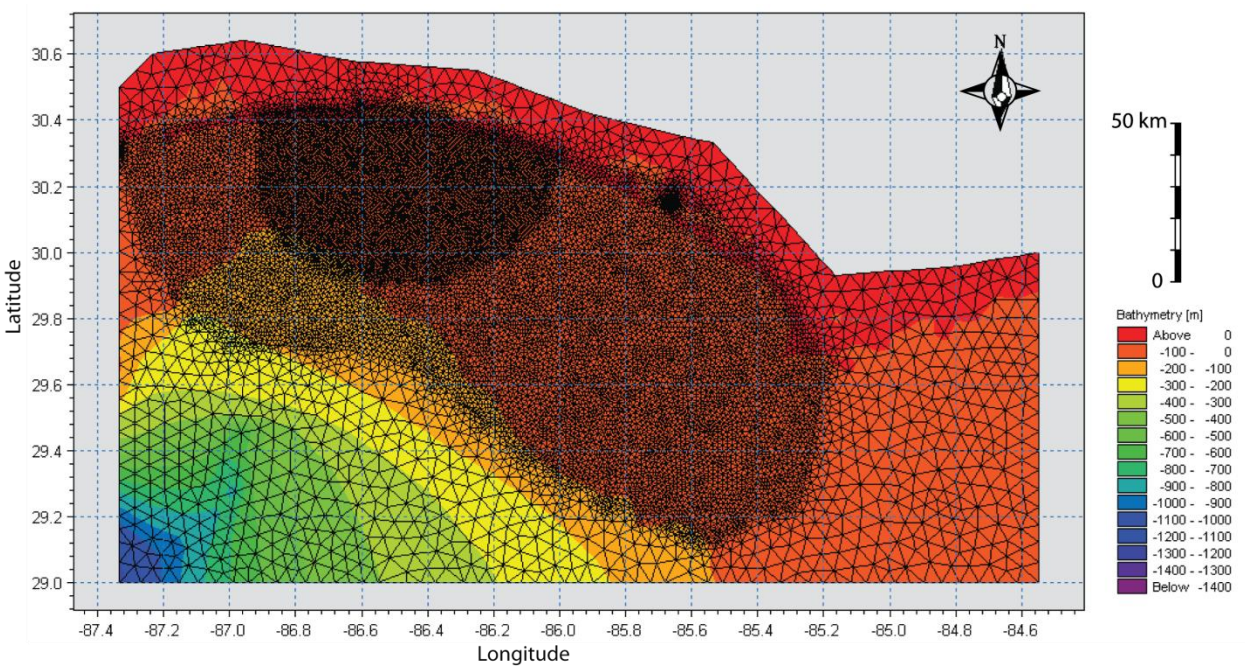

Figure 2.8. Computational domain, mesh grid and bathymetry for the coupled hydrodynamic model. Bathymetry for this model run was converted from mean low lower water (MLLW) to mean sea level (MSL), using VDatum (NOAA Coastal Services Center), in order to maintain compatibility with the HYCOM boundary conditions.

Bed resistance was determined from Nikuradse roughness length, k_s, which was determined by k_s=200D (Nielsen, 1992). D is the mean grain diameter from sediment samples in this study and usSEABED data. In wave models with a sandy bottom, a roughness length of 4 cm has been determined to yield the best results (Tolman, 1991; Siadatmousavi et al., in review). Back calculation from this value yields a constant of 200 based on a mean sediment size of 2×10^{-4} m. The result of this calculation was filtered by a lower minimum of 0.001 to avoid very small numbers for which Nikuradse's model may not be valid.

The wave and flow models are integrated using a fully spectral formulation that allows for dynamic coupling of flow and wave calculations (DHI Water & Environment, 2007). Wave-induced currents in the flow model are based on radiation stresses resulting from the wave

model. Water level in the wave model varies as a result of the flow model simulation. Five sigma layers were used for the 3D flow calculations.

2.3 Results

2.3.1 Wind/Wave Regimes Pre- During- and Post-Hurricane Landfall

Fair-weather conditions in the northeastern GoM show a consistent wind and wave direction from the south-southeast to north-northwest (Mossa, 1984). Wind speeds are generally low, less than 5 m/s, and hence significant wave heights are accordingly low, generally less than 0.8 m (Fig. 2.9). Peak wave periods are often short, due to the limited fetch of the GoM, generally under 5 s. Long period waves with significant wave height (SWH) greater than 10 m are formed when tropical cyclones pass through the region.

Ivan's wind field was much larger than that of Dennis, especially in terms of the extent of hurricane-strength winds (Fig. 2.3). Dennis was, in general, a much more compact storm. Wind speeds for Ivan over the northern GoM reached over 55 m/s, while maximum wind speeds for Dennis were approximately 50 m/s. Post-landfall wind patterns differed slightly: post-Ivan, wind was directed to the east-northeast, and the wind speed remained elevated in the eastern quadrant. During post-Dennis, wind was directed due north, and the wind speed was accordingly distributed more evenly.

Data from a nearby NDBC buoy 42039 (Fig. 2.6), the closest buoy to the study area and located to the east of the hurricane tracks (Fig. 2.2), showed a peak in significant wave height of approximately 11 m, during the pass of Ivan and approximately 10 m during the pass of Dennis (Fig. 2.9), the latter occurring much closer to the buoy. During Ivan, long period waves (approximately 14 s) were consistently measured at NDBC 42039 early 13 September 2004. Figure 2.9 also shows that the peak wave period for Ivan was recorded at 14 s, while Dennis'

peak wave period was recorded at approximately 12.5 s. A similar spike in wave activity, with much reduced intensity, was also recorded at nearby stations during Tropical Storm Cindy, with a significant wave height of approximately 3 m and a peak wave period of approximately 8 s. In general, the results of the wave model showed excellent correlation with the NDBC buoy observations, particularly with data measured at the site directly offshore of the study area (42039). Discrepancy noticed between the field-measured data and modeled data are mostly due to the smoothing effect by the modeled data output at 3 hours as opposed to measured data for every hour. This output interval was chosen to correspond with the input wind data interval of 3 hours. All validation plots for NDBC buoys around the GoM are located in Appendix B.

2.3.2 Post-Hurricane Plume Structure from Satellite Images

During fair-weather conditions, coastal plumes were not detected in red channel imagery or observed in true color composites on the open northeast GoM shelf. Due to the lack of sediment input during fair-weather, satellite imagery can be very clear, and the bottom sediments may be observed or detected in reflectance from shallow water (Walker, N., personal communication).

MODIS true color images during Hurricane Ivan were of high quality and revealed a substantial plume of material covering the entire shelf during post-landfall (Fig. 2.14). This plume persisted for at least three and a half days post-landfall, until 19 September 2004, after which satellite images were not available due to cloud cover. In Figure 2.14, three distinctly colored portions of the plume can be seen: the outer, lighter and bluish portions of the image, especially prominent on the 17th and 18th, the bright white portion that comprises most of the offshore portion of the image on the 17th, and the darker, brownish portion of the image that appears to be concentrated around the bays. The time series of the true color images in Figure

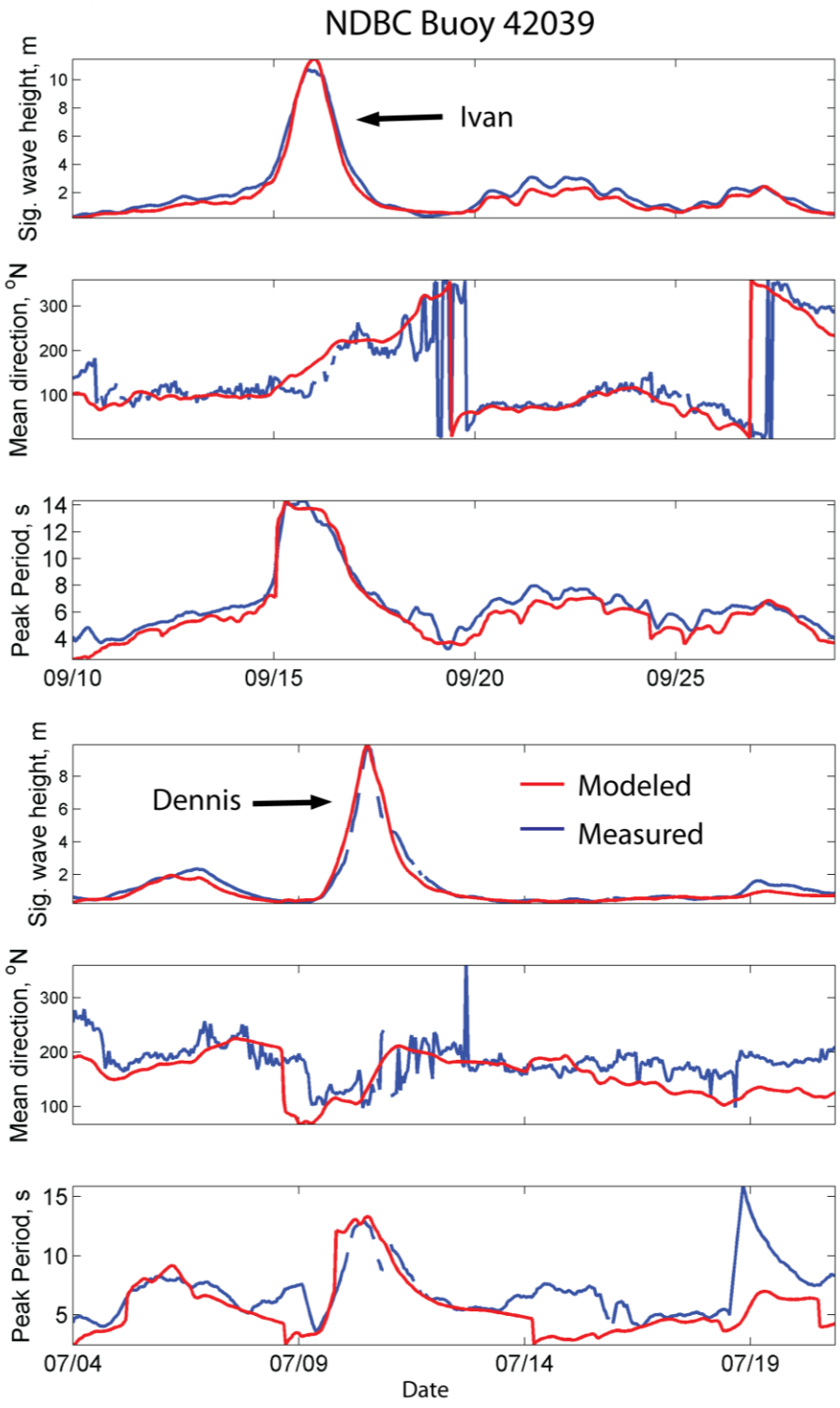

Figure 2.9. Significant wave heights, mean wave directions and peak wave periods measured during Ivan (top three graphs) and Dennis (bottom three graphs) at NDBC buoy 42039 (see Figure 2.4 for location of buoy) plotted against simulated parameters from the wave model. Strong correlation between modeled and field-measured data is observed, especially for significant wave heights.

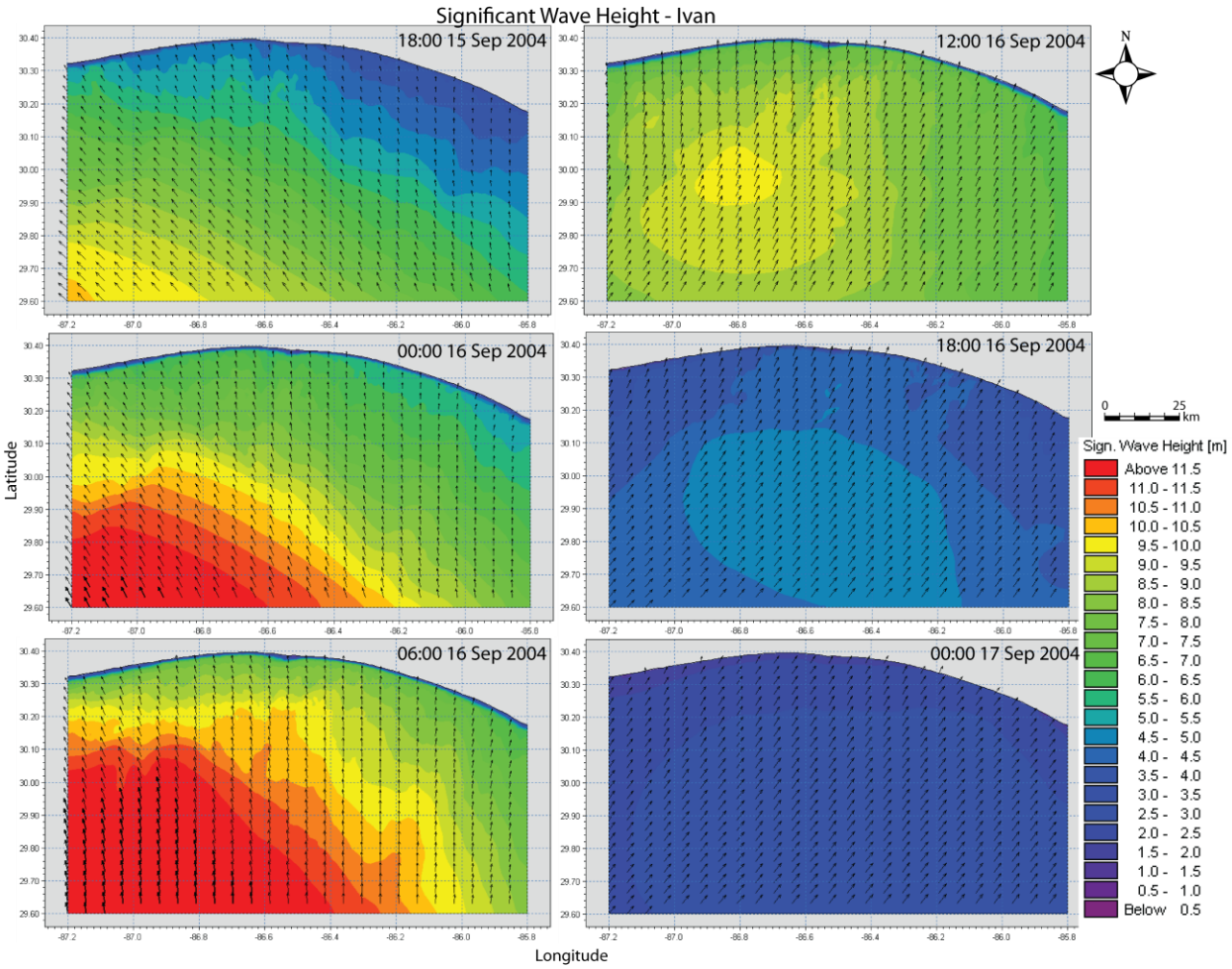

Figure 2.10. Simulated significant wave height and mean wave direction distributions during Hurricane Ivan. Arrows indicate direction of waves. Bottom left image approximates landfall of the hurricane. Extremely large waves (> 12 m) were observed over a large region of the inner – mid shelf, while rapid dissipation of waves occurred post-landfall (right column). All times are in UTC.

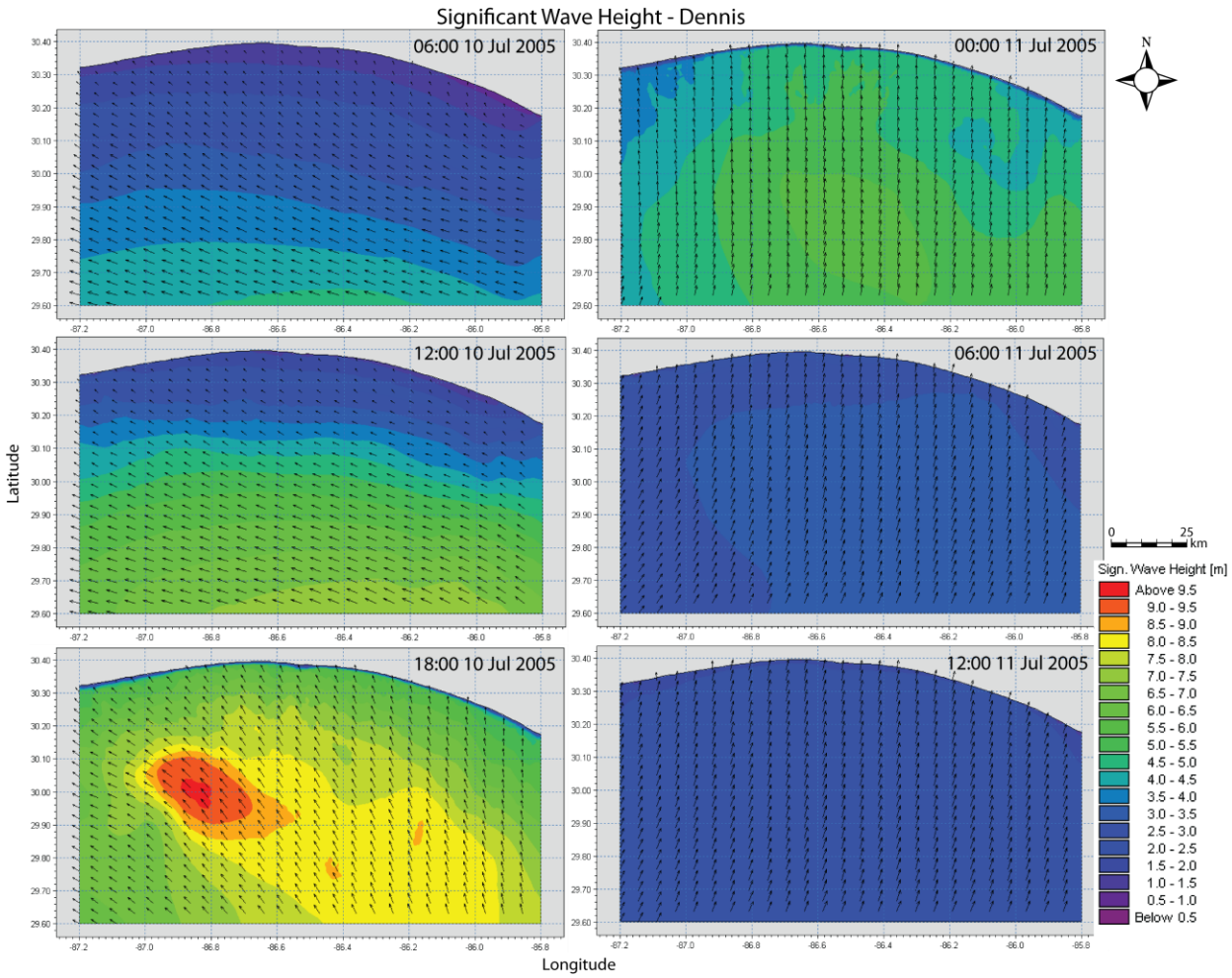

Figure 2.11. Simulated significant wave height and mean wave direction distribution during Hurricane Dennis. Arrows indicate wave direction. Bottom left image approximates landfall of the hurricane. Similar to that of the wind field, Dennis' high waves were concentrated over a much smaller region as the hurricane made landfall, indicating the dependence of waves on wind for wave generation and sustenance.

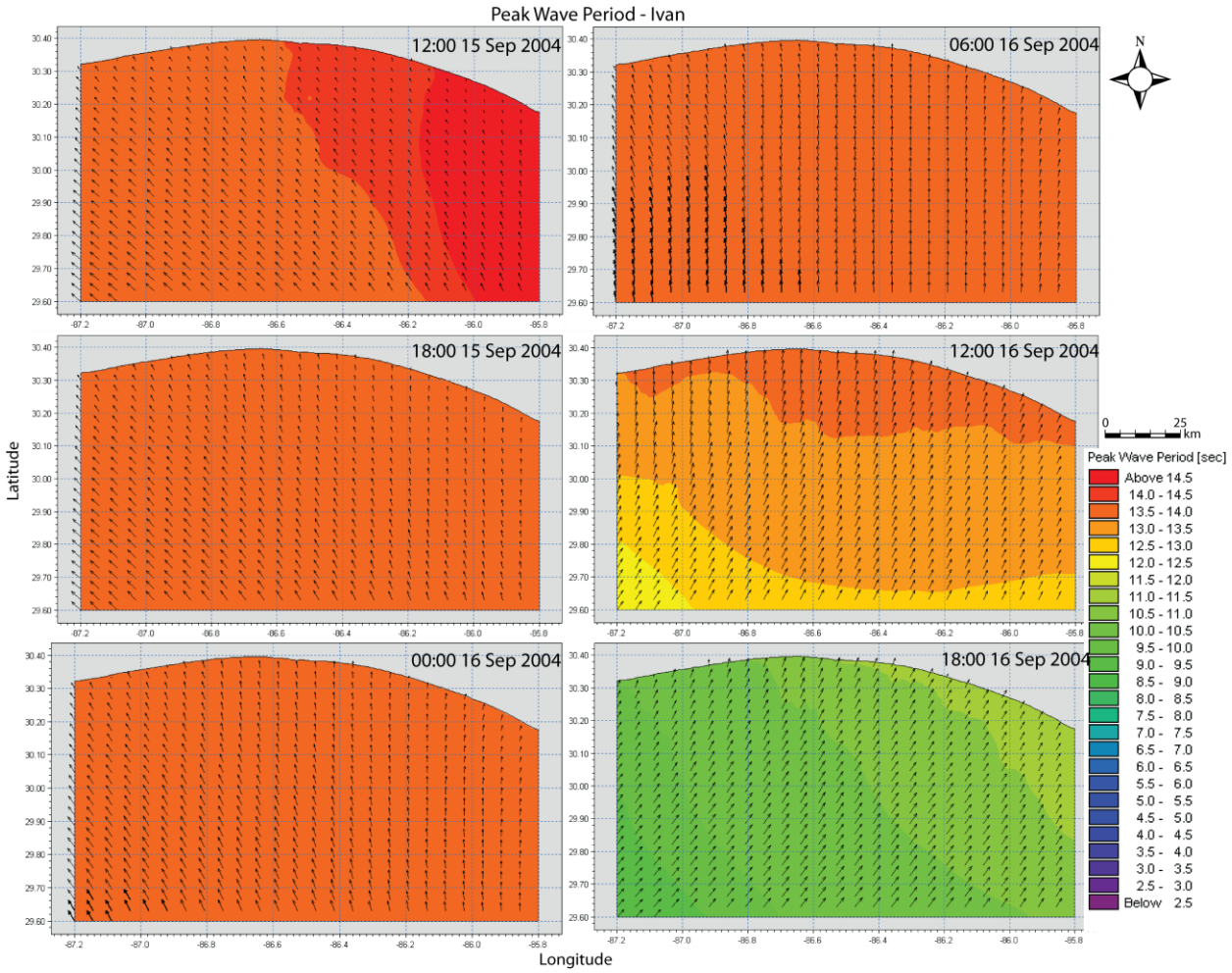

Figure 2.12. Peak wave period distributions during Hurricane Ivan. Arrows indicate wave direction. Landfall is approximated by the top right image (06:00 16 September). Notice that the highest peak wave period occurred approximately 18 hrs prior to landfall of the storm (middle left, 18:00 September) and remained extremely elevated through landfall (next three images). All times are in UTC.

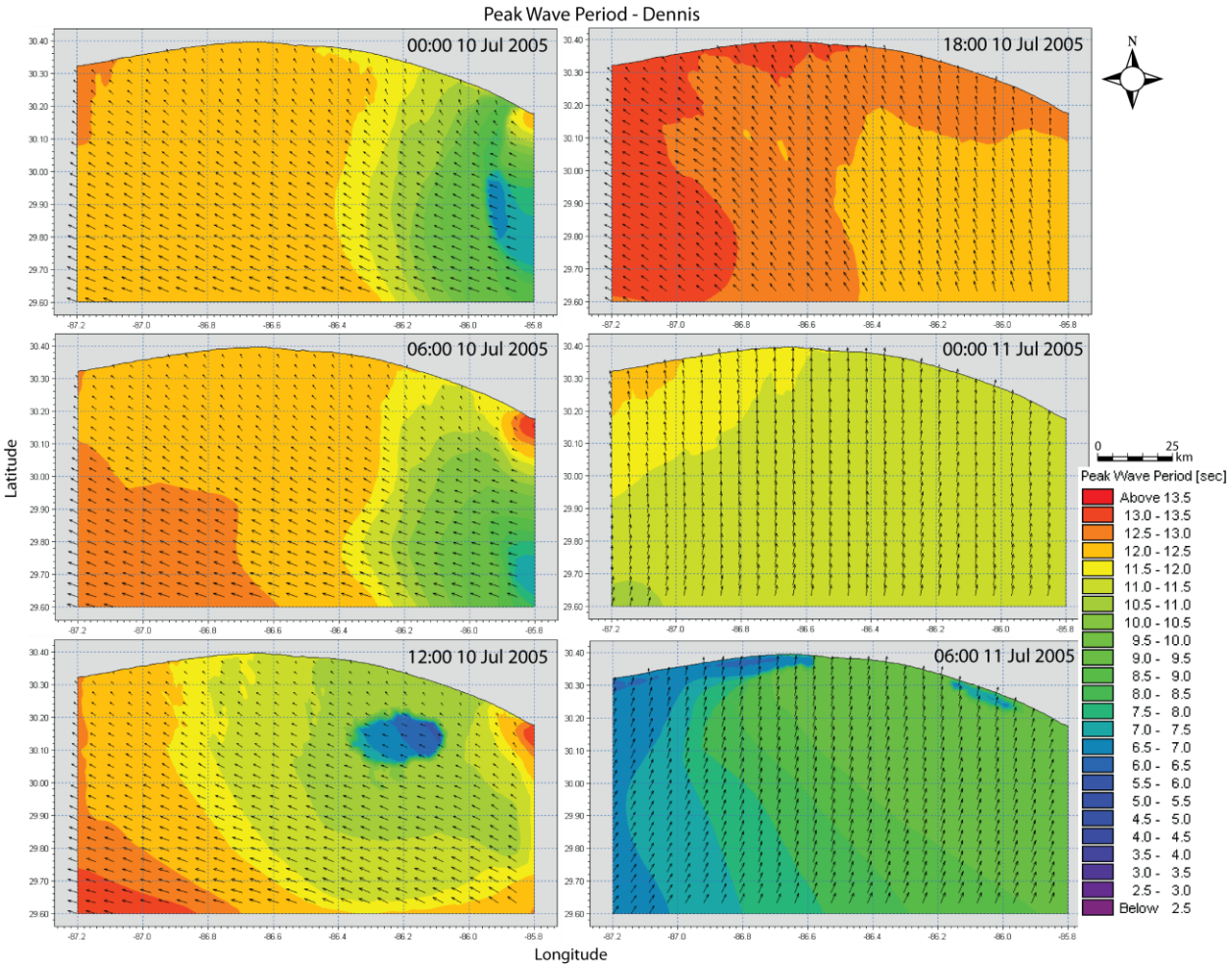

Figure 2.13. Peak wave period distributions during Hurricane Dennis in six hour increments. Arrows represent wave direction. Landfall is approximated by the top right image (18:00 10 July). Unlike Ivan, peak wave periods during Dennis occurred during landfall. The low period anomaly in the bottom left image may be a local feature that the model may not have adequately resolved, and is therefore not included in the results and interpretations. All times are in UTC.

2.14 show the plume becoming more transparent to the west and surrounding the mouths of the estuaries along the coast. The plume remains the thickest and most opaque on the shelf off Apalachicola. The plume also appears to strictly adhere to the shelf edge, clearly showing the outline of the De Soto Canyon. However, eddies can be seen forming in the later time series and moving off the shelf into deeper water.

Comparison of the true color images with channel 1 red images show a substantial plume in the red channel, with similar shape and qualities (Fig. 2.15). Reflectance extracted from the red channel (see the time series in Figs. 2.15, 2.16) indicates the presence and dissipation of the plume in a smaller region of the inner to mid shelf. The SeaWiFS image of suspended particulate material indicates that the denser portion of the plume visible in the in the MODIS true color images has a concentration of more than 10 mg/L (Fig. 2.16).

Unfortunately due to excessive cloud cover and oblique sensor angles during its pass over the GoM, satellite images for Dennis were of lesser quality than Ivan. However, a plume remained visible on 11 and 12 July 2005, indicating it persisted for at least two days post-landfall. The plume showed a similar pattern to Ivan's, which formed around the De Soto Canyon and protruded from the Apalachicola Embayment (Fig. 2.17). The plume is more uniformly colored post-Dennis, and in particular, lacks the different colored material that appears emerge from the bays post-Ivan. A jet-like projection of suspended material can be seen directly offshore Panama City, Florida. In addition, red channel images from post-Dennis landfall indicate a plume on the shelf. Images from post landfall of Tropical Storm Cindy were examined in true color; however no noticeable plume was detected and therefore not included in this research.

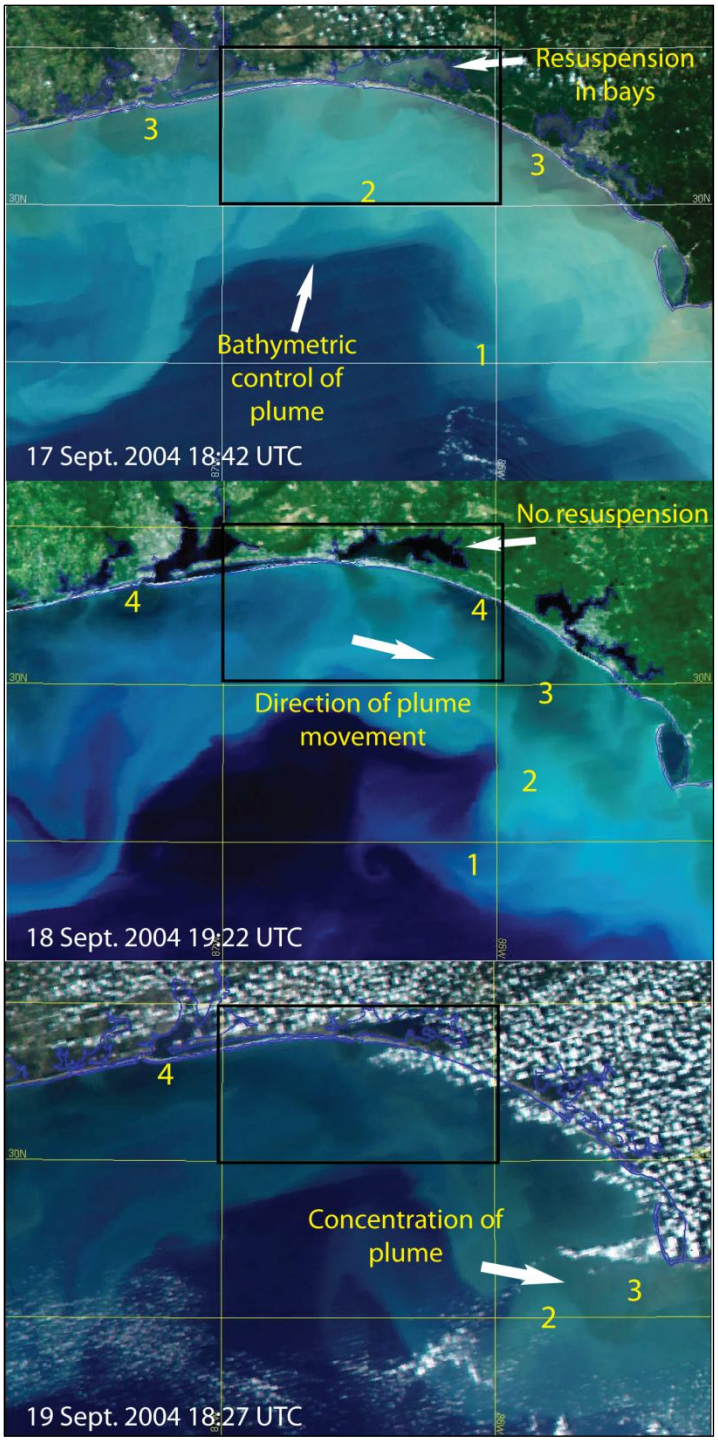

Figure 2.14. True color satellite imagery time series during Hurricane Ivan. Black rectangle indicates study area. The resuspension on the 17th and 18th was especially obvious on the shelf. The numbers on the images correspond to the different colored portions of the plume. The number 1 indicates the lighter outer portion of the plume, 2 is the bright white, main portion of the plume, 3 is dark material coming out of the bays, and 4 is clear dark water from the bays. For interpretation of these regions see the discussion section of the text.

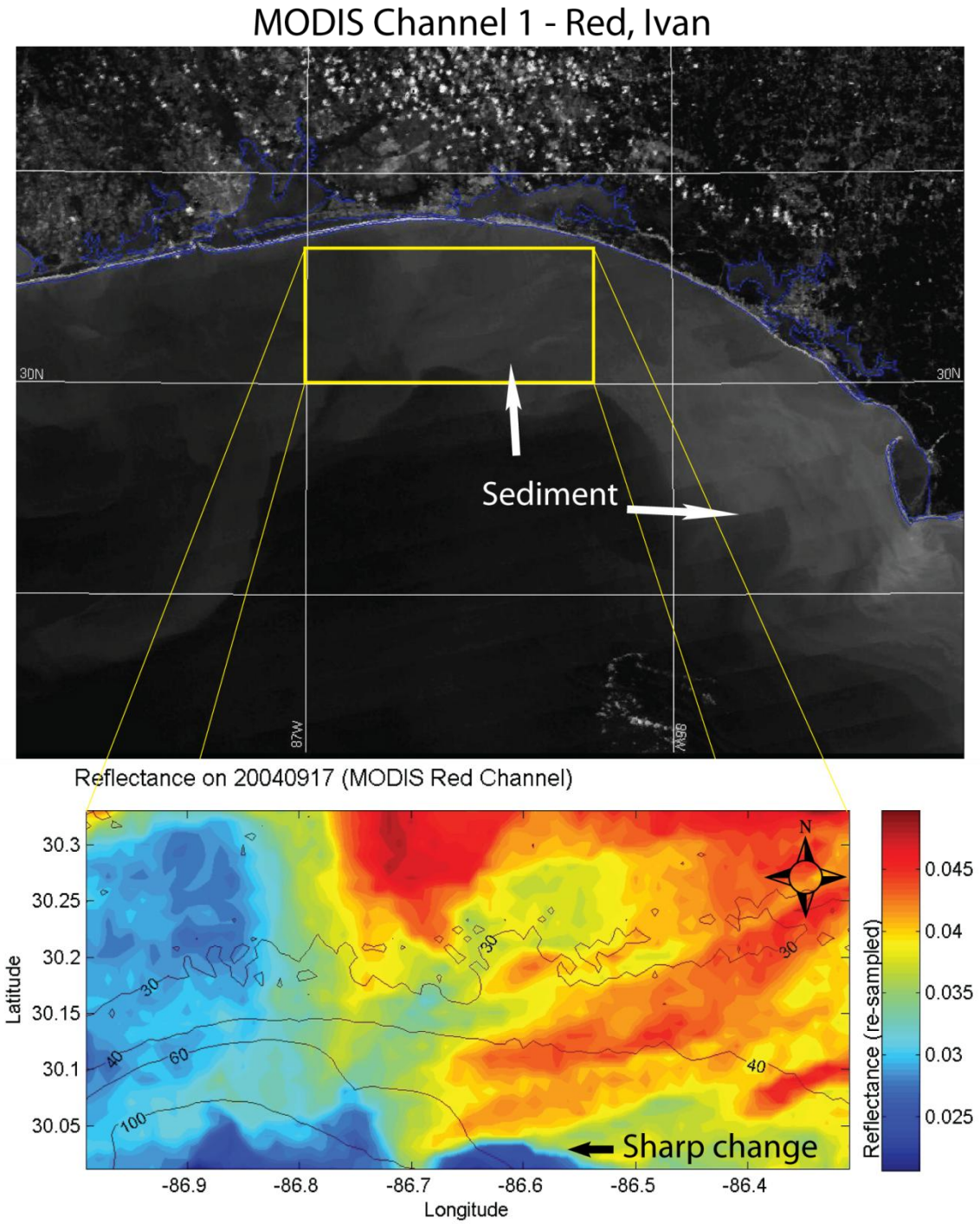

Figure 2.15. Top: mapped reflectance values extracted from band 1, red color images. Bottom: red color image indicating the presence of sediment in the plume. Note the concentration and apparent movement of the plume to the east, indicated by hotter colors in the top map, and by lighter gray color of the bottom image. Also, a sharp change in the concentration of the plume is noted at the base of the top image, and is interpreted as a sharp change in bathymetry. The yellow box in the bottom image demarcates the extent of the upper image.

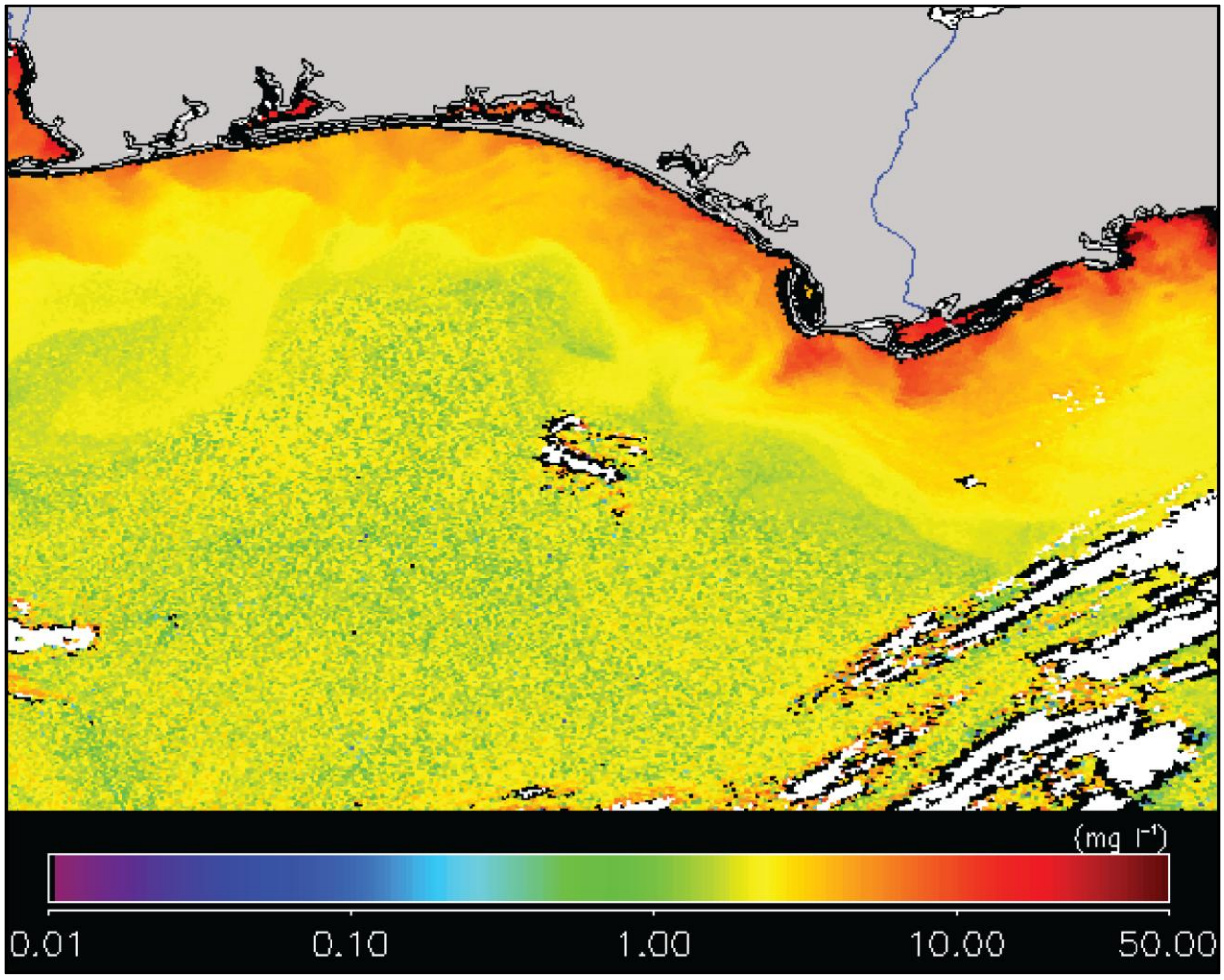

Figure 2.16. Mapped suspended particulate matter concentration from SeaWiFS data. Note the elevated concentrations (~6-20 mg/L) along the shelf, adjacent coast and bays.

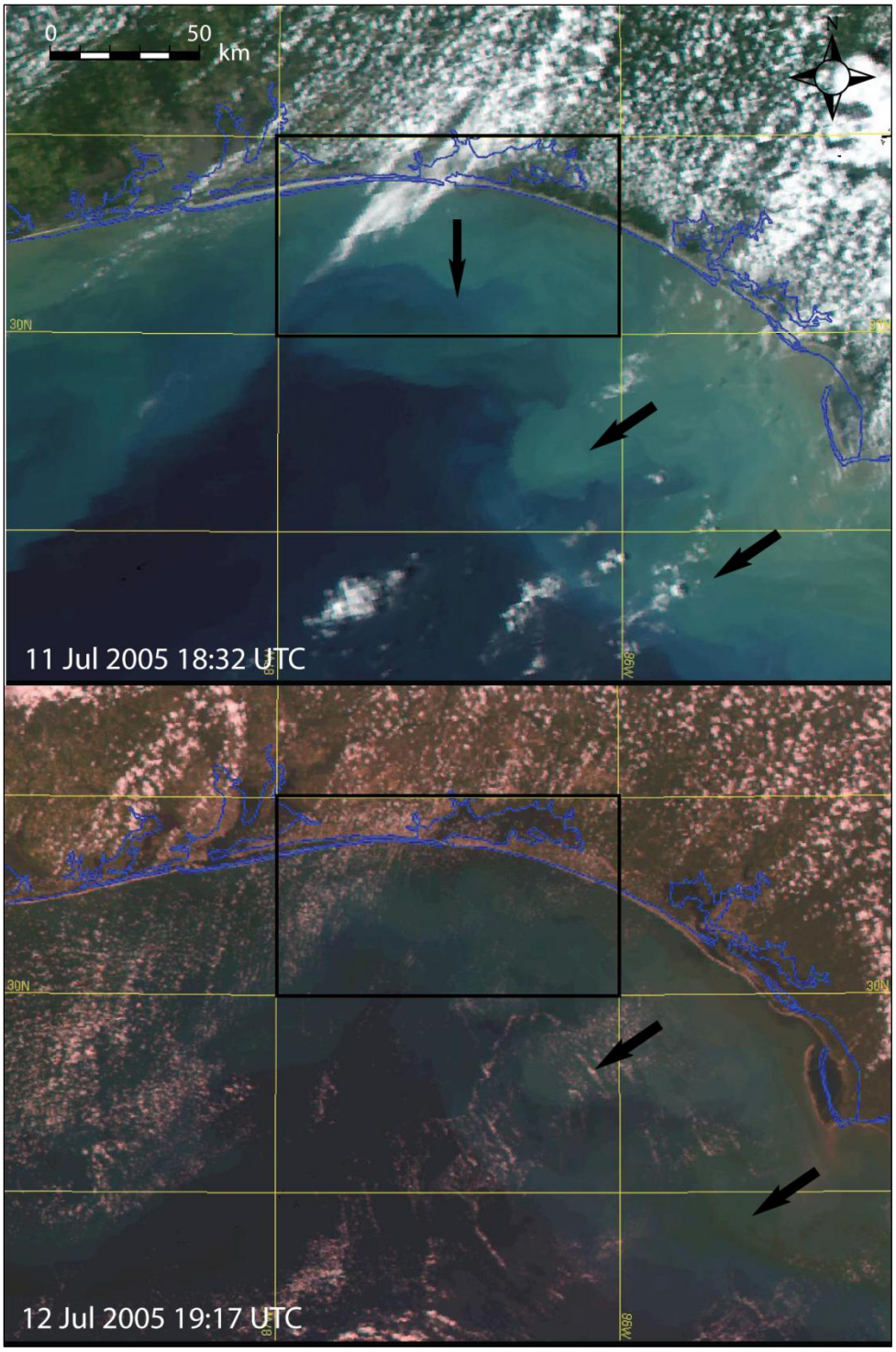

Figure 2.17. True color satellite images from post-Dennis. The arrows indicate direction of motion of the visible plume. Note how the post-Dennis plume distribution differs from that of post-Ivan. Also, post-Dennis plume was less intense than Ivan's, indicated by lack of highly reflective sediment in the shelf water. However, the pattern of the plume is nearly identical to that of Ivan's, indicating shelf bathymetry and prevailing coastal currents are very important to plume evolution on the shelf.

2.3.3 Bottom Shear Stress and Resuspension Intensity

During fair-weather conditions only the coastal zone and nearshore (greater than 10 m isobath) has bottom shear stresses high enough to resuspend sediment, and therefore has a positive RI. Sediment resuspension does not occur during fair-weather conditions.

East and west longitudinal profiles of bottom shear stress for both Ivan and Dennis are seen in Figure 2.18 and 2.19. Pre-Ivan, shear stresses along the western transect are much higher than those in the eastern transect. Pre-Dennis, shear stresses in the east were slightly lower than that in the west, and attenuated towards the coast. Shear stress increased very rapidly during the approaching phase of Dennis, especially when compared to Ivan-induced shear stress levels which remained elevated over a longer period of time; approximately 12 hours. During both Ivan and Dennis, the highest shear stress zones occurred over the large shoal in the study area (Fig. 2.20) and at the head of the De Soto Canyon. During Dennis, the peak shear stress occurred along the coast, reaching 1.7 N/m^2. During the pre- and landfall phases of the hurricanes, particularly during Ivan, the peak in shear stress (Fig. 2.18) was amplified at the head of the DeSoto Canyon, peaking at 2 N/m^2. Computed shear stress values during Dennis at the apex of the DeSoto Canyon were lower, peaking at 1.4 N/m^2. These values were considerably higher than the mean critical shear stress value of 0.4 N/m^2. Figure 2.18 illustrates that additional peaks in shear stress occur over smaller shoals and scatter across the domain as well as along the coast. Shear stress computations for both hurricanes clearly showed an increasing trend with decreasing water depth. Shear stress is significantly reduced landward of the shoals and in the canyon. During landfall of the hurricanes, shear stress is reduced along the coast, where the bathymetry steepens and is less than 10 m water depth. During post-Ivan, shear stresses in the east remain slightly elevated compared to those in the west. However, post-

Dennis landfall, shear stress values were slightly higher in the east. Post-hurricanes, shear stress remained elevated during Ivan, for an additional 6 hours, and then rapidly decreased, as opposed to the gradual decrease during post-landfall.

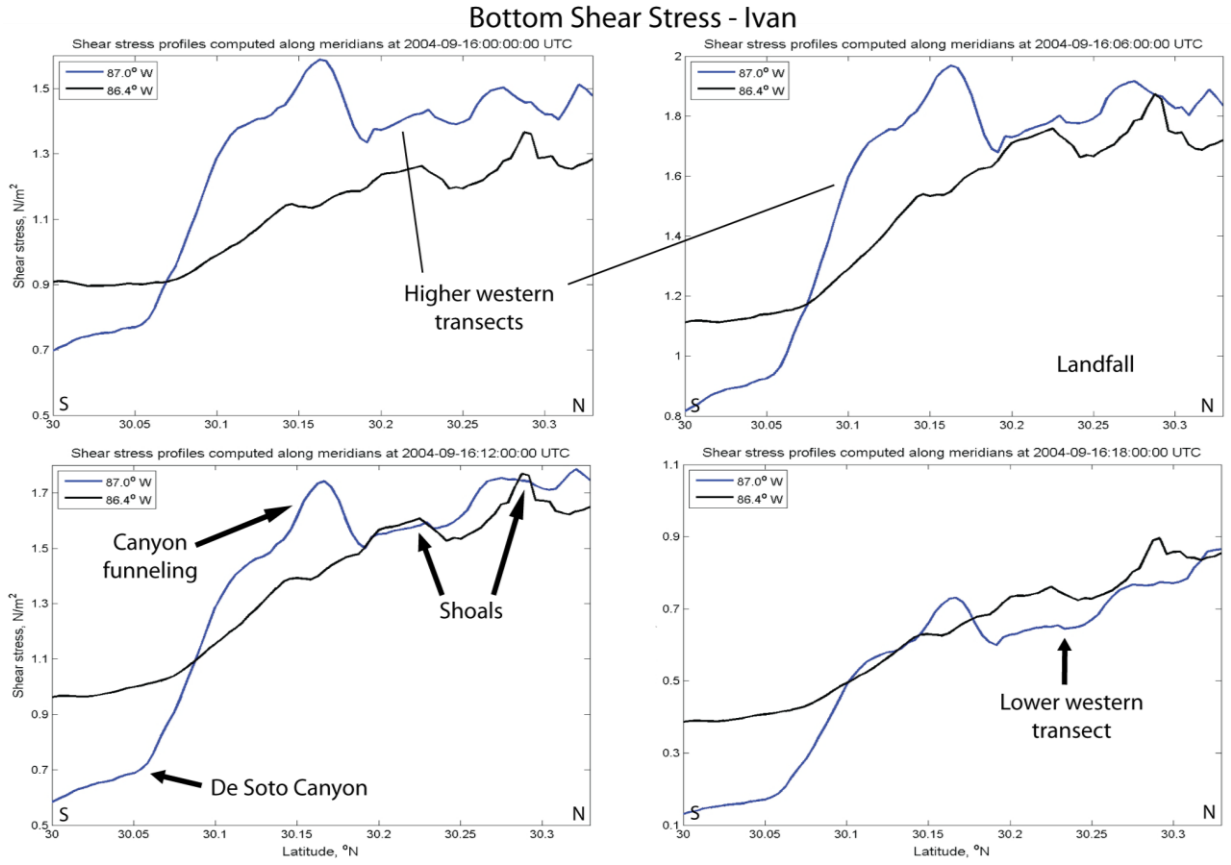

Figure 2.18. Shear stress profiles for an eastern and western transect of the study area during Hurricane Ivan. The profiles extend from the nearshore (on the right) to approximately the shelf break (on the left).

Reflectance values were also plotted against resuspension intensity values for the period corresponding to the satellite overpass, and are provided in Figure 2.21. These methods were used in Miller et al. (2005) and Booth et al. (2000). Figure 2.21 shows that there is almost no correlation between reflectance values and resuspension intensity.

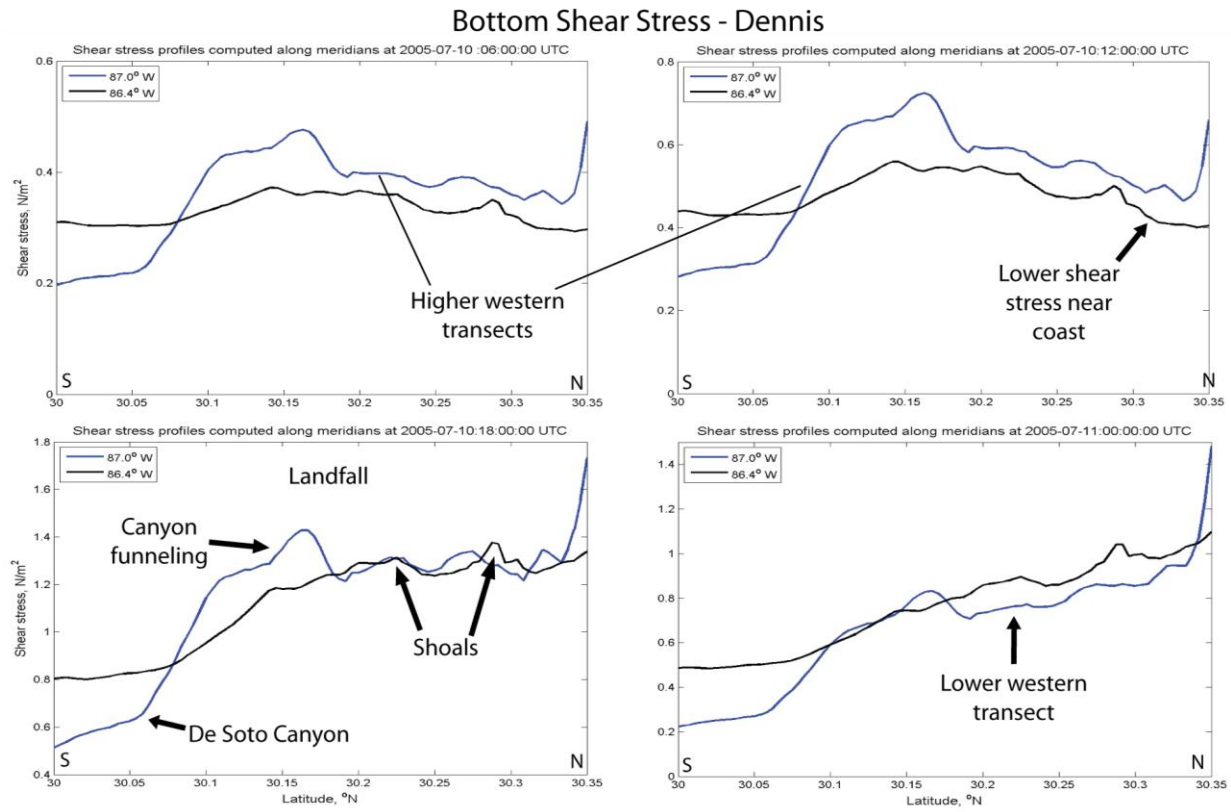

Figure 2.19. Shear stress profiles for an eastern and western transect of the study area during Hurricane Dennis.

During Ivan resuspension intensity (RI) turned positive over much of the domain almost 24 hours prior to landfall. Resuspension intensity built up west of the DeSoto Canyon and moved east with increasing intensity, as the storm approached the northern GoM. As expected maximum resuspension, that is, the highest RI in the region for the given event occurred at landfall, peaking at 1.9 N/m^2, and was highest over the shoals and at the mouth of the DeSoto Canyon (Fig. 2.22). However, resuspension potential (positive RI) was confined to the 100 m isobath. Most of the resuspension was constrained along the inner shelf to the west and directly north of the DeSoto Canyon. Higher RI values were persistent west of the canyon and over the shoals on the inner shelf, even after the hurricane made landfall. Lower RI was observed immediately landward of the shoals. The RI began to decrease by 12:00 UTC, on 16 September.

Resuspension potential for Ivan lasted for 18 hours (until 17 September 00:00 UTC) post-landfall, and overall, for 42 hrs (pre- and post-hurricane).

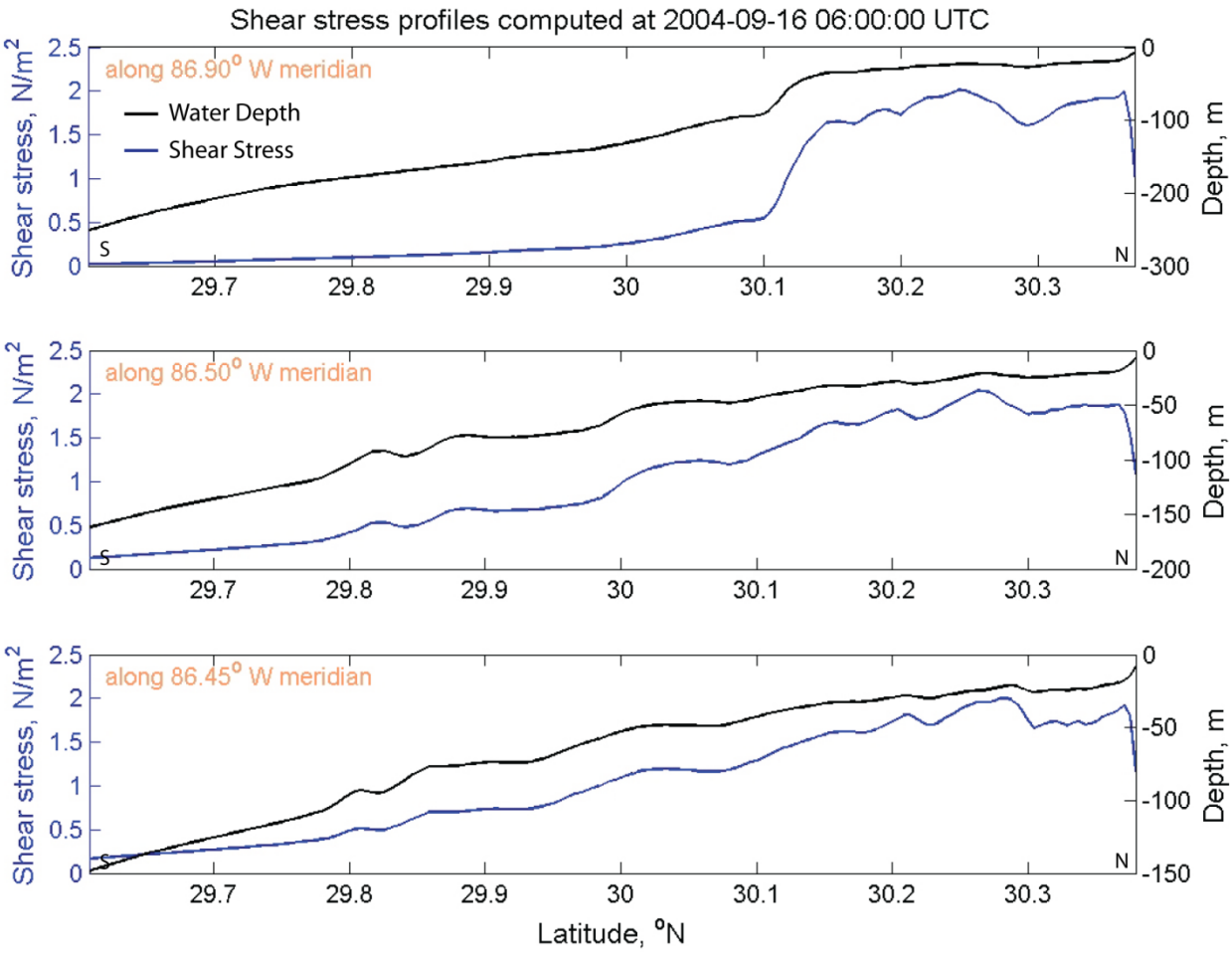

Figure 2.20. Shear profiles plotted with water depth across the shelf during Hurricane Ivan. Profiles extend from the outer shelf (left) to the coast (right). Transects were taken from the western portion of the study area (top), the middle of the study area (middle, at the mouth of Choctawhatchee Bay) and the eastern portion (bottom) during landfall of the storm. Shear stress is clearly influenced by bathymetry, particularly over large shoals, canyon and shelf break.

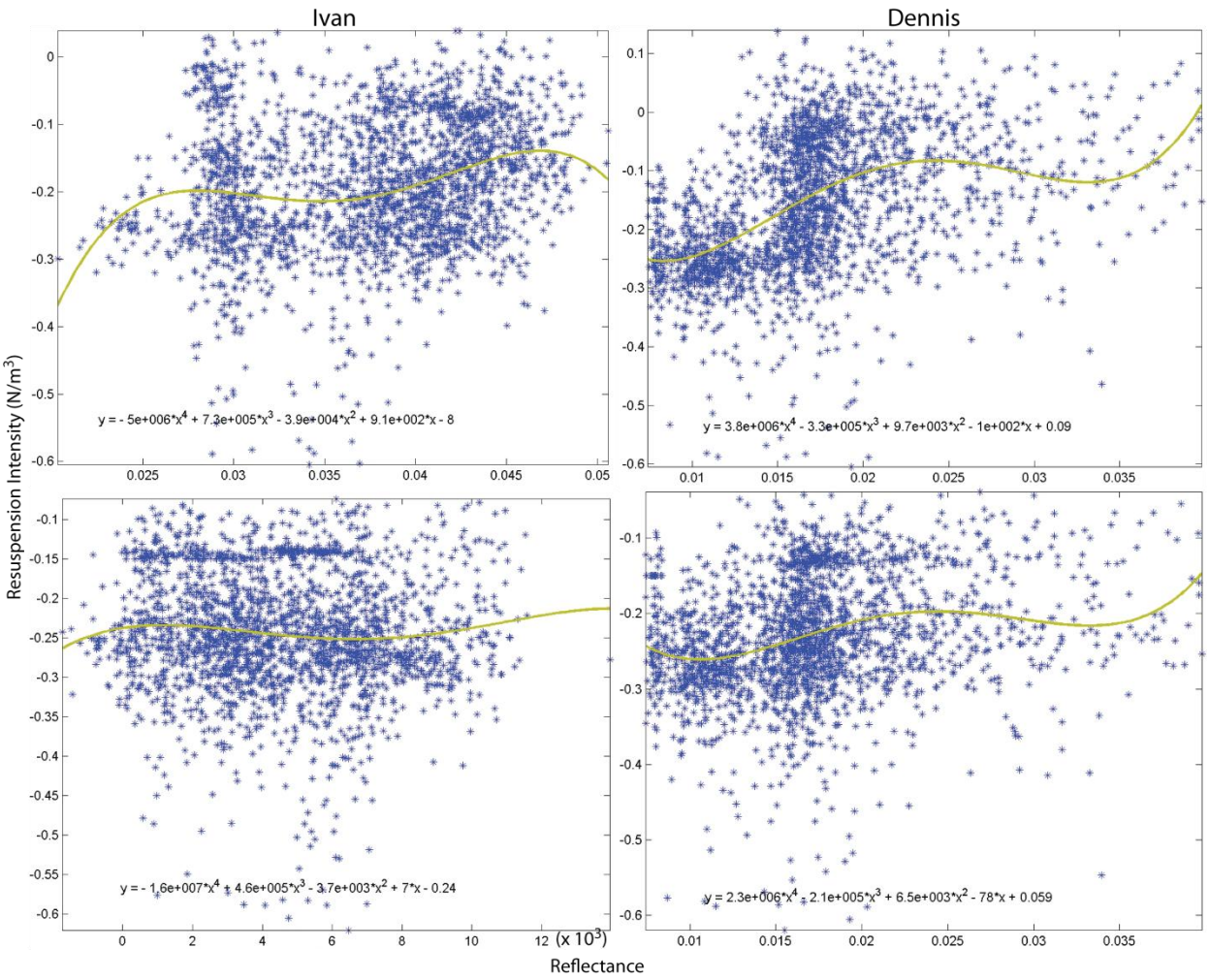

Figure 2.21. Resuspension intensity plotted against reflectance from red channel MODIS images. Lack of correlation indicates that the majority of the plume does not originated from the shelf. However, the isolated zones of positive RI value during the post-landfall phase of both hurricanes indicate that sediment transport processes remained active on portions of the shelf after landfall of the hurricane.

Values of RI during Dennis's approach began increasing 18 hours before landfall (10 July 2005 00:00). Zones of higher RI values were less uniform than that of Ivan's (Fig. 2.23), however were uniform from the coast to offshore. As in the case of Ivan, RI was the highest (1.4 N/m^2) during landfall, peaks were observed at the head of the DeSoto Canyon and along the crests of shoals. The RI during Dennis also remained elevated for an extended period of time over the crest of shoals (Fig. 2.23). Resuspension potential lasted for 24 hours over the shelf

(until 11 July 2005 18:00 UTC) and remained noticeable along the coastal zone for several more hours. Pre- and post-landfall combined resuspension continued for 42 hours during Dennis also.

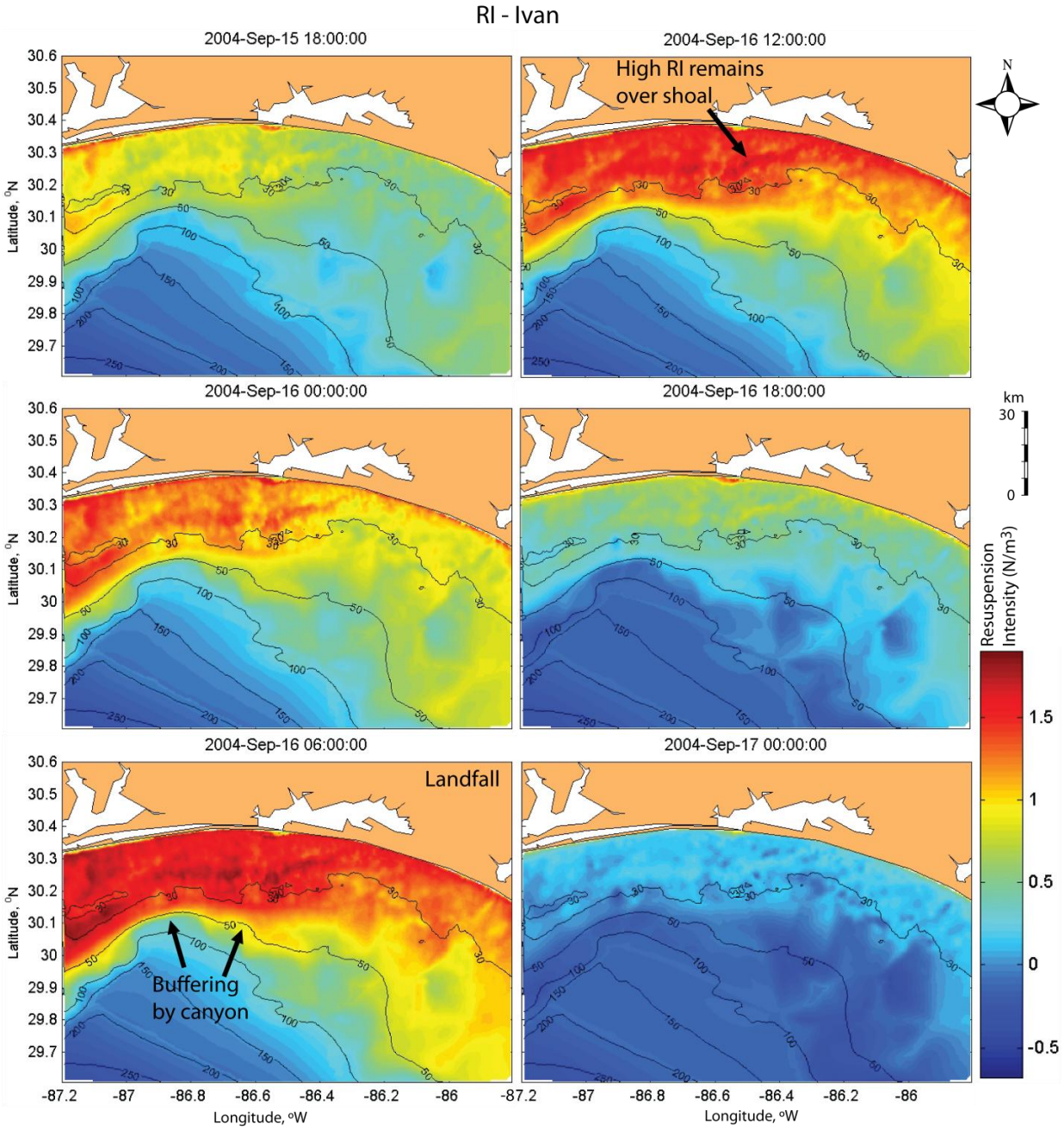

Figure 2.22. Shelf distribution of RI during Hurricane Ivan in 6 hr intervals (time in UTC). During landfall (bottom left image) RI was positive over the entire shelf, indicating most of the shelf experienced sediment resuspension. During the post-landfall phase, RI decreased rapidly. A large shoal on the inner shelf is apparent in all images and has the highest RI in the study area.

Tropical storm Cindy generated a comparatively weak resuspension profile, peaking at 0.6 N/m^2 in the western-most zone of the study area, off the Florida/Alabama border, and mostly along the inner shelf and coastal areas. Due to this lower level of resuspension on the shelf during this storm, the morphodynamic response of the inner shelf to tropical storms was not further investigated.

2.3.4 Hydrodynamic Model

During fair-weather conditions, currents are predominately directed to the northwest (Stone et al., 1985) and are less than 0.3 m/s at all depths. Along the coast and shallow inner shelf, currents have a dominant western component. Water levels, obtained from coastal tide gauges were used to validate the hydrodynamic model for Hurricane Ivan, and showed reasonably good correlation; especially at the station at Panama City, Florida (Fig. 2.24). The model overestimated less than 20 cm of sea surface height during pre and post surge, while an overestimation of less than 10 cm of surge was evaluated (Fig. 2.24), during the peak of the surge. This consistent overestimation may be due to the non-uniformity in the resolution and datum of the bathymetry used in the coastal model and the HYCOM regional model, from which the boundary conditions were extracted for the coastal model. Approximately 1.22 m of storm surge was recorded at Panama City and approximately 1.3 m was simulated by the hydrodynamic model. The MIKE 21/3 model also showed good agreement with the HYCOM model outputs (Figs. 2.25 and 2.26).

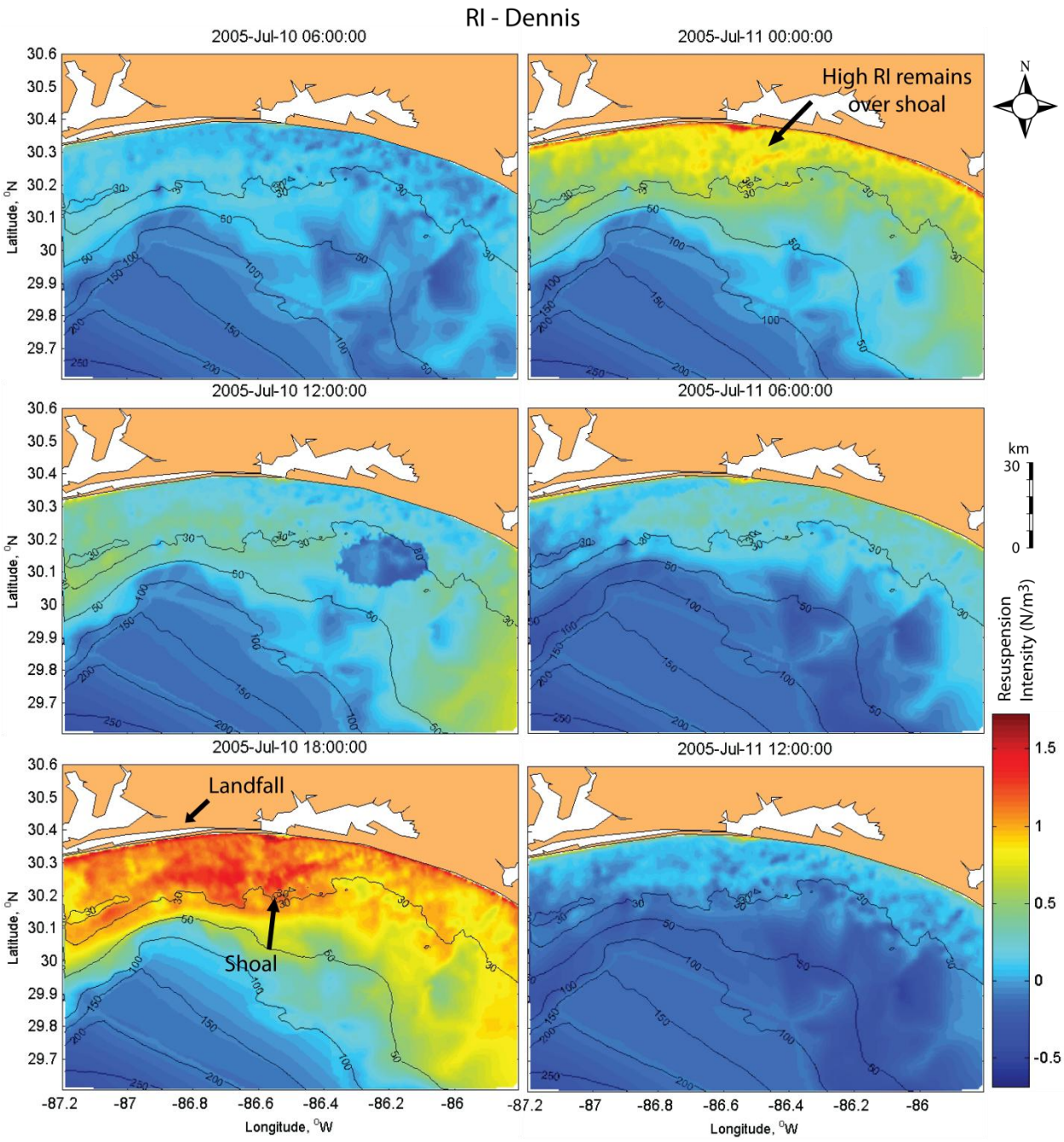

Figure 2.23. Shelf distribution of RI during Hurricane Dennis, over 6 hour time intervals (time in UTC). Peak RI occurred at landfall (bottom left image), and was not as high or widespread as in Ivan. However, Dennis' RI increased very rapidly over a short time (left column) and dissipated more slowly (right column), particularly along the coast.

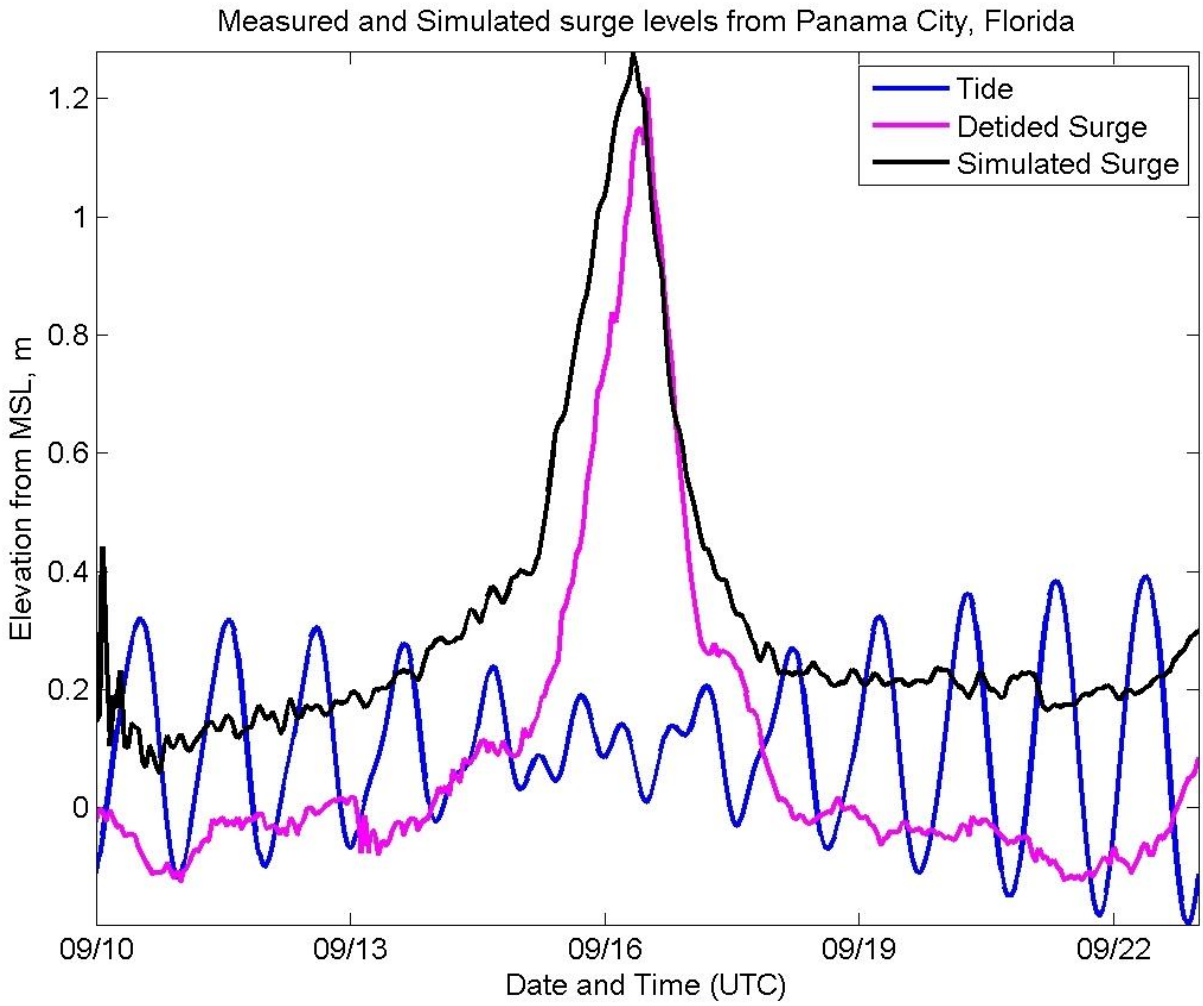

Figure 2.24. Time series of water level from MSL at Panama City, Florida tidal station during Ivan. The blue curve corresponds to the tidal fluctuations; the pink curve is de-tided measured surge at Panama City station; the black curve is the simulated surge (without tide) from the hydrodynamic model.

2.3.4.1 Pre-landfall Flow Patterns

Currents around the Apalachicola Embayment intensified first, as much as 5 days prior to landfall. The current speed on the surface and at 10 m water depth peaked approximately 7 hrs prior to landfall (Figs. 2.25 and 2.26). Peak current flow pre-landfall has been shown to occur in other areas of the coast and for other tropical cyclones as well (Snedden and Nummedal, 1991). Pre-hurricane flow is predominantly directed onshore (north) during the approaching phase of the hurricane, until approximately 2 hours post-hurricane landfall, at nearly all levels. After this

point, eddies develop in the west at all levels and to the east at the surface. Maximum surface speeds reached approximately 1.6 m/s, although speeds were typically between 1 and 1.4 m/s during the pre and landfall of the hurricane (Figs. 2.25 and 2.26). These flow speeds were the maximum over the water column for pre-, landfall, and post-hurricane conditions.

2.3.4.2 Post-landfall Surface Flow

At 12:00 UTC on 16 September surface currents began to flow to the south along the western boundary south of Pensacola Bay. By 15:00 UTC 16 September, surface currents began to orient to the east and then to the southeast. One day later, 15:00 UTC 17 September, surface currents moved to the south (Figs. 2.25 and 2.26). Surface currents remain directed south until 12:00 UTC 19 September, when they rotated to the west. Current speed remained high and directed offshore over the De Soto Canyon (approximately 1 m/s) for approximately a day and a half. Currents in the southern, offshore direction remained this way over most of the shelf, until fair-weather conditions were reestablished several days post-landfall.

2.3.4.3 Post-landfall Sub-surface Flow

Post-hurricane flow is complex, particularly with depth, but overall flow was directed to the west or southwest. A small anticlockwise eddy was formed at 9:00 UTC 16 September over the head of the De Soto Canyon, after which current fields moved to the south in the western portion over the De Soto Canyon. This eddy persists throughout the water column, and currents sustaining the eddy remain active for 3 days after the hurricane made landfall. At 20 m and 30 m water depth, peak flow occurs 18 hrs prior to landfall, south of Apalachicola, at approximately 1.4 m/s. Peak distribution of flow occurs approximately 4 hours prior to landfall at 3:00 UTC 16 September.

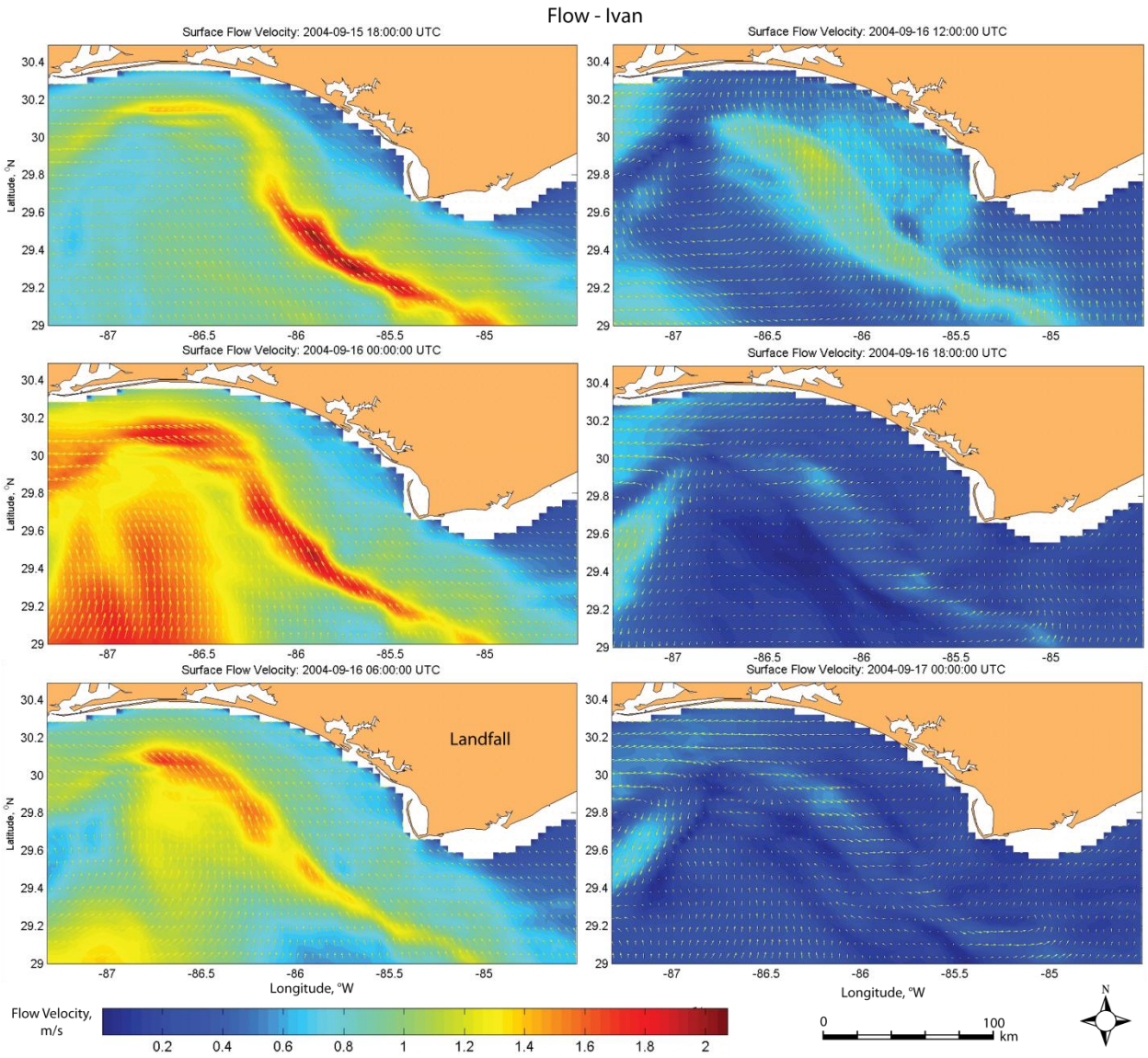

Figure 2.25. Simulated surface current speeds and direction obtained from HYCOM during Ivan in 6 hr increments. A fast, narrow jet-like current can be seen in the vicinity of Apalachicola in the left column images. Peak current speeds occurred more than 6 hrs prior to landfall (middle left image). Data courtesy of Prasad and Hogan (2007).

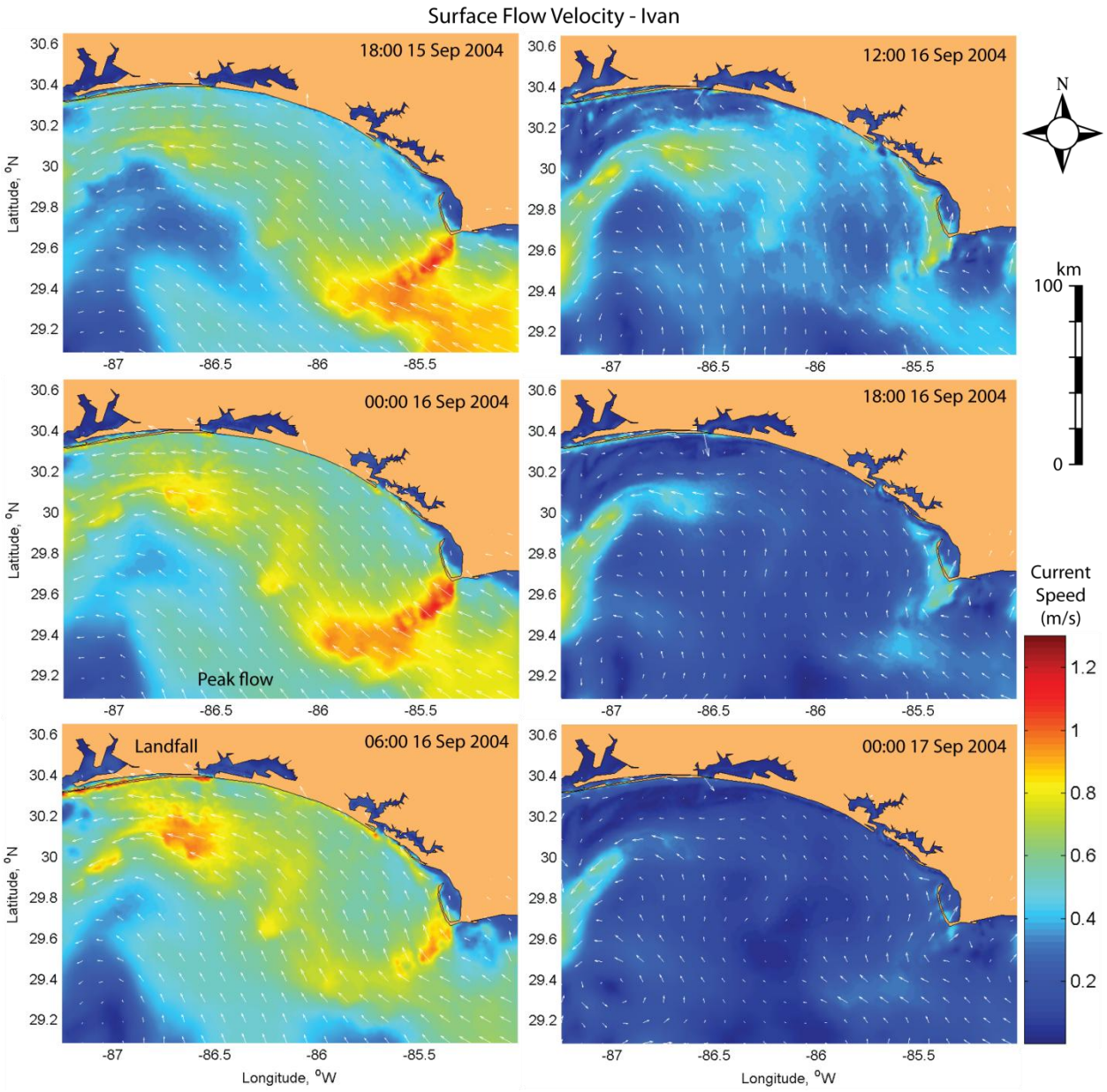

Figure 2.26. Sea surface flow for the study area, simulated from MIKE 21/3 in 6 hr increments. Arrows indicate the direction of flow.

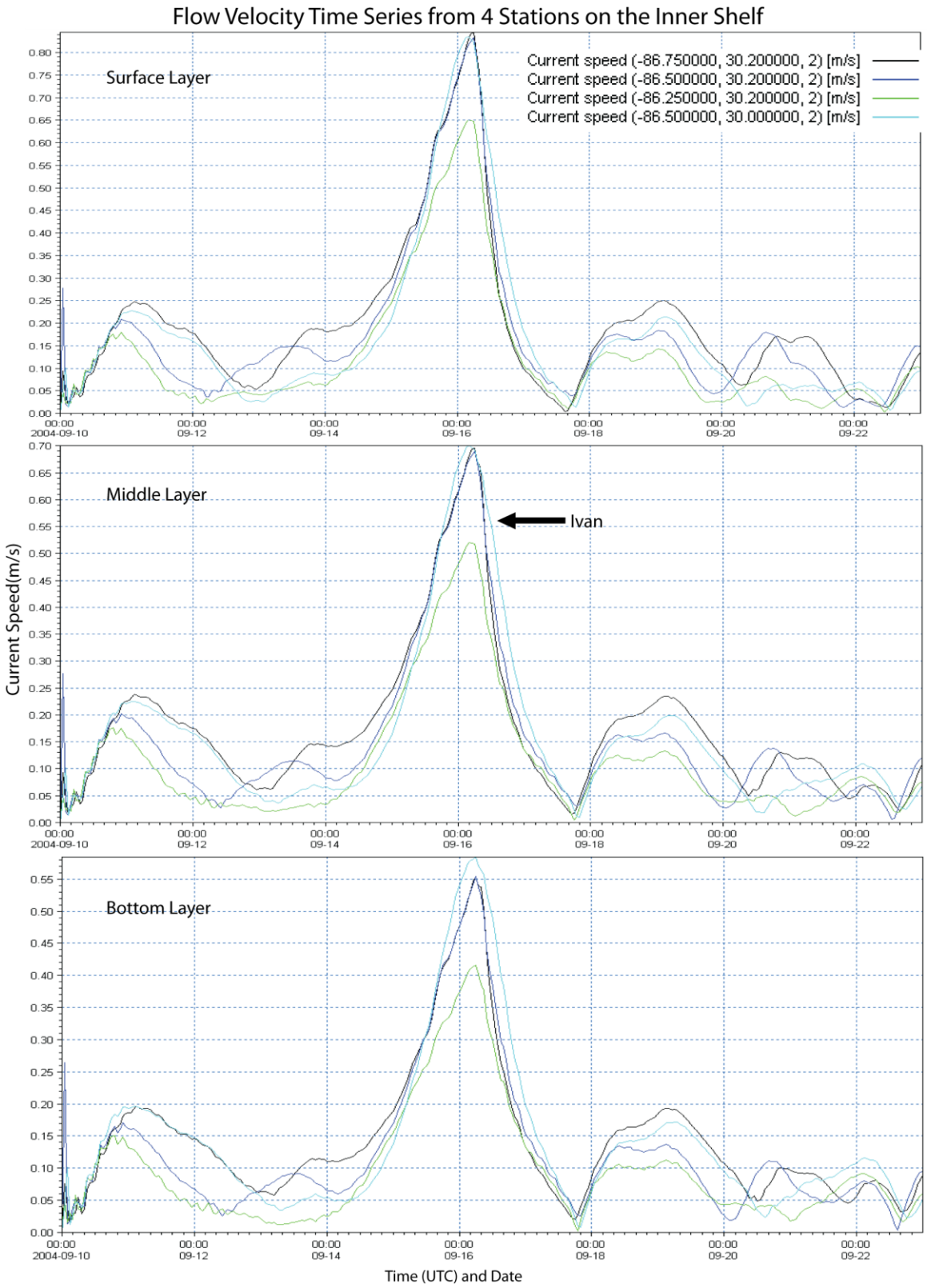

Figure 2.27. Time series of simulated flow velocity over several days extracted from 4 stations on the inner shelf, from the surface, middle and bottom layers.

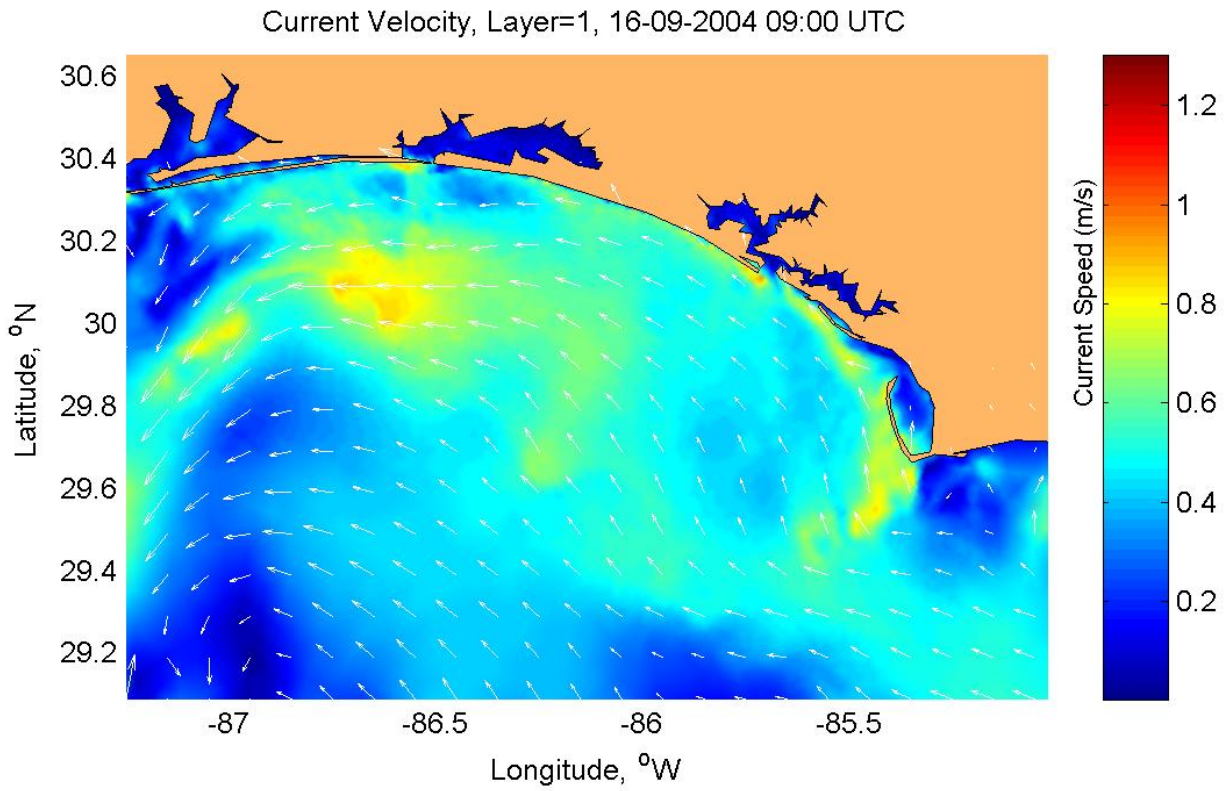

Figure 2.28. Bottom layer currents simulated using MIKE 21/3, two hours after the hurricane made landfall. Arrows indicate flow direction.

Flow field stratified just after the hurricane made landfall with surface currents moving onshore and bottom currents moving offshore (Fig. 2.29). However, several hours post-landfall, almost all velocity in the y-direction (north-south) is negative, indicating offshore flow. Velocity in the y-direction strengthens at approximately 00:00 UTC 18 September along the mid-shelf, and continues to increase until approximately 20 September, after which flow begins to rotate back to the north-northwest. Directly north of the head of the De Soto Canyon, an elevated flow field is almost always noticed with direction offshore. To the east and west of the canyon, strong currents are visible in the flow velocity profiles; however, current velocity remains low over the head of the canyon. Very strong onshore currents persist around the Panama City region of the shelf. Currents also became stratified post-hurricane in the x-direction as well, with the surface currents moving to the east and the weak bottom currents often moving west (Fig. 2.29).

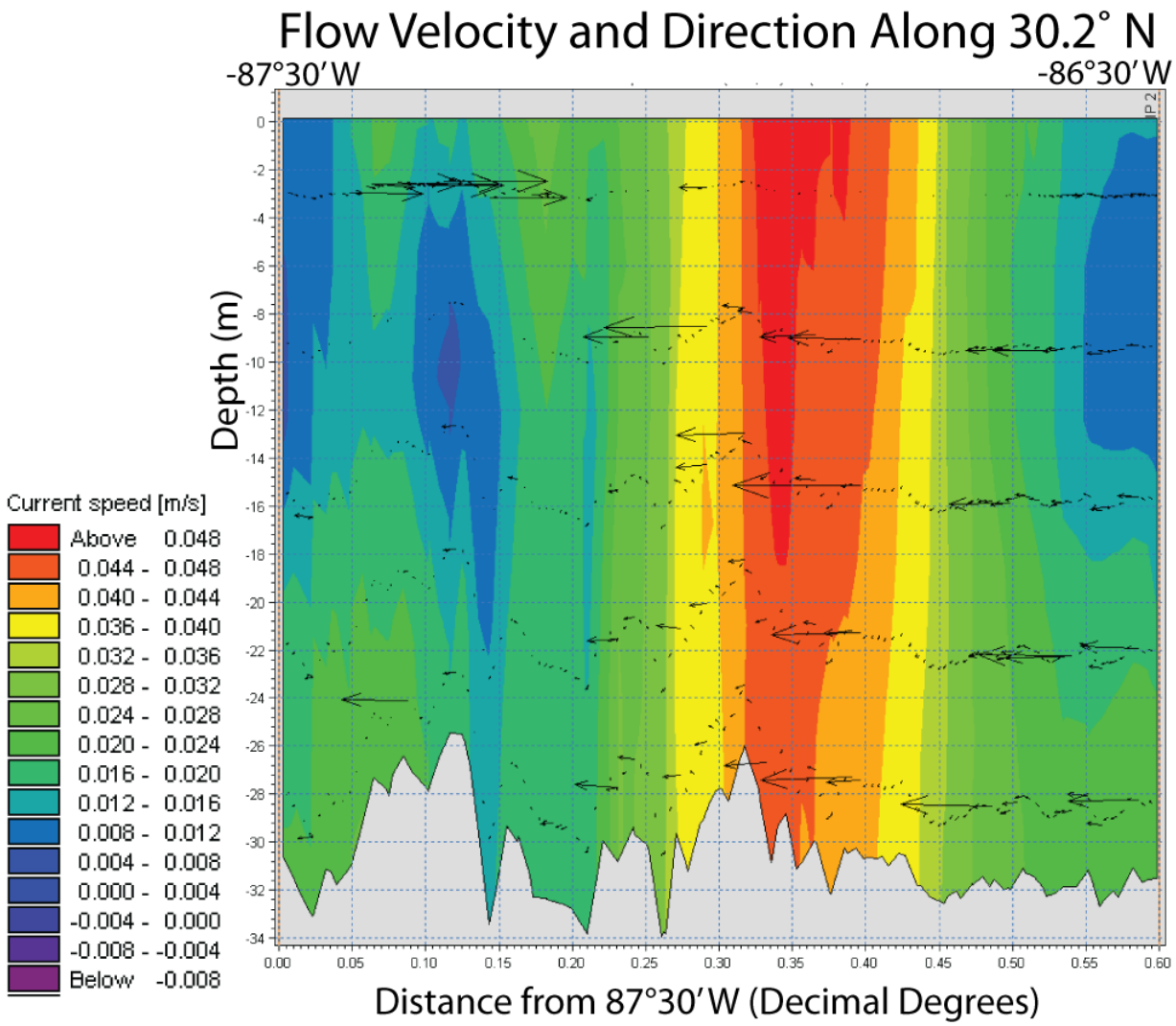

Figure 2.29. Current velocity transect at landfall along the 30.2°N latitude.

2.4 Discussion

The series of wave and hydrodynamic modeling studies along with the analysis of met-ocean data collected during the hurricanes suggests that hurricane-generated high energy waves and associated flow characteristics all have significant impacts on bottom shear stress and resuspension potential on the inner shelf. Prevailing wind fields decide the trajectory of the coastal sediment plumes, especially during the post-landfall phase. Flow was increasingly complex with the hurricane's evolution and approach, and stratified during and post-hurricane. Sediment resuspension during hurricanes Ivan and Dennis was apparent, even in deeper water on

the mid-outer shelf. In terms of the hydrodynamic impacts on the sediments on the shelf, storms can be broken into three phases: Phase 1, the resuspension phase during the approach of the hurricane and similar to stage 1 by Mitchell et al. (2005); phase 2, the mixing phase during the landfall and just after landfall (~ 2 hrs), similar to stage 3 (Mitchell et al., 2005) or Forced Stage (Price et al., 1994); phase 3, the deposition phase post-hurricane, similar to Stage 4 (Mitchell et al., 2005), or Relaxation Stage (Price et al., 1994). Table 2.1 summarizes these phases and the hydrodynamic response and transport pattern associated with each phase, while Figure 2.29 illustrates the pattern of wind stress and flow during each phase. This model to describe flow and transport is also consistent with and adapted from the 'temporal acceleration' model for shelf storm deposits proposed by Swift and Rice (1984).

2.4.1 Pre-Hurricane: "Resuspension Phase"

The increase in wave period prior to the storms, particularly during Ivan, was due to long period swells travelling across the GoM days before the storms made landfall. These long period waves propagating ahead of the storm (Fig. 2.12) would create favorable hydrodynamic conditions across the shelf that allow for a steady increase in RI with increasing wave energy. The RI increased steadily over two days during the approaching phase of Hurricane Ivan (Fig. 2.22), even when local wave heights were relatively low (Fig. 2.10). Resuspension intensity dramatically increased during Ivan when the peak wave period increased; however, RI persists even when wave period decreases. During Hurricane Dennis, RI increased very rapidly in a short period of time prior to landfall. The difference in resuspension potential during the set up phases of the two hurricanes may be due to the orientation of their track through the Caribbean: Ivan entered the Gulf south of Cuba, propagating long period waves to the northern GoM for a longer period of time and from a greater distance. Dennis however, traversed over Cuba,

prohibiting swell waves from forming while it was over land. Dennis was also a much smaller storm (category 1) while over Cuba, and did not reach category 4 status until it had entered the GoM and encountered the warm waters of the Loop Current (Beven, 2005; Prasad and Hogan, 2007). Being a much larger storm, Ivan's hurricane-strength winds affected roughly the same area that Dennis's tropical storm-strength winds did (Fig. 2.3), indicating a wider swath of storm influence. A good example of this is illustrated by lowered shear stresses on the inner shelf during pre-Dennis. Ivan's immense size was able to produce a larger realm of hurricane-force winds and long period waves that would affect the entire shelf, while Dennis affected a smaller portion. Moreover, Hurricane Cindy made landfall over southeastern Louisiana on 6 July as a Category 1 hurricane, creating wave heights along the Florida inner shelf large enough to initiate resuspension along the crests of the shoals and ridges. It is possible that the sediment resuspension, which may have been induced by Hurricane Cindy, facilitated more resuspension during Dennis, due to already elevated hydrodynamic conditions in the region. This difference in RI development indicates the dependency of shear stress and RI, and therefore sediment transport, on wave period. Grain size is also important to RI evolution, which is evident along a coarse patch of sand offshore Panama City, Florida (Figs. 2.22, 2.23). In this region of coarse material, RI takes longer to evolve, and is lower when compared to other areas with similar water depth and wave fields.

Table 2.1. Met-ocean hydrodynamic parameters and RI during the three phases of storm transport.

Met-Ocean parameter/Sediment Response	**Resuspension Phase**	**Mixing Phase**	**Deposition Phase**
Wind Speed	Increasing	Maximum	Decreasing
Wind Direction	West	North	Northeast
Sig. Wave Height	Increasing	Maximum	Decreasing to fair-weather conditions
Wave Direction	West	North	Northeast
Peak Wave Period	Increasing to Maximum	Maximum	Decreasing to fair-weather conditions
Flow Speed	Maximum (x and y direction)	Decreasing (with z direction peaking)	Fair-weather conditions
Flow Direction	West/northwest Some upwelling	Surface flow to the north bottom flow to the south = downwelling	Surface = east/southeast Middle = west Bottom = southwest
RI Due to Waves	Increasing resuspension	Maximum resuspension	Decreasing resuspension to deposition
Effect on sediment motion	Sediment agitation and motion initiates	Sediment is entrained in bedload (dominant) or suspension; Peak transport occurs	Sediment in plume falls out of suspension; Sediment transport (bedload) ceases
Direction of sediment transport	Limited onshore	Limited vertical; Maximum offshore	Alongshore and offshore

Peak current speed occurred in a narrow current that extended to all depths many hours prior to landfall, suggesting that this current gained speed from the setup of sea level against the coast and the forward motion of the hurricane track. This setup may have accelerated the already persistent Loop Current, a prominent feature in the Gulf particularly in the summer, and a jet associated with the current on the west Florida shelf (Hetland et al., 1999; He and Weisberg, 2002) (Figs. 2.25, 2.26). This current can even be seen in fair-weather conditions, although, not as pronounced. While the pre-landfall phase accelerated this current, it appears that the post-landfall phase was dominated by downwelling (Fig. 2.30), effectively abating this jet, as observed by the lack of this current during and post-landfall (Fig. 2.25). Peak flow conditions (for all vertical layers) occurred several hours in advance of the hurricane. This was in good agreement with the observations from Mitchell et al. (2005) of Ivan on the outer shelf, that of winter storms on the Scotian Shelf by Li et al. (1997), and Hurricane Allen observations on the

Texas shelf by Snedden et al. (1988). At this time period, Ekman layers showed minimal veering with depth, in agreement with the findings from Mitchell et al. (2005) on the outer continental shelf, who used a cluster of 14 acoustic Doppler current profilers (ADCPs) to examine the oceanic response to Ivan. The alignment of current vectors throughout the water column and with the wind direction indicates that the strong winds driving hurricanes dominates the current flow during its peak, particularly surface waves and currents (Chen et al., 2008). The strong westward flow over the entire domain of the model was also in good agreement with observations by Teague et al. (2006). This demonstrates the impact of wind as a forcing mechanism during hurricanes. The small amount of Ekman veering to the northwest allowed for some upwelling to occur as the hurricane approached.

During this phase, it is unlikely that any significant transport of sediment occurs, particularly because the shear stresses are just progressively increasing above the critical shear stress. Any transport that may occur would be directed onshore, in agreement with the work of Hayes (1966, 1967). Even though the current velocity peaks at this point, most of the impact on the bottom sediment would likely be bed agitation and the initiation of sediment motion.

2.4.2 Hurricane Landfall: "Mixing Phase"

As might be expected, maximum RI and shear stress occurred with maximum wind speed, wave heights and wave period that occurred at the peak of the storm, that is, landfall. At this point, RI extended through all depths of the shelf, out to the shelf break (~ -100 m), during Ivan, and over most of the shelf (~ -80 m) during Dennis. This extensive distribution of RI and the ability of storms to resuspend sediments at such depths, indicates the ability of waves to influence the entire shelf (Wang et al., 2005; Teague et al., 2006), with the majority of the energy impacting the inner shelf. Correlation of positive RI to the shelf break and high RI values along

the crests of shoals also demonstrates the importance of water depth and morphology in RI evolution (Fig. 2.20). The shallowest regions sustained the highest RI for an extended period of time. However, shallow features were significantly impacted, such as large shoals on the inner shelf. Model results indicate that RI is the highest and remains persistent over the crests of these shoals. The results also show a slight decrease immediately landward of the shoals, indicating that the shoals act as a buffer of wave energy shear stress (Figs. 2.22 and 2.23). These extremely high values of RI (2.0 N/m^2 during Ivan) also implies that high wave energy expended over these shoals would be translated into additional resuspension (Figs. 2.22 and 2.23) and mixing over the shoal, and ultimately would result in winnowing of the shoal sediments (Mehta, 2002). In a similar but much larger fashion, the DeSoto Canyon acts as a funnel for shear stress. When waves move over the canyon and suddenly encounter shallow water, an increase in shear stress and RI results due to the convergence of the wave crests. Waves are steepened, the speed slows, and convergence occurs. It was also observed that the De Soto Canyon buffered RI along the shelf to the east during Ivan and along the shelf to the west during Dennis. Due to the effect of depth control on shear stress, the shelf edge and canyon are very important in RI evolution and sediment mobility (Fig. 2.22). The higher values of RI to the right of the hurricanes indicate that the majority of sediment motion is focused on the eastern side of the storm's track.

During the peak of the storm, most of the higher energy swell waves (period > 8s) break further offshore and there was a substantial reduction in shear stress in the nearshore (<5 m depth). The rapid forward speed of the hurricane likely resulted in the breaking of long period southerly swells farther offshore, which resulted in the lower shear stress values simulated near the coast. An additional explanation may be the non-inclusion of water level variability in the wave model. Wave simulations used a constant water level and did not account for the effects of

storm surge. If it were included the swells may have propagated further inshore before they would become unstable and break. However, if waves are breaking farther offshore, as one might expect with the large wave heights that were simulated, it is indicated that the inner shelf would sustain the major impact of the storm. Bentley et al., (2002) found that numerically modeled resuspension depths increased seaward post-Camille offshore Mississippi. By means of complex wave-wave interaction, wave energy would be effectively transferred from low period swells to locally generated waves in the intermediate and shallow waters.

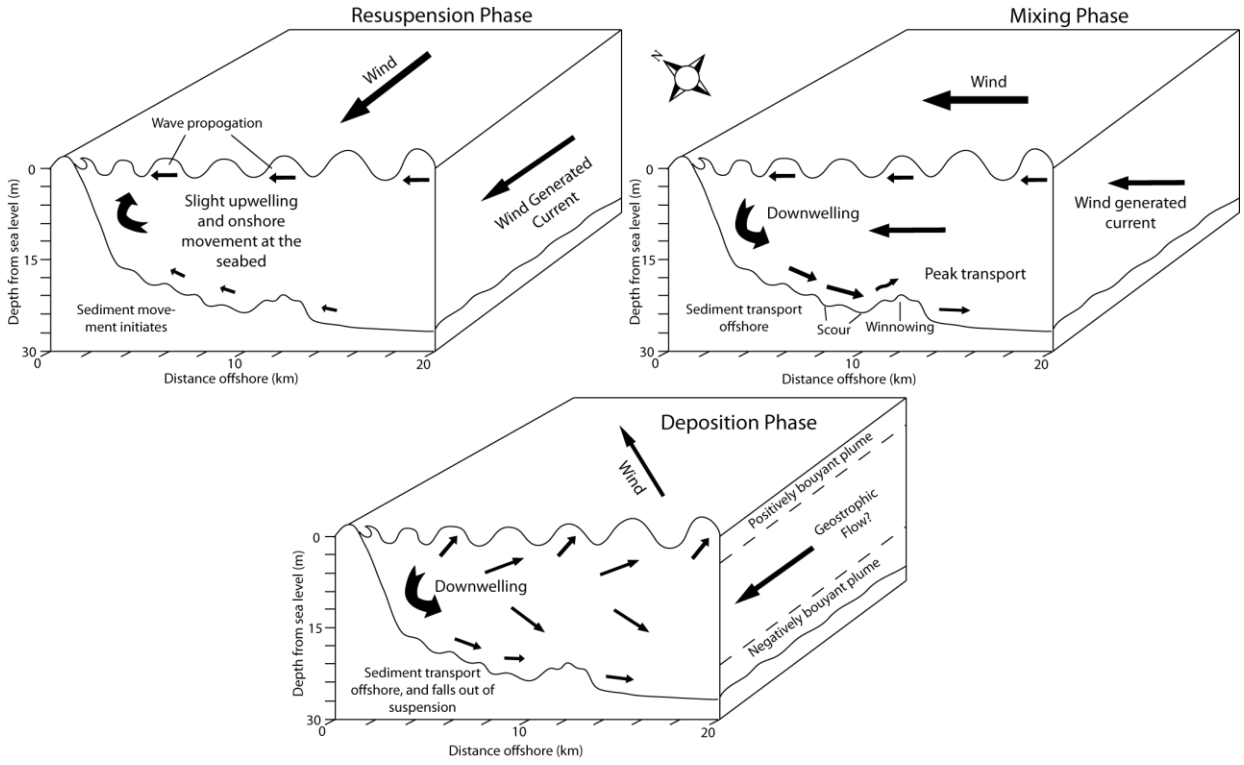

Figure 2.30. Three phases of sediment movement on the shelf before (resuspension phase), during (mixing phase) and after (deposition phase) hurricane landfall. The small vectors directly below the wave crests indicate wave direction. Modified from Wright (1995) and Swift et al. (1983).

The peak current during pre-landfall and relaxing of the current speed during landfall indicated that hurricane-induced flow is somewhat like a semi-diurnal tidal signal. Water level sets up against the coastal boundary as the storm approaches. At the peak of the storm, like peak

of high tide, the flow tends to become stagnated even though the surge is at the highest. This decrease in current speed during the peak of the storm may also be due to the forward wind speed of the hurricane relaxing as it makes landfall, due to increased friction the hurricanes would encounter over the land. A significant decrease in current speed was observed in the model over the De Soto Canyon (Fig. 2.29), and is attributed to the conservation of mass (continuity equation). Horizontal advection and vertical velocity was greatest at this time, indicating a well-mixed homogenized water column. This idea of a well-mixed water column is supported by Mitchell, et al. (2005)'s observations of current velocities on the outer shelf. At this point, downwelling began to initiate as surface flow was directed onshore and bottom flow offshore. Also, winds rotate faster than currents, ultimately slowing them after the hurricane passes (Mitchell et al., 2005). The rotation of the surface currents to the east and offshore is due to Ekman transport (Wright, 1995).

Studies have indicated that transport peaks at the peak of the storm (Li et al., 1997) and during the ebb-surge (Bentley et al., 2002). The highest values of RI, in particular during the landfall of both storms, support this idea, and the flow direction of bottom currents at this time would indicate an offshore, south-west to south-southwest dominant transport direction, part of the ebb-surge or geostrophic flow.

2.4.3 Post-Hurricane: "Deposition Phase"

Presence of the plume in red channel satellite images indicates that the plume is primarily comprised of particulate matter. The plume may not be entirely sediment-laden; however it appears to be dominated by it. Brownish areas may indicate tannins and organics transported from the bay. Stone et al. (2005) indicates that some algal blooms may exist along the edges of the plume. The bright white/light brown material that comprises the majority of the plume is

interpreted as predominately sediment, from its presence in red channel images (Fig. 2.15). The clear dark areas immediately seaward of the bays are interpreted as freshwater during the ebb-induced return flow associated with storm surge.

While the computed RI decreased substantially, solid material remained in suspension in the study area, as confirmed by the satellite imagery, indicating the presence of fine-grained material than sand. A correlation of RI to reflectance in Booth et al. (2000) and Miller et al. (2005) indicate that material in the plume they detected in satellite images was from the bottom of Lake Pontchartrain. The lack of this correlation in this study, along with the low correlation with wind speed, indicates that wind speeds, wave heights, and therefore RI, has returned to more fair-weather magnitudes at this time. Therefore, material in the plume is most likely being expunged from the bays, with less than 0.1 % of the material in the plume originating from the shelf. However, Walker and Hammack (2000) argue that 75-80 % of the plume visible in satellite imagery post-cold front storms on the Louisiana shelf is from resuspension on the inner shelf, and not material from the rivers. They argued that the sediment in the plume could not travel as far offshore as it did with the current speed measured during that time. They also argued that the plume's alignment with the isobaths indicated resuspension, as material from the river would not occupy such a wide space of the shelf and terminate along the 15 m isobath. While the water depth in the Louisiana study was similar to the Florida shelf, the majority of sediment on the Louisiana shelf was fine-grained material, which would stay in suspension much longer than that of the sand that dominates the northeast GoM. Also, the adherence of the plume to a particular isobath, the -15 m on the Louisiana shelf post-cold front, or the shelf edge post-hurricane in the northeast GoM would more likely be due to a steeper slope in bathymetry causing a significant decrease in wave-bottom interaction, current speed and bottom shear stress.

The sediment would rapidly fall out of suspension in this case. Finally, a mechanism is needed for bringing the sediment from the seafloor to the surface, or at least the top meter of the ocean surface, in order for material from the shelf to be visible in satellite imagery. The most probable cause would be strong mixing and currents in the z-direction (vertical). While mixing does occur, it is primarily during the peak of the storm (phase 2), and even then magnitudes of vertical velocity of currents are relatively low (maximum = 0.01 m/s) in comparison to velocity in the u and v directions. Given a settling velocity of approximately 0.15 m/s of the average grain size in this region (based on measurements from Baba and Komar (1981)), sand in suspension from the shelf would settle out much faster than the rate at which it was resuspended.

This is apparent in the plume observed in the MODIS imagery post-hurricanes. From these images, sediment sinks can be inferred from the behavior of the plume. The DeSoto Canyon, the upper slope, and the point off Apalachicola all indicate potential sinks for sediment.

One exception may indicate that an estimate of less than 0.1% of material in the plume of the shelf is a low estimate. The calculated resuspension intensity is only from shear stress due to waves. Many studies have shown the importance of combined wave-current flow in sediment transport (Grant and Madsen, 1979; Grant and Madsen, 1986; Snedden et al., 1988; Drake et al., 1992; Wiberg, 2000), however shear stress due to currents is difficult to calculate due to the variability in roughness coefficients. Furthermore, the combination of shear stresses is not linear and cannot simply be combined (Li et al., 1997). Li et al. (1997) concluded that shear stress due to currents would only impact the total combined shear stress by as much as 20 % if the ratio of wave shear stress to current shear stress approximated 1. If either wave shear stress or current shear stress was much higher or lower than the other, the effect on total shear stress would be less than 5 %. In addition, the angle between wave and current direction must be taken into

account, and often the result is less of an effect on total shear stress, unless the currents and waves are completely aligned or completely against each other. Given that the peak current speed occurs in the study area are out of phase with significant wave heights and peak wave period, the influence of current shear stress during storms should be significantly less, as when current shear stress is high, wave shear stress is not, and when wave shear stress is high, current is not. Finally, bottom currents are nearly opposite to wave direction, post-hurricane, when the ratio shear stresses might be closer to one, indicating less effect from current shear stress.

After 12 – 18 hrs, the inner shelf energy dissipation pattern returns back to fair-weather magnitudes and high shear stress is observed near the coast/beach, particularly during Dennis. The rapid dissipation of energy is attributed to the rapid decrease in wind speed when the hurricane makes landfall. Warm waters are not available along the shelf to fuel the hurricane, plus coastal friction decreases wind speed. The elevated shear stresses along the coast during post-Dennis are attributed to the elevated wind speeds due to the hurricane's trajectory to the north-northwest. This maintains high winds along the right side of the hurricane, concentrated over one area for a longer period of time.

The eastern transect retains elevated stress values for a prolonged period compared to a sharp drop on the western transect for both hurricanes (Figs. 2.22, 2.23). The reason for Dennis is likely due to the location of landfall and the weaker left side of the hurricane being observed along the western transect of the study area. A plausible reason for the decrease in stress, simulated for Ivan may be due to the north-eastward trajectory after landfall (Fig. 2.2). Wind stress was elevated along the eastern portion of the transect directing the flow and dominant wave direction to the east. Also, pre-landfall funneling of wave energy would cause sudden dissipation that likely resulted in lower shear stresses of the western transect.

During this post-landfall deposition phase, direction becomes more important than magnitude in terms of wave field and coastal currents. Flow is especially complex during this time and exhibits increasingly more downwelling along with Ekman veering. Surface flow moves to the east, in concert with wind and wave direction, and supports the time series satellite images during Ivan (Fig. 2.9) that indicate movement of the plume to the east. The north wind during post-Dennis indicates that material in the Dennis plume did not migrate along the coast as much as that during Ivan, as seen in the time series of images. This surface plume is interpreted as the positively buoyant, hypopycnal plume. The mid-depth flow simulated in the model is interpreted as a geostrophic flow that develops along the mid-outer shelf post-storm. Geostrophic flows have been recognized in shelf deposits due to pressure gradients from the set up of sea level during storms (Snedden et al., 1988; Snedden and Nummedal, 1991; Siringan and Anderson, 1994). Geostrophic flow that develops during the landfall and/or post-landfall of the hurricane may be the primary factor driving downwelling and sediment transport offshore towards the DeSoto Canyon. Frictional forces along the seafloor cause the flow to turn to the left, relative to the direction of the flow, creating offshore transport (Swift, 1985). However, it is difficult to say conclusively from the data presented here that tropical cyclone transport is a result of geostrophic flow or storm ebb-surge, even though current vectors in the middle of the water column are dominated by flow to the west, nearly 180 degrees opposite of the surface flow. The bottom offshore flow is the negatively buoyant, hyperpycnal plume. This flow is likely still laden with sediment entrained from the storm. This tripartite flow scheme supports the model proposed by Snedden et al. (1991), Nittrouer and Wright (1994), and Wright (1995), and reproduced in Figure 2.28c. An event characterized by three distinct transport phases is also

further substantiated by depositional sequences of storm surge deposits interpreted in Bonaire by Spiske and Jaffe (2009).

The RI calculations for both Ivan and Dennis indicate that the time period for sediment movement is approximately 42 hours for a category 3 hurricane. However, many studies have indicated that while waves cause sediment motion, currents play the role of an actual transport carrier (Keen and Glenn, 2002). With this in mind, sediment movement, may last longer than 42 hours especially that of finer grained material than sand. The results of this study indicate that large storms, such as Ivan, have the capability of moving much sediment on the shelf during the peak of the storm, but also moving a tremendous amount of sediment from the bays offshore, in suspension. However, the mechanism of transport on the shelf is not clear: the results of the RI calculations show that there is clearly some suspended transport of material; however it is uncertain what depth it is suspended to, due to the relatively small vertical velocity component. In addition, much of the sediment on the shelf is likely transported along the bottom, in either sheet flow conditions (Trembanis et al., 2004) or episodic pulses of bedload transport (Spiske and Jaffe, 2009). Very little is understood by way of distinguishing types of transport during storms (Li et al., 1997), especially in the study area, and more research is required for a more accurate description and quantification of transport types. De Soto Canyon acts as an efficient drain for hurricane-induced surge and sediment in suspension from the inner shelf and material is being worked further offshore than the inner shelf. Smaller storms may have significant potential to move sediment on the shelf bottom, however sediment in the plume may settle out on the outer reaches of the shelf.

2.5 Summary

Results from a suite of wave, hydrodynamic and sediment resuspension models indicate that significant amounts of sediment were resuspended on the inner shelf, particularly on bathymetric highs such as shoals and ridges, during high-energy storm events such as tropical cyclones. Long period waves arriving days ahead of the storm facilitate an environment for increasing RI with increasing wave height and energy. Resuspension potential was generated on the entire inner shelf and extended to depths of 100 m and persisted for several days following landfall of the hurricanes. The head of the De Soto Canyon was consistently the lowest values of RI, indicating sediment is being winnowed off the shoal and deposited farther offshore.

These model results were confirmed by true color satellite images and measured reflectance values from the red channel. However, satellite imagery indicated that the suspended material plume persisted several days after RI decreased when deposition began to occur, indicating that much of the surface plume sediment is not derived from the shelf, but most likely finer grained material from the bays. Peak current flow occurs several hours before hurricane landfall, during which the current becomes completely wind-dominated. Flow and sediment movement during the approach, landfall and aftermath of a hurricane can be broken into three phases: the resuspension phase, mixing phase, and deposition phase. Significant downwelling occurs during the mixing and deposition phases. Flow vectors indicate movement of the plume and possibly bottom sediment further offshore than most of the inner shelf.

CHAPTER 3. STRATIGRAPHY, SEDIMENTOLOGY AND GEOMORPHOLOGY OF AN INNER SHELF, NORTHEASTERN GULF OF MEXICO

3.1 Introduction

The northeastern GoM is a tectonically stable region, experiencing a relatively slow, almost stable rate, of sea level rise in comparison to the most recent transgression (Donoghue et al., 2003). This stability has created an excellent natural laboratory for the study of sediment and stratigraphy since the last glacial period and lowstand. In fact, many studies (i.e. Donoghue, 1992; Sydow and Roberts, 1994; Fleischer et al., 1996; McBride et al., 1999) have been conducted offshore around Apalachicola and eastern Louisiana, Mississippi and Alabama. However, few comprehensive studies exist detailing the stratigraphic framework of the western Florida Panhandle, west of Apalachicola, and those that do exist are not well dated (Hyne and Goodell, 1967) or lack core data (Ludwick, 1964; Doyle and Sparks, 1980; Locker and Doyle, 1992). New technology in seismic surveys and coring methods are available now that allow for more precise and accurate scientific analysis. A study of this kind would be significant in closing an "information gap" of the geology of the shelf in this region. In addition, results from such a study would be useful to many entities, including local and state environmental and coastal organizations and communities involved with borrowing offshore sand resources for replenishing beaches. Understanding the geology of shelf sheet sands would also serve as a modern analog to ancient sheet sands and oil sands, benefiting the oil and gas industry and exploration (Mancini, 2008). Finally, knowledge of bottom sediments and geomorphology is essential for understanding the effect of physical processes that affect this region, in particular sediment transport.

Given previous studies from the region, especially sea-level studies in the GoM, the inner shelf off the Florida Panhandle should reflect the last major lowstand followed by a major transgression and then a decrease in the rate of sea level rise. The stability of the region in the past few thousand years would allow for modern hydrodynamic processes to take over and further rework this sediment and possibly modify the upper stratigraphy. The purpose of this portion of the study is to examine the late Quaternary (approximately, the last glacial lowstand to present day sea level) stratigraphy, sedimentological and bathymetric expression on the inner shelf offshore of the western Florida Panhandle.

Specific objectives of this portion of the study include: 1) to identify the stratigraphic components and environmental interpretation of the late Quaternary on the inner shelf, 2) to identify the Pleistocene contact and Holocene reworked material, 3) to determine the bathymetric expression of the seafloor and its stability in the modern system, and 4) to apply a conceptual model of the history of the inner shelf over the late Quaternary.

3.2 Previous Work

While many studies have examined the sediments and sub-bottom stratigraphy of the northeastern GoM, there are still details lacking in discrete areas across the shelf (see Table 3.1). One of these regions is offshore Choctawhatchee Bay, on the western Florida Panhandle (Figs. 1.2, 3.1). Many studies in the region have been large regional studies of the geology comprising the shelf (Ludwick, 1964; Doyle and Sparks, 1980; Mazzullo and Bates, 1985; Locker et al., 1988; Locker and Doyle, 1992; Koch, 2006), and therefore have not been able to focus on the detail required to determine short term changes to the shelf geology. Many studies of the region are also now dated, using more obsolete methods and less precise techniques (Ludwick, 1964; Hyne and Goodell, 1967; Doyle and Sparks, 1980). Other studies lack core detail or age

constraints (Locker and Doyle, 1992). Table 3.1 summarizes the major geologic studies, dates, locations, and type of data collected, including this study.

Table 3.1. Summary of major studies within the northeastern GOM, the published date of the study, approximate location, and type of data collected.

Study	Year	Location	Data Collected
Ludwick	1964	Along and across shelf transects off Chandeleur Is., MS Sound, Mobile Bay, Choctawhatchee Bay, and St. Vincent Is.	Surface samples and gravity cores
Hyne and Goodell	1967	Inner-mid shelf off Choctawhatchee Bay	Seismic and short cores
Doyle and Sparks	1980	Mid-outer shelf off Mobile Bay, St. Andrew Bay and Cape San Blas	Surface and water samples
Mazzullo and Bates	1985	Shelf off MS to St. Andrew Bay	Surface grab samples
Kindinger	1988	Shelf off MS to birdsfoot delta	Seismic
Otvos	1988	Barrier/nearshore/inner shelf off MS, AL, and NW FL	drill samples
Donoghue	1989	Nearshore/inner shelf off St. Andrew Bay to St. Georges Sound	Vibracores and seimic
Locker and Doyle; Locker et al.	1988, 1992	Shelf off Perdido Bay to St. Andrew Bay	Seismic, side scan sonar, surface grab samples, and well data
McBride and Byrnes; McBride; McBride et al.	1995, 1997, 1999, 2004	Shelf off Mobile Bay to Pensacola Bay	Vibracores, surface grab samples
Bart and Anderson	2004	Mid-outer shelf off Mobile Bay to Choctawhatchee Bay	Seismic
Gardner et al.	2005	Outer shelf off Choctawhatchee Bay to St. Andrew Bay	Multibeam echosounder
Koch	2006	Inner-mid shelf in transects off Pensacola, Choctawhatchee, St. Andrew, Bays, with detail offshore Apalachicola Bay	Seismic and vibracores
This study	2010	Nearshore and inner shelf off Choctawhatchee Bay	Vibracores, shallow high resolution seismic, bathymetry

3.2.1 Geologic Framework

The Quaternary history of the northern GoM includes a complexity of sea-level change during the last glacial and interglacial events which have been recorded in the stratigraphic structure of the continental shelf. A shelf-wide early Wisconsinan erosional unconformity characterizes the northern GoM during a sea level drop below the shelf edge (Kindinger, 1988). Anderson et al. (2004) describes this time period, from approximately 120 ka to 70 ka (where ka is 1,000 years ago) as the Early Highstand. Below this, the northern GoM and much of Florida, Alabama and Missisippi are underlain by Miocene sediments, and in some places Pliocene limestone and calcarenites that were severely eroded during Wisconsinan glaciations (Schnable and Goodell, 1968; Donoghue, 1992). The northeastern GoM has been described as tectonically stable since Pamlico (Sangamon, Oxygen Isotope Stage (OIS) 3 to 5 (Fullerton, 1997)) time by Doering (1956), however, some studies acknowledge the occurrence of subsidence of sediment and the possibility of isostatic readjustment due to the weight of advancing seas since the last glaciation (Schnable and Goodell, 1968). From approximately 70 ka to 22 ka, sea level fell then rose rapidly, then fell again during the last glacial, referred to as the Late Highstand 'Falling Stage' (Anderson et al., 2004). It was during this time period that deposition of many shelf-edge deltas began, allowing the deltas to become quite large, despite the short lowstand (Sydow and Roberts, 1994; Roberts et al., 2004).

During the last glacial period (Late Wisconsinan), rivers along the northern GoM incised deep valleys on the inner and mid shelf, debouching a large amount of sediment on the outer shelf and facilitating the formation of shelf-edge deltas (Curray, 1964; Mazzullo and Bates, 1985). Sea level dropped approximately 120 m to the shelf break and a sequence boundary is documented across the northern Gulf during this lowstand, approximately 22 ka (Anderson et al.,

2004). Incised valleys are well documented from the Mississippi and Pearl rivers (Kindinger, 1988; Sydow and Roberts, 1994), the Choctawhatchee River (Hyne and Goodell, 1967; Locker et al., 1988), and Apalachicola River (Schnable and Goodell, 1968; Donoghue, 1992; McKeown et al., 2004) (Fig. 3.1). Shelf-edge deltas have also been documented along the outer shelf in the northeastern GoM (Kindinger, 1988; Sydow and Roberts, 1994; Winn et al., 1998; Bart and Anderson, 2004; Gardner et al., 2005).

The post-glacial rise of sea level caused a major transgression during the early to mid-Holocene in the GoM, approximately 16 ka to 4 ka (Anderson et al., 2004). The vast amount of sediment deposited on the outer shelf during the Late Pleistocene lowstand was subsequently reworked and deposited on the inner shelf as a major sheet sand, one of the most dominant stratigraphic features in the region, known as the Mississippi Alabama and Florida (MAFLA) sand sheet (Ludwick, 1964; Doyle and Sparks, 1980; McBride, 1997; McBride et al., 1999; McBride et al., 2004). The rapid rise in sea level during most of the Holocene drowned the river valleys incised during the lowstand and forming the estuaries seen along the Gulf coast today. As sea level rose, at least one, possibly more, still stands are documented by offshore shoals and bars on the inner shelf, in particular, offshore Perdido and Pensacola bays (McBride, 1997; McBride et al., 1999), Choctawhatchee Bay (Hyne and Goodell, 1967), and Apalachicola Bay (Gunter, 1931; Schnable and Goodell, 1968; Koch, 2006).

Post stillstand, a slower rate of sea-level rise is proposed (McFarlan, 1961a; Coleman and Smith, 1964; Schnable and Goodell, 1968) since the past 6 to 3 ka. This slower rate has allowed the modern coastal system of coastal estuaries and barrier islands to form (Stapor, 1973; Donoghue and Tanner, 1992), and in particular, the sediment-starved, flooded shelf that characterizes the northeastern GoM today. Anderson et al. (2004) refers to this as the Late

Holocene Highstand and suggests that a condensed section is forming, the maximum flooding surface, particularly in the estuaries along the coast.

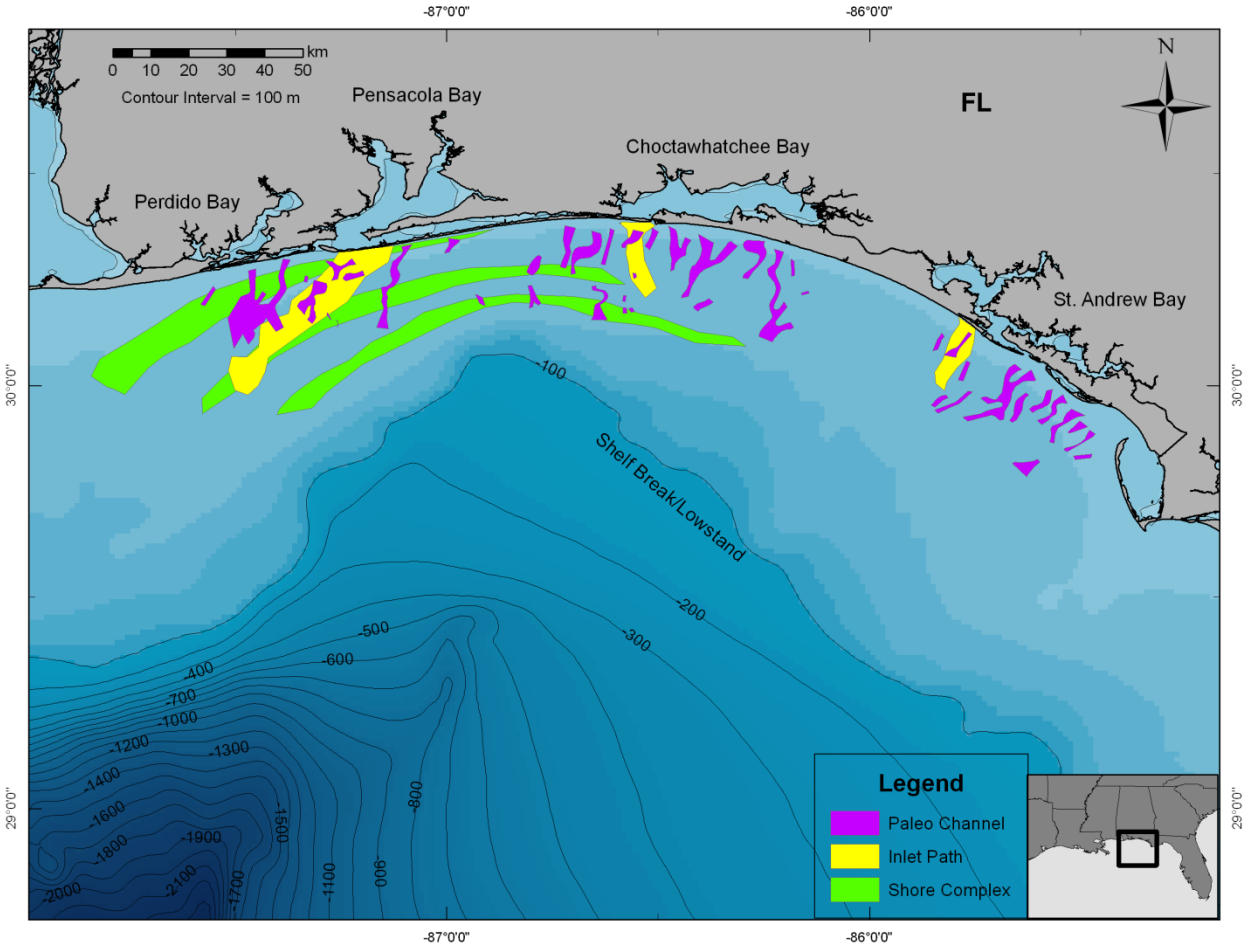

Figure 3.1. Relict features on the northwest Florida shelf from the last glacial period. Created with http://ross.urs-tally.com/Default.aspx.

3.2.2 Stratigraphy and Sedimentology

Previous studies of the northeastern GoM have been abundant in seismic collection (Locker et al., 1988; Locker and Doyle, 1992) and sediment surface samples (Ludwick, 1964; Doyle and Sparks, 1980; Mazzullo and Bates, 1985) (See Table 3.1). Many studies have also documented the late Quaternary stratigraphy adjacent to the study area. McBride et al. (1999; 2004) examined the late Quaternary stratigraphy in detail offshore Mobile, Perdido and

Pensacola Bay, via vibracores, bathymetric data, macro-, and microfauna, and formed the foundation for this research. The study described six facies and three surfaces based on sedimentology, paleontology and radiocarbon dates, essentially documenting the falling stage systems tract of the late Pleistocene to the modern Holocene seafloor. Donoghue (1992) describes the Miocene to Holocene seismic stratigraphy of Apalachicola but primarily groups the Pleistocene and Holocene stratigraphy together as undifferentiated sands and the Citronelle Formation. Locker et al. (1988) and Locker and Doyle (1992) investigated the Neogene to recent shelf/slope geology of the northwestern Florida shelf, but delineated basic seismic packages with no detail of the thin Holocene sediments. Otvos (1988) focused on detailed Neogene to recent stratigraphy along the coast of the northeastern GoM. Koch (2006) determined the top of the Intracoastal (Pliocene/Miocene) Formation via three cores and seismic lines on the inner shelf off Choctawhatchee Bay. Hyne and Goodell (1967) described the sedimentology of the inner shelf and shoal off Choctawhatchee Bay and the geologic history based on shallow cores (see Table 3.1 for more details of these studies).

The sediments are dominated by the transgressive, predominately quartz, sand sheet and therefore are a product of transport and reworking during sea-level rise. Most of the sediment from the Choctawhatchee River is deposited in the bay. Therefore, sediment on the shelf is relict from the lowstand, and is very mature quartz sand (Mazzullo and Bates, 1985). Quartz sand grains of the eastern Gulf tend to be more elongate and angular, indicating a source provenance in the lower Appalachian Mountains (Mazzullo and Bates, 1985). Heavy mineral assemblages of the sand offshore are also characteristic of Appalachian origins (Van Andel and Poole, 1960). In addition, a kaolinite suite dominates the clay fraction and also suggests material from the Appalachians, as the Mississippi River is dominated by an illite-montmorillonite suite of clays

(Hyne and Goodell, 1967; Schnable and Goodell, 1968). These studies also suggest westward sediment transport along the northeastern GoM coast, due to the dominance of kaolinite suite of clay minerals. However, increasing illite-montmorillonite suite down-core suggests eastern transport and current direction, for short durations, in the past (Hyne and Goodell, 1967) and is substantiated by Curry (1960) in his study of the northwestern GoM. Due to the westward flow, grain size decreases from east to west along the coast of the northeastern GoM coast, while sorting increases (Koch, 2006). Mean grain size of offshore sands also decreases seaward (Ludwick, 1964).

3.2.3 Geologic Features

It is clear that the geology and geologic features of the northeastern GoM is quite complex, and can be explained as a direct response of the sea-level fluctuations previously described. The coast is characterized by four estuarine systems: Perdido Bay, Pensacola Bay, Choctawhatchee Bay and St. Andrew Bay (Figs. 1.2 and 3.2). Further to the east, the Apalachicola Embayment and Cape San Blas protrude into the Gulf, forming a concave seaward coastline (Donoghue and Tanner, 1992). While there have been numerous studies in the northern Gulf, it is acknowledged that there is considerable variability in stratigraphic architecture across the margin (Anderson et al., 2004).

The Choctawhatchee River enters Choctawhatchee Bay in the eastern-most portion of the bay (Mazzullo and Bates, 1985) where it is slowly filling in (Jackson et al., 1991). Choctawhatchee Bay is a drowned estuary and almost entirely closed from the Gulf, except via Destin East Pass, where an ebb tide delta is forming (Hyne and Goodell, 1967) (Fig. 3.2) and is frequently dredged (Rosati, J.D., personal communication). Two jetties on either side of the pass help maintain a channel (Fig. 3.3). Santa Rosa Island (approximately 84 km long and 1.5 to 1 km

wide), is an elongate barrier island in the western portion of the study area, is the largest barrier in the eastern Gulf and consists of a broad beach backed by dunes (Boone, 1973). East of Destin East Pass, a Pleistocene "headland" comprises the coast from Grayton Beach to Destin East Pass (Stone and Penland, 1992).

Beyond the beach and barriers, relict paleo-shorelines are present in both the nearshore and offshore (Koch, 2006) (Fig. 3.1). The shelf is gently sloping (<3°) and is described as a passive ramp margin (Sydow and Roberts, 1994; Bart et al., 1998; Richmond et al., 2000; Bart and Anderson, 2004; McKeown et al., 2004). Subsidence is relatively low, approximately 0.5 mm/yr (Anderson et al., 2004). In the study area, the shelf varies in width from 30 km (at the head of the DeSoto Canyon) to over 50 km to the east. Two offshore shoals are recognized in the study area (Fig. 3.4): one at approximately 25 m water depth and a smaller one at 30 m water depth, as well as numerous ridges and troughs with smaller dimensions (Hyne and Goodell, 1967).

3.3 Methods

A comprehensive geophysical and geological data set was utilized in this project, originally collected for the Department of Environmental Protection of the state of Florida for the assessment of offshore resources (borrow areas) for beach restoration. The collection of the data was done by several geophysical companies as noted in this chapter. All laboratory work and interpretations were done by the author unless otherwise noted. Because the data was collected by and for engineering firms and the state of Florida, all collection, laboratory and interpretation measurements were performed in English units (feet) and later converted to metric for this thesis. Therefore, measurements will be given in both systems for this chapter. All depths in this chapter are referenced to MLLW unless otherwise noted.

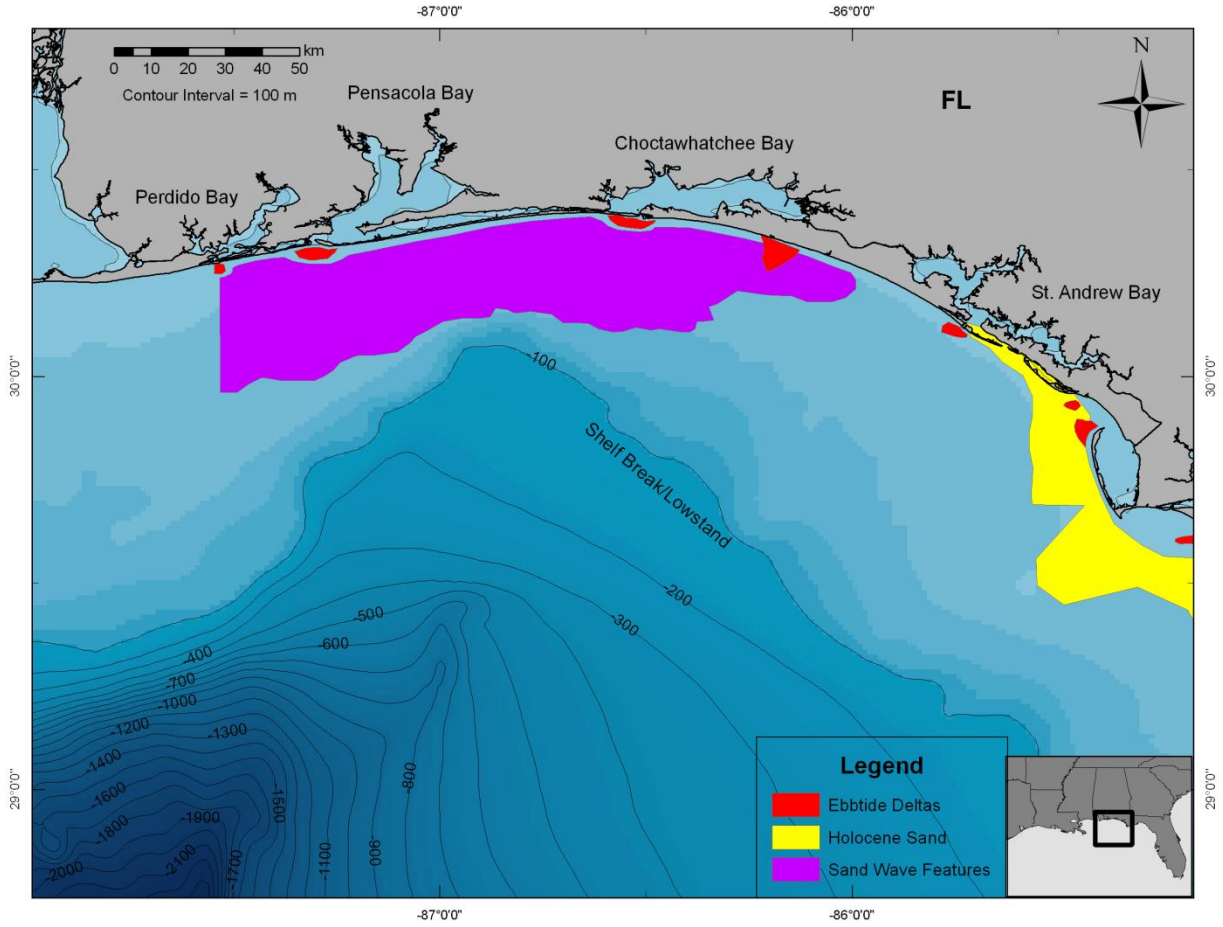

Figure 3.2. Late Pleistocene/Holocene features of the northwest Florida shelf. Created from http://ross.urs-tally.com/Default.aspx.

Figure 3.3. Rock jetty at Destin East Pass, which traps a significant amount of sand along the coast.

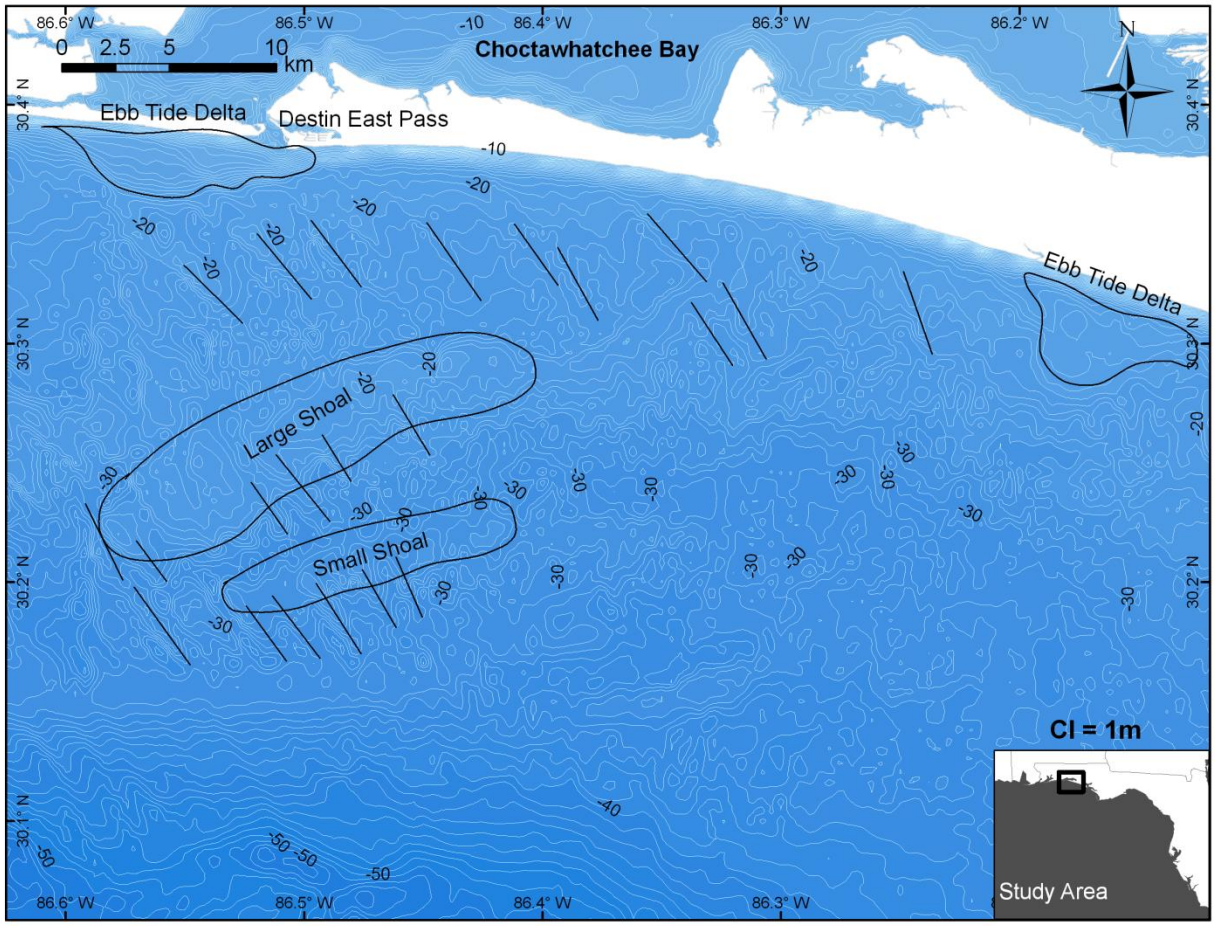

Figure 3.4. Bathymetric features in the study area. Three distinct features are recognized: two shoals on the inner to mid shelf; two ebb tide deltas, one that is still active; and small ridges and troughs on the nearshore to mid shelf. Some of the crests of the major ridges are highlighted with black lines.

3.3.1 Seismic Data

Approximately 1,100 km of sub-bottom seismic profiles were collected by Alpine Ocean Seismic, Inc., in October 2004 and Sonographics, Inc., in October 2006, covering the nearshore to inner shelf to the east and west of Destin East Pass and a large sand shoal on the shelf (Fig. 3.5). The seismic profiles were shallow, high resolution, ranging from approximately 2 – 4 m and were collected with a DataSonics CHIRP II system or an ORE Geopulse "boomer-type" profiling system. For the CHIRP data (Alpine), standard DGPS navigation input was used with Hypack Max software for generating the X-Y data from the GPS system with a reading every

150 ft. The frequency ranged from 2 – 10 kHz. Unfortunately, the navigation did not record to the .seg files, and were subsequently damaged. The data were printed directly from the logger at 5 milliseconds (ms) of two-way travel time per inch, or approximately 4 m vertical resolution. Sonograph profiles were recorded using a 125 ms sweep with bandpass filters set for .5 – 6 kHz. Navigation for the survey was provided by LORAN C. Positions were acquired every 10 minutes for the high-resolution seismic, and depth profile data. These data were also scaled for prints at 5 ms two way travel time per inch. The .segy files were not provided. Seismic data was interpreted from the unprocessed print outs for key reflectors and characteristics of major facies bounded by these reflectors. Seismic data were then correlated to vibracores and utilized in cross-sections. Selected raw and interpreted profiles are provided in Appendix D. Depths reported in this section are in meters below the seafloor and are based on a standard acoustic velocity of 1500 m/s.

3.3.2 Vibracores

Three hundred and five vibracores were collected along the nearshore and inner shelf and further offshore on the shoal (Fig. 3.6 and Appendix E, for annotated core logs). Most of the cores were approximately 6 m (~20 ft) in length, although some were a little shorter, and 7.6 cm (3 in) in diameter. The cores were collected by Alpine Ocean Seismic, Inc., on contract to Taylor Engineering Inc., to confirm the presence and quality of offshore sand resources for beach restoration. Because the coring purpose was with the intent to locate large quantities of sand viable for restoration, the core locations were somewhat skewed towards sand bodies identified from the seismic data. Coring cruises were completed by Taylor Engineering in 2002, November 2005, February 2006, September 2006, and February 2007, to calculate the volume of sand available of sufficient quality for beach restoration. Cores were split longitudinally and

photographed by Floyd De Mers, and logged for approximate lithology (gravel, sand, fines), heavy bioturbation, and presence of organics, by Drs. Baozhu Liu, Harry Roberts, and Felix Jose at the Coastal Studies Institute at LSU. Photographs and logs from 258 cores (Appendix E) were later analyzed in more detail by the author to identify all possible structures, such as bedding and laminations, and material type. Selected annotated core photographs and logs are available in Appendix E. Stratigraphic columns were interpreted and the core depths were corrected for MLLW. Correlations were made in strike and dip cross sections, and compared to seismic and radiocarbon ages for interpretation of facies.

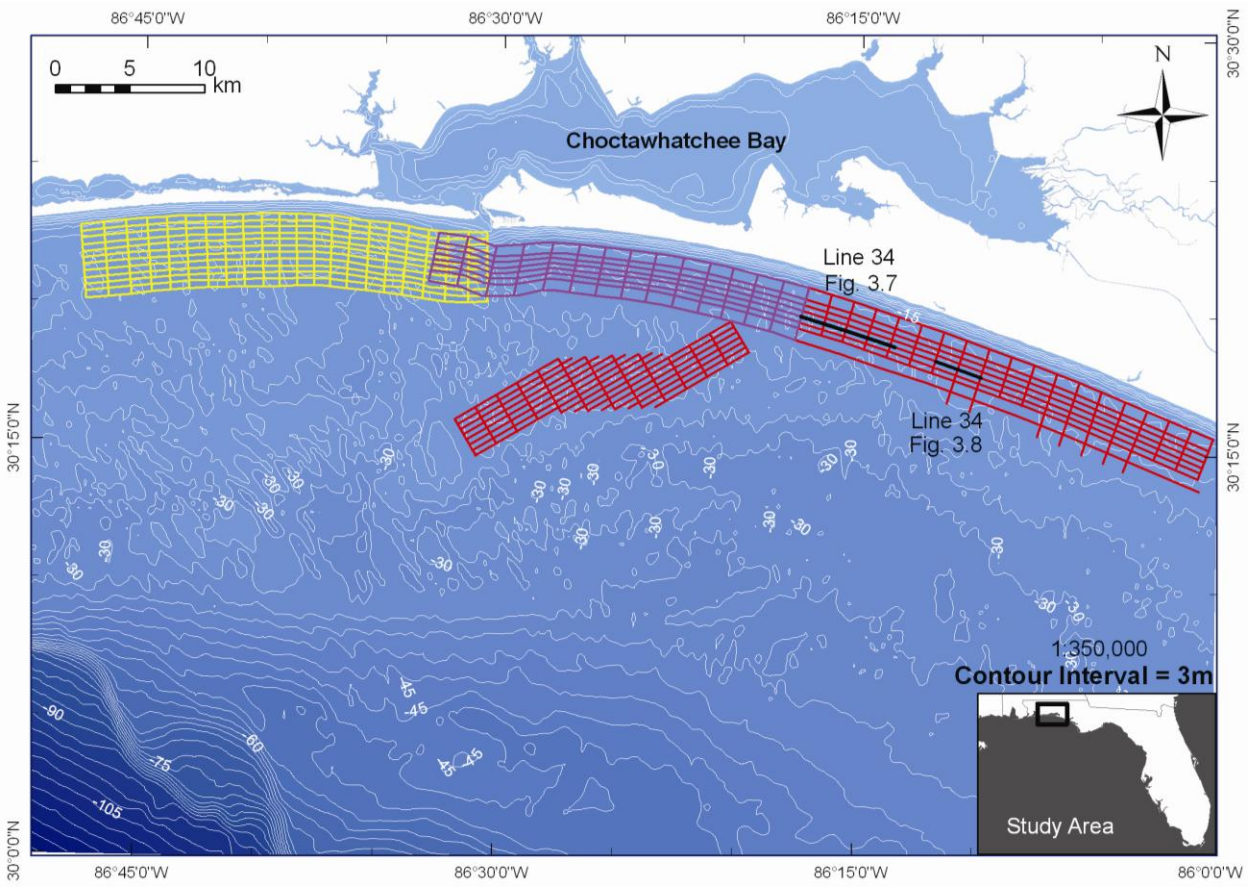

Figure 3.5. Location of seismic lines with figure numbers labeled for sections to be shown and discussed later in the chapter.

3.3.3 Bathymetry

Bathymetry data were obtained from two sources for the study: the data compiled from the NGDC website (Divins and Metzger, 2008) used in the modeling study and from the coring and seismic cruises. Bathymetry data from the NGDC Digital Elevation Model is a 3 arc-second coastal relief model that utilizes almost a century of compiled bathymetric soundings and topographic data from the USGS. Data can be downloaded in a variety of horizontal spatial resolutions, ranging from 10 minutes to 3 seconds. The horizontal resolution of the bathymetry data downloaded for this section was based on the closest approximation of the data collected that it was being compared to, for precise calculations and comparison. The data compiled for the study area covered a range of surveys dating from 1935 – 1992, with the majority of it collected in the late 1970s.

Bathymetry was collected by Alpine Ocean Seismic, Inc., in both low and medium resolution grids during the coring cruises in 2002, November 2005, February 2006, September 2006, and February 2007. Alpine also collected bathymetry data in high resolution grids during seismic surveys in September 2004, September 2005, September 2007, and November 2007. All navigation locations were collected in Florida North State Plane system. The horizontal projection was later converted to UTM, using ArcGIS software, for all data sets, including NGDC data, for coherence in horizontal datum and for later calculations of area and volumetric change due to the influence of hurricanes Ivan and Dennis. The vertical datum varied for each cruise, so all data were corrected to MLLW using VDatum (NOAA Coastal Services Center). The tracks for bathymetry surveys that were not part of the seismic or core cruises (i.e. Figures 3.5 and 3.6) are shown in Appendix C.

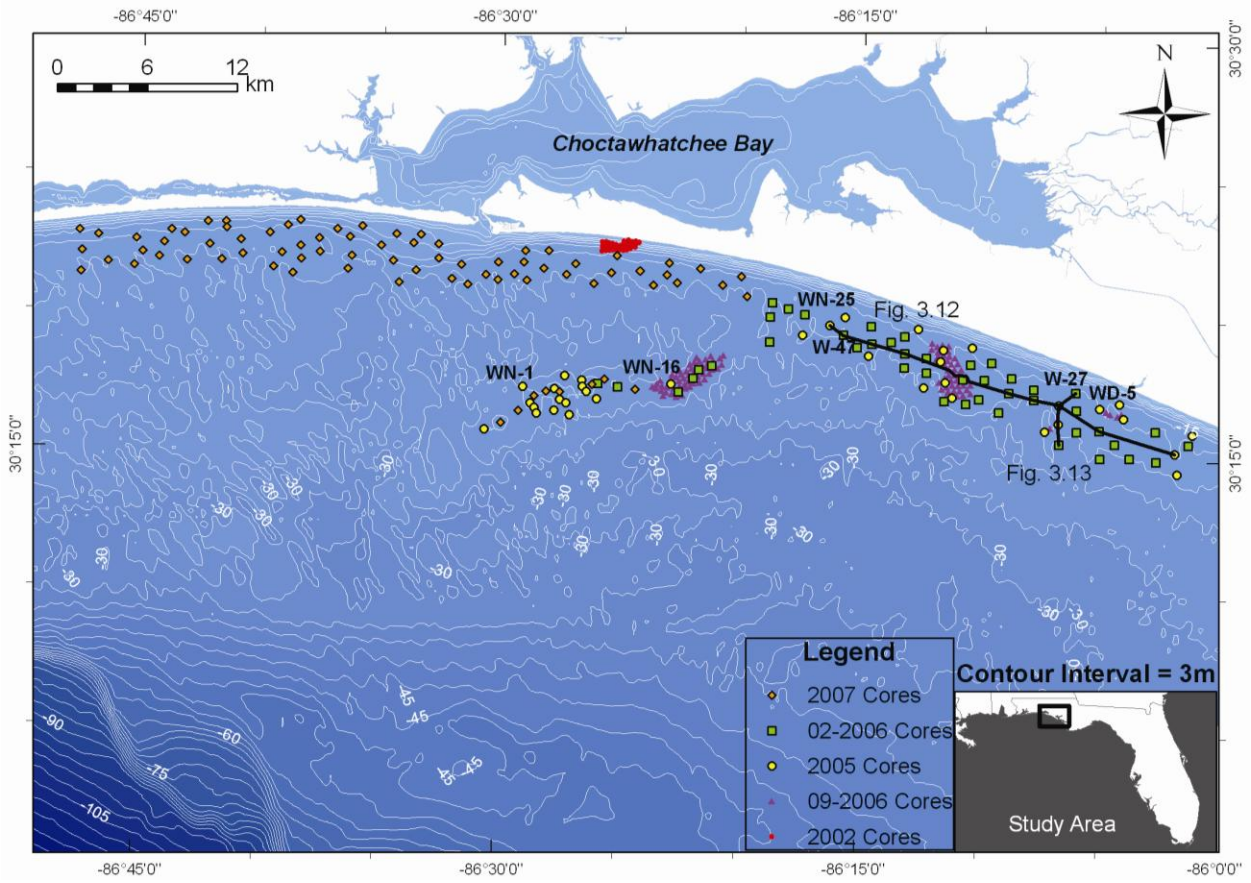

Figure 3.6. Locations of cores collected. The labeled cores indicate the location of cores, in particular those sampled for radiocarbon dating, discussed later in this chapter. Stratigraphic correlations illustrated in subsequent figures are also labeled.

The ArcGIS spatial data analysis package, from ESRI, was used to create surfaces and contours for each data set and to assess the bathymetric features generated on the shelf from high energy events occurring prior to the surveys. Data that were determined having sufficiently high enough resolution to visualize most of the morphologic features on the inner shelf were used for erosion/accretion and volumetric analysis. This analysis utilized the spatial analysis feature in ArcGIS and methods outlined in Price (2002) and Pepe and Coutu (2008). Specifically, this involved using a subtraction technique on the bathymetry data from two consecutive surveys, in the raster calculator feature, to assess depth changes, and the cut/fill feature, to assess volumetric changes, both under spatial analyst. Analyses were preformed for a longer interval (24 years)

pre- and post-Ivan, and a shorter interval (2.5 years) pre- and post-Dennis. The longer time interval utilized the NGDC and October 2004 data sets, immediately following Hurricane Ivan, and the shorter interval utilized the October 2004 and November 2007 data sets, post-Dennis.

3.3.4 Granulometry

Granulometric analysis was performed at the Coastal Studies Institute at LSU by the author, Drs. Felix Jose, Baozhu Liu, Daijiro Kobashi, Yixin Luo, and Yuliang Chen. Vibracores were sampled at 46 cm intervals (1.5 ft) for granulometric analysis to obtain a quantitative assessment of the lithologic changes in the cores. This also provided accurate and up-to-date data with sufficient spatial resolution as input for the models discussed in the previous chapter (2). Cores or sections of cores that were predominantly fine-grained (>4.0 phi) upon visual inspection were not sampled. Thus, sampling often did not extend all the way to the base of the core. Approximately 20 g of sediment were used in each sample for the sieving process. Samples were washed to remove any salts, dried overnight in a low temperature oven (approximately 40°C), and the large shell fraction (>2 mm) was weighed and removed to avoid skewing the particle size distribution (Ellis and Stone, 2006). Dry sieving was accomplished using 0.25 phi intervals with the GilSonic AutoSiever™ in accordance with methods outlined in Ellis and Stone (2006). This technique was chosen because the samples of interest (for beach restoration) were largely free of clay and silt (Folk, 1980). The GilSonic AutoSiever™ combines three different motions that provide rapid and accurate grain size results (Gilson, 1992). Acrylic sieves of 7.6 cm (3 in) were used in sets of seven, running the sample through the siever a total of three times per sample. Sieve mesh ranged in size from 0 to 4 phi. All sets were run for 2.5 minutes each. Sieves were brushed and cleaned daily with an ultrasonic bath to prevent accumulation of lodged grains in the mesh.

Grain size statistics were calculated using the graphic method as defined by Folk and Ward (1957), using the MicroCal™ Origin software package that allows weights by sieve to be directly imported to into a spread sheet. Initial sieve weight, final sieve weight, sample weight, weight percent and cumulative weight percent per sieve interval and saved in a text file, while a graph of weight percent versus cumulative weight percent are automatically generated for each sample. Mean phi, sorting, skewness, and kurtosis are also calculated using Folk and Ward method (1957). This method was selected over other methods (i.e. Inman, moments) to allow comparisons of results with previous studies in the northern Gulf of Mexico. Additionally, if small errors associated with the sieves or methods were present, the resulting statistical output would still be valid if the graphic methods were used (Folk, 1980). All calculations were done in phi (φ) and millimeters (mm), with phi being used primarily, except for the sediment size data used in the previous chapter (2) for the numerical modeling. Mean grain size data from all cores are provided in Appendix F.

Mean grain sizes for all surface samples were compiled for input to the models in Chapter 2. Mean grains of surface samples were also used to map the size distribution of surficial sediments for major sand size divisions (0.5 and 0.1 phi increments). Where cores were not sampled due to surface sediments being too fine, a value of 4.0 phi was arbitrarily assigned for mapping, to indicate areas of fine grained material.

In order to assess how much calcium carbonate was present in the samples, three cores were chosen for traditional acid digestion test. A "representative" sample was created by taking samples from the top of selected cores, down to 3.6 or 4.5 m (12-15 ft) core depth, dried and weighed. Five hundred mL beakers were filled with the dried sediment and hydrochloric (HCl) acid (10 %) and left on a shaker for two days. The samples were then triple washed to remove

any remaining solubles, dried, and weighed. The results of the analysis are provided in Table 3.2.

Table 3.2. Percentage of carbonate content in selected cores.

Sample	Sample Wt (g)	Final Wt (g)	% Carbonate
WA-10	96.4	94.292	2.186721992
WA-38	40.311	38.821	3.696261566
WA-43	37.44	35.691	4.671474359

3.3.5 Radiocarbon Dating

To accurately establish the beginning of the Holocene and/or the end of the Pleistocene (roughly, the end of the lowstand or beginning of the highstand) with hard dates, radiocarbon (^{14}C) dating techniques were utilized. Many of the cores, particularly the bottom portions, contained extensive deposits of peat, organics and organic-mixed sediments, and woody fragments, some of which were excellent samples for radiocarbon dating. Sixty samples of wood and peat were extracted from 45 different cores, and stored in a cool, dark location. From these samples, five peat samples (see Table 3.3) were chosen from two different cores, one on the nearshore, and one on the shoal (Fig. 3.6) to be sent to BETA Analytic, Inc., to be dated. The samples were chosen based on location, multiple samples down core, and the presence of peat and absence of wood. Peat was chosen over other materials present to be dated because basal peats have been proven to be suitable in use for sea-level indicators (Gould and McFarlan, 1959; McFarlan, 1961b; Tornqvist et al., 2004). In addition, samples at considerable depth were chosen in order to avoid the surface mixed layer. The rationale of this approach is that a widespread peat deposit would be *in situ*, particularly if found within a back lagoon-type environment, overlies a relatively consolidated (commonly Pleistocene) basement experiencing negligible compaction, and can be related to the paleo-(ground)water level, which is assumed to

be closely related to mean-sea level (Tornqvist et al., 2004). Wood was rejected because rootlets may contaminate the sample with younger dates, while shell was rejected due to the possibility of recrystallization.

Accelerated Mass Spectrometer (AMS) technique was used for low carbon/bulk sediment samples, commonly used with peat. Samples were sent to BETA for pretreatment and all were washed with acid. Calibration of the ^{14}C data to calendar years was performed with the INTCAL04 database (INTCAL04, 2004). The 2-sigma (95 % probability) and 1-sigma (68 % probability) results were calculated (Talma and Vogel, 1993) for results less than 20,000 ^{14}C years BP. These results were then compared to radiocarbon results from Hyne and Goodell (1967) and Koch (2006), the only other dates published in this region (Table 3.3).

Stable carbon isotopes ($^{13}C/^{12}C$) were also measured at BETA and their ratio was calculated (Table 3.4). A serious limitation of basal peats as sea-level indicators is the difficulty to interpret their environment of deposition and establish their dates with respect to sea-level (Tornqvist et al., 2004). Stable carbon isotope ratios ($\delta^{13}C$) have been proven to be extremely useful in estimating the salinity regime of vegetation and sediments in modern Mississippi Delta wetlands (Chmura et al., 1987), and is therefore used in this study to determine the relative location of samples in relation to sea-level.

3.4 Results

3.4.1 Seismic Facies

Four facies are distinguishable in the seismic based on acoustic signature and bounding surfaces. Selected annotated profiles are provided in Appendix D.

3.4.1.1 Facies D

Facies D (Fig. 3.7) is relatively clear and featureless, containing almost no reflections in the profiles and is therefore acoustically impenetrable. The bottom of Facies D is obscured by the seafloor multiple, but generally at least 12 m or more is present in the profiles. However, Facies D is generally absent where Facies C is present. This facies is correlated to AE3 from Locker and Doyle (1992) (Table 3.5).

Table 3.3. Radiocarbon ages from sediment cores extracted from this study, compared to ages from Hyne and Goodell (1967), and Koch (2006).

Study	Sample	Core Depth (m)	Total Depth (m)	Material	Radiocarbon Age (yrs BP)	Horizontal Error (+/- yrs BP)
Hyne and Goodell (1967)	19	0.24	21.54	clastic limestone fragment	22042	200
Hyne and Goodell (1967)	10	0.36	21.66	shells, *Macrocallista maculata*	4918	200
Hyne and Goodell (1967)	10	0.36	21.66	fragmented calcareous skeletal material	6000	200
Koch (2006)	PC1A	4.66	18.891	organic sediment	37470	1060
Koch (2006)	EP1A	3.72	26.891	Wood - rootlet	46850	1500
Koch (2006)	SR3A	3.72	31.9998	Wood - stem or branch	38370	760
This Study	W-16A	4.801	25.5274	peat, woody material removed, some burrowing	18400	100
This Study	W-16B	5.486	26.2124	peat, woody material removed, some burrowing	19560	100
This Study	W-27A	4.572	25.87752	pure peat, slightly oxidized	25290	160
This Study	W-27B	5.004	26.30952	pure peat, slightly oxidized	27560	170
This Study	W-27C	5.486	26.79152	pure peat, slightly oxidized	29150	240

3.4.1.2 Surface 1

Surface 1 (Fig. 3.7) is a discontinuous reflection above Facies D. It most commonly occurs where Facies A is missing from the profile. Where it does occur, it is slightly irregular or is the outer-most surface of large channels. The depth to Surface 1 is quite variable: generally on the order of 10 m or greater. This surface is correlated to BD in the eastern region of the Locker and Doyle (1992) study and C of the northwest Florida shelf region of their study. Kindinger (1988) refers to this surface as Horizon D. Koch (2006) interprets this surface as the top of the Intracoastal Formation (Donoghue, 1992) (Table 3.5). This surface is much closer to the seafloor in the eastern section of the study area than anywhere else.

Table 3.4. Stable carbon isotope ratios, conventional radiocarbon dates and calendar calibrated ages with 1- and 2- sigma ranges where applicable.

Core	$\delta^{13}C$ (0/00)	Conventional Radiocarbon Age (yrs)	Error (+/- yrs)	Calendar (yrs BP)	1-sigma range (yrs BP)	2-sigma range (yrs BP)
W-16A	-26.6	18400	100	22010	21520-22150	21350-22230
W-16B	-24	19560	100		23115-23630	22814-23740
W-27A	-24.4	25290	160			
W-27B	-24.2	27560	170			
W-27C	-23.8	29150	240			

3.4.1.3 Facies C

Facies C (Fig. 3.8) is present only in certain strike lines, and is obvious in a large channel feature. It is characterized by multiple small channel-like reflectors that appear to cut into each other and are possibly truncated at Surface 3. Reflections are spotty at best and sometimes difficult to interpret due to lack of continuity. Locker and Doyle (1992) interpret this as possibly AE4, and AE5.

3.4.1.4 Facies B

Facies B (Fig. 3.7) is more noticeable in dip sections, and characterized by long, gently dipping seaward, weakly acoustic clinoforms. The reflections are faint and difficult to determine the type of termination. Locker and Doyle (1992) call this section AE5. Koch (2006) interprets this as mid-Wisconsinan.

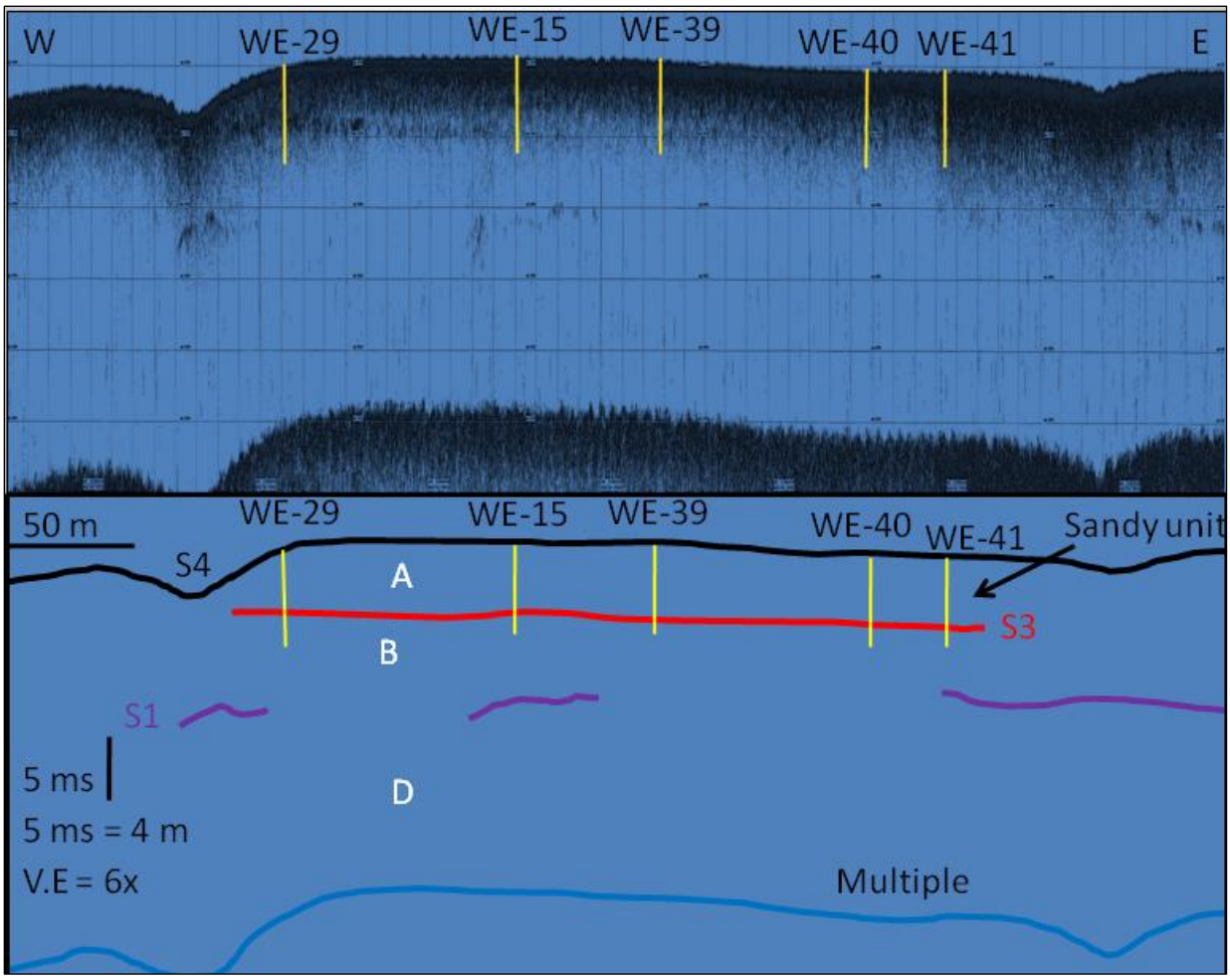

Figure 3.7. Top image, raw seismic, un-interpreted. Bottom image, interpreted line drawing of image. The yellow vertical lines are cores. The black line in the bottom image is surface 4, the seafloor.

3.4.1.5 Surface 2

Surface 2 is somewhat sparse in the nearshore, or disrupted, but more common on the shoal. It is sometimes very gently dipping seaward, in very long, clinoform-like features. Koch

(2006) interprets this reflector as the maximum flooding surface (MFS) of the mid-Wisconsinan before sea level dropped (Table 3.5).

3.4.1.6 Surface 3

Surface 3 (Figs. 3.7, 3.8) is a fairly continuous and flat reflector, visible in almost all profiles. It ranges from at the seafloor to approximately 4 m below the seafloor in depth (Table 3.5).

Table 3.5. Seismic and litho-facies of this study correlated to facies described by other previous studies.

This study		Locker and Doyle 1992	McBride et al. 1999	Koch 2006	
Seismic	Core			Seismic	Core
Surface 4	Surface 4		Surface 3		
	5		Facies 6, 5		Beach/Barrier
A	Surface 3	AE5	Erosional surface 2	Holocene	
	4		Facies 2, 3, 4?		lagoon, delta
Surface 2		n/a		MFS	
B	3	AE4?	n/a	Mid-Wisconsinan	Estuarine/lagoon/ delta
C	2		Facies 1		
Surface 1		BD/C	Erosional surface 1		
D	1	AE3	n/a	Intracoastal Fm	n/a

3.4.1.7 Facies A

Facies A (Figs. 3.7, 3.8) contains high amplitude reflections that are difficult to penetrate with the seismic. High amplitude features are present but rare and difficult to see due to the highly acoustic facies. Due to the impenetrability of this facies, it is interpreted as the quartz sand that is common in the area. Facies A is at most 4 m thick, however, often disappears where

troughs in Surface 4 dissect it. Locker and Doyle (1992) call this facies AE5. Koch (2006) interprets this facies as Holocene reworked beach, nearshore and barrier sands (Table 3.5).

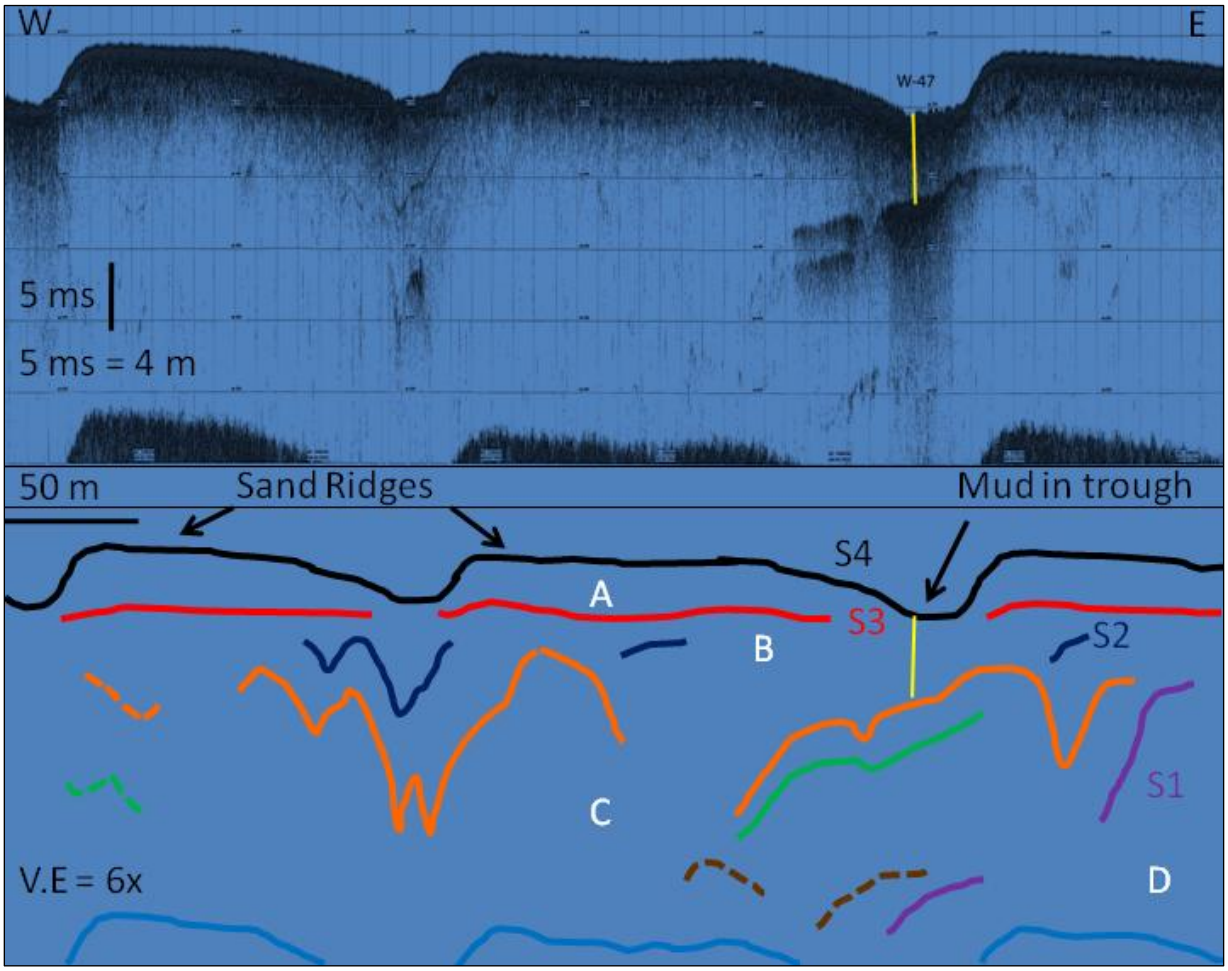

Figure 3.8. Top image, un-interpreted raw seismic image. Bottom, interpreted line drawing of the above image. The image is part of a large incised channel, in which multiple smaller channels occur. The black line in the bottom image is Surface 4, the seafloor, with multiple ridges and troughs, down cutting into Surface 3.

3.4.1.8 Surface 4

Surface 4 is the seafloor, bounding the top of Facies A and occasionally B. It is characterized by ridge and trough like features, particularly noticeable in strike sections (Fig. 3.8). Where these troughs occur Facies A is often missing, however, where the ridges occur Facies A shows maximum extent. The ridges are asymmetric, with a steeply dipping side to the

west or southwest and a gently dipping side to the east or northeast. The troughs, on the other hand, are nearly symmetric. The shoal itself also appears to be slightly asymmetric, with a slightly steeper side dipping landward. This morphology was also noted by McBride et al. (1999) on the landward sides of North and South Perdido shoals on the inner shelf offshore westernmost Florida Panhandle. These shoals also had similar orientation to the shoal in this study.

3.4.2 Lithological Facies

Five facies are described from the cores based on lithology, composition, and to some extent sedimentary structures. In addition to the figures, selected annotated cores are located in Appendix E. Table 3.5 lists the lithological facies correlated to the seismic and other studies.

3.4.2.1 Facies 1 – Quartz and Carbonate-cemented Calcarenite

Facies 1 (Fig. 3.7) is a weakly carbonated-cemented sand that is very uniform in particle size and color. The facies is featureless and dark gray. Where the facies is found with other sediments, it is always at the base of the core. Refusal of the vibracoring often came soon after penetrating this facies. The facies is most common in eastern cores and closer to the shore. It is never found beneath the shoal. A few cores are entirely composed of this facies. The extent of the formation is unknown in this area. Locker et al. (1988) and Locker and Doyle (1992) indicate that this unit may outcrop along the eastern section of the study area (Fig. 3.9). It is correlated to Facies D in the seismic.

3.4.2.2 Facies 2 – Silt and Clay

Facies 2 (Fig. 3.10) is a fine-grained silt and clay deposit with shells mixed throughout. The facies is dark gray-brown in color. Thin beds of silt and clay often alternate (Fig. 3.10).

Facies 2 is correlated to Facies C in the seismic (Table 3.5). The facies is not present in most cores, but when present, is substantial.

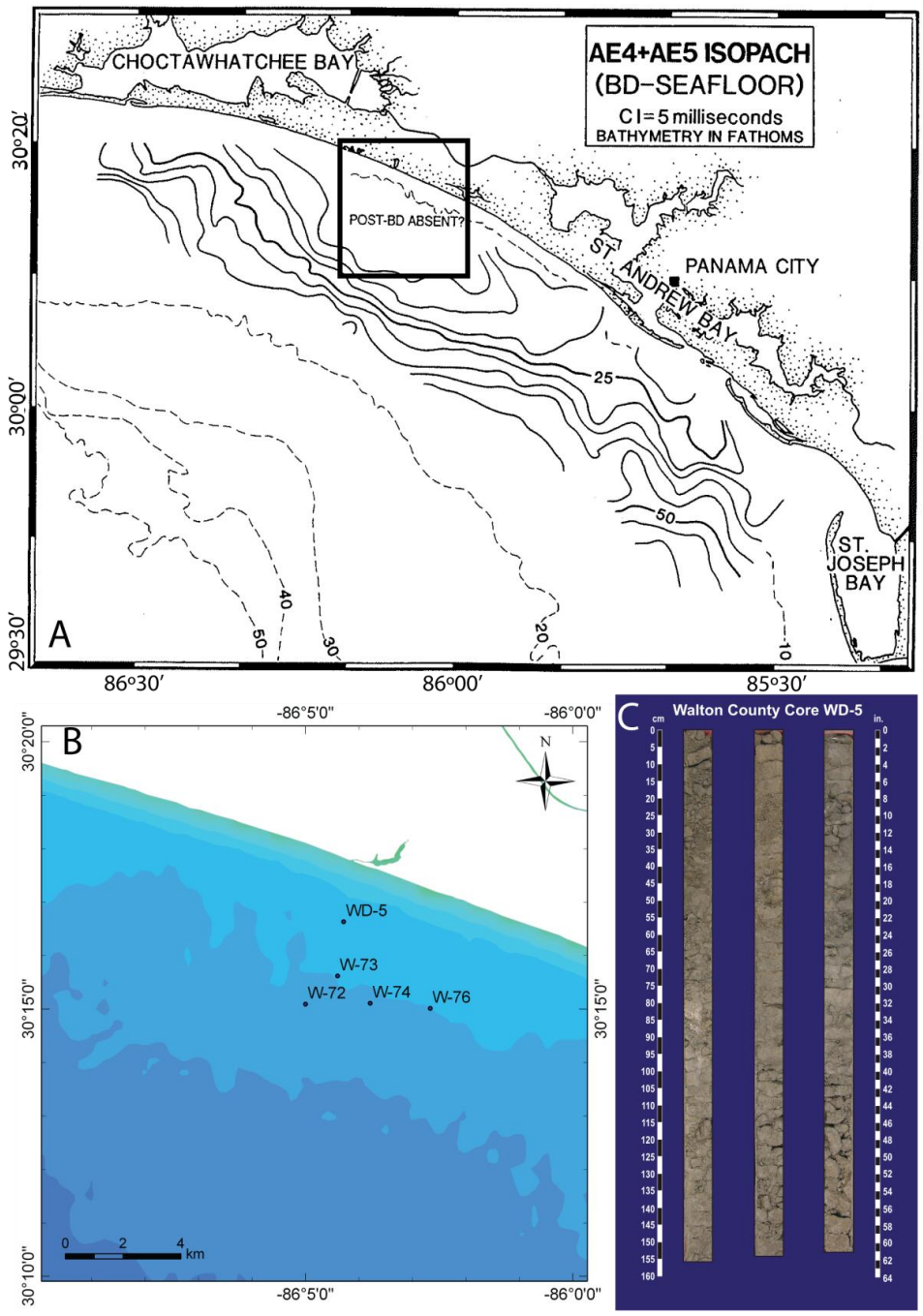

Figure 3.9. Intracoastal Formation (Facies 1). A. Isopach map from the seafloor to surface BD, modified from Locker et al. (1988). B. Location of cores from this study containing mostly Facies 1: cores WD-5, W-74, and W-72 were completely composed of this facies, while cores W-73 and W-76 contained the facies within the first meter of the core to the bottom of the core. C. Core WD-5 is completely composed of Facies 1.

3.4.2.3 Facies 3 – Oxidized Clay and Peat

Facies 3 (Figs. 3.11) is an oxidized clay and peat section that is mottled orange, brown and black in color. It is very fine grained, clayey, and organic-rich. Thin (~ 2 – 5 cm) peat beds are present in many of these cores, often containing more than one bed of peat. Peat is also mixed in with clay and silt in the cores. Wood fragments are common as well, and some rootlets are observed. In the east, the base is on occasion truncated by Facies 1, but most of the cores do not contain the base of Facies 3. In seismic profiles, a reflector is often observed at or very near the top of this layer (Fig. 3.8). It is correlated to Facies B in the seismic (Table 3.5).

3.4.2.4 Facies 4 – Bioturbated Muddy Sand

Facies 4 (Fig. 3.12) is a moderately to highly bioturbated muddy sand. The color of the facies is variable, ranging in color from whitish sands swirled with brown and grey sediment to dark brown-grey sediment. The sand in this facies is often organically stained and is characterized by abundant shells, scattered throughout, and/or in a significant hash layer, generally towards the top of the facies. This layer is small, on the order of approximately 10 cm. Facies 4 is approximately 0.5 to 2 m in vertical extent. The bottom boundary is often distinct, noted by the lack of shells in Facies 2 or lack of sand in Facies 3, while the top boundary grades into the shelly sands and clean sand facies above. Correlation to the seismic (Table 3.5) is to the upper portion of Facies B. In the seismic, reflections often bound both the top and bottom of Facies 4. This facies is easily correlated across the study area (Fig. 3.12).

3.4.2.5 Facies 5 – MAFLA Sand

Facies 5 (Figs. 3.11, 3.12, and 3.13) is a mature quartz sand with little shell fragments. The facies is white to light brown in color and contains some scattered burrows. This unit is very clean, but some mud is present in a few cores, mostly contained to flaser bedding or vertical

burrows. Shell content often increases toward the base of the facies. The facies is approximately 0.5 to 4 m in vertical extent, and is correlated to Facies A of the seismic (Table 3.5). The facies is easily correlated across the region (Figs. 3.12 and 3.13).

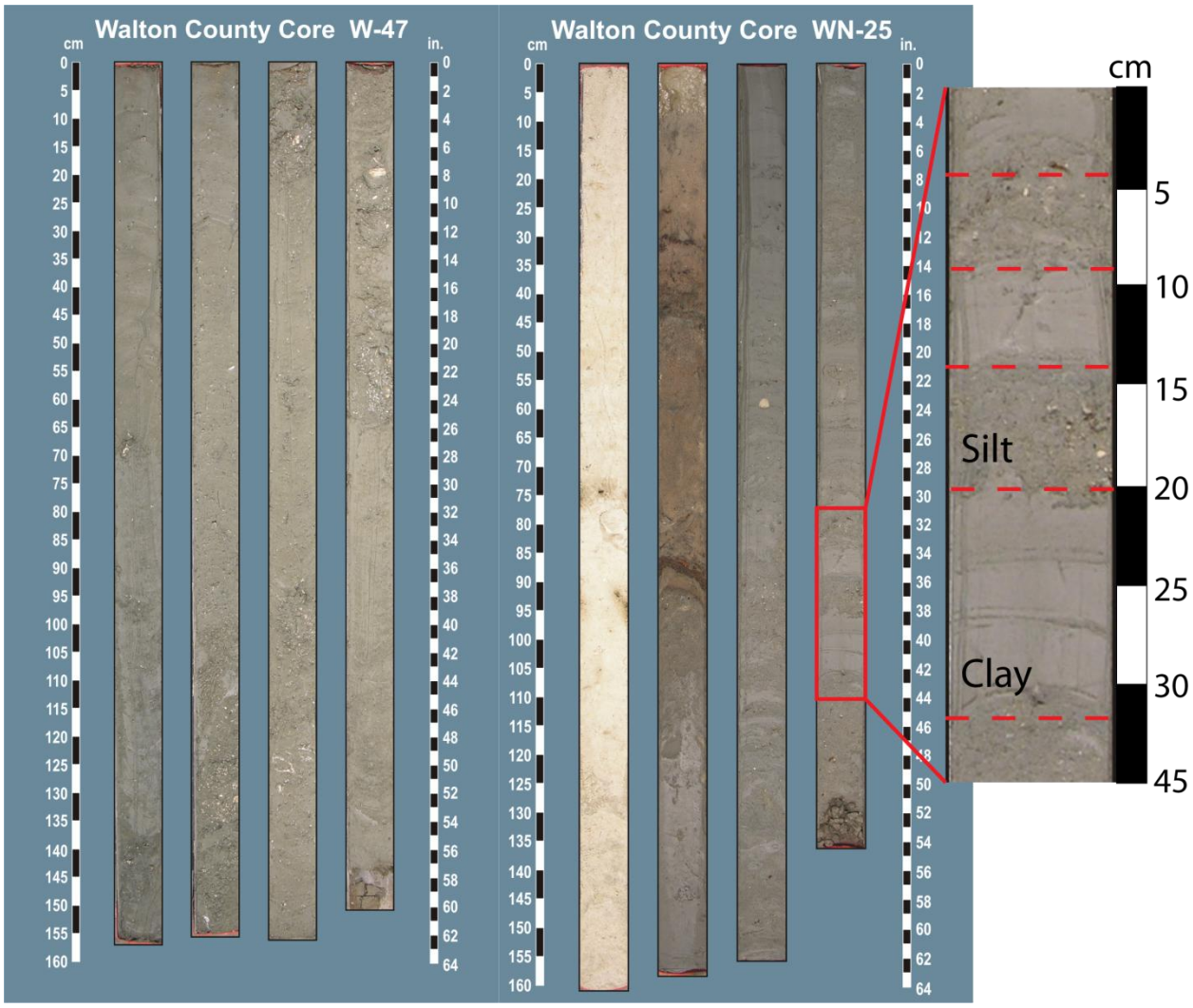

Figure 3.10. Channel deposits (Facies 2) of fine-grained material. Core W-47 (left) is completely composed of Facies 2. The channel deposit in core WN-25 was covered with an organic layer (Facies 3) and MAFLA sand (Facies 5). Beds of alternating silt and clay are visible core WN-25.

3.4.3 Radiocarbon Ages

Two radiocarbon ages were obtained from core WN-16 (Table 3.4) on the middle of the crest of the shoal on the inner shelf. These samples were taken from peat (Facies 2 (lithology), B

(seismic)) with some wood in the sample. The wood was removed for radiocarbon analysis. The samples were dark brown, organically stained sand and silt mixed with peat. A few burrows were present within several centimeters of the sample. The samples yielded ages of 18,400 ^{14}C years BP (WN-16A) and 19,560 ^{14}C years BP (WN-16B). The 2-sigma range (95% confidence) calendar calibrated result for sample WN-16A was 21,350 – 22,230 years BP (where BP is before 1950, according to radiocarbon standard). The 2-sigma range for WN-16B was 22,814 – 23,740 years BP.

The stable carbon isotope ratio (δ^{13}C) result for sample WN-16A was -26.6 ‰, indicating a freshwater environment of deposition (Chmura et al., 1987). The δ^{13}C result for WN-16B was -24 ‰, indicating a more intermediate depositional environment for this peat.

Three radiocarbon ages were obtained from core W-27 (Table 3.4, Fig. 3.14) on the eastern inner shelf region. These samples were of pure peat (litho-Facies 2, seismic Facies B). The samples were slightly oxidized and dark brown, a thick, very uniform and featureless peat deposit. No burrowing was evident for over a meter of the core surrounding this deposit (Fig. 3.14). Silt and clay interbedded the peat. The shallowest sample, W-27A yielded an age of 25,280 ^{14}C years BP. The next deepest sample, W-27B, yielded an age of 27,550 ^{14}C years BP. The deepest sample, W-27C, yielded an age of 29,130 ^{14}C years BP. Due to the age of these samples, they were not calibrated to calendar years.

The δ^{13}C of these samples ranged from -24.4 ‰ (W-27 A) to -23.8 ‰ (W-27C). While these samples were predominately intermediate (Chmura et al., 1987), the increasing ratios indicate increasing salt influence (towards brackish or marine) environments down-core.

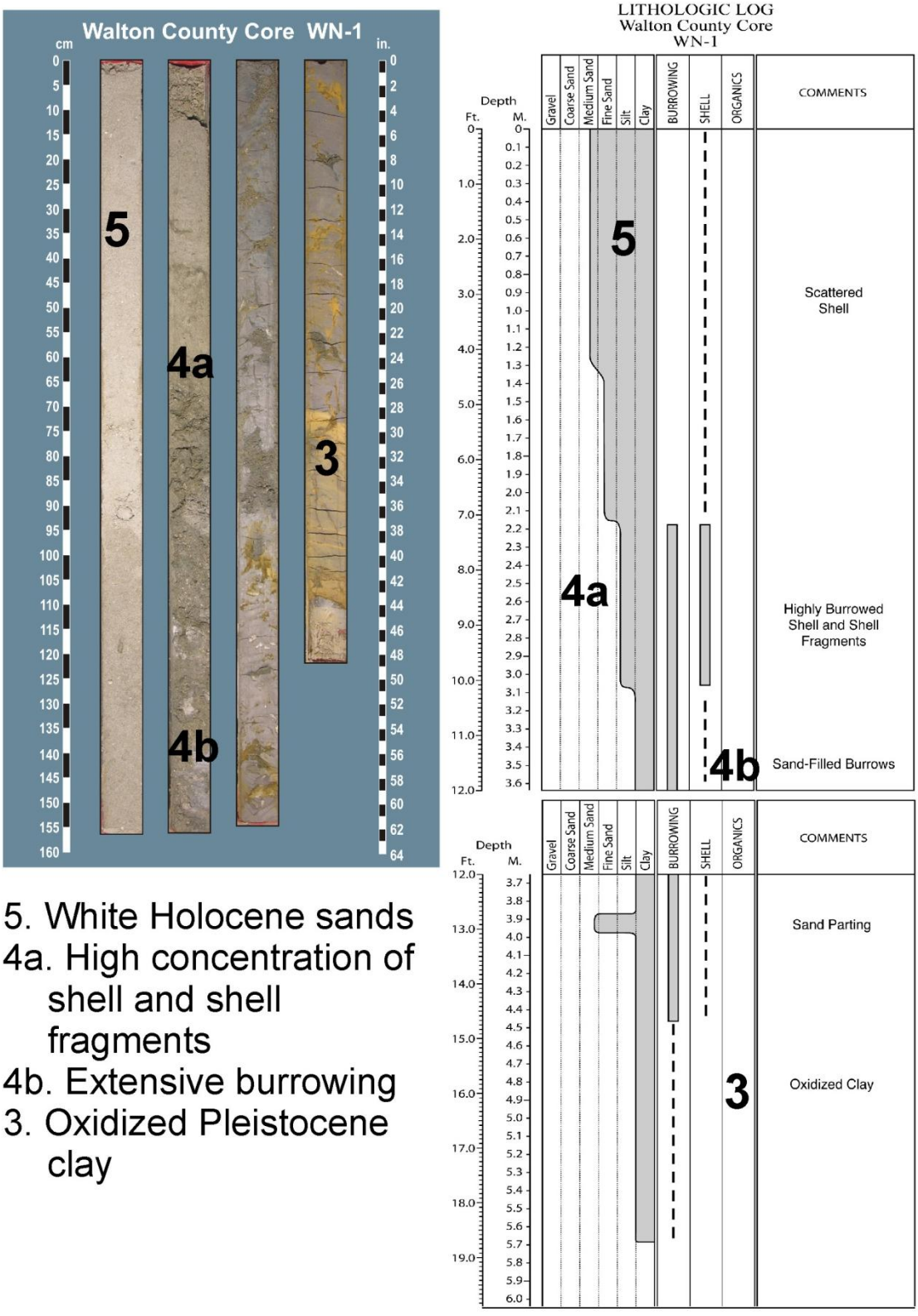

Figure 3.11. Core WN-1, with an extensive, well oxidized clay unit (Facies 3), overlain by burrowed muddy shelly sand (Facies 4) and clean quartz sand (Facies 5).

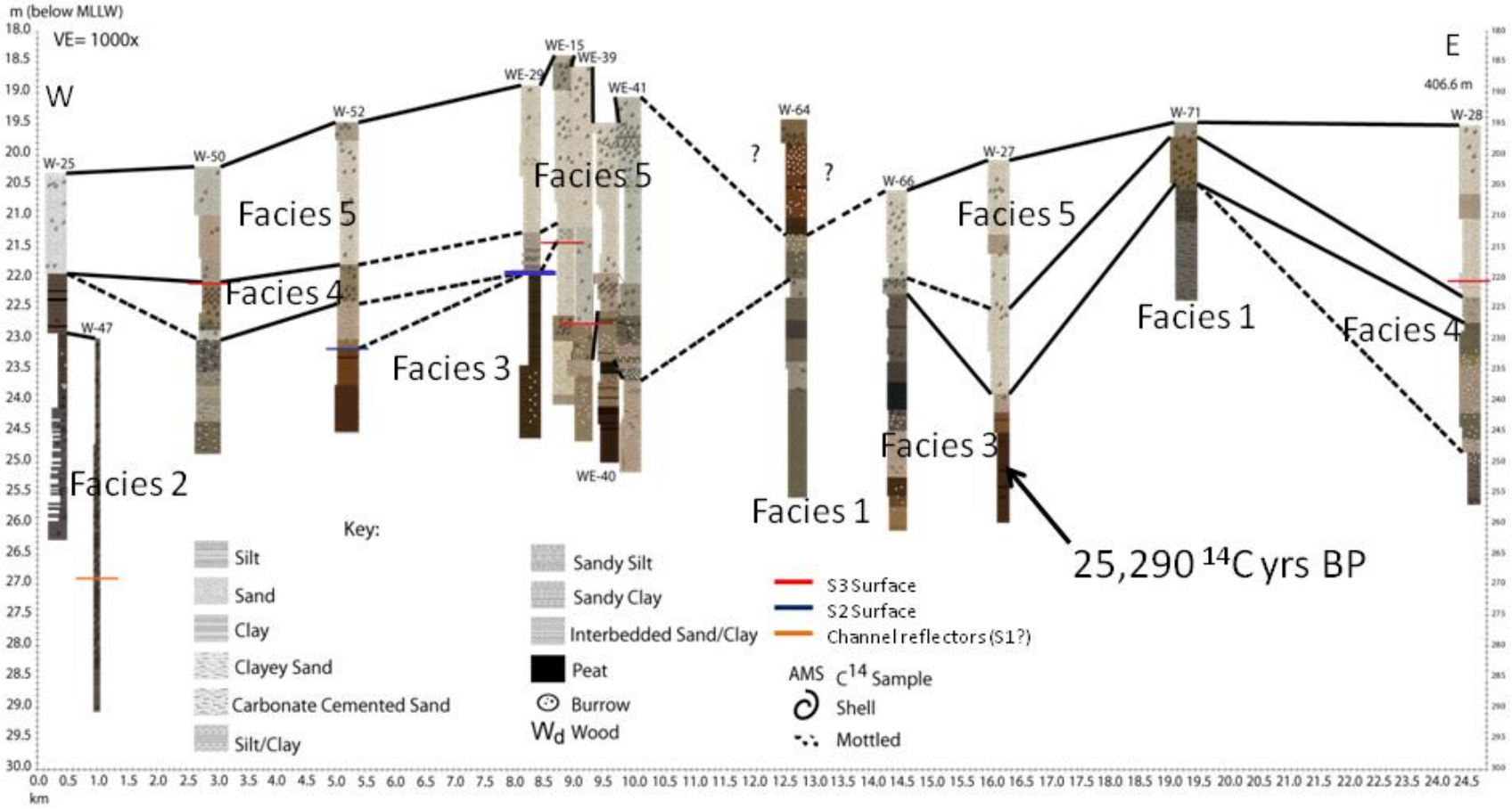

Figure 3.12. Strike cross-section of facies discussed in the text. Red lines indicate reflectors in the seismic, most likely Surface 3. The cluster of cores with the large depth of Facies 5 may be a relict ebb tide delta or paleo-sand body. Core W-47 occurs in the trough that has eroded into a channel shown in Figure 3.8. Three radiocarbon samples were taken from the peat unit at the base of core W-27.

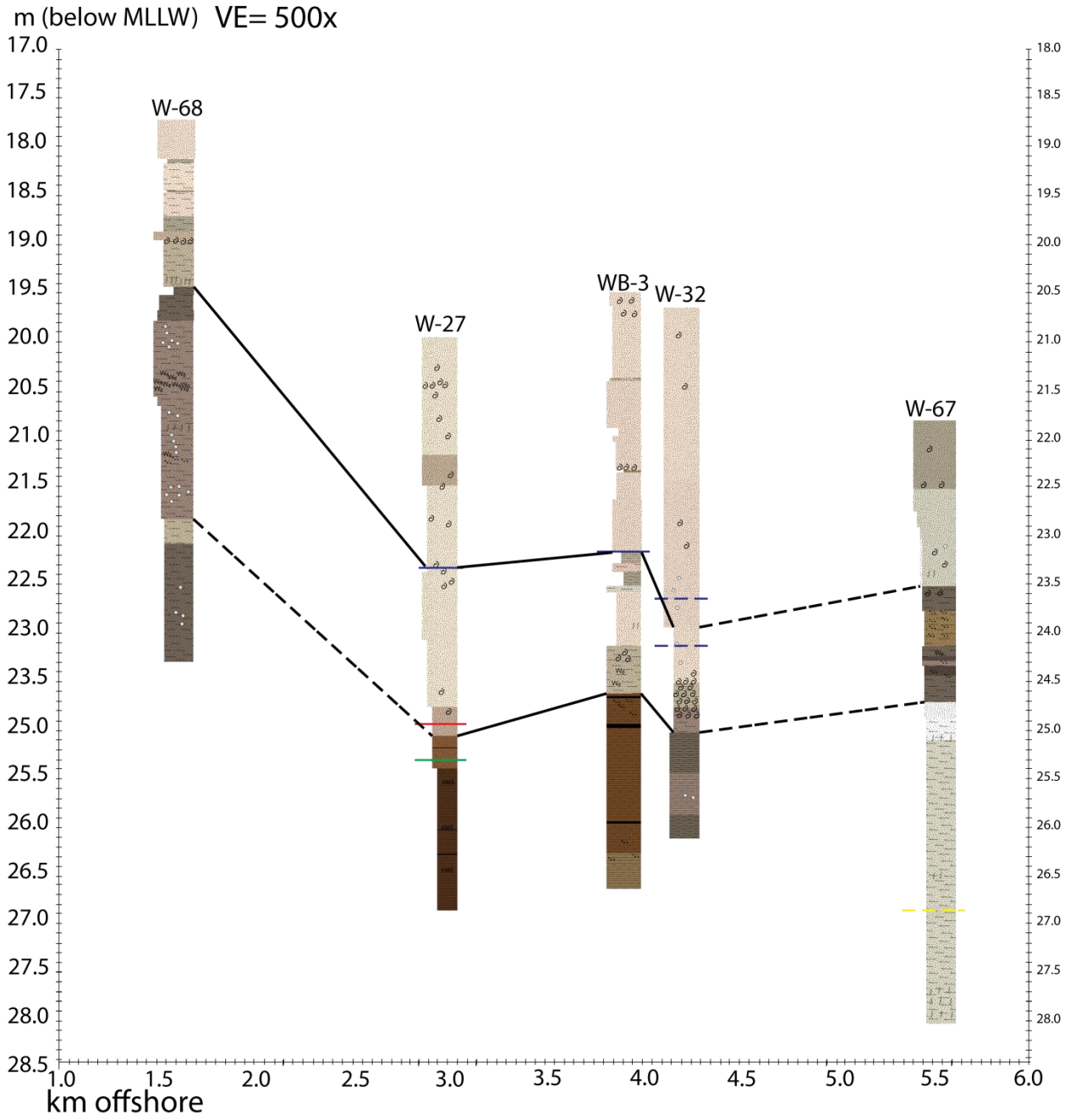

Figure 3.13. Dip cross section shown in Figure 3.6. Facies 5 (top) is easily correlated across the region but the other facies are much more variable. The middle unit is indicative of Facies 4, while the bottom unit is Facies 3; except for the core W-67 contains Facies 1 at the base. Refer to Figure 3.12 for the key.

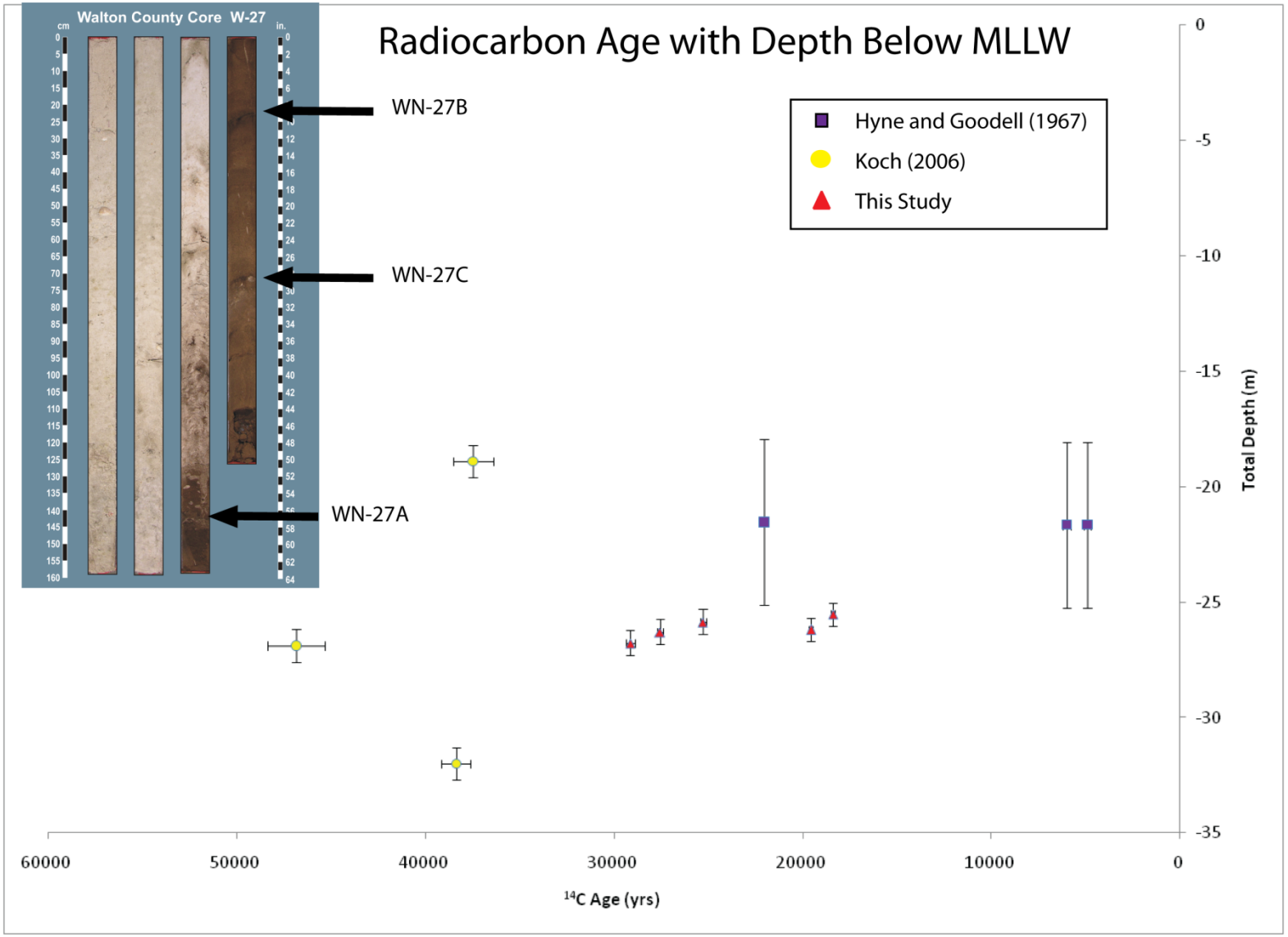

Figure 3.14. Radiocarbon ages from previous study and this study plotted against total depth. Inset, core WN-27, with sample locations.

The comparison to other age results from studies in this region (Fig. 3.14) is complicated in that very little correlation is readily seen. The two younger dates from Hyne and Goodell (1967) are extremely young for such depths, and do not compare well with the rest of the data. Also, according to their study, if these dates are accurate, and represent the drowning of the shoals, then sea level would have had to have risen 25 m in the last 4,000 – 6,000 years. It may be possible that dates from Hyne and Goodell (1967) have been contaminated by younger material, likely recrystalization of the shell material, due to the type of material that was dated (shells) or vertical mixing of the Holocene material. A significant amount of older carbon is required to contaminate a sample; however, younger contamination is possible with a small amount of material (Hatfield, R., personal communication). Because of this, the age results of core WN-16 may be slightly younger than reality. This may be due to younger contamination from burrows or woody fragments (fresh water). Comparison of the dates from core W-27 and Koch's sample SR3A to Frazier (1974) curve of sea-level ages from the Texas and Louisiana coast (Fig. 3.15), however Frazier's data was sparse for pre-20 ka, and are not supported by other sea-level histories outside of the GoM. Other studies in the region (i.e. Balsillie and Donoghue, 2004) do not extend far enough into the past for comparison. Comparison to global sea level curves (Lambeck and Chappell, 2001; Siddall et al., 2003) indicate that the samples should be much deeper, however, a hiatus of sedimentation that would have occurred when sea level was further lowered (i.e. during the late Pleistocene lowstand) and this region fully exposed, was not corrected for in this study's depth error calculations. The surface that would have been exposed and eroded during this time period can be seen by reflectors in the seismic (Surface 3). Therefore, the ages of core W-27 are interpreted to be *in situ* due to the extensive deposit of the

peat in the core, the lack of burrowing and wood, and the presence of a major reflection in the seismic bounding of this facies.

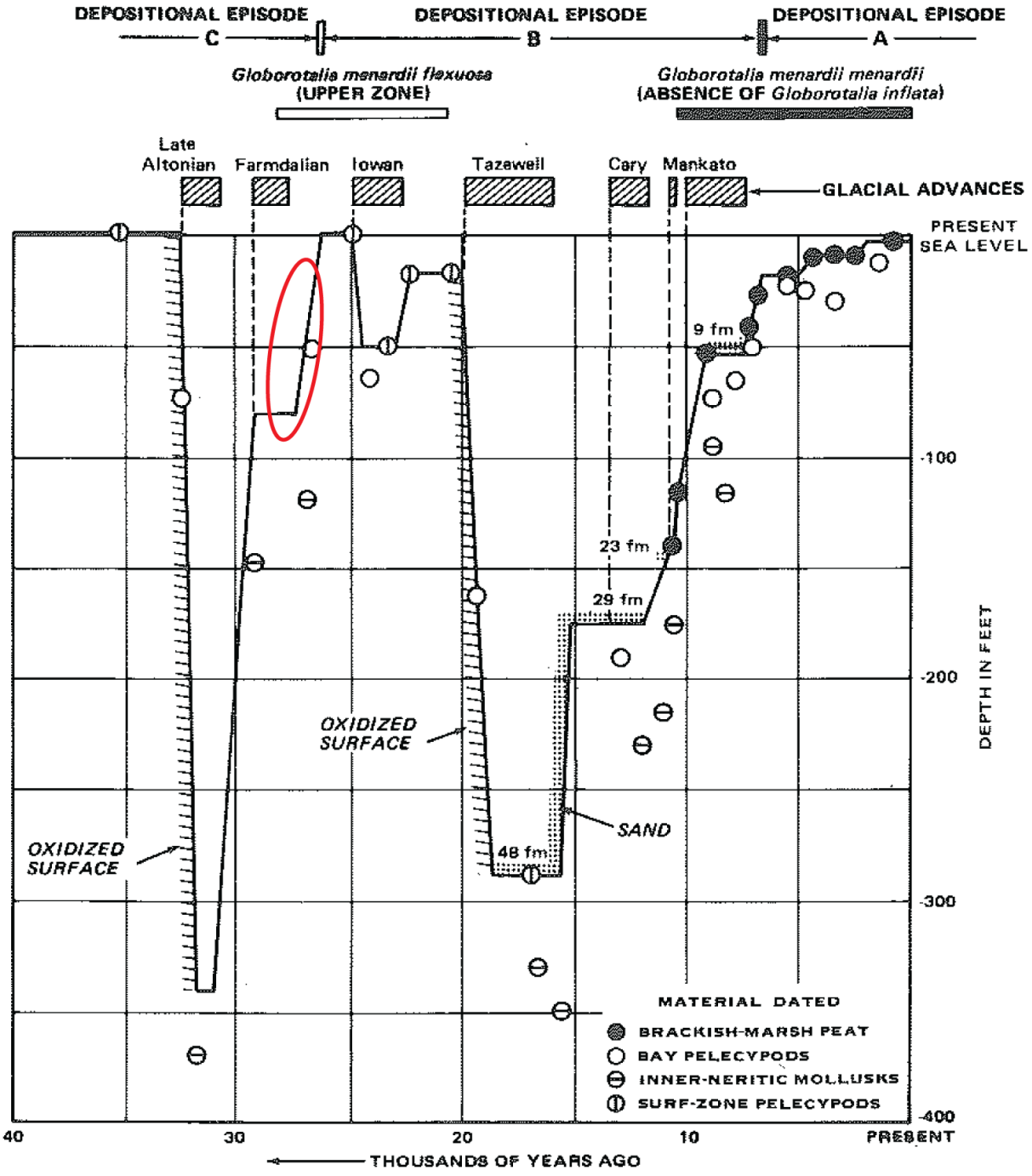

Figure 3.15. GoM sea-level curve for the last 40,000 years agrees well with the radiocarbon dates from this study. The approximate depths and ages from radiocarbon dates from this study are highlighted in red, indicating that Facies 3 was deposited upland from a transgressing coast in the mid-Wisconsinan. Modified from Frazier (1974).

3.4.4 Sedimentology

Results from the granulometric analysis confirmed the presence of fine grained material in Facies 2, 3, mixed sand with some mud and finer grained material in Facies 4, clean sand in Facies 5. However, the results also indicated that an overall coarsening upward signature occurs within Facies 4 to 5. The sand coarsens from approximately 3 phi (very fine sand) to less than 0.5 phi (coarse sand), with a mean sediment size per depth interval range of 2.5 phi at the bottom to less than 1 phi (Fig. 3.16).

The surface sediment size distribution map indicates that most of the sediment at the surface is approximately medium sand (1.5 – 1.0 phi) (Fig. 3.17). Some patches of coarse sand (less than 1.0 phi) occur at the mouth of the Destin East Pass and near a large patch of sand (Fig. 3.10) in the east (Fig. 3.17). Analysis of sediment size on the surface of the shoal indicates that the shoal is finest in the middle, and coarsens slightly to the northeast and southwest, ranging from 1.3 to 1.6 phi.

Mean grain sizes were graphed with depth down core, and then cores were chosen from the crest of the shoal and the nearshore to create a transect of mean grain size with depth (Fig. 3.18). The transect cuts the inner shelf from the nearshore in the northeast to the southwest tip of the shoal, through which a fining trend is observed in the offshore direction (Fig. 3.17). The nearshore cores are quite homogenous with uniform grain sizes through most of the core, while the offshore southern shoal cores exhibit a fining downward trend through the core. In addition, more shell, particularly shell hash, existed on the stoss (seaward) side of the shoal, and cores on this side tended to be more variable in grain size down core, due substantial burrowing and shell hash. In comparison, cores on the crest of the shoal decreased uniformly in mean grain size with depth (Fig. 3.18).

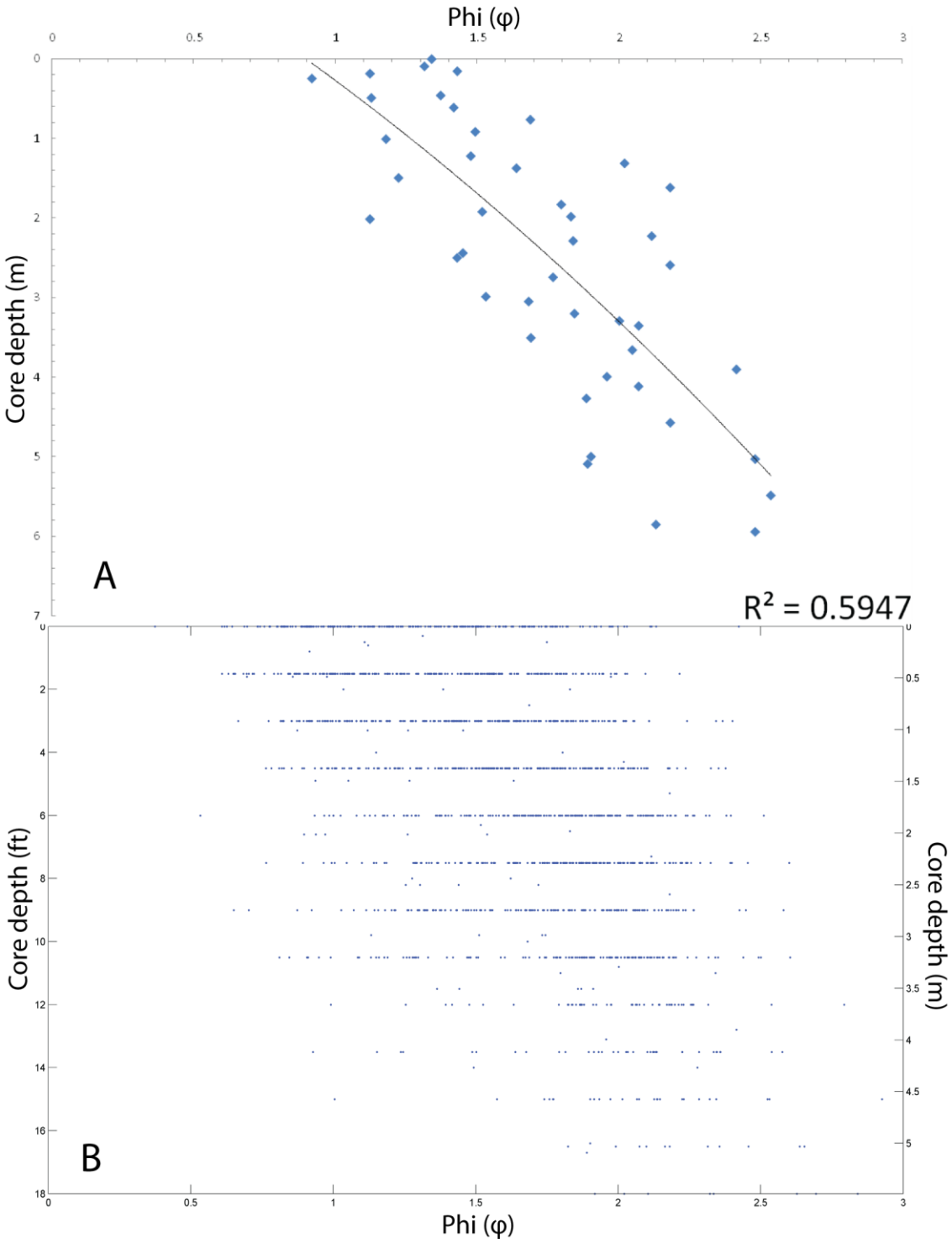

Figure 3.16. Mean grain sizes in the cores showing a significant coarsening upward trend. A. Mean grain size per depth interval for the entire study area. B. Mean grain size per sample for all samples.

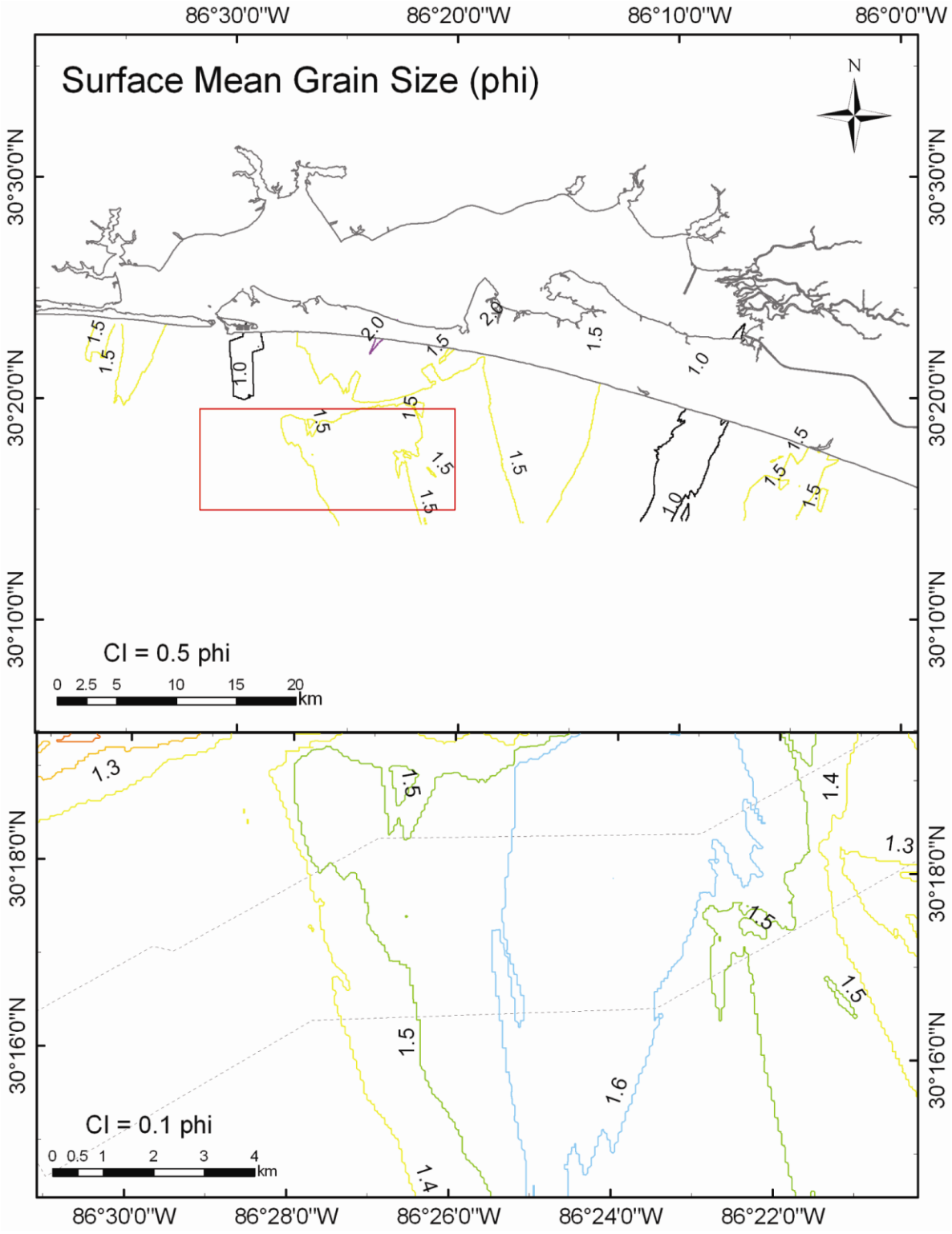

Figure 3.17. Mean grain size of surface samples from the cores in the study area (top map) and mean grain size over the shoal (bottom map). The shoal is highlighted by the light gray dotted lines in the bottom map, and the extent of the bottom map is indicated by the red box in the top map.

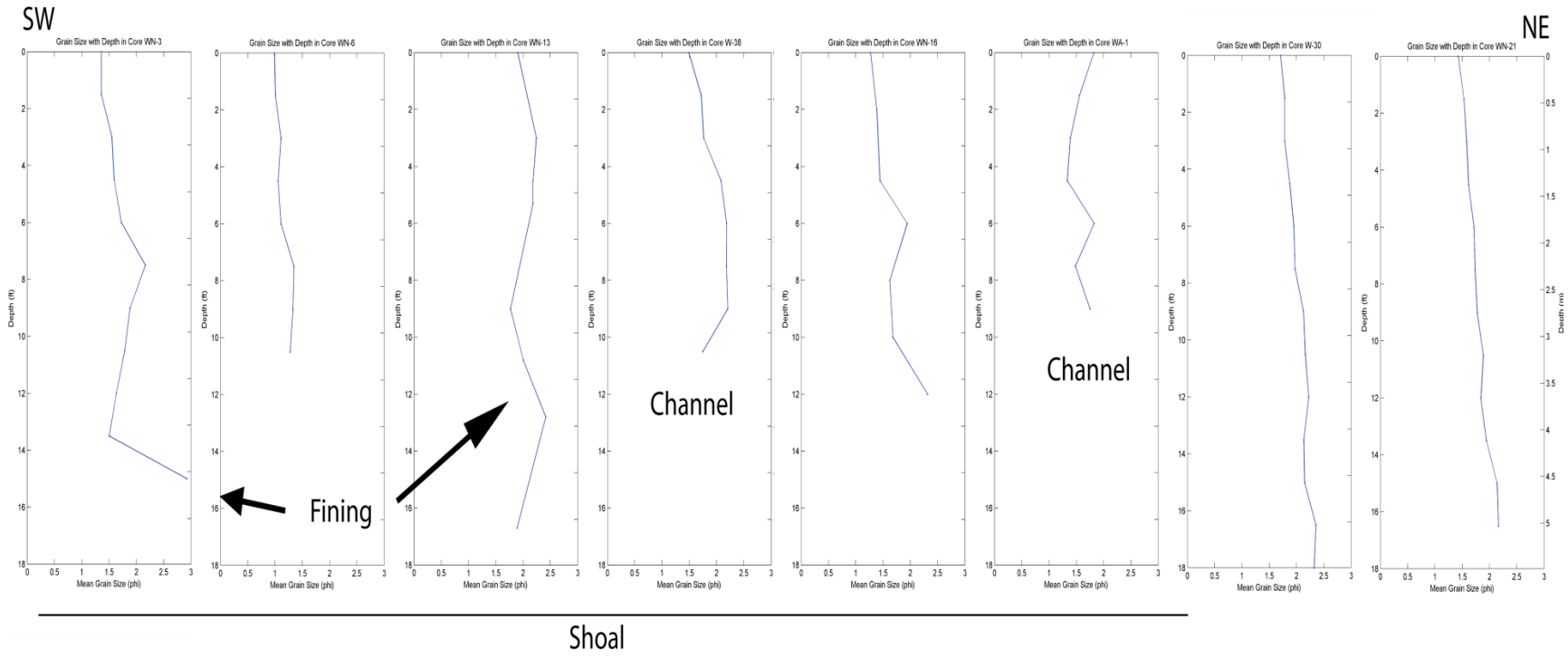

Figure 3.18. Mean grain size distribution with core depth along a shelf transect from the nearshore, northeast of the shoal to the southwest tip of the shoal. Note that the nearshore cores are fairly homogenized through the core, but the southwestern cores fine downcore.

3.4.5 Bathymetric Calculations

It is well established that the features on the seafloor of the northeastern GoM are relict from the latest rise in sea level (Hyne and Goodell, 1967; McBride et al., 1999; Donoghue et al., 2003; Koch, 2006). Large shoals are visible on the shelf, as well as smaller ridges super-imposed over these shoals and the majority of the shelf (Fig. 3.4). The shoals range in length from approximately 10 – 17 km, are 2 – 3.5 km wide, and less than 8 m above the surrounding bathymetry. The shoals are generally sub-parallel to the coast, oriented east-northeast to west-southwest, and may be analogous ridges described on the Atlantic coast (Figueiredo et al., 1981; Swift and Field, 1981; McBride and Moslow, 1991; Snedden et al., 1994; Snedden and Dalrumple, 1999; Snedden et al., 1999; Hayes and Nairn, 2004) and ridges/shoals described in the Gulf (McBride, 1995; McBride et al., 1999; Edwards et al., 2003; Twichell et al., 2003; McBride et al., 2004; Rogers et al., 2009). The ridges, also noted in the seismic (Fig. 3.8), are secondary features that are roughly perpendicular and super-imposed on the shoals. These ridges are shore-oblique, with a steep side facing roughly southwest, and gently sloping on the northeast side, similar to dune or large ripple morphology. The troughs appear more symmetric than the ridges (Fig. 3.6). The ridges are approximately 50 m wide or less, less than 4 m high, and are quite variable in length from less than a kilometer to approximately 4 km. These ridges have been recognized by Fleischer et al. (1996) post-hurricane impact offshore Panama City, Florida.

Simple calculations of the symmetry and size of the ridges can provide information regarding the type of flow or parameter forming these features. The rippled index (ripple length/ ripple height) (Collinson and Thompson, 1982) was calculated for a few selected ridges and yielded a value of 12.05. The ripple symmetry (length of the stoss side/length of the lee side) (Collinson and Thompson, 1982) was calculated for the same ridges, yielding a value of 6.7.

Results from the subtraction of bathymetry data over a 24 year period (Fig. 3.19) indicated that a significant amount of erosion occurs along the both sides of the shoal and the northeast end of the shoal, over a multi-decadal scale and post-Ivan. Erosion, possibly scour, occurs in a trough pattern, perpendicular to the axis of the shoal, parallel to the ridges. However, deposition appears to be more uniform and blanket-like, particularly at the southwest end of the shoal. On the landward side of the shoal, deposition is more ridge-like. A net volume of 16.75 million m^3 was lost over this time period (Table 3.6). Maximum depth of erosion was 2.4 m, while maximum deposition thickness was 3.3 m.

Due to limitations of high resolution bathymetry data change analysis from the short term pre- and post-hurricane scenario was restricted to a much smaller area, confined to a sand-rich area within the shoal; therefore the comparison is not exhaustive. It appears that the highest volume and vertical accretion occured on the backside of the shoal; however, the deepest scour occured here as well, with a value of 4.1 m of scour depth (Fig. 3.20). This was much higher than erosion rates calculated from a numerical model, post-Camille in the Mississippi Sound, by 2.7 m (Bentley et al., 2002). This may be attributed to substantial energy attenuation of hurricane-generated waves, prior to their reaching the barrier islands, and a reduction in shear stress during the maximum influence of the hurricane (see Chapter 2, section 2.3.3 and 2.4.2). Maximum thickness of the deposition is the same as in the long-term calculation: 3.3 m. The seaward side of the shoal experiences more erosion than the landward side; however it is not as deep, and more uniform than the landward side erosion. Fleischer et al. (1996) noticed similar features offshore Panama City post-hurricanes Elena and Kate, that they referred to as mega-ripples.

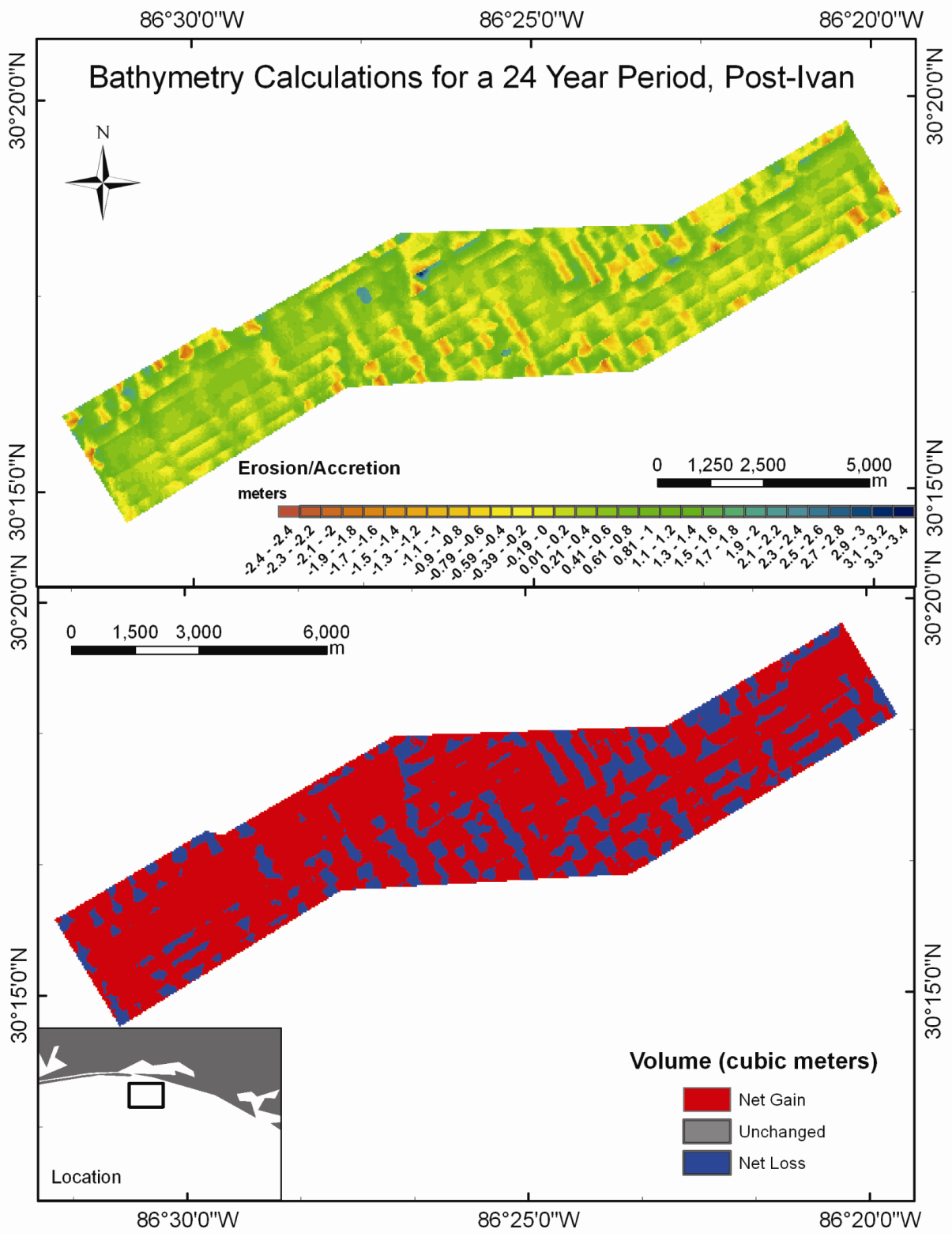

Figure 3.19. Bathymetry subtraction (top) and volumetric analysis (bottom) using the cut/fill tool in ArcGIS, for a 24 year period. The top map shows depth of scour and accretion thickness, while the bottom map contrasts the spatial patterns in erosion and deposition.

Table 3.6. Statistics for the volumetric calculations for both area and volume for surface sediment eroded and accreted over a 24 year time period (left, Ivan) and 2.5 year time period (right, Dennis).

2004-1978 (Ivan/Long Term Analysis)			2007-2005 (Dennis/Short Term Analysis	
	Volume	Area	Volume	Area
Count	225	225	117	117
Minimum	-22891717.188	1600.000	-129220.963	2500.000
Maximum	330825.146	44929600.000	5040728.455	1380000.000
Sum	-16745377.249	59268800.000	3750763.683	14690000.000
Mean	-74423.899	263416.889	32057.809	125555.556
Std Dev	1525639.043	2986454.122	465719.067	1045959.366

3.5 Discussion

3.5.1 Depositional Environment Interpretation

All facies, bounding surfaces, environments of deposition, and geologic and actual ages can be seen in Table 3.7, in summary of this discussion (see also Fig. 3.8). Facies 1 is correlated to Facies D (Table 3.5) in the seismic and below the BD surface from Locker and Doyle (1992). Koch (2006) calls this facies the Intracoastal Formation. The cemented sand would create an impenetrable surface for shallow seismic, as seen in the Chirp data (Fig. 3.7, Appendix D). The Intracoastal Formation is interpreted to be Middle Miocene to Late Pliocene in age and stratigraphically equivalent to the Choctawhatchee Formation of Miocene age (Schnable and Goodell, 1968; Donoghue, 1992) (Table 3.6). Donoghue (1992) attributes the variation in depth to the top of the Intracoastal Formation to subaerial exposure and fluvial erosion.

Facies 2 was not noted in other studies, except for Locker and Doyle (1992), who note the presence of channels in the BD and C reflector in their profiles near Choctawhatchee Bay.

Due to the irregularity of this facies, its fine-grained nature, and the presence of the facies in channel-like reflectors in the seismic, this Facies 2 is interpreted as channel fill.

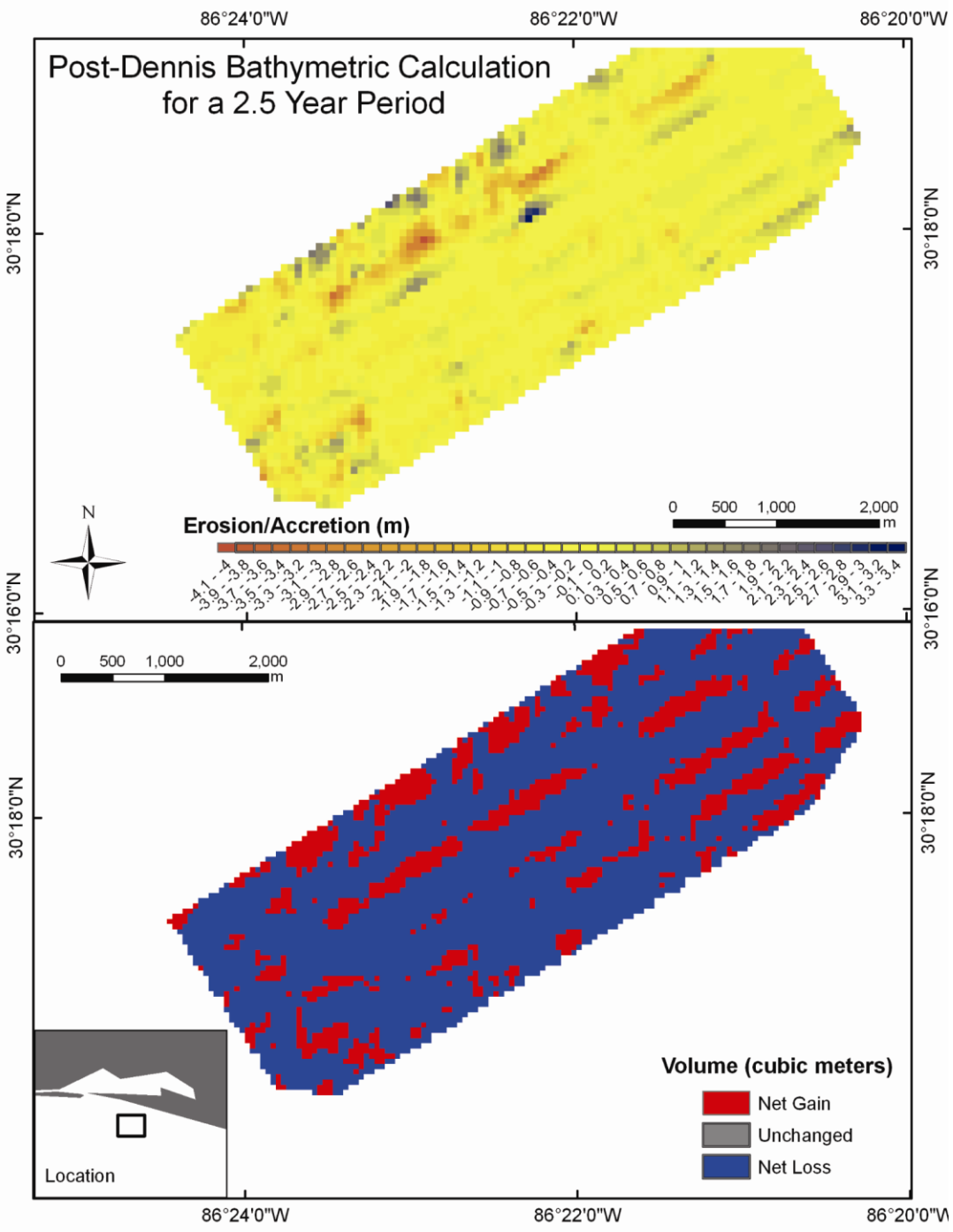

Figure 3.20. Bathymetric subtraction (top) and volumetric calculation (bottom) using the cut/fill tool in ArcGIS for a 2.5 year period following the landfall of Hurricane Dennis. The top map shows the depth of erosion and thickness of accretion, while the bottom map shows the spatial distribution patterns of net erosion and accretion.

McBride (1997) and McBride et al. (1999) interpret Facies 3 (this study) as Facies 1 in their cores, a continental or coastal environment and strand plain masked by the soil horizon, part of the highstand and falling stage systems tract (Table 3.5). Koch (2006) interprets this as a mid-Wisconsinan deposit. This study interprets the facies as a soil horizon or marsh deposit, sub aerially exposed during a lowstand (Table 3.6), and possibly the Pleistocene Prairie Formation (Otvos, 1988; McBride, 1997; McBride et al., 1999), due to the oxidation that is visible within the core (Fig. 3.11) and the radiocarbon dates obtained from this unit (Table 3.4 and Fig. 3.14).

Facies 4 is correlated to Facies 2, 3, and 5 in McBride et al. (1999), who interprets this facies as an estuarine environment, part of the lower transgressive systems tract. Koch 2006 describes this facies as estuarine, back barrier lagoon or delta. This study interprets this facies as back barrier lagoon or prograding delta, due to mixed sediment content, extensive burrowing and shells. It is underlain by a sharp reflector that marks the ravinement surface separating it from erosional ravinement surface, possibly the last lowstand, which separates Facies 4 from fluvial and terrestrial sediments below (Figs. 3.7, 3.8, 3.10, and 3.11).

Facies 5, the surface deposits of the seafloor, is the MAFLA sand sheet recognized in numerous studies of the northeastern GoM shelf (Ludwick, 1964; Doyle and Sparks, 1980; Mazzullo and Bates, 1985; Kindinger, 1988; Locker et al., 1988; Locker and Doyle, 1992; McBride, 1995, 1997; McBride et al., 1999; McBride et al., 2004; Koch, 2006). It is interpreted as beach/nearshore/barrier sand that was deposited on the outer shelf/upper slope during the lowstand and reworked onshore as sea level rapidly rose during the Holocene.

Table 3.7. Lithologic and seismic facies with bounding surfaces and environmental interpretations. Modified and updated from McBride, et al. (1999).

Lithological Facies	Seismic Facies	Description	Environmental Interpretation	C^{14} Age (yrs BP)	Chronology	Sequence Stratigraphy
	Surface 4	Ridges, troughs and large hummocks	Modern seafloor			Stillstand/Highstand
Facies 5	Facies A	Mature clean quartz sand; high amplitude	Nearshore to inner shelf sand sheet	N/A	Mid-Late Holocene reworked sheet sand, MAFLA (Doyle and Sparks, 1980	Major transgression
	Surface 3	Continuous below ridges	Ridge base			Erosional ravinement
Facies 4	Facies A	Slighly muddy to shelly quartz sand, highly burrowed, flaser bedding; spotty reflections	Back barrier beach, lagoon, or ebb tide delta	N/A	Early Holocene	Early transgression
	Surface 2	Sparse, but relatively flat to gently sloping				Maximum flooding surface
Facies 3	Facies B	Muddy sand to sandy mud, highly oxidized, some burrowing, lots of organics, peat, wood; some clinoforms	Intrafluvial marsh, paleosol	25290 - 29150	Mid-Wisconsinan	Late trangression to highstand
Facies 2	Facies C	Fine grained silts and clays; multiple channels	Incised valley fill, estuary fill	N/A	Early - Mid Wisconsinan/Late Pleistocene	Early - mid transgression
	Surface 1	Highly variable and disconneted, large channels				Lowstand/Sequence Boundary
Facies 1	Facies D	Carbonated cemented sands	Open marine (Schnable and Goodell, 1968)	N/A	Miocene - Pliocene (Donoghue, 1992)	

3.5.2 Geological History and Shelf Evolution

During the Early Wisconsinan, a major lowstand exposed the entire shelf and upper slope, allowing fluvial processes to cut large channels across the shelf into Miocene strata. A major lowstand with fluvial activity extending across the shelf is substantiated by the presence of channels in the seismic profiles collected in this study and the presence of a peat bed overlying portions of these channels (Fig. 3.10). Other studies have concluded that the area has been incised by Early Wisconsinan channels adjacent to this study area as well (Locker and Doyle, 1992). As sea level rose during the Middle Wisconsinan, the channels were filled in with fine grained fluvial sediment. Figure 3.21 shows a model of shelf development for the northeastern GoM modified from McBride et al. (1999)

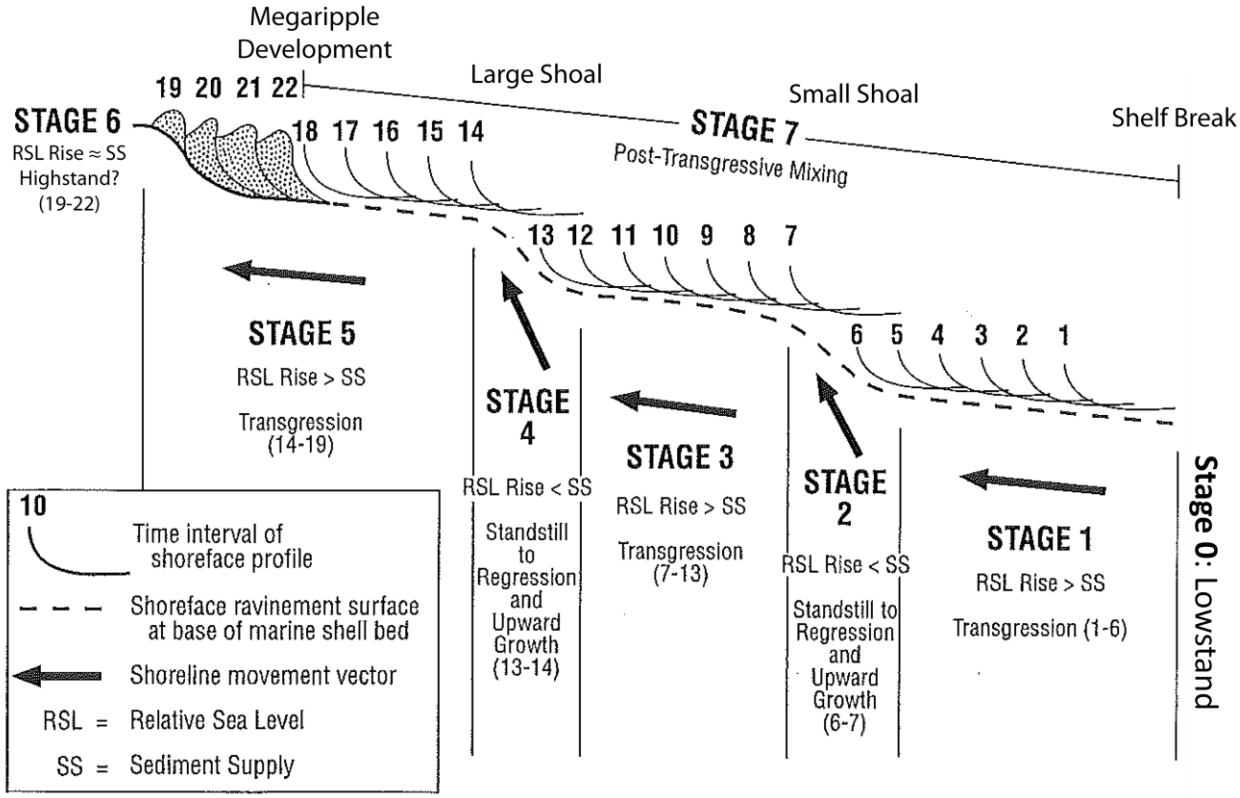

Figure 3.21. Shelf evolution and development modified from McBride et al. (1999) for the northeastern GoM.

The results of the radiocarbon dates indicate that litho-Facies 3 and seismic-Facies B are Late Pleistocene in age, deposited during a transgression as sea level rose for the last time during the last glacial period (Fig. 3.15). These dates and the depth at which they occur are in good agreement with Frazier's (1974) curve from the northwestern GoM (Fig. 3.15). Timing of this deposit would be during the end of the Mid-Wisconsinan and oxygen isotope stage 3 (OIS3) (Beard et al., 1982; Gibbard and Kolfschoten, 2004). Results from the $\delta^{13}C$ indicate that the samples are becoming increasing fresh water up-core, thus indicating a fall in sea level. All samples indicate that sea level is below (seaward) of the sample location in the core. The intermediate samples indicate that the environment of this peat was an intermediate marsh, much like what one would see around Lake Salvador, south of New Orleans, today (Chmura et al., 1987). Given this type of system, sea level may have been approximately 30-50 km basin-ward, but perhaps only a few meters (or less) below the environment of Facies 3 where the radiocarbon samples were taken.

As sea level dropped again, the most recent lowstand and Last Glacial Maximum, the organic sediments were exposed and oxidized. This lowstand is represented by a ravinement surface of erosion in the seismic (Fig. 3.7), and the transition of peat and organic material to sandy deposits with little organics, representing the Pleistocene-Holocene boundary (Figs. 3.12 and 3.13). At this time period, shelf-edge deltas debouched sediment on the outer shelf (Gardner et al., 2005). A rapid rise in sea level during the subsequent transgression allowed for this material on the outer shelf to be reworked on the middle to inner shelf, depositing a major sheet sand known as the MAFLA sand sheet (Doyle and Sparks, 1980).

The trangression may have paused twice on the inner shelf (McBride et al., 1999). During these pauses, ebb tide deltas would have formed in sand sinks on the shelf, similar to the

ebb tide delta at Destin East Pass (Fig. 3.4). These stillstands are consistent with those elsewhere in the GoM (i.e. Frazier, 1974) and this region (Hyne and Goodell, 1967; Schnable and Goodell, 1968; McBride et al., 1999). Waves and currents would cause these features to become detached ridges on the shoreface (McBride and Moslow, 1991), possibly barrier islands (Hyne and Goodell, 1967). The shoals in this region are in a reasonable path of retreat from the modern Choctawhatchee Bay, and are along the same isobaths as North and South Perdido shoals (McBride et al., 1999), suggesting that these features formed at concurrently via the same processes. Figure 3.22 illustrates this idea of shoal development from ebb tide deltas detaching from the shoreface. The smaller shoal in this study, along with South Perdido shoal, lies just landward of the region where isobaths begin to straighten and parallel the shelf break. This region is also approximately the boundary of maximum RI and wave influence during storms (Chapter 2). As sea level began to rise again, these features were likely overstepped and drowned. The presence of a relict ebb tide delta to the northeast of the shoal, along with the fining of shoal sediments offshore and with depth (Fig. 3.18), support the idea that this shoal was formed from a detached ridge of an ebb tide delta. The presence of thin flaser mud beds along the northeastern point of the shoal also is consistent with this idea of a detached ebb tide delta.

Sea level reached its present level approximately 3,000 years ago (Coleman and Smith, 1964) and ebb tide deltas and barriers formed again along the coast. High energy processes associated with tropical cyclones and cold front storms began to take over as the dominant process affecting and shaping shelf features and sediments. This has caused modification of both the seafloor and the sedimentology/stratigraphic nature of the inner shelf. The coarsening upward trend of sediments throughout Facies 5 (Fig. 3.16), and in particular on the shoal, indicates that this sand sheet is being reworked at considerable depths. The reworking and

winnowing of sediment in the near-seafloor shallow stratigraphy is substantiated by both the short term and long term bathymetric calculations (Figs. 3.19 and 3.20). Bathymetric calculations also indicate that the stoss side of the shoal is eroded, but at minimal depths overall, with deposition on the backside of the shoal. The steeper landward side and erosion on the seaward side of the shoal may indicate some barrier migration onshore. However, bathymetric calculations also indicate deposition over the crest and to the southwest, suggesting that the shoal is being maintained over time and migrating offshore, in the direction illustrated by the shoal detachment model (Fig. 3.22). The bathymetric calculations also indicate the further development of ridge and troughs on the inner shelf, which is well illustrated in the seismic (Fig. 3.8) and long term bathymetric calculations (Fig. 3.19). These calculations show that there is a large volume of sediment that is lost to the inner shelf, both over a longer time period, and a short interval (Table 3.6). The concept that storms are impacting the shelf is further corroborated by the results of the ripple index and symmetry from the ridges. These results indicate that the ridges are formed by strong waves and currents, to predominantly current conditions, (Collinson and Thompson, 1982) associated with hurricanes and large storms.

3.6 Summary

Vibracores, shallow seismic, and bathymetry data were utilized to interpret the stratigraphic framework and depositional environments of the late Quaternary inner shelf in the northeastern GoM. Four seismic facies with four bounding surfaces were recognized in the seismic, and five lithological facies were recognized within the cores. These facies represent a major portion of the late Quaternary history, including the Mid-Wisconsinan incised channels and transgression, and the Late-Pleistocene lowstand and Holocene trangression. Radiocarbon ages confirm the large temporal distribution of these facies.

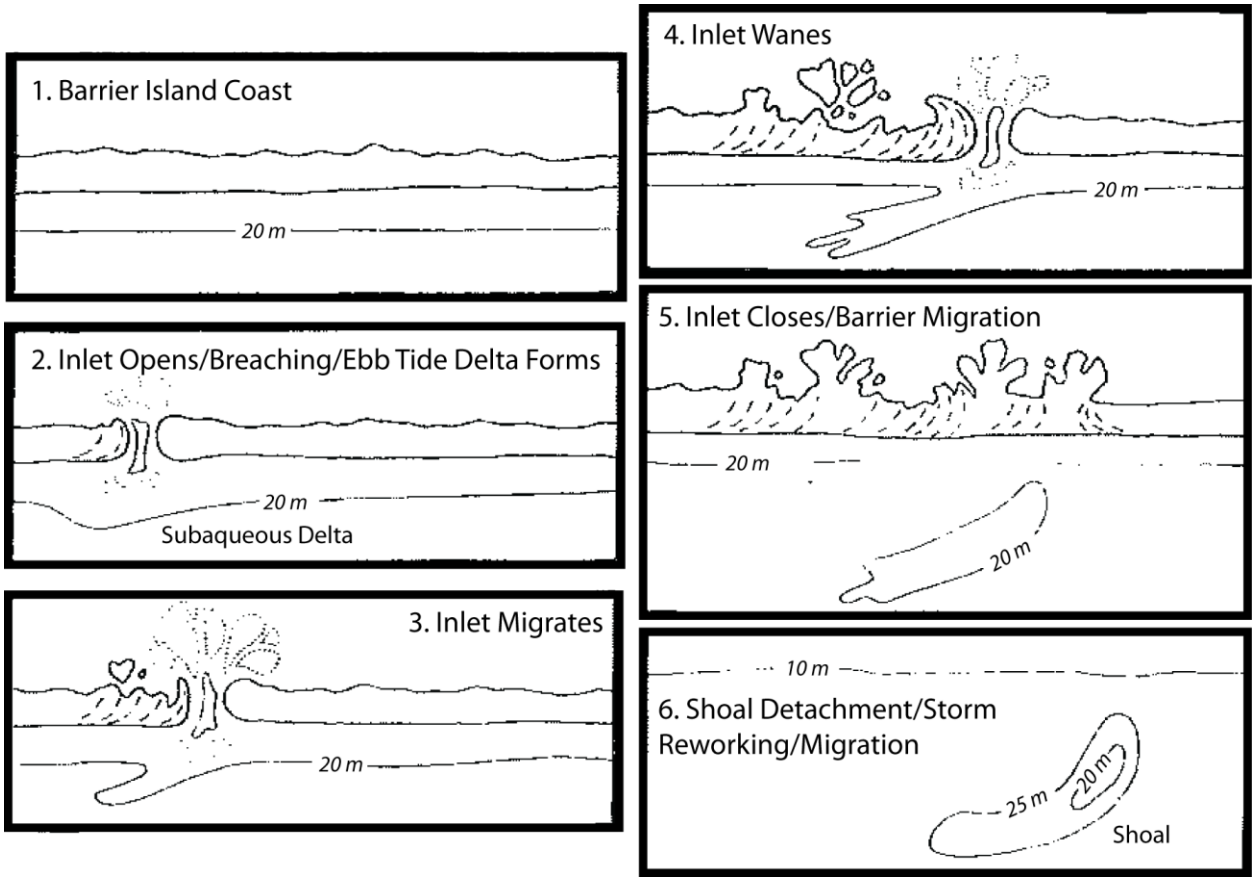

Figure 3.22. Shoal development from a detached ebb tide delta, explaining the origin of the shoals in this study. Dotted lines represent former tidal inlet shorelines. Modified from McBride and Moslow (1991).

Two shelf shoals represent stillstands during the last trangression. The shelf shoals formed from an ebb tide delta that was reworked and detached from the shoreface as sea level rose. Since sea level has stabilized in the last couple thousand of years, the shelf has undergone substantial reworking and winnowing of sediment due to storms. This well-mixed sediment has created a sheet sand that coarsens upward to the seafloor, and over time has evolved into numerous ridge and trough bathymetric features. Erosion and deposition is often localized due to these patterns, and has further modified the stratigraphic framework.

CHAPTER 4. SYNTHESIS AND A CONCEPTUAL MODEL FOR THE LATE HOLOCENE GEOMORPHIC EVOLUTION OF THE WEST FLORIDA SHELF

4.1 Conceptual Model for Shelf Evolution

While no single layer of sediment on the inner shelf can be attributed to a specific hurricane or "event", significant changes have occurred on the shelf due to the impact of frequent storms. While studies such as those from bays or lagoons (i.e. Bentley et al., 2000; Liu and Fearn, 2000) or the Texas coast (Snedden et al., 1988; Snedden and Nummedal, 1991; Siringan and Anderson, 1994) describe discreet sand layers from individual storms, this cannot be applied to the northeastern GoM shelf due to the fact that the composition of the shelf is nearly identical to that of the coast and barrier islands. Other influences are noticed however, based on sedimentology and geomorphic changes, which have been integrated with the hydrodynamic forcing, specifically when powerful hurricanes crossed the region, and computed using third generation numerical models. Figure 4.1 summarizes these influences of storms on the inner shelf. This study will corroborate the results of the numerical modeling by correlating the geologic features observed on the shelf with the processes that impact the shelf during major storms.

4.1.1 Sediment Redistribution

One general trend that is noticed on the shelf is the winnowing of sediments of the MAFLA sand sheet and the deposition of patchy thin beds of clay on the shelf. The coarsening

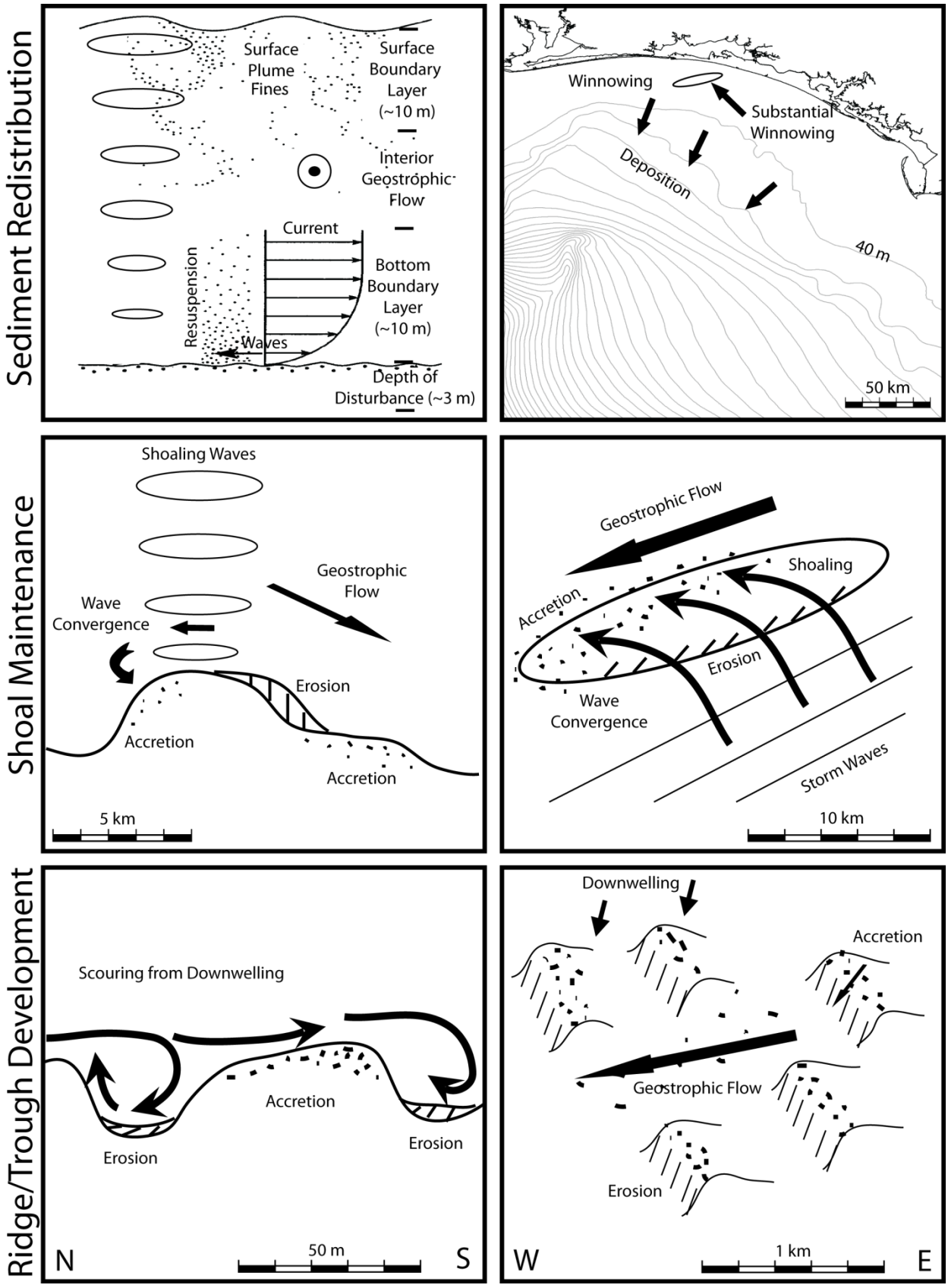
Sediment Redistribution
Surface Plume Fines
Surface Boundary Layer (~10 m)
Interior Geostrophic Flow
Current
Resuspension
Bottom Boundary Layer (~10 m)
Waves
Depth of Disturbance (~3 m)
Winnowing
Substantial Winnowing
Deposition
40 m
50 km
Shoal Maintenance
Shoaling Waves
Geostrophic Flow
Wave Convergence
Erosion
Accretion
Accretion
5 km
Geostrophic Flow
Shoaling
Accretion
Erosion
Wave Convergence
Storm Waves
10 km
Ridge/Trough Development
Scouring from Downwelling
Accretion
Erosion
Erosion
N
50 m
S
Downwelling
Accretion
Geostrophic Flow
Erosion
W
1 km
E

Figure 4.1. A conceptual model demonstrating the three dominant geomorphic/sediment transport processes originating from the passage of frequent storms across the northeastern GoM. From the top, reworking and winnowing of shelf material, and deposition of fine grained bay material; shoal maintenance due to shoaling waves and wave convergence, and geostrophic flow; trough scour and ridge building due to downwelling and geostrophic flow. For flow description and phases see Figure 2.29, Chapter 2. Diagrams were modified and synthesized from several studies (Snedden and Nummedal, 1991; Myrow and Southard, 1996; Snedden et al., 1999; Suter and Clifton, 1999; Wiberg, 2000; Hayes and Nairn, 2004).

upward trend of the entire shelf (Figs. 3.16 and 4.1) is indicative of a substantially reworked deposit. The calculations of material lost and gained over time (Fig. 3.19), and before and after Hurricane Dennis (Fig. 3.20), indicate that sediments are being reworked at a considerable depth and that can be as much as a few meters for one event. The movement of large volumes of sediment during storms has resulted in extensive vertical mixing of the sediment column (Anderson et al., 1997), likely causing sedimentary structures to be obliterated with the frequency of storms. Therefore, there is little preservation potential of the transgression on the shelf, only the effects of the highstand. Nittrouer et al. (1979) describes this region as the "surface-mixed layer", the region where sediments are under the influence of surface activity. Seismic profiles indicate that this surface-mixed layer may extend through the entire transgressive deposit to Pleistocene material (Fig. 3.8). Dellapenna et al. (2008) also describes a section on the Texas shelf near the Colorado River delta that is exposed Pleistocene sediments due to strong storm currents and erosion.

It is possible that storms, particularly smaller ones, such as tropical storms or cold fronts, may also deposit a drape of mud from the bays on the shelf or some patchier deposits of fine grained material. The presence of fine grained material is noted in some cores as flaser mud bedding, and in some cross-sections (Fig. 3.10) as larger deposits of mud and organics. Dellapenna et al. (2008) noted scour pits on the shelf that were filled with as much as a meter of mud after Hurricane Claudette. On the Louisiana shelf, ADCP's deployed at Coastal Studies Institute stations 15 and 6 were also buried well below 1 m of sediment post-hurricane Gustav and were subsequently lost (Gibson, W., personal communication). Bentley et al. (2002) described a mechanism in which sand is transported and advected on the shelf after which a mud drape is deposited. They also found that reworking of the sediment extends well below the

erosional depth cause by transport. This mud is subsequently burrowed and reworked so that the drape becomes fill for the burrows in the sand sheet. As storms impact the region again and again, the sediment is repeatedly winnowed, and material is worked off the shelf (see discussion in Chapter 2). It has been suggested that some of this material being worked off the shelf, particularly the material being deposited in the De Soto Canyon, may be forming a highstand wedge at the slope toe (Bart, P., personal communication).

4.1.2 Shoal Morphology and Maintenance

It is evident from the bathymetric calculations (Figs. 3.19 and 3.20) that the general morphology of the shoal is being maintained (Fig. 4.1). It is difficult to ascertain whether the shoal is migrating onshore, as suggested by other studies (Penland et al., 1988; Byrnes et al., 1999), due to the limited bathymetry data collected; however, it may be likely that the shoal is migrating onshore due to the steeper northern side of the shoal seen in seismic images (McBride et al., 1999). The shoal is likely being maintained by the approaching hurricane waves (Rogers et al., 2009), which increase in height and decrease in length when approaching the shoal, thus converging and shoaling on its crest (Hayes and Nairn, 2004). This convergence and shoaling of waves would create the erosion seen in the bathymetric calculations, particularly for Dennis (fig. 3.20). Deposition along the crest indicates that the crest is being built up, in agreement with the model proposed by Hayes and Nairn (2004) of shoal maintenance by converging waves on the crest. Convergence of wave would likely occur during storm events, particularly during phases 1 and 2, given the high shear stresses along the shoal crest, discussed in Chapter 2. The deposition of material in the west-southwestern section of the shoal may indicate a pathway for these currents that are winnowing the shoal crest or a pathway for the removal of sediment that is being lost from the shoal, shown in the volumetric calculations. Further research may be needed

to substantiate this idea, but this pathway is consistent with flow vectors of the central portion of the flow in the current model and discussed in Chapter 2. This may also support the idea of the presence of geostrophic flows during storms (Swift et al., 1983; Snedden et al., 1988; Snedden and Nummedal, 1991). Fining of the shoal to the west, particularly with depth (Fig. 3.18) also supports the idea that sediment on the shoal is moving in a southwesterly directions due to storm flow. The sides of the shoal, in particular the seaward side, are being dissected by ridges and troughs on the seafloor.

4.1.3 Ridge and Trough Topography

Many researchers have recognized the presence of sand ridges or megaripples on the shelf and attributed them to the influence of storms but virtually no one has attempted to explain their origin in the northeastern GoM beyond that of wave reworking (Kindinger, 1988; Locker and Doyle, 1992; McBride, 1995, 1997; McBride et al., 1999; Bart and Anderson, 2004). Due to the depths of these ridges, it is likely that they are the direct result of storm erosion and sedimentation. Many have suggested that a nucleus be available for the ridges to form, and it is postulated that these ridges were formed when sea level was lower and the fair-weather wave base could interact with the sand wave field. The storminess of the inner shelf in the northeastern GoM has further shaped these ridges. The results of the bathymetric calculations suggest that the troughs are being deepened while the swales are being built up and flattened out. The images of the seafloor in the seismic profiles also confirm this, having broad, somewhat flat swales, and narrow, deep troughs (Fig. 3.6). The steep facing sides on the southwest of the ridges indicate flow to the southwest, consistent with the ebb flow and downwelling post-hurricane landfall (Chapter 2, Fig. 2.29). In addition, studies indicate that bedform growth takes place during current deceleration (Yalin, 1977; Snedden and Nummedal, 1991) suggesting that

these features are being maintained on the ebb flow or downwelling post-storms. The ridges are very similar to megaripples recognized offshore Panama City, FL (Fleischer et al., 1996). It was concluded from this study that these ridges were formed post-hurricanes Elena and Kate, from isobath following flows. These features described by Fleischer (1996) differ slightly in orientation than the megaripples in this study, indicating a direction of flow to the northwest. This could be due to the variability in currents off the Apalachicola Embayment, and eddies that resulted in the flow model (Chapter 2).

4.2 Factors Controlling Geology in the Northeastern Gulf of Mexico: Revisited

It is clear that the major factor affecting the modern northeastern GoM inner shelf is the frequent impact of storms and their associated hydrodynamics. All three phases of hydrodynamics associated with storms, described in Chapter 2, can be seen in the sedimentology, stratigraphy, and geomorphology of Chapter 3. The pre-landfall, resuspension phase of the hurricane is important in terms of wave action on the sediments. This high-energy wave action fosters resuspension on the shelf, particularly on the shoal, as waves converge and shoal over it (Fig. 4.1). This helps maintain the shoal feature and winnow the sediments. During landfall, the mixing phase, also allows for winnowing the MAFLA sediments on the shelf, particularly of the shoal. Post-landfall downwelling and geostrophic flow become especially important in the maintenance of the shoal, development of ridge and trough topography, and carrying the fine grained material from the bays further offshore. The development of ridges and the maintenance of the shoal, in particular, is evidence for geostrophic flow during and/or post-hurricane landfall.

While the role of storms on the inner shelf is primary, other factors are secondary in shelf development that has allowed the precedence for storm impact. As discussed in Chapter 3, the stratigraphy below the inner shelf is a direct function of sea level fluctuations and has formed the

foundation for this setting. The relative stability currently associated with the northeastern GoM is important in allowing storms to significantly affect the sediments and stratigraphy. Also important is the lack of sediment input from riverine sources during fair-weather conditions. Lack of burial of storm deposits or erosional features has created a layer of sediment that is being constantly reworked and refined.

4.3 Directions for Further Research

One of the most prominent concerns in this area of research is quantifying sediment transport during a storm event, as well as over a longer period of time, such as decadal or century time scales. These models, however, are extremely complex and require a significant amount of computational power, resources, host of input data; not to mention the complex model parameterization and calibration procedures. Requirements for the success of such a model would require skill assessment of the flow model for different metocean conditions. Wind forcing may be the single most important factor in any hydrodynamic modeling and therefore improvements to the quality of wind data and modeling are essential. The availability of current data could also greatly assist such a study, allowing for both input and calibration. Also, updated bathymetry data could significantly enhance the flow simulations; particularly for the shallow water environments.

The collection of suspended sediment data during hurricanes would be useful for providing both a means for calibration and the development of an algorithm for sediment resuspension from satellite imagery. Such an algorithm has been successfully developed for parts of Louisiana and Mobile Bay (Booth et al., 2000; Miller and McKee, 2004; Miller et al., 2005) and can be useful to subsequent research in the same area.

Another area of research that has very limited understanding is that of combined flow (wave and current) properties. While it may be relatively small, understanding the shear stress due to currents combined with that of waves is essential to any sediment transport modeling, but the equations governing such properties are rather limited in their applications. This in turn would be important to understanding the dominant type of movement of sediment on the shelf, that is, geostrophic flows, episodic bed load transport, or sheet flows of sediment.

Many questions were also raised in regard to the stratigraphy of the inner shelf due to the limited extent of data collected for this study. One question is the timing of the channel fill and the creation of these channels on the shelf. Radiocarbon dates/depths of adjacent peat material suggest that these channels, particularly the large ones may be Mid-Wisconsinan, but it is difficult to ascertain if these channels were filled during the Mid-Wisconsinan transgression or the last Holocene transgression. In addition, peat deposits occurred at a variety of depth intervals on the shelf, even the surface. By determining the origin of these deposits, it would greatly facilitate a better understanding of the reworking processes that occur on the shelf. Both of these issues could be addressed by more random coring methods across the shelf, and better processing of the seismic data.

Finally, the bathymetric calculations were extremely useful in understanding the degree of change that occurred on the shelf both over longer and shorter time periods. More calculations with a wider spatial distribution would be extremely useful in corroborating a sediment transport model and would constitute a study on its own. These calculations would require the collection of data before, and immediately after large storms, as well as over longer time scales (decadal or multi-decadal). Very few studies have been attempted in this direction. With the advancement in data collection technologies, such as high resolution LIDAR data for

coastal mapping, or real time observations of metocean data for model validation, smaller features and more ephemeral changes can be observed. In addition, enhanced understanding of the geological impact of major storms would be beneficial to science.

CHAPTER 5. CONCLUSIONS

It is clear from this thesis research that storms are the dominant factor currently shaping the geology and geomorphic features of the northeastern GoM inner shelf. The overall purpose of this research was to assess how these storms affect the northeastern GoM and what these impacts are was accomplished through both physical modeling and geologic interpretations from an extensive data set combing met-ocean data with stratigraphic, sedimentological, and bathymetric data. The results of this work indicate that storm influence is manifested in three distinct features obvious on the shelf, which are the product of several different mechanisms that influence the region during major storm events. These features include 1) winnowing of sediment that creates a coarsening upward sand sheet in the upper Quaternary/Holocene stratigraphy; 2) the maintenance of sand shoals on the inner shelf; and 3) the development of ridge and trough topography on the shelf, particularly the inner shelf.

The upper Quaternary stratigraphy is a direct product of sea level change in the northern GoM and the cores and seismic, supported with radiocarbon ages are indicative of two major transgressions (the Mid-Wisconsinan and the Holocene), separated by the last lowstand at the end of the Pleistocene. Granulometry data from the facies deposited during the Holocene transgression indicates that it is a substantially reworked deposit, not only from the rise in sea level, but the continued winnowing from storms that can move at least a few meters of sediment in one event. The hydrodynamic model simulation suggests that this material is likely moved in episodic bedload transport during the peak of the storm. The model coupled with satellite imagery suggests that a large amount of fine-grained bay material is moved out on the shelf post-storms, but the lack of this material in the majority of cores indicates that finer-grained material from the bays and shelf is deposited in deeper water, further offshore than the inner shelf.

Alternatively, if this material is never buried on the shelf, it is possible that with the coring technique used this material may not be recorded.

The shoal on the inner shelf is being well-maintained, indicated by the deposition of material along the crest calculated for a 24 year period. This deposition on the crest of the shoal is likely due to the convergence of wave crests during approaching storms, in the pre-landfall phase, and geostrophic flow that develops in the landfall and post-landfall phases. Wave convergence over the shoal has also caused a migration of the shoal to the southwest and further offshore. This migration of the shoal is consistent with the detached ridge and ebb tide delta model for inner shelf shoal evolution.

Ridges and troughs have formed on the inner shelf as secondary features, possibly tertiary to larger sand wave features. The ridge and trough topography is fairly ephemeral but consistent: while the ridges almost always exist on the shelf due to the frequency storms in the northeastern GoM, their locations and depths may vary. The ridges and troughs are most pronounced post-storms, while quiescent periods allow for dissemination of the ridges, in particular. These ridges and troughs are a product of scour from return flow downwelling during the post-landfall phase of the storm.

The presence of these three features on the inner shelf, a winnowed sand sheet, the maintenance of a shoal, and the development of ridges and troughs, indicate that the northeastern GoM stratigraphy is a result of frequent and complex storm influence.

REFERENCES

Anderson, H.E., and Bart, P.J., 1999, Evolution of the Apalachicola Delta: The last glacial eustatic cycle: Transactions-Gulf Coast Association of Geological Societies, v. XLIX, p. 7.

Anderson, J.B., Rodriguez, A., Abdulah, K.C., Fillon, R.H., Banfield, L.A., McKeown, H.A., and Wellner, J.S., 2004, Late Quaternary stratigraphic evolution of the northern Gulf of Mexico Margin: A synthesis, *in* Anderson, J.B., and Fillon, R.H., eds., Late Quaternary Stratigraphic Evolution of the Northern Gulf of Mexico Margin, Volume 79: SEPM Special Publication: Tulsa, OK, Society for Sedimentary, SEPM, p. 1-23.

Anderson, L.C., Sen Gupta, B.K., McBride, R.A., and Byrnes, M.R., 1997, Reduced seasonality of Holocene climate and pervasive mixing of Holocene marine section: Northeastern Gulf of Mexico shelf: Geology v. 25, p. 127-130.

AOML, 2006, Atlantic Oceanographic and Meteorological Laboratory, *in* (NOAA), N.O.a.A.A., ed., Volume 2007, National Oceanic and Atmospheric Administration (NOAA).

Arnante, C., and Eakins, B.W., 2009, ETOPO1 1 Arc-Minute Gobal Relief Model: Procedures, Data Sources and Analysis, NOAA Technical Memorandum NESDIS NGDC-24, National Oceanic and Atmospheric Administration (NOAA), p. 19.

Baba, J., and Komar, P.D., 1981, Measurements and analysis of settling velocities of natural quartz sand grains: Journal of Sedimentary Petrology, v. 51, p. 0631-0640.

Bart, P.J., Anderson, J.B., and Richmond, R.V., 1998, Pleistocene lowstands on the Alabama/West Florida continental shelf: Implications for the importance of shelf-edge fluvial incision as an initiator of slope canyons: Transactions-Gulf Coast Association of Geological Societies, v. XLVIII, p. 527-528.

Bart, P.J., and Anderson, J.B., 2004, Late Quaternary stratigraphic evolution of the Alabama and west Florida outer continental shelf, *in* Anderson, J.B., and Fillon, R.H., eds., Late Quaternary Stratigraphic Evolution of the Northern Gulf of Mexico Margin, Volume 79: Special Publication - Society for Sedimentary Geology: Tulsa, OK, United States, Society for Sedimentary Geology (SEPM), p. 53-43.

Basillie, J.H., 1987, Seasonal variation in sandy beach shoreline position and beach width, *in* Resources, F.D.o.N., ed., Beach and Shores Technical and Design Memorandum, p. 18.

Beard, J.H., Sangree, J.B., and Smith, L.A., 1982, Quaternary chronology, paleoclimate, depositional sequences, and eustatic cycles: AAPG Bulletin, v. 66, p. 158-170.

Bentley, S.J., Keen, T.R., Blain, C.A., and Vaughan, W.C., 2002, The origin and preservation of a major hurricane event bed in the northern Gulf of Mexico; Hurricane Camille, 1969: Marine Geology, v. 186, p. 446-423.

Bentley, S.J., Sr., Furukawa, Y., and Vaughan, C.W., 2000, Record of event sedimentation in Mississippi Sound: AAPG Bulletin, v. 84, p. 1672-1672.

Beven, J., 2005, Tropical Cyclone Report: Hurricane Dennis, National Hurricane Center, p. 25.

Boone, P.A., 1973, Depositional systems of the Alabama, Mississippi, and western Florida coastal zone: GCAGS Transactions, v. XXIII, p. 266-277.

Booth, J.G., Miller, R.L., McKee, B.A., and Leathers, R.A., 2000, Wind-induced bottom sediment resuspension in a microtidal coastal environment: Continental Shelf Research, v. 20, p. 785-806.

Bryant, W.R., Lugo, J., Cordova, C., and Salvador, A., 1991, Physiography and bathymetry, *in* Salvador, A., ed., The Gulf of Mexico Basin, Volume J: Boulder, Colorado, Geological Society of America.

Byrnes, M.R., Hammer, R.M., Vittor, B.A., Ramsey, J.S., Snyder, D.B., Bosma, K.F., Wood, J.D., Thibaut, T.D., and Philips, N.W., 1999, Environmental survey of identified sand resource areas offshore Alabama, *in* Applied Coastal Research and Engineering, I., ed.: Mashpee, MA, Minerals Management Service, p. 327.

Byrnes, M.R., Griffee, S.F., and Osler, M.S., 2008, Evaluation of channel dredging on shoreline response at and adjacent to Mobile Pass, Alabama: Mashpee, MA, Applied Coastal Research and Engineering, p. 316.

Chen, Q., Wang, L., and Tawes, R., 2008, Hydrodynamic response of northeastern Gulf of Mexico to hurricanes: Estuaries and Coasts, v. 31, p. 1098-1116.

Chmura, G.L., Aharon, P., Socki, R.A., and Abernethy, R., 1987, An inventory of 13C abundances in coastal wetlands of Louisiana, USA: Vegetation and sediments: Oecologia, v. 74, p. 264-271.

Coleman, J.M., and Smith, W.G., 1964, Late recent rise of sea level: GSA Bulletin, v. 75, p. 833-840.

Coleman, J.M., Prior, D.B., and Roberts, H.H., 1986, Geologic development and characteristics of the continental margins, Gulf of Mexico: Gulf Coast Association of Geological Societies Transactions, v. XXXVI, p. 61-64.

Collinson, J.D., and Thompson, D.B., 1982, Sedimentary Structures: London, UK, George Allen & Unwin Ltd. , 194 p.

Curray, J.R., 1960, Sediments and history of Holocene Transgression, continental shelf, northwest Gulf of Mexico, p. 221-266.

Curray, J.R., 1964, Transgressions and regressions, [Chapter] 10: International, p. 203-175.

D'Sa, E.J., Miller, R.L., and McKee, B.A., 2007, Suspended particulate matter dynamics in coastal waters from ocean color: Application to the northern Gulf of Mexico: Geophysical Research Letters, v. 34, p. 23611-.

Davis, R.A., 1997, Regional coastal morphodynamics along the United States Gulf of Mexico: Journal of Coastal Research, v. 13, p. 595-604.

Dellapenna, T.M., Majzlik, E., and Allison, M., 2008, Sand sources and seabed processes of the Colorado River Delta: CMP Cycle 7 Final Report: Galveston, Texas A & M University.

Department of Environmental Protection, 2008, Strategic Beach Management Plan for the Panhandle Gulf Coast Region, State of Florida, p. 39.

DHI Water & Environment, 2006, MIKE 21 & MIKE 3 Flow Model FM, *in* DHI, ed.: Horsholm, Denmark, DHI, p. 36.

DHI Water & Environment, 2007, MIKE 21/3 coupled Model FM, *in* DHI, ed.: Horsholm, Denmark, DHI, p. 1-62.

Divins, D.L., and Metzger, D., 2008, NGDC Coastal Relief Model, *in* (NGDC), N.G.D.C., ed., Volume 2007-2009, National Oceanographic and Atmospheric Administration.

Doering, J.A., 1956, Review of Quaternary Surface Formations of Gulf Coast Region: Bulletin of the American Association of Petroleum Geologists, v. 40, p. 1816-1862.

Donoghue, J.F., 1992, Late Quaternary coastal and inner shelf stratigraphy, Apalachicola Delta region, Florida, *in* Donoghue, J.F., Davis, R.A., Fletcher, C.H., and Suter, J.R., eds., Quaternary Coastal Evolution, Volume 80: Sedimentary Geology: Amsterdam, Elsevier Science Publishers B.V., p. 293-304.

Donoghue, J.F., Niedoroda, A.W., Hatchett, L., Locker, S.D., Clark, R., Koch, J., and Butler, K., 2003, Model for identifying and characterizing offshore sand sources using an interactive GIS, Coastal Sediments '03, American Society of Civil Engineers.

Doyle, L.J., and Sparks, T.N., 1980, Sediments of the Mississippi, Alabama, and Florida (MAFLA)) continental shelf: Journal of Sedimentary Petrology, v. 50, p. 915-905.

Drake, D.E., Cacchione, D.A., and Grant, W.D., 1992, Shear stress and bed roughness estimates for combined wave and current flows over a rippled bed: Journal of Geophysical Research, v. 97, p. 2319-2326.

Edwards, J.H., Harrison, S.E., Locker, S.D., Hine, A.C., and Twichell, D.C., 2003, Stratigraphic framework of sediment-starved sand ridges on a mixed siliciclastic/carbonate inner shelf; west-central Florida: Marine Geology, v. 200, p. 195-217.

Ellis, J., and Stone, G.W., 2006, Numerical simulation of net longshore sediment transport and granulometry of surficial sediments along Chandeleur Island, Louisiana, USA: Marine Geology, v. 232, p. 115-129.

Figueiredo, A.G., Swift, D.J.P., Stubblefield, W.L., and Clarke, T.L., 1981, Sand ridges on the inner Atlantic shelf of North America: morphometric comparisons with the Huthnance stability model: Geo-Marine Letters, v. 1, p. 187-191.

Finkle, C.W., Benedet, L., and Andrews, J.L., 2005, Submarine geomorphology of the continental shelf off southeast Florida based on interpretation of airborne laser bathymetry: Journal of Coastal Research, v. 21, p. 1178-1190.

Fisk, H.N., McFarlan, E., Kolb, C.R., and Wilbert, L.J., 1954, Sedimentary framework of the modern Mississippi Delta: Journal of Sedimentary Petrology, v. 24, p. 76-99.

Fleischer, P., Sawyer, W.B., Fiedler, H., and Stender, I.H., 1996, Spatial and temporal variability of a coarse-sand anomaly on a sandy inner shelf, northeastern Gulf of Mexico: Geo-Marine Letters, v. 16, p. 266-272.

Flocks, J.G., Ferina, N.F., Dreher, C., Kindinger, J.L., FitzGerald, D.M., and Kulp, M.A., 2006, High-resolution stratigraphy of a Mississippi subdelta-lobe progradation in the Barataria Bight, north-central Gulf of Mexico: Journal of Sedimentary Research, v. 76, p. 429-443.

Folk, R.L., and Ward, W.C., 1957, Brazos River bar [Texas]; a study in the significance of grain size parameters: Journal of Sedimentary Petrology, v. 27, p. 3-26.

Folk, R.L., 1980, Petrology of Sedimentary Rocks: Austin, TX, Hemphill Publishing Company, 190 p.

Frazier, D.E., 1974, Depositional - Episodes: Their relationship to the Quaternary stratigraphic framework in the northwestern portion of the Gulf Basin: Geological Circular, v. 74, p. 1-28.

Freeman, A., 2010, Analysis and Modeling of Hurrican Impacts on a Coastal Louisiana Lake Bottom: Baton Rouge, LA, Louisiana State University.

Fullerton, D., 1997, Sangamon and Sangamonian time divisions, chronostratigraphic unit, and geosol - clarification of terminology: Quaternary Research, v. 48, p. 247-248.

Gardner, J.V., Dartnell, P., Mayer, L.A., Hughes Clarke, J.E., Calder, B.R., and Duffy, G., 2005, Shelf-edge deltas and drowned barrier-island complexes on the northwest Florida outer continental shelf: Geomorphology, v. 64, p. 133-166.

Gibbard, P., and Kolfschoten, T.V., 2004, The Pleistocene and Holocene Epochs, p. 441-454.

Gould, H.R., and McFarlan, E., 1959, Geologic history of the Chenier Plain, southwestern Louisiana: Gulf Coast Association of Geological Societies Transactions, v. IX, p. 261-271.

Grant, W.D., and Madsen, O.S., 1979, Combined wave and current interaction with a rough bottom: Journal of Geophysical Research, v. 84, p. 17971808.

Grant, W.D., and Madsen, O.S., 1986, The continental shelf bottom boundary layer: Annual Review of Fluid Mechanics, v. 18, p. 265-305.

Guidroz, W.S., Poole, K.R., Stone, G.W., Dartez, D., and Pond, L.G., 2007, Contrasting sediment transport along the southwestern Louisiana and upper Texas shorelines: Impacts from Hurricane Rita, 2005: Shore and Beach, v. 75, p. 57-64.

Gunter, H., 1931, The Pensacola Terrace and associated beaches and bars in Florida: Florida State Geological Survey Bulletin, v. 7, p. 44.

Hapke, C.J., and Christiano, M., 2007, Long-term and storm-related shoreline change trends in the Florida Gulf Islands National Seashore, Volume 2007-1392, U.S. Geological Survey, p. 18p.

Hayes, M.O., 1966, Some observations on the geological effects of hurricanes south Texas coast: Houston Geological Society Bulletin, v. 9, p. 18-26.

Hayes, M.O., 1967, Hurricanes as geological agents, south Texas coast: AAPG Bulletin, v. 51, p. 937-956.

Hayes, M.O., and Nairn, R.B., 2004, Natural maintenance of sand ridges and linear shoals on the U.S. Gulf and Atlantic continental shelves and the potential impacts of dredging: Journal of Coastal Research, v. 20, p. 138-148.

He, R., and Weisberg, R.H., 2002, A Loop Current intrusion case study on the West Florida shelf: Journal of Physical Oceanography, v. 33, p. 465-477.

Hetland, R.D., Hsueh, Y., Leben, R.R., and Niiler, P.P., 1999, A Loop Current-induced jet along the edge of the West Florida shelf: Geophysical Research Letters, v. 26, p. 2239-2242.

Hyne, N.J., and Goodell, H.G., 1967, Origin of the sediments and submarine geomorphology of the inner continental shelf off Choctawhatchee Bay, Florida: Marine Geology, v. 5, p. 299-313.

Isphording, W.C., and Imsand, F.D., 1991, Cyclonic events and sedimentation in the Gulf of Mexico, *in* Kraus, N.C., Gingerich, K.J., and Kriebel, D.L., eds., Coastal Sediments '91, Volume 2, American Society of Civil Engineers, p. 1122-1136.

Isphording, W.C., and Isphording, G.W., 1991, Identification of ancient storm events in buried Gulf Coast sediments: Transactions - Gulf Coast Association of Geological Societies, v. 41, p. 347-339.

Jackson, R.B., Isphording, W.C., Caputo, M.V., and Gibbons, T.L., 1991, The sedimentology and clay mineralogy of Choctawhatchee Bay, Northwest Florida: AAPG Bulletin, v. 75, p. 1527-1526.

Jensen, J.H., Viggosson, G., Elfrink, B., and Broker, I., 2007, Bakkafjara: Sediment Transport and Morphology Phase 2, *in* Environment, D.W., ed.: Horsholm, Denmark, DHI Water & Environment, p. 118.

Jose, F., Kobashi, D., and Stone, G.W., 2007, Spectral wave transformation over an elongated sand shoal off south central Louisiana, USA: Journal of Coastal Research, p. 757-761.

Kahn, J.H., and Roberts, H.H., 1982, Variations in storm response along a microtidal transgressive barrier-island arc: Sedimentary Geology, v. 33, p. 129-146.

Keen, T.R., and Allen, S.E., 2000, The generation of internal waves on the continental shelf by Hurricane Andrew: Journal of Geophysical Research, v. 105, p. 26,203-26,224.

Keen, T.R., and Stone, G.W., 2000, Anomalous response of beaches to hurricane waves in a low-energy environment, northeast Gulf of Mexico, USA: Journal of Coastal Research, v. 16, p. 1100-1110.

Keen, T.R., and Glenn, S.M., 2002, Predicting bed scour on the continental shelf during Hurricane Andrew: Journal of Waterway, Port, Coastal and Ocean Engineering, p. 249-259.

Keen, T.R., Bentley, S.J., Vaughan, W.C., and Blain, C.A., 2004, The generation and preservation of multiple hurricane beds in the northern Gulf of Mexico: Marine Geology, v. 210, p. 105-79.

Keim, B.D., Muller, R.A., and Stone, G.W., 2007, Spatiotemporal patterns and return periods of tropical storm and hurricane strikes from Texas to Maine: Journal of Climate, v. 20, p. 3498-3509.

Kindinger, J.L., 1988, Seismic stratigraphy of the Mississippi-Alabama shelf and upper continental slope: Marine Geology, v. 83, p. 79-94.

Kobashi, D., Jose, F., and Stone, G.W., 2007, Heterogeneity and dynamics on a shoal during spring-winter storm season, south-central Louisiana, USA, Coastal Sediments '07: New Orleans, LA, ASCE, p. 1-14.

Kobashi, D., 2009, Bottom Boundary Layer Physics and Sediment Transport Along a Transgressive Sand Body, Ship Shoal, South-Central Louisiana: Implications for Fluvial Sediments and Winter Storms [Dissertation thesis]: Baton Rouge, LA, Louisiana State University.

Kobashi, D., and Stone, G.W., 2009, Spatially-varying morphodynamics over a shore-parallel transgressive shoal, south-central Louisiana, U.S.A., Coastal Dynamics 2009: Tokyo, Japan, p. 1-12.

Koch, J.L., 2006, Late Quaternary Evolution of the Northwest Florida Coast and Margin: Development of a Conceptual Model for Identifying and Characterizing Shelf Sediment Deposits, The Florida State University.

Lambeck, K., and Chappell, J., 2001, Sea level change through the last glacial cycle: Science, v. 292, p. 679-686.

Li, M.Z., Amos, C.L., and Heffler, D.E., 1997, Bottom boundary layer dynamics and sediment transport under storm and non-storm conditions on the Scotian shelf: Marine Geology, v. 141, p. 157-181.

Liu, K.-b., and Fearn, M.L., 2000, Reconstruction of prehistoric landfall frequencies of catastrophic hurricanes in northwestern Florida from lake sediment records: Quaternary Research, v. 54, p. 238-245.

Liu, Y., Islam, M.A., and Gao, J., 2003, Quantification of shallow water quality parameters by means of remote sensing: Progress in Physical Geography, v. 27, p. 24-43.

Locker, S.D., Logue, K.T., and Doyle, L.J., 1988, Neogene stratigraphy, bedforms, and surface sediments: NW Florida state waters: St. Petersburg, FL, University of South Florida, p. 75.

Locker, S.D., and Doyle, L.J., 1992, Neogene to Recent stratigraphy and depositional regimes of the northwest Florida inner continental shelf: Marine Geology, v. 104, p. 123-138.

Ludwick, J.C., 1964, Sediments in northeastern Gulf of Mexico, *in* Miller, R.L., ed., Papers in Marine Geology: New York, Macmillan Co., p. 204-238.

Madsen, O.S., 1976, Wave climate of the continental margin: Elements of its mathematical description, *in* Stanley, and Swift, eds., Marine Sediment Transport and Environmental Management, p. 65-87.

Mancini, E.A., 2008, Paleogene lowstand systems tract sand deposits of the eastern Gulf Coastal Plain: Potential reservoir facies in the offshore northeastern Gulf of Mexico: Gulf Coast Association of Geological Societies Transactions, v. 58, p. 669-675.

Mazzullo, J., and Bates, C., 1985, Sources of Pleistocene and Holocene sand for the Northeast Gulf of Mexico Shelf and the Mississippi Fan: GCAGS Transactions, v. 35, p. 457-466.

McBride, R.A., and Moslow, T.F., 1991, Origin, evolution, and distribution of shoreface sand ridges, Atlantic inner shelf, U.S.A.: Marine Geology, v. 97, p. 57-85.

McBride, R.A., 1995, Surficial sediments and morphology of the southwestern Alabama/western Florida Panhandle coast and shelf: Transactions - Gulf Coast Association of Geological Societies, v. 45, p. 404-393.

McBride, R.A., 1997, Seafloor morphology, geologic framework, and sedimentary processes of a sand-rich shelf offshore Alabama and northwest Florida: Northeastern Gulf of Mexico: Baton Rouge, LA, Louisiana State University.

McBride, R.A., Anderson, L.C., Tudoran, A., and Roberts, H.H., 1999, Holocene stratigraphic architecture of a sand-rich shelf and the origin of linear shoals: Northeastern Gulf of Mexico, *in* Bergman, K.M., and Snedden, J.W., eds., Isolated shallow marine sand bodies; Sequence stratigraphic analysis and sedimentologic interpretation, Volume 64: Special Publication - Society for Sedimentary Geology: Tulsa, OK, United States, Society for Sedimentary Geology (SEPM), p. 95-126.

McBride, R.A., Moslow, T.F., Roberts, H.H., and Diecchio, R.J., 2004, Late Quaternary geology of the northeastern Gulf of Mexico shelf; sedimentology, depositional history, and ancient analogs of a major shelf sand sheet of the modern transgressive systems tract, *in* Anderson, J.B., and Fillon, R.H., eds., Late Quaternary Stratigraphic Evolution of the Northern Gulf of Mexico Margin, Volume 79: Special Publication - Society for Sedimentary Geology: Tulsa, OK, United States, Society for Sedimentary Geology (SEPM), p. 55-83.

McFarlan, E., Jr., 1961a, Radiocarbon dating of late Quaternary deposits, South Louisiana: GSA Bulletin, v. 72, p. 129-158.

McFarlan, E., Jr., 1961b, Radiocarbon dating of Late Quaternary deposits, South Louisiana: Geological Society of America Bulletin, v. 72, p. 129-158.

McKeown, H.A., Bart, P.J., and Anderson, J.B., 2004, High-resolution stratigraphy of a sandy, ramp-type margin; Apalachicola, Florida, U.S.A, *in* Anderson, J.B., and Fillon, R.H., eds., Late Quaternary Stratigraphic Evolution of the Northern Gulf of Mexico Margin, Volume 79: Special Publication - Society for Sedimentary Geology: Tulsa, OK, United States, Society for Sedimentary Geology (SEPM), p. 41-25.

Mehta, A.J., 2002, Mudshore dynamics and controls, *in* Healy, T., Wang, Y., and Healy, J.-A., eds., Muddy Coasts of the World: Processes, Deposits and Function: Amsterdam, The Netherlands, Elsevier Science B.V., p. 19-60.

Miller, M.C., McCave, I.N., and Komar, P.D., 1977, Threshold of sediment motion under unidirectional currents: Sedimentology, v. 24, p. 507-527.

Miller, R.L., and McKee, B.A., 2004, Using MODIS Terra 250 m imagery to map concentrations of total suspended matter in coastal waters: Remote Sensing of Environment, v. 93, p. 259-266.

Miller, R.L., McKee, B.A., and D'Sa, E.J., 2005, Monitoring bottom sediment resuspension and suspended sediments in shallow coastal waters, Remote Sensing of Coastal Aquatic Environments: Netherlands, Springer, p. 259-276.

Mitchell, D., Teague, W.J., Jarosz, E., and Wang, D.W., 2005, Observed currents over the outer continental shelf during Hurricane Ivan: Geophysical Research Letters, v. 32, p. L11610.

Moeller, C.G., Huh, O.K., Roberts, H.H., Gumley, L.E., and Menzel, W.P., 1993, Response of Louisiana coastal environments to a cold front passage: Journal of Coastal Research, v. 9, p. 434-447.

Mossa, J., 1984, Wave climate studies in the northern Gulf of Mexico: Comparisons of visual surf, SSMO, hindast, and gage data, Oceans '84, Volume 2, MTS/IEE, p. 717-724.

Muller, R.A., and Stone, G.W., 2001, A climatology of tropical storm and hurricane strikes to enchance vulnerability prediction for the southeast U.S. Coast: Journal of Coastal Research, v. 17, p. 949-956.

Myrow, P.M., and Southard, J.B., 1996, Tempestite deposition: Journal of Sedimentary Research, v. 66, p. 875-887.

NARR, 2007, North American Regional Reanalysis, *in* (NOAA), N.O.a.A.A., ed., Volume 2007, National Oceanic and Atmospheric Administration (NOAA).

NDBC, 2008, National Data Buoy Center, *in* (NOAA), N.O.a.A.A., ed., Volume 2008, National Oceanic and Atmospheric Administration (NOAA).

Nielsen, P., 1992, Coastal Bottom Boundary Layers and Sediment Transport: Singapore, World Scientific Publishing Co. Pte. Ltd. , 324 p.

Nittrouer, C.A., and Wright, L.D., 1994, Transport of particles across continental shelves: Reviews of Geophysics, v. 32, p. 85-113.

NOAA Coastal Services Center, 2009, Historical Hurricane Tracks, *in* NOAA, ed., Volume 2009: Charleston, SC, NOAA.

Otvos, E.G., 1988, Pliocene age of coastal units, Northeastern Gulf of Mexico: Transactions-Gulf Coast Association of Geological Societies, v. XXXVIII, p. 485-494.

Palacas, J.G., 1968, Organic matter in bottom sediments, Choctawhatchee Bay, Florida.

Penland, S., Boyd, R., and Suter, J.R., 1988, Transgressive depositional systems of the Mississippi Delta Plain: A model for barrier shoreline and shelf sand development: Journal of Sedimentary Petrology, v. 58, p. 932-949.

Pepe, G., and Coutu, G., 2008, Beach morphology change study using arcGIS spatial analyst: Middle States Geographer, v. 41, p. 91-97.

Pepper, D.A., Stone, G.W., and Wang, P., 1999, Bottom boundary layer parameters and sediment transport on the Louisiana inner-shelf during cold front passages: Gulf Coast Association of Geological Societies Transactions, v. XLIX, p. 432-439.

Prasad, T.G., and Hogan, P.J., 2007, Upper-ocean response to Hurricane Ivan in a $1/25^{o}$ nested Gulf of Mexico HYCOM Journal of Geophysical Research, v. 112, p. 1-18.

Price, M., 2002, Deriving volumes with ArcGIS spatial analyst, ArcUser, ESRI, p. 52-56.

Reid, J.A., Williams, S.J., and Torresan, L.Z., 2006, usSEABED, *in* Program, C.a.M.G., ed., Volume 2009, U.S. Geological Survey.

Reza, M.M., 2008, Assessment of suspended sediments concentration in surface waters, using MODIS images: American Journal of Applied Sciences, v. 5, p. 798-804.

Richmond, R.V., Bart, P.J., and Anderson, J.B., 2000, Late Quaternary sequence development on a slowly subsiding, ramp margin: offshore Alabama/northwest Florida: AAPG Annual Meeting Program with Abstracts.

Roberts, H.H., 1997, Dynamic changes of the Holocene Mississippi River Delta Plain: The delta cycle: Journal of Coastal Research, v. 13, p. 605-627.

Roberts, H.H., Fillon, R.H., Kohl, B., Robalin, J.M., and Sydow, J.C., 2004, Depositional architectur of the Lagniappe Delta: Sediment characteristics, timing of depositional events, and temporal relationship with adjacent shelf-edge deltas, *in* Anderson, J.B., and Fillon, R.H., eds., Late Quaternary Stratigraphic Evolution of the Northern Gulf of Mexico Margin, Volume 79: SEPM Special Publication: Tulsa, OK, SEPM (Society for Sedimentary Geology), p. 143-188.

Robinson, I.S., 2004, Measuring the Oceans From Space: The principles and methods of satellite oceanography: Chichester, UK, Springer, 669 p.

Rodriguez, A.B., Anderson, J.B., Siringan, F.P., and Taviani, M., 1999, Sedimentary facies and genesis of Holocene sand banks on the east Texas inner continental shelf, *in* Bergman, K.M., and Snedden, J.W., eds., Isolated shallow marine sand bodies: Sequence stratigraphic analysis and sedimentologic interpretation, Volume 64: SEPM Special Publication: Tulsa, OK, Society for Sedimentary Geology (SEPM), p. 165-178.

Rogers, B.E., Kulp, M.A., and Miner, M.D., 2009, Late Holocene chronology, origin, and evolution of the St. Bernard Shoals, northern Gulf of Mexico, USA: Geo-Marine Letters, v. 30.

Schnable, J.E., and Goodell, H.G., 1968, Pleistocene-recent stratigraphy, evolution, and development of the Apalachicola Coasta, Florida, Geological Society of America, Special Paper, Volume 112: Boulder, Colorado, Geological Society of America, Inc. , p. 72p.

Siadatmousavi, S.M., Jose, F., and Stone, G.W., in review, The effects of bed friction on wave simulation: Implementation of an unstructured third-generation wave model, SWAN: Journal of Geophysical Research, v. XX, p. XXX-XXX.

Siddall, M., Rohling, E.J., Almogi-Labin, A., Hemleben, C., Meischner, D., Schmelzer, I., and Smeed, D.A., 2003, Sea-level fluctuations during the last glacial cycle: Nature, v. 423, p. 853-858.

Siegel, D.A., Wang, M., Maritorena, S., and Robinson, W., 2000, Atmospheric correction of satellite ocean color imagery: the black pixel assumption: Applied Optics, v. 39, p. 3582-3591.

Siringan, F.P., and Anderson, J.B., 1994, Modern shoreface and inner-shelf storm deposits off the East Texas Coast, Gulf of Mexico: Journal of Sedimentary Research, Section B: Stratigraphy and Global Studies, v. 64, p. 99.

Snedden, J.W., Nummedal, D., and Amos, A.F., 1988, Storm- and fair-weather combined flow on the central Texas continental shelf: Journal of Sedimentary Petrology, v. 58, p. 580-595.

Snedden, J.W., and Nummedal, D., 1991, Origin and geometry of storm-deposited sand beds in modern sediments of the Texas continental shelf: Special Publications of the International Associating of Sedimentologists, v. 14, p. 283-308.

Snedden, J.W., Tillman, R.w., Kreisa, R.D., Schweller, W.J., Culver, S.J., and Winn, R.D., 1994, Stratigraphy and genesis of a modern shoreface-attached sand ridge, Peahala Ridge, New Jersey: Journal of Sedimentary Research, v. 4, p. 560-581.

Snedden, J.W., and Dalrumple, R.W., 1999, Modern shelf sand ridges: From historical perspective to a unified hydrodynamic and evolutionary model, *in* Bergman, K.M., and Snedden, J.W., eds., Isolated shallow marine sand bodies: Sequence stratigraphic analysis and sedimentologic interpretation, Volume 64: Tulsa, OK, SEPM, p. 13-28.

Snedden, J.W., Kreisa, R.D., Tillman, R.W., Culver, S.J., and Schweller, W.J., 1999, An expanded model for modern shelf sand ridge genesis and evolution on the New Jersey Atlantic shelf, *in* Bergman, K.M., and Snedden, J.W., eds., Isolated Shallow Marine Sand Bodies: Sequence Stratigraphic Analysis and Sedimentologic Interpretation, Volume 64: Tulsa, OK, SEPM, p. 147-163.

Sorensen, O.R., Kofoed-Hansen, H., Rugbjerg, M., and Sorensen, L.S., 2004, A third-generation spectral wave model using an unstructured finite volume technique, 29th International Conference on Coastal Engineering, Volume 29, p. 894-906.

Spaziani, A.L., Jose, F., and Stone, G.W., 2009, Sediment dynamics on an inner shelf shoal during storm events in the northeastern Gulf of Mexico, USA: Journal of Coastal Research, v. SI 56, p. 668-672.

Spiske, M., and Jaffe, B.E., 2009, Sedimentology and hydrodynamic implications of a coarse-grained hurricane sequence in a carbonate reef setting: Geology, v. 37, p. 839-842.

Stewart, S.R., 2004, Tropical Cyclone Report: Hurricane Ivan: Miami, National Hurricane Center, p. 6.

Stewart, S.R., 2006, Tropical Cyclone Report: Hurricane Cindy, National Hurricane Center, p. 21.

Stone, G.W., Fischer, D.W., and Morgan, J.P., 1985, The variability of Florida's coasts to storm wave susceptibility: Journal of Shoreline Management, v. 1, p. 81-104.

Stone, G.W., 1991, Differential Sediment Supply and the Cellular Nature of Longshore Sediment Transport Along Coastal Northwest Florida and Southeast Alabama Since the Late Holocene [unpublished thesis]: College Park, University of Maryland.

Stone, G.W., and Penland, S., 1992, Historic shoreline change along the northern Gulf of Mexico, *in* Majumdar, S.K., Forbes, G.S., Miller, E.W., and Schmalz, R.F., eds., Natural and technological disasters: Causes, effects and preventative measures, The Pennsylvania Academy of Science, p. 267-279.

Stone, G.W., Stapor, F.W., May, J.P., and Morgan, J.P., 1992, Multiple sediment sources and a cellular, non-integrated, longshore drift system: Northwest Florida and southeast Alabama coast, USA: Marine Geology, v. 105, p. 141-154.

Stone, G.W., and Stapor, F.W., 1996, A nearshore sediment transport model for the northeast Gulf of Mexico coast, USA: Journal of Coastal Research, v. 12, p. 786-792.

Stone, G.W., Liu, B., Pepper, D.A., and Wang, P., 2004, The importance of extratropical and tropical cyclones on the short-term evolution of barrier islands along the Gulf of Mexico, USA: Marine Geology, v. 210, p. 63-78.

Stone, G.W., Walker, N.D., Hsu, S.A., Babin, A., Liu, B., Keim, B.D., Teague, W., Mitchell, D., and Leben, R., 2005, Hurricane Ivan's impact along the northern Gulf of Mexico: EOS, Transactions, v. 86, p. 497-508.

Stone, G.W., 2006, Tropical cyclone and winter storm impacts on the short-term evolution of barriers along the northeastern Gulf of Mexico: Gulf Coast Association of Geological Societies Transactions, v. 56, p. 793-795.

Stone, G.W., Liu, B., and Jose, F., 2007, Winter storm and tropical cyclone impacts on the short-term evolution of beaches and barriers along the northeastern Gulf of Mexico, *in* Kraus, N.C., and Rosati, J.D., eds., Coastal Sediments '07, Volume 2: New Orleans, LA, American Society of Civil Engineers, p. 935-950.

Stumpf, R.P., and Pennock, J.R., 1989, Calibration of a general optical equation for remote sensing of suspended sediments in a moderately turbid estuary: Journal of Geophysical Research, v. 94, p. 14,363-14,371.

Suter, J.R., and Clifton, H.E., 1999, The Shannon Sandstone and isolated linear sand bodies: Interpretations and realizations, *in* Bergman, K.M., and Snedden, J.W., eds., Isolated shallow marine sand bodies: Sequence stratigraphic analysis and sedimentologic interpretations, Volume 64: SEPM Special Publication: Tulsa, OK, Society for Sedimentary Geology (SEPM), p. 321-356.

Swift, D., J. P. , 1985, Response of the shelft floor to flow, SEPM Short Course, Volume 13: Tulsa, OK, SEPM, p. 135-241.

Swift, D.J.P., and Field, M.E., 1981, Evolution of a classic sand ridge field: Maryland sector, North American inner shelf: Sedimentology, v. 28, p. 461-482.

Swift, D.J.P., Figueiredo, A.G., Freeland, G.L., and Oertel, G.F., 1983, Hummocky cross-stratification and megaripples: A geological double standard?: Journal of Sedimentary Petrology, v. 53, p. 1295-1317.

Swift, D.J.P., and Rice, D.D., 1984, Sand bodies on muddy shelves; A model for sedimentation in the western interior seaway, North America. , *in* Tillman, R.W., and Siemers, C.T., eds., Siliclastic Shelf Sediments, Volume 34: Tulsa, OK, SEPM, p. 43-63.

Sydow, J., and Roberts, H.H., 1994, Stratigraphic framework of a late Pleistocene shelf-edge delta, Northeast Gulf of Mexico: AAPG Bulletin, v. 78, p. 1276.

Tanner, W.F., 1960, Florida Coastal Classification: Gulf Coast Association of Geological Societies Transactions, v. X, p. 259-268.

Teague, W.J., Jarosz, E., Keen, T.R., and Wang, D.W., 2006, Bottom scour observed under Hurrican Ivan: Geophysical Research Letters, v. 33, p. 7607-7610.

Tolman, H.L., 1991, A third-generation model for wind waves on slowly varying unsteady, and inhomogeneous depths and current: Journal of Physical Oceanography, v. 21, p. 782-797.

Tornqvist, T.E., Gonzalez, J.L., Newsom, L.A., van der Borg, K., de Jong, A.F.M., and Kurnik, C., W., 2004, Deciphering Holocene sea-level history on the U.S. Gulf Coast: A high-resolution record from the Mississippi Delta: Geological Society of America Bulletin, v. 116, p. 1026-1039.

Trembanis, A.C., Wright, L.D., Friedrichs, C.T., Green, M.O., and Hume, T., 2004, The effects of spatially complex inner shelf roughness on boundary layer turbulence and current and wave friction: Tairua embayment, New Zealand: Continental Shelf Research, v. 24, p. 1549-1571.

Twichell, D., Brooks, G., Gelfenbaum, G., Paskevich, V., and Donahue, B., 2003, Sand ridges off Sarasota, Florida: A complex facies boundary on a low-energy inner shelf environment: Marine Geology, v. 200, p. 243-262.

Van Andel, T.H., and Poole, D.M., 1960, Sources of recent sediments in the northern Gulf of Mexico: Journal of Sedimentary Petrology, v. 30, p. 91-122.

Wang, D.W., Mitchell, D.A., Teague, W.J., Jarosz, E., and Hulbert, M.S., 2005, Extreme waves under Hurricane Ivan: Science, v. 309, p. 896.

Wiberg, P., 2000, A perfect storm: formation and potential for preservation of storm beds on the continental shelf: Oceanography, v. 13, p. 93-99.

Winker, C.D., 1991, Summary of the Quaternary framework, Northern Gulf of Mexico, Coastal Depositional Systems in the Gulf of Mexico: Quaternary Framework and Environmental Issues, Volume 1: Houston, TX, Society of Economic Paleontologists and Mineralogists Foundation: Gulf Coast Section, p. 280-284.

Winn, R.D., Roberts, H.H., Kohl, B., Fillon, R.H., Crux, J.A., Bouma, A.H., and Spero, H.W., 1998, Upper Quaternary strata of the upper continental slope, northeast Gulf of Mexico: Sequence stratigraphic model for a terrigenous shelf edge: Journal of Sedimentary Research, v. 68, p. 579-595.

Woodroffe, C.D., 2003, Coasts: Form, Process and Evolution: Cambridge, Cambridge University Press, 623 p.

Wright, L.D., 1995, Morphodynamics of Inner Continental Shelves: Boca Raton, Florida, CRC Press, Inc., 241 p.

Yalin, M.S., 1977, Mechanics of Sediment Transport: Oxford, England, Pergamon Press, 298 p.

APPENDIX A: SELECTED SATELLITE IMAGES

A.1 MODIS Images

Table A-1. MODIS Bandwidths used in this study, modified from http://modis.gsfc.nasa.gov.

Image	Channel	Bandwith (nm)
True Color Composite (Red, Green, and Blue)	1,3 and 4	620 – 670; 459 – 479; 545 – 565
Red	1	620 – 670
Near Infrared (NIR)	2	841 – 876

A.1.1 Ivan Images

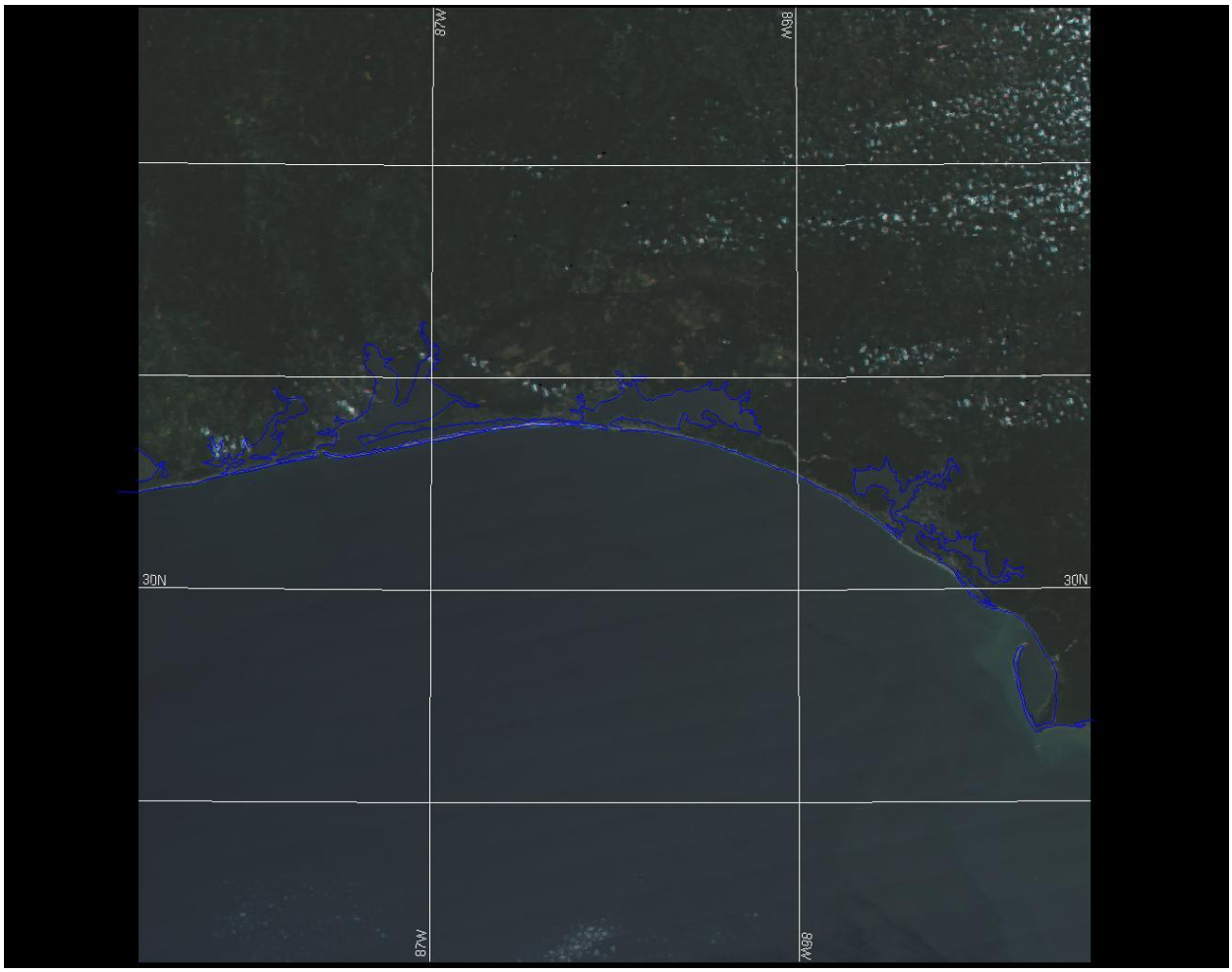

Figure A.1. Aqua, True Color Composite: 18:47 UTC, 08 September 2004.

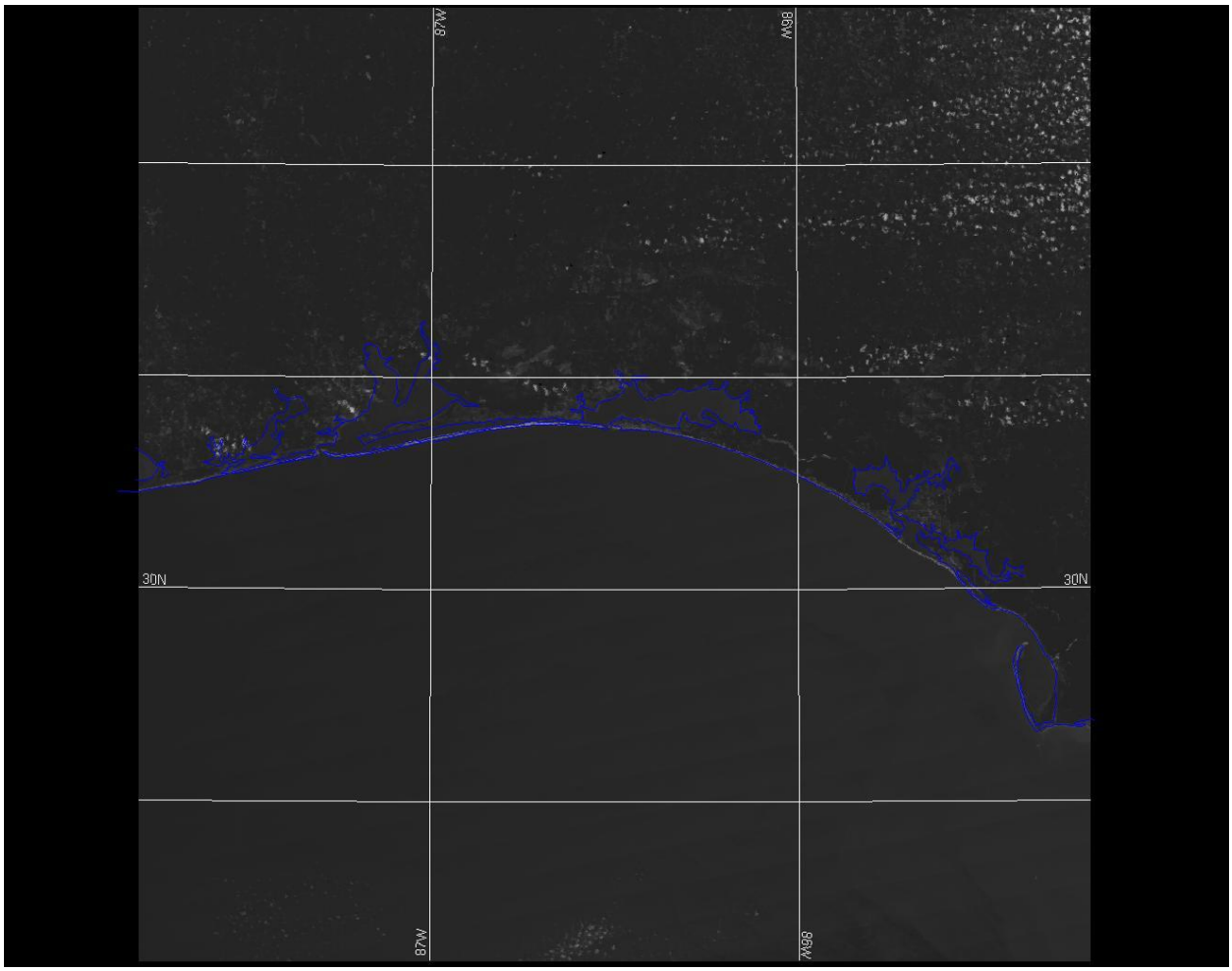

Figure A.2. Aqua, Red Channel: 18:47 UTC, 08 September 2004.

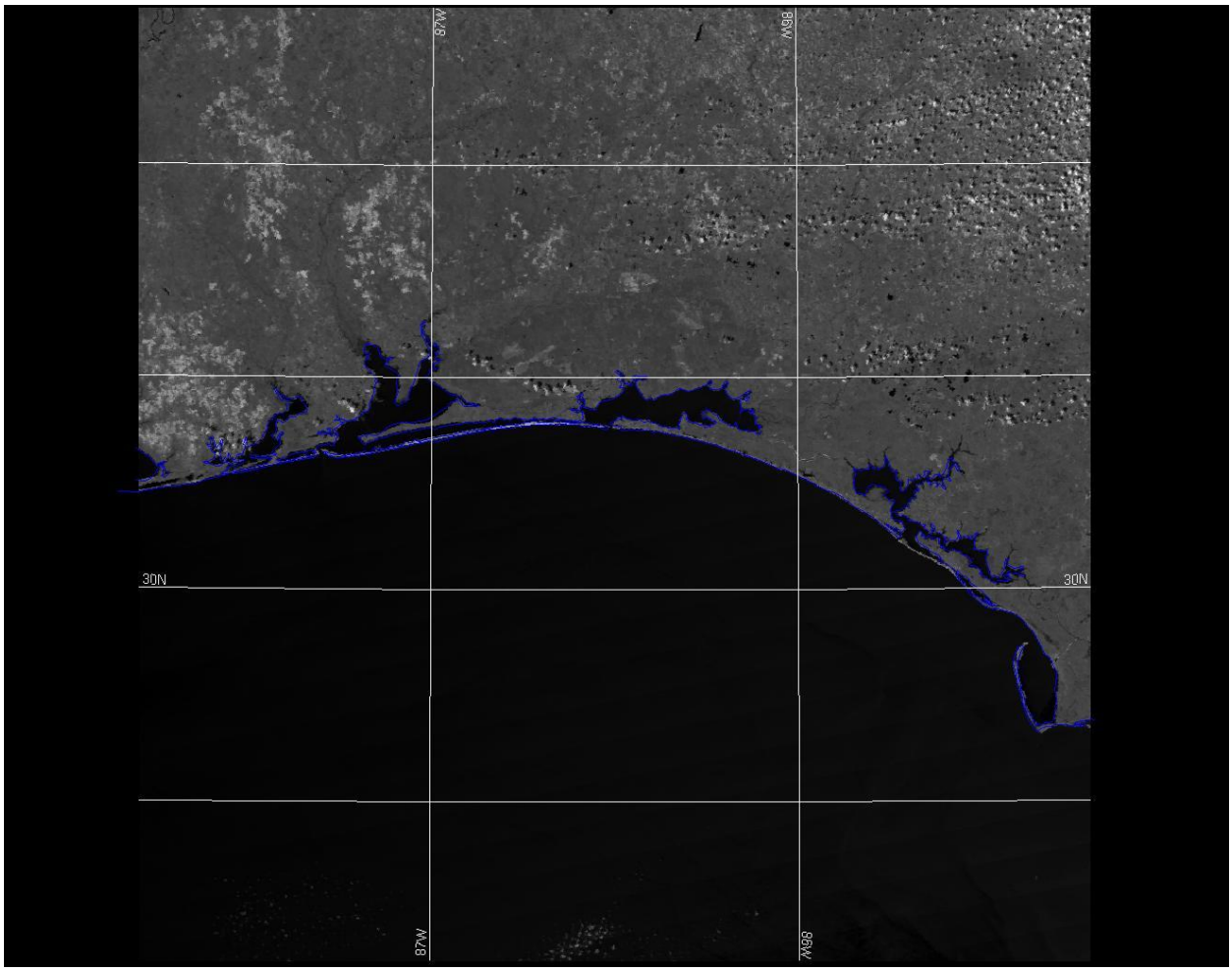

Figure A.3. Aqua, NIR Channel: 18:47 UTC, 08 September 2004.

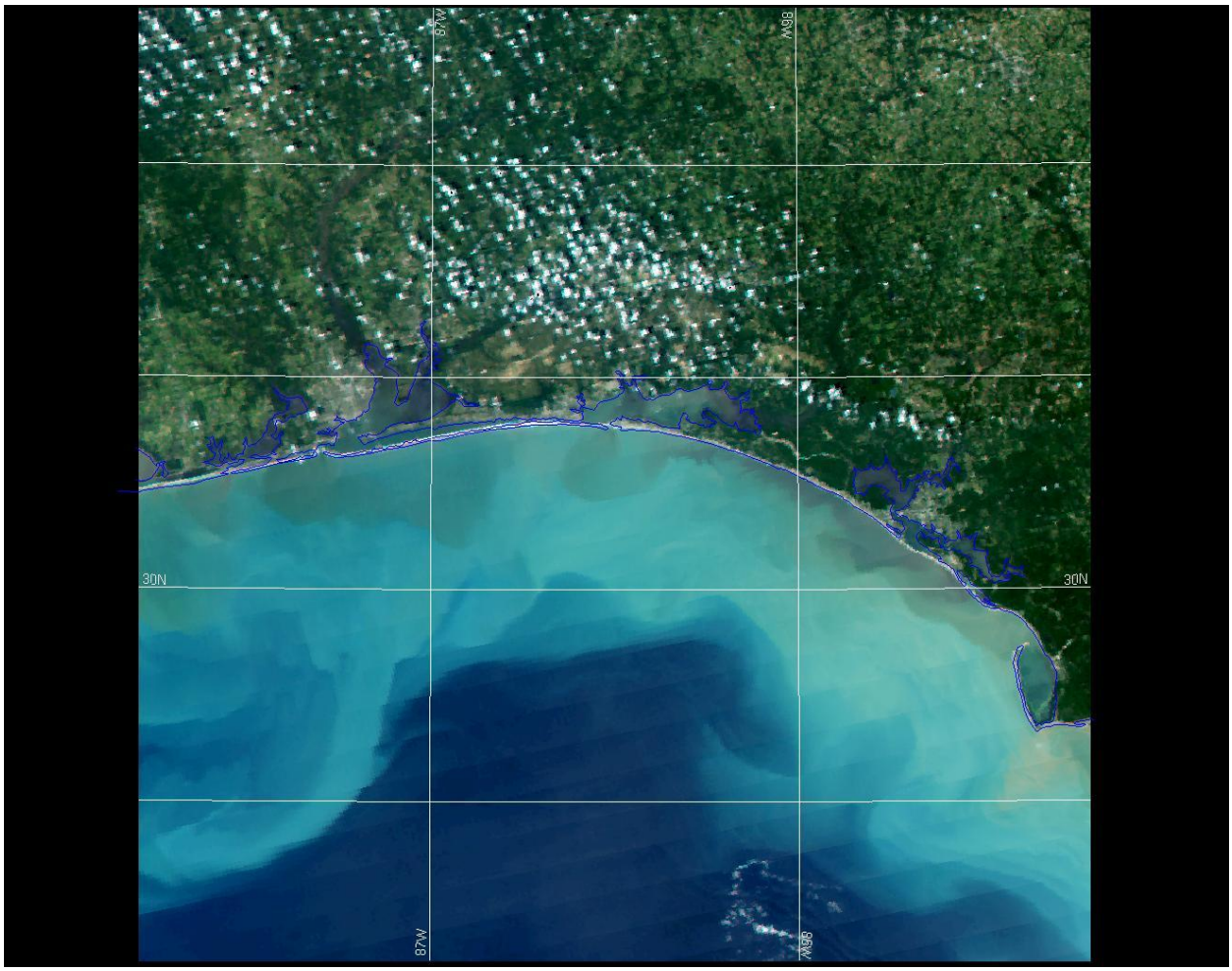

Figure A.4. Aqua, True Color Composite: 18:42 UTC, 17 September 2004.

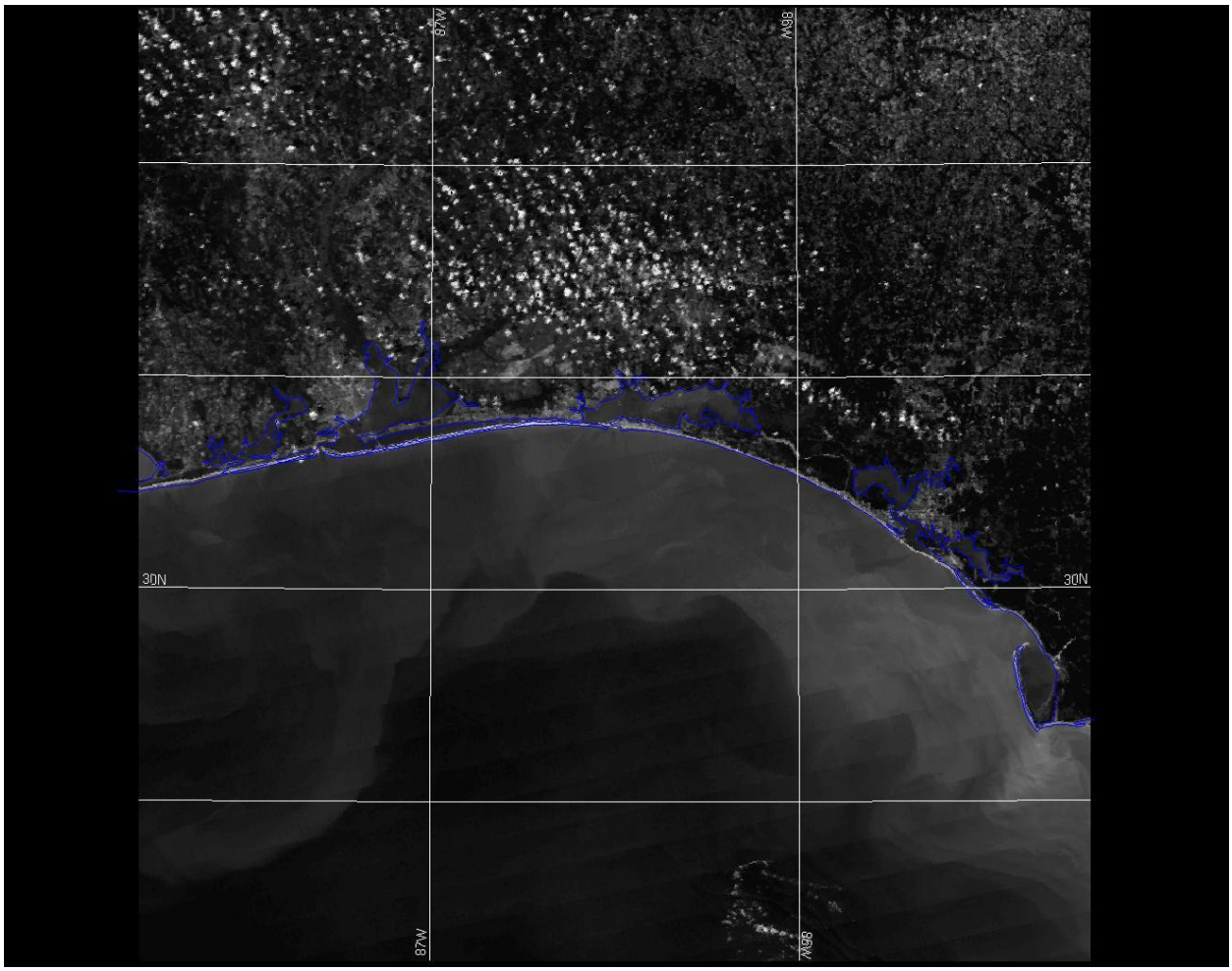

Figure A.5. Aqua, Red Channel: 18:42 UTC, 17 September 2004.

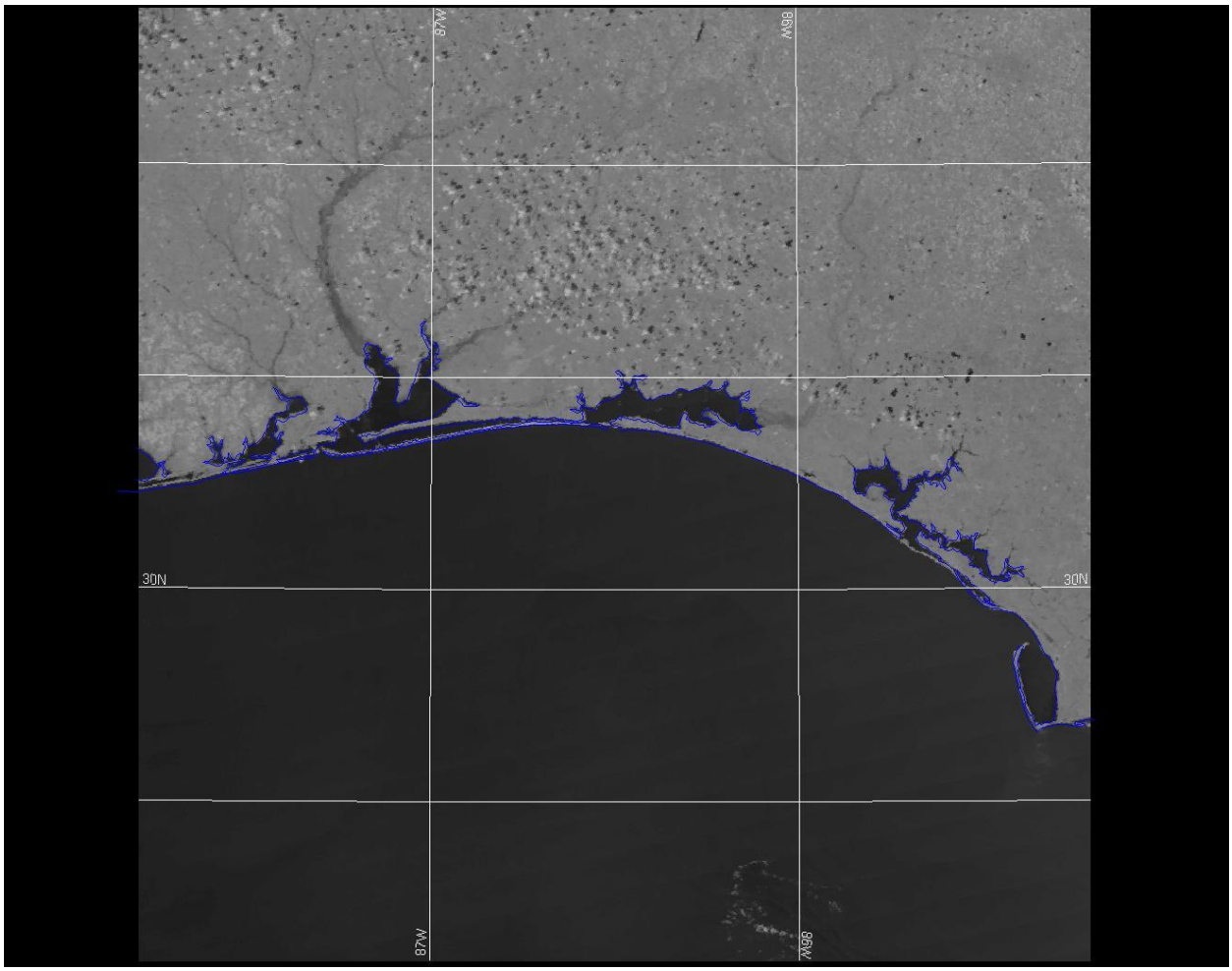

Figure A.6. Aqua, NIR Channel: 18:42 UTC, 17 September 2004.

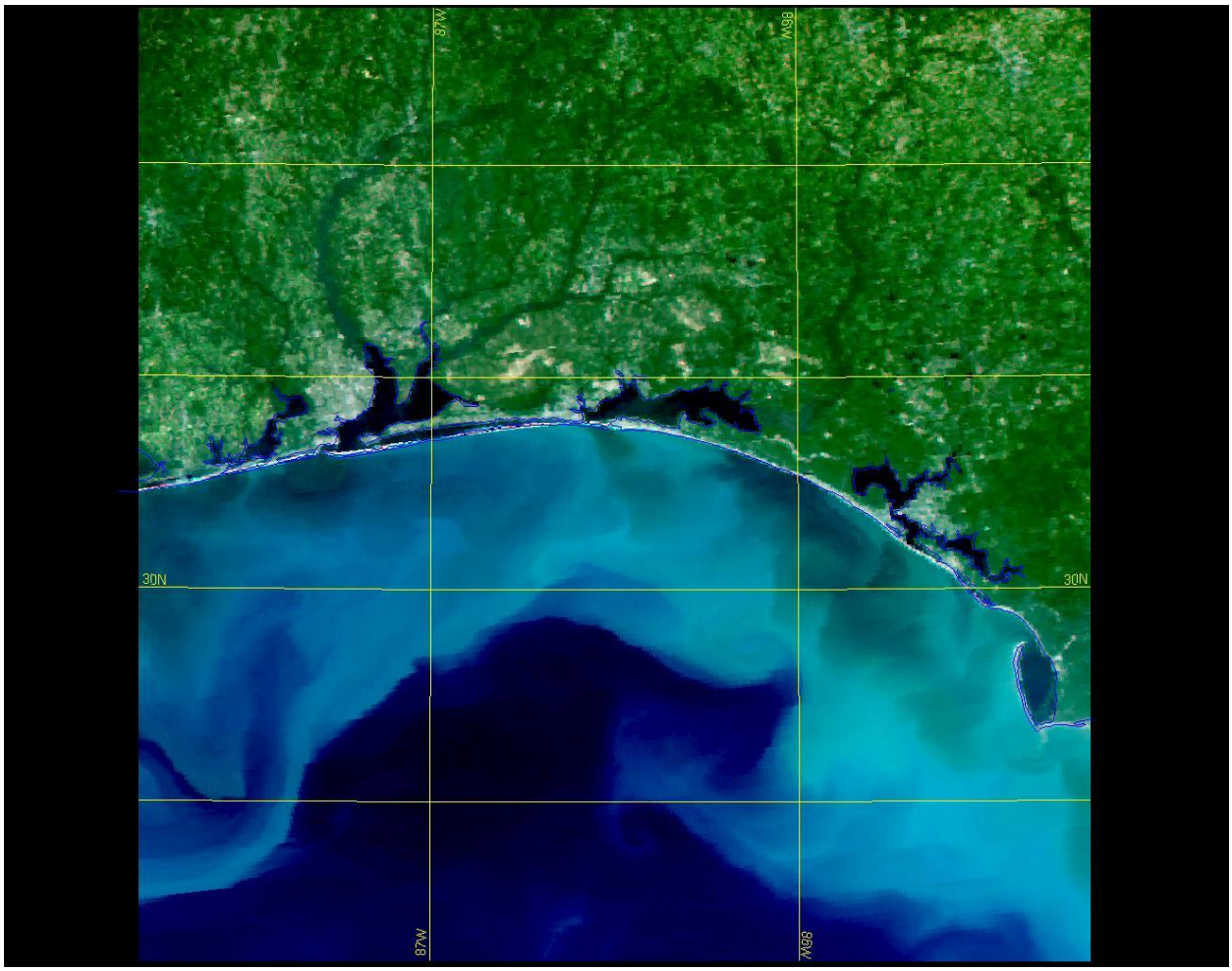

Figure A.7. Aqua, True Color Composite: 19:22 UTC, 18 September 2004.

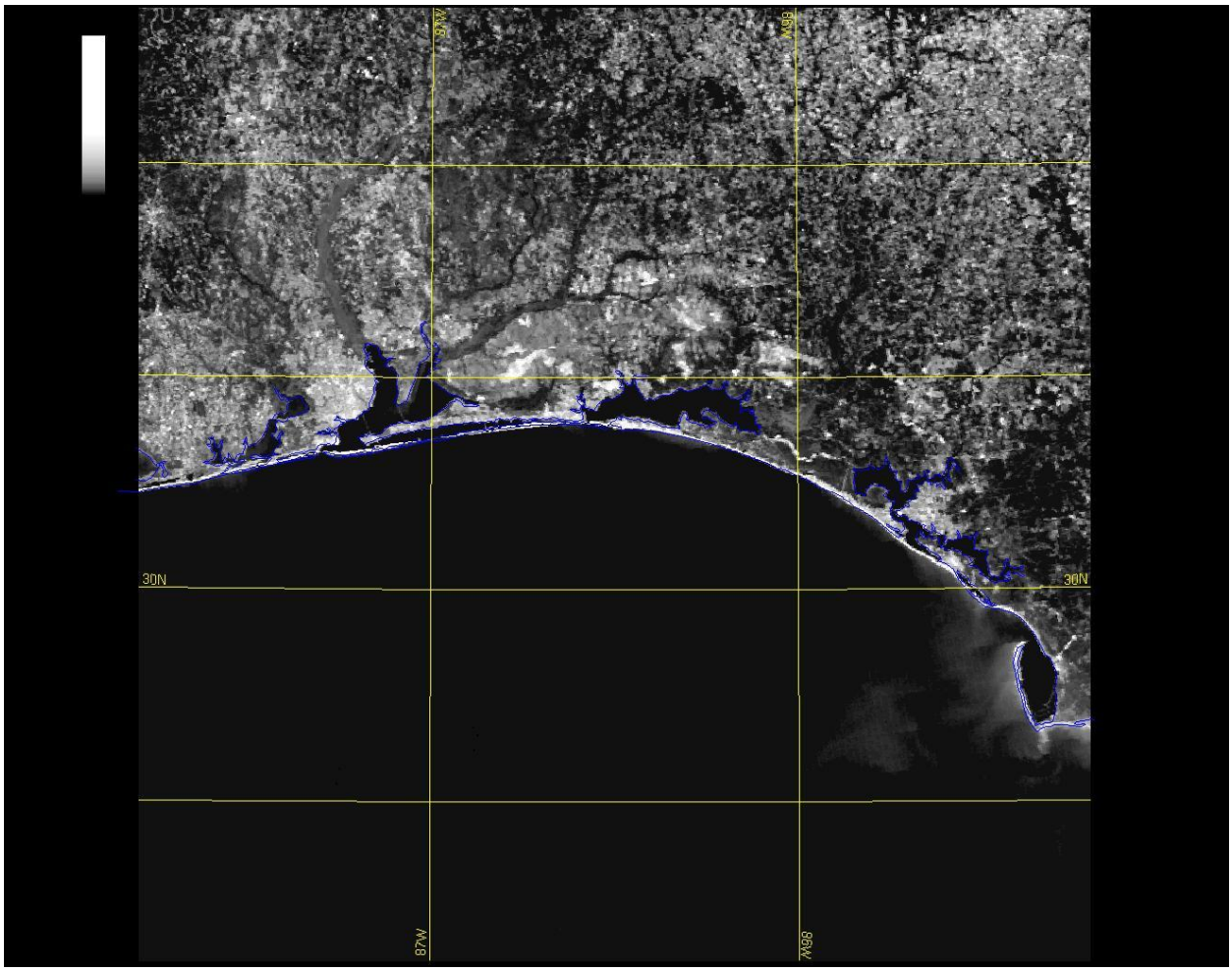

Figure A.8. Aqua, Red Channel: 19:22 UTC, 18 September 2004.

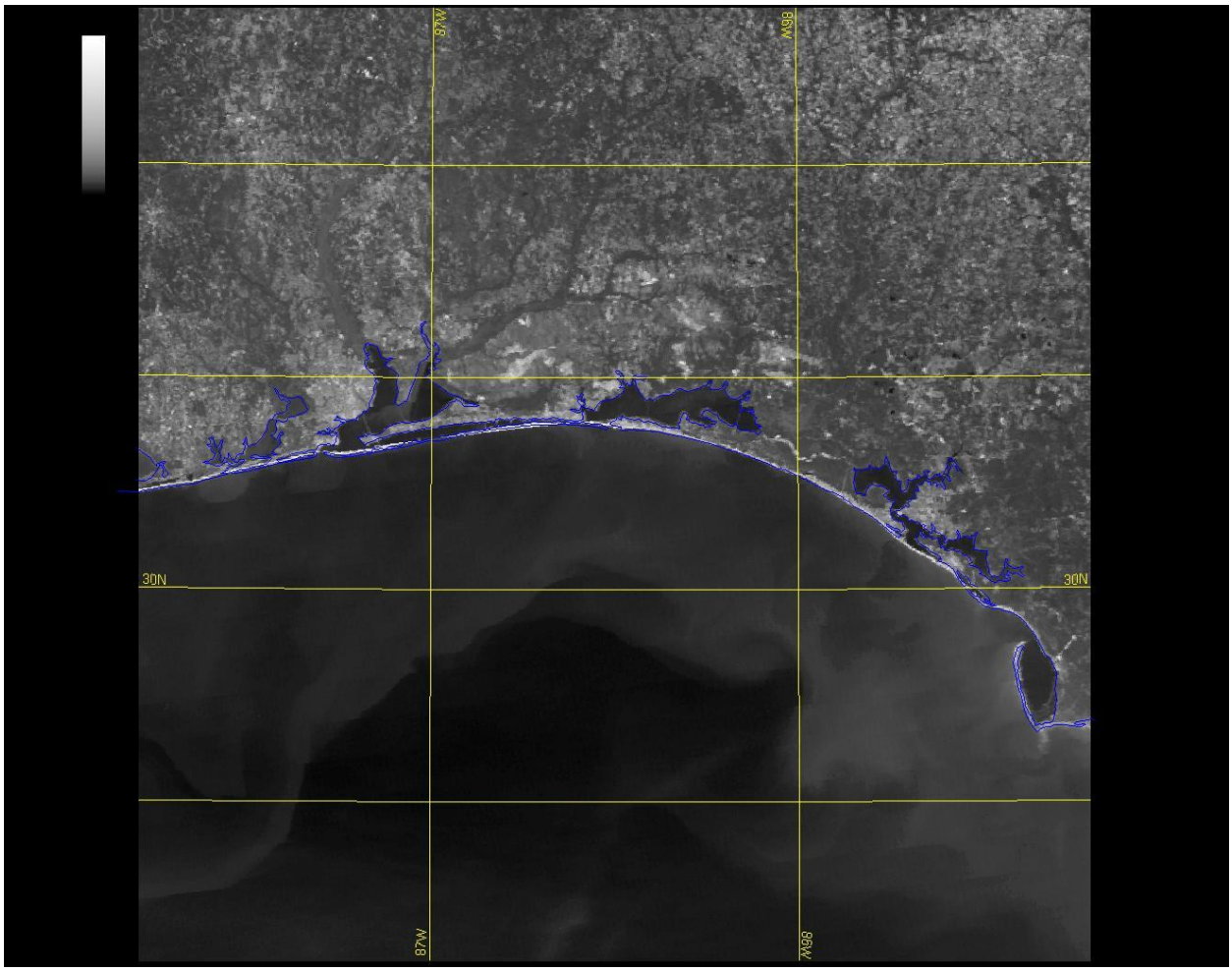

Figure A.9. Aqua, NIR Channel: 19:22 UTC, 18 September 2004.

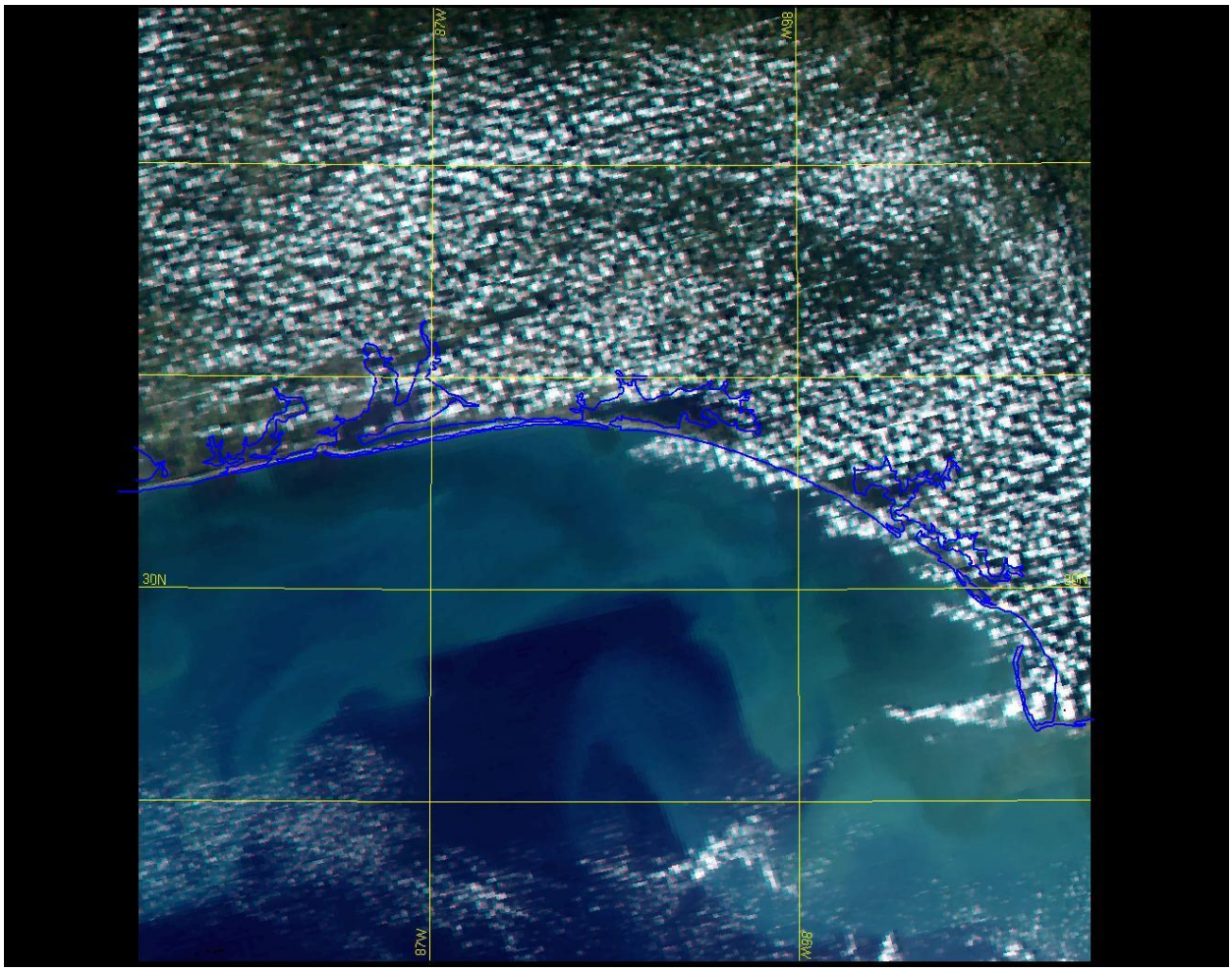

Figure A.10. Aqua, True Color Composite: 18:27 UTC, 19 September 2004.

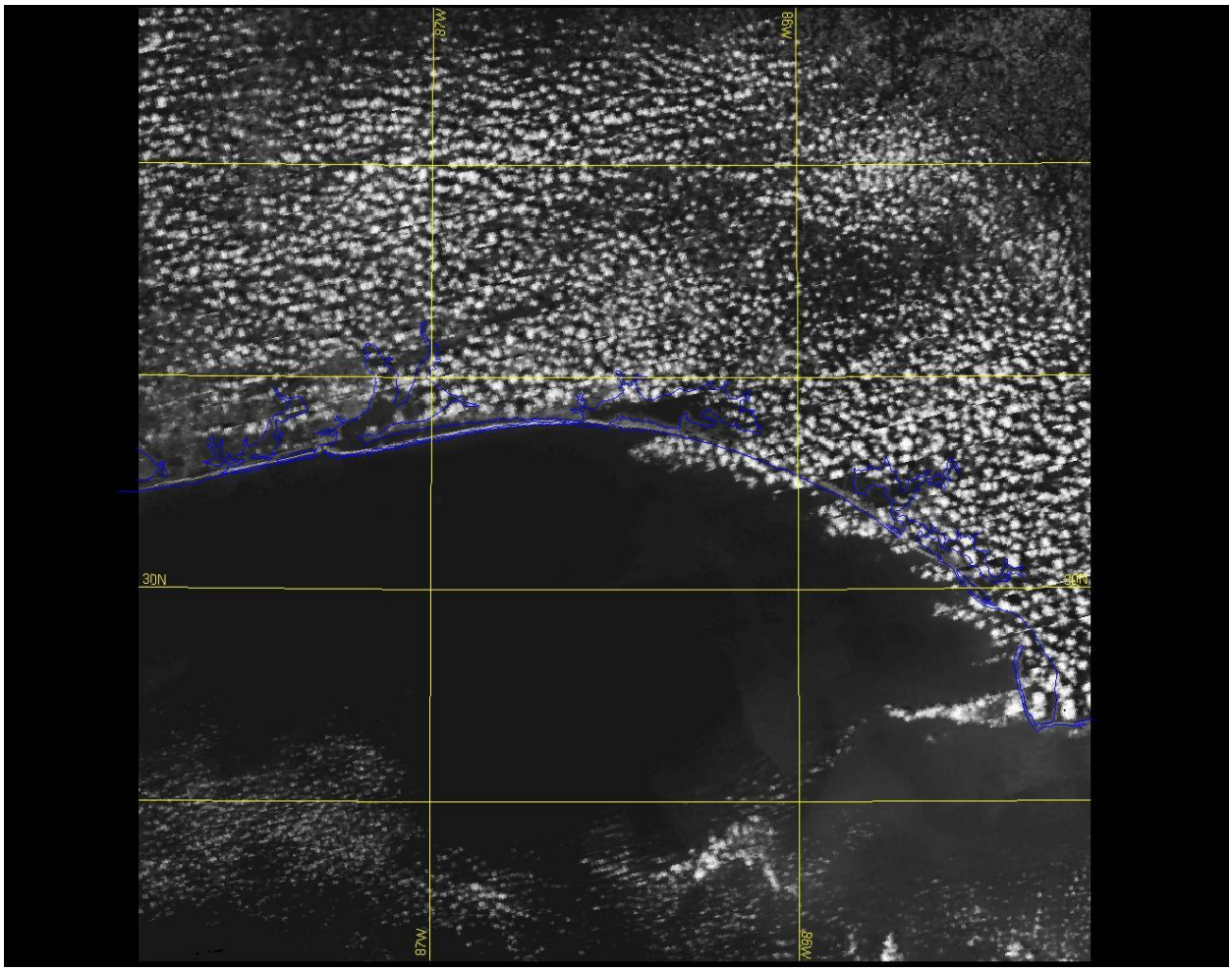

Figure A.11. Aqua, Red Channel: 18:27 UTC, 19 September 2004.

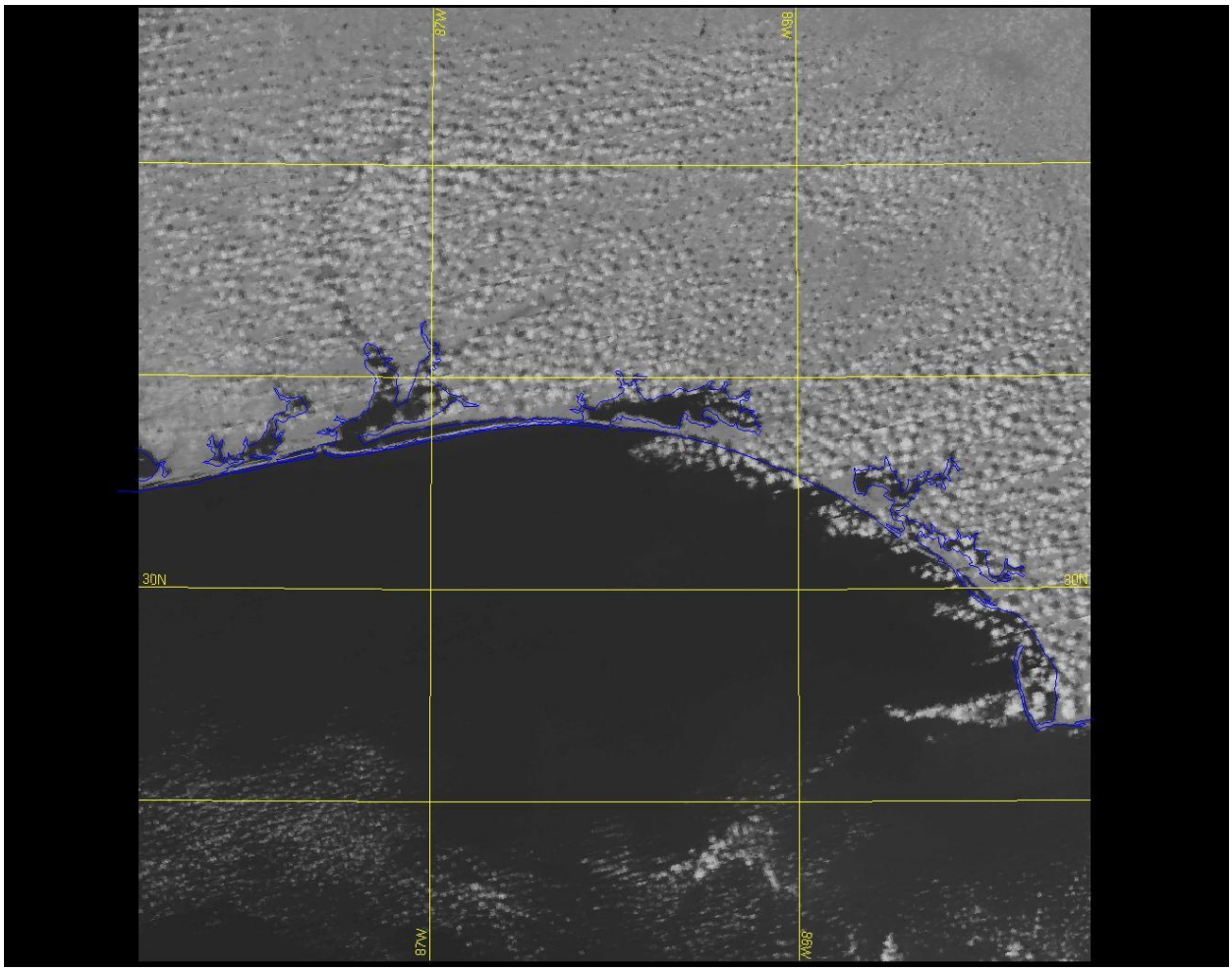

Figure A.12. Aqua, NIR Channel: 18:27 UTC, 19 September 2004.

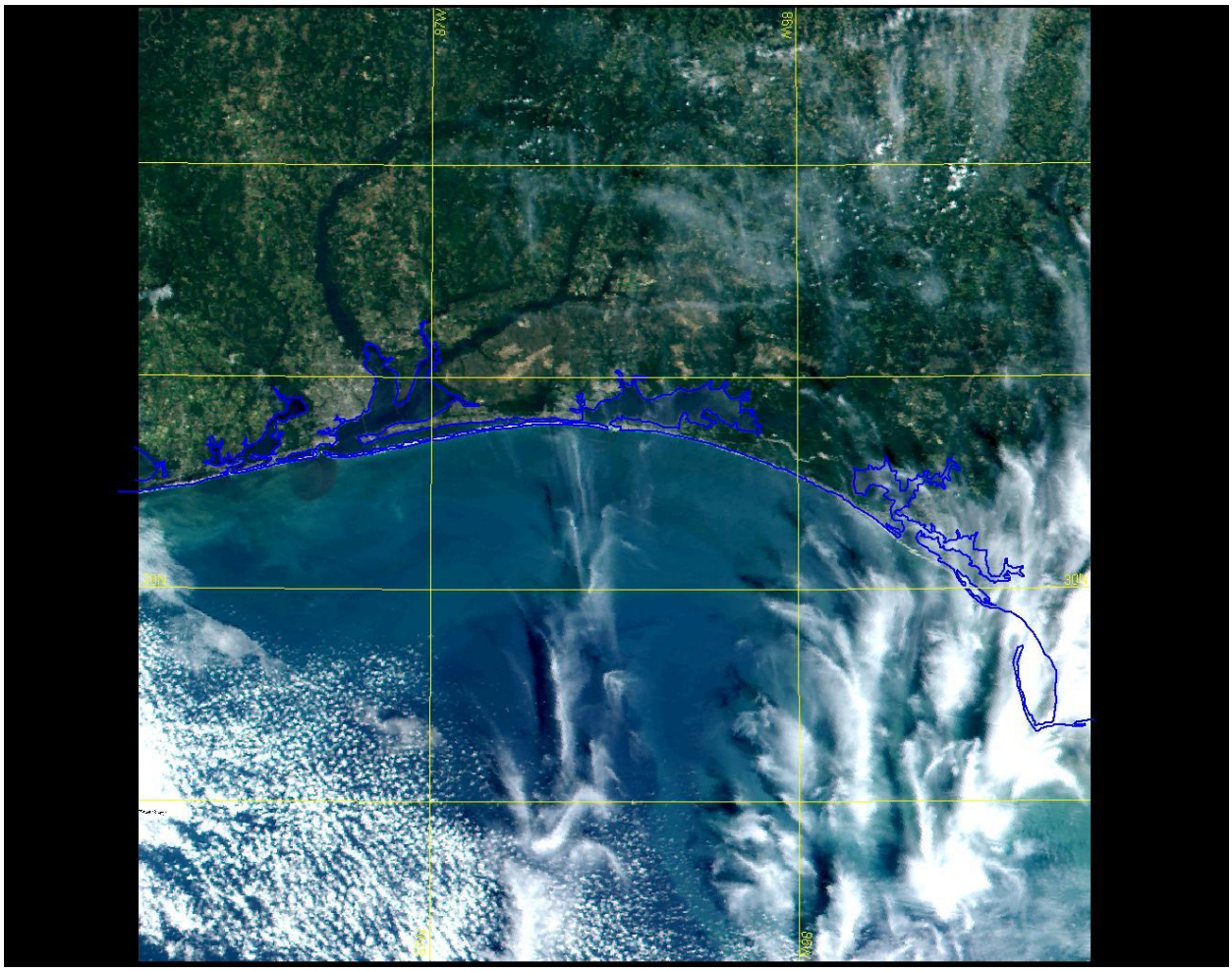

Figure A.13. Terra, True Color Composite: 16:42 UTC, 21 September 2004.

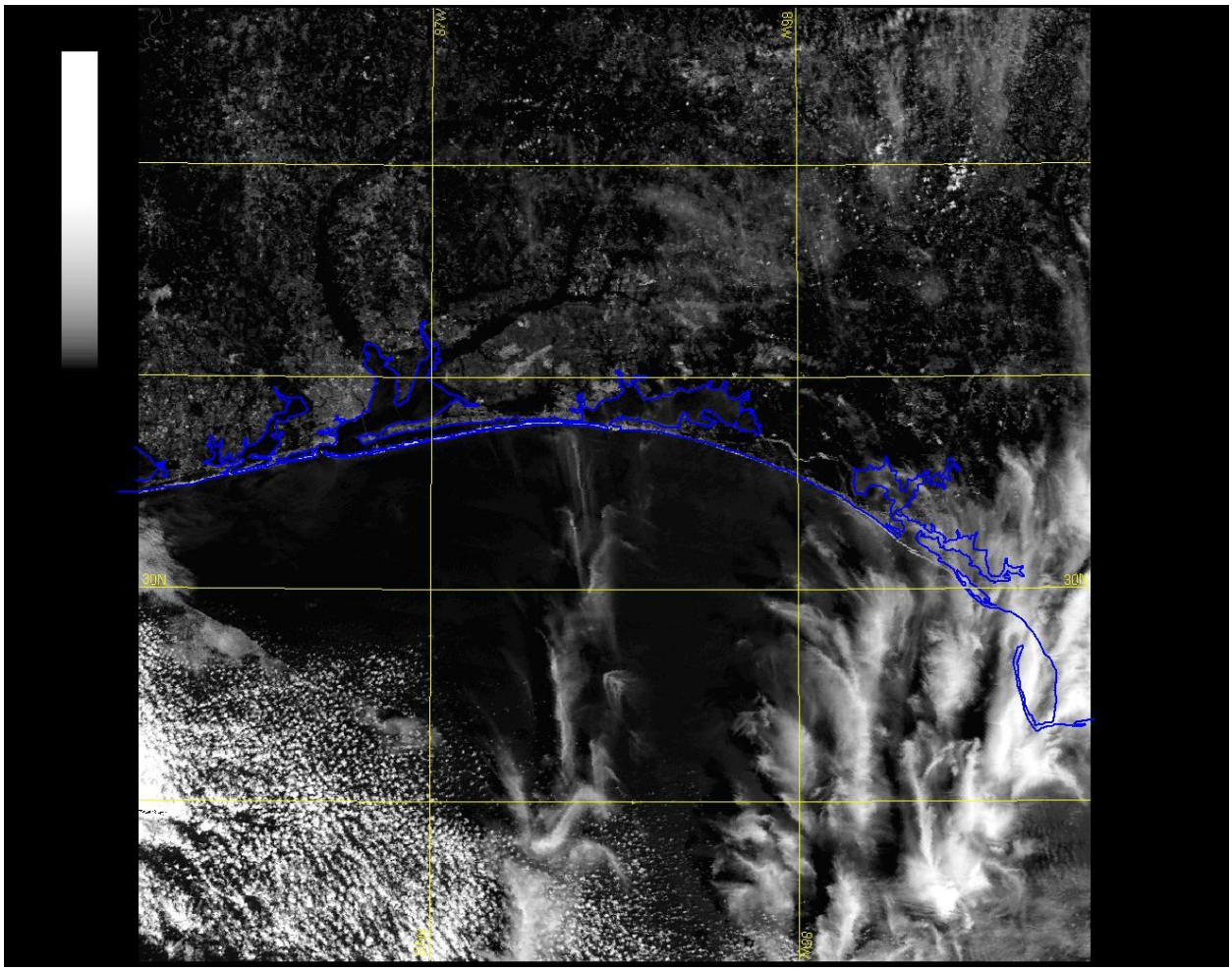

Figure A.14. Terra, Red Channel: 16:42 UTC, 21 September 2004.

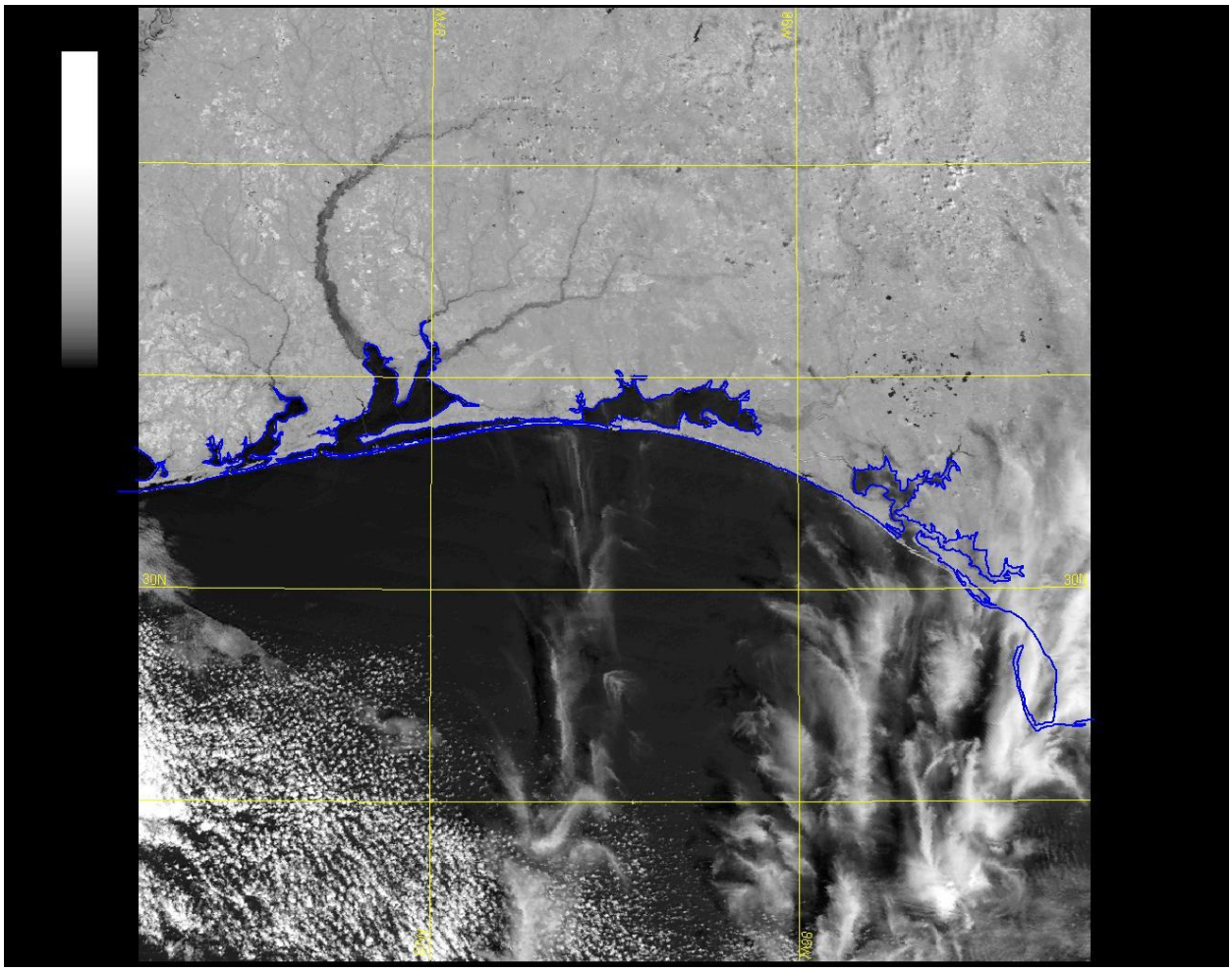

Figure A.15. Terra, NIR Channel: 16:42 UTC, 21 September 2004.

A.1.2 Dennis Images

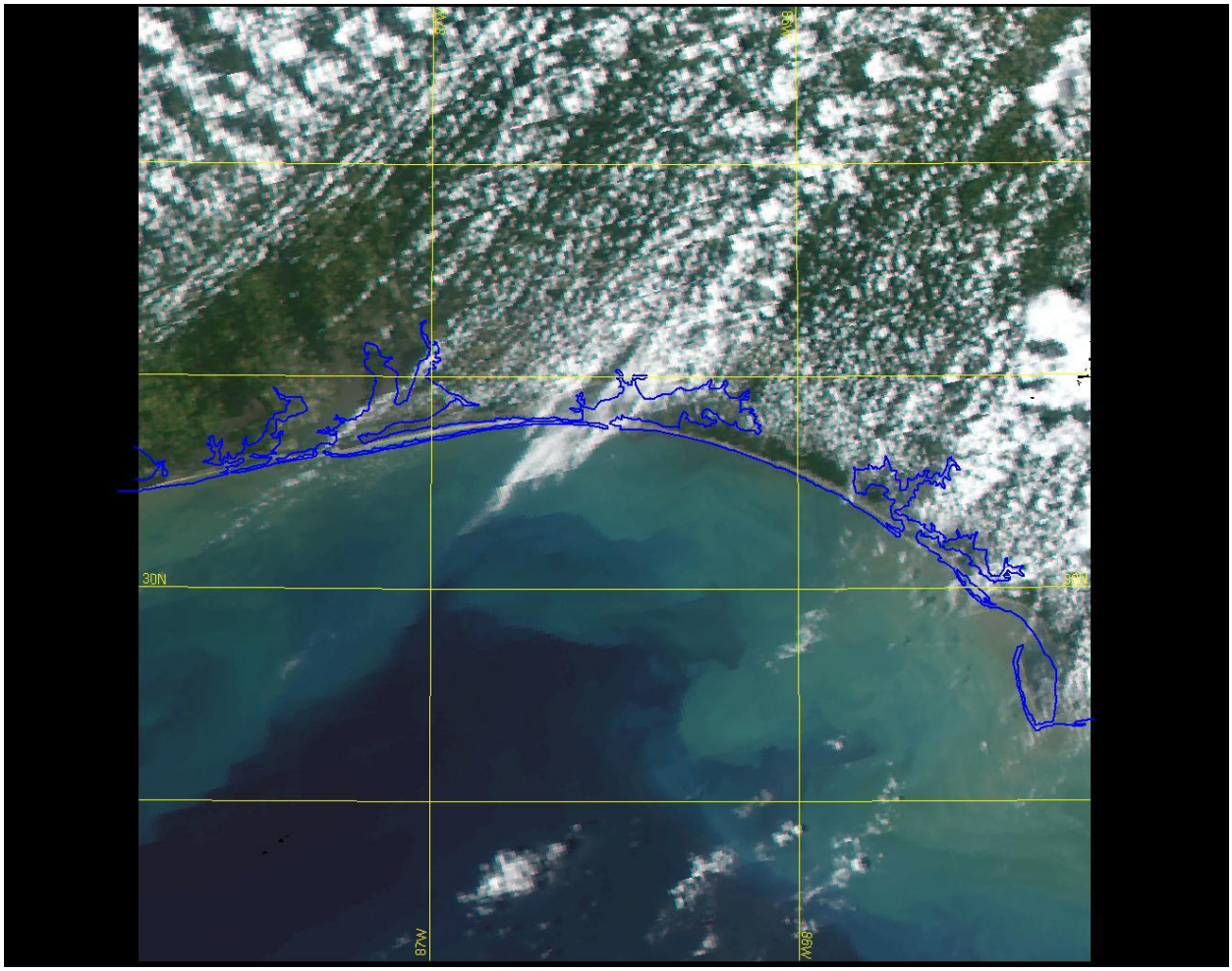

Figure A.16. Aqua, True Color Composite: 18:32 UTC, 11 July 2005.

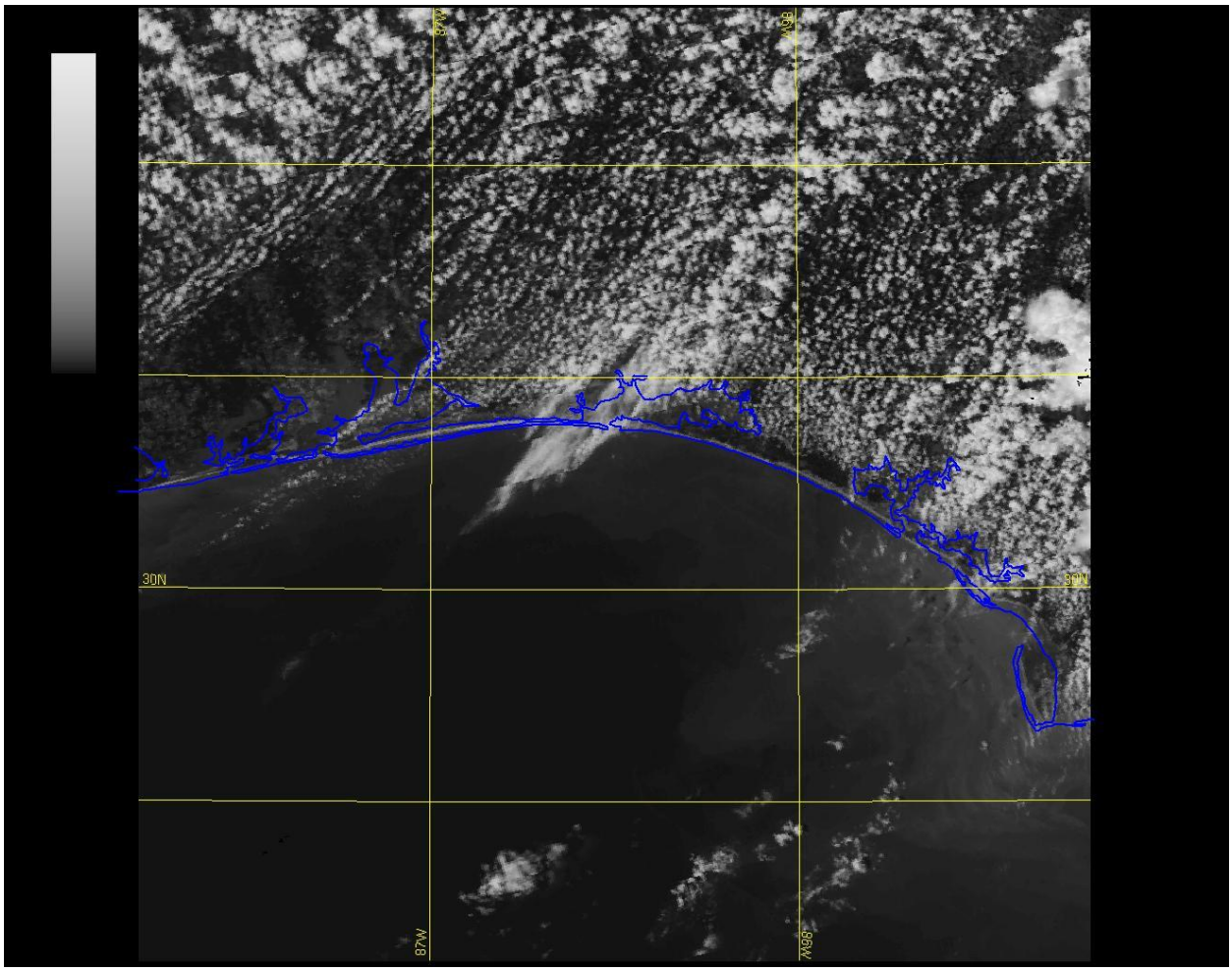

Figure A.17. Aqua, Red Channel: 18:32 UTC, 11 July 2005.

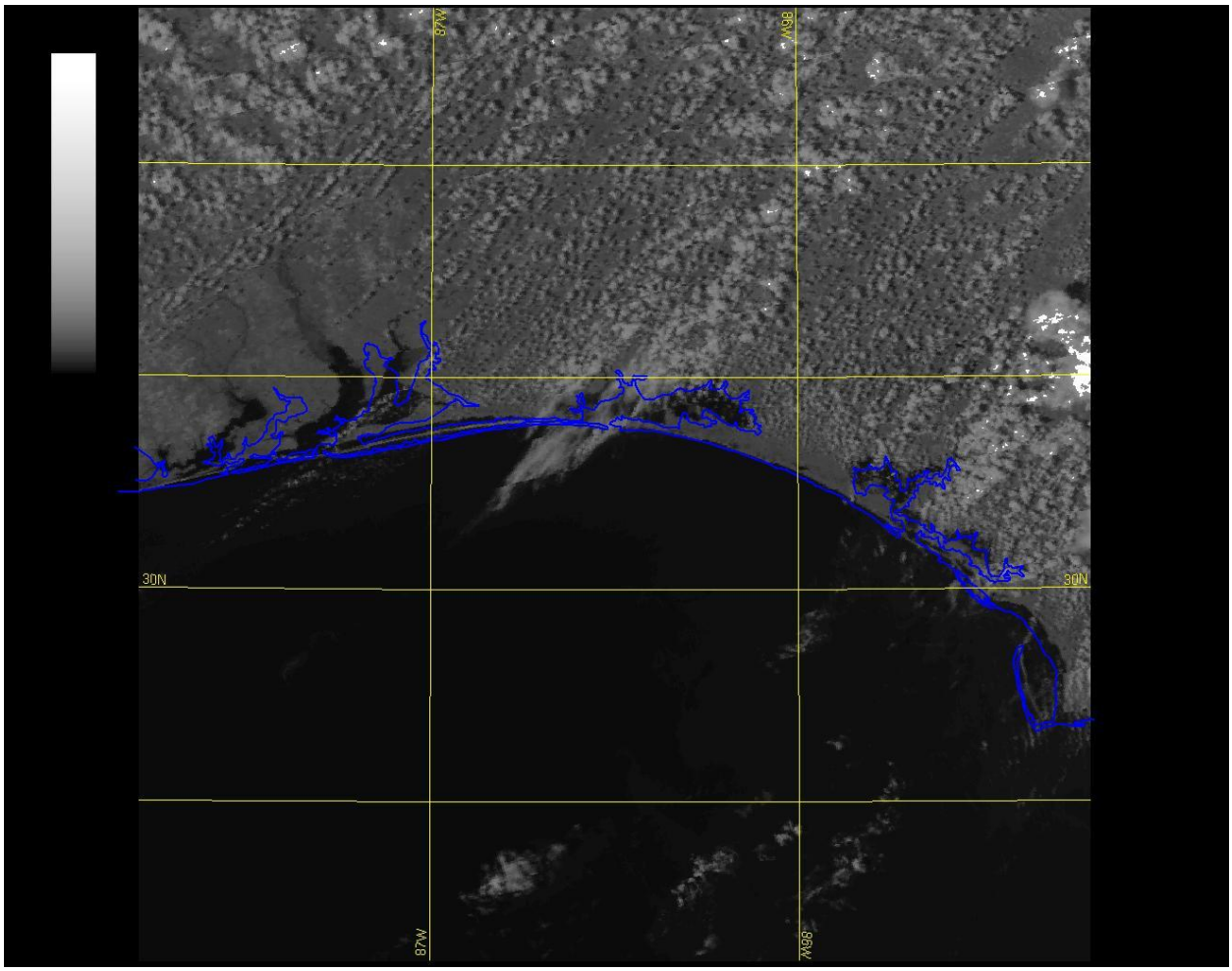

Figure A.18. Aqua, NIR Channel: 18:32 UTC, 11 July 2005.

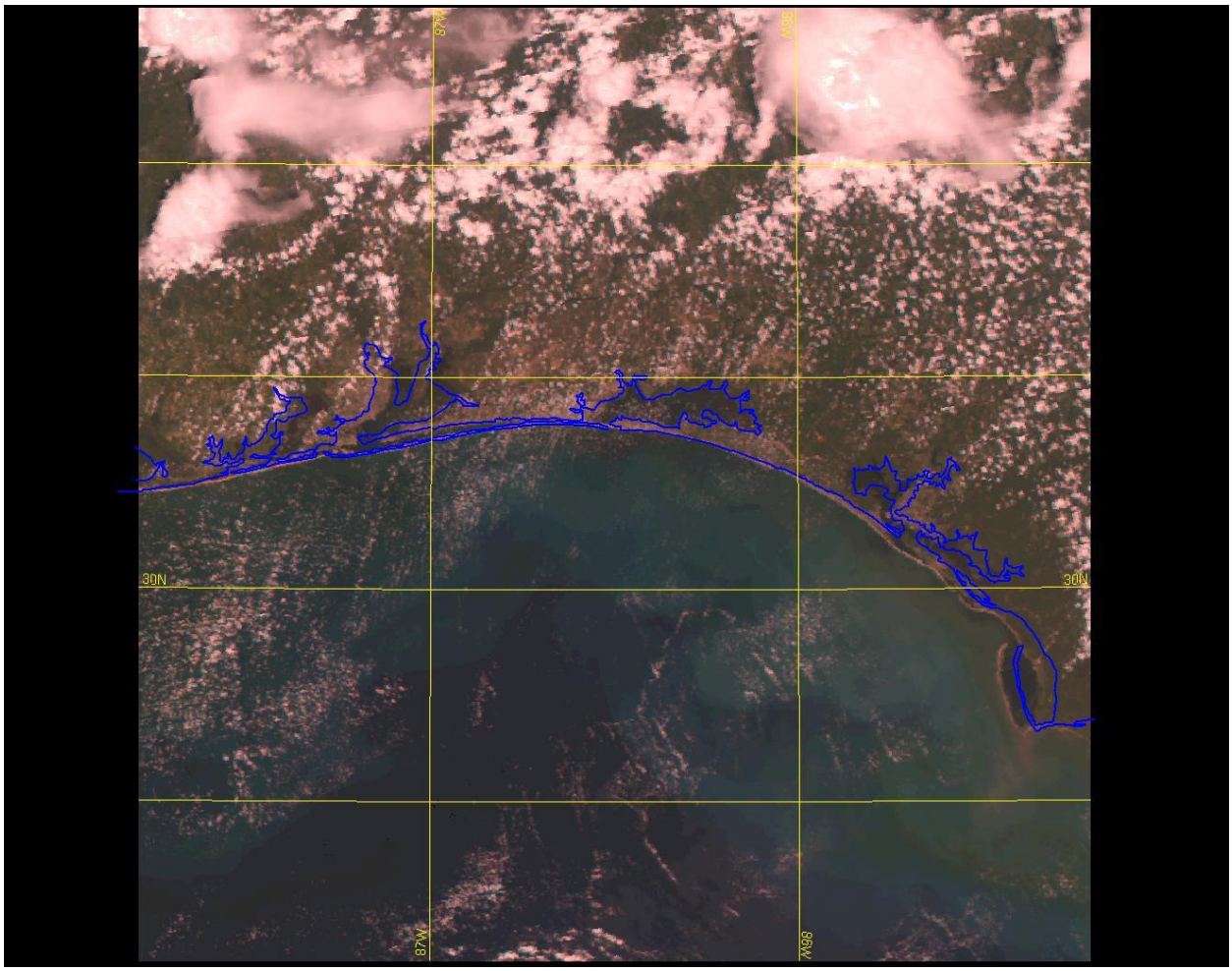

Figure A.19. Aqua, True Color Composite: 19:17 UTC, 12 July 2005.

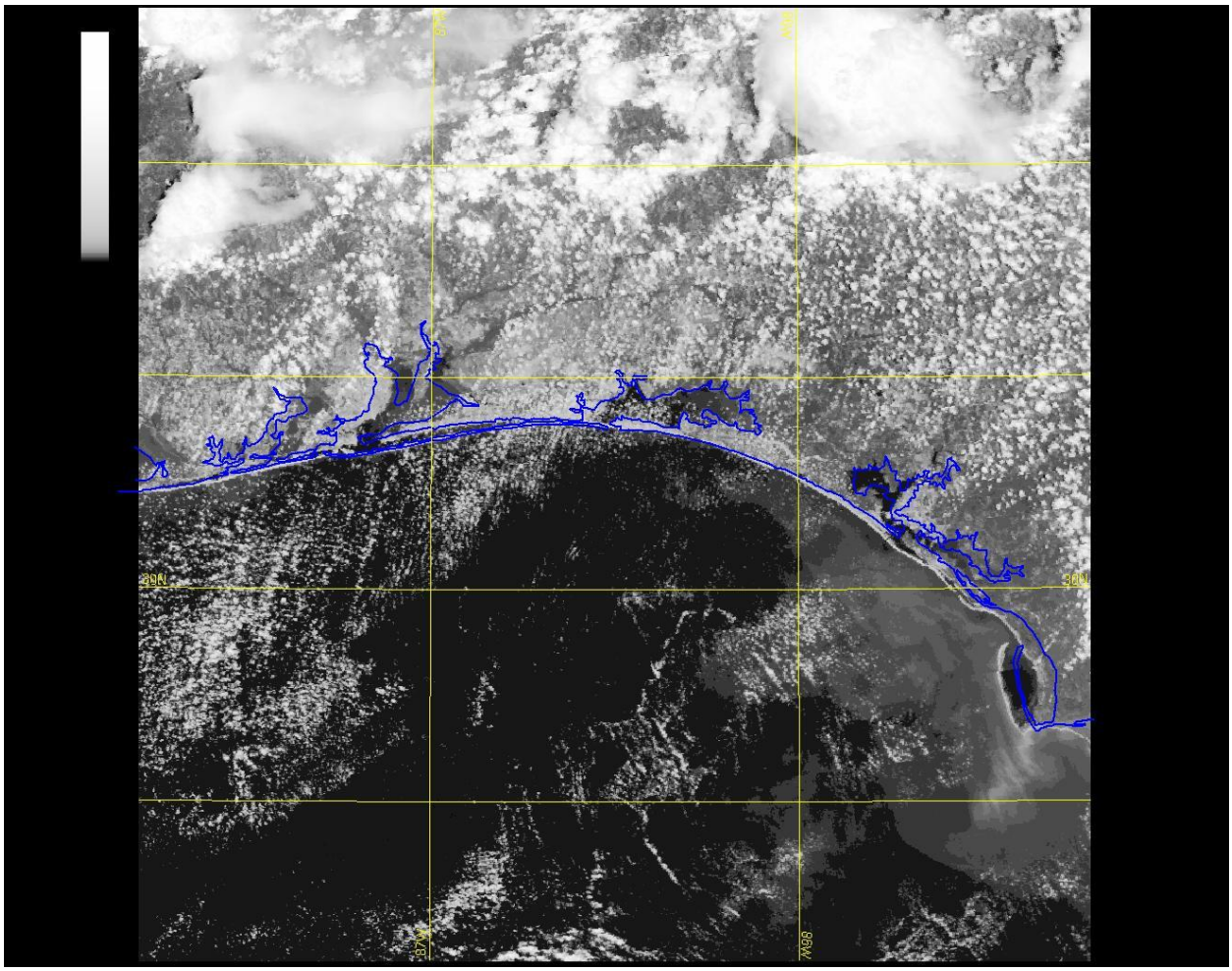

Figure A.20. Aqua, Red Channel: 19:17 UTC, 12 July 2005.

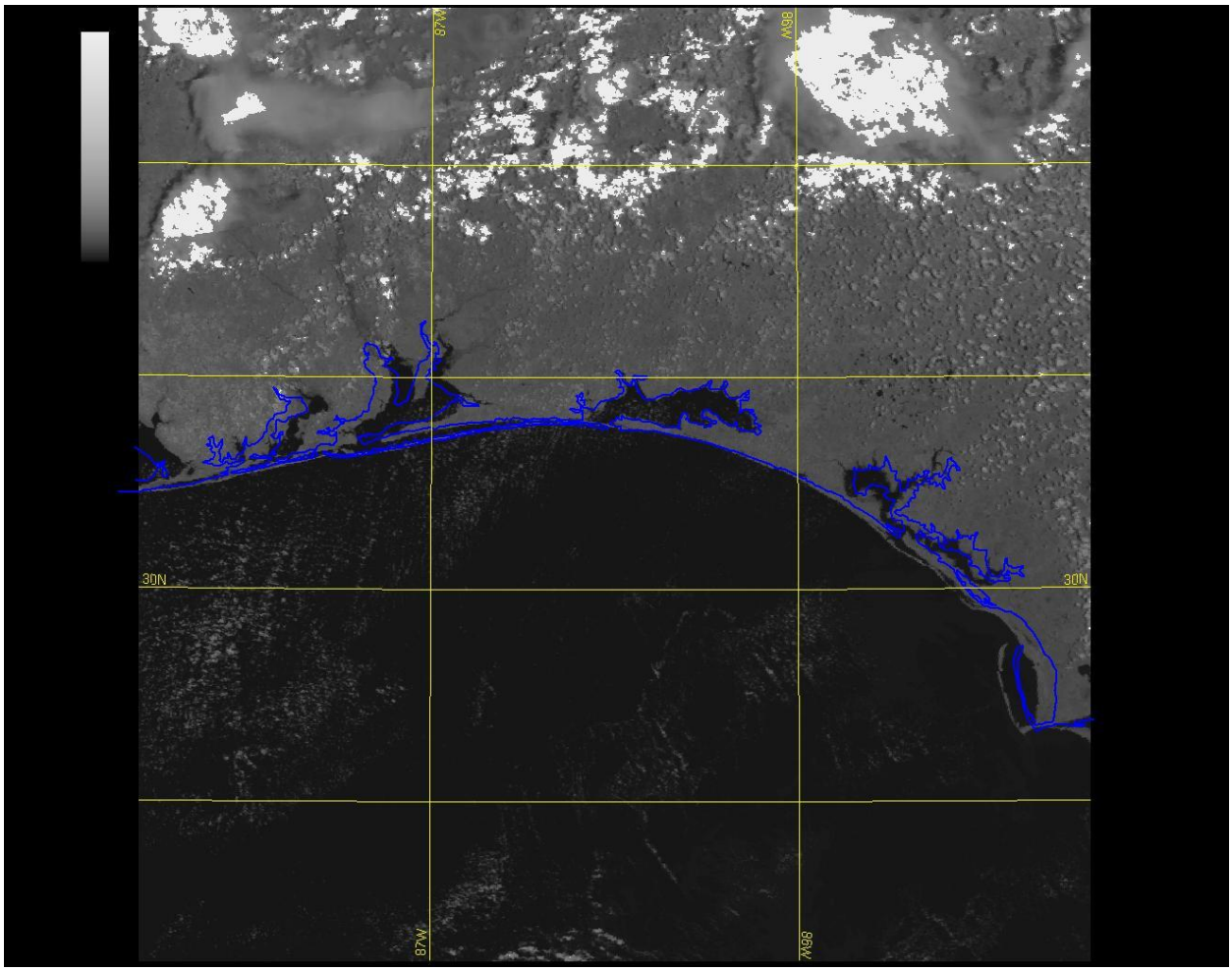

Figure A.21. Aqua, NIR Channel: 19:17 UTC, 12 July 2005.

A.2 SeaWiFS Suspended Particulate Images

Table A.2. SeaWiFS Bandwidths used in this study.

Channel	Bandwith (nm)
5	555
6	670

A.2.1 Ivan Images

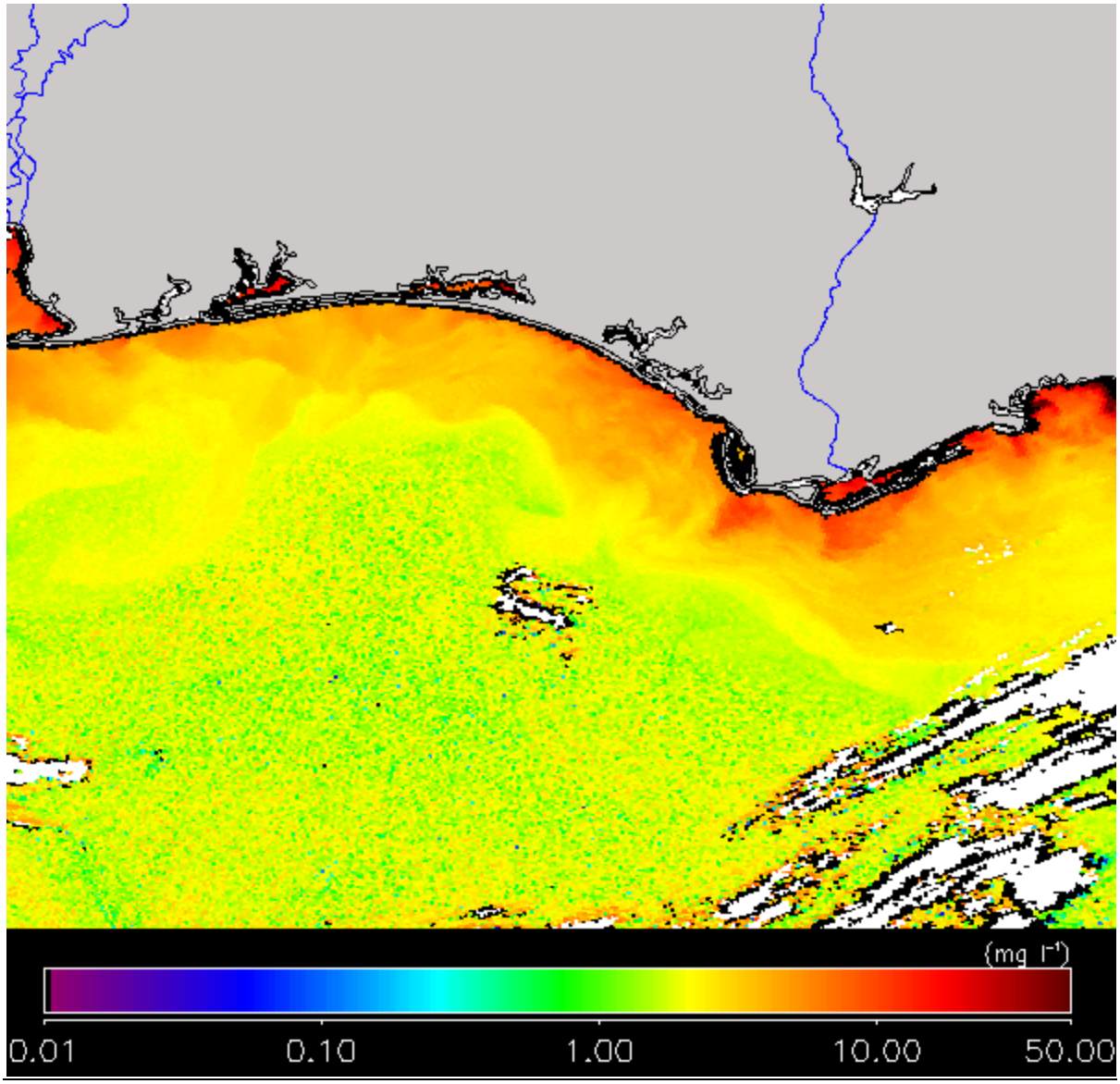

Figure A.22. 18:23:58 UTC, 17 September 2004.

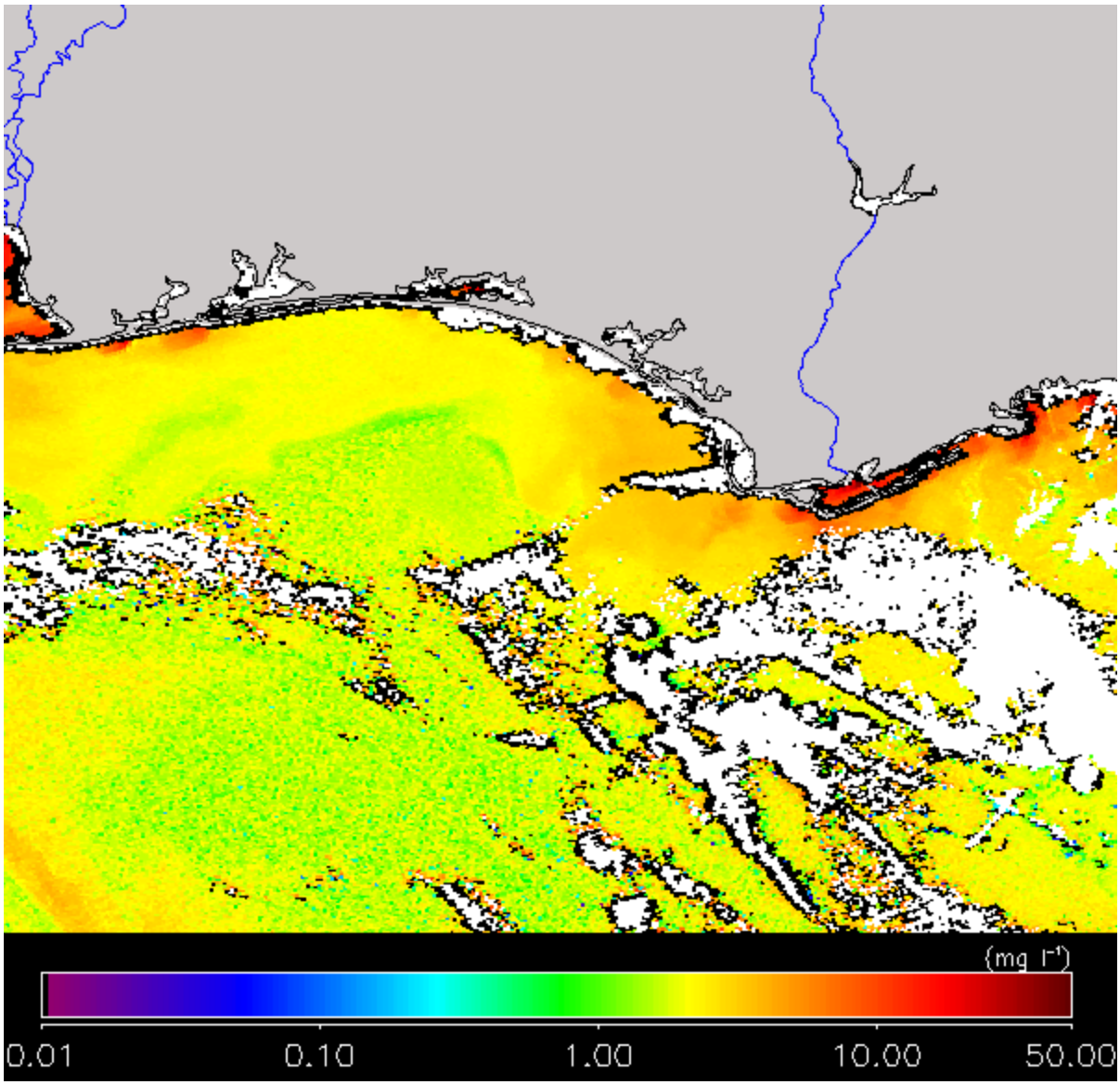

Figure A.23. 18:06:48 UTC, 19 September 2004.

A.2.2 Dennis Images

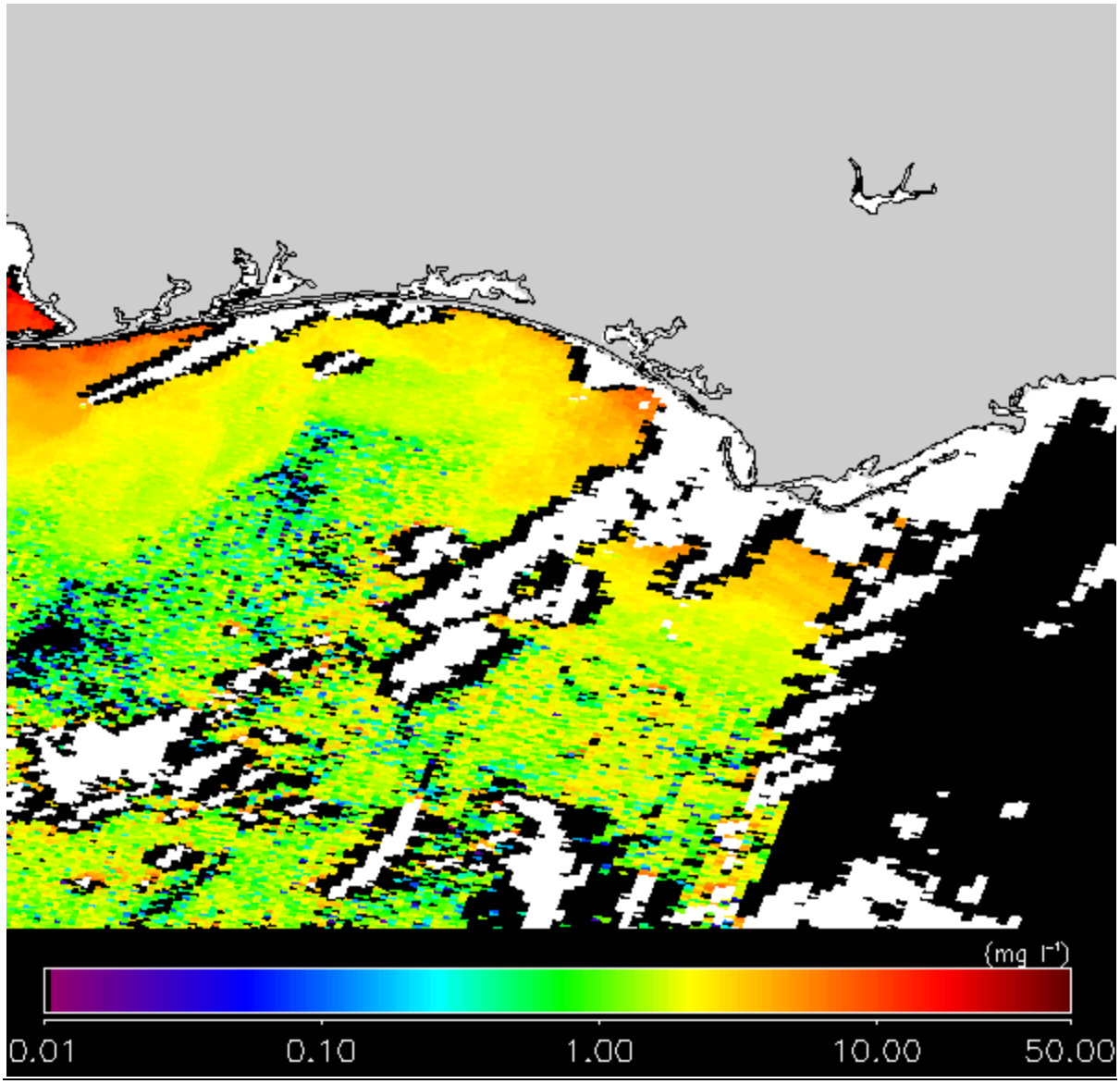

Figure A.24. 18:57:53 UTC, 11 July 2005.

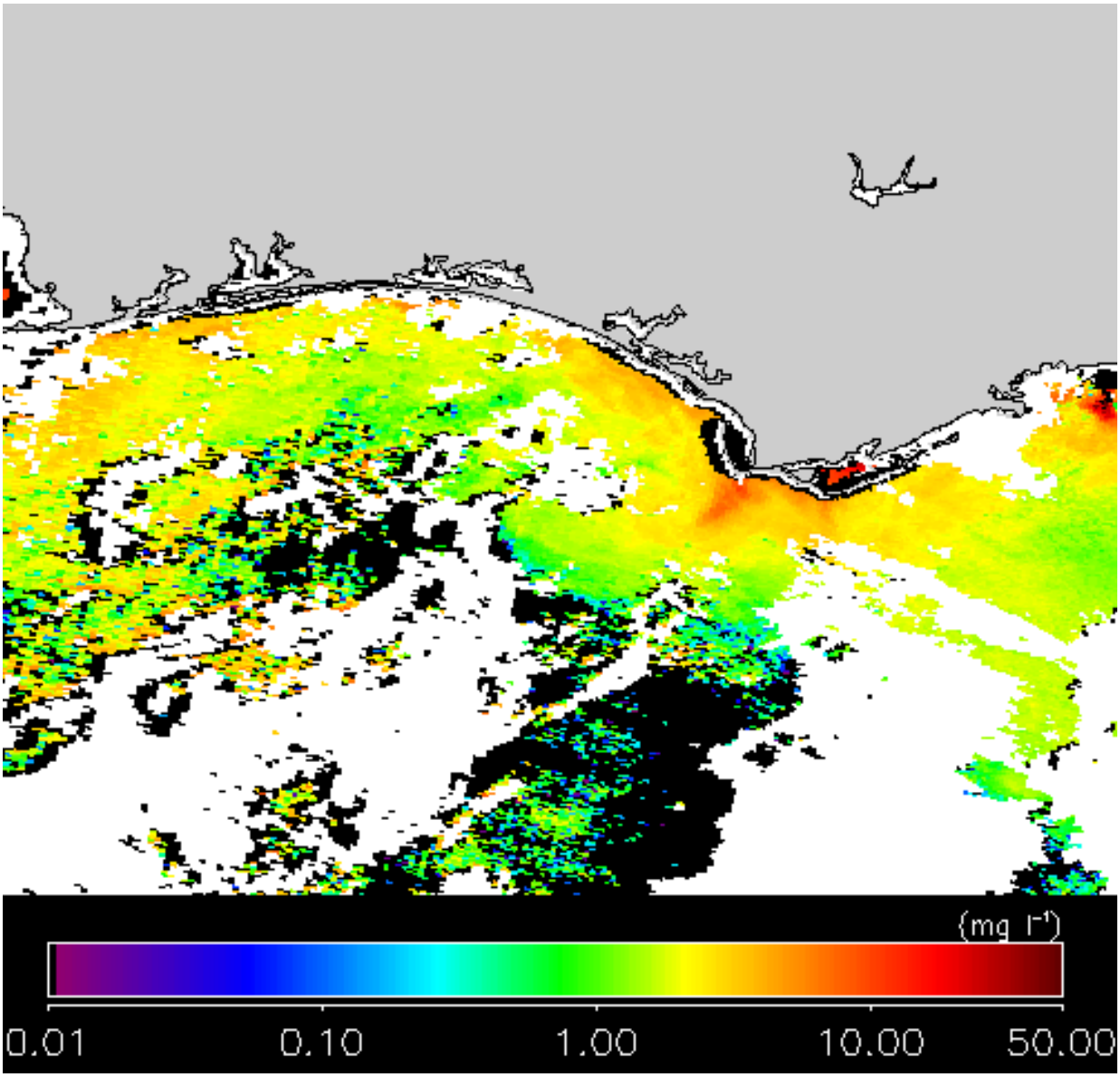

Figure A.25. 17:59:11 UTC, 12 July 2005.

APPENDIX B. MODEL VALIDATION PLOTS

B.1 Ivan Wave Model Validation

For all figures in this section, blue is measured data, red is modeled data.

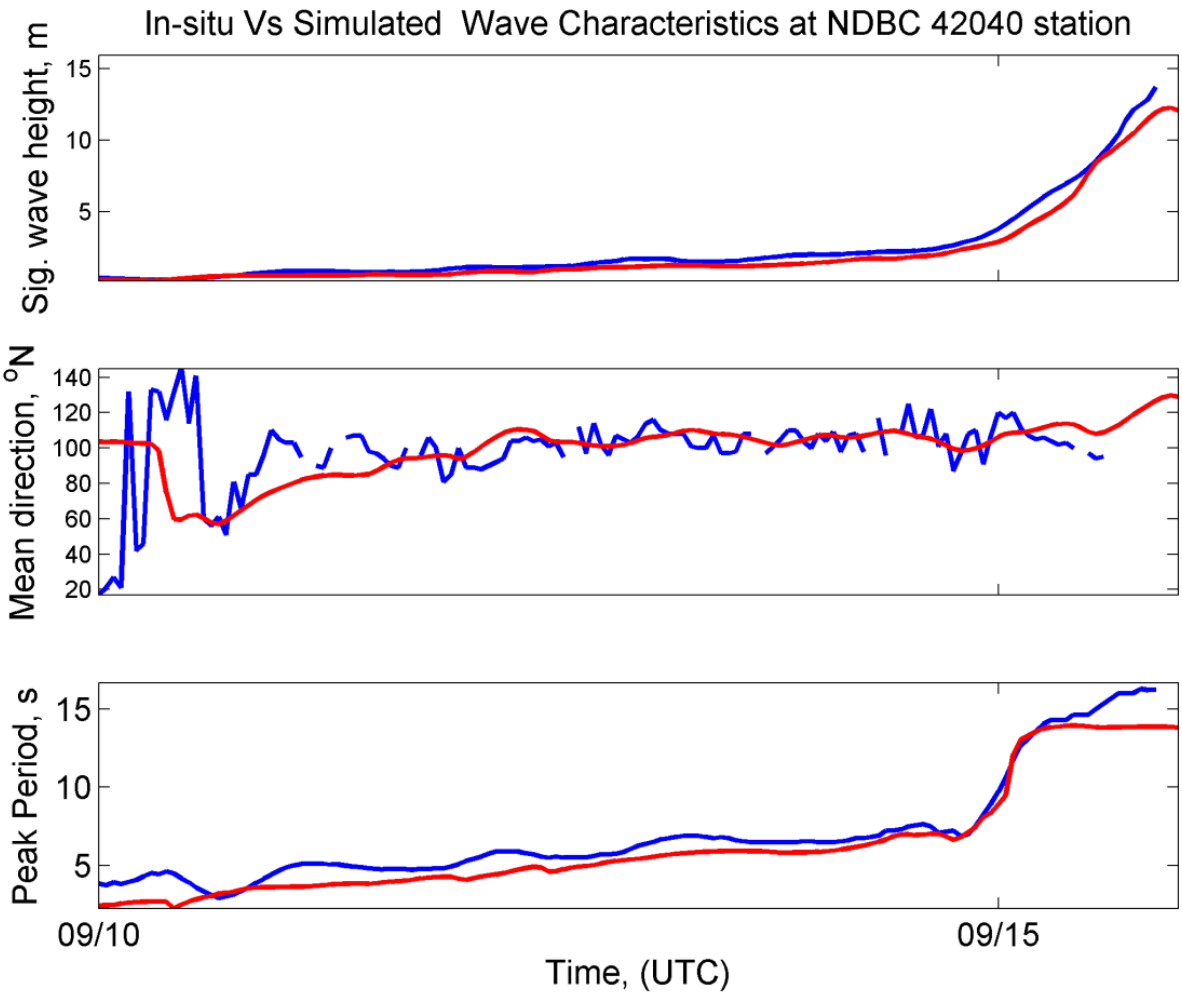

Figure B.1. Validation at NDBC 42040 for modeled data.

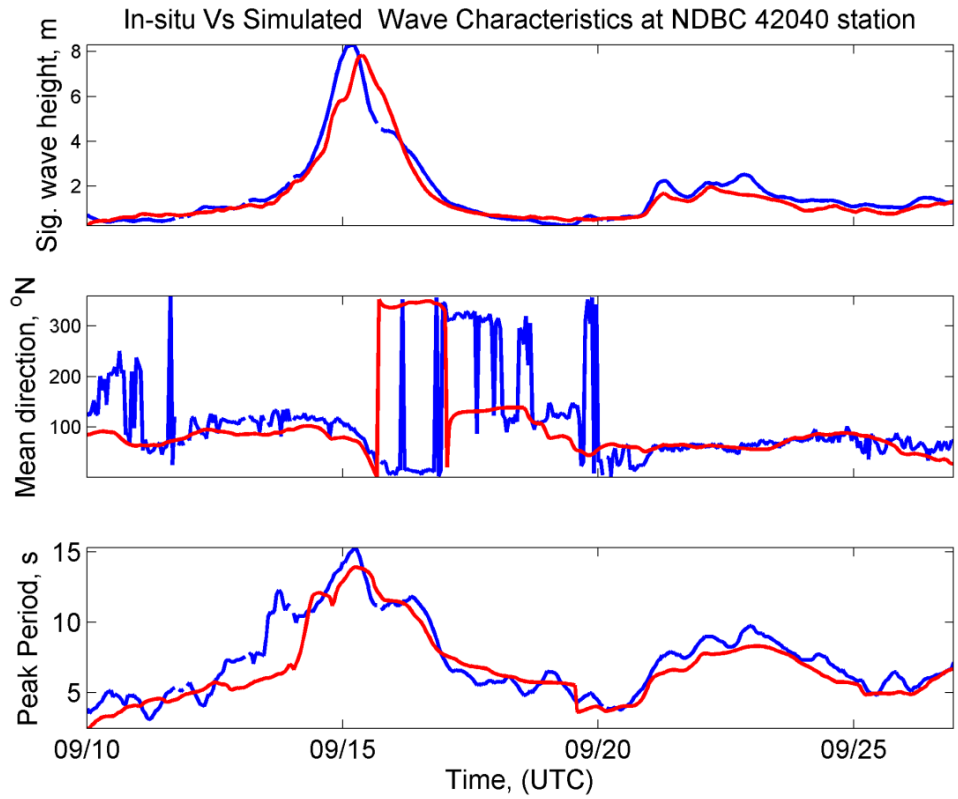

Figure B.2. Model validation at NDBC buoy 42040.

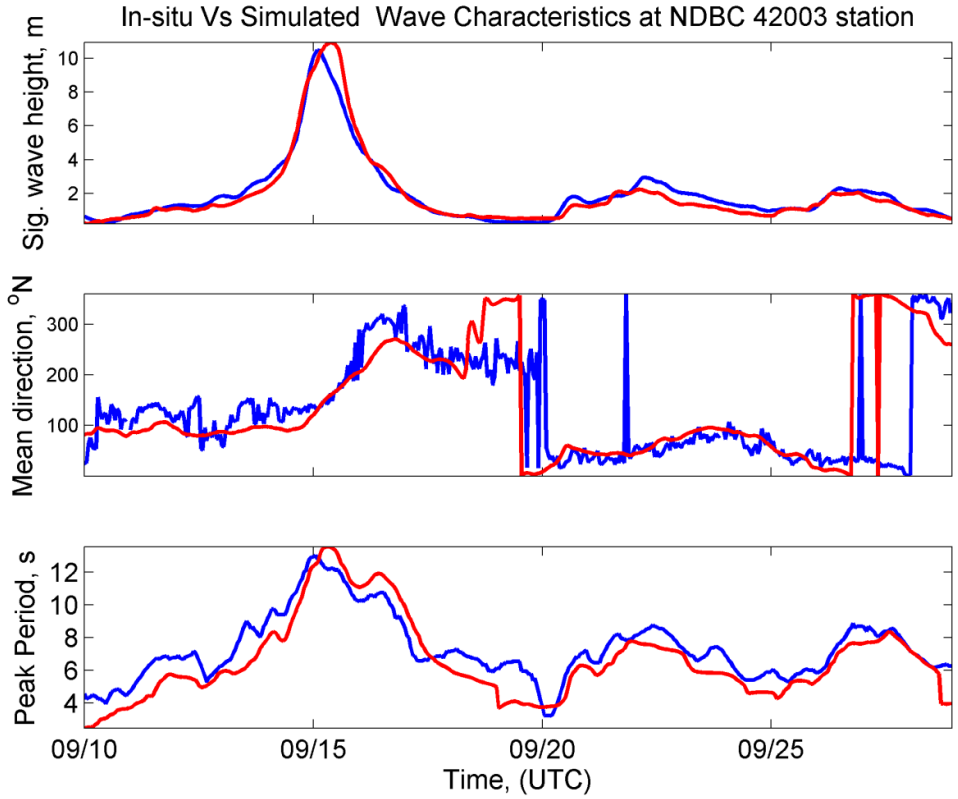

Figure B.3. Model validation at NDBC buoy 42003.

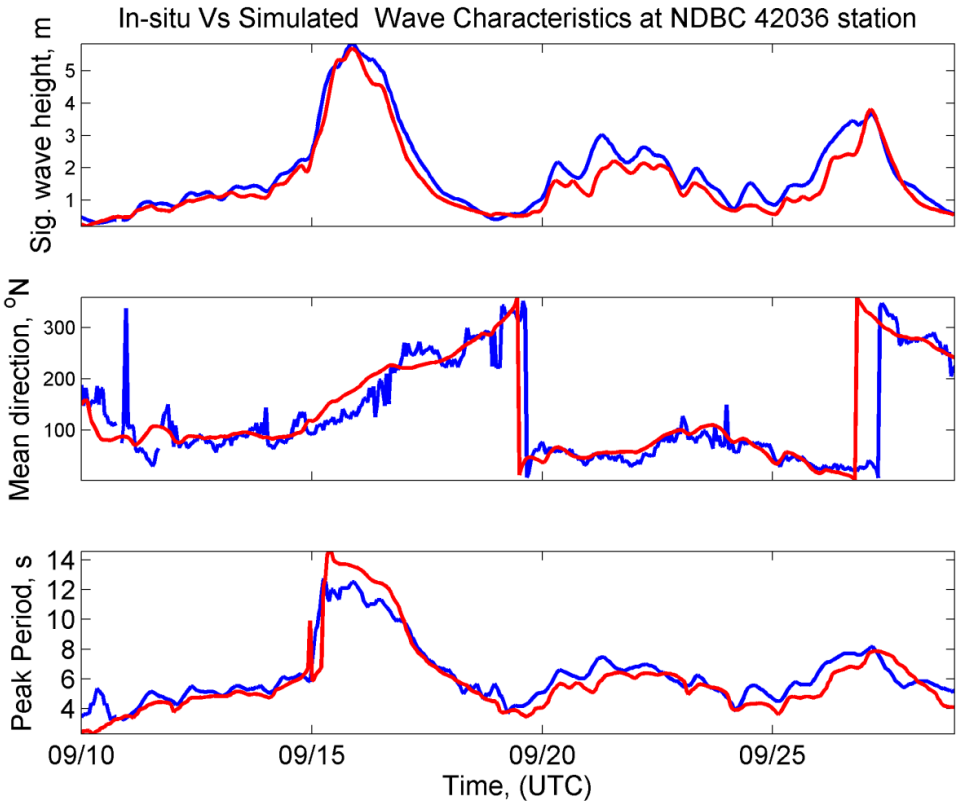

Figure B.4. Model validation at NDBC buoy 42036.

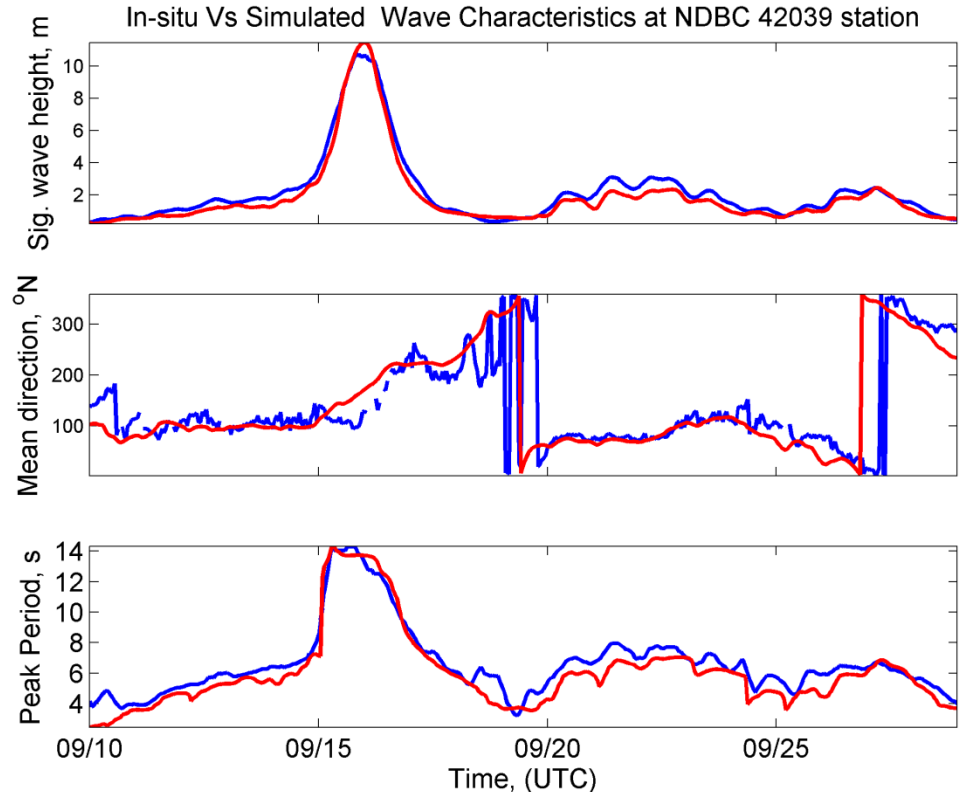

Figure B.5. Model validation at NDBC buoy 42039.

B.2 Dennis Wave Model Validation

For all figures in this section, blue is measured data, red is modeled data.

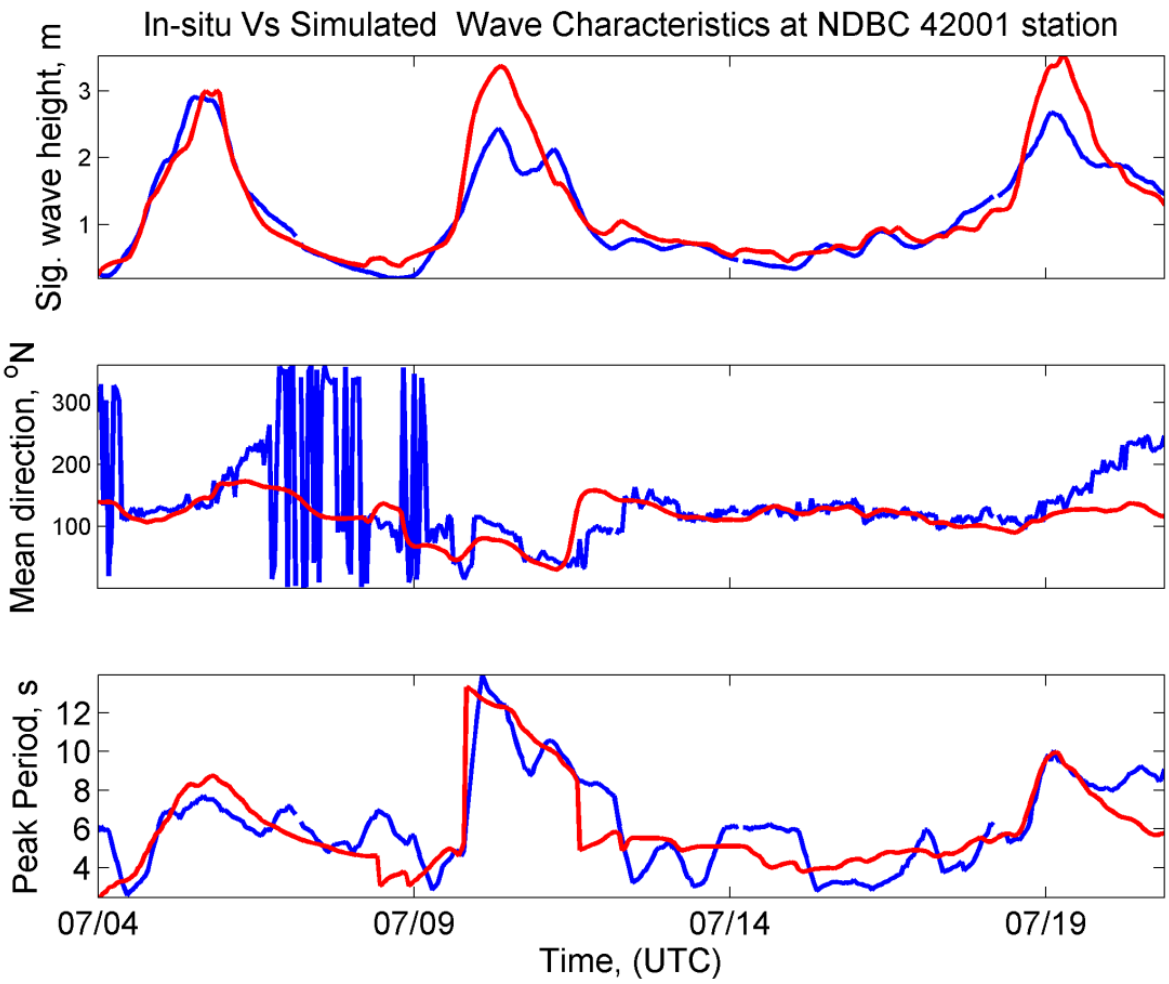

Figure B.6. Model validation at NDBC buoy 42001.

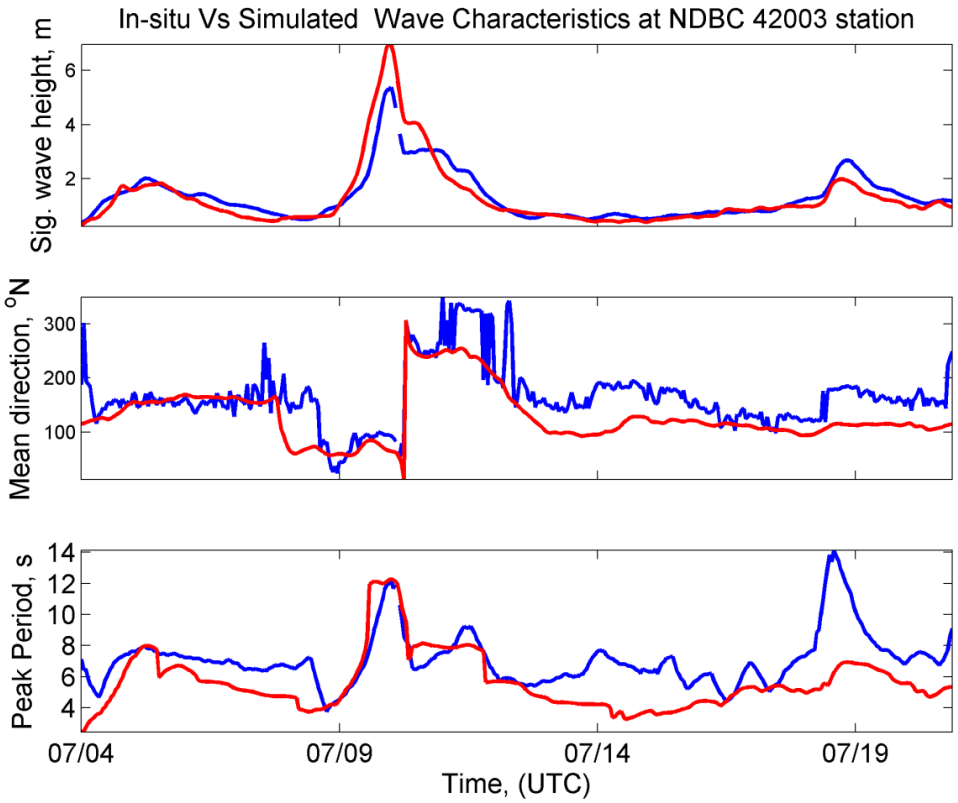

Figure B.7. Model validation at NDBC buoy 42003.

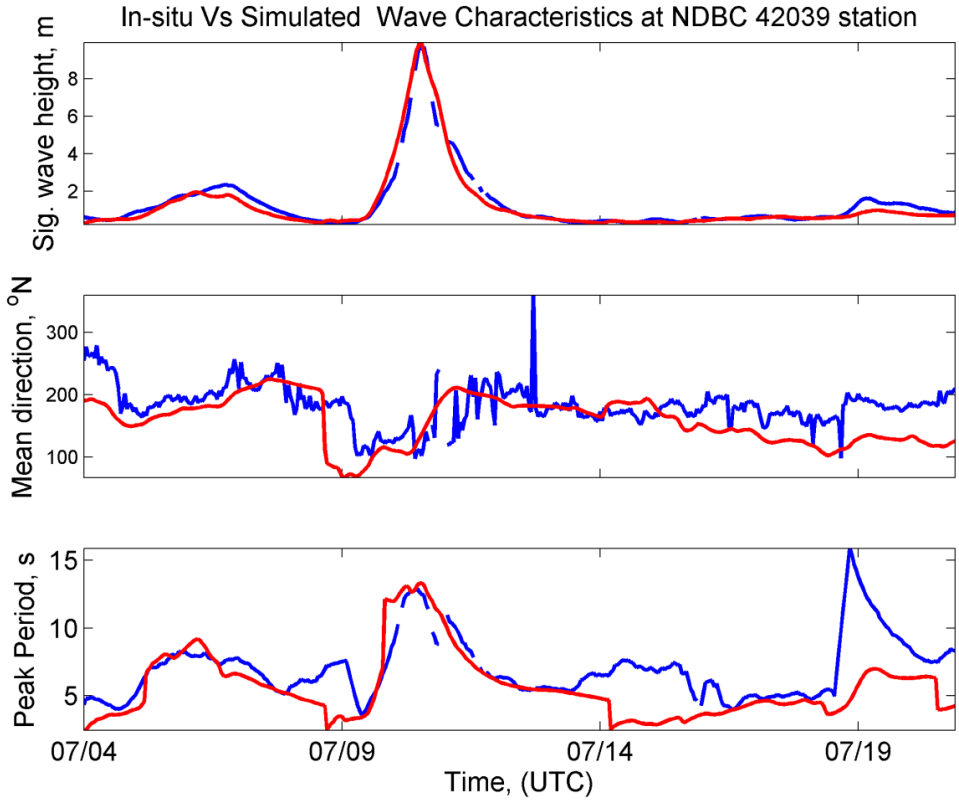

Figure B.8. Model validation at NDBC buoy 42039.

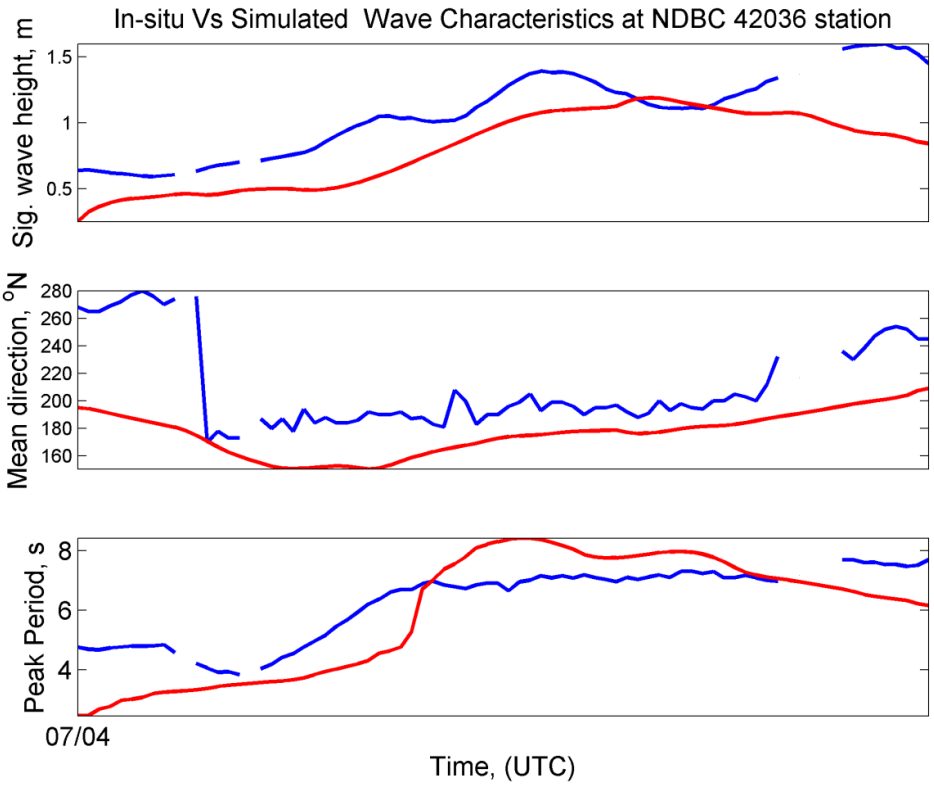

Figure B.9. Model validation at NDBC buoy 42036.

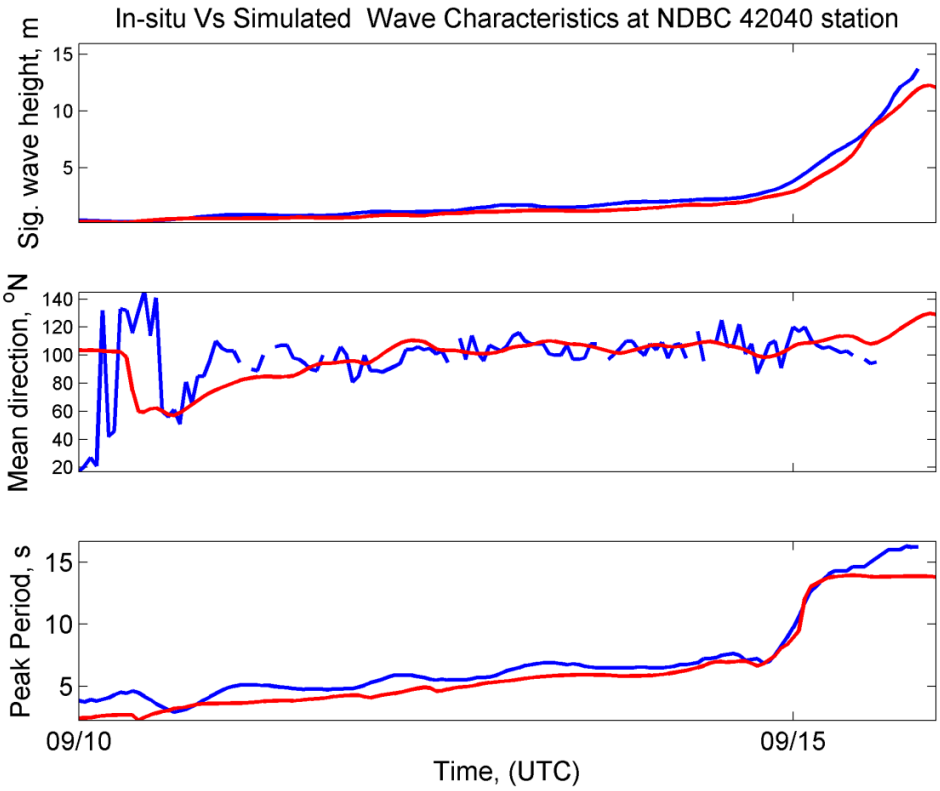

Figure B.10. Model validation at NDBC buoy 42040.

B.3 Ivan Hydrodynamic Model Validation

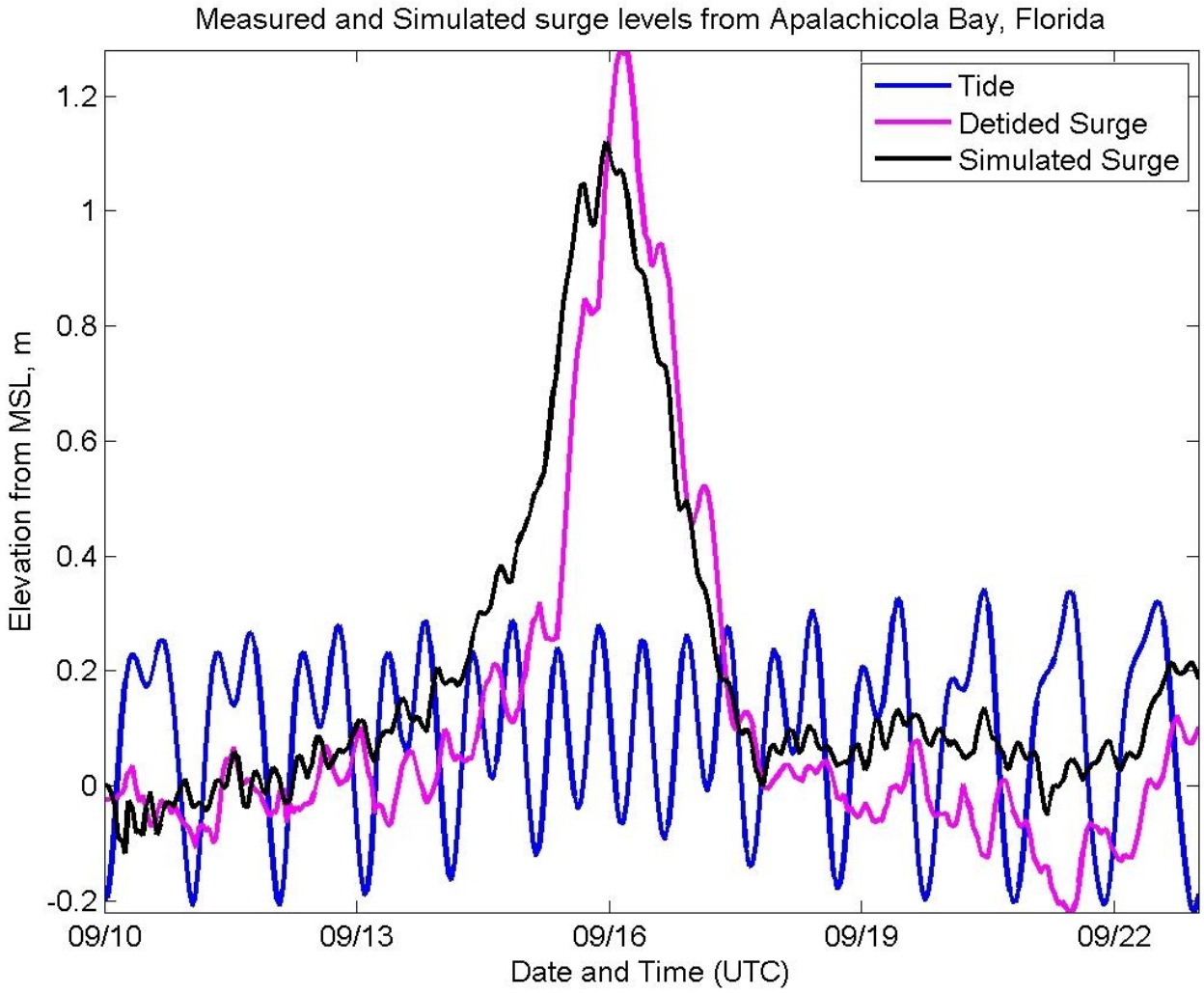

Figure B.11. Model validation at Apalchicola Bay tidal gauge station in Florida.

APPENDIX C. INDIVIDUAL CRUISE TRACKS

Cruise tracks for bathymetry collected and used in bathymetric calculations.

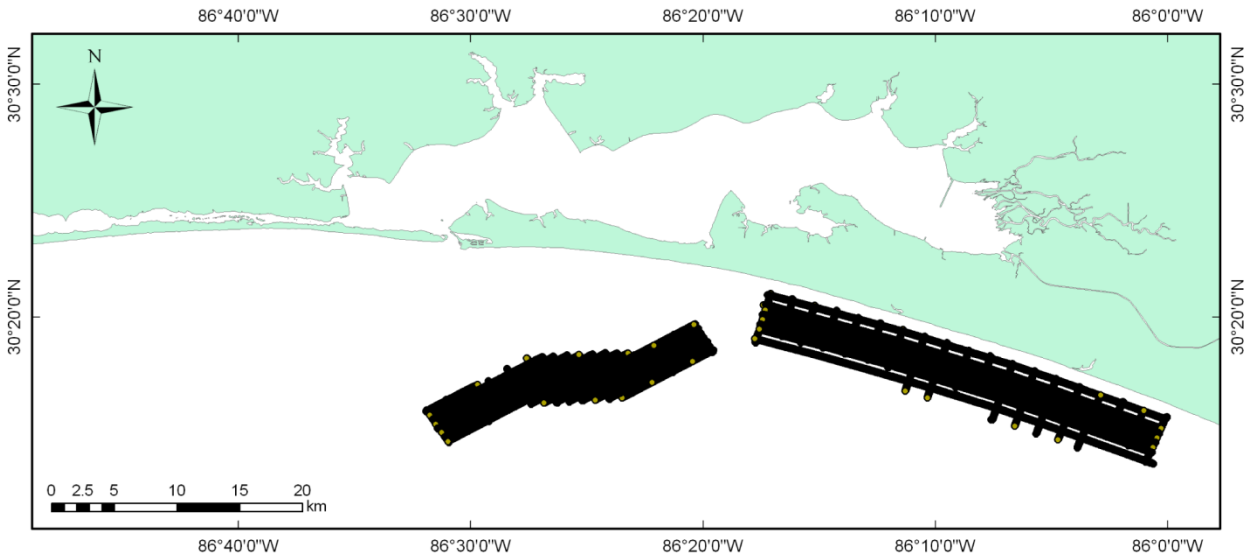

Figure C.1. Collected by Alpine Ocean Seismic, Inc., October 2004: seismic cruise.

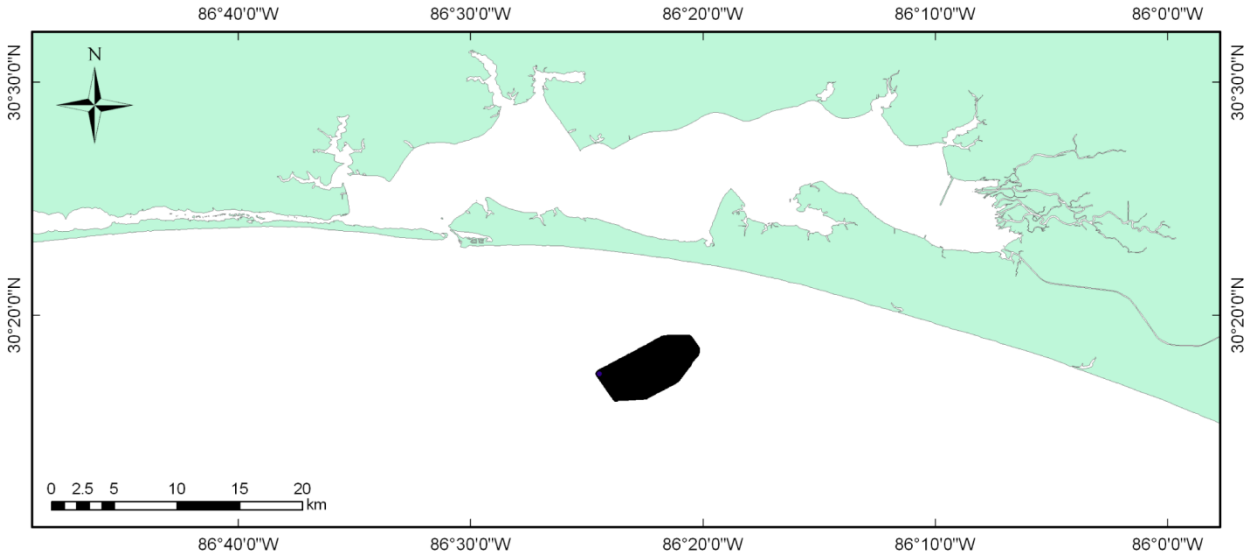

Figure C.2. Collected by Morgan and Eklund, Inc., November 2007.

APPENDIX D. ANNOTATED SELECTED SEISMIC IMAGES*

*Because most of these lines were not digital, the interpretations were done on paper and later transferred to digital copies for this study. During the process, Line 33 was extensively interpreted and annotated, containing a large channel and many clear reflectors. Unfortunately, this line was lost before the seismic profiles could be made digital. For all images, one inch equals 5 ms of two-way travel time, or approximately 4 m. The vertical exaggeration varies per figure.

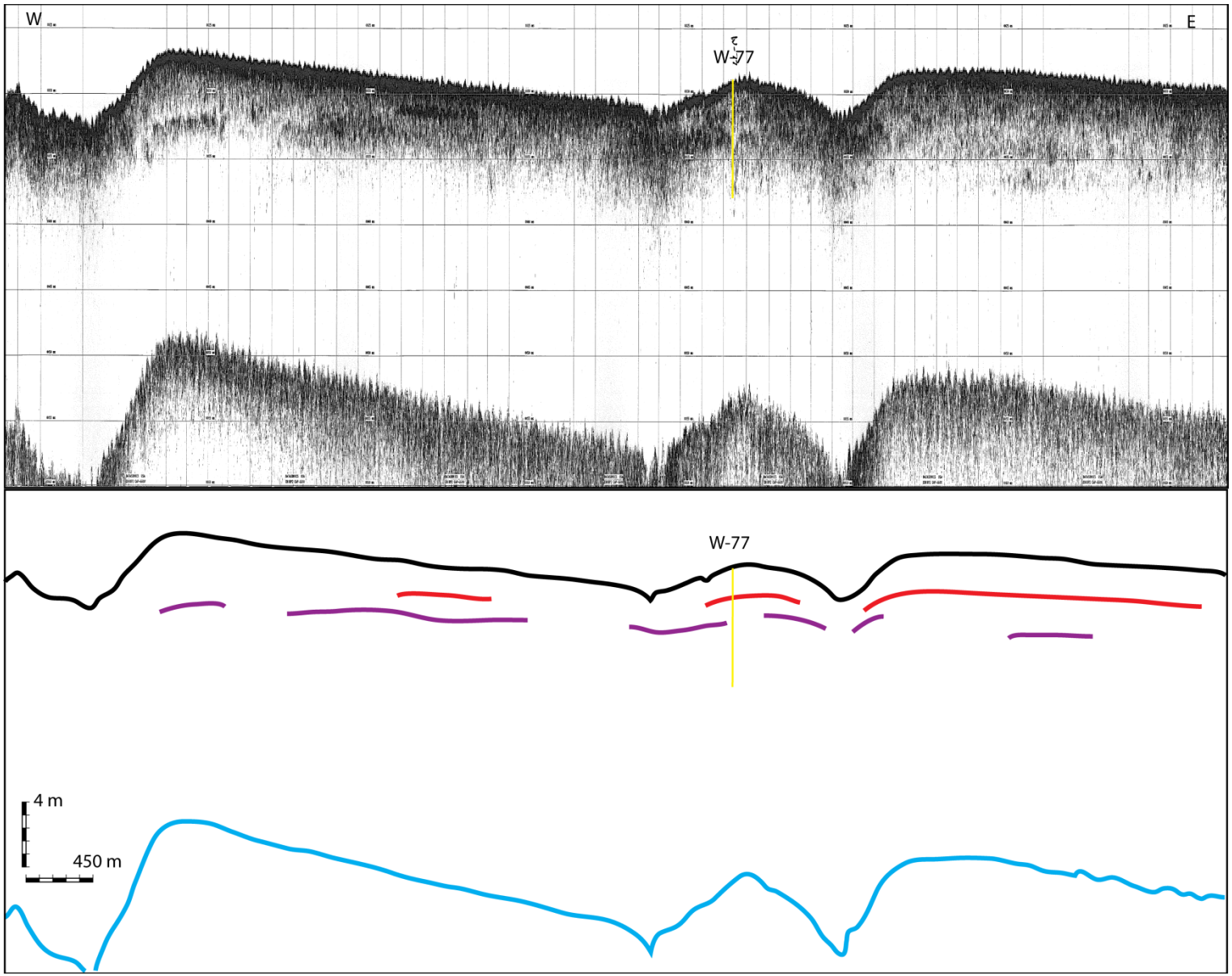

Figure D.1. Line 31.

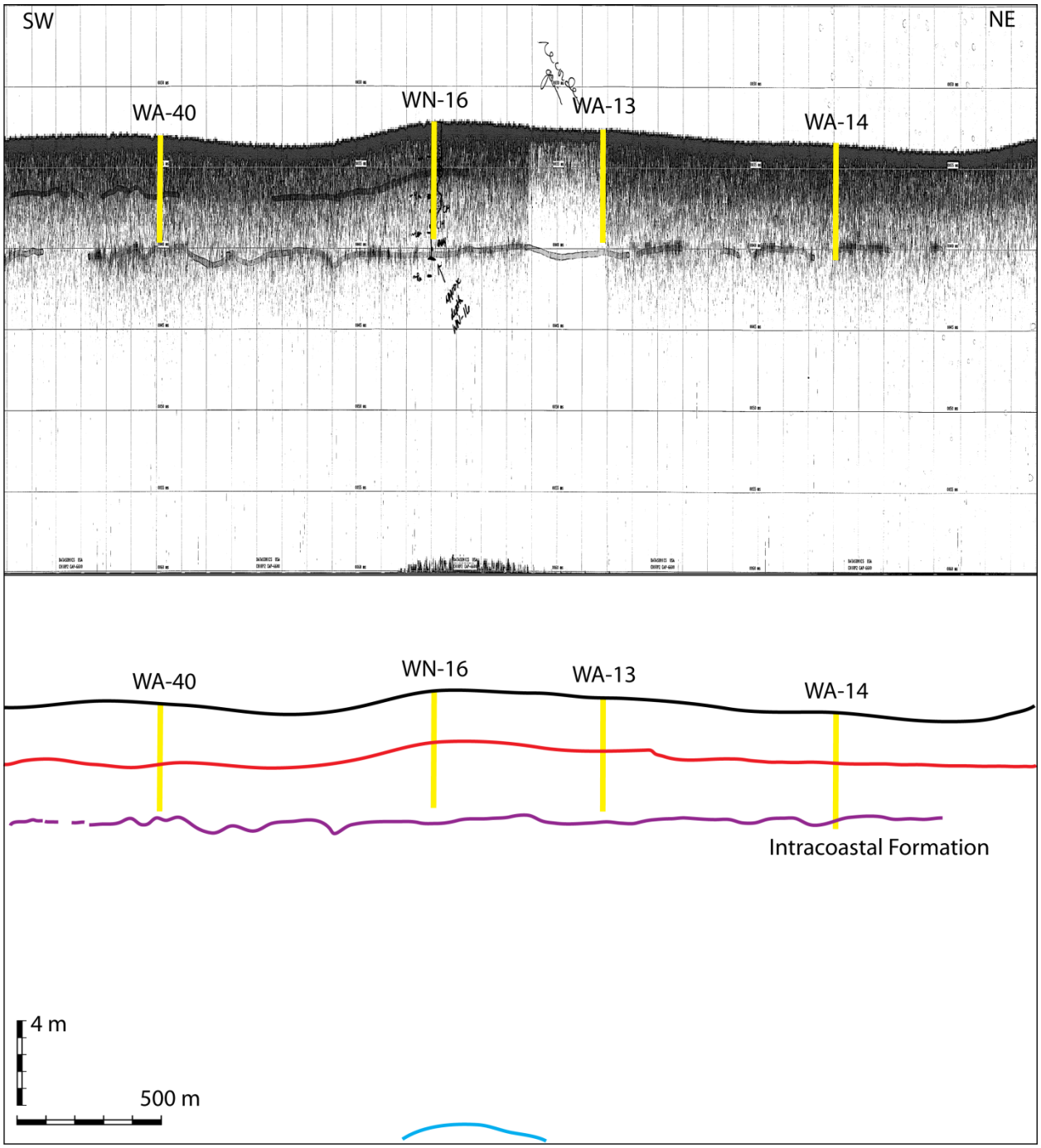

Figure D.2. Line 26.

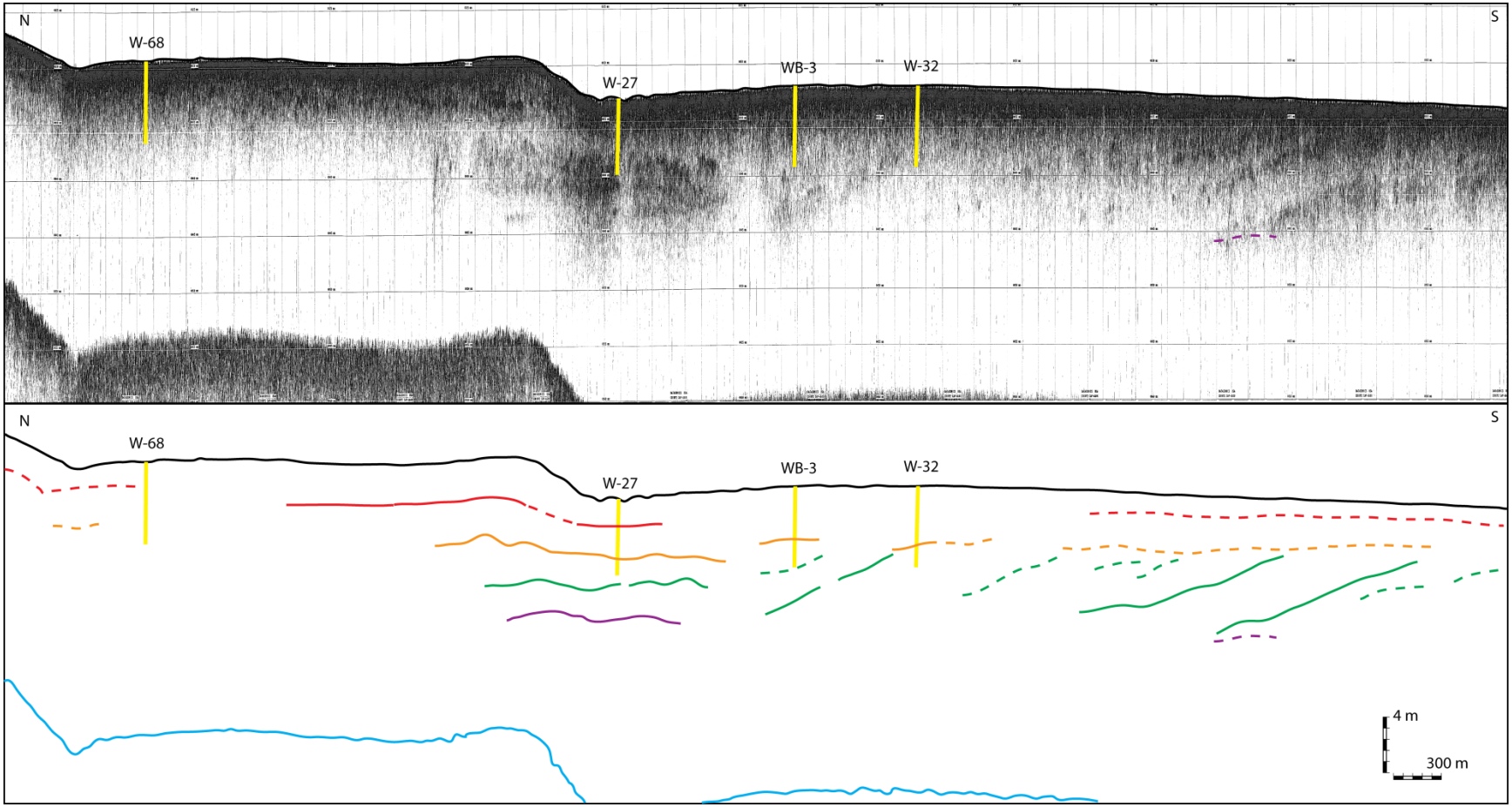

Figure D.3. Line 50.

APPENDIX E. SELECTED ANNOTATED CORE LOGS

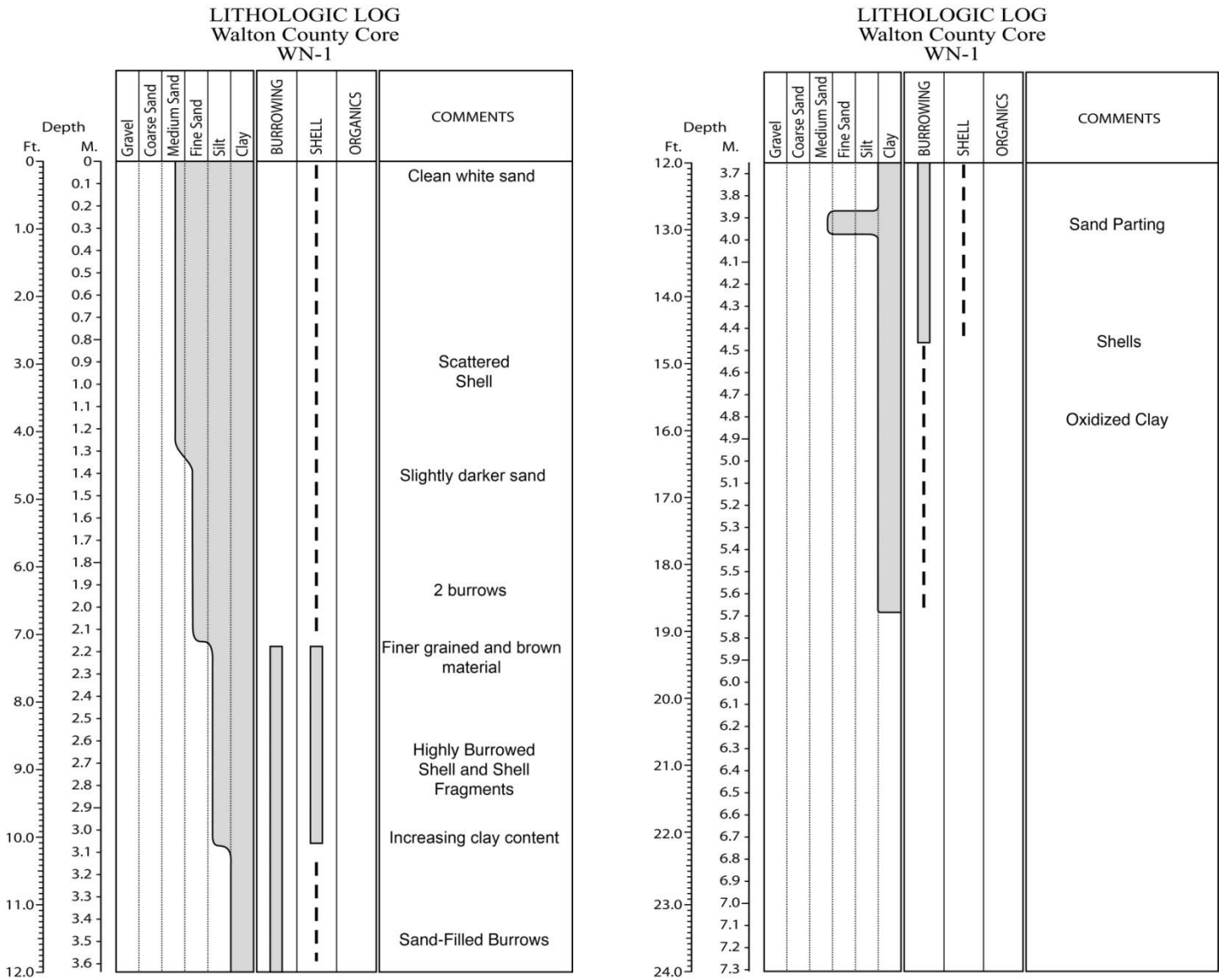

Figure E.1. Core WN-1 log.

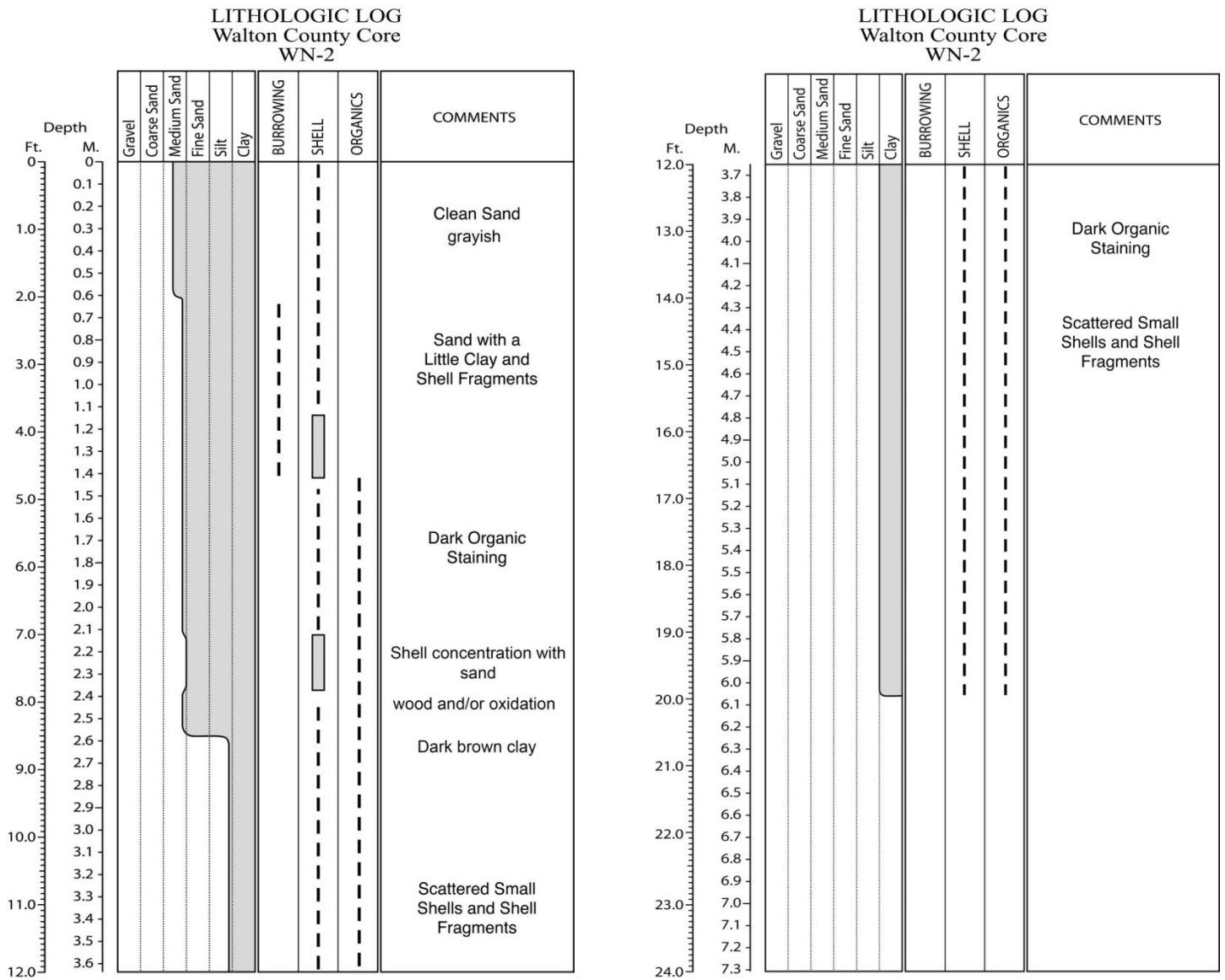

Figure E.2. Core WN-2 log.

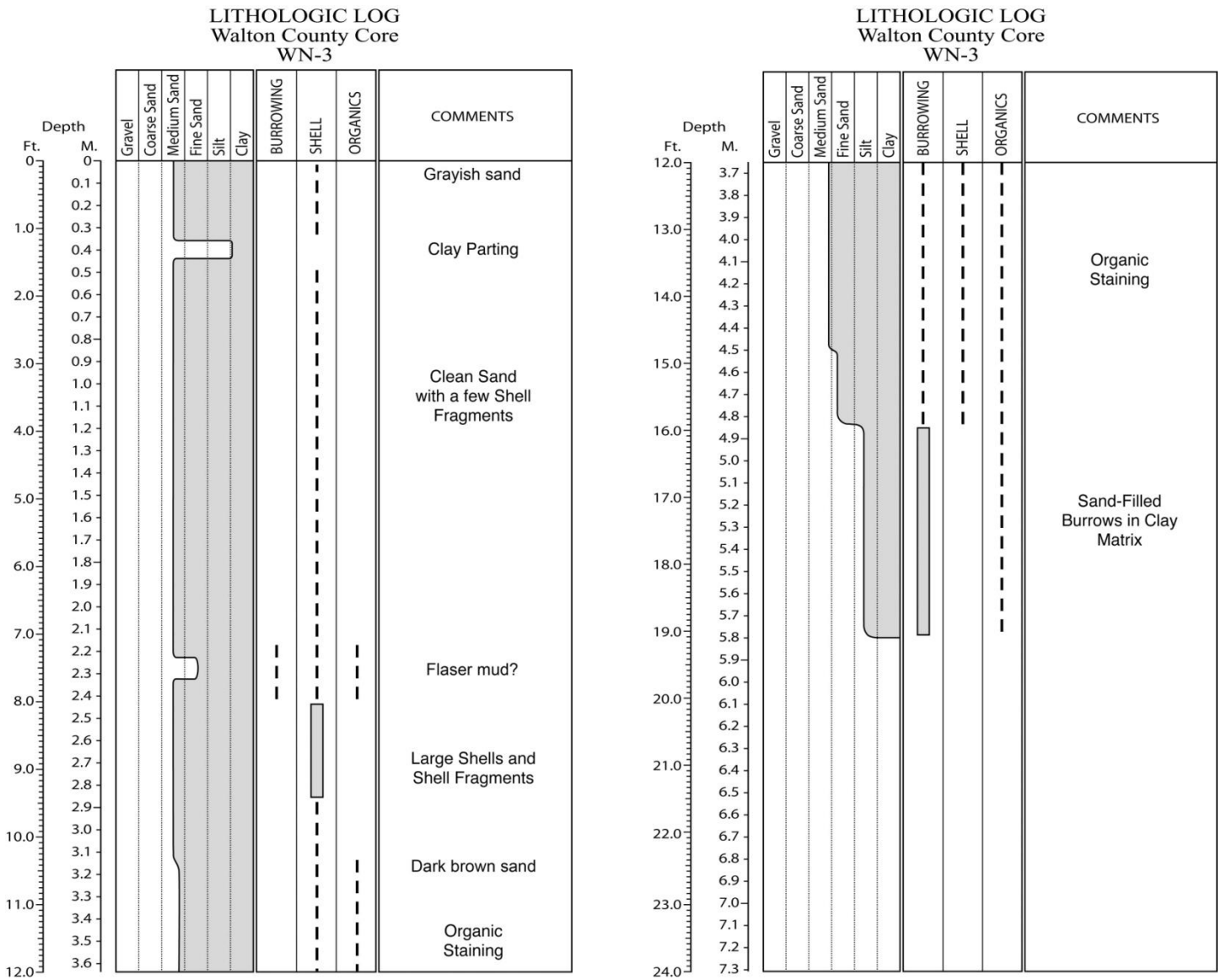

Figure E.3. Core WN-3 log.

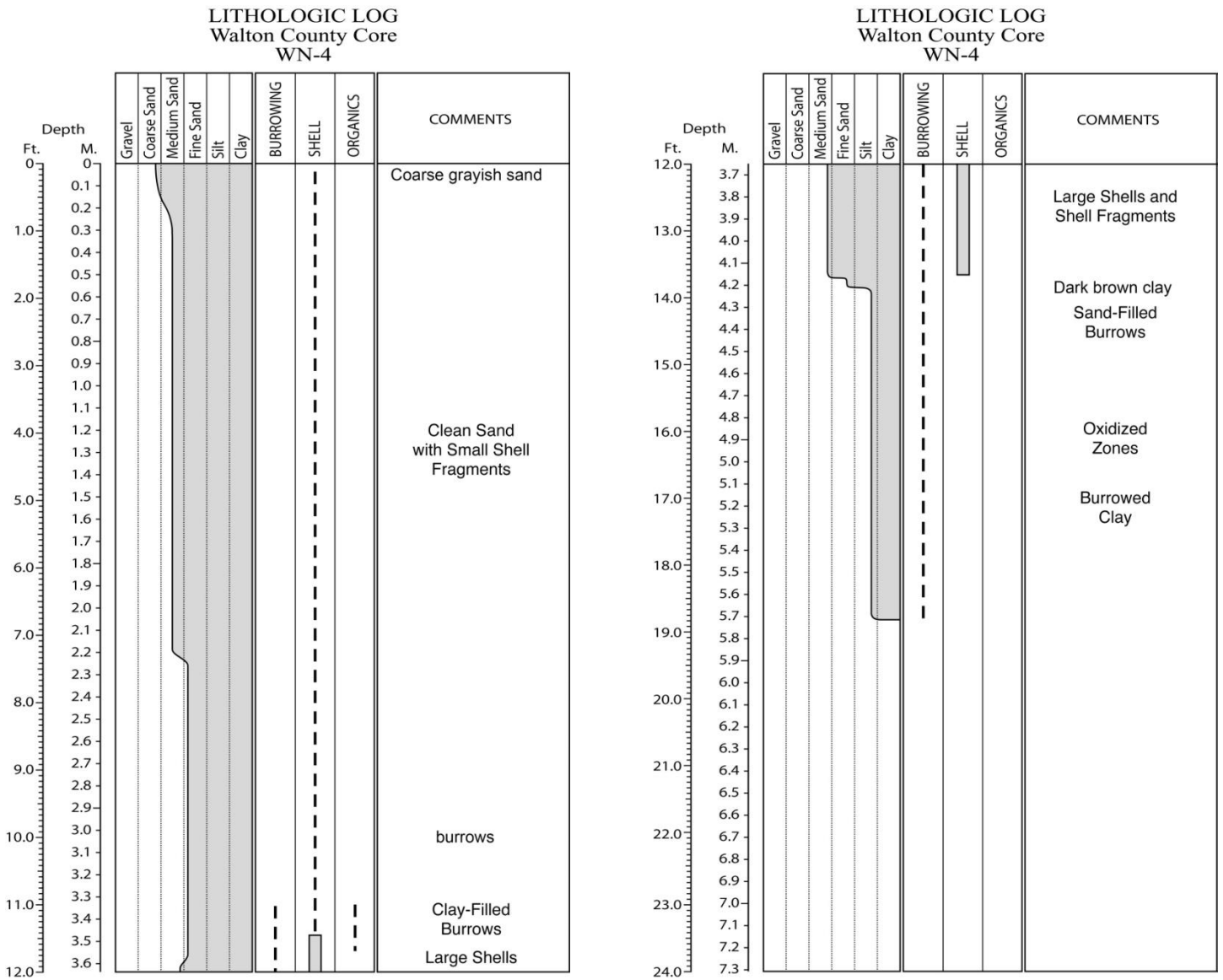

Figure E.4. Core WN-4 log.

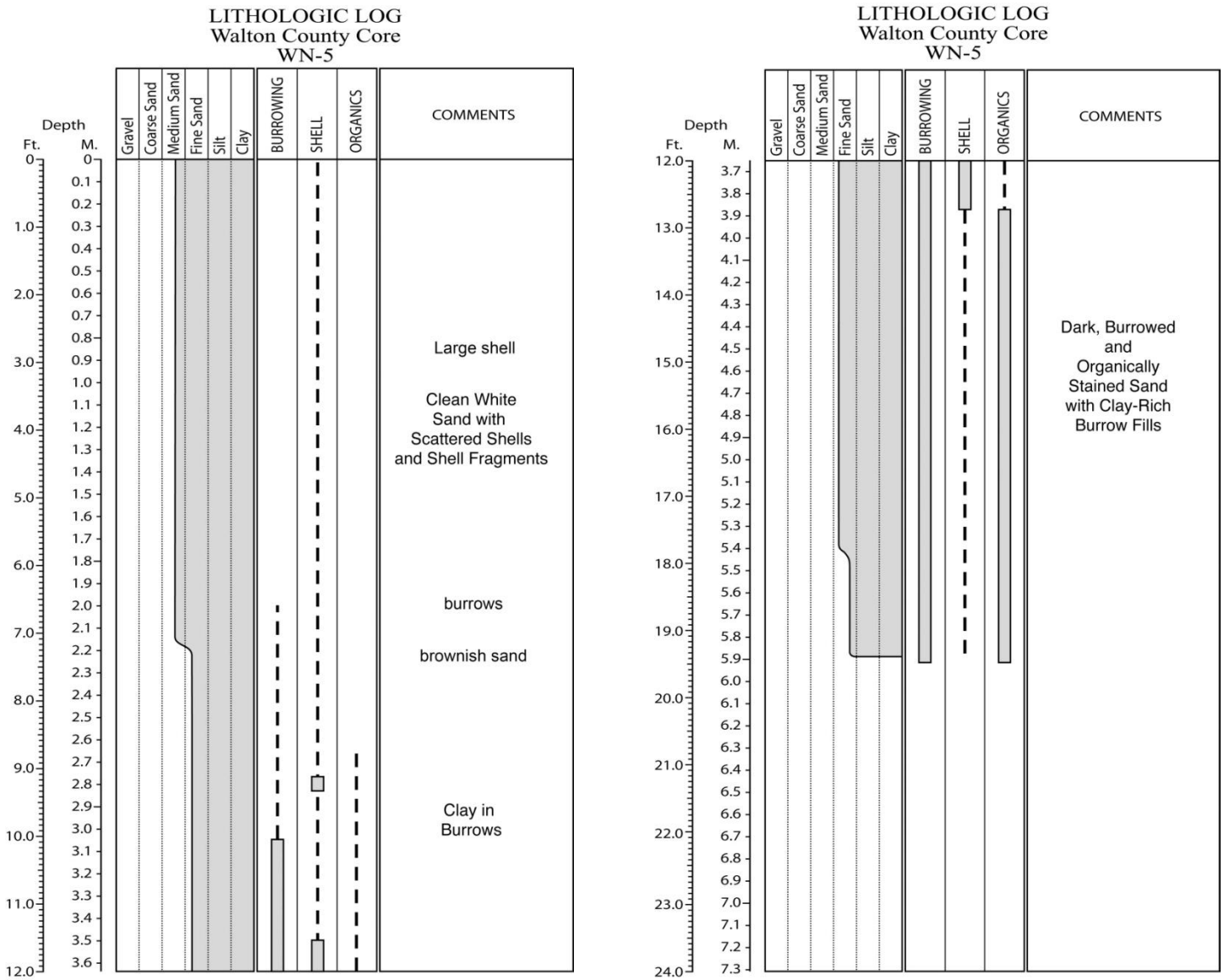

Figure E.5. Core WN-5 log.

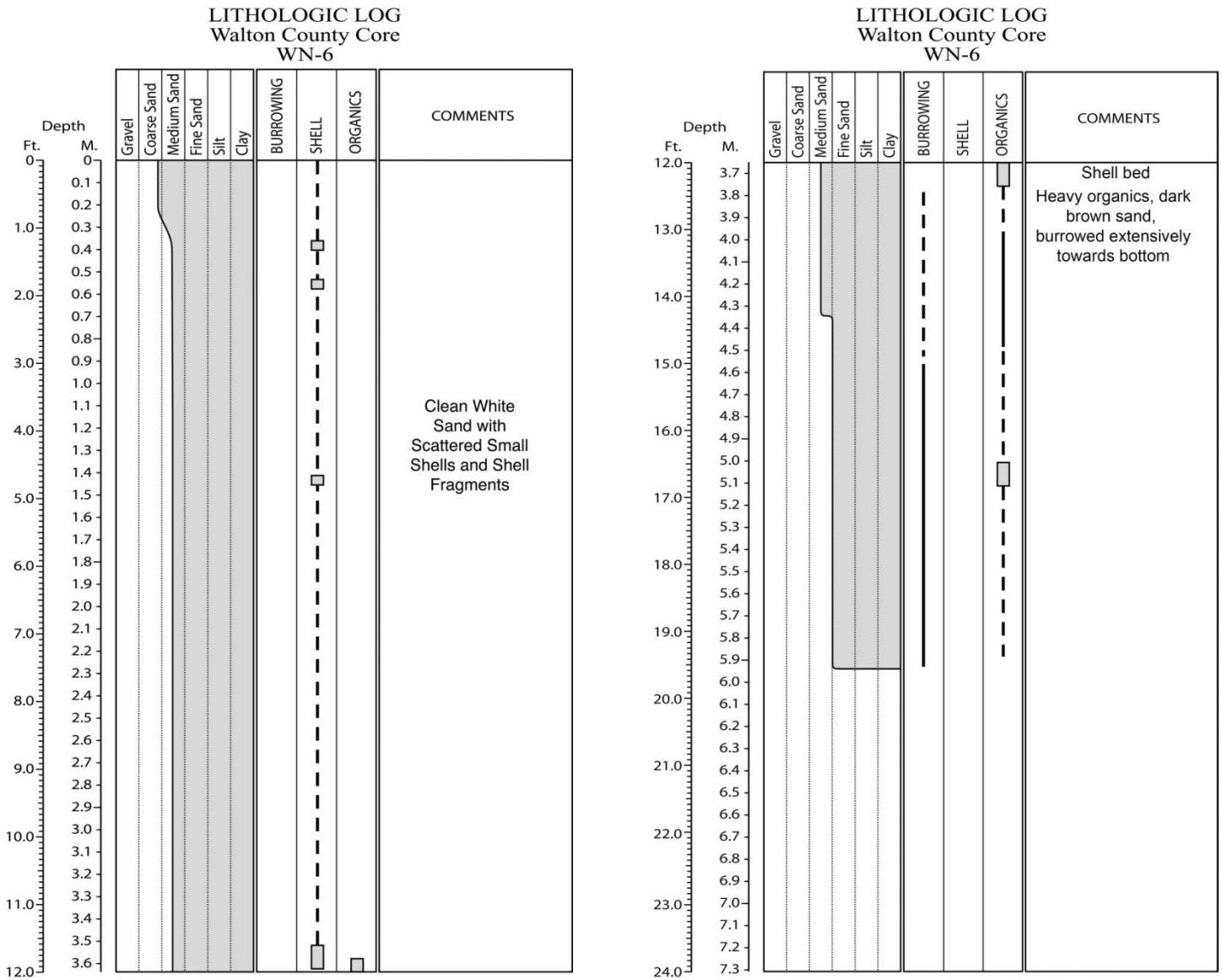

Figure E.6. Core WN-6 log.

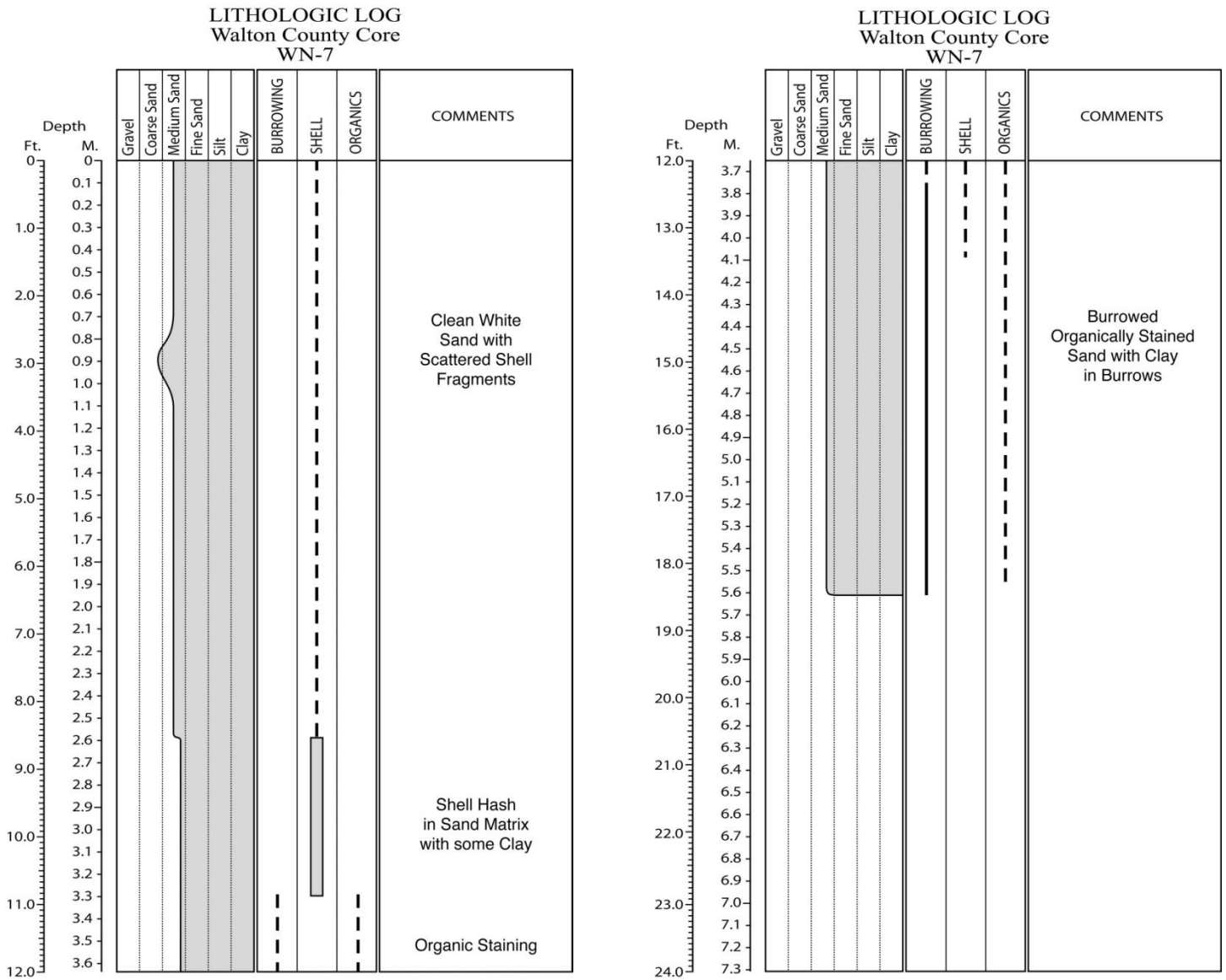

Figure E.7. Core WN-7 log.

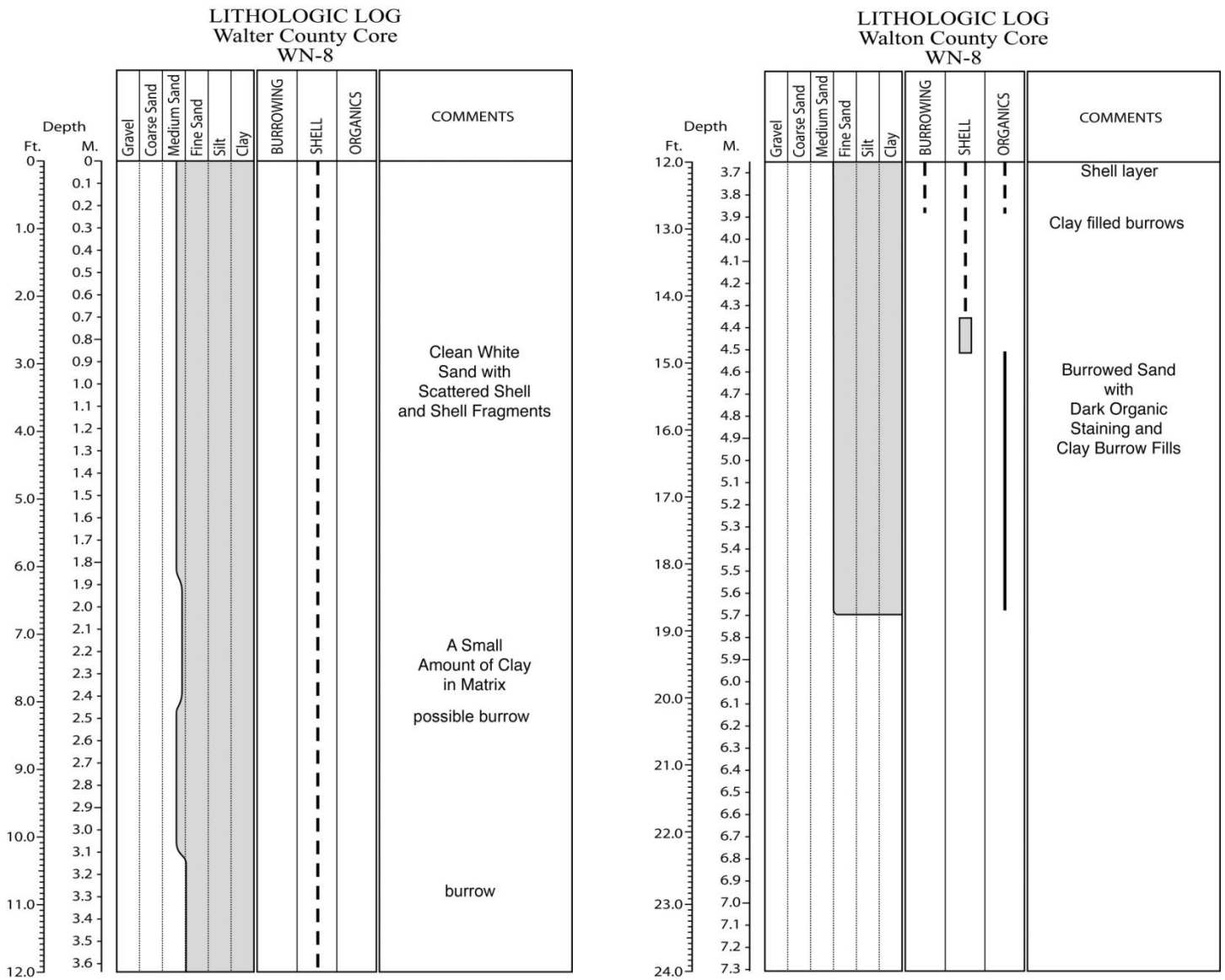

Figure E.8. Core WN-8 log.

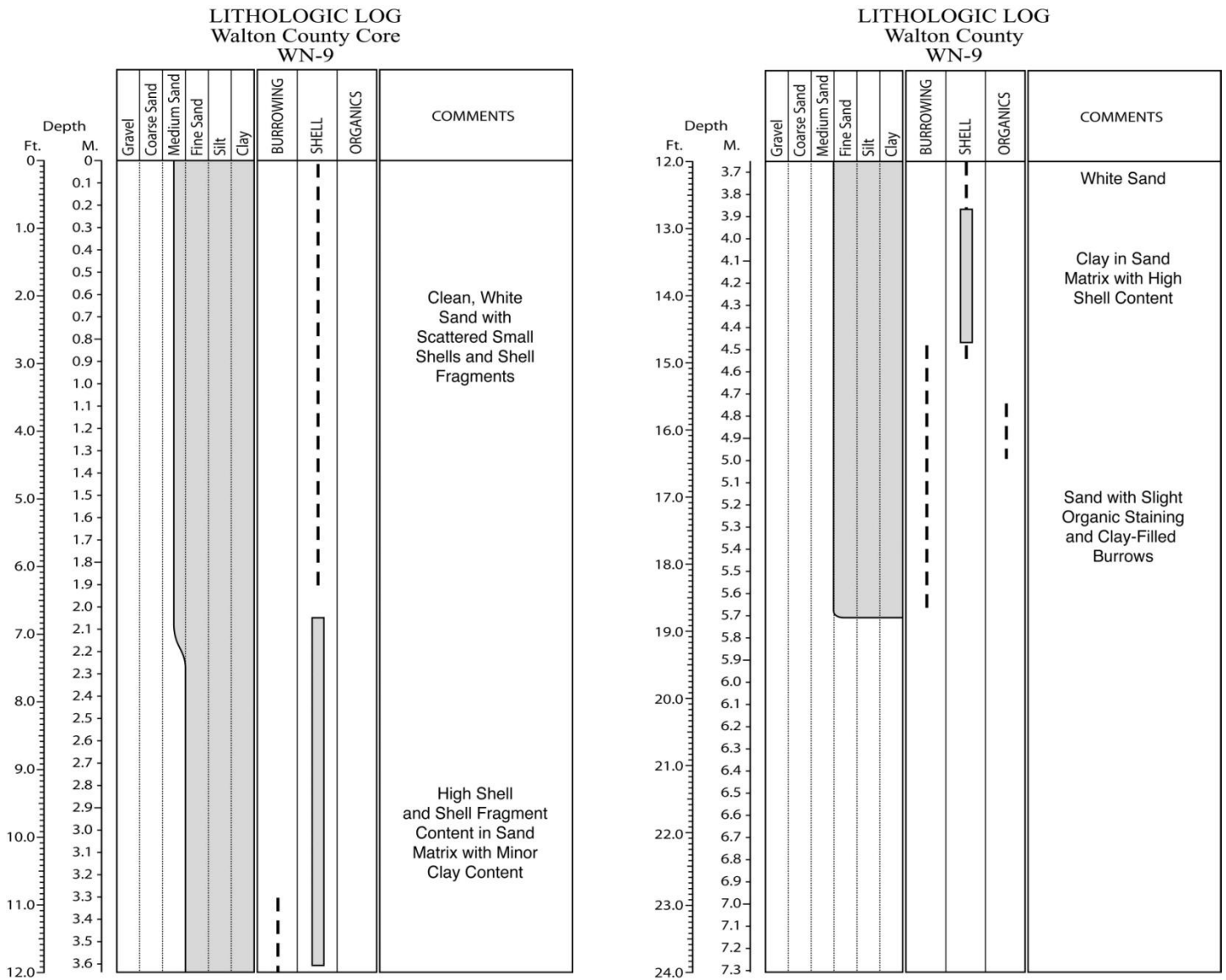

Figure E.9. Core WN-9 log.

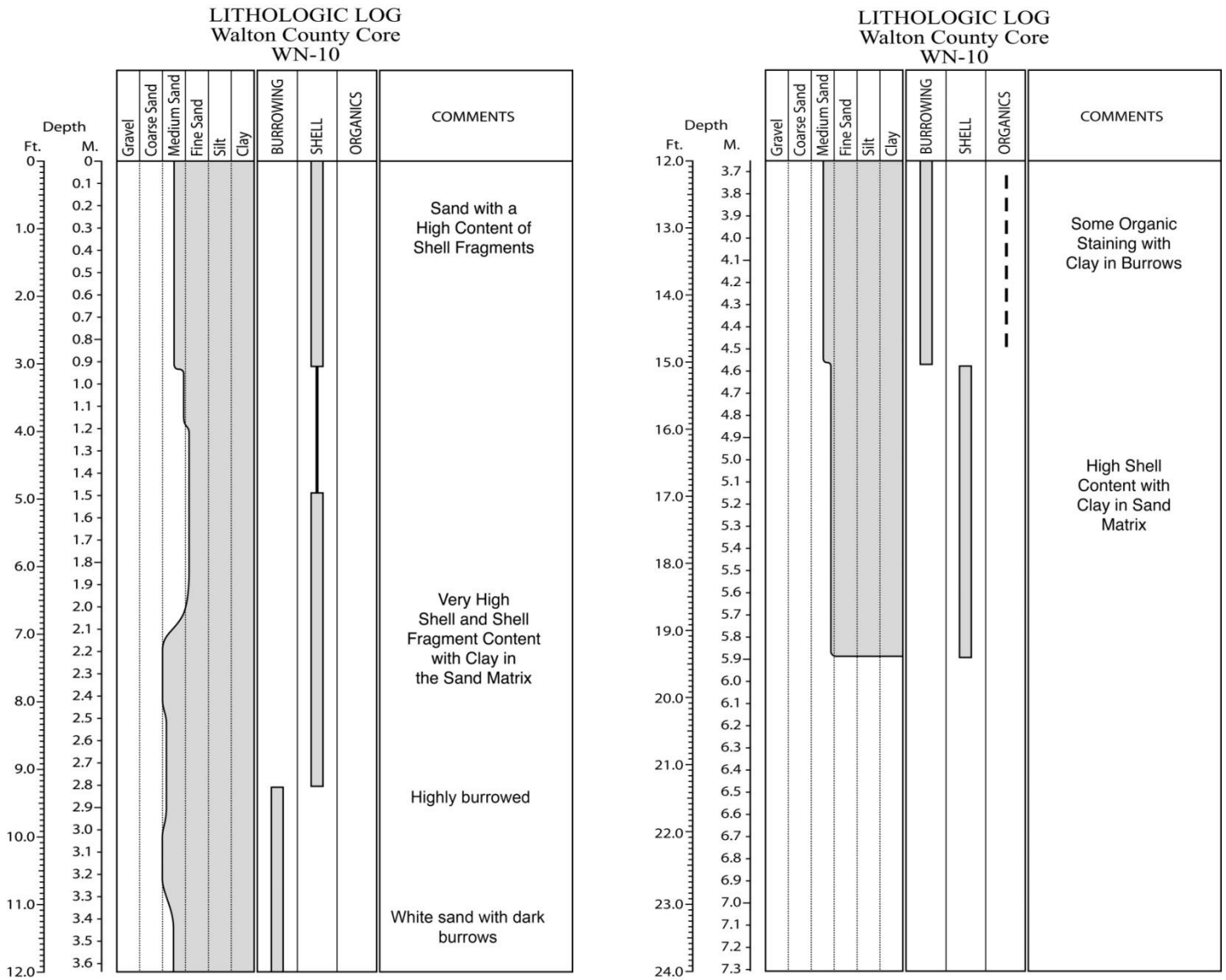

Figure E.10. Core WN-10 log.

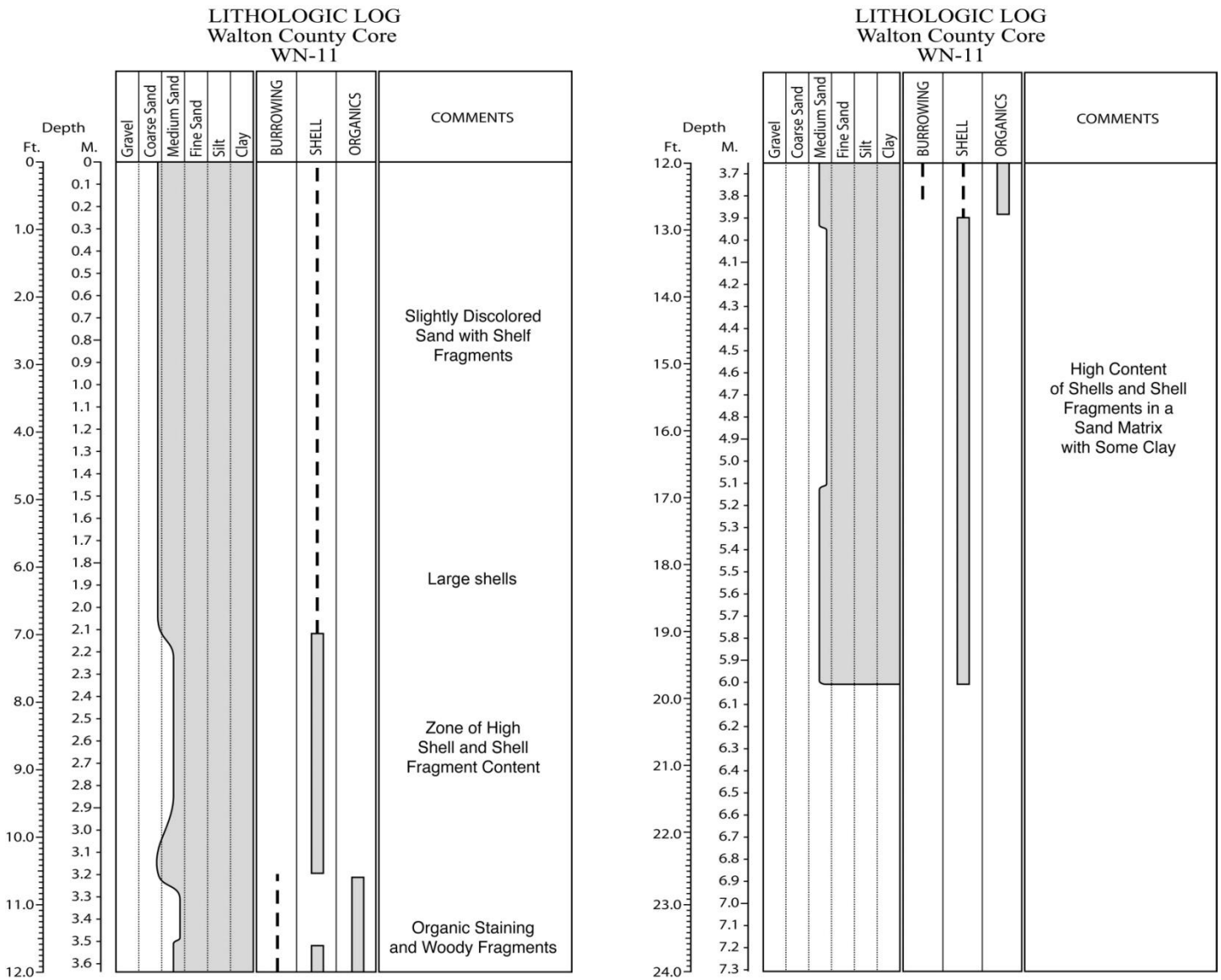

Figure E.11. Core WN-11 log.

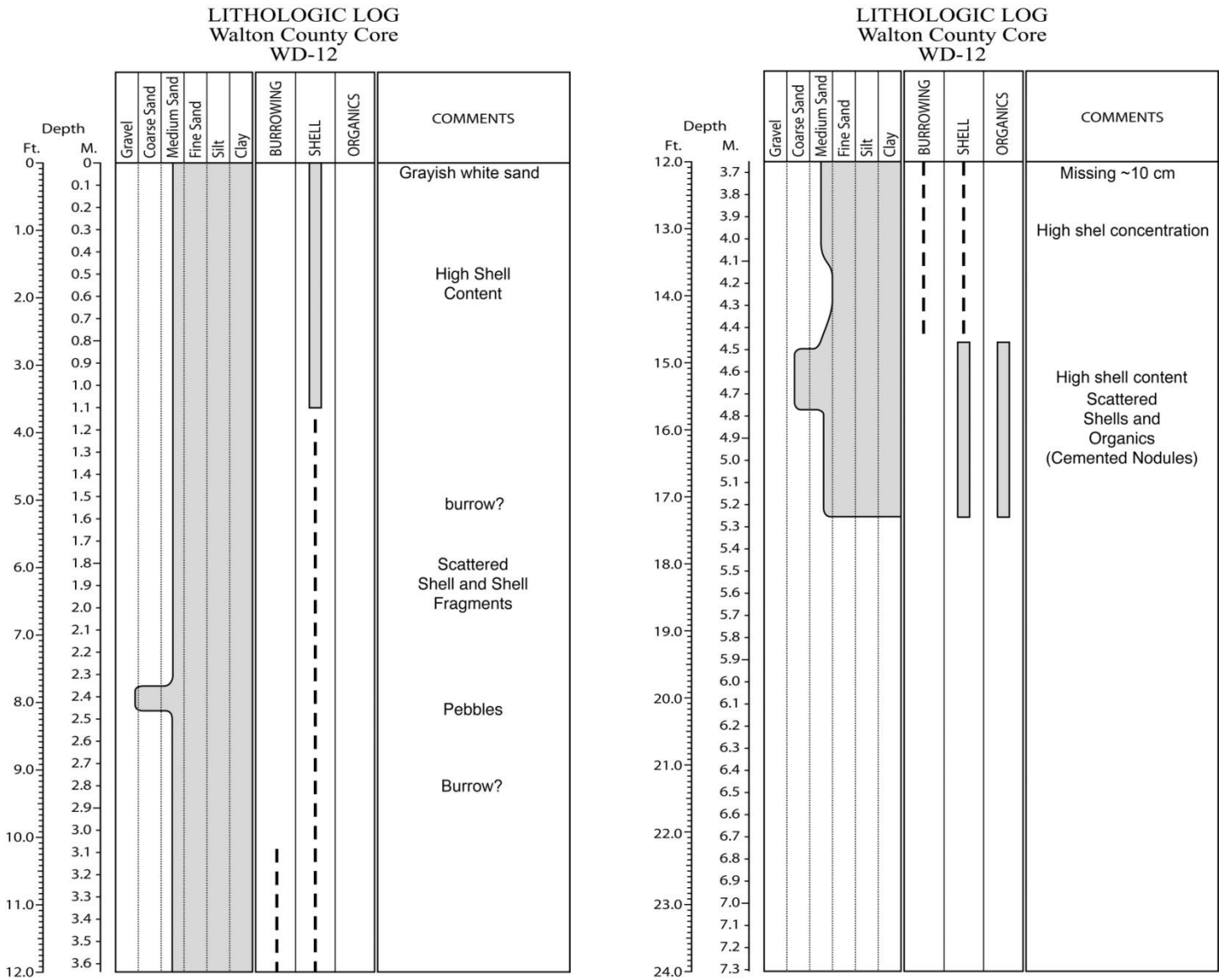

Figure E.12. Core WD-12 log.

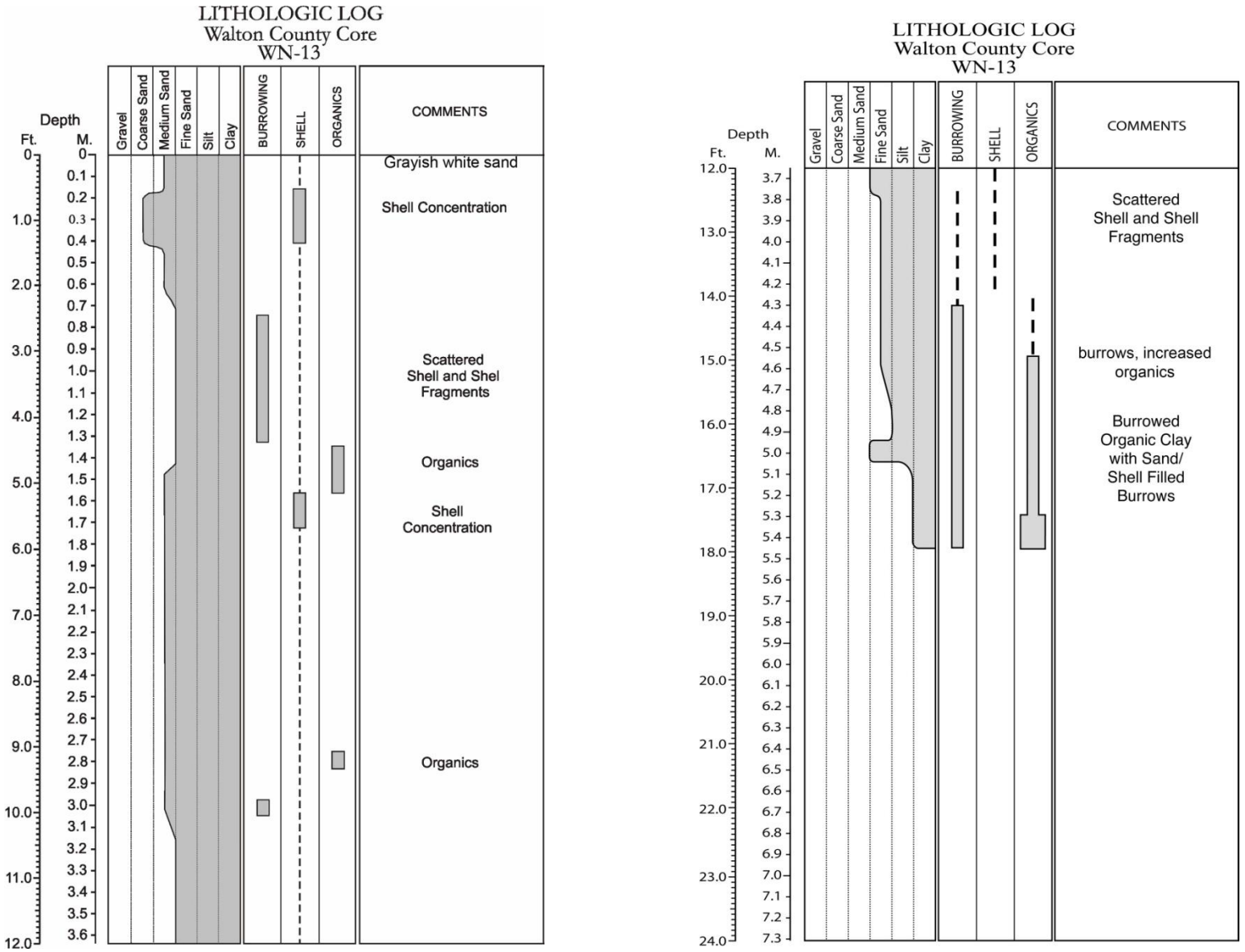

Figure E.13. Core WN-13 log.

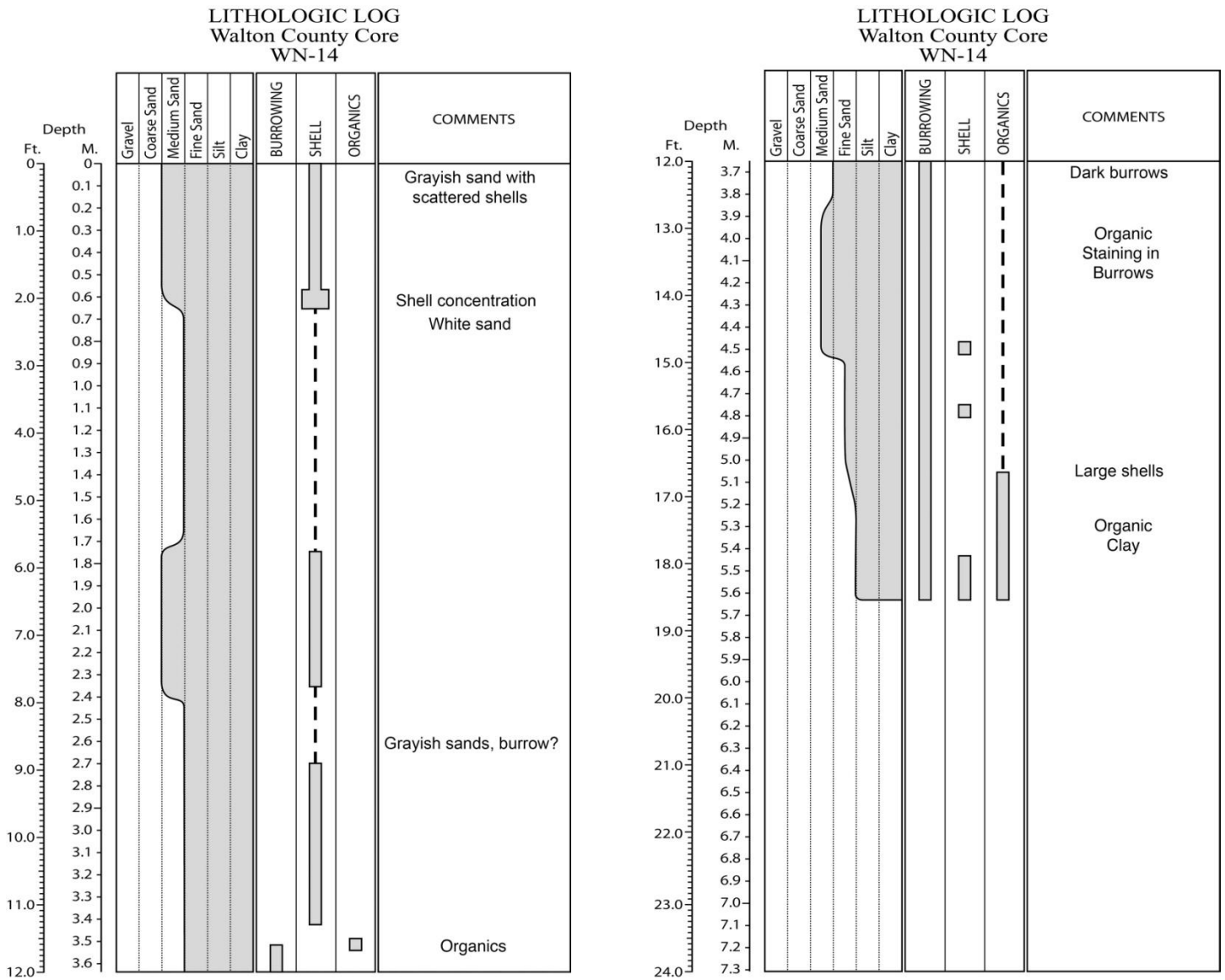

Figure E.14. Core WN-14 log.

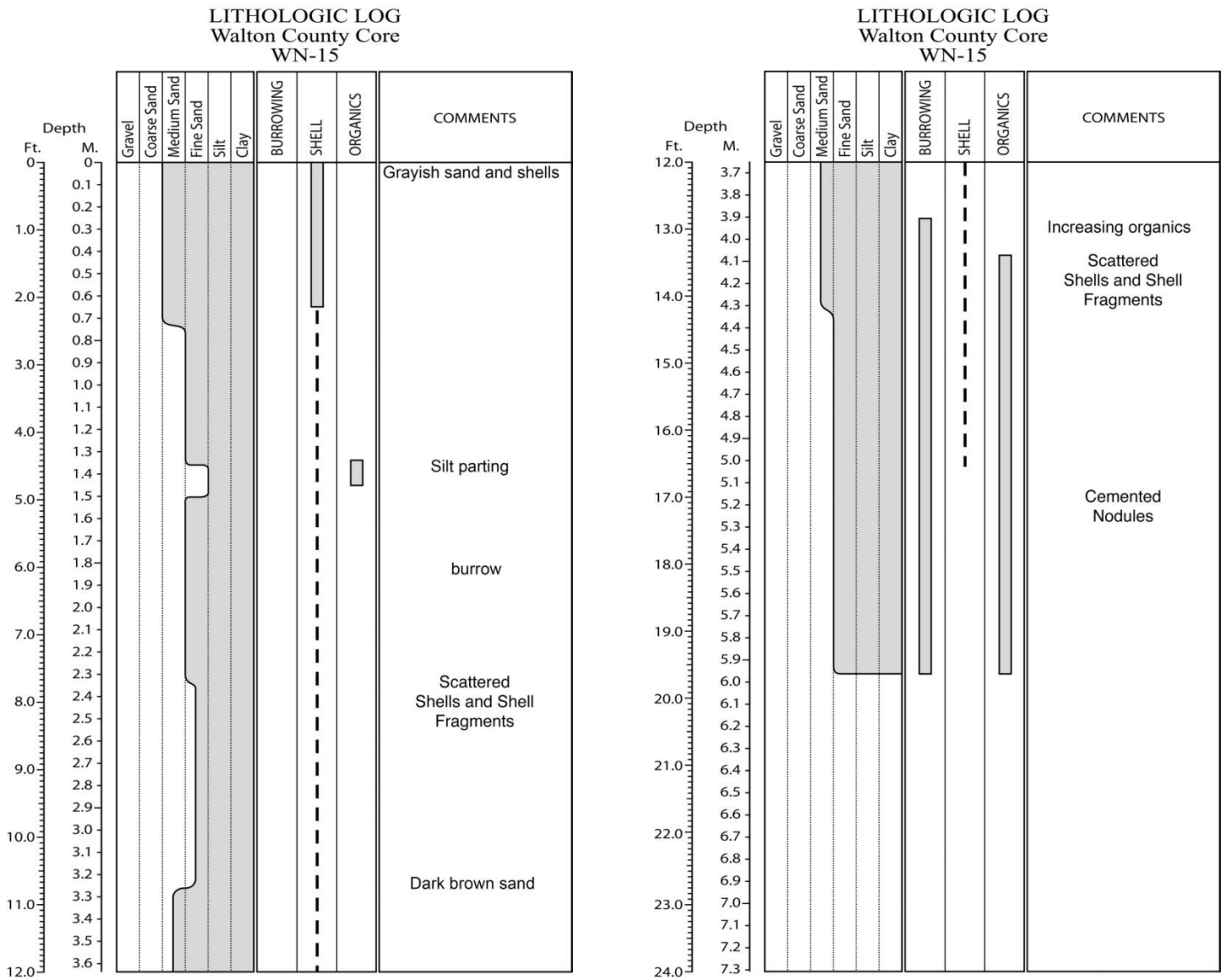

Figure E.15. Core WN-15 log.

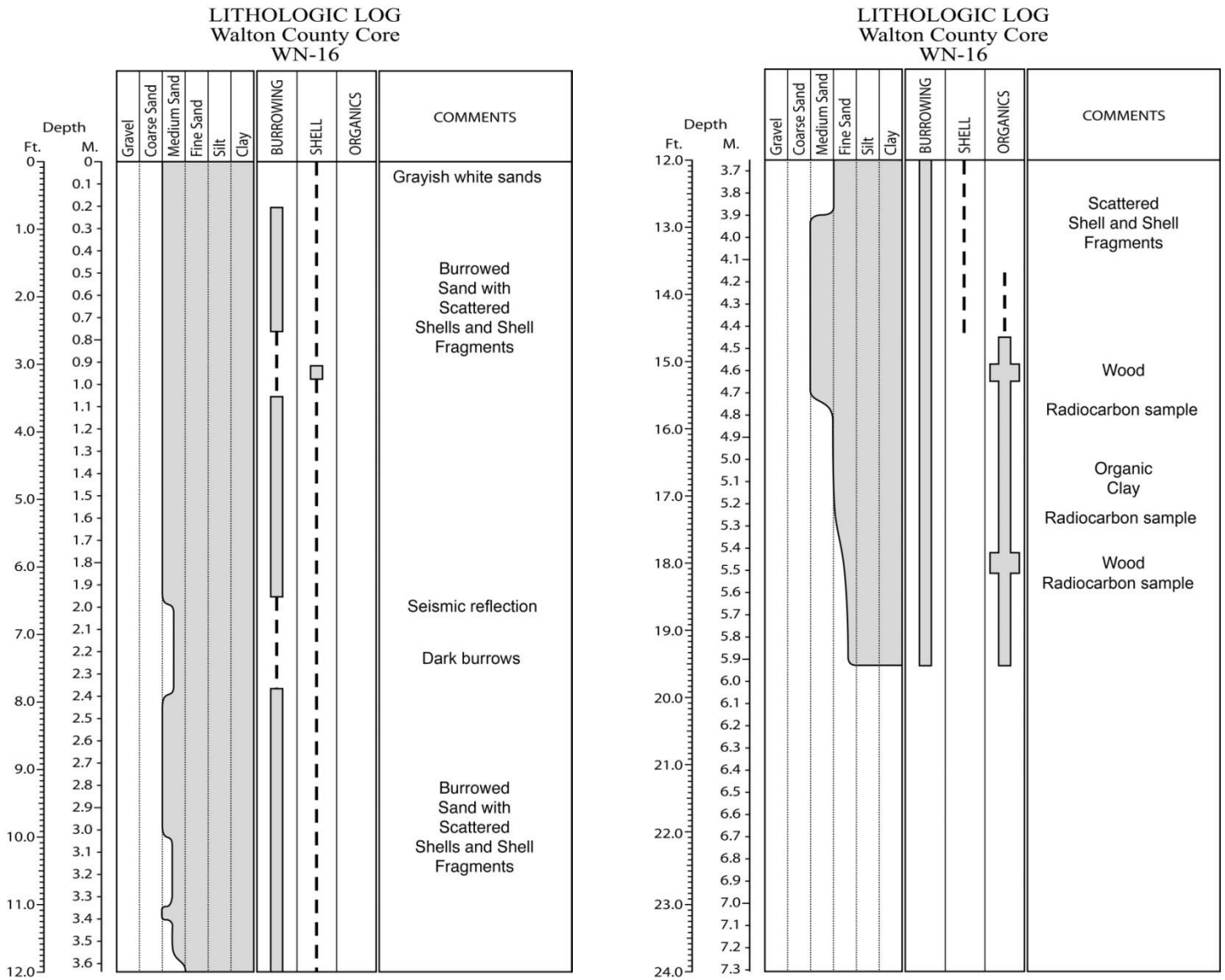

Figure E.16. Core WN-16 log.

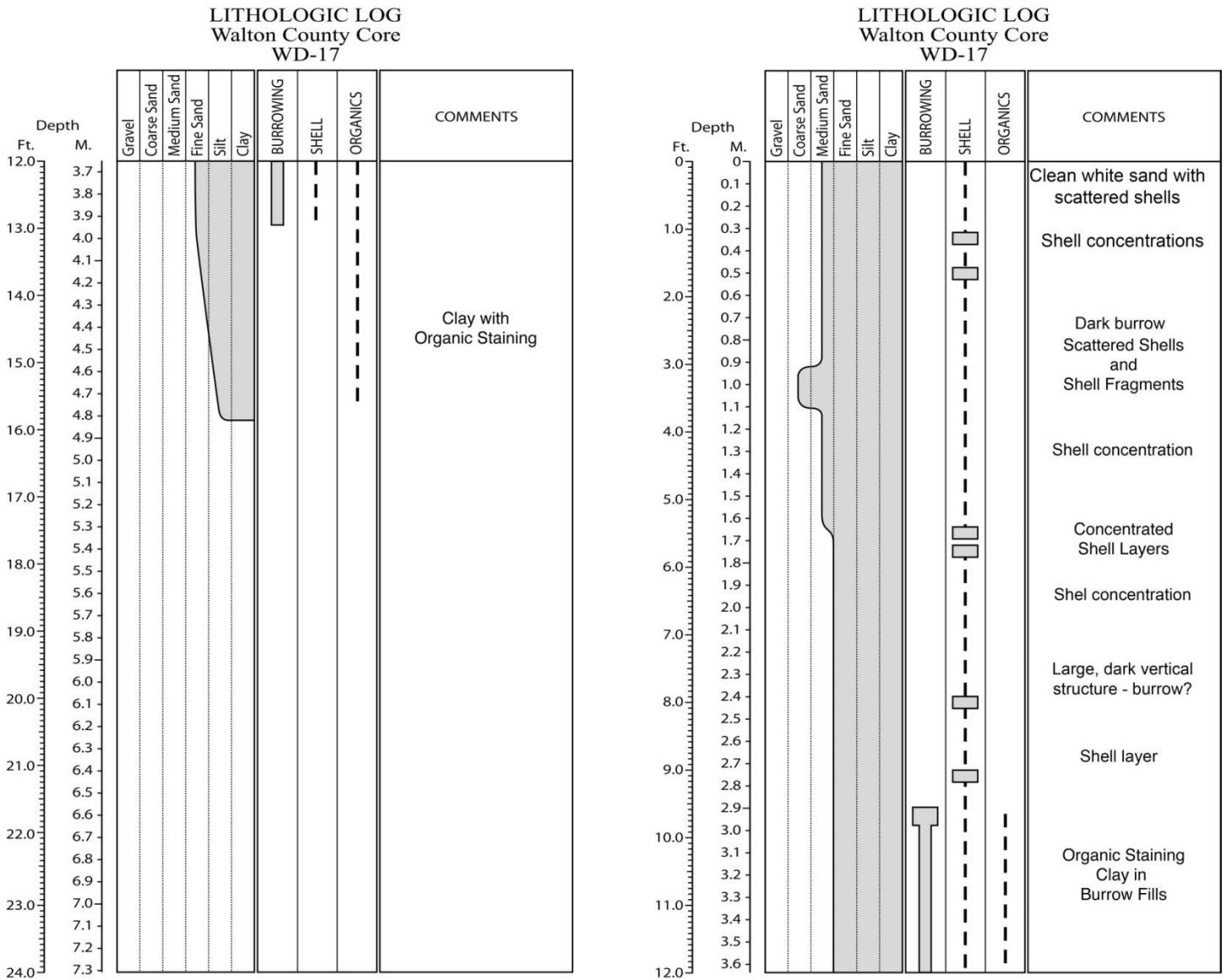

Figure E.17. Core WN-17 log.

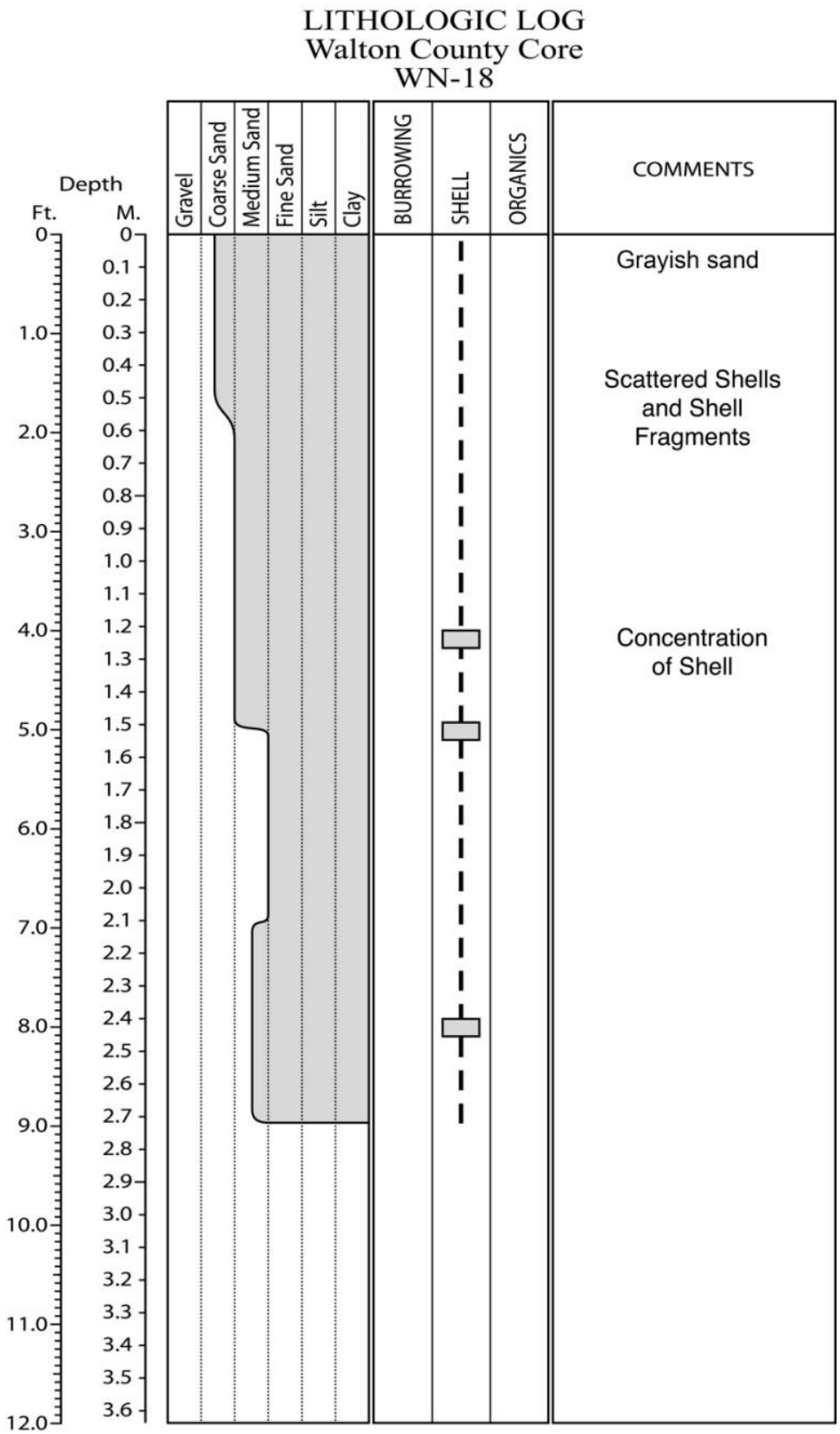

Figure E.18. Core WN-18 log.

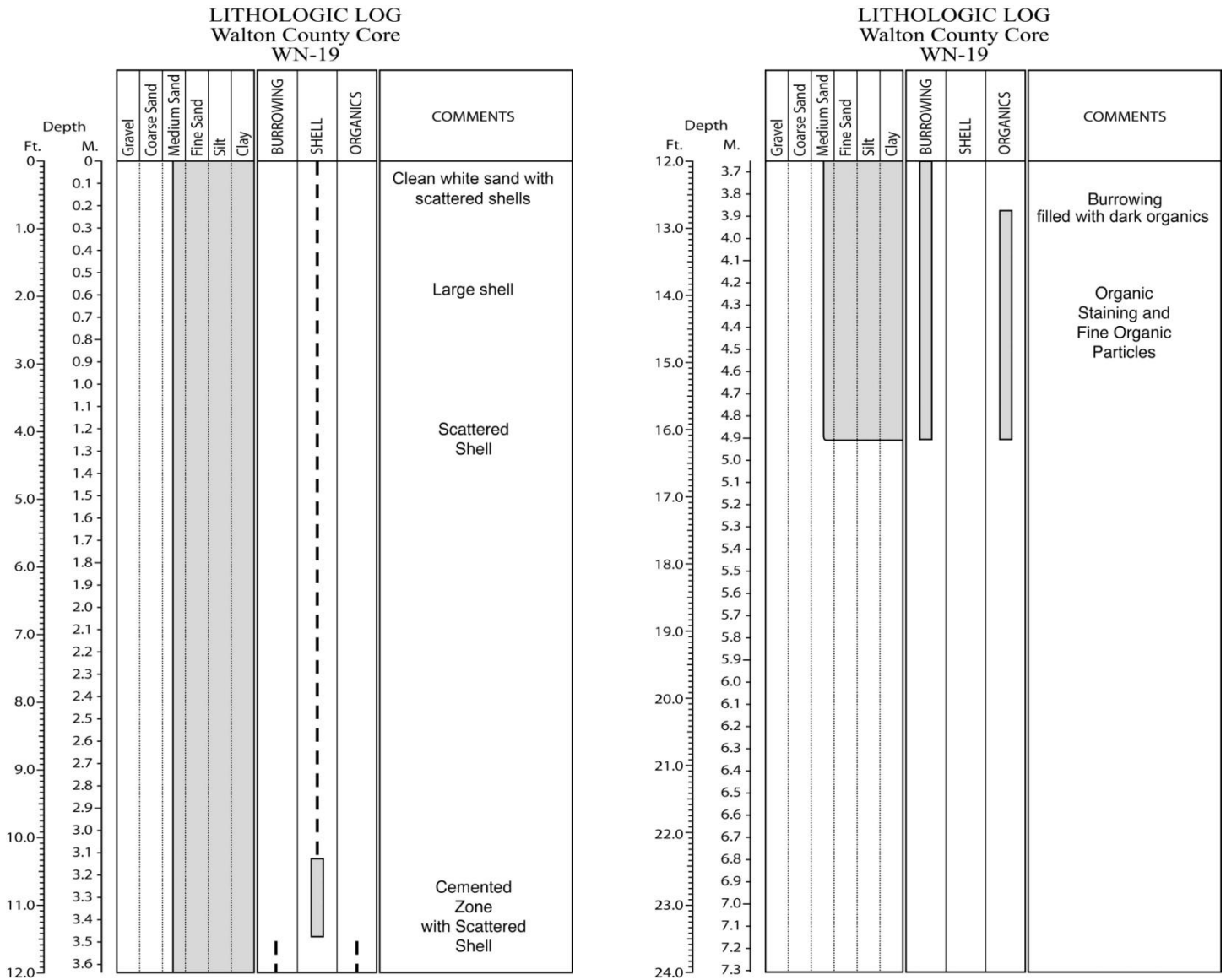

Figure E.19. Core WN-19 log.

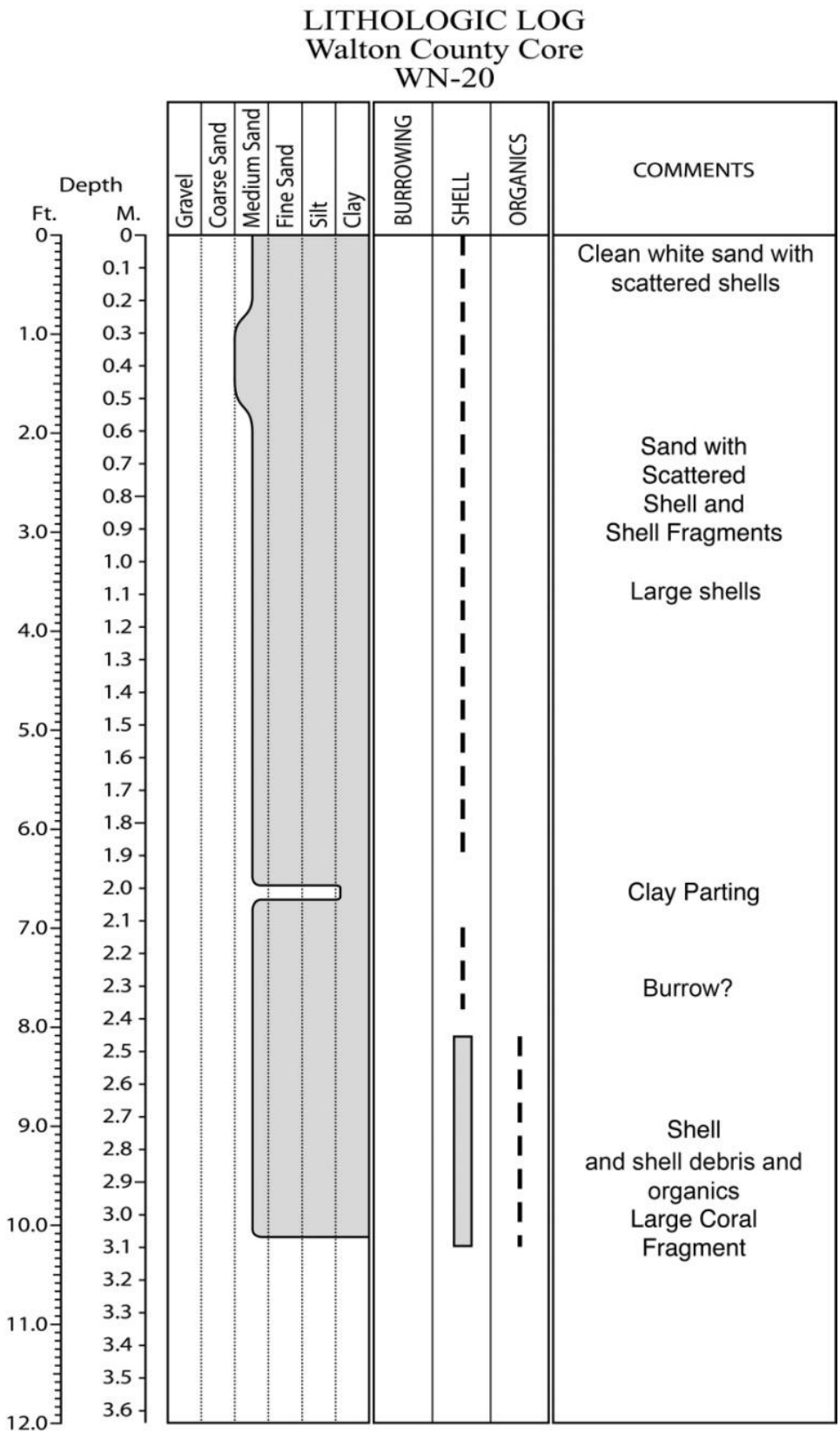

Figure E.20. Core WN-20 log.

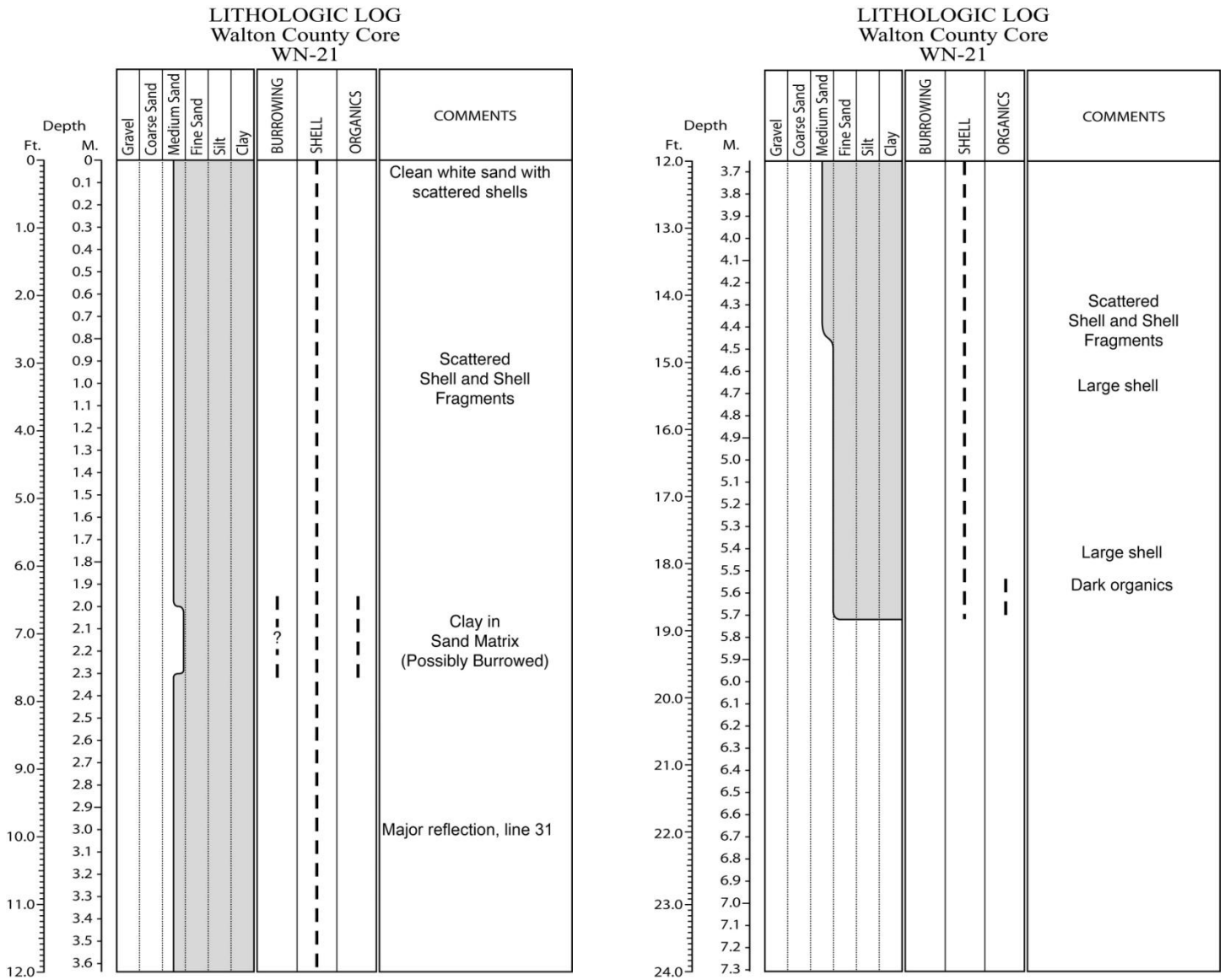

Figure E.21. Core WN-21 log.

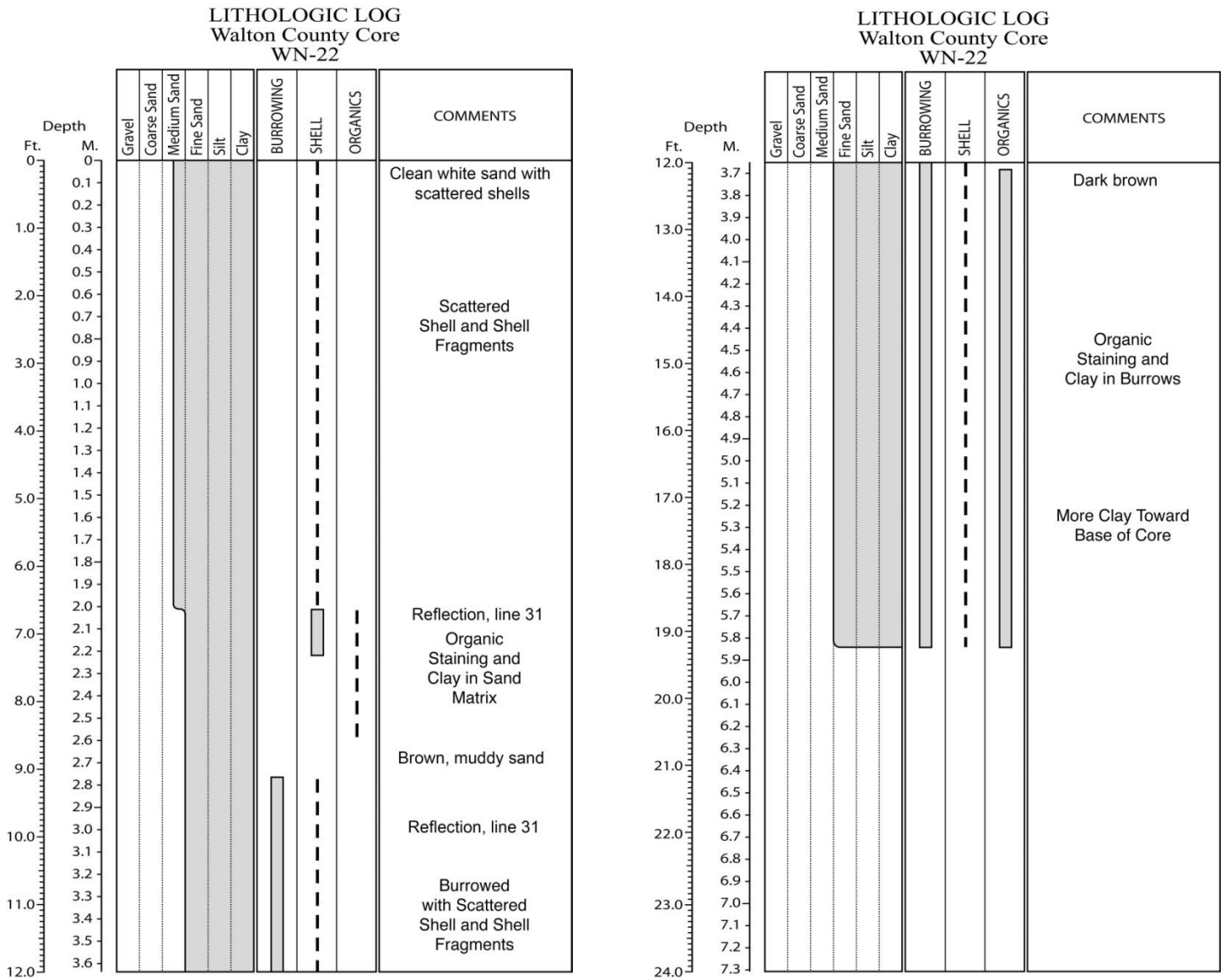

Figure E.22. Core WN-22 log.

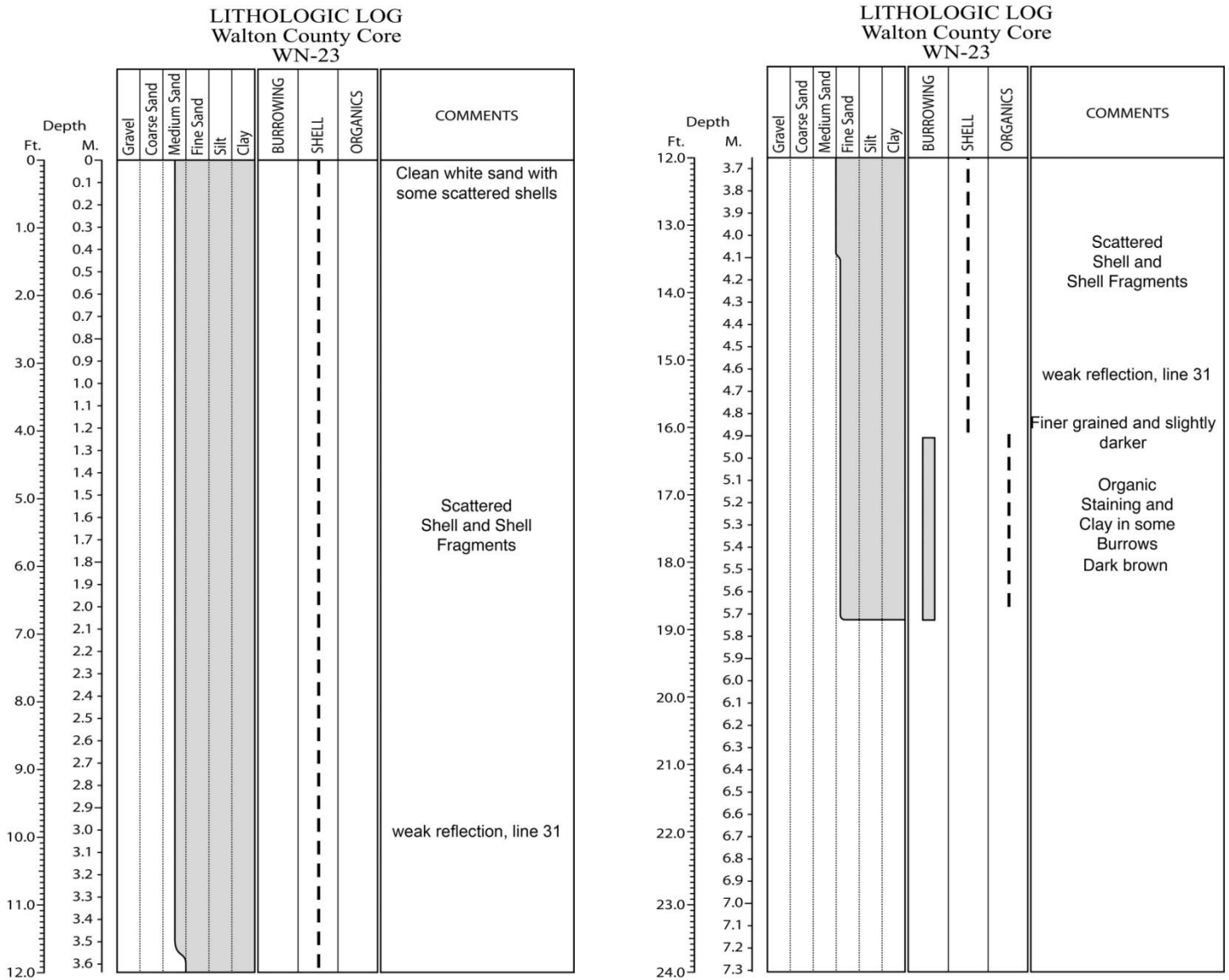

Figure E.23. Core WN-23 log.

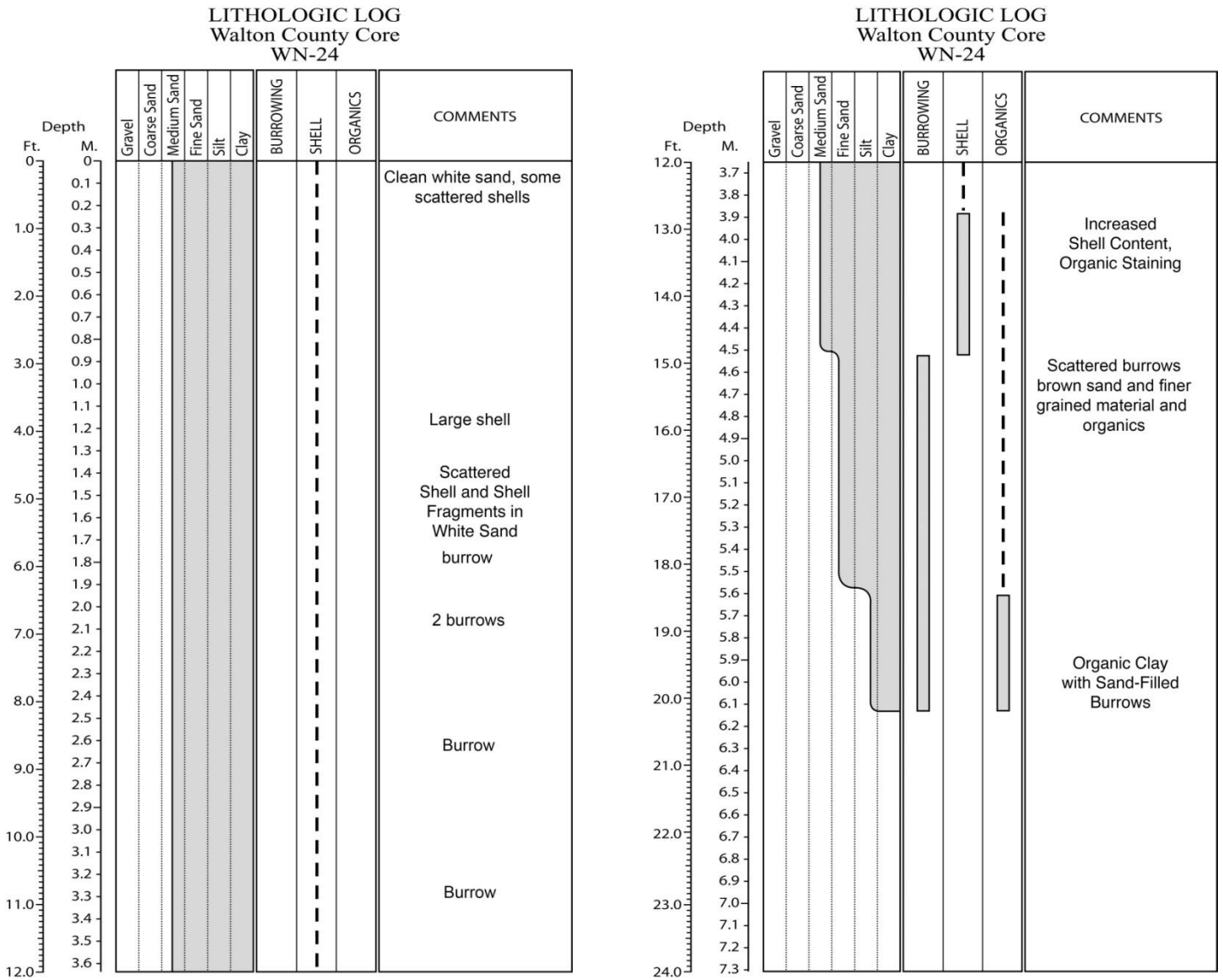

Figure E.24. Core WN-24 log.

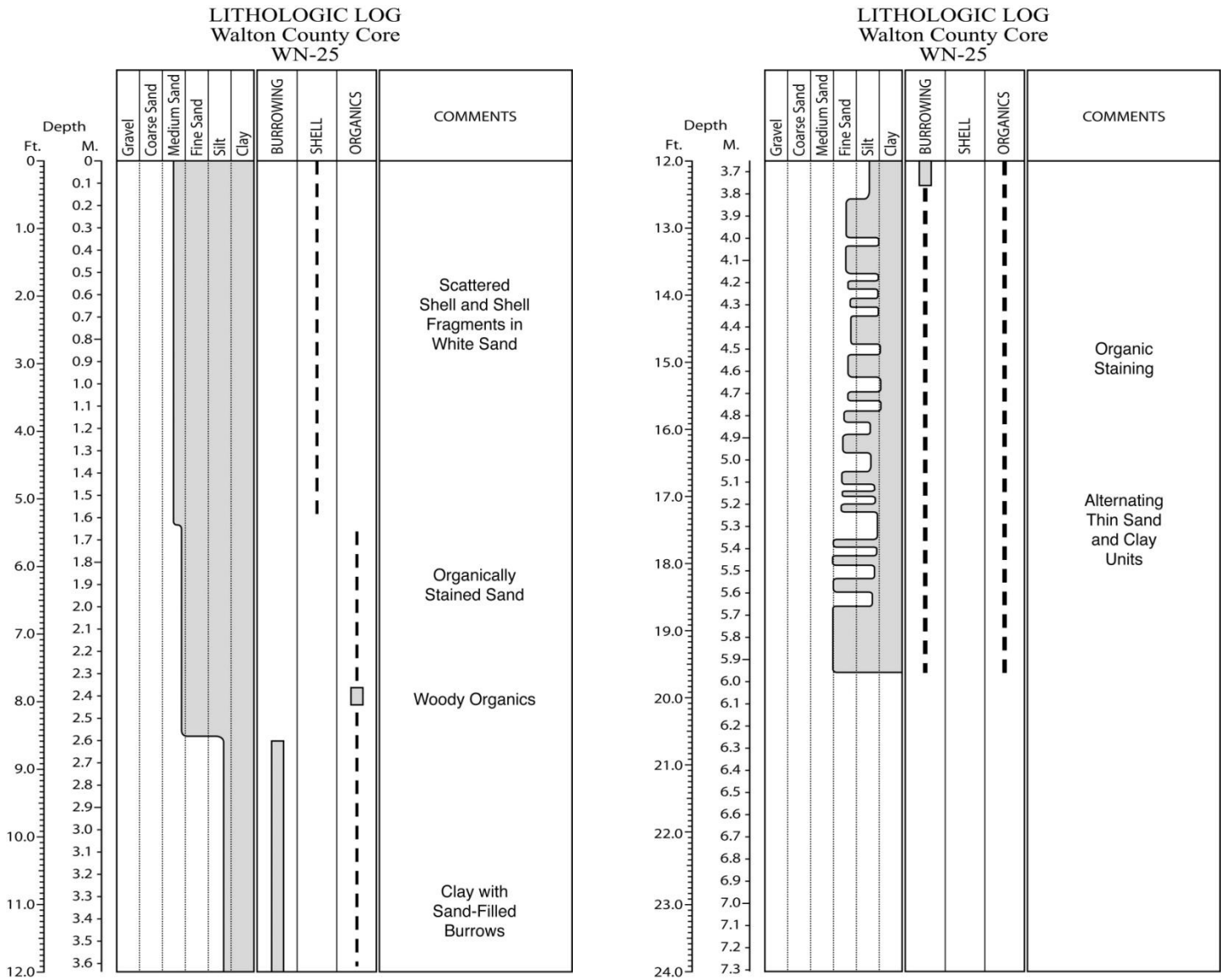

Figure E.25. Core WN-25 log.

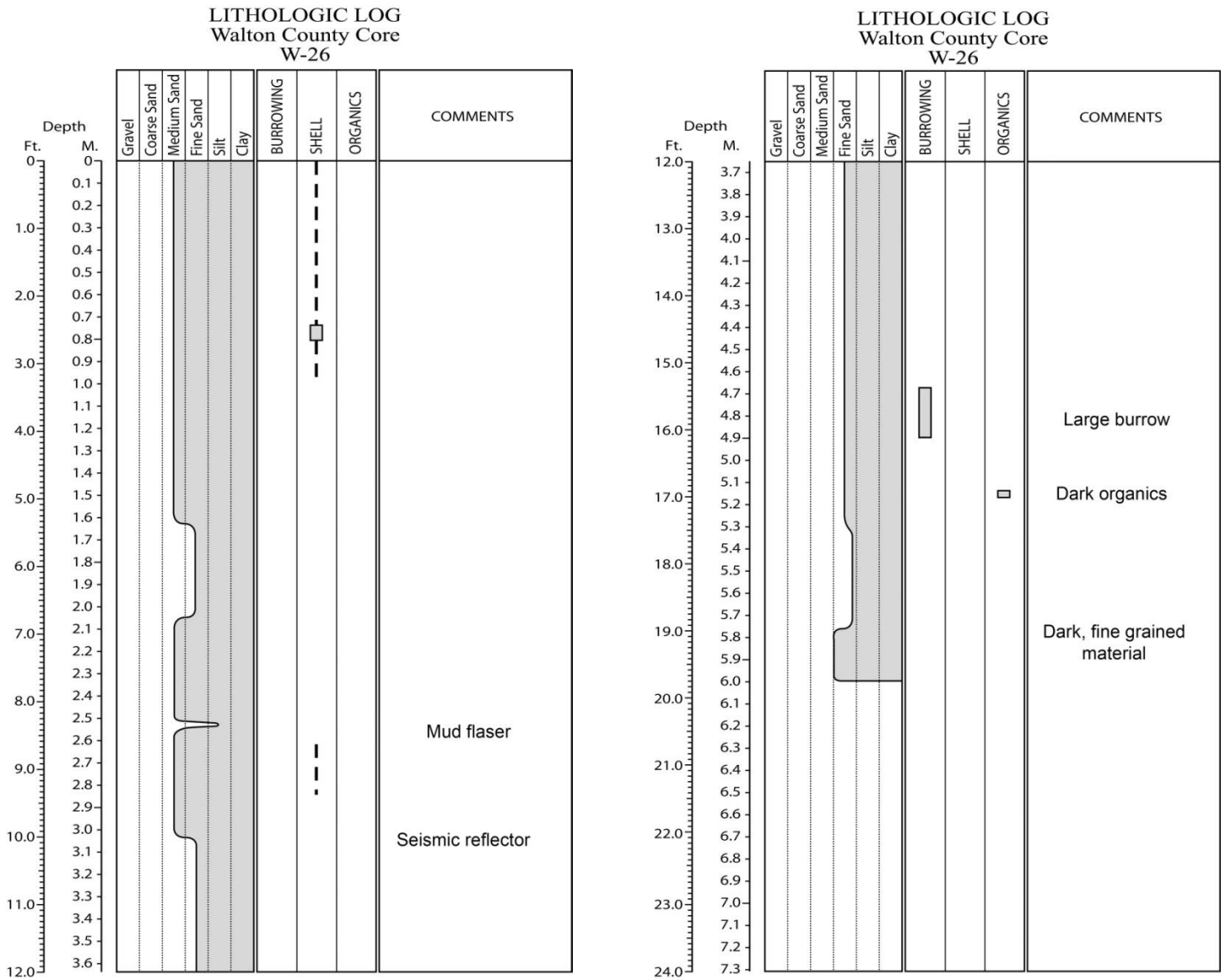

Figure E.26. Core W-26 log.

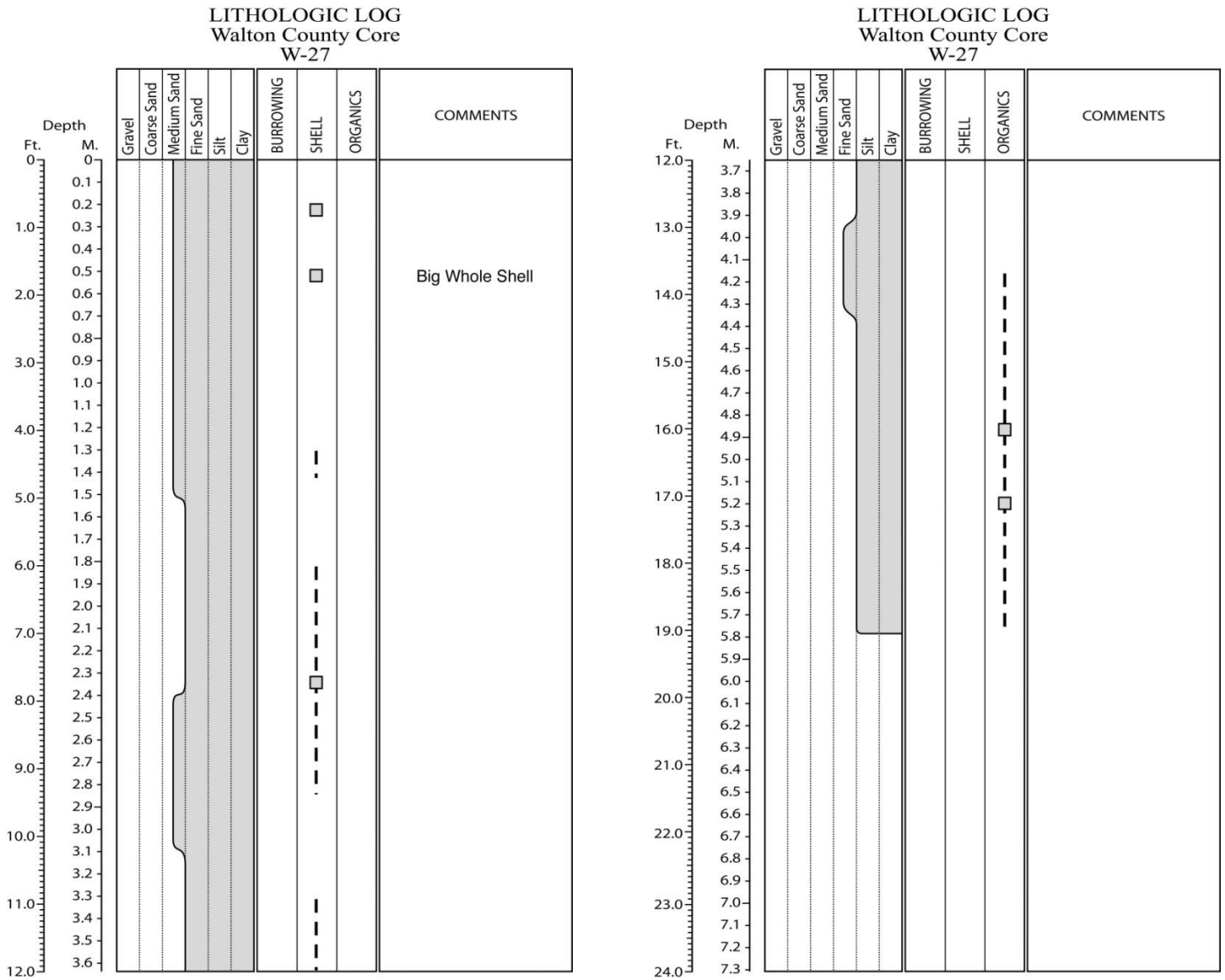

Figure E.27. Core W-27 log.

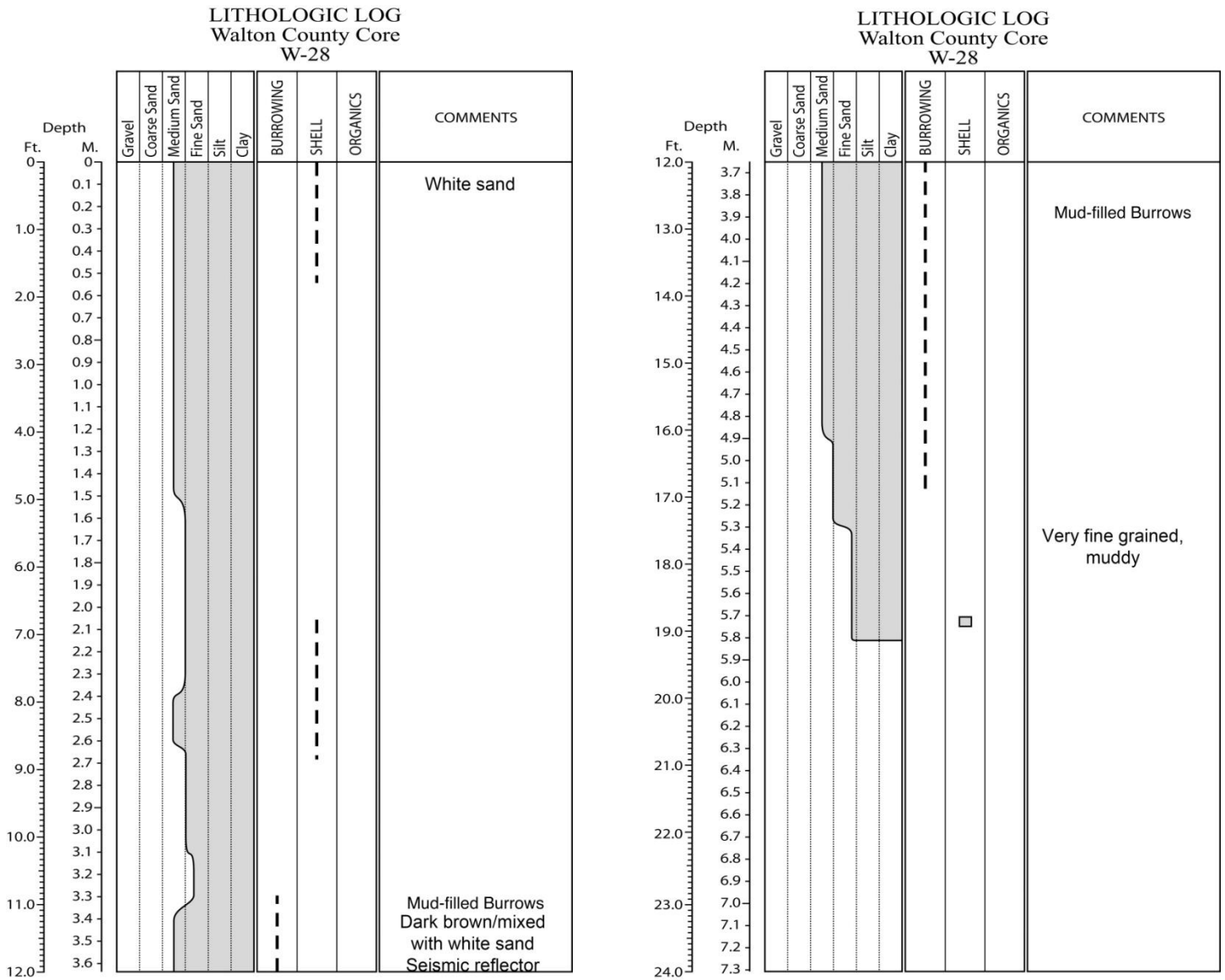

Figure E.28. Core W-28 log.

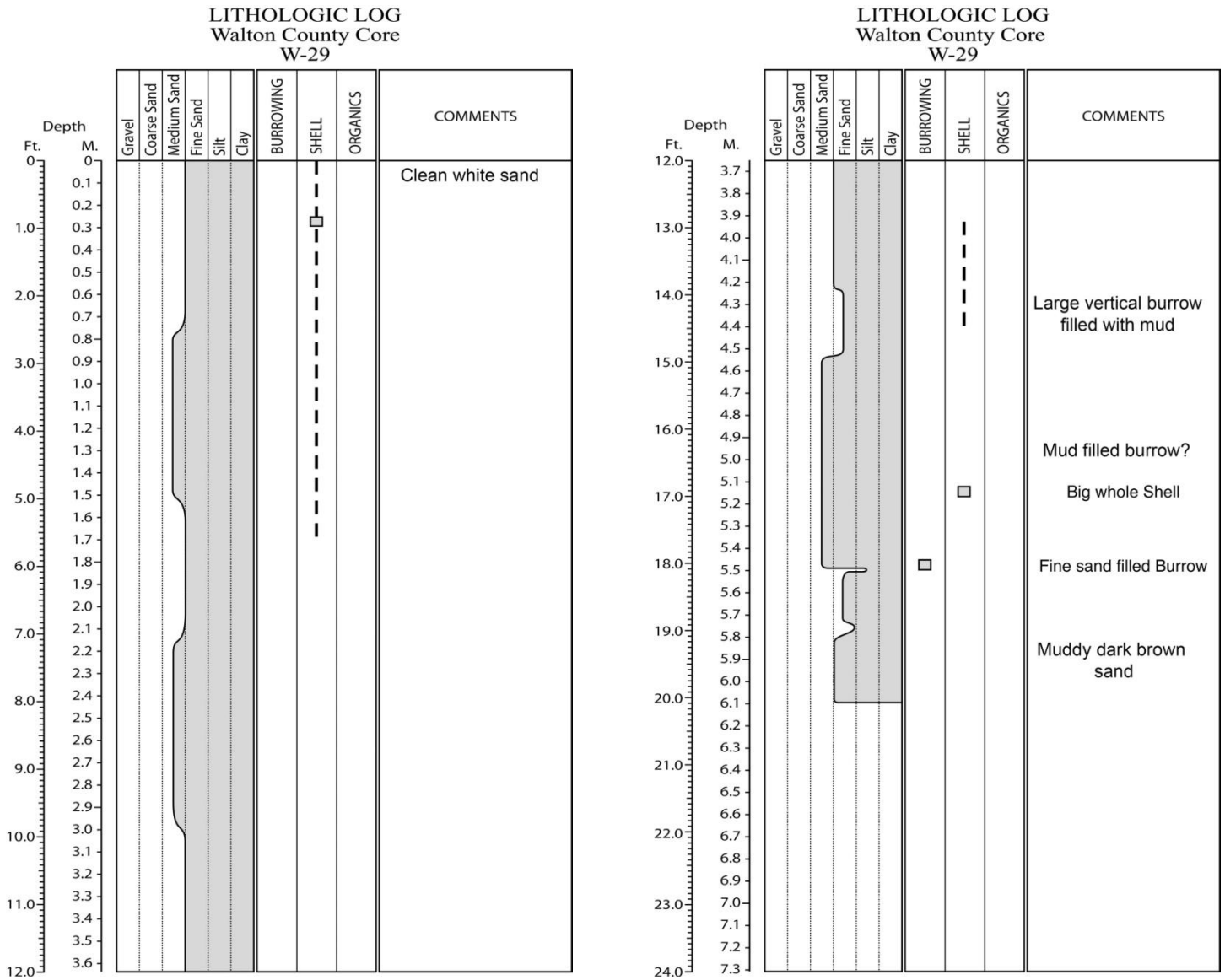

Figure E.29. Core W-29 log.

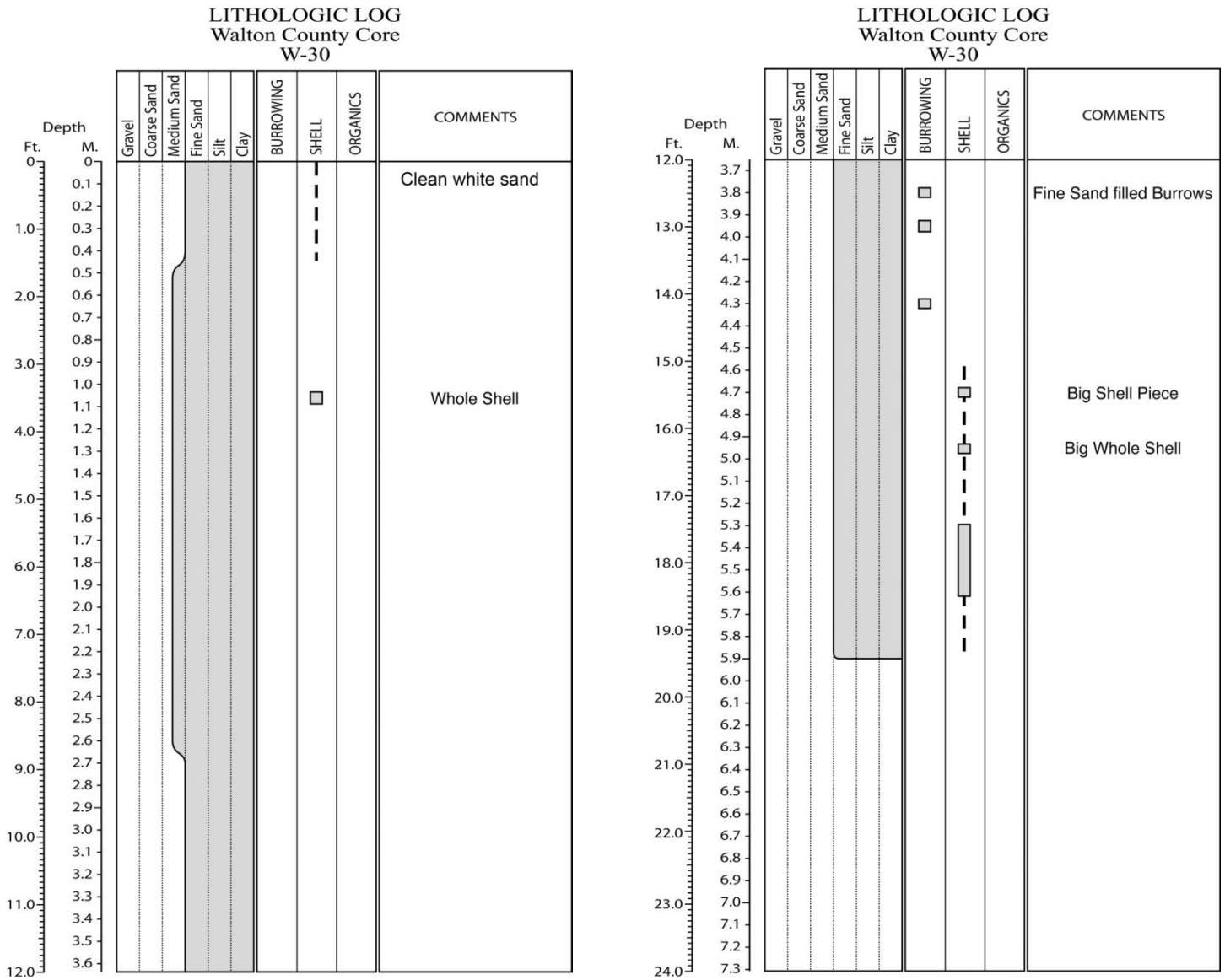

Figure E.30. Core W-30 log.

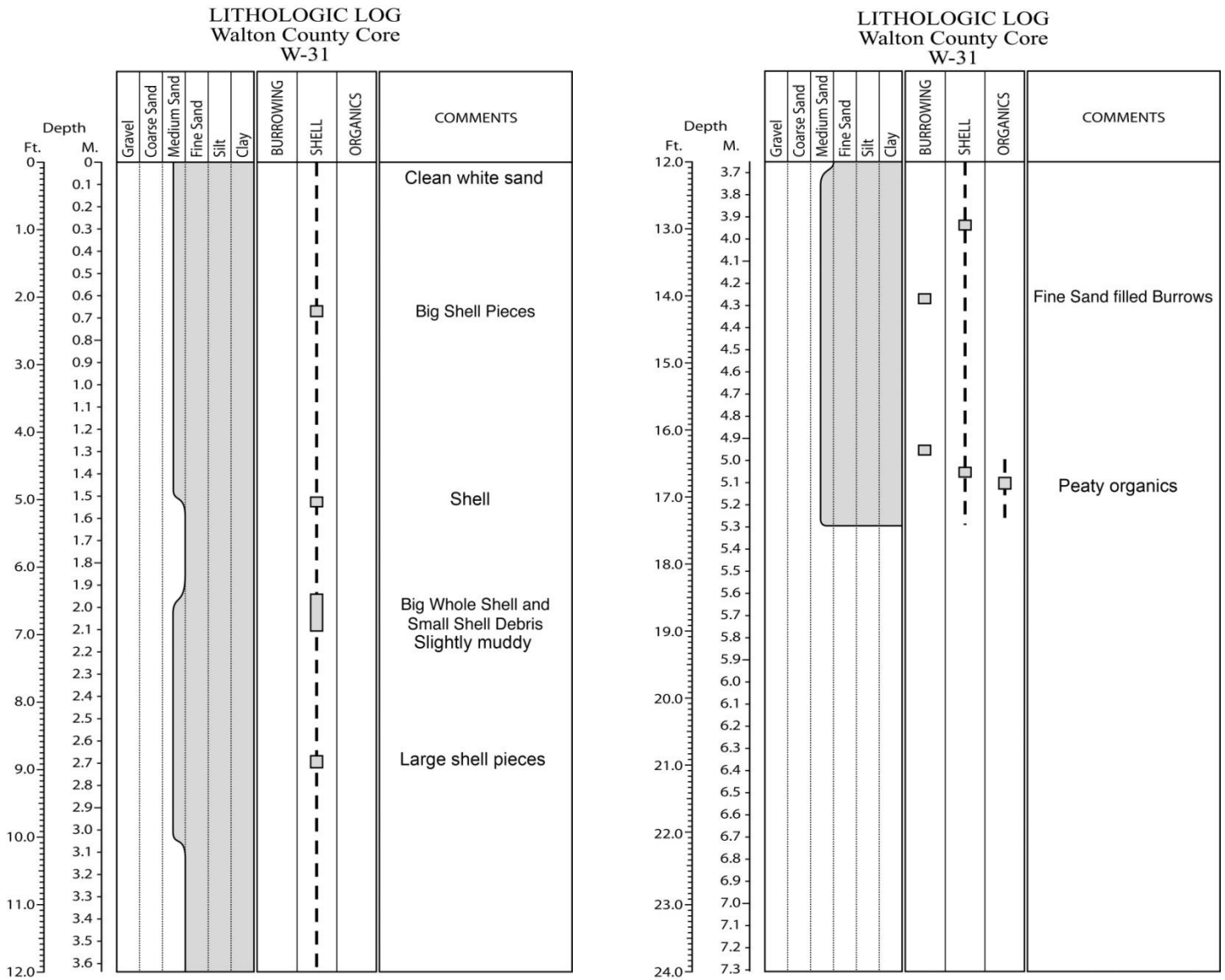

Figure E.31. Core W-31 log.

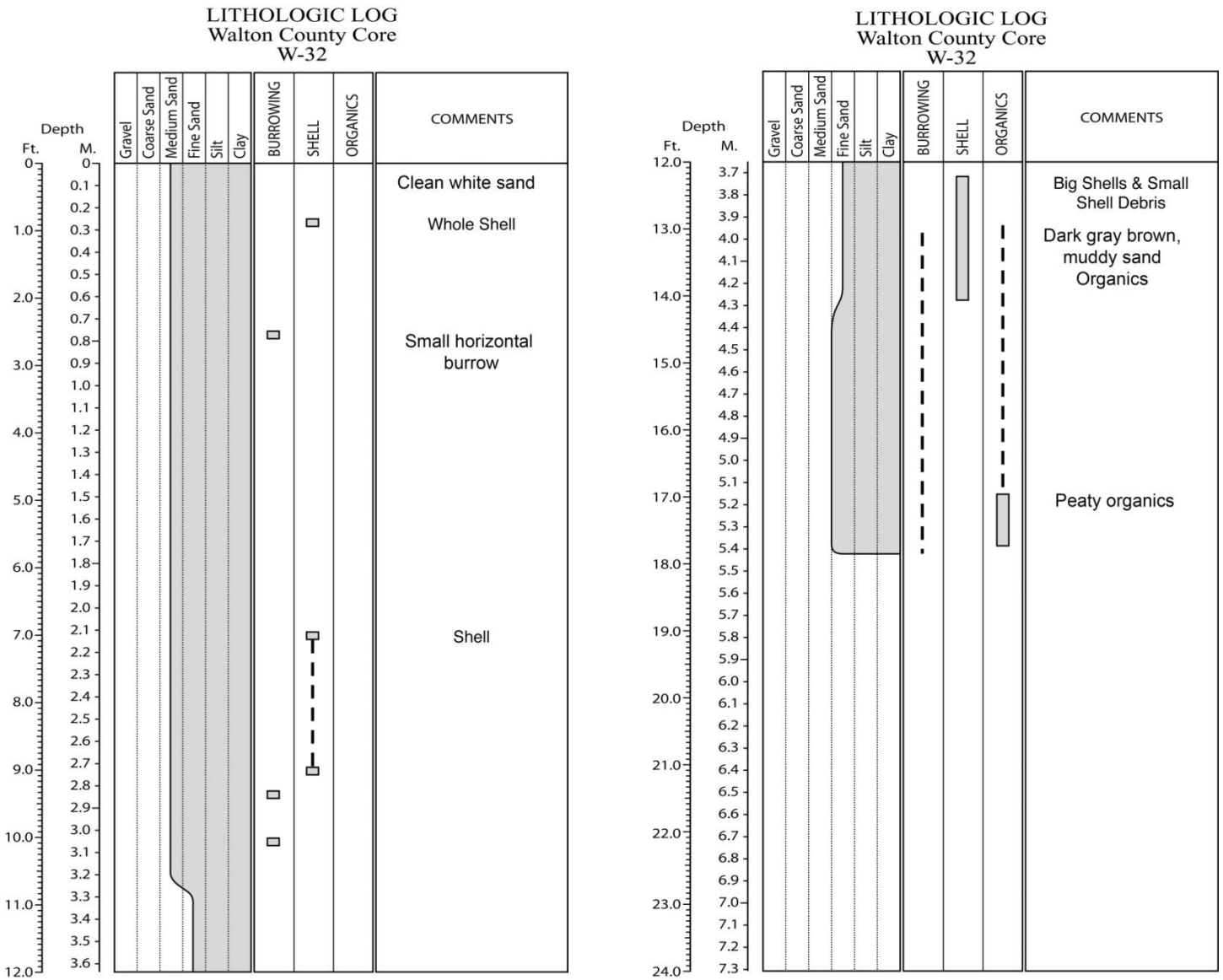

Figure E.32. Core W-32 log.

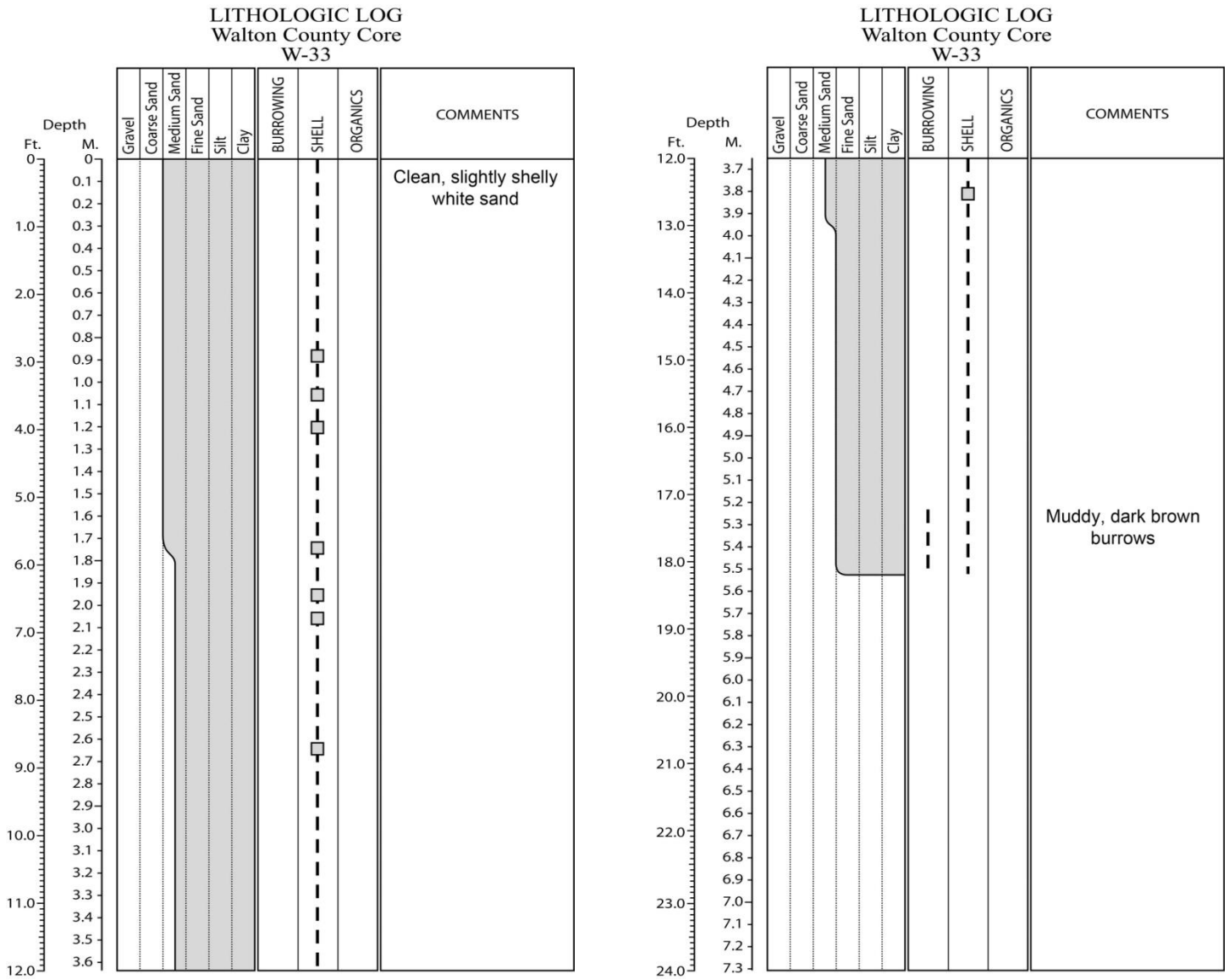

Figure E.33. Core W-33 log.

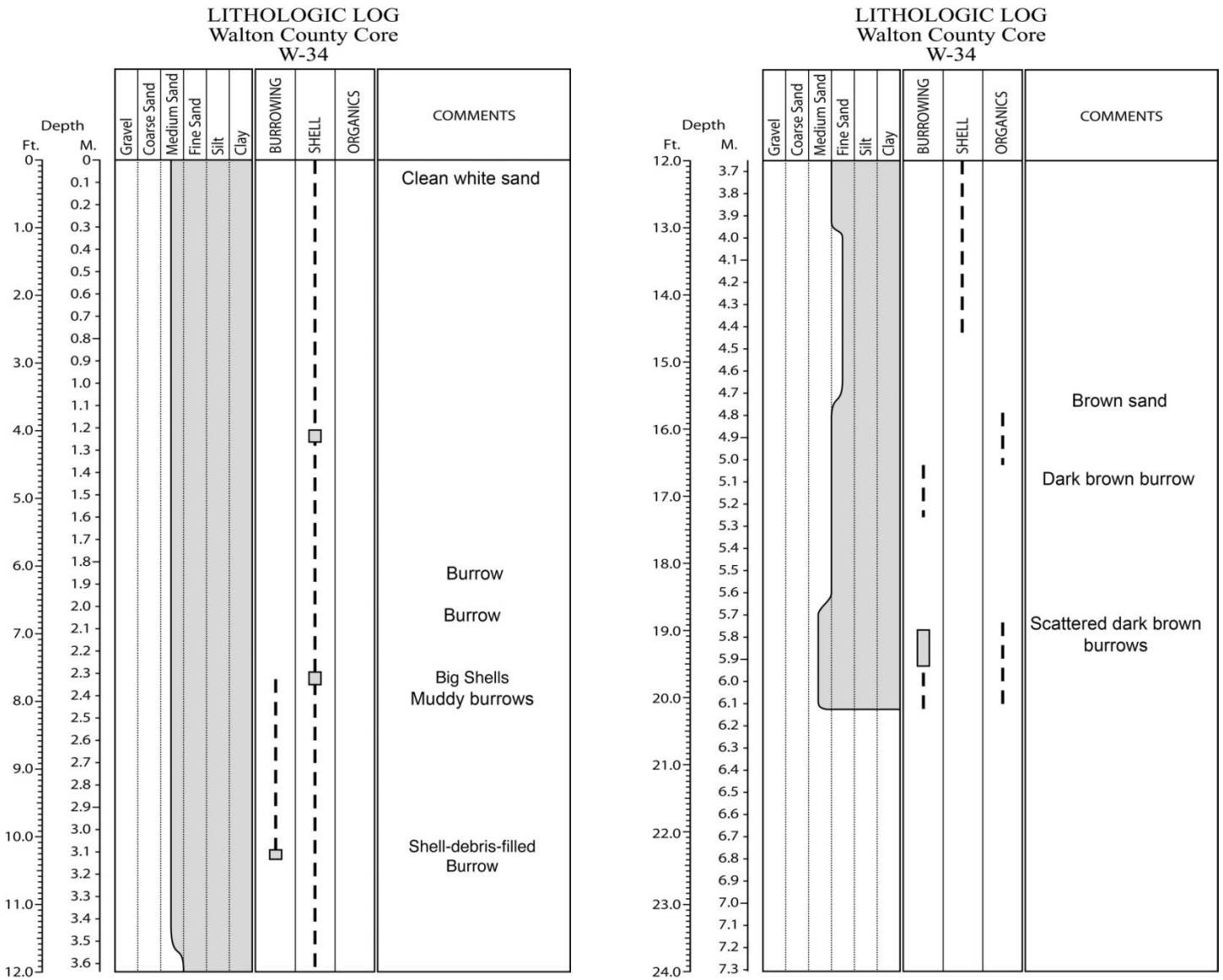

Figure E.34. Core W-34 log.

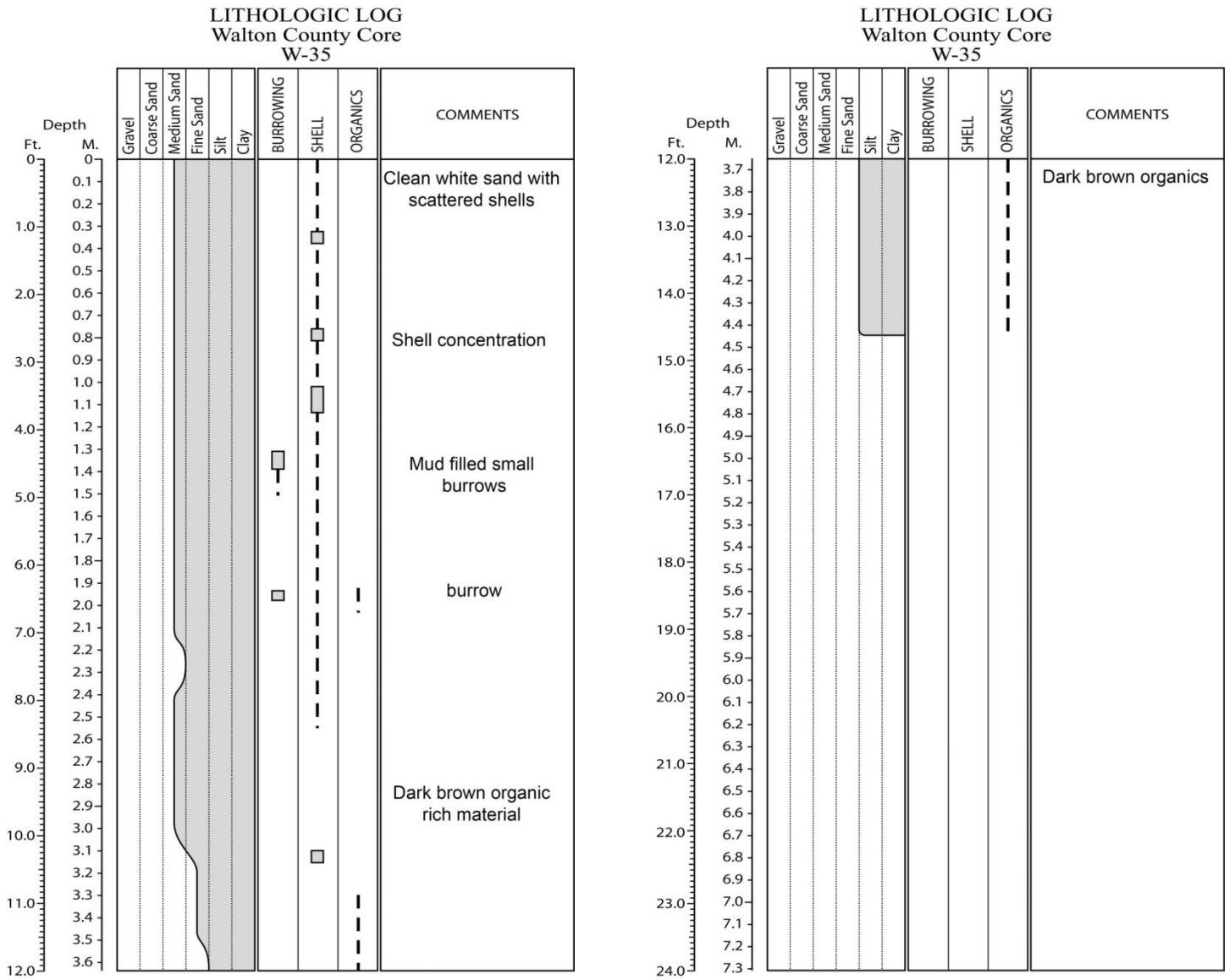

Figure E.35. Core W-35 log.

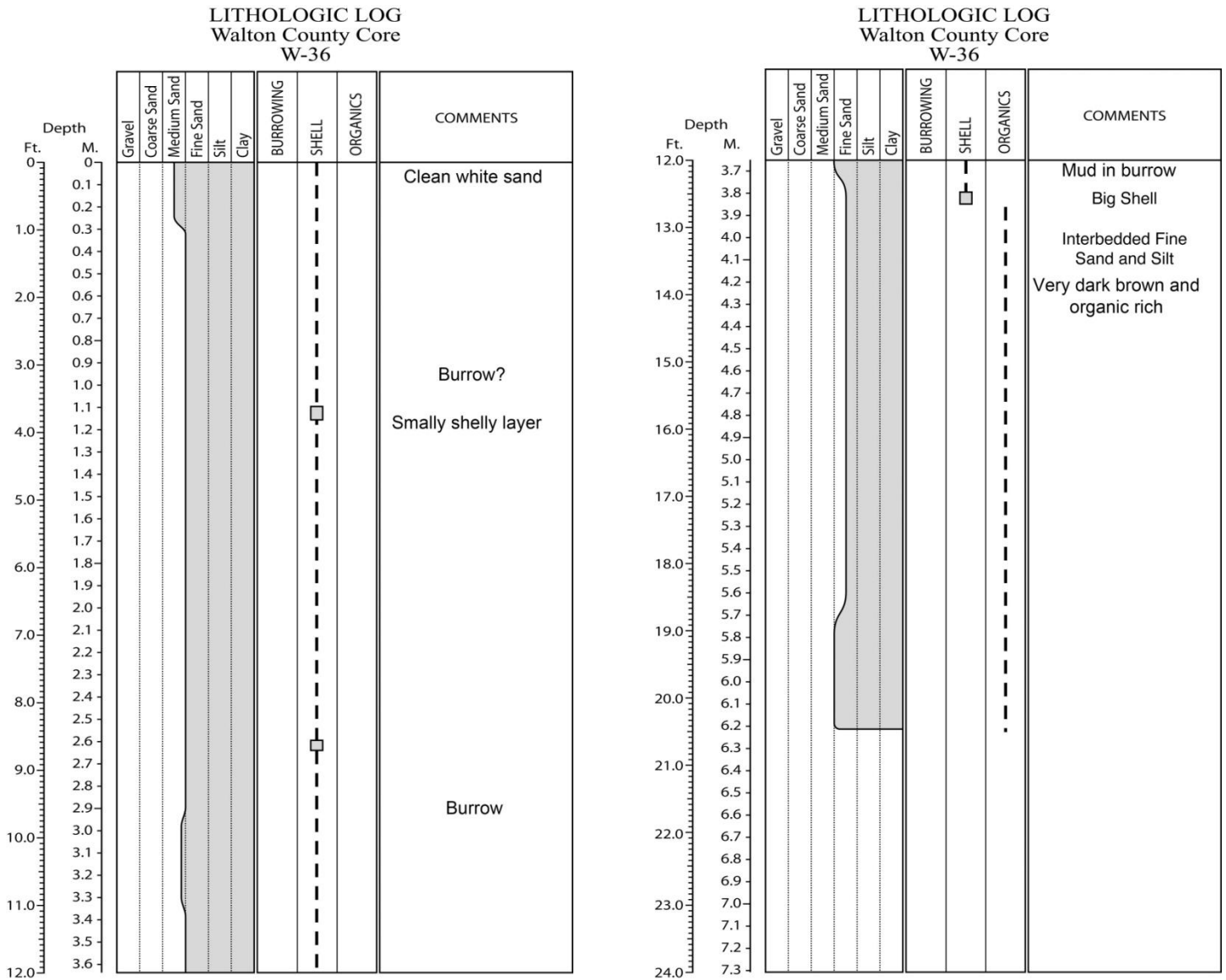

Figure E.36. Core W-36 log.

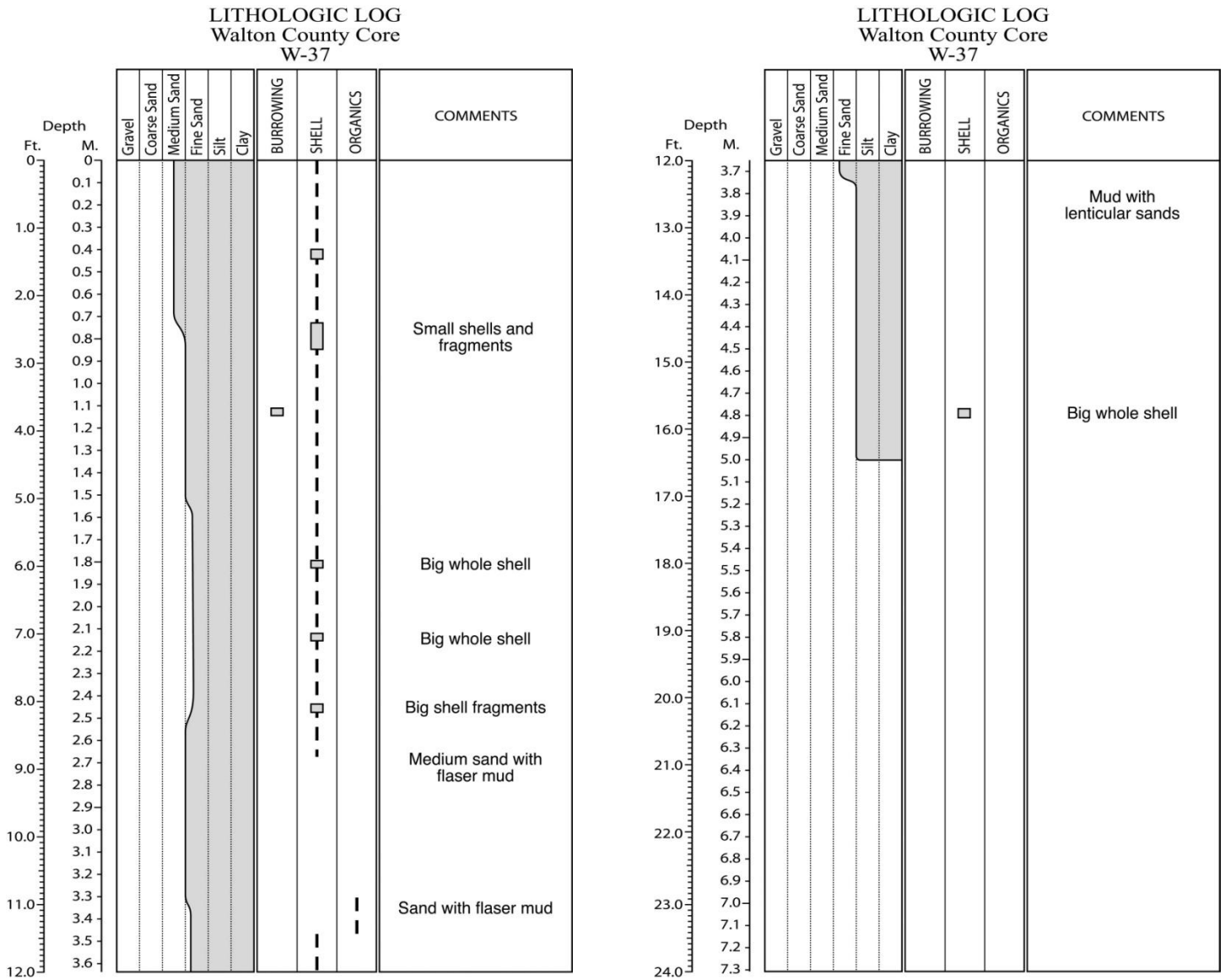

Figure E.37. Core W-37 log.

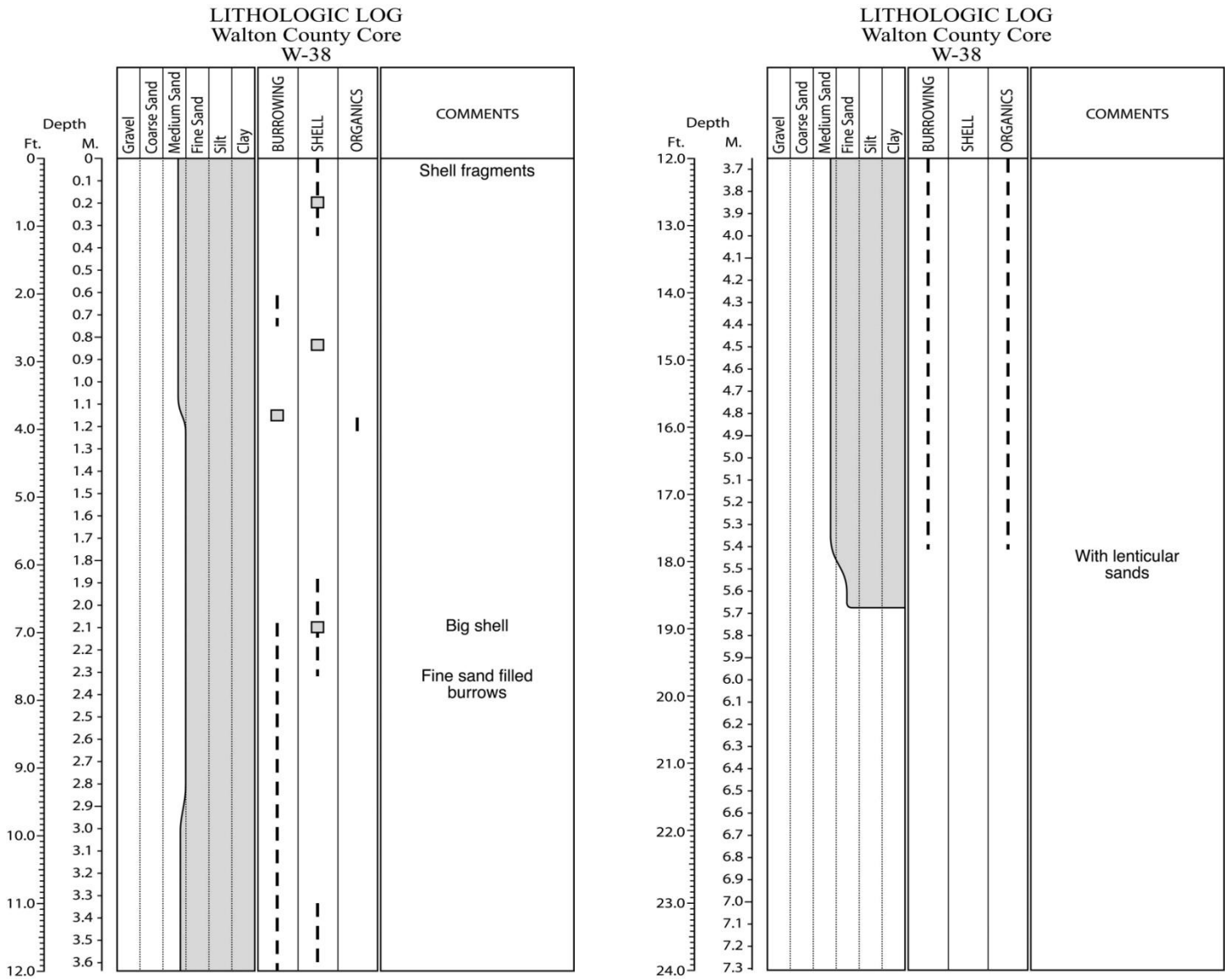

Figure E.38. Core W-38 log.

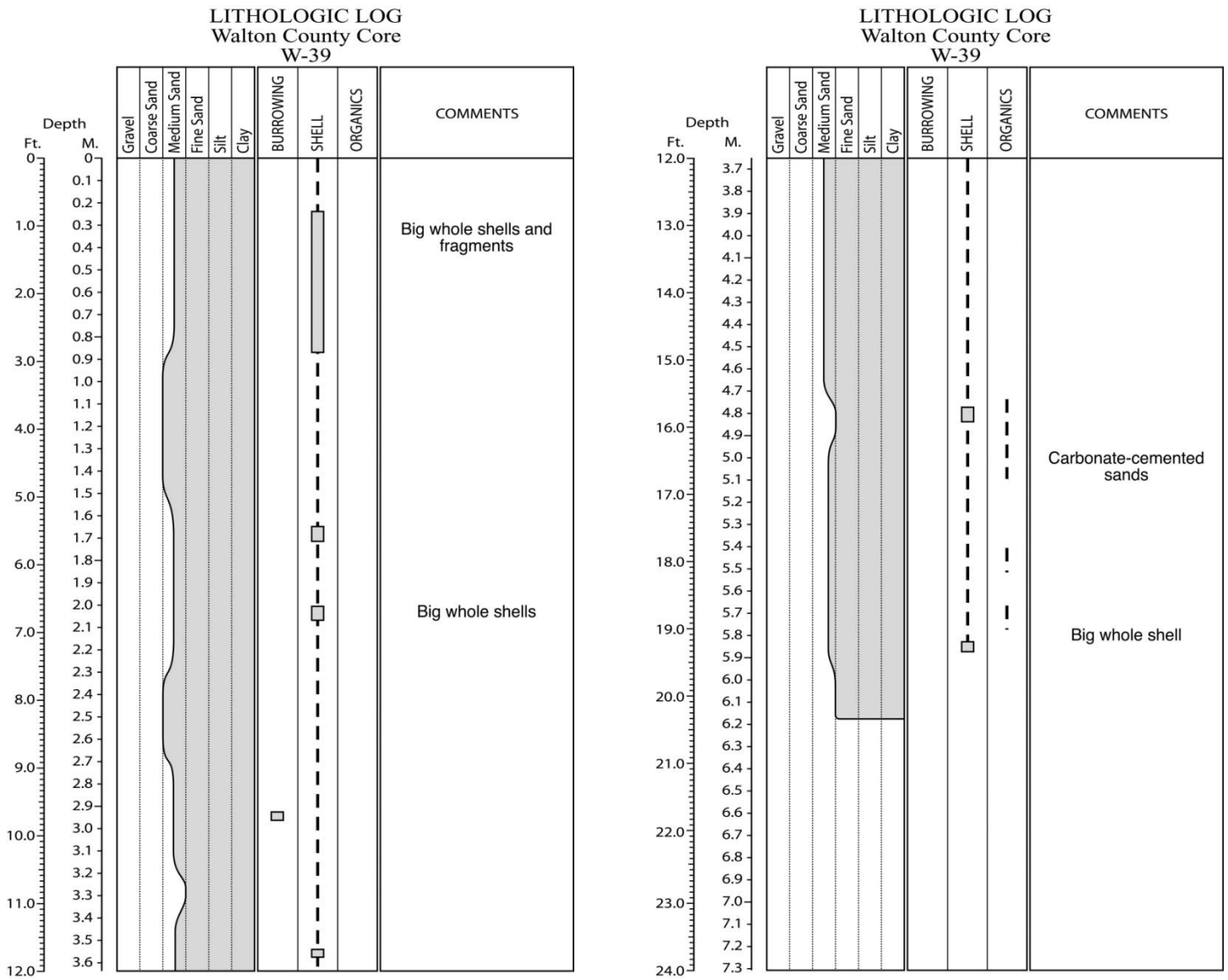

Figure E.39. Core W-39 log.

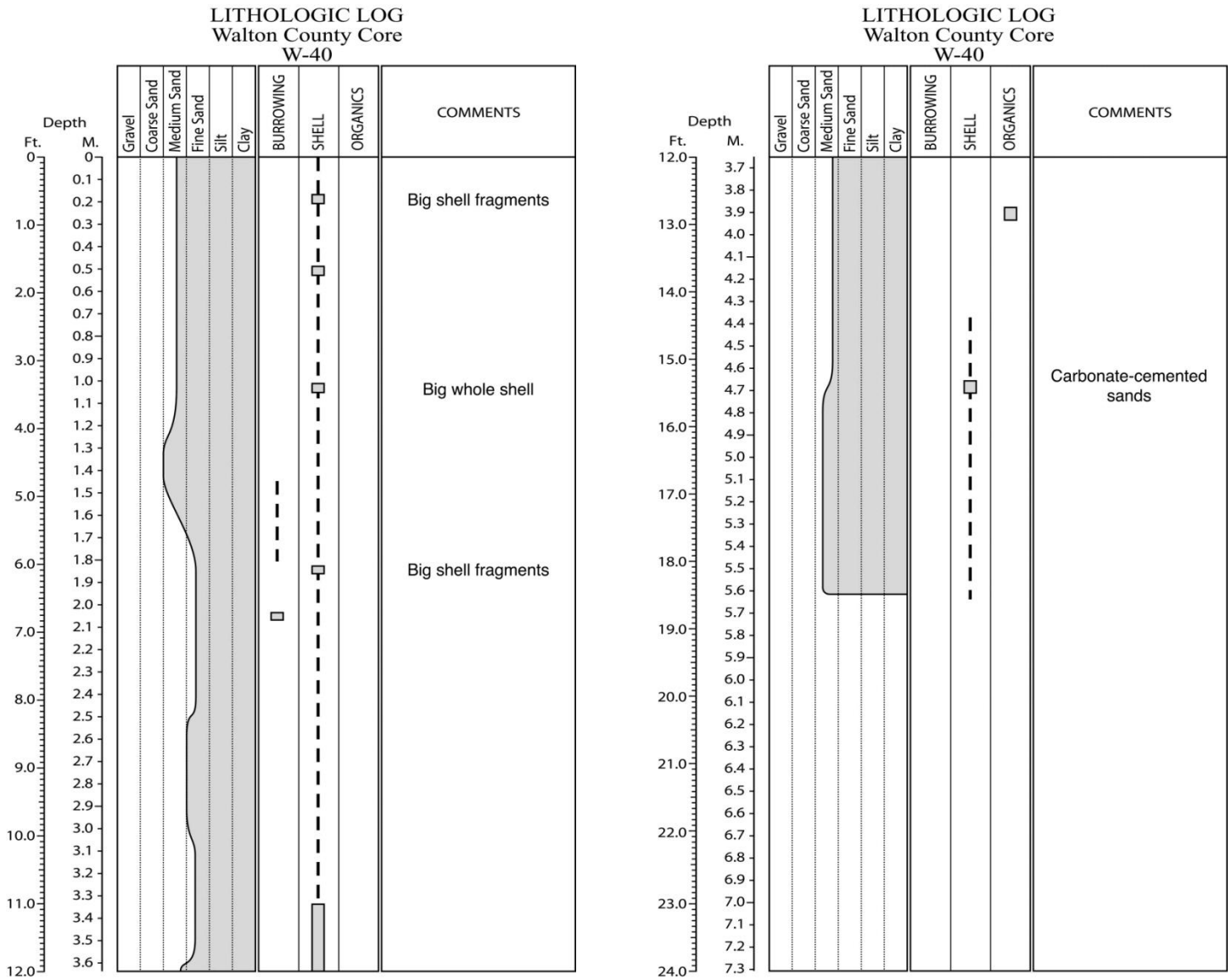

Figure E.40. Core W-40 log.

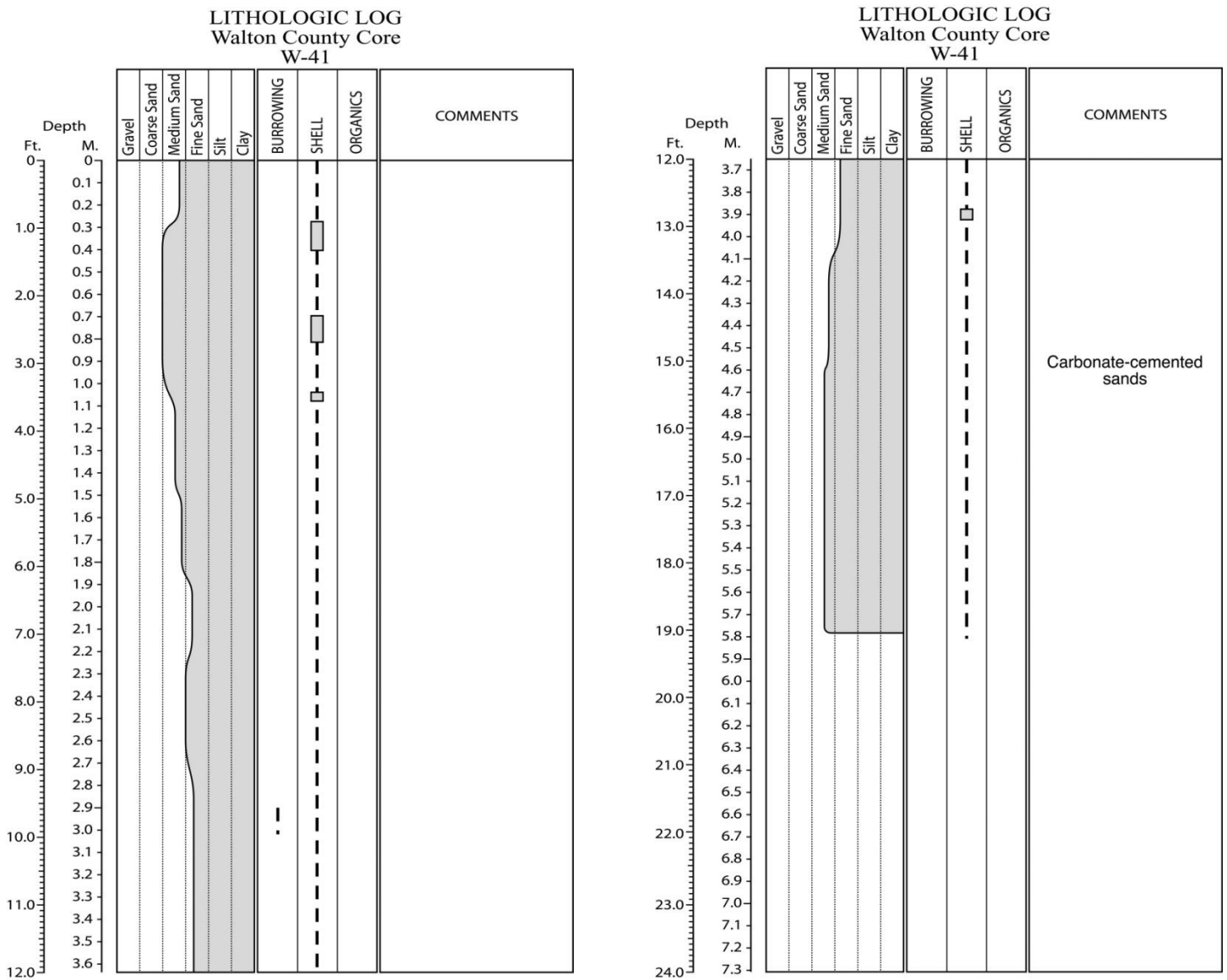

Figure E.41. Core W-41 log.

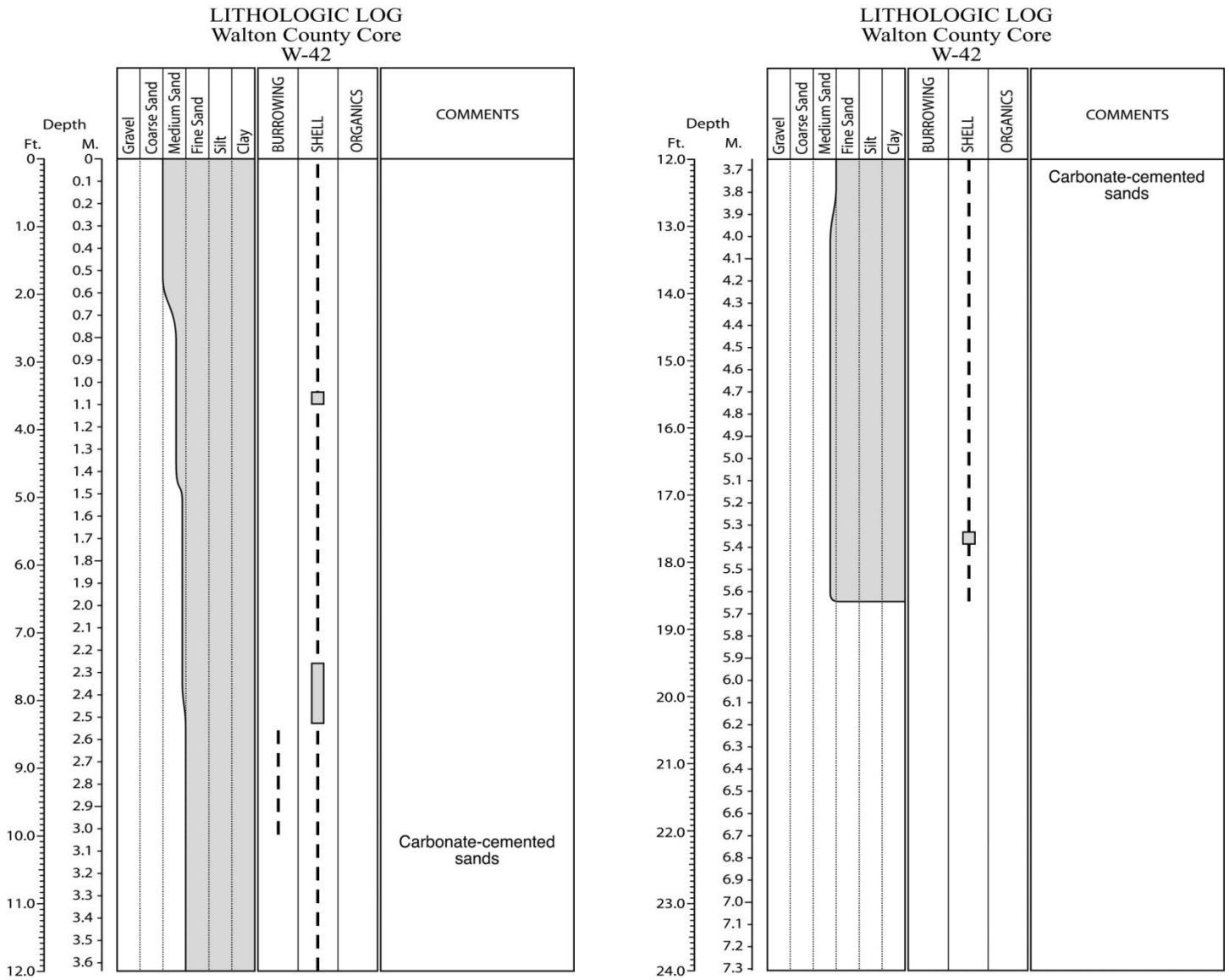

Figure E.42. Core W-42 log.

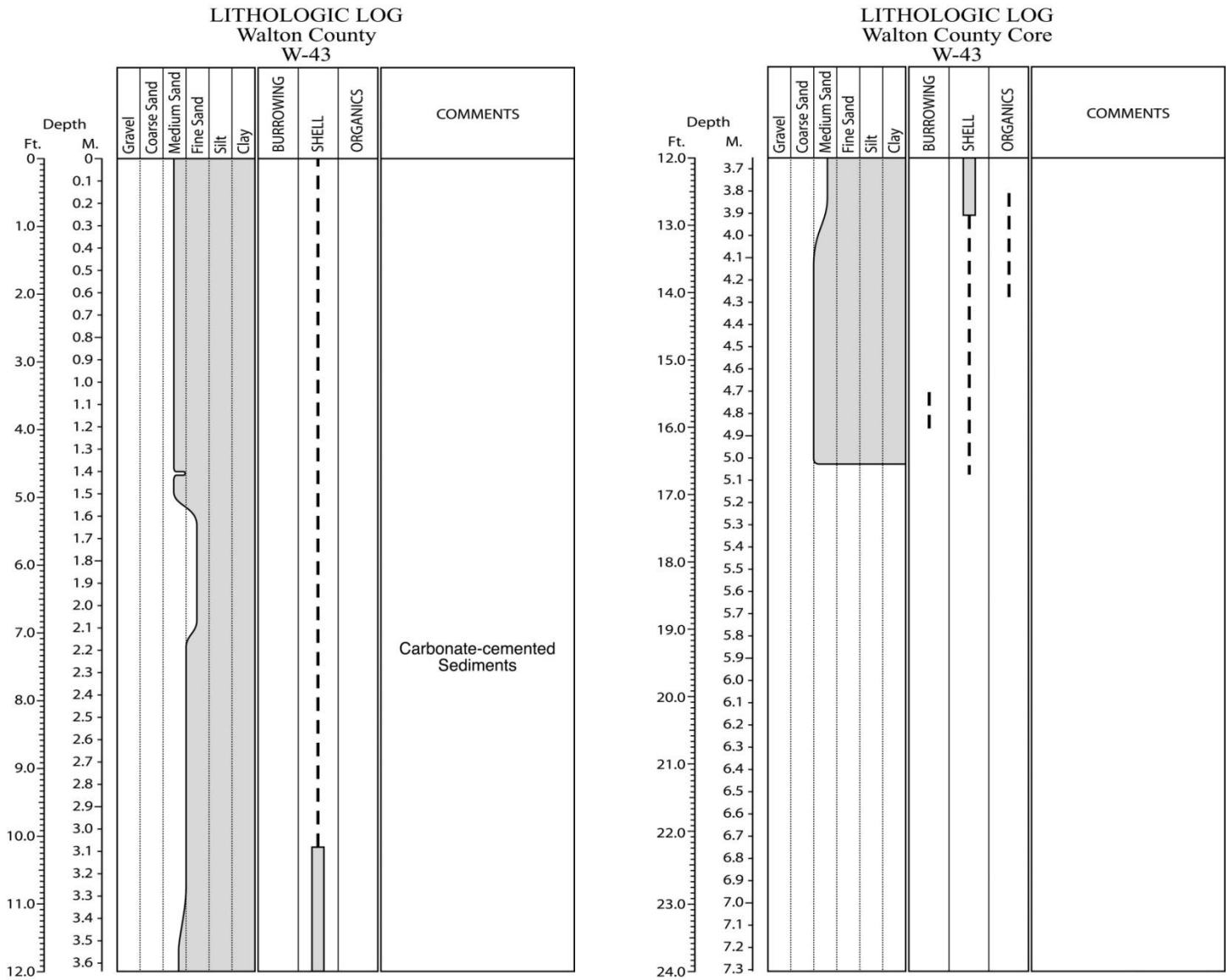

Figure E.43. Core W-43 log.

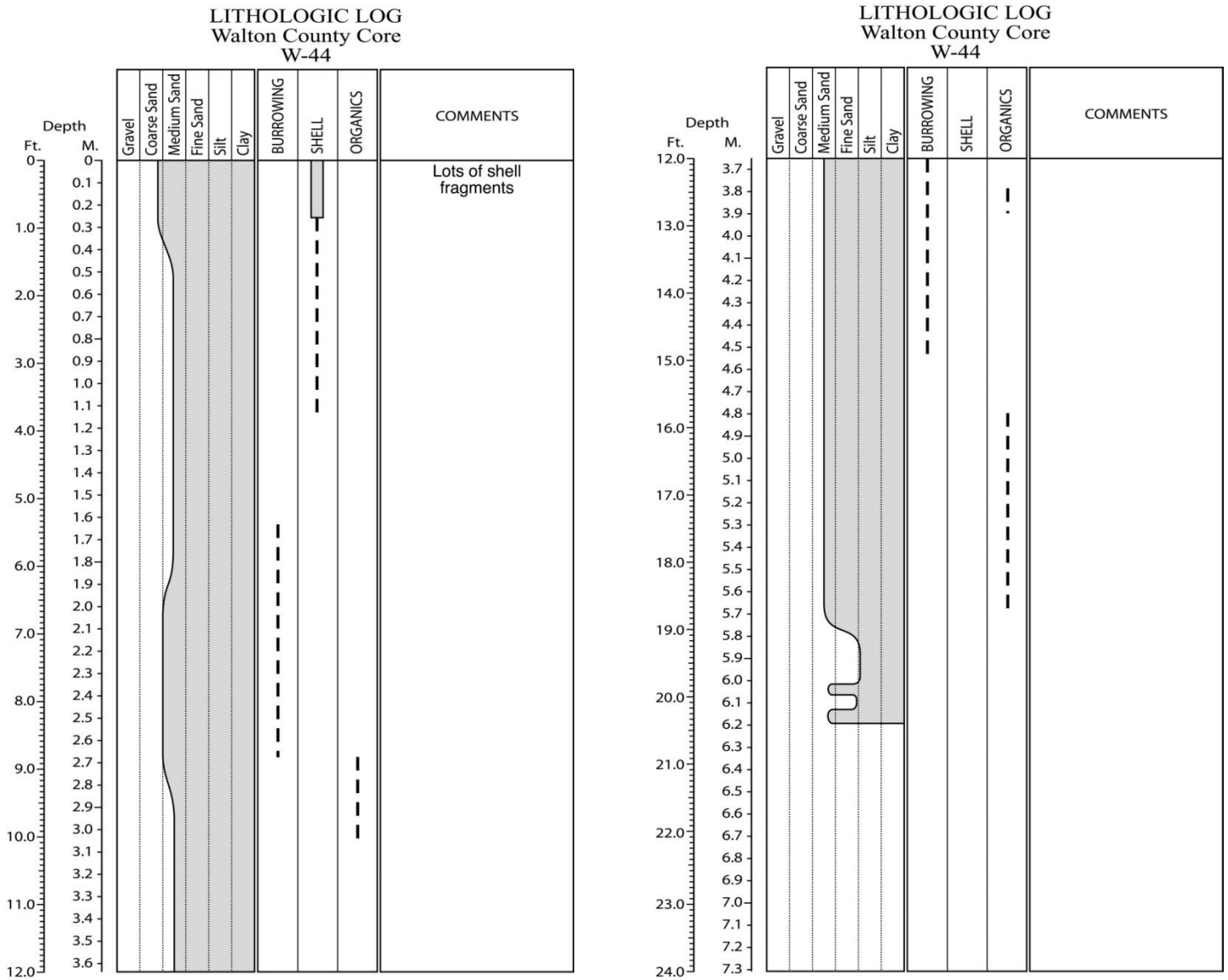

Figure E.44. Core W-44 log.

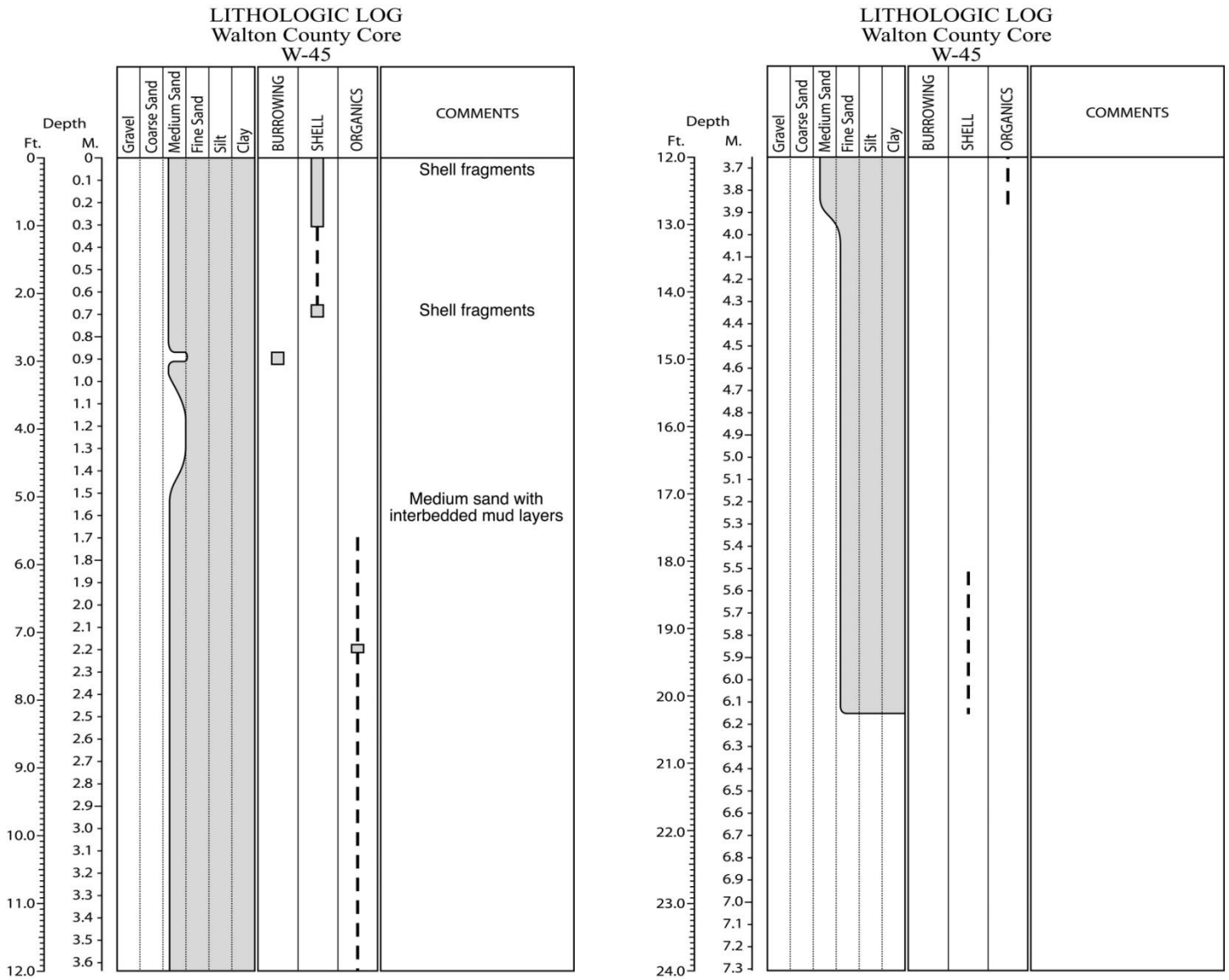

Figure E.45. Core W-45 log.

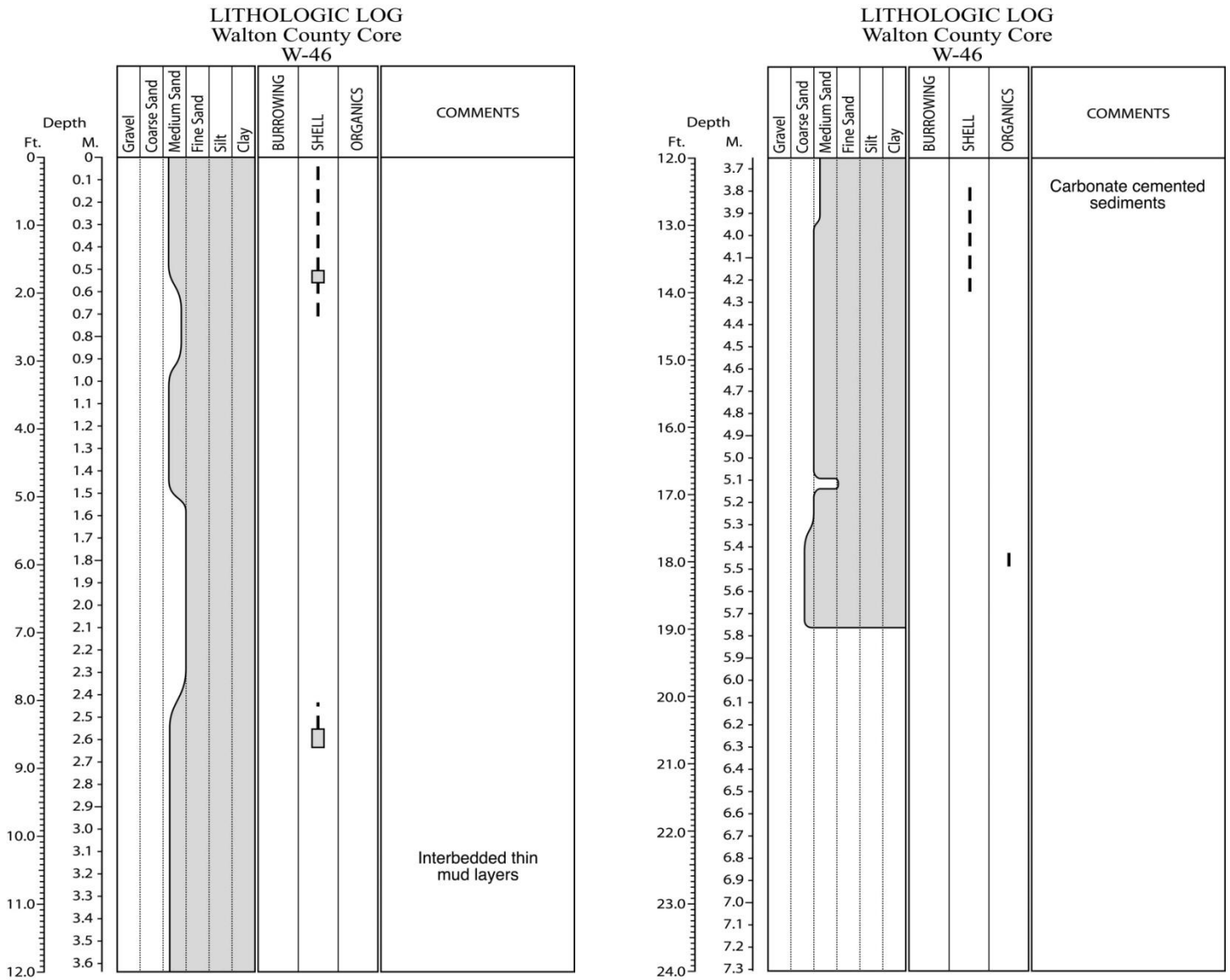

Figure E.46. Core W-46 log.

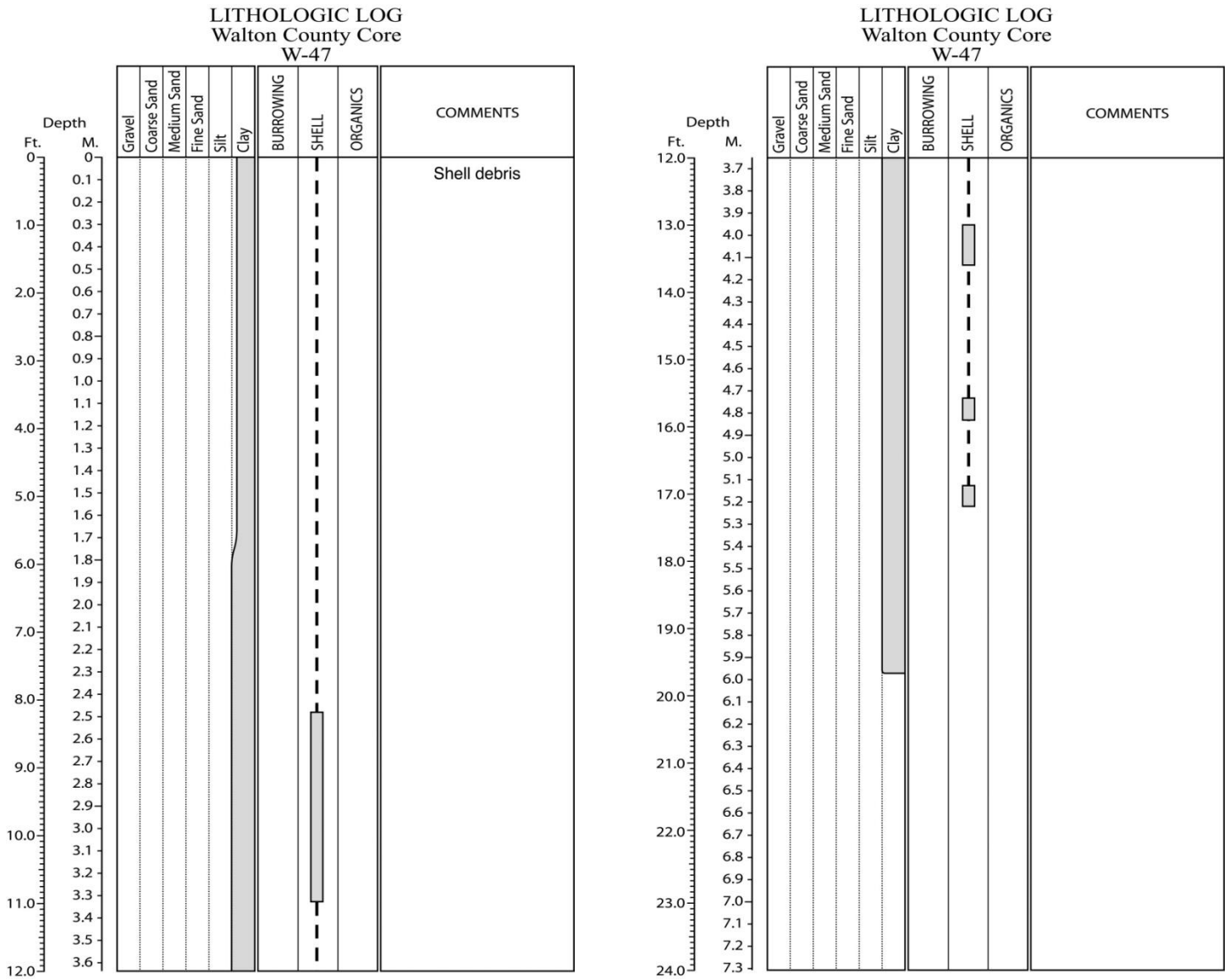

Figure E.47. Core W-47 log.

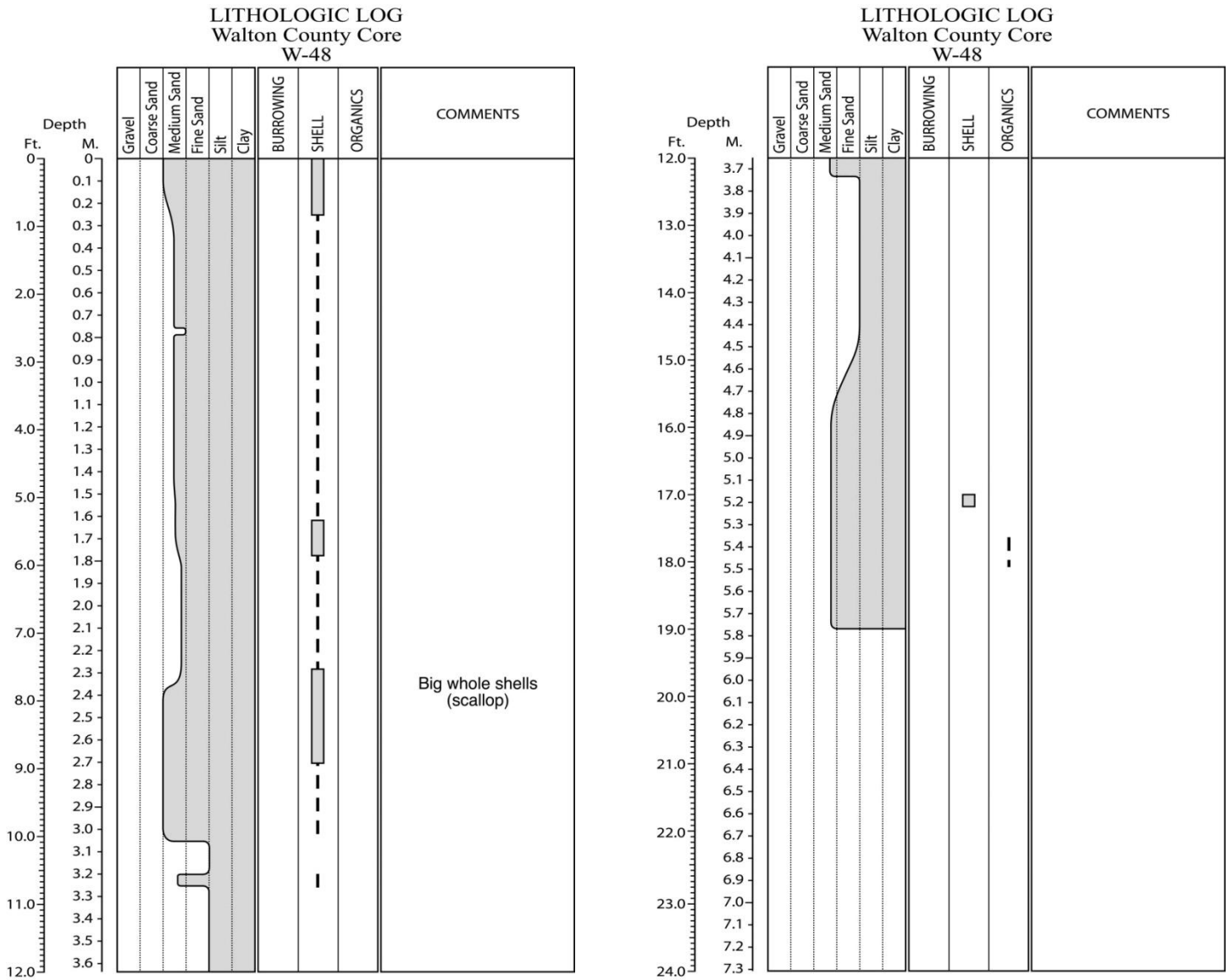

Figure E.48. Core W-48 log.

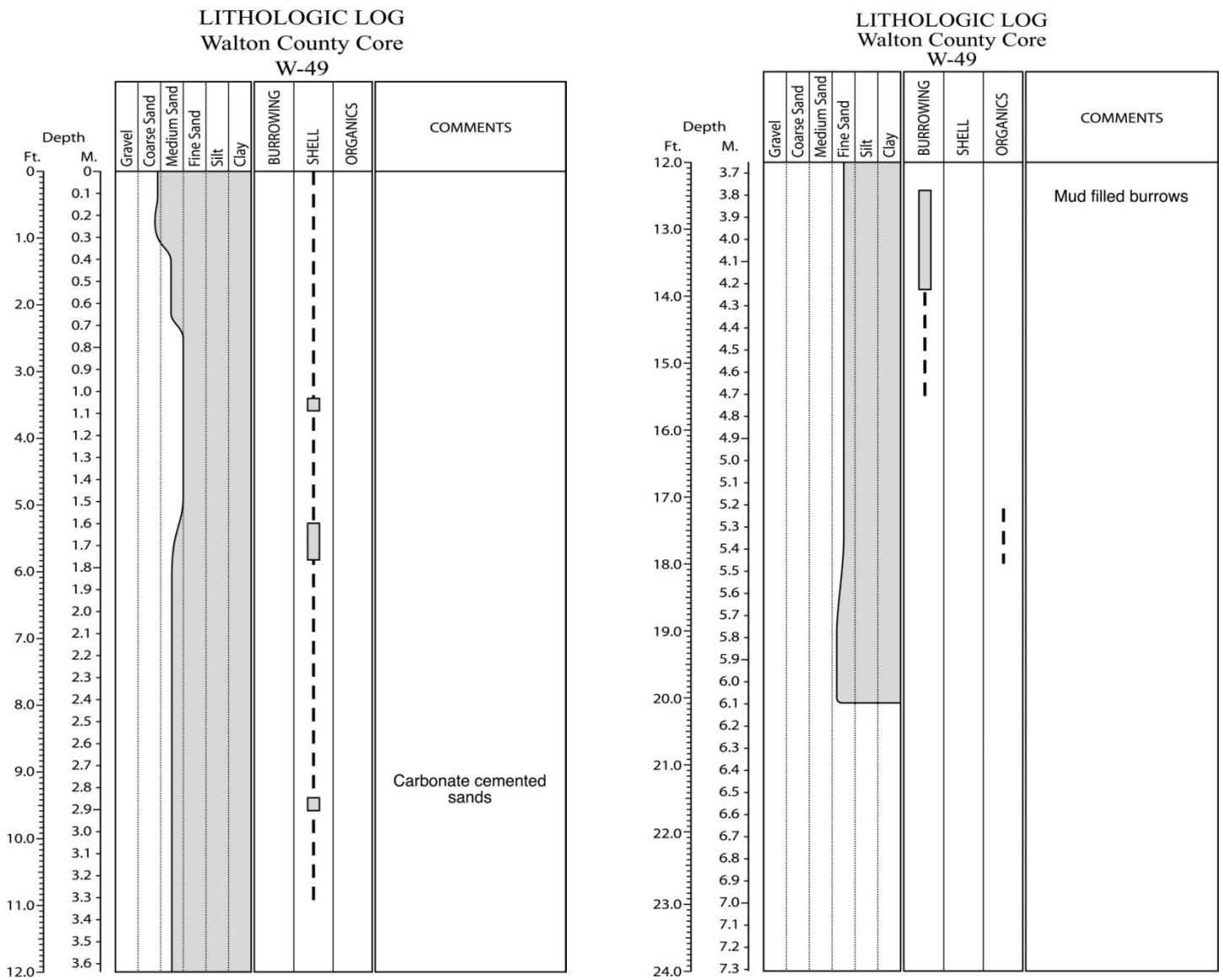

Figure E.49. Core W-49 log.

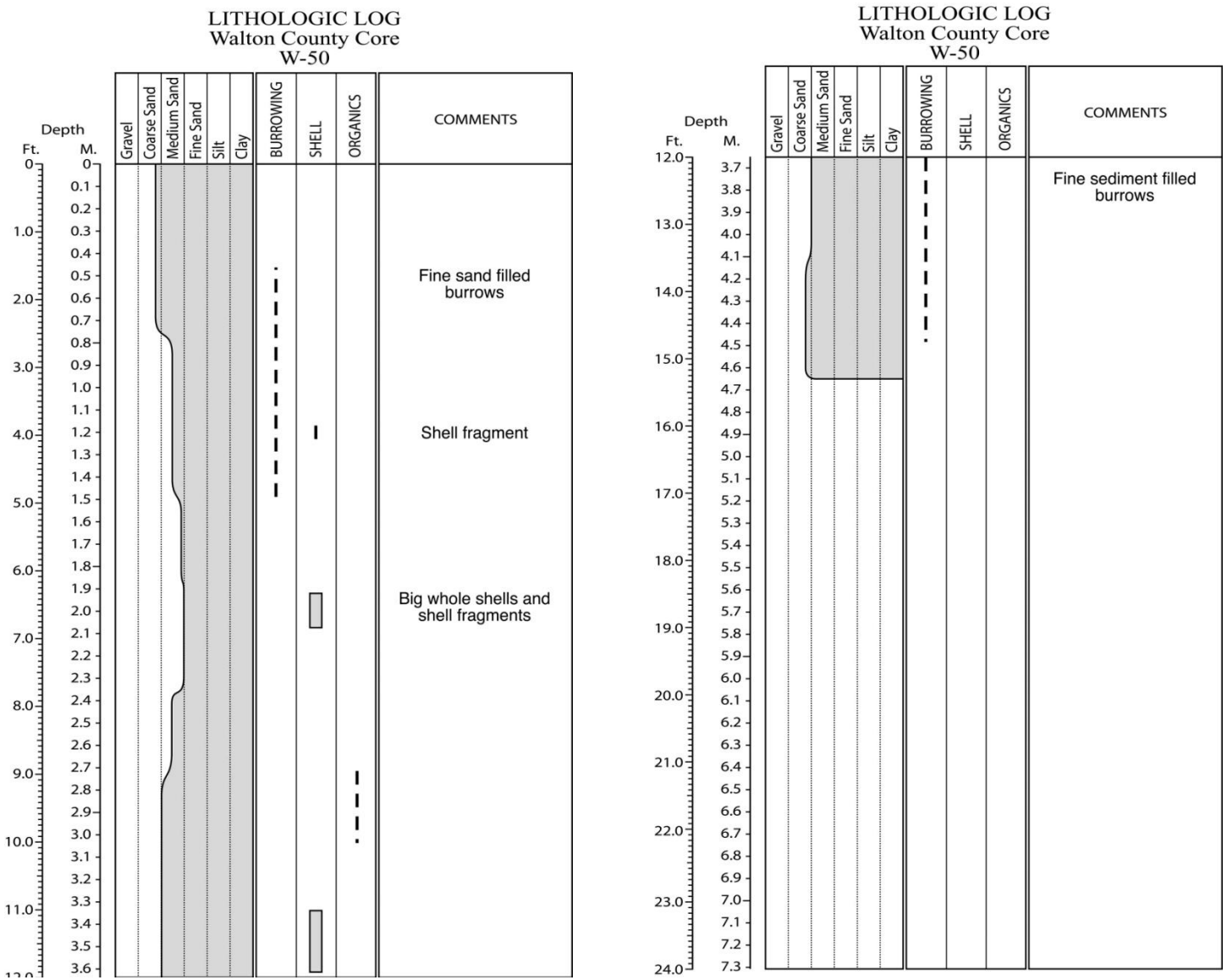

Figure E.50. Core W-50 log.

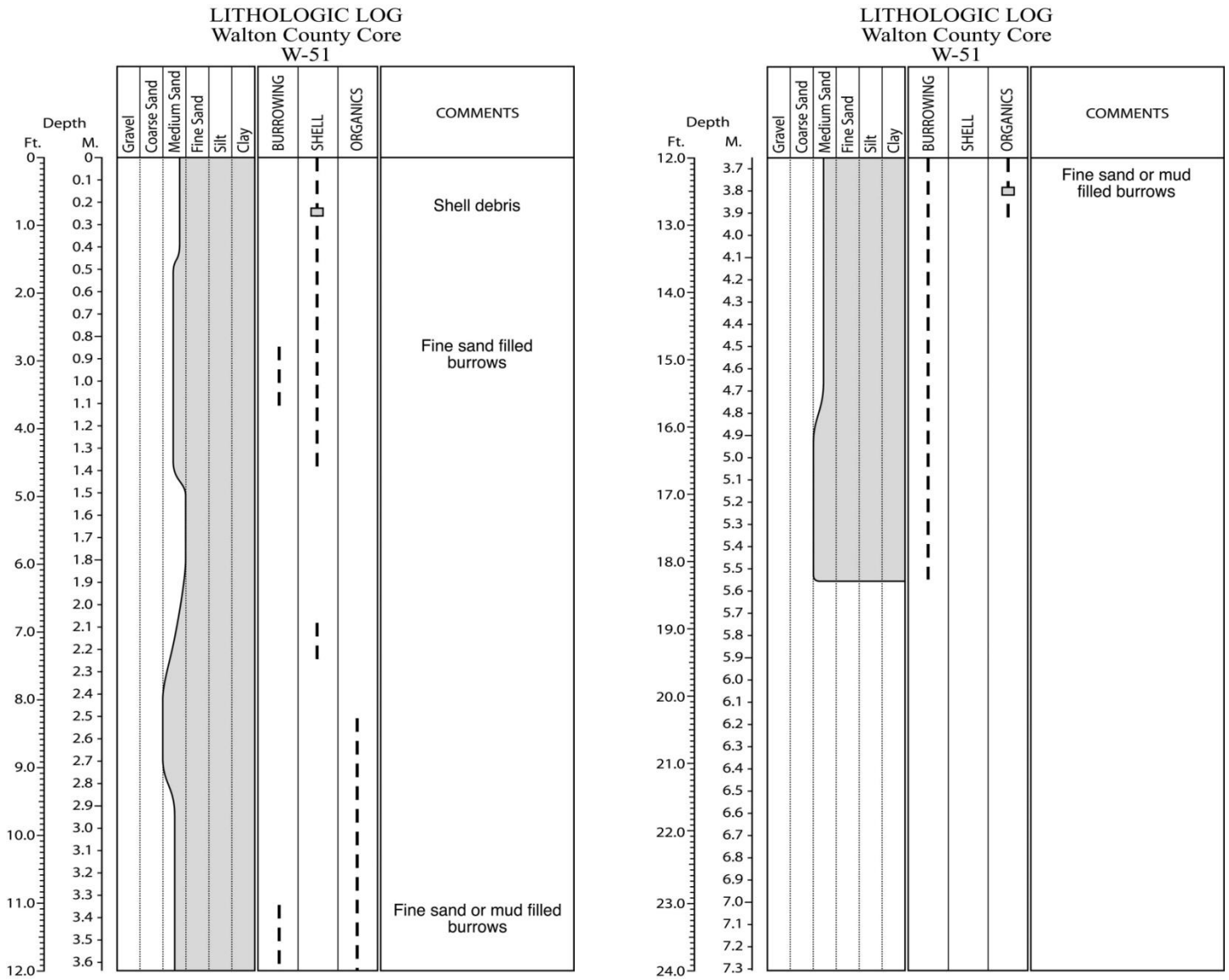

Figure E.51. Core W-51 log.

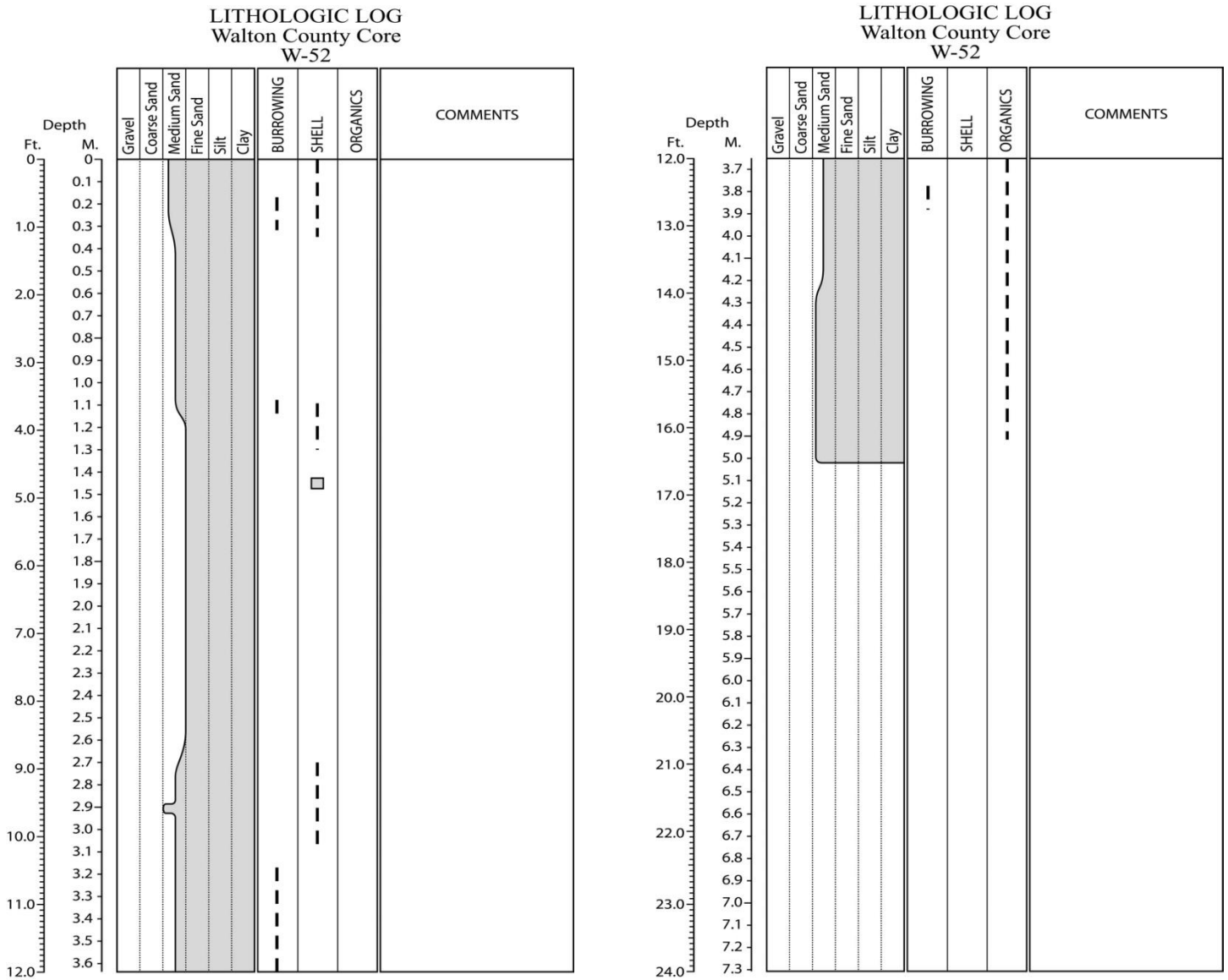

Figure E.52. Core W-52 log.

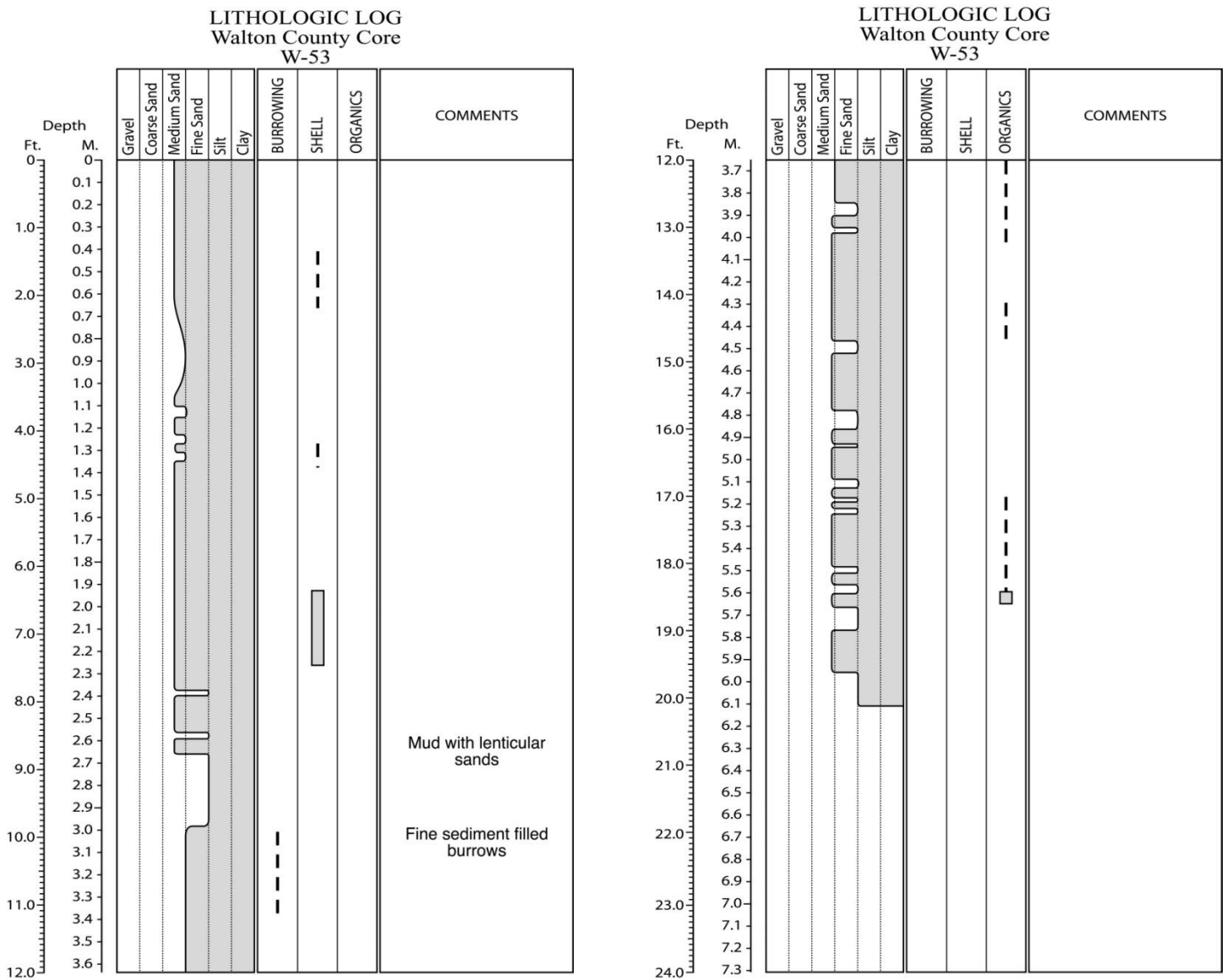

Figure E.53. Core W-53 log.

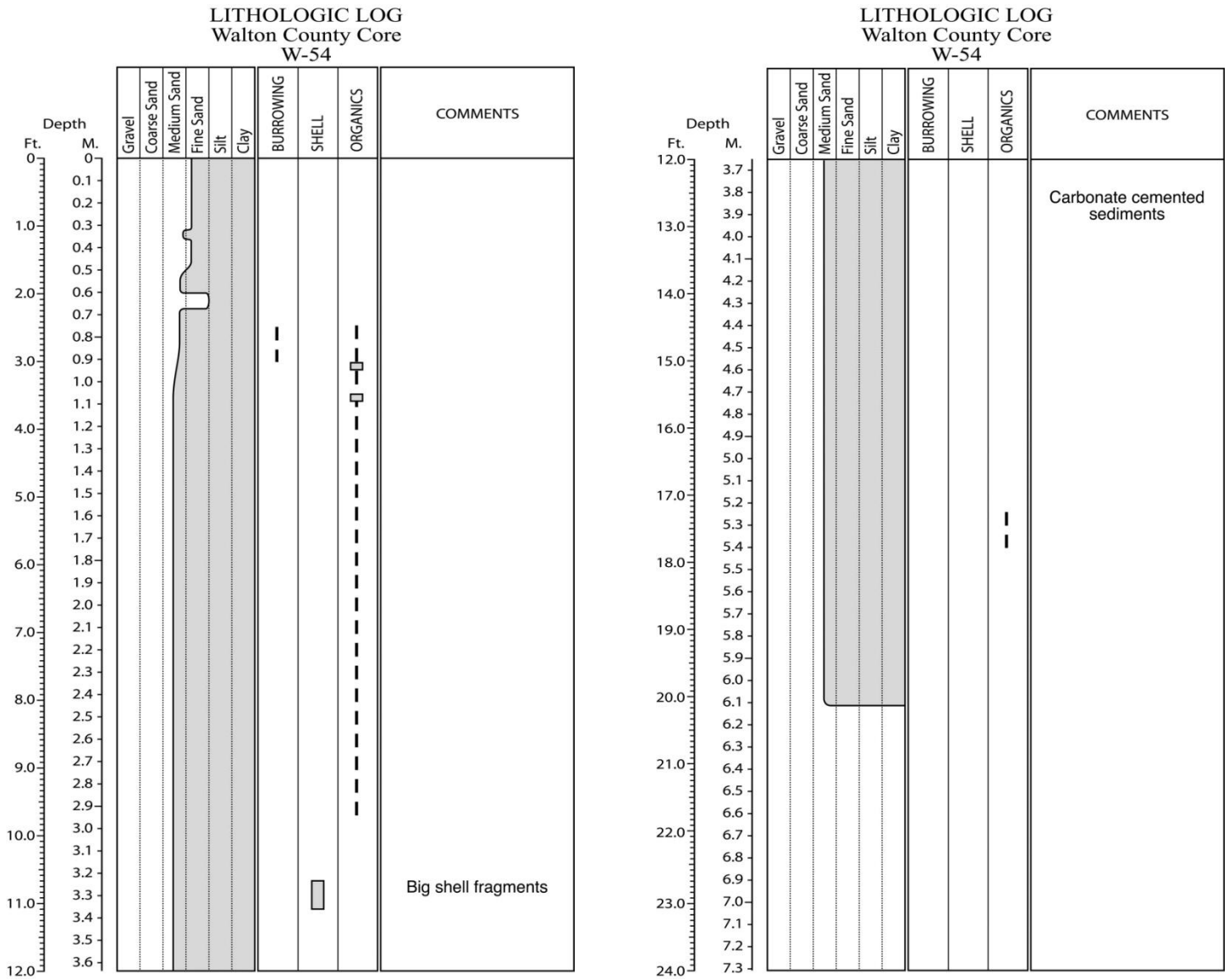

Figure E.54. Core W-54 log.

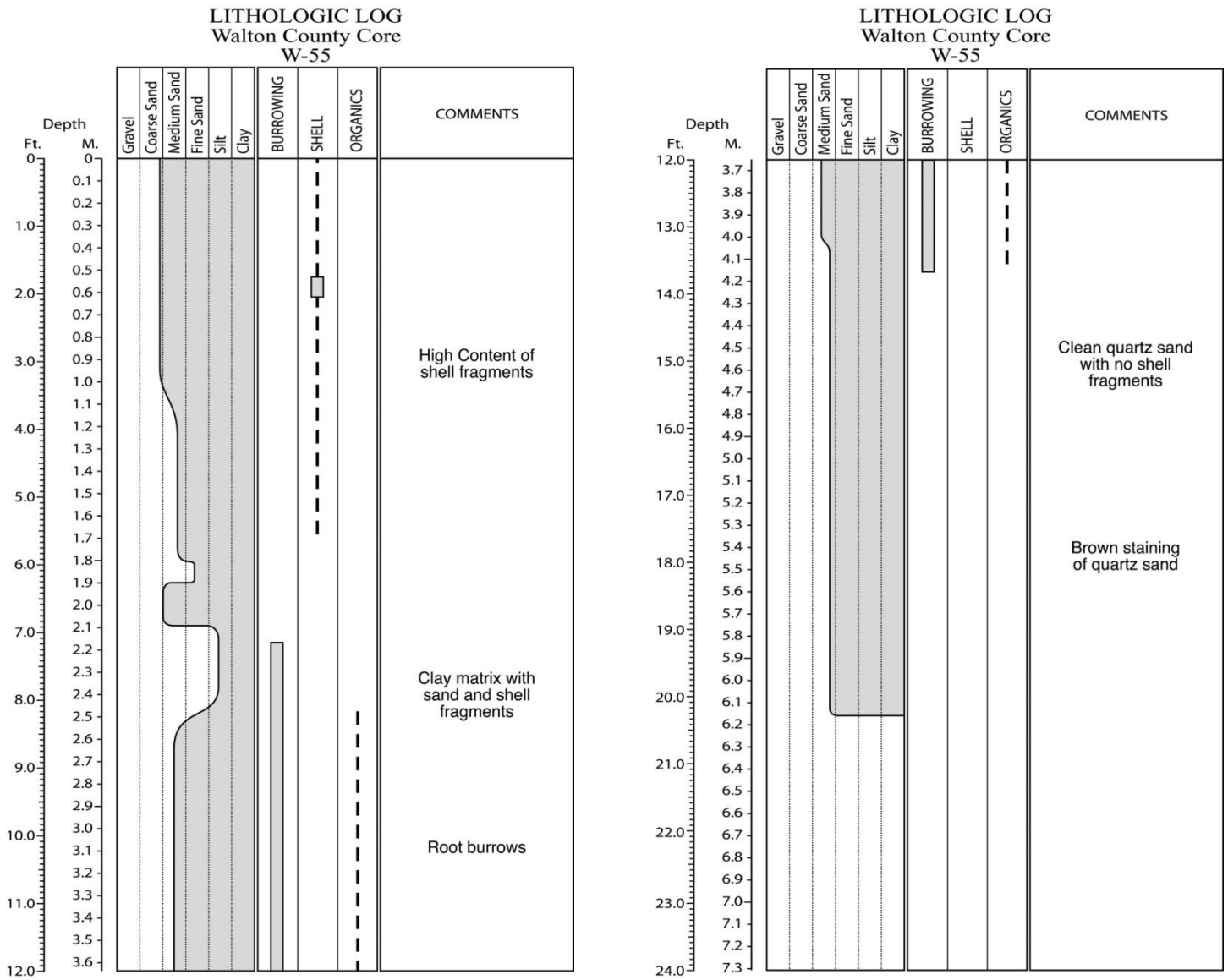

Figure E.55. Core W-55 log.

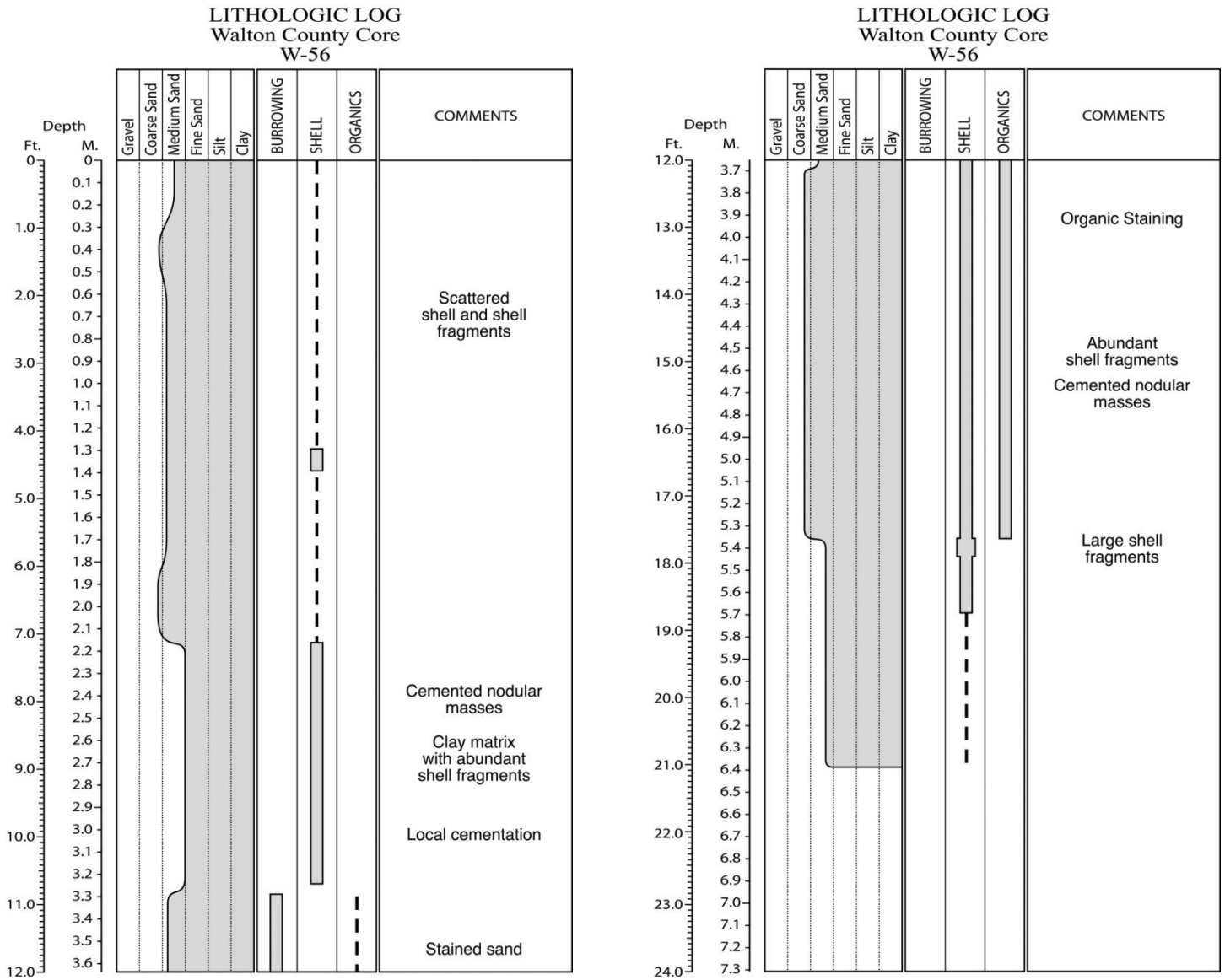

Figure E.56. Core W-56 log.

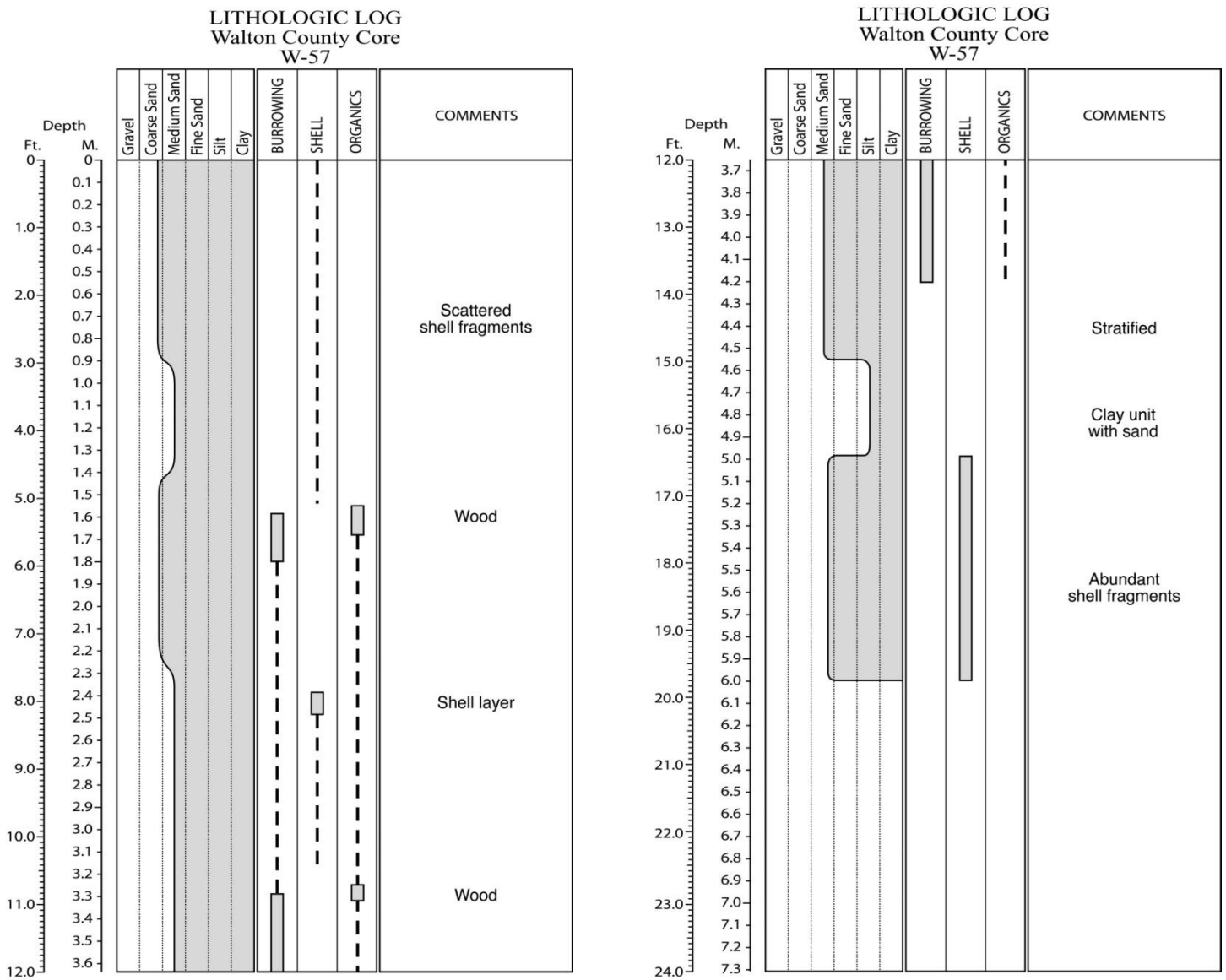

Figure E.57. Core W-57 log.

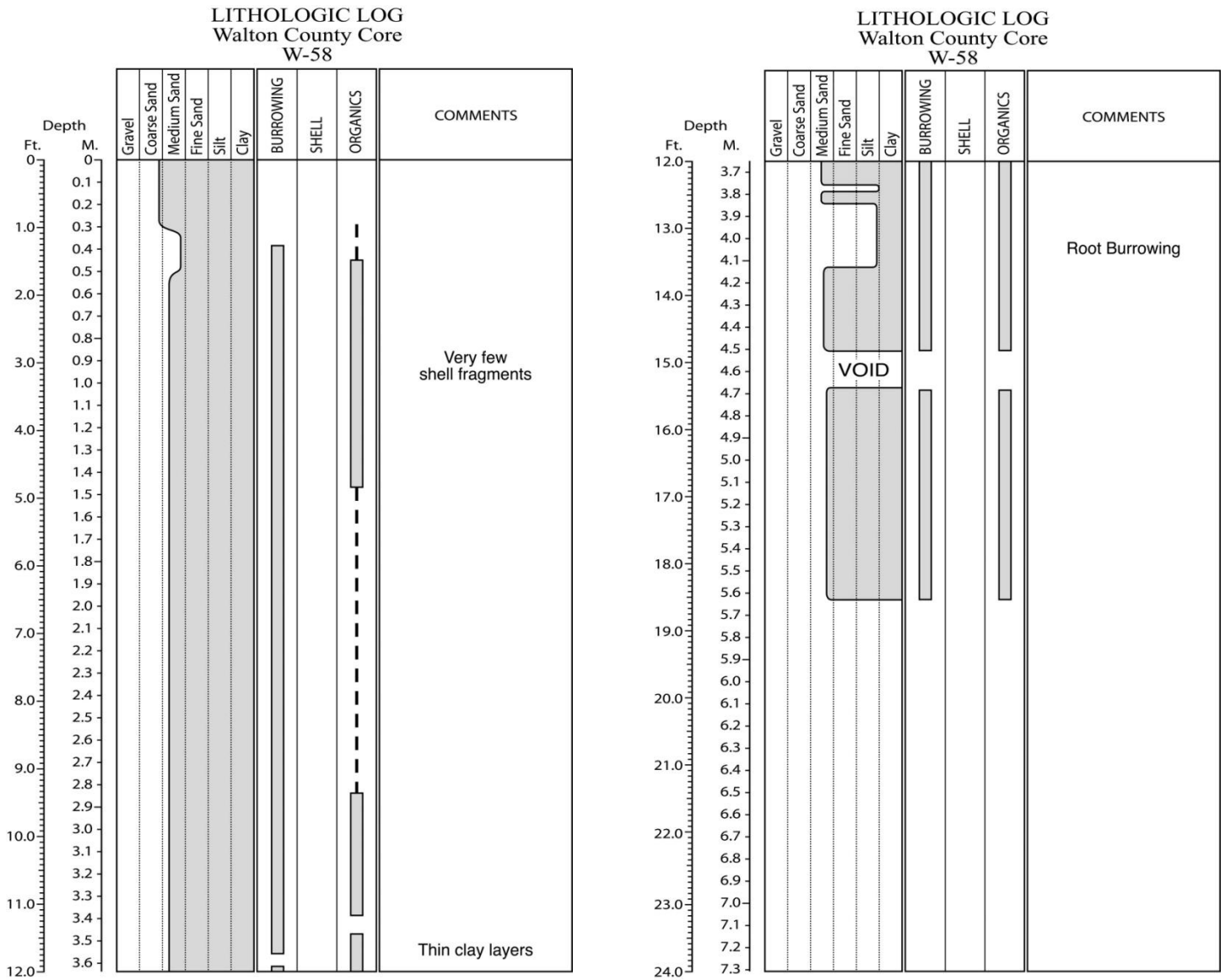

Figure E.58. Core W-58 log.

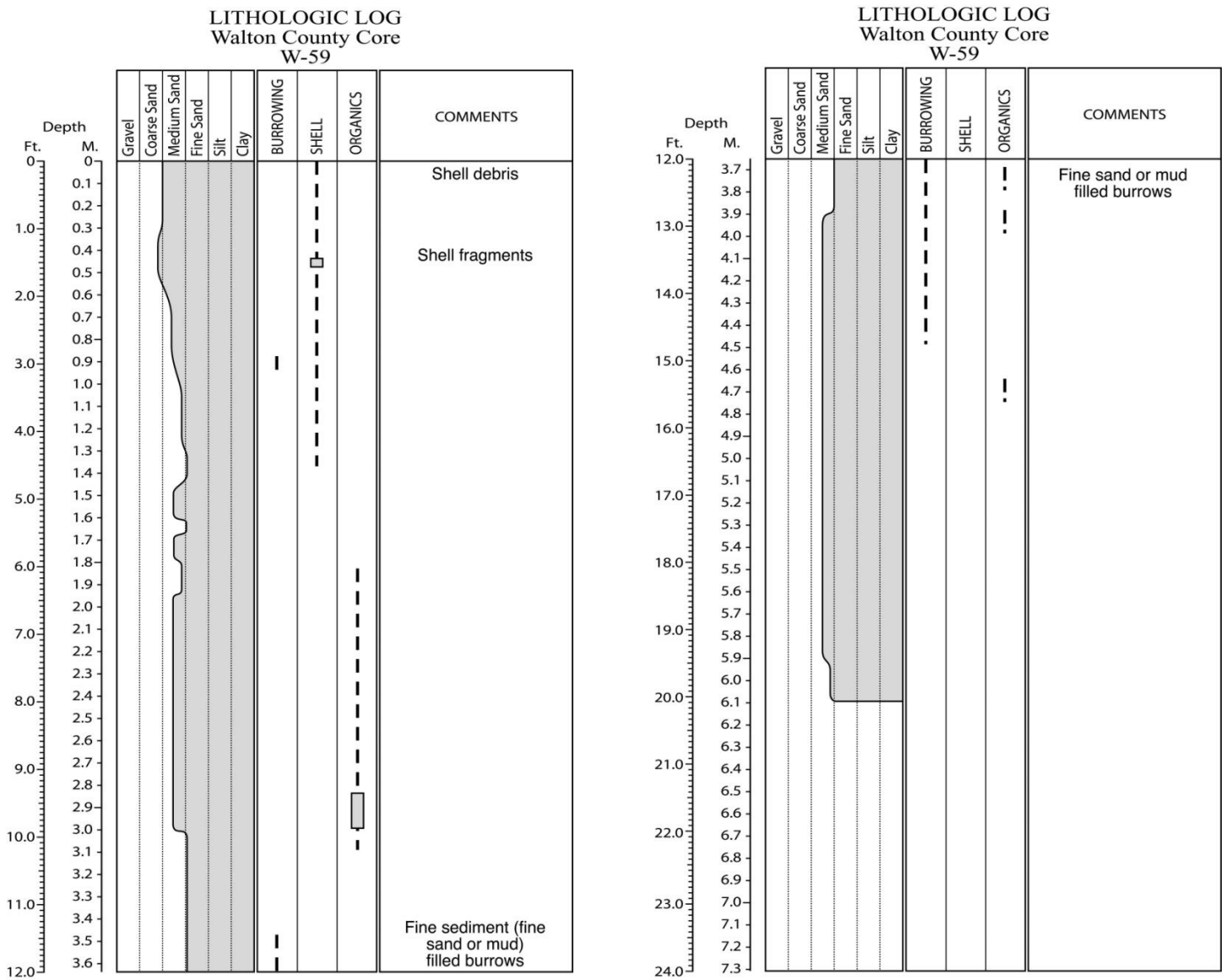

Figure E.59. Core W-59 log.

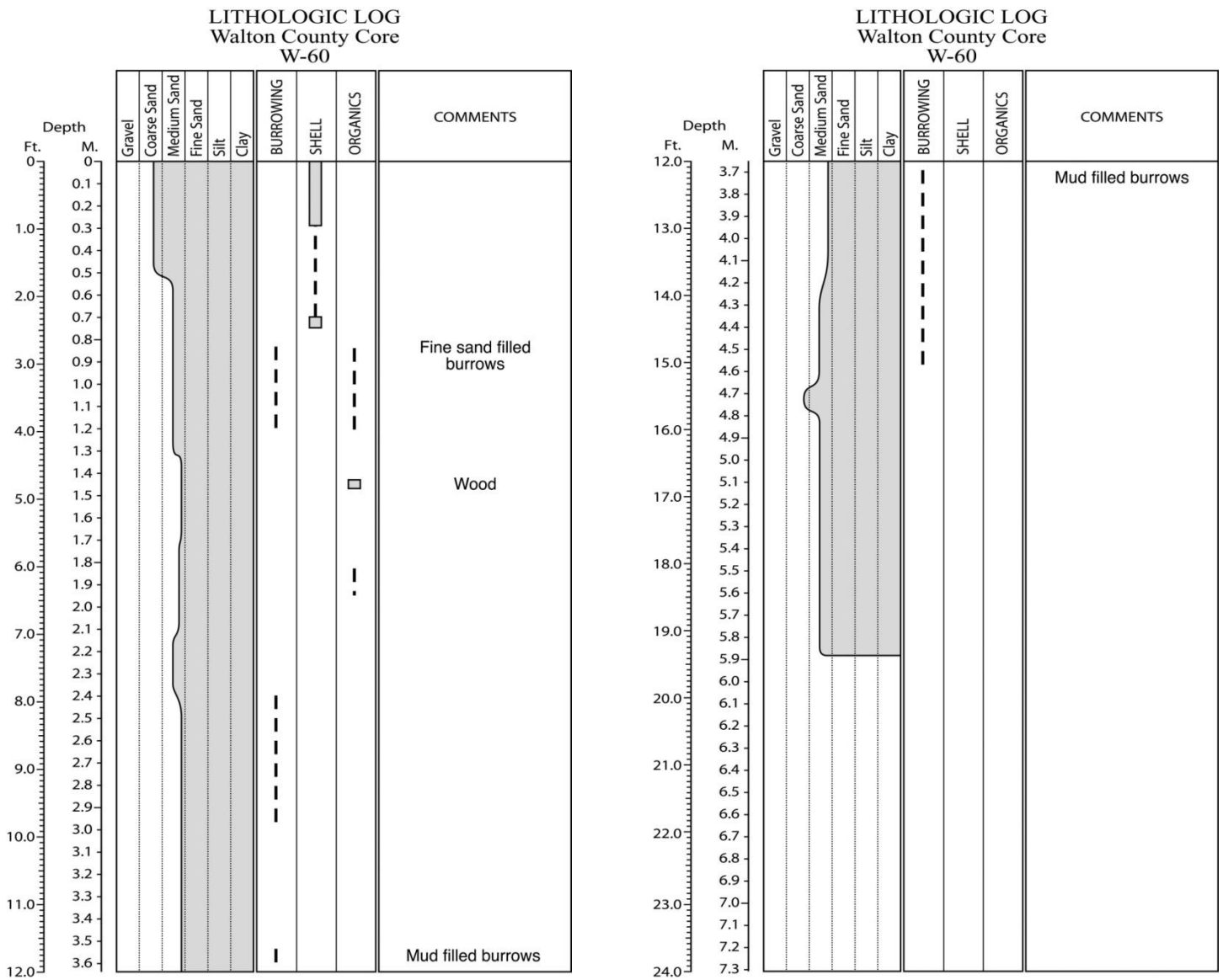

Figure E.60. Core W-60 log.

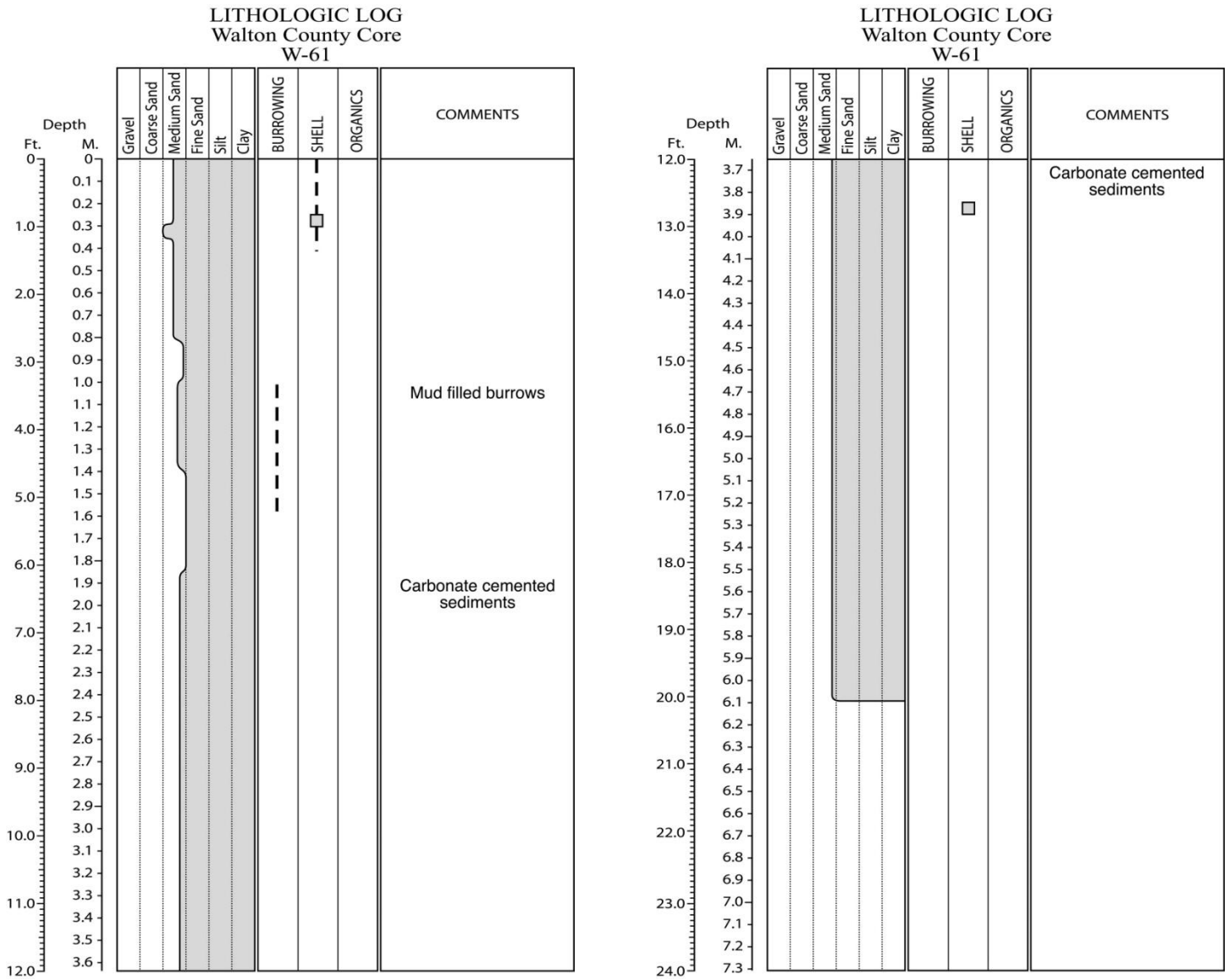

Figure E.61. Core W-61 log.

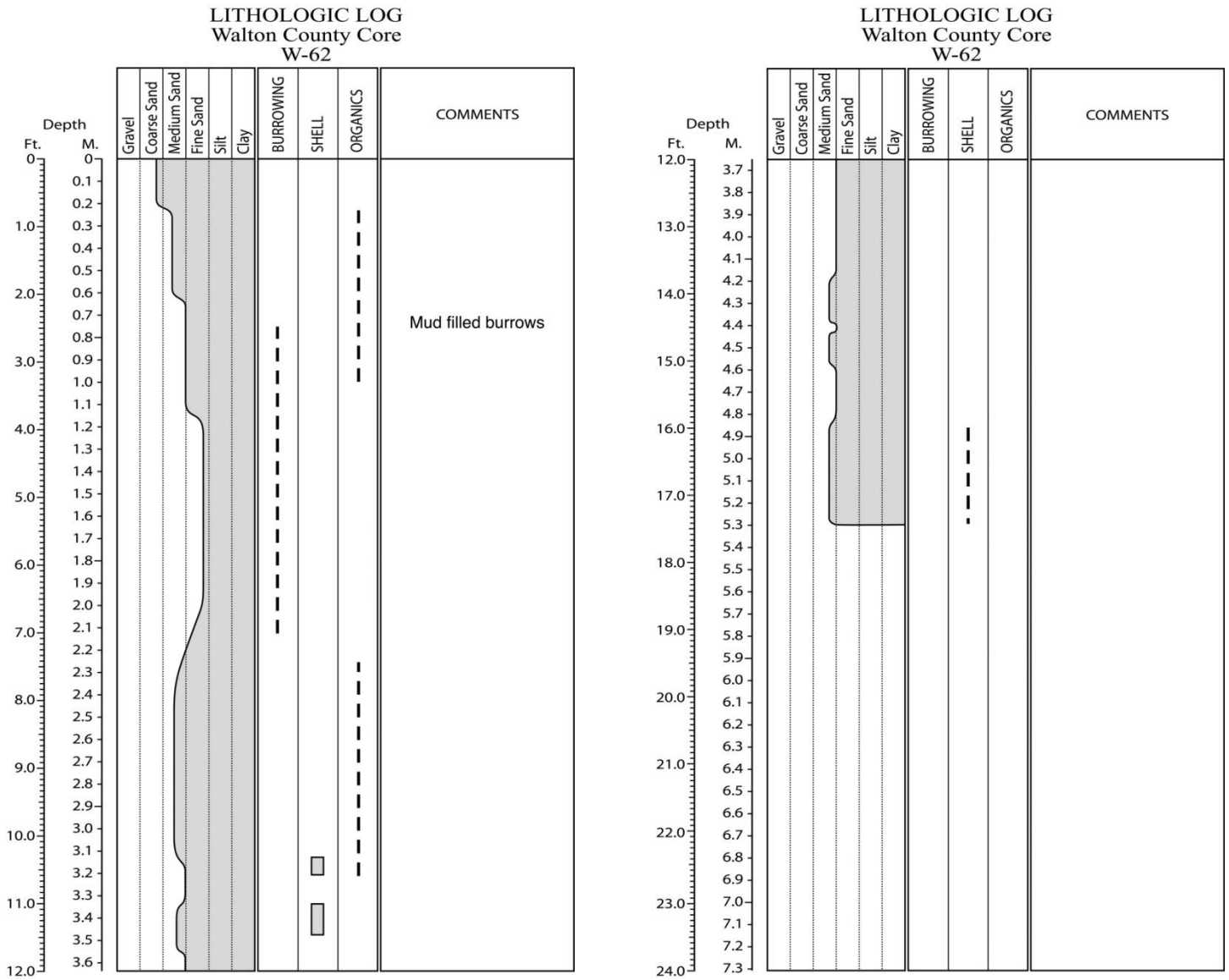

Figure E.62. Core W-62 log.

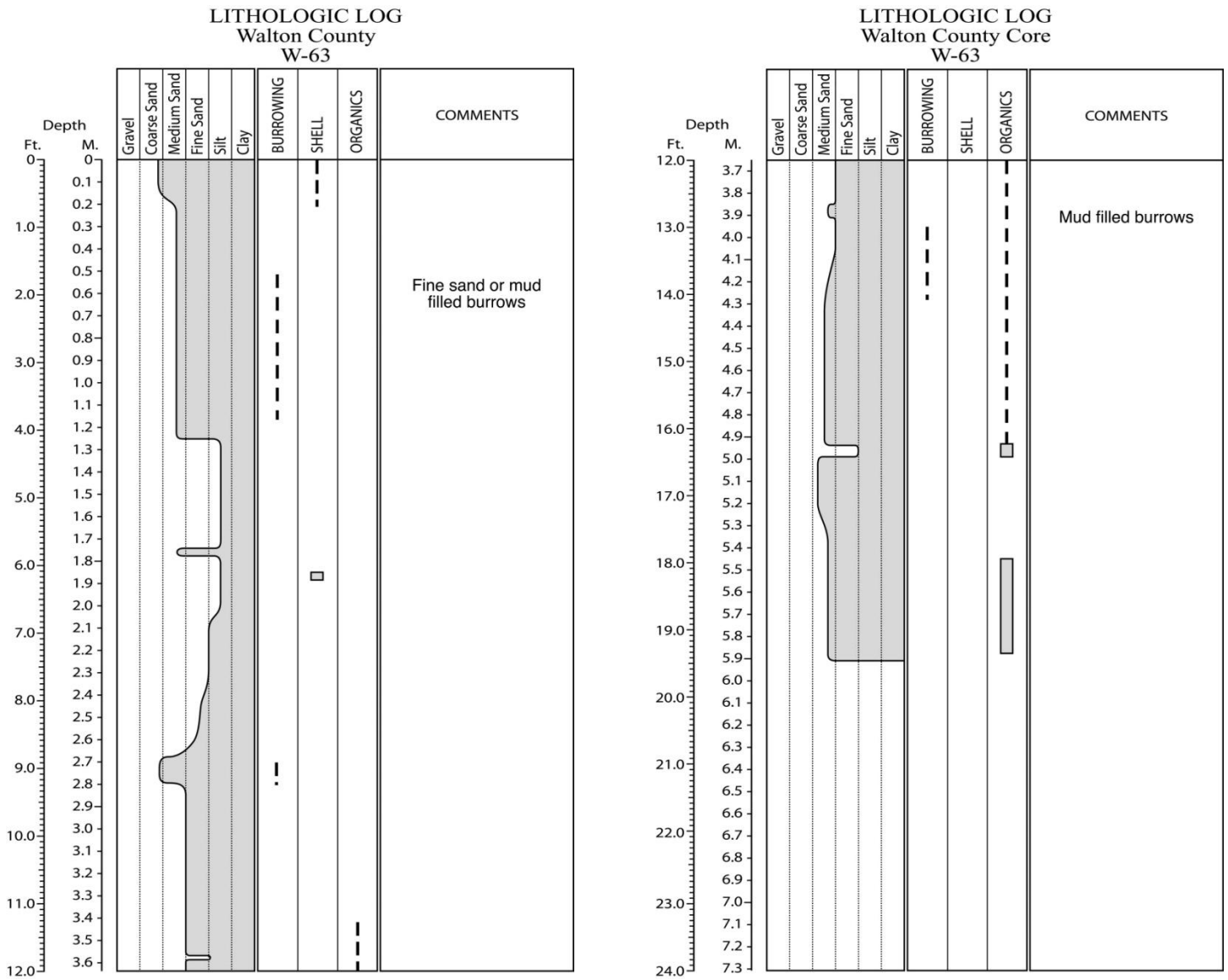

Figure E.63. Core W-63 log.

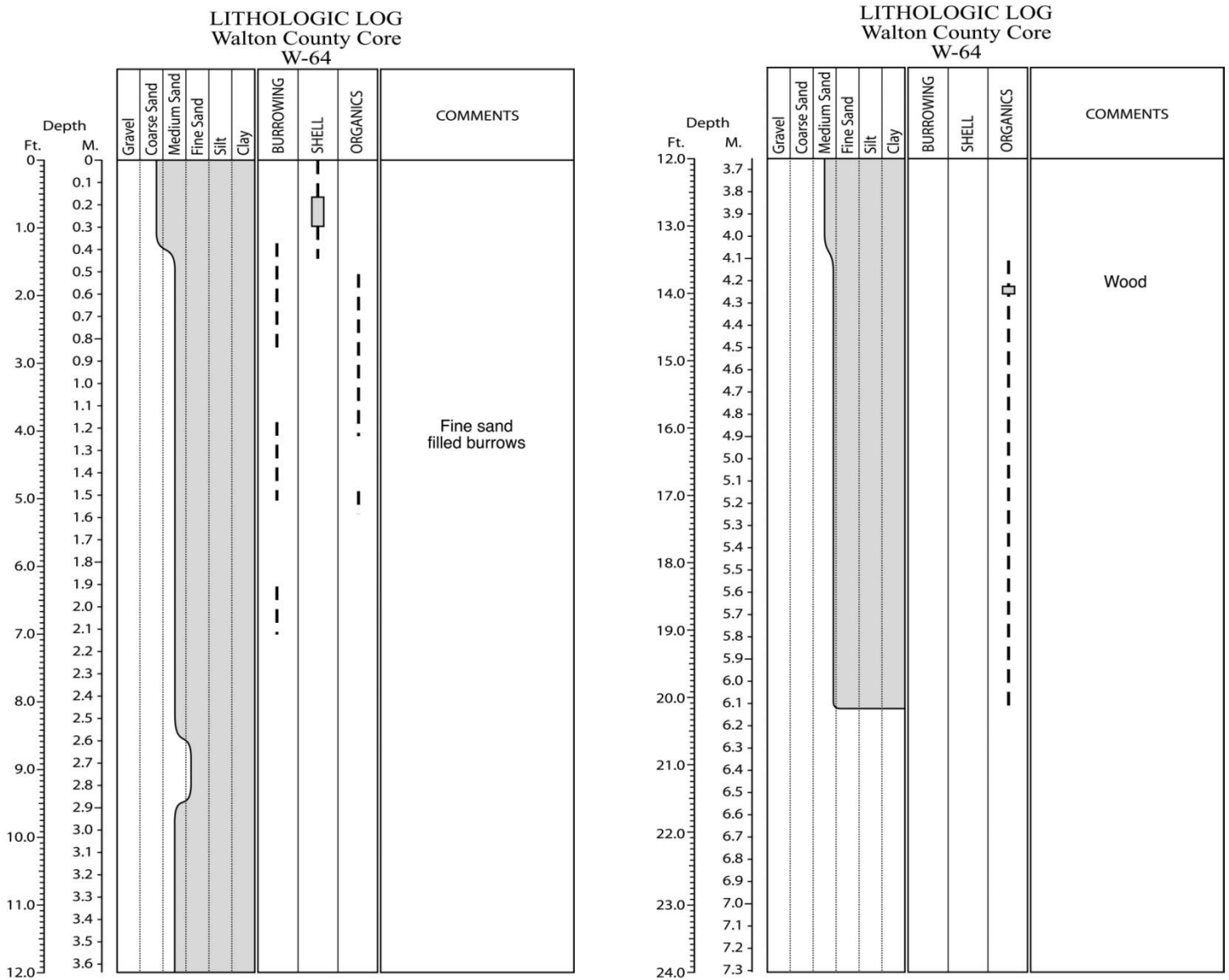

Figure E.64. Core W-64 log.

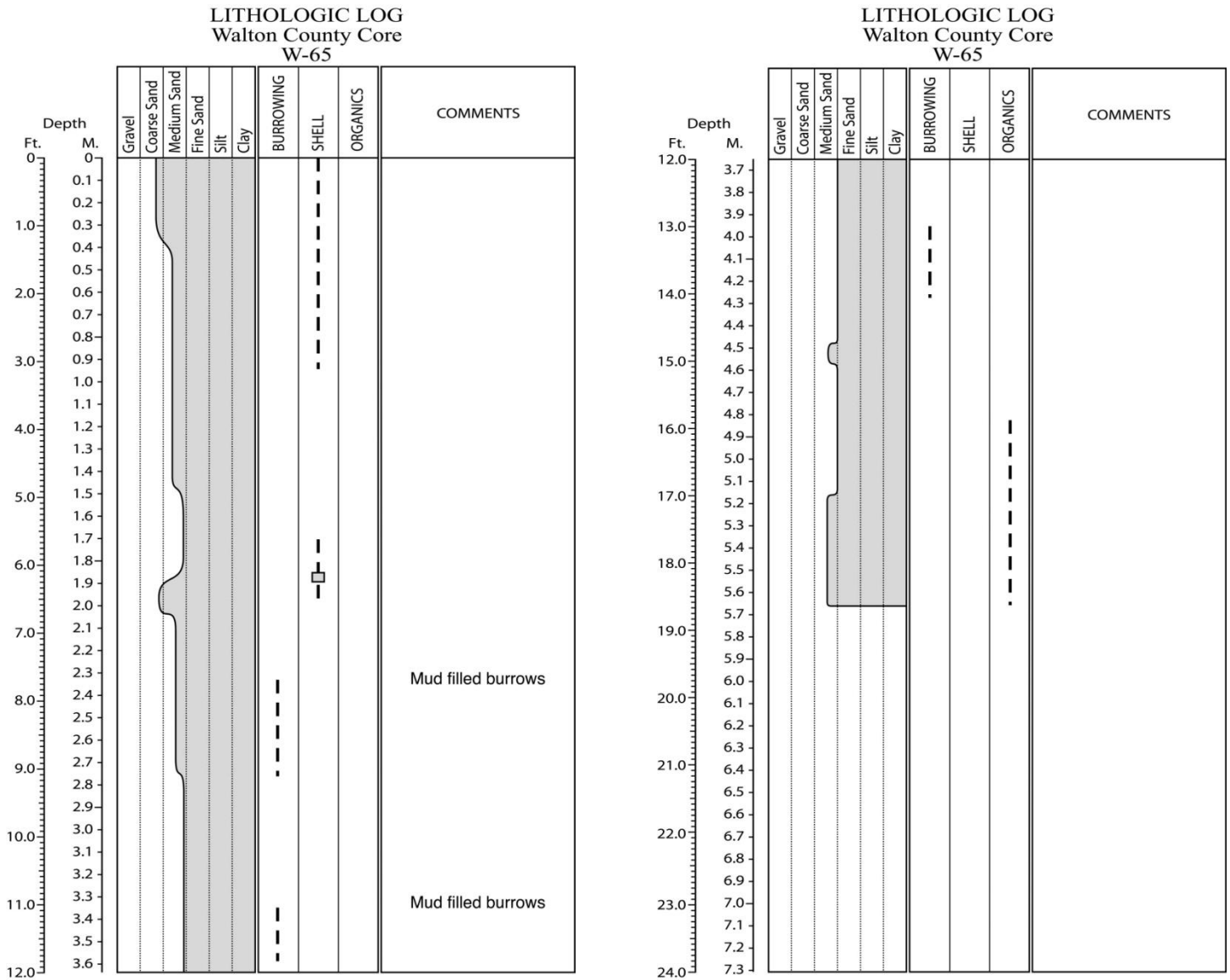

Figure E.65. Core W-65 log.

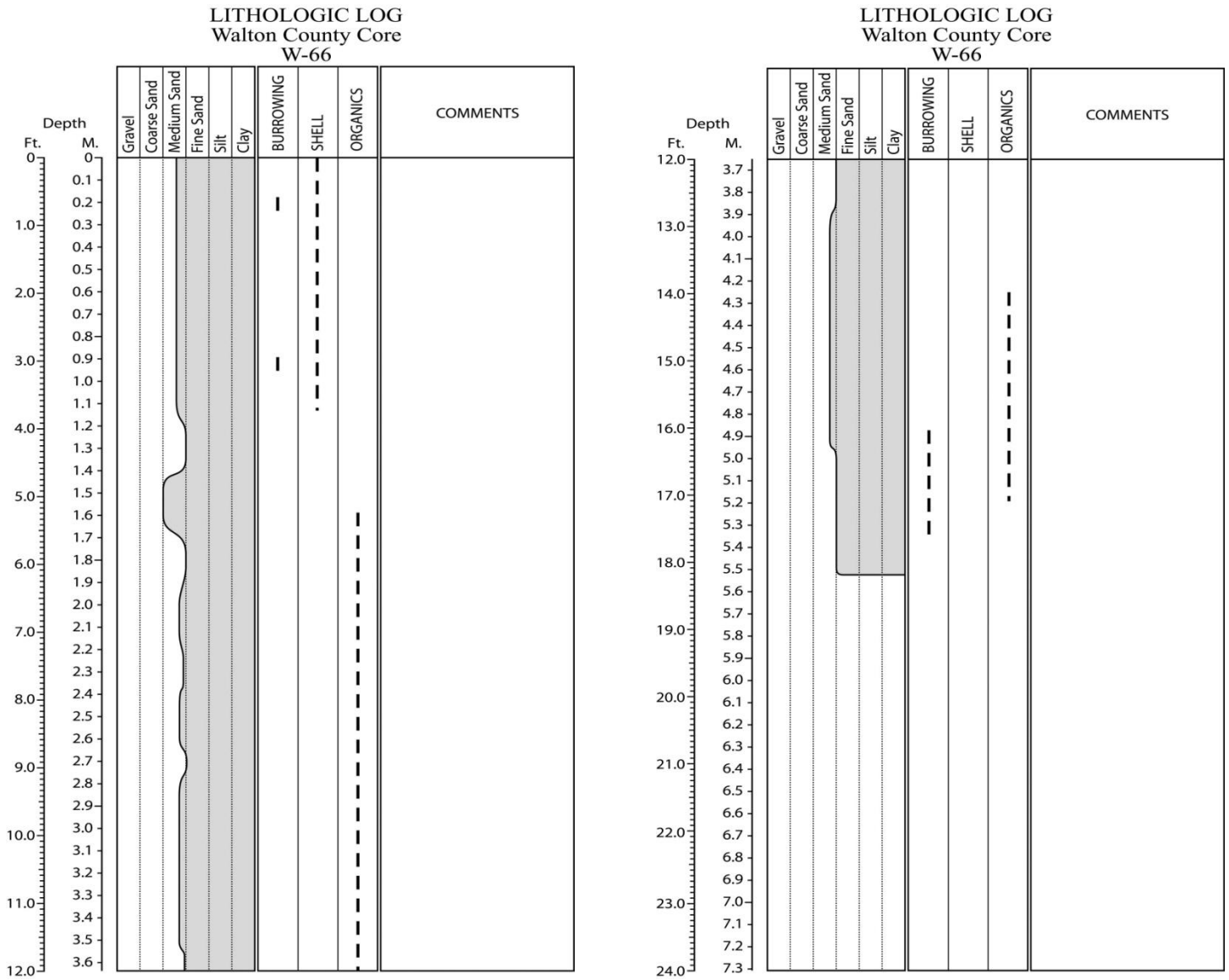

Figure E.66. Core W-66 log.

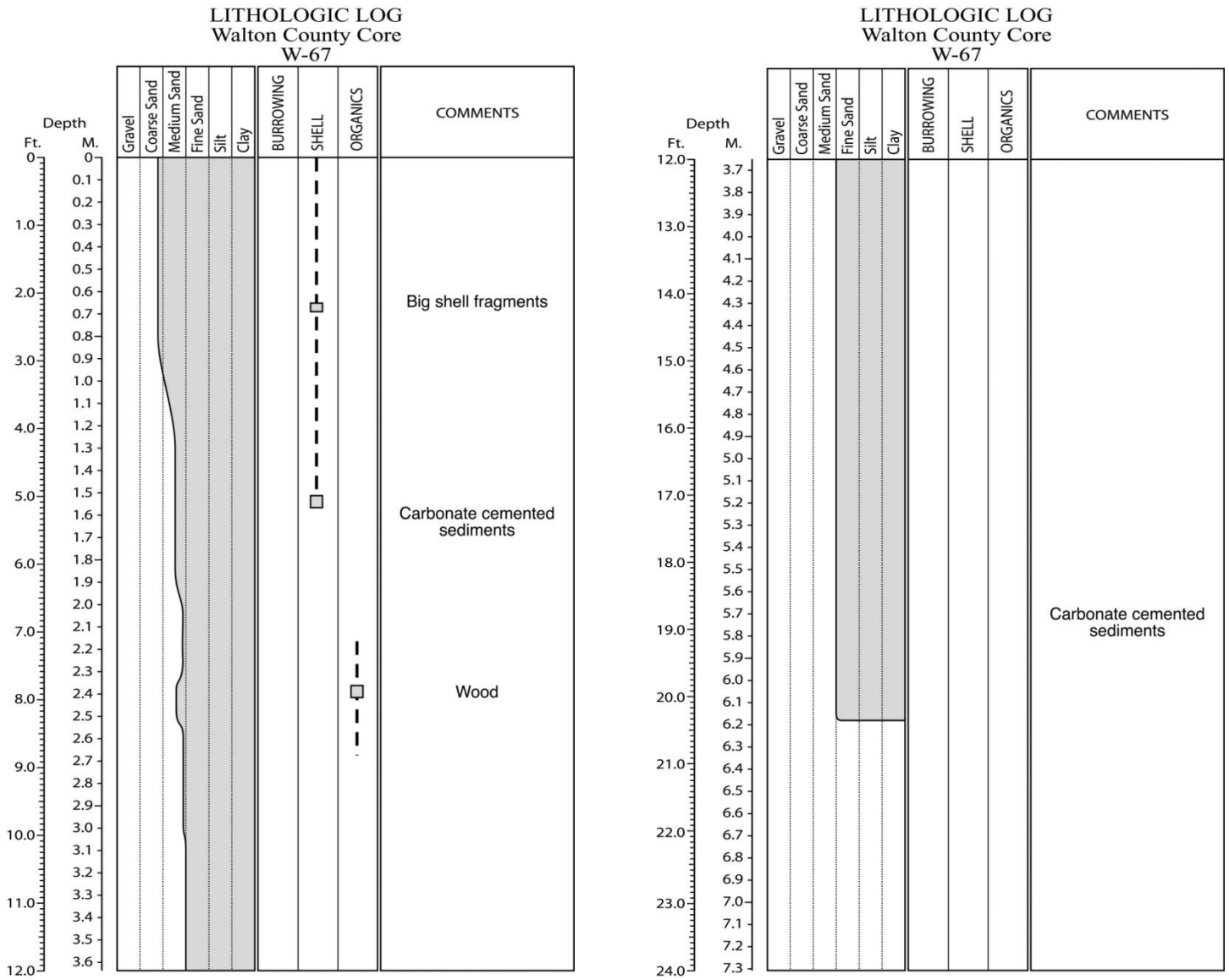

Figure E.67. Core WN-67 log.

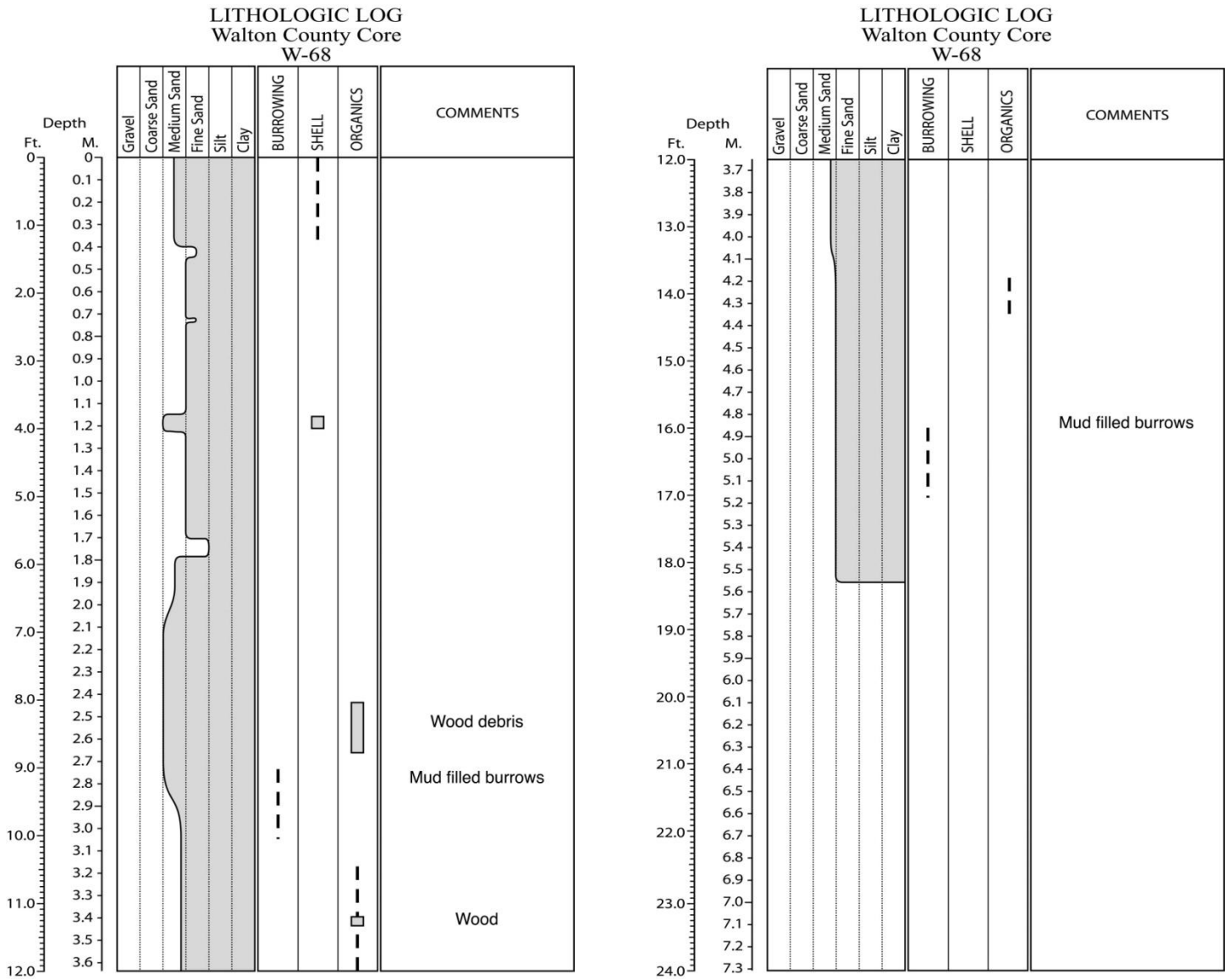

Figure E.68. Core W-68 log.

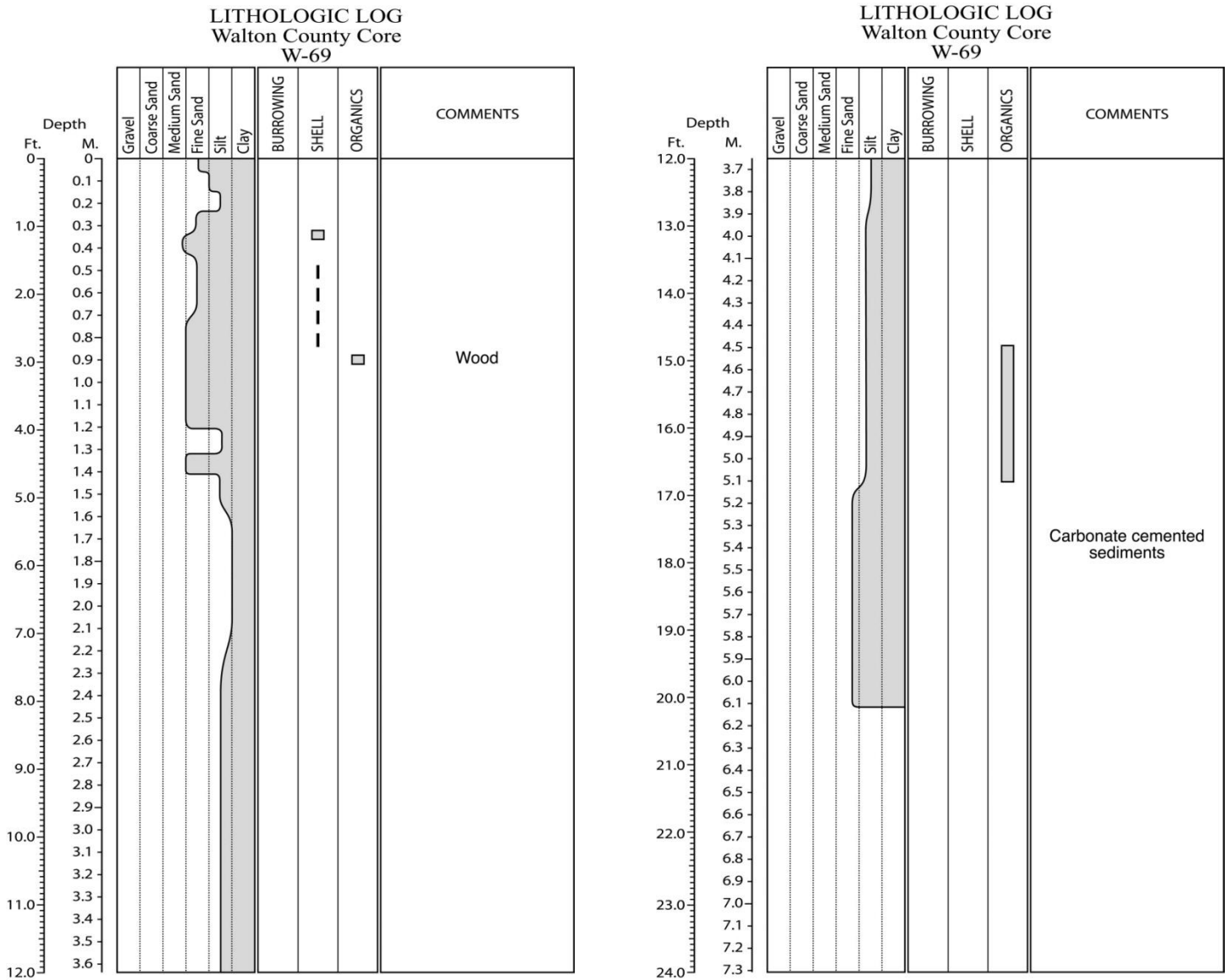

Figure E.69. Core W-69 log.

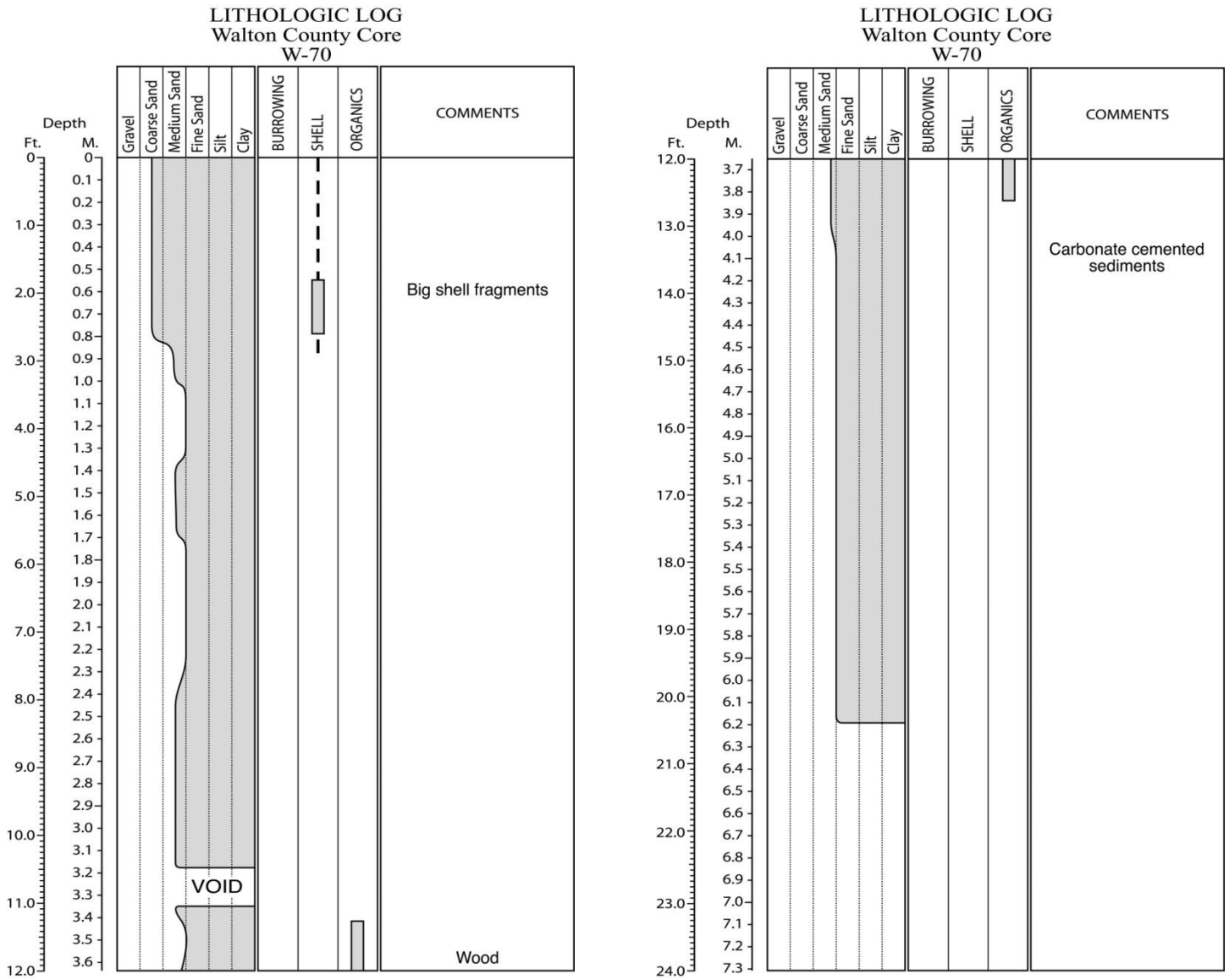

Figure E.70. Core W-70 log.

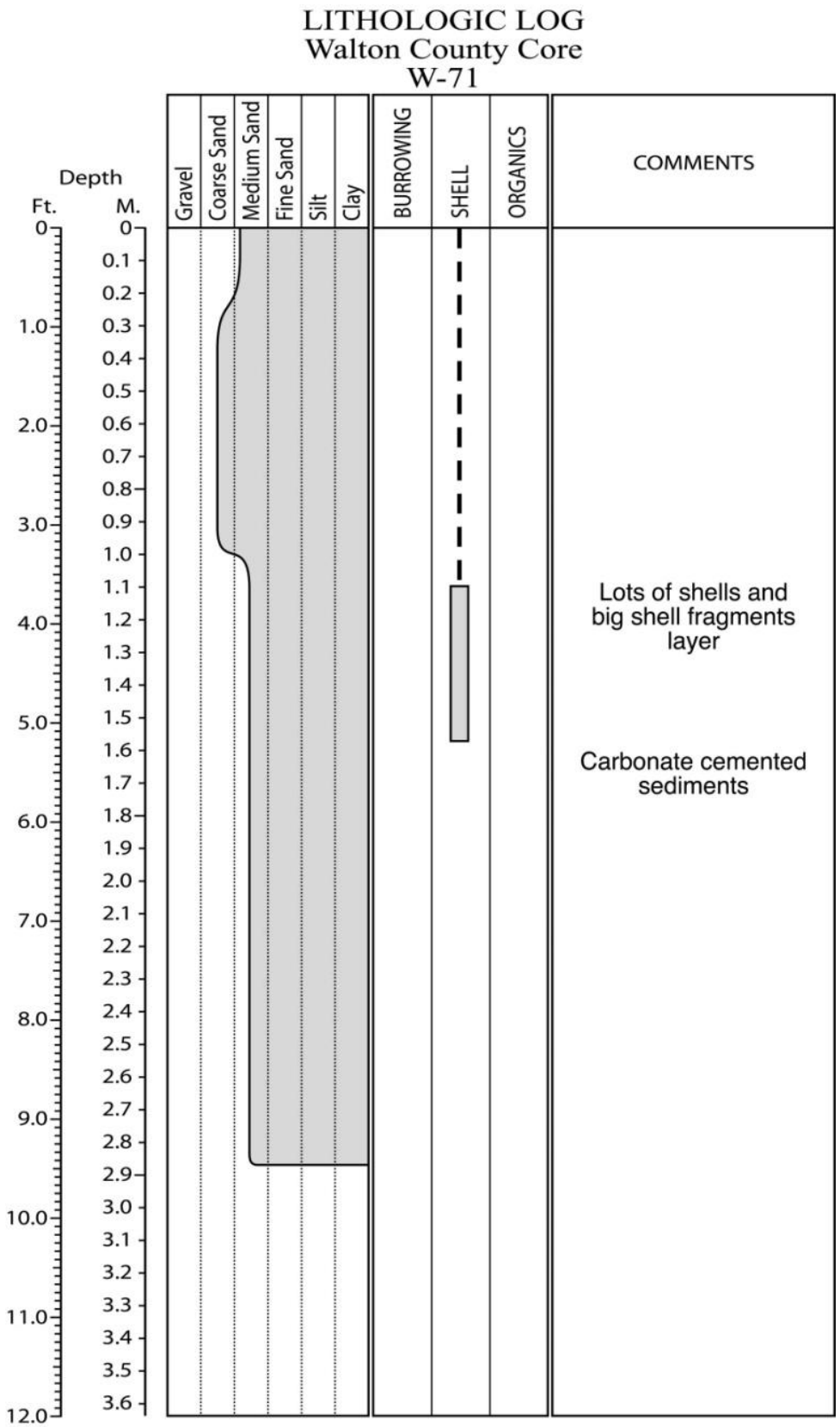

Figure E.71. Core W-71 log.

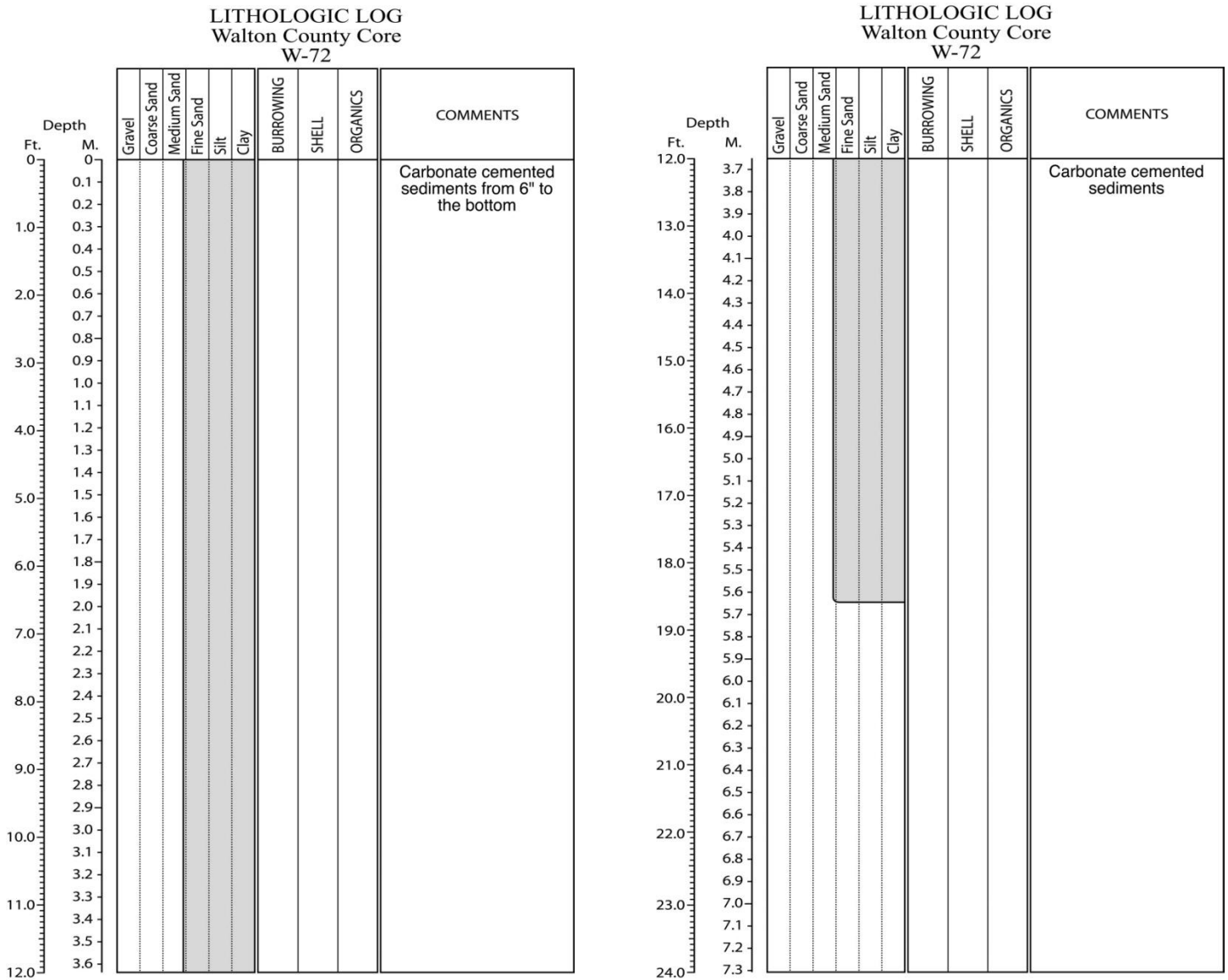

Figure E.72. Core W-72 log.

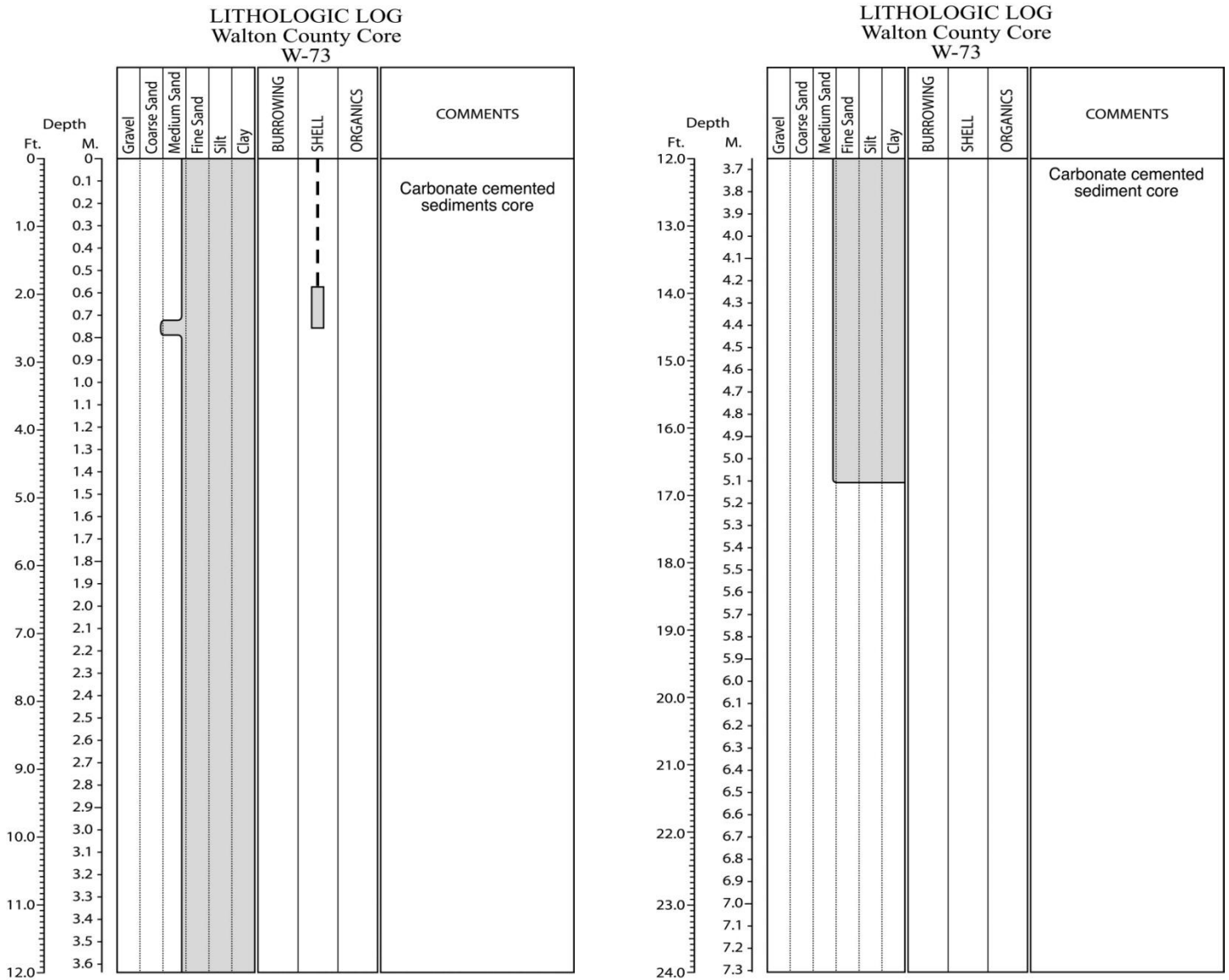

Figure E.73. Core W-73 log.

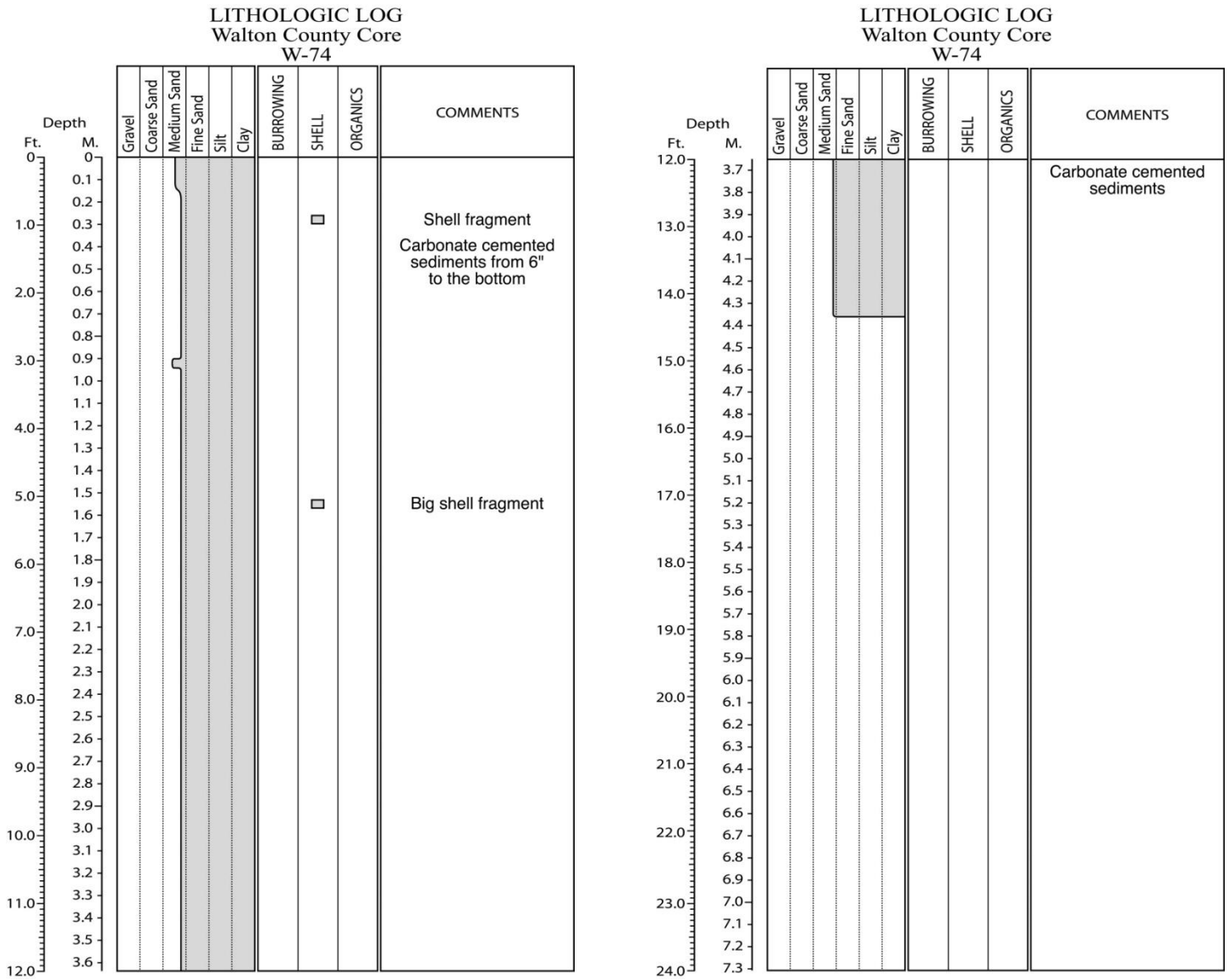

Figure E.74. Core W-74 log.

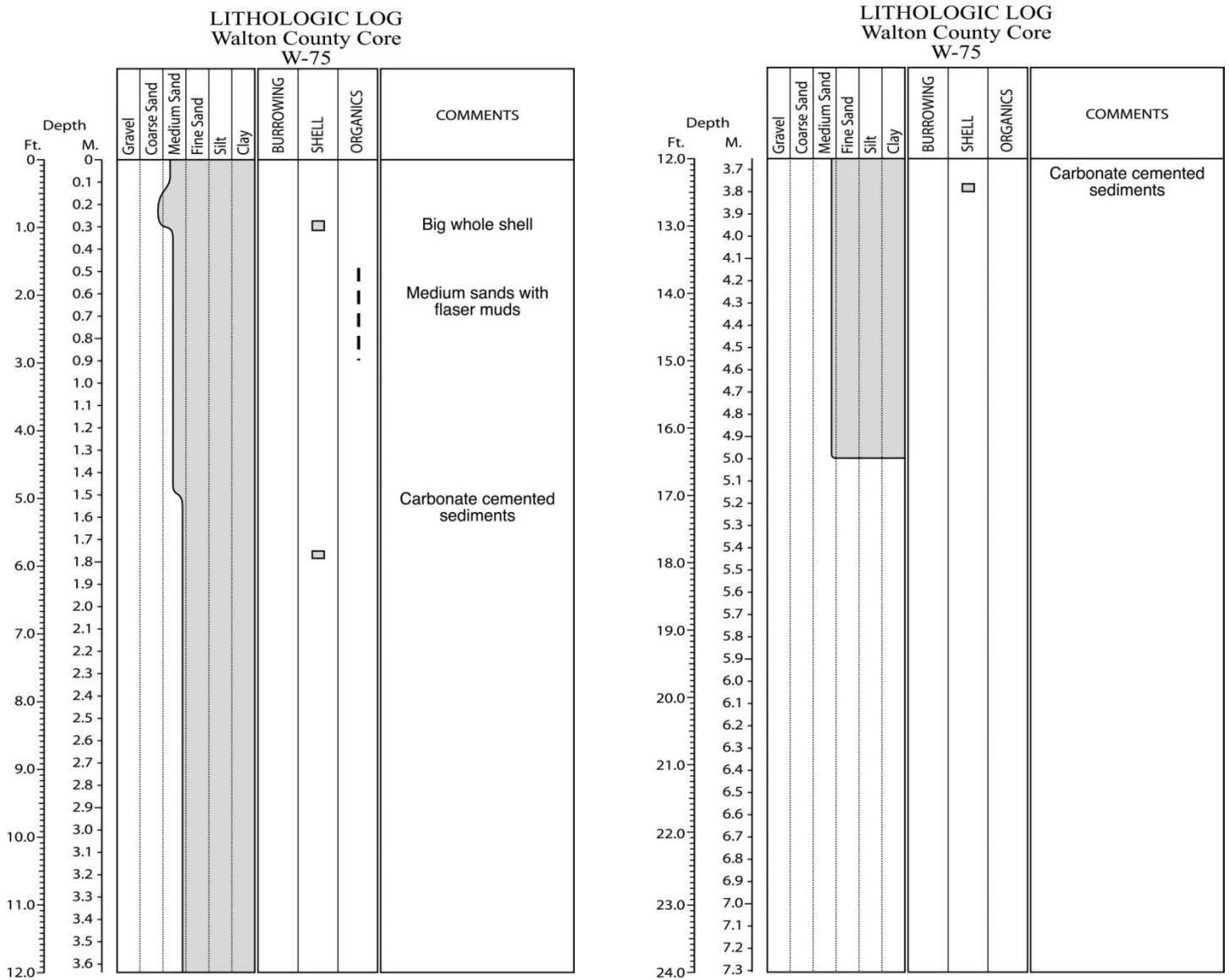

Figure E.75. Core W-75 log.

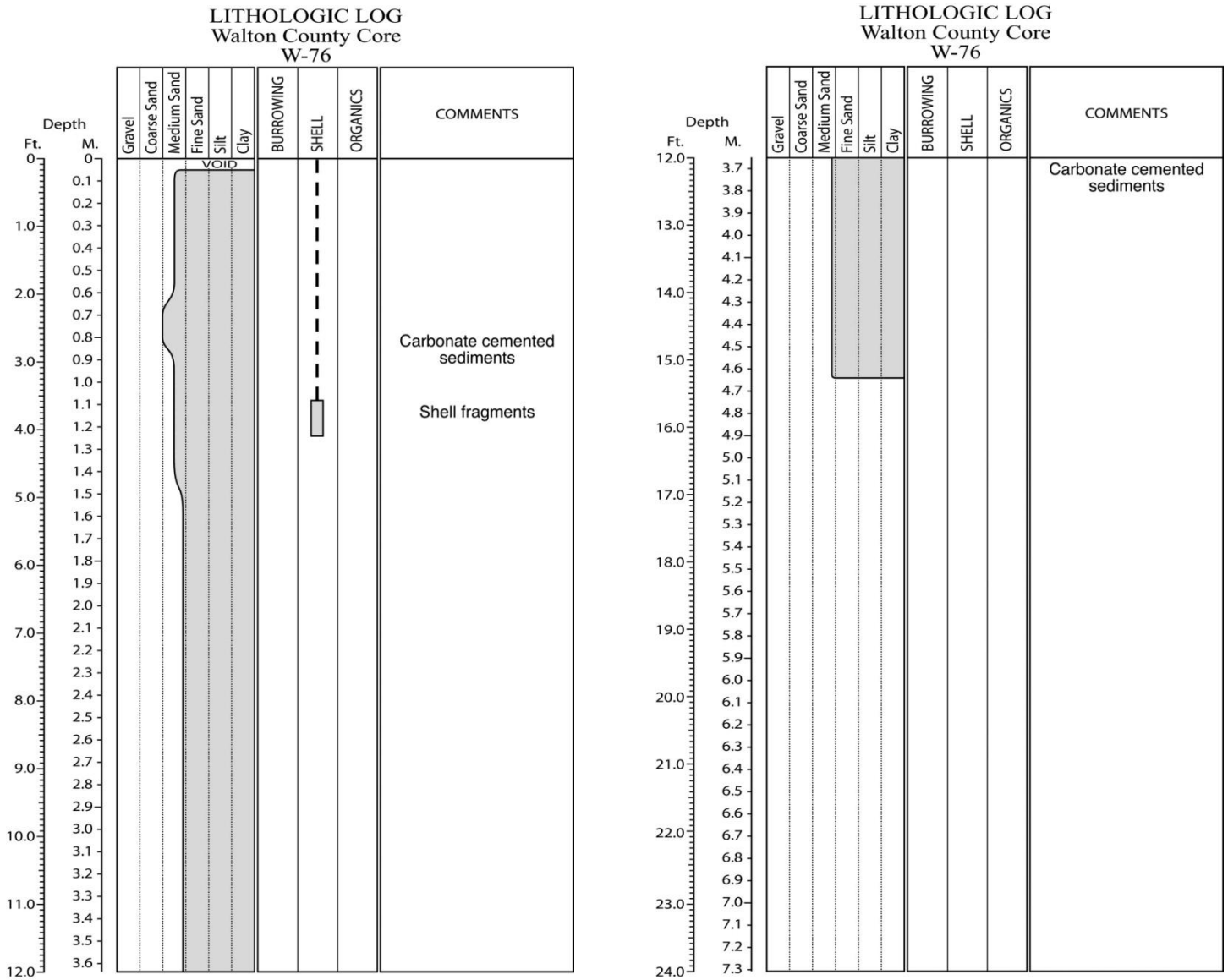

Figure E.76. Core W-76 log.

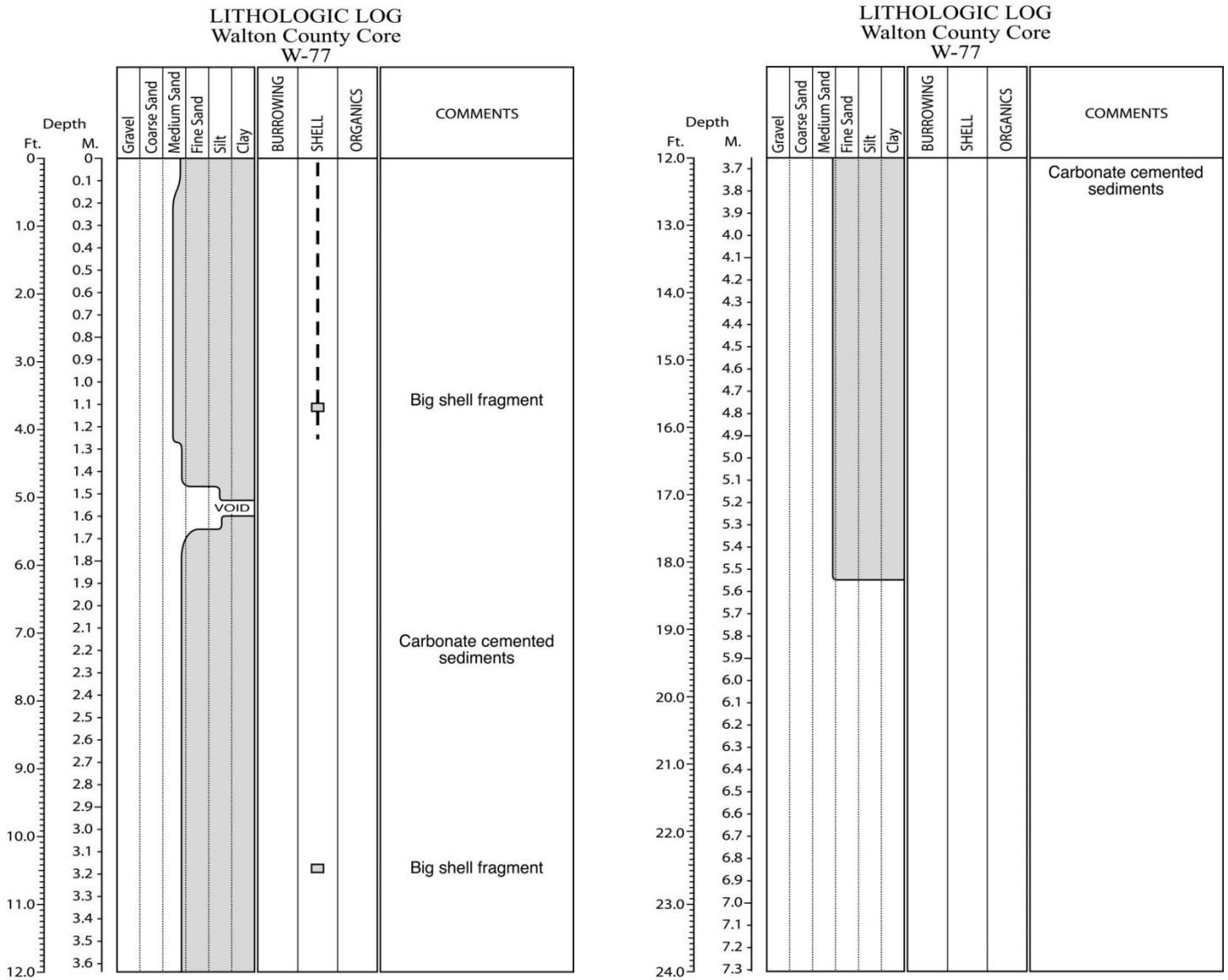

Figure E.77. Core W-77 log.

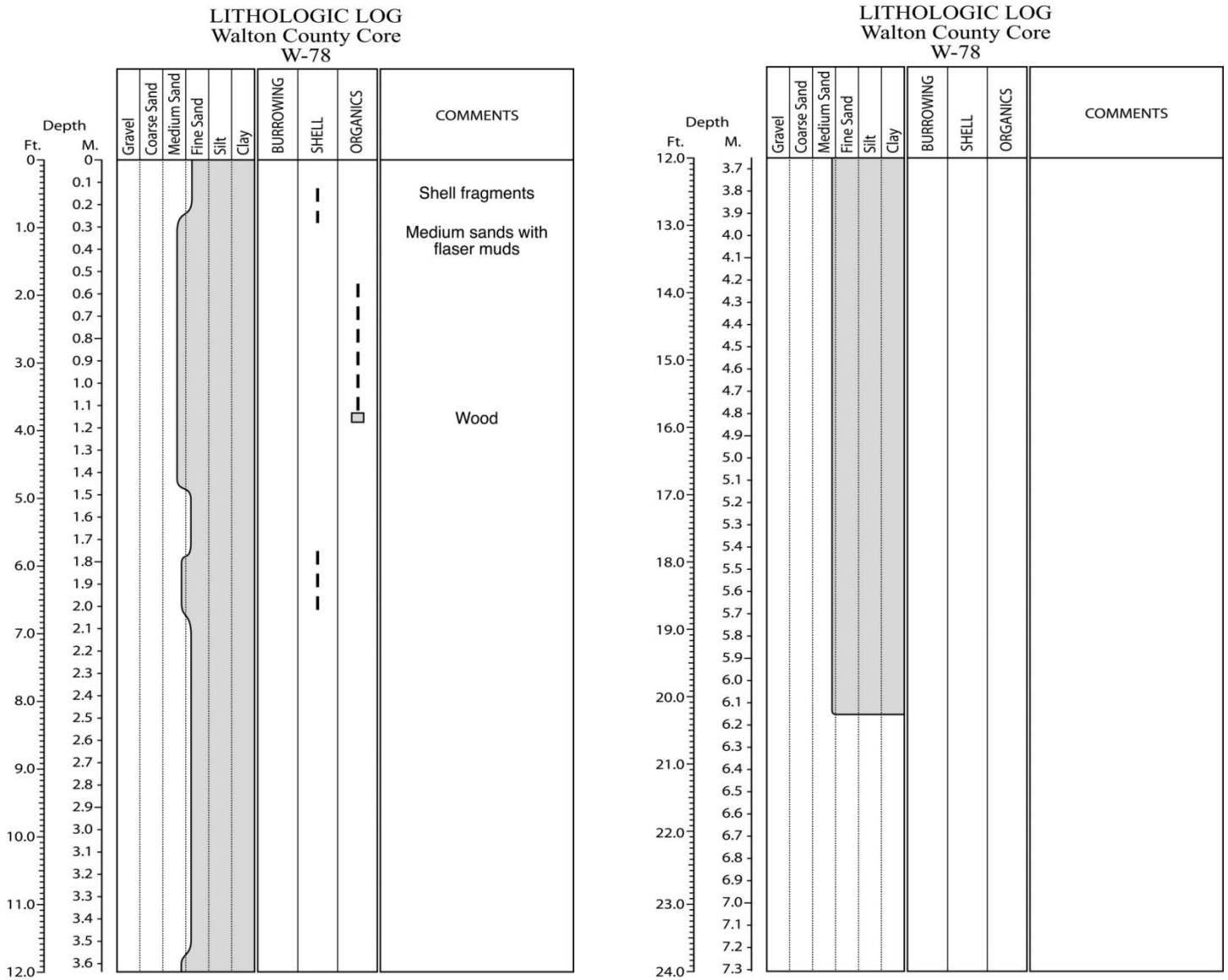

Figure E.78. Core W-78 log.

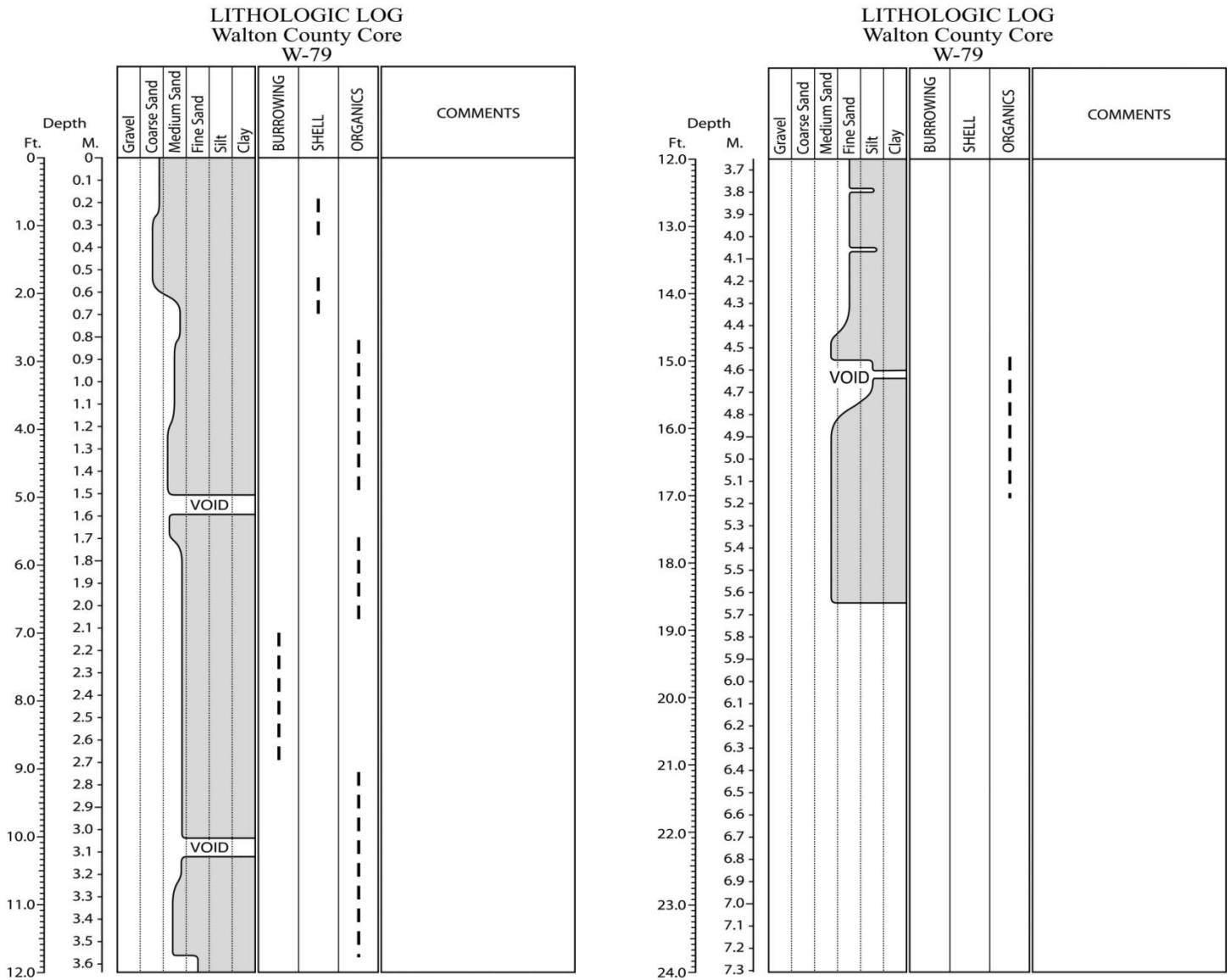

Figure E.79. Core W-79 log.

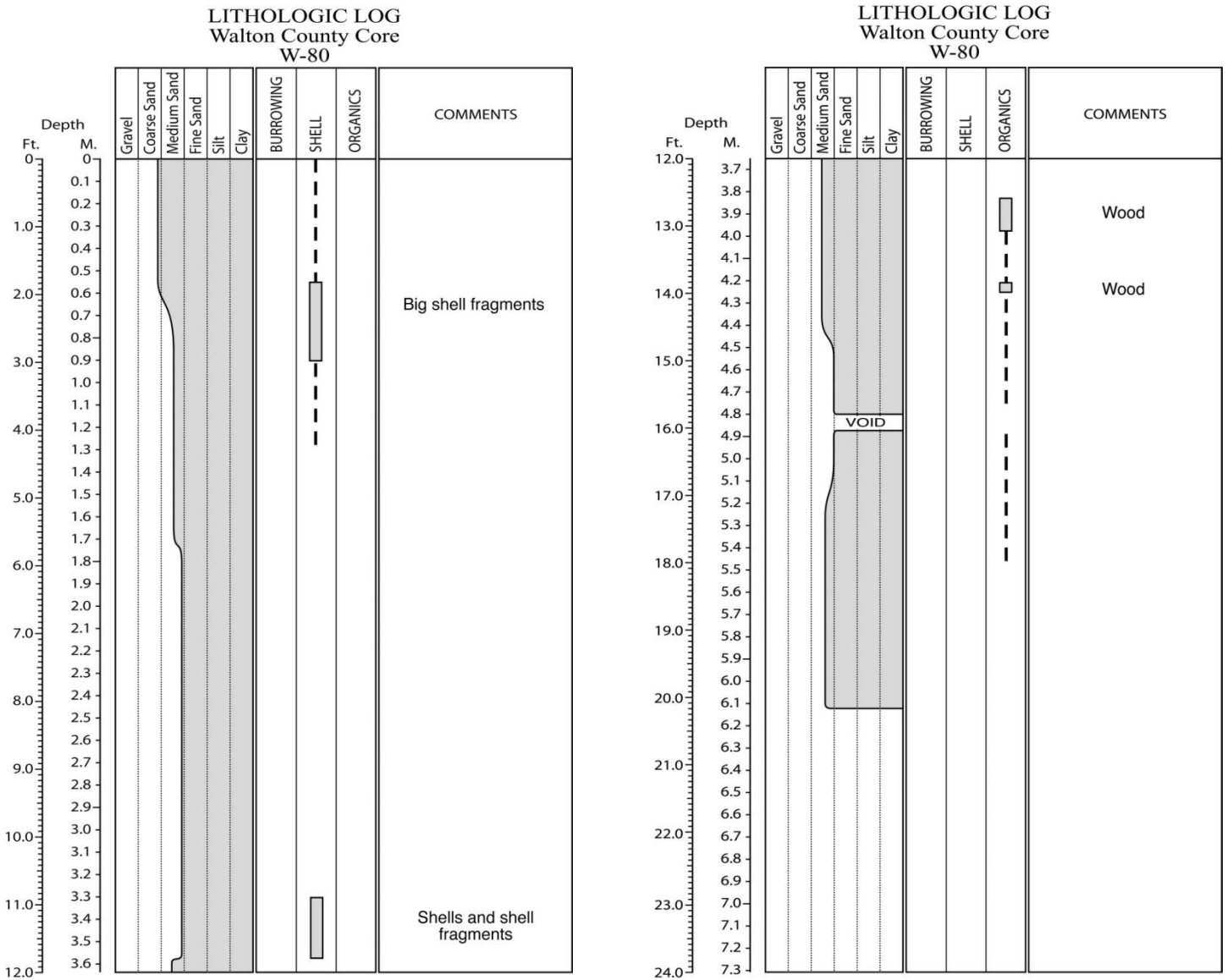

Figure E.80. Core W-80 log.

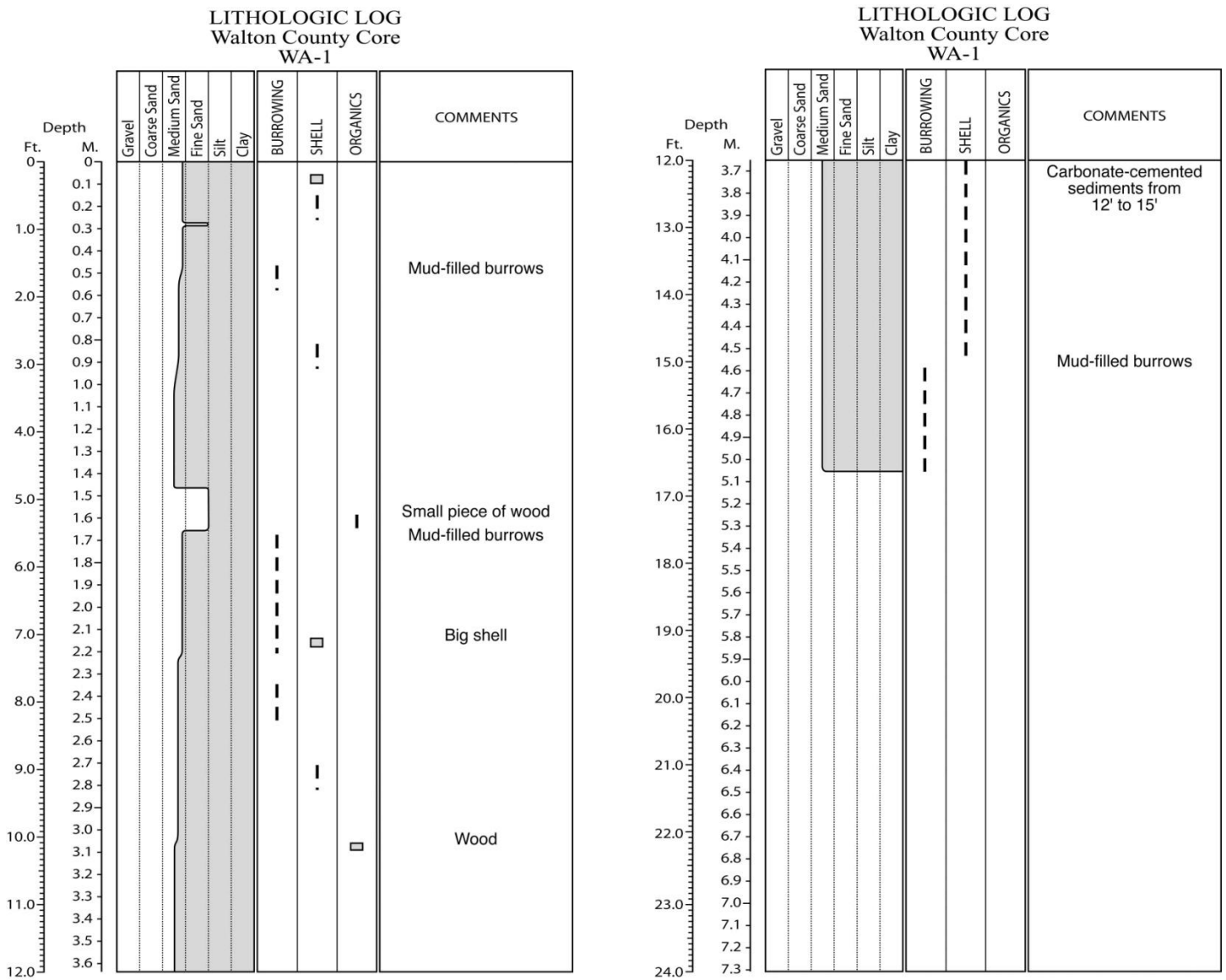

Figure E.81. Core WA-1 log.

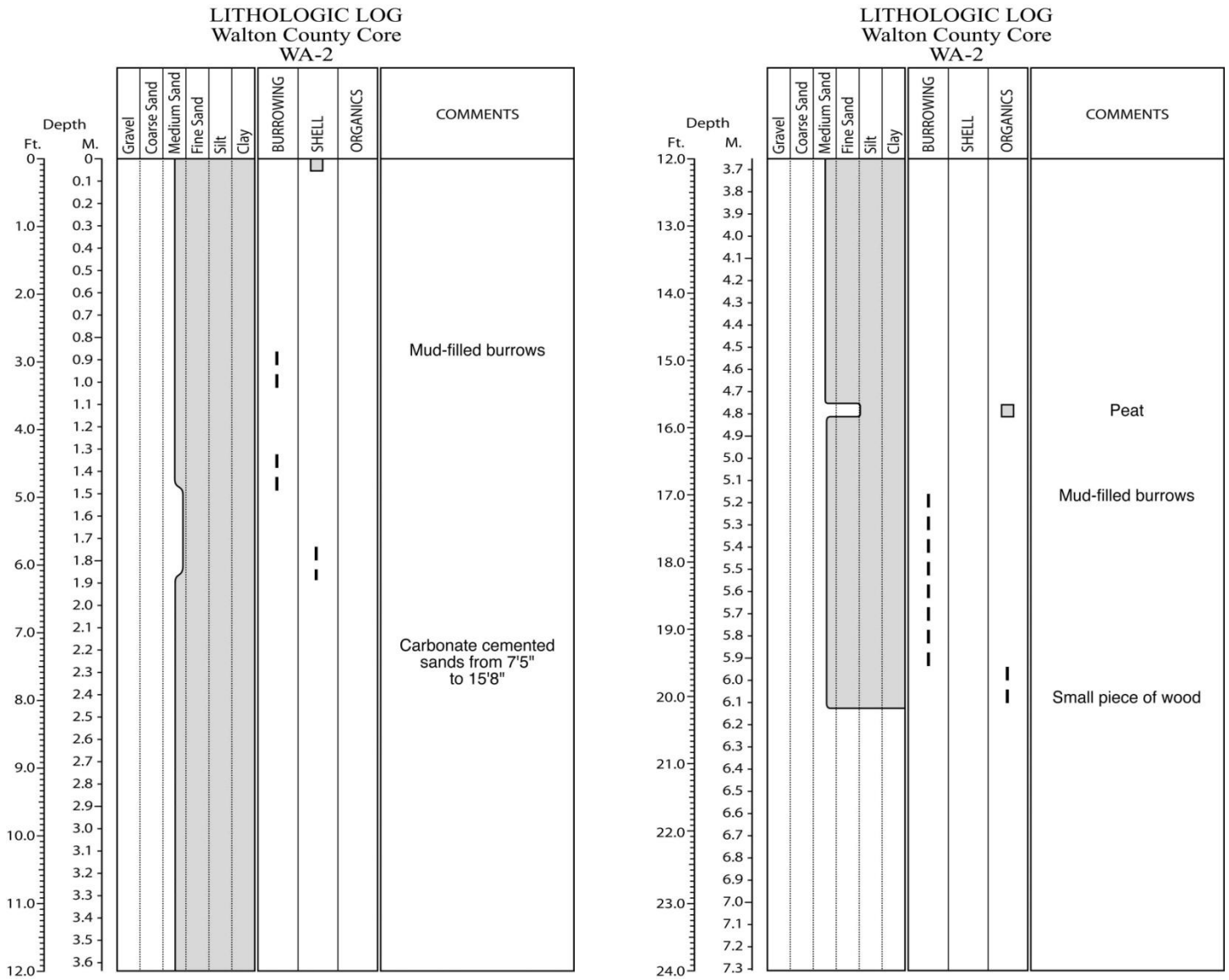

Figure E.82. Core WA-2 log.

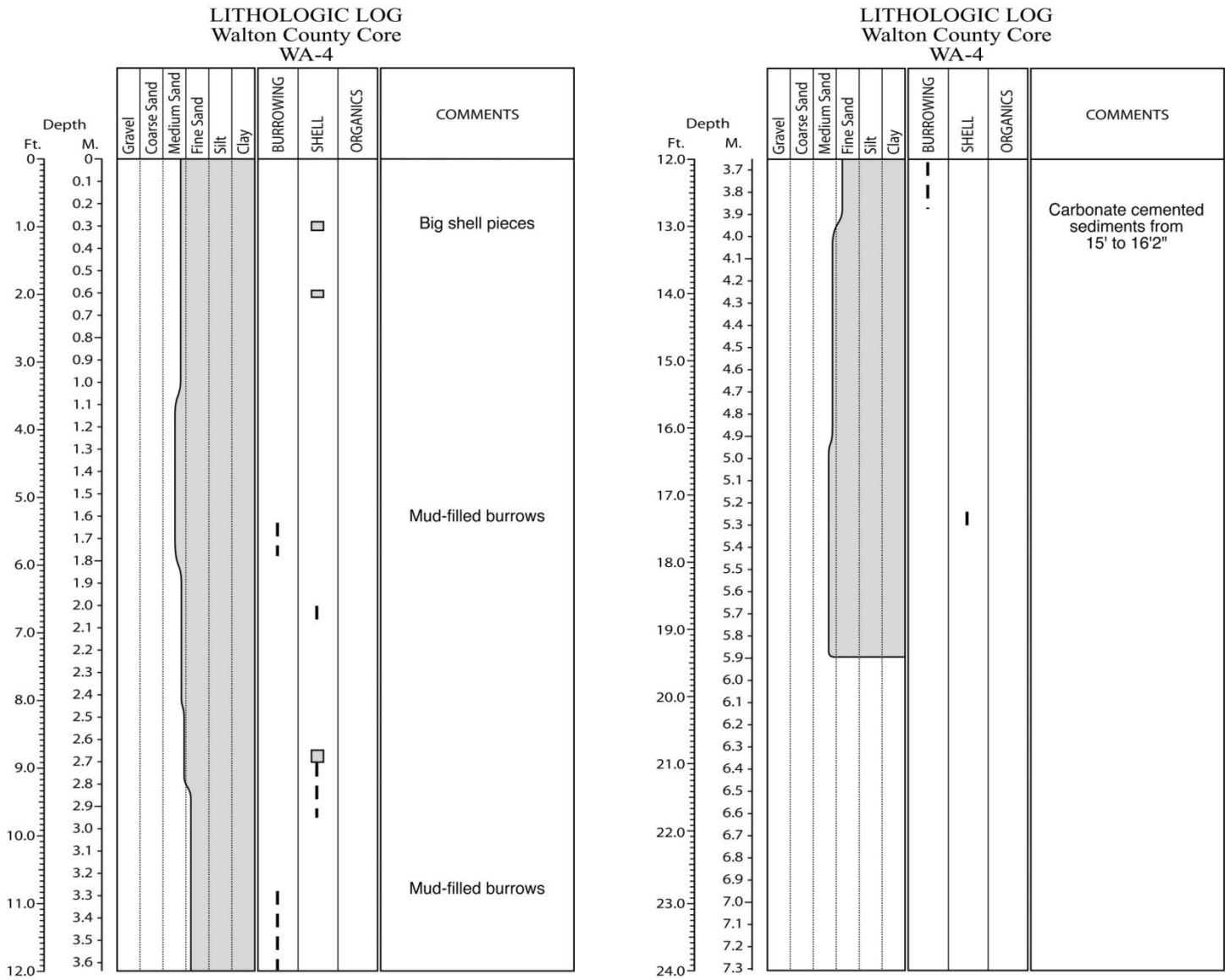

Figure E.83. Core WA-4 log.

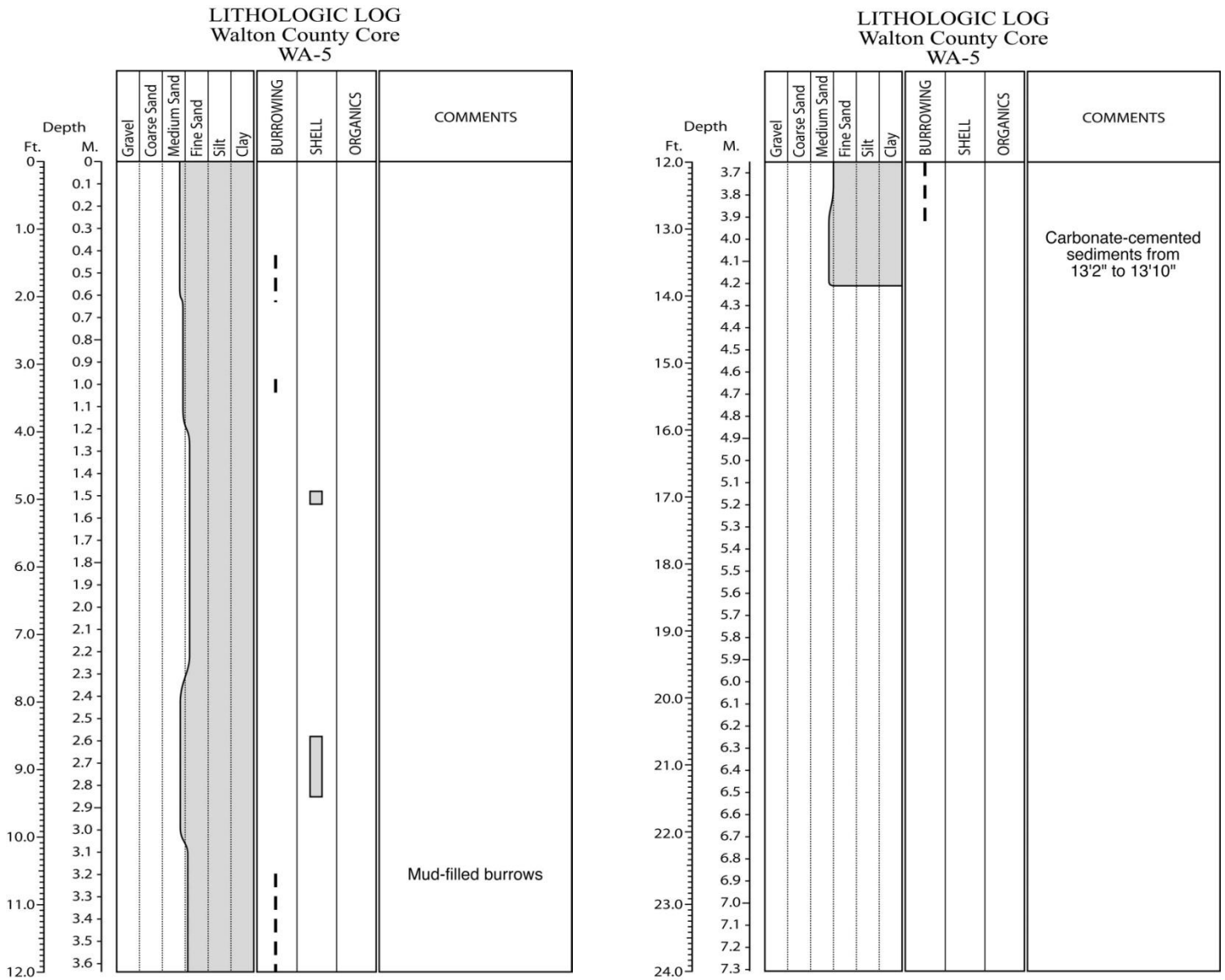

Figure E.84. Core WA-5 log.

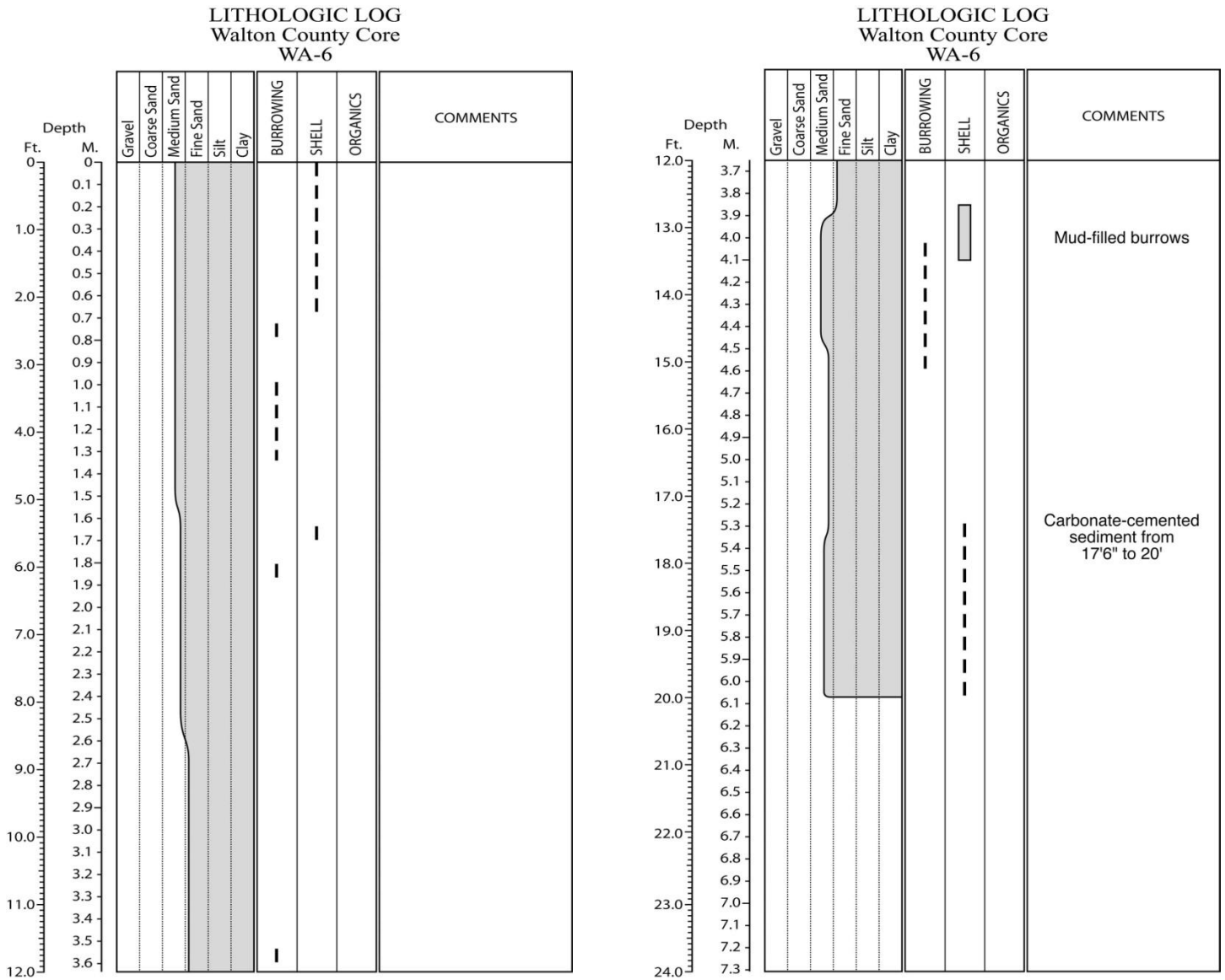

Figure E.85. Core WA-6 log.

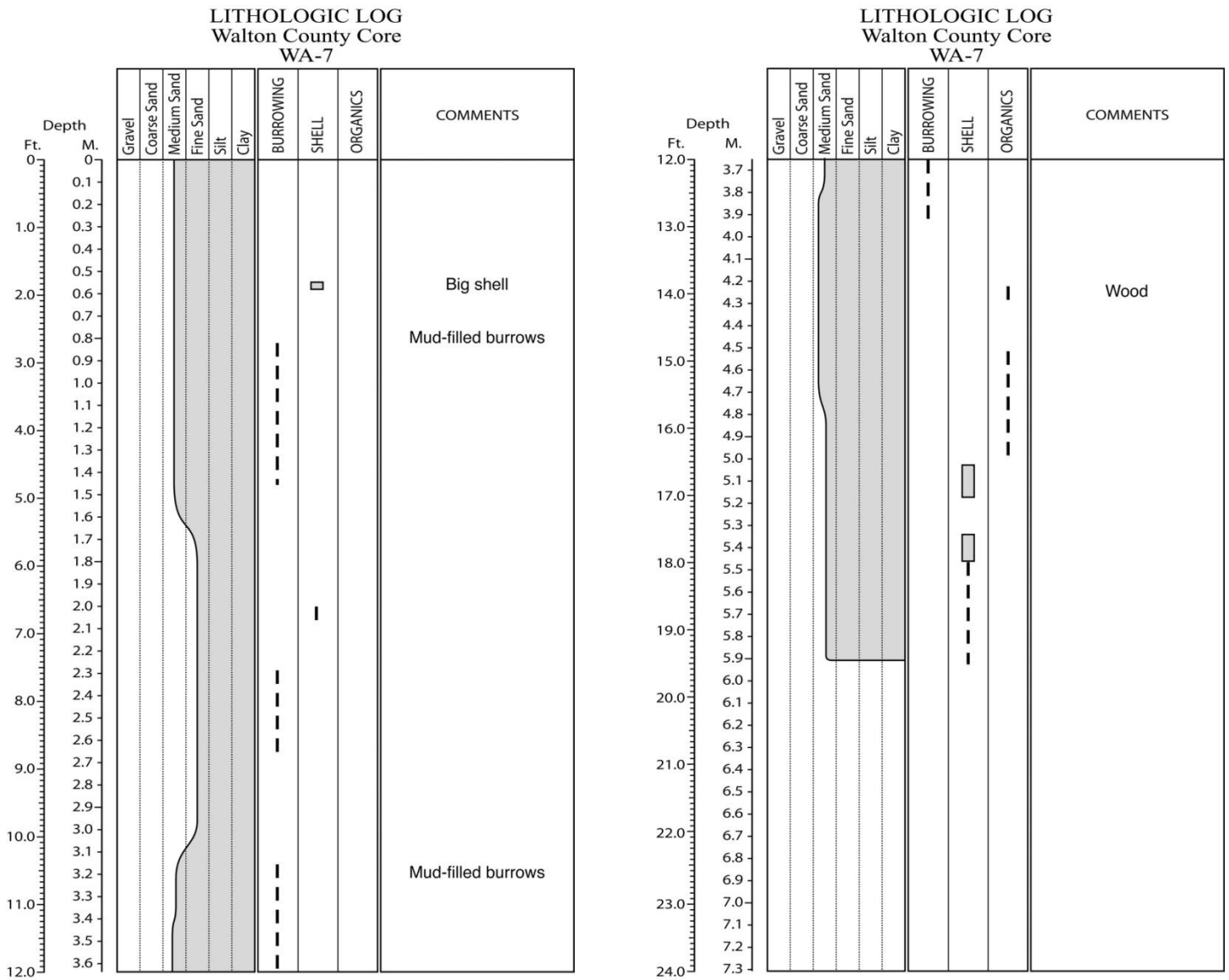

Figure E.86. Core WA-7 log.

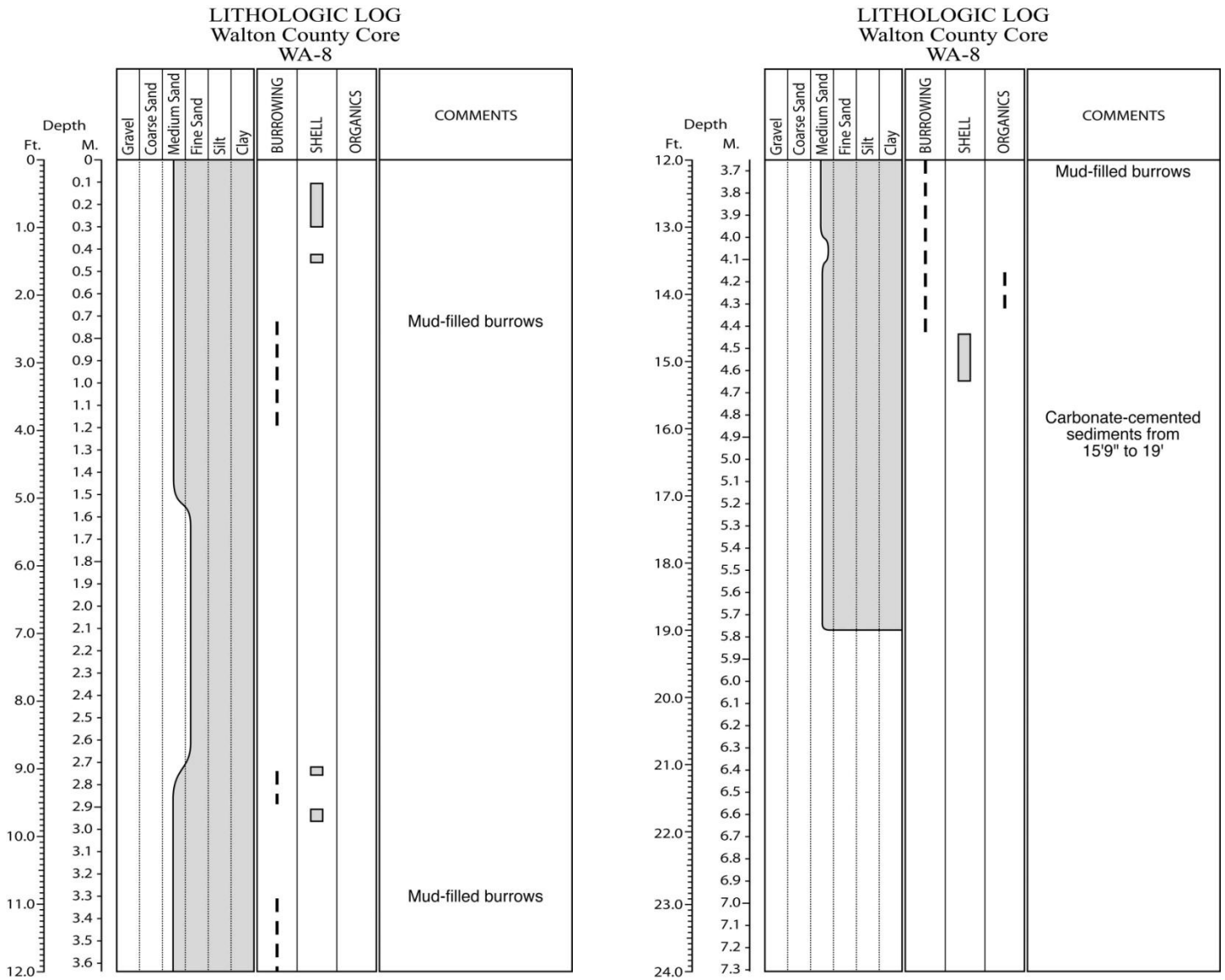

Figure E.87. Core WA-8 log.

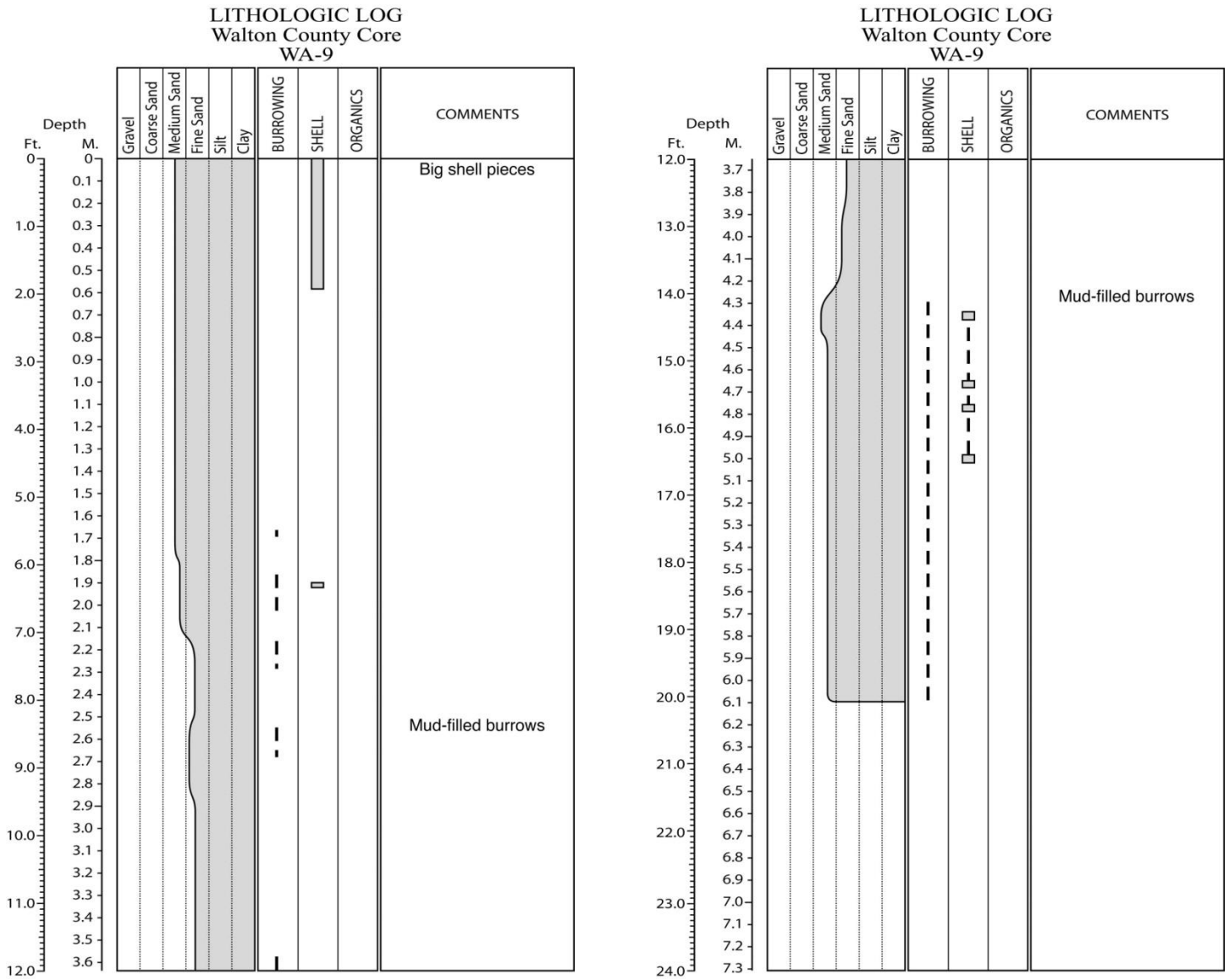

Figure E.88. Core WA-9 log.

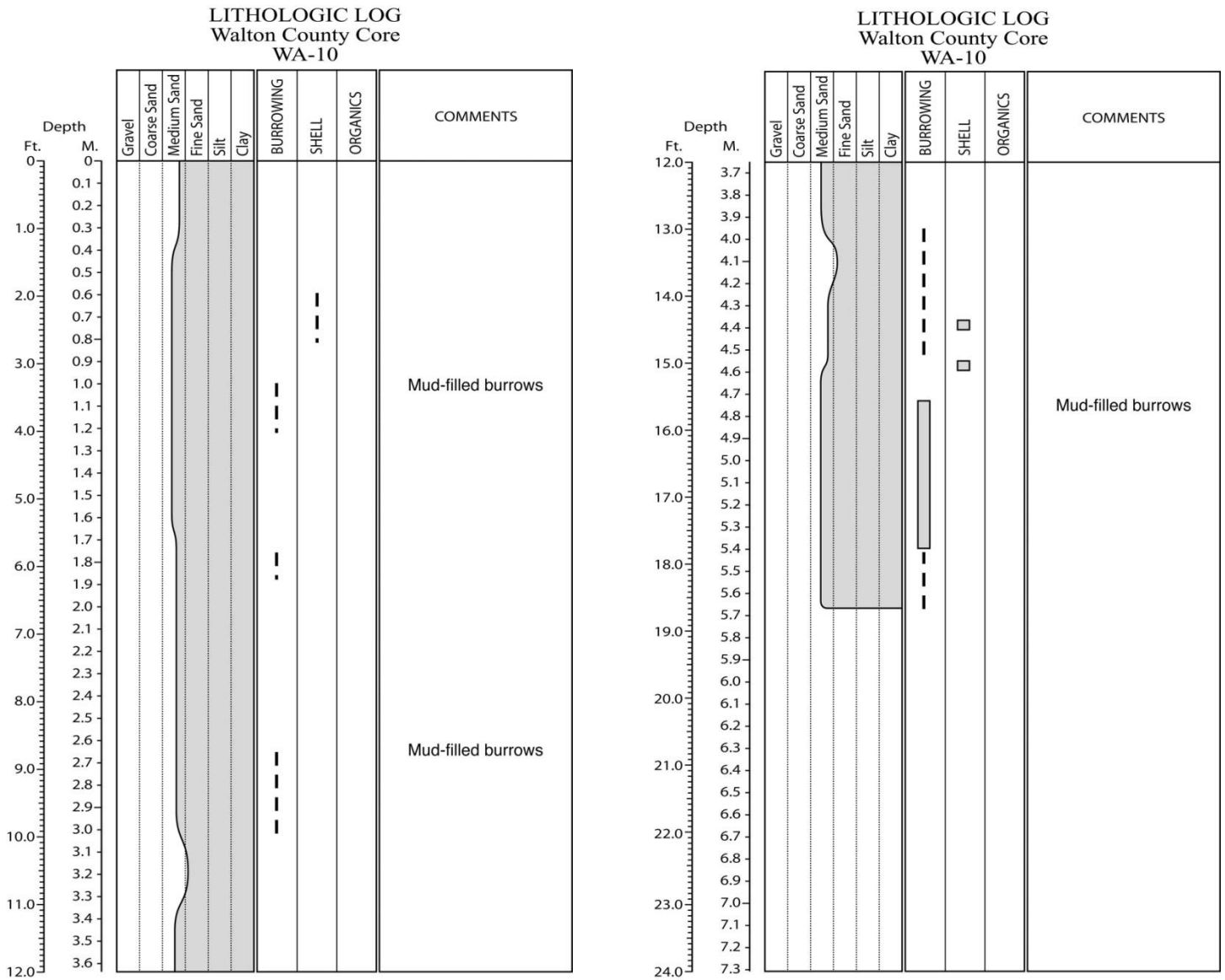

Figure E.89. Core WA-10 log.

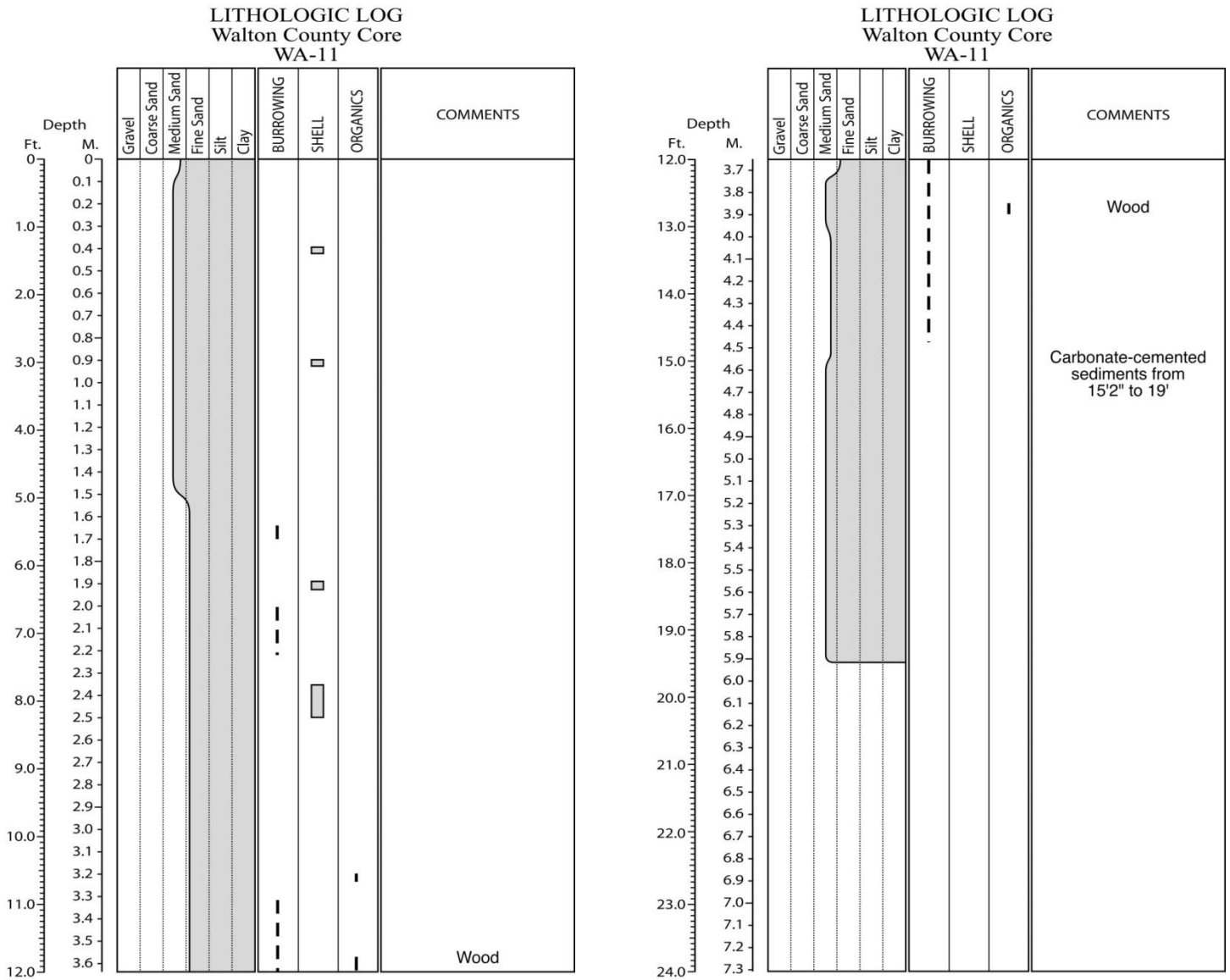

Figure E.90. Core WA-11 log.

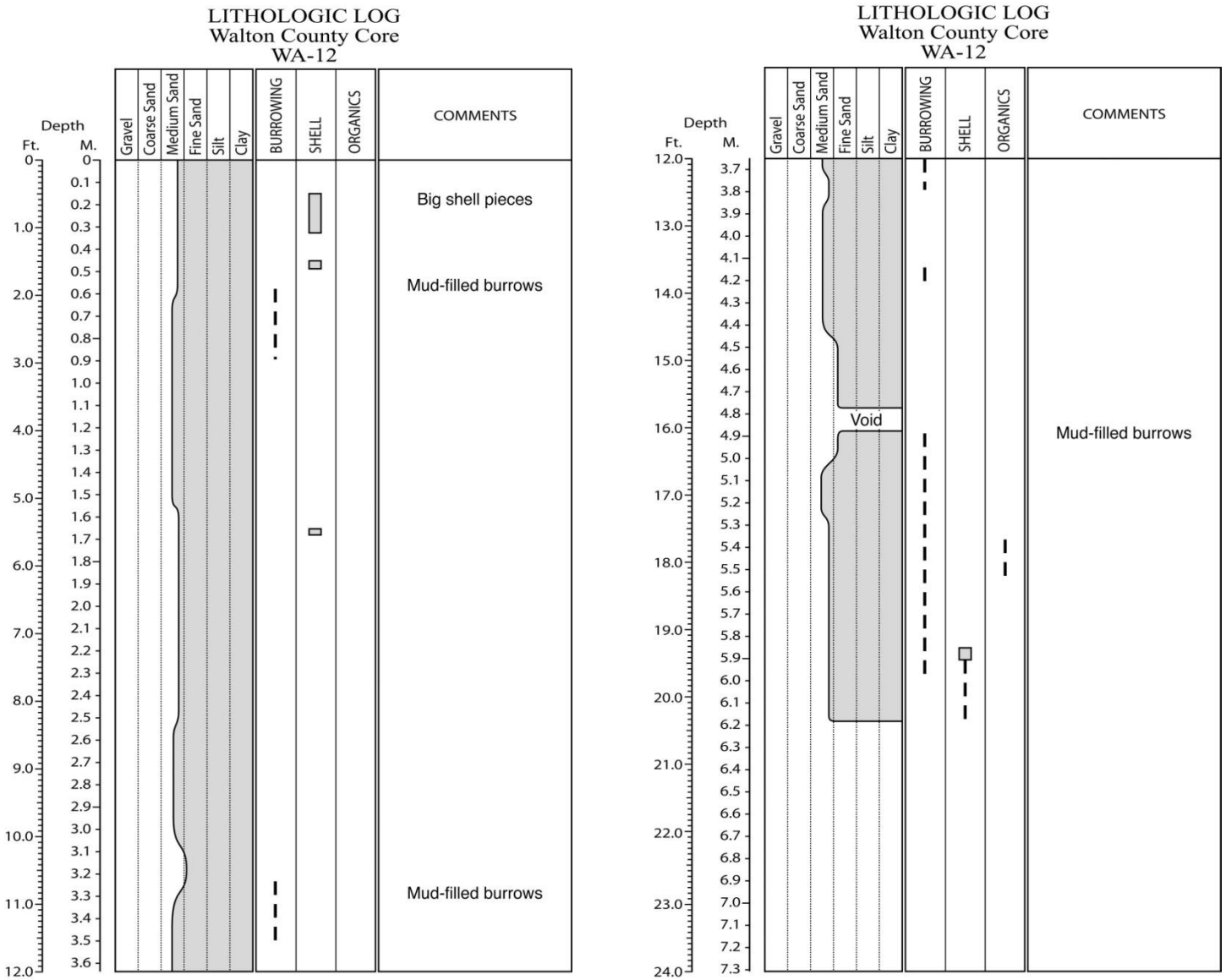

Figure E.91. Core WA-12 log.

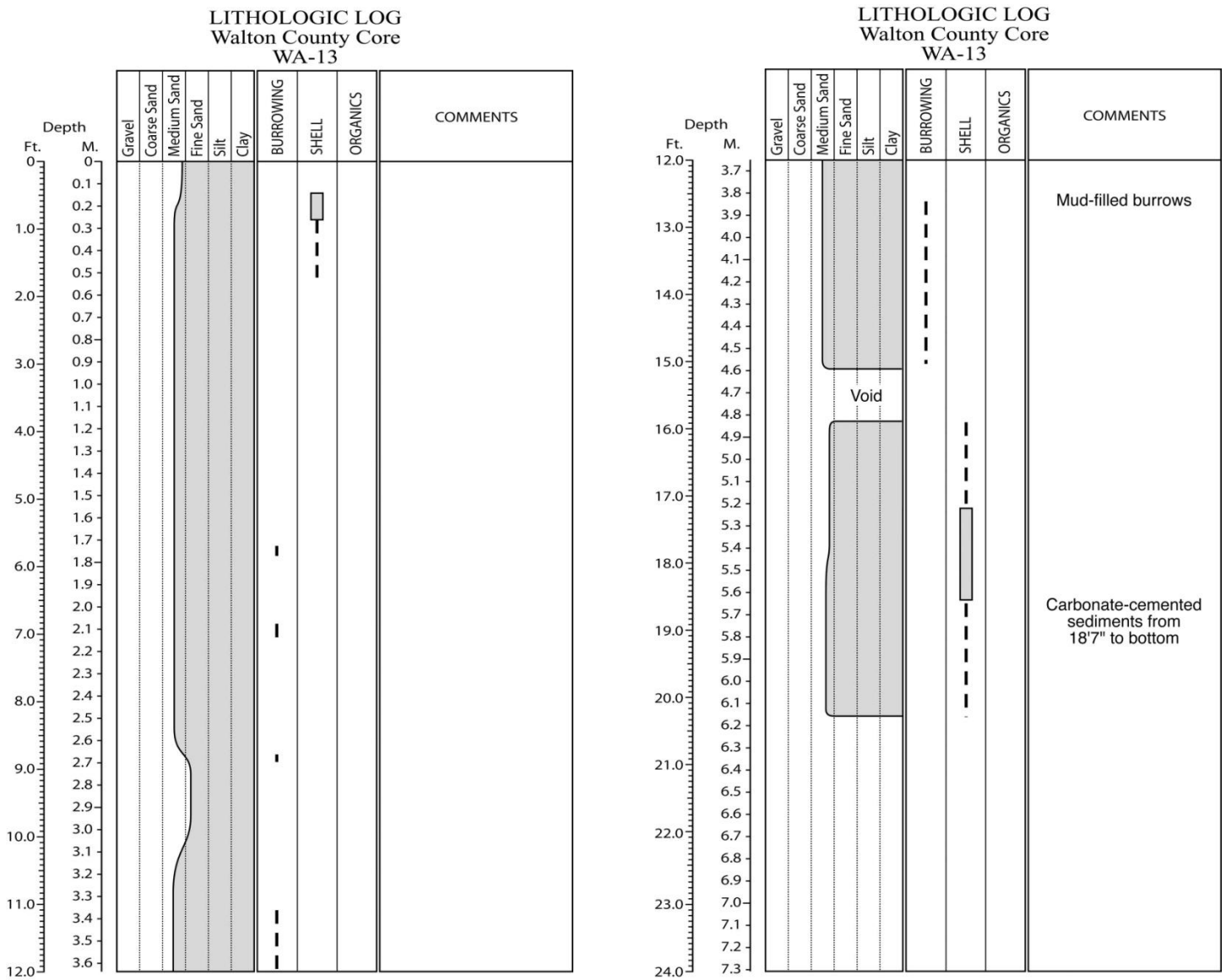

Figure E.92. Core WA-13 log.

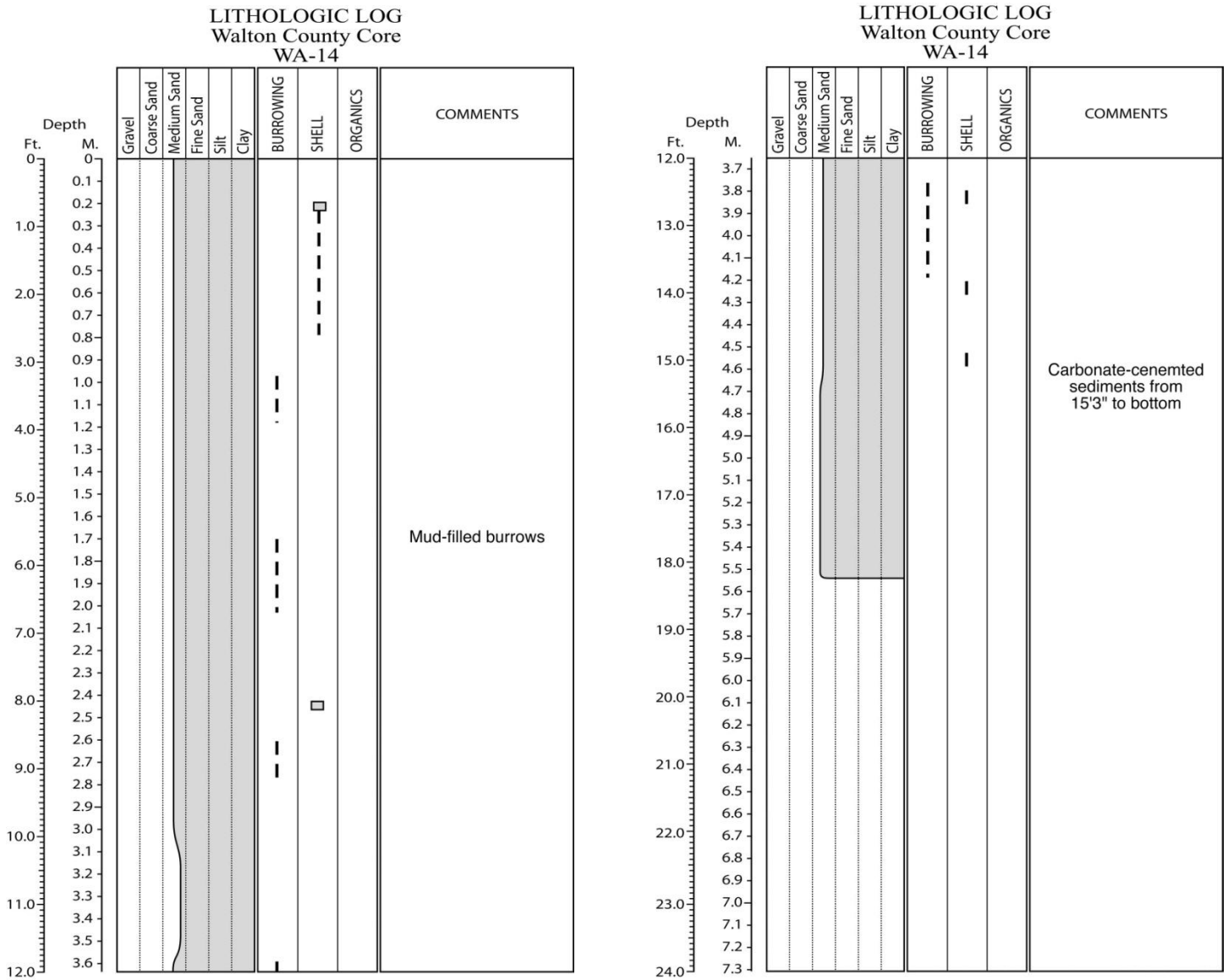

Figure E.93. Core WA-14 log.

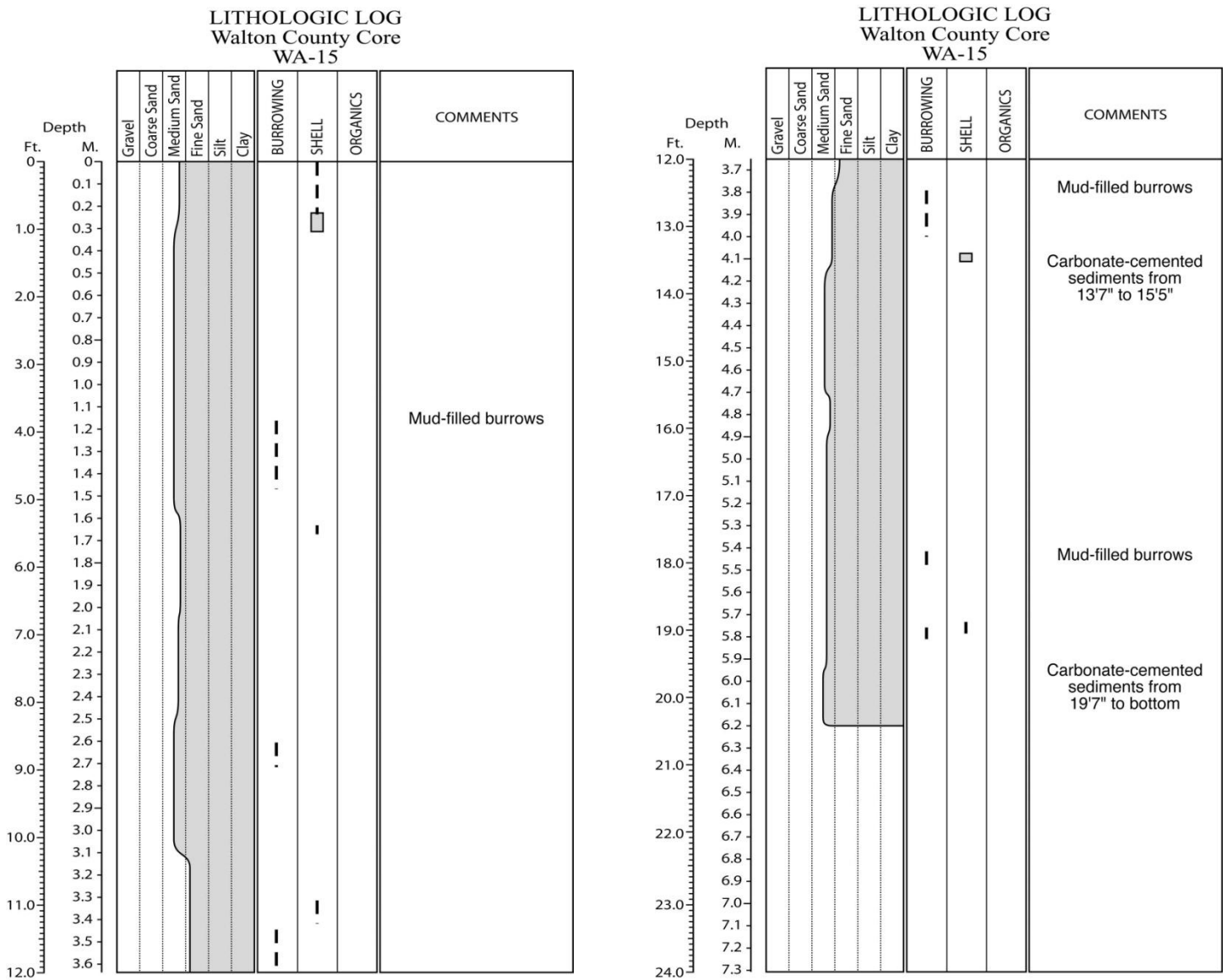

Figure E.94. Core WA-15 log.

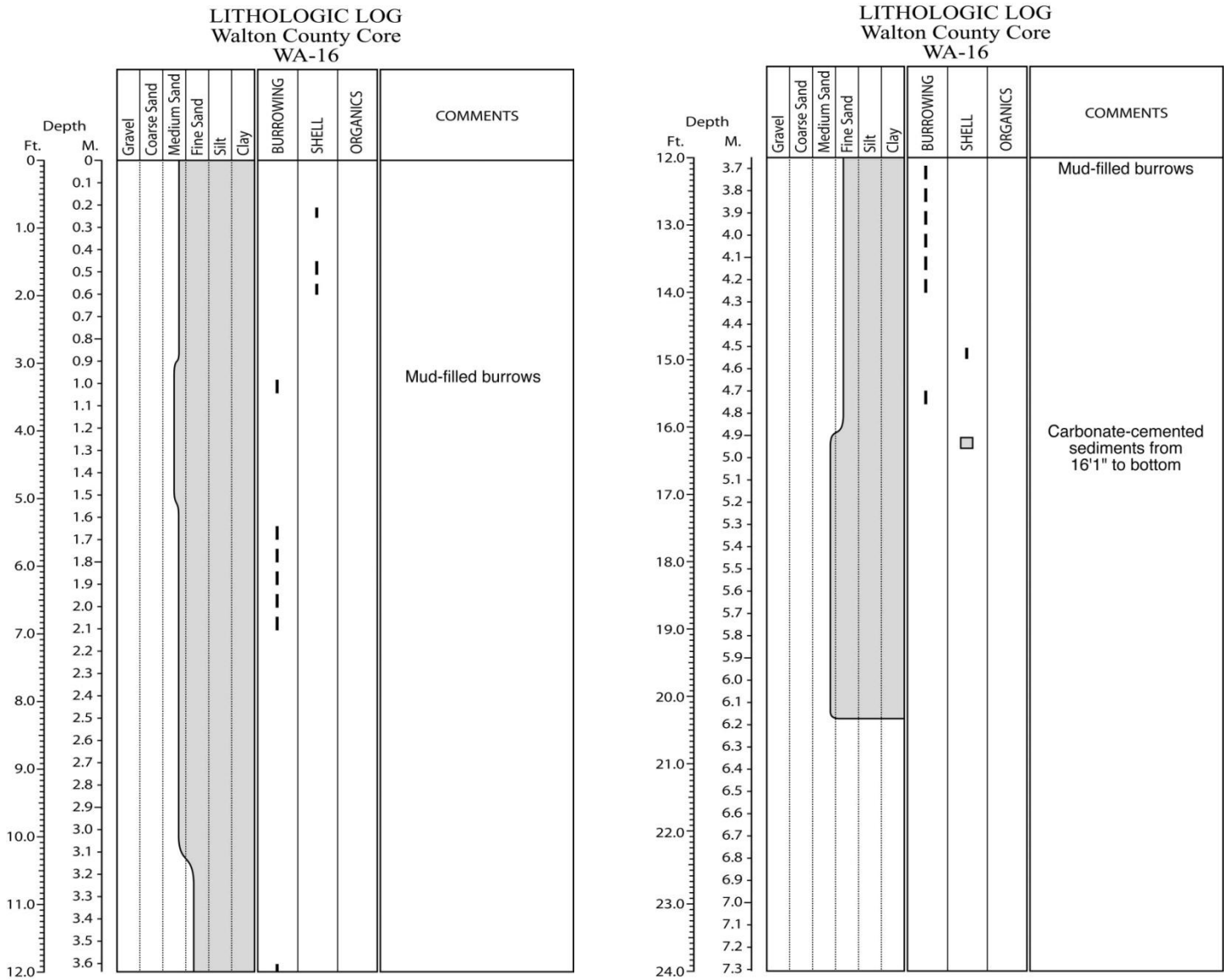

Figure E.95. Core WA-16 log.

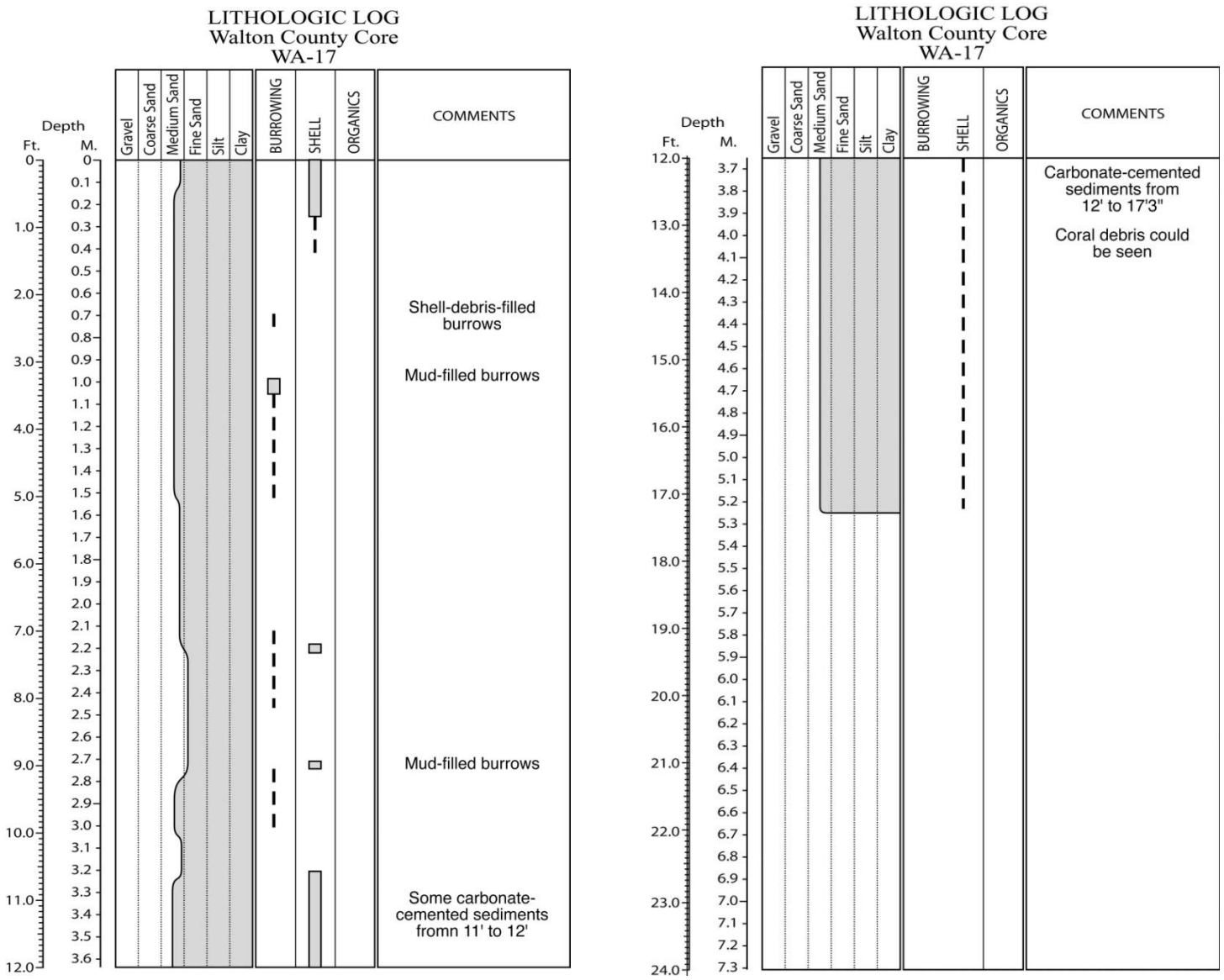

Figure E.96. Core WA-17 log.

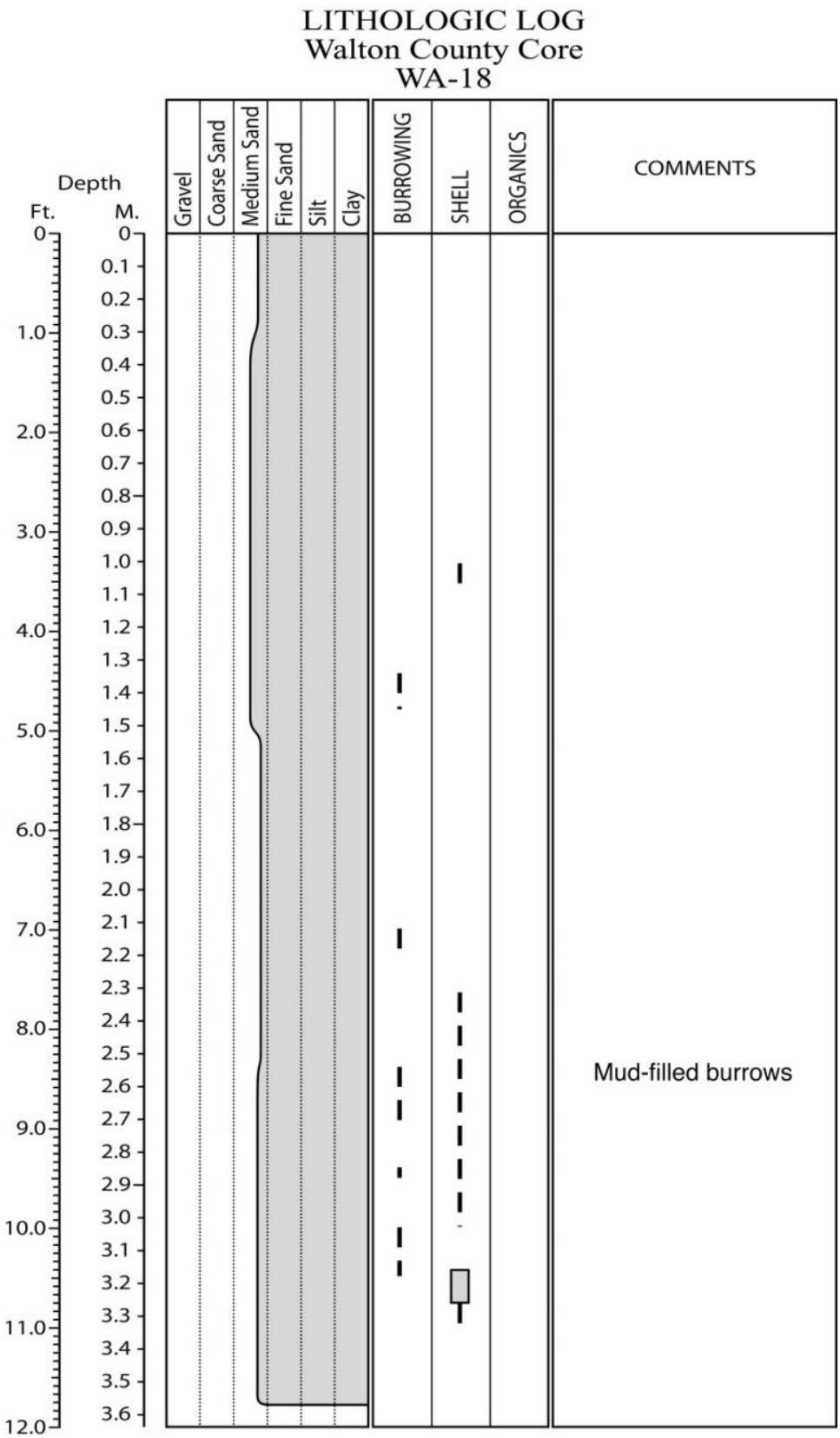

Figure E.97. Core WA-18 log.

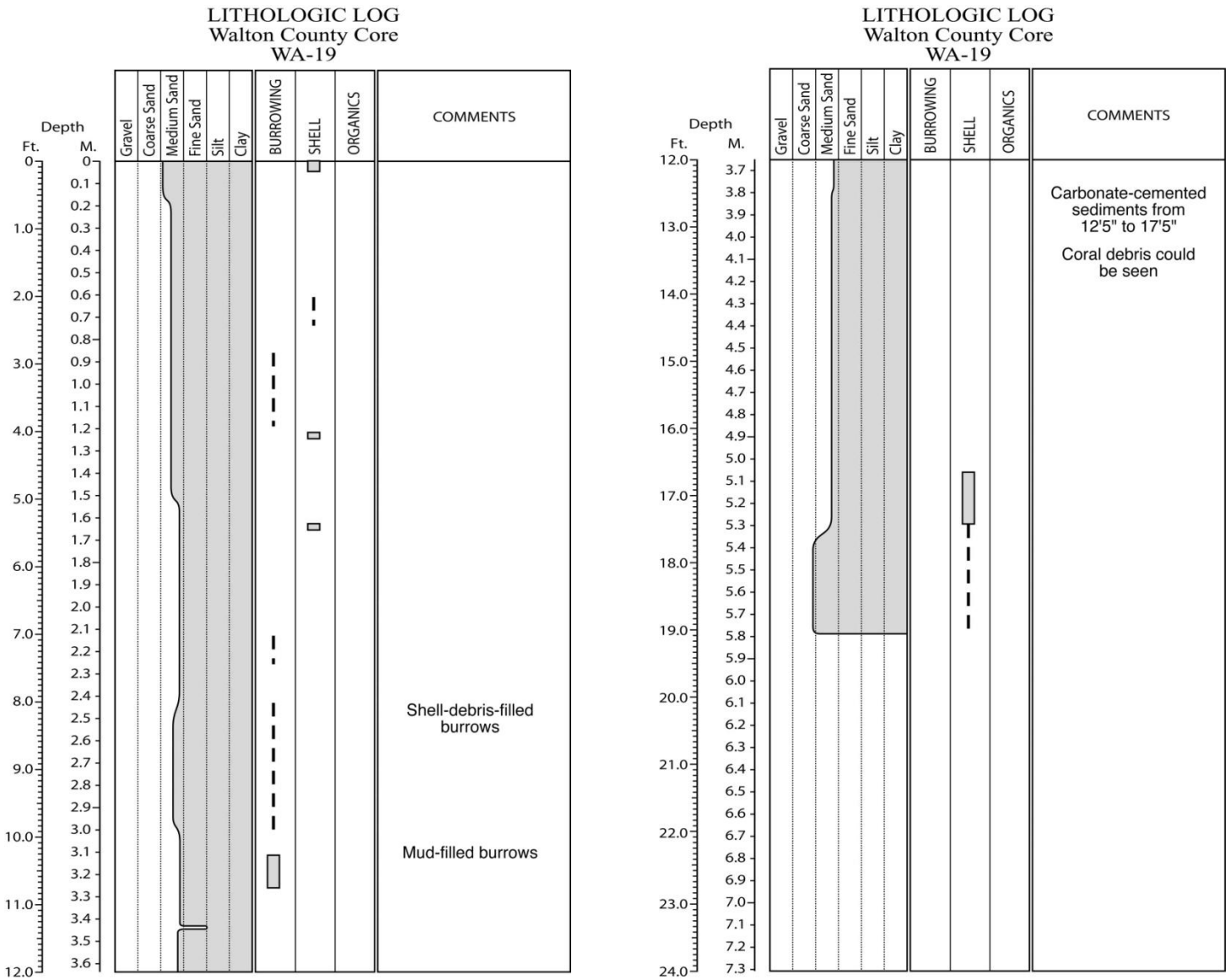

Figure E.98. Core WA-19 log.

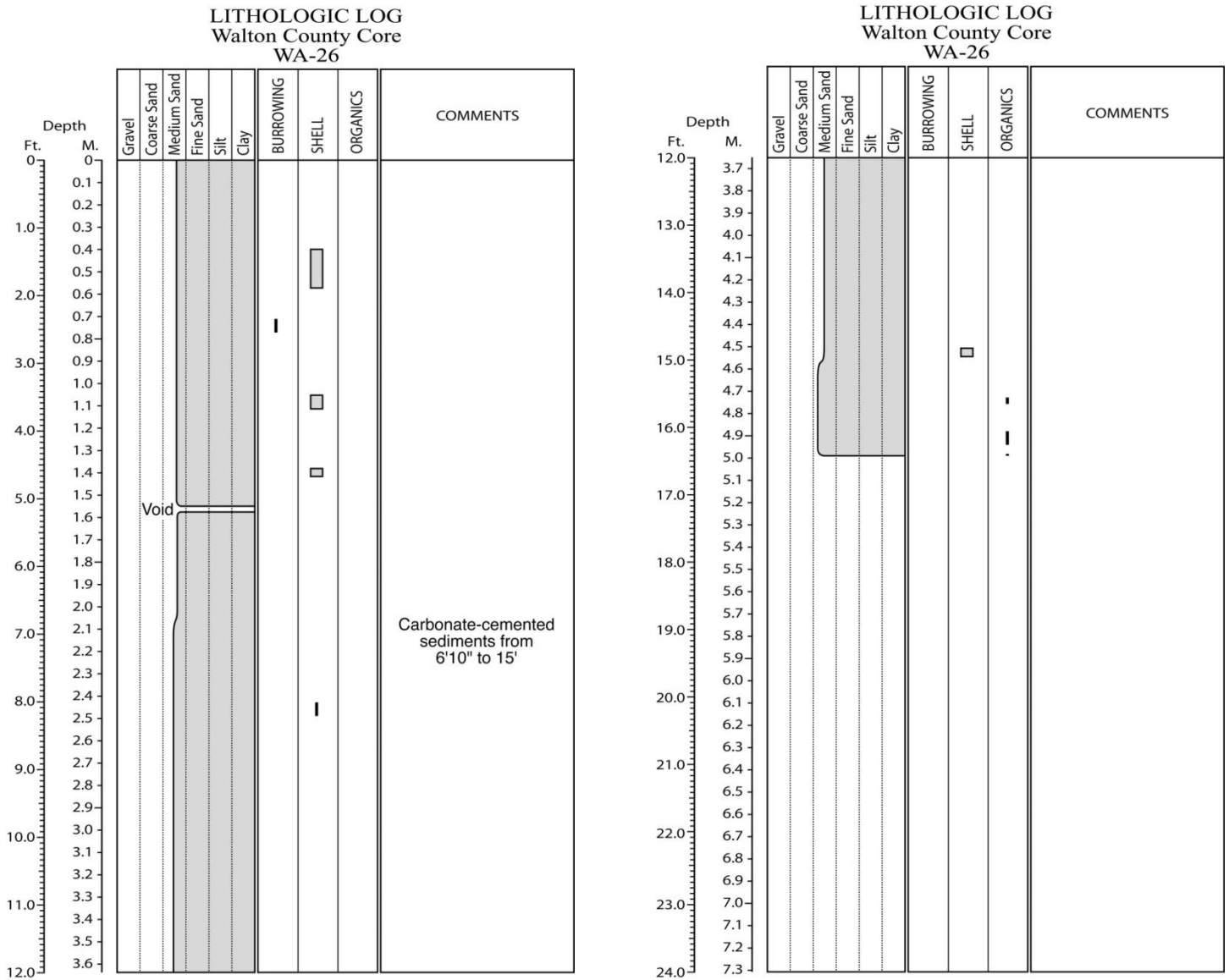

Figure E.99. Core WA-26 log.

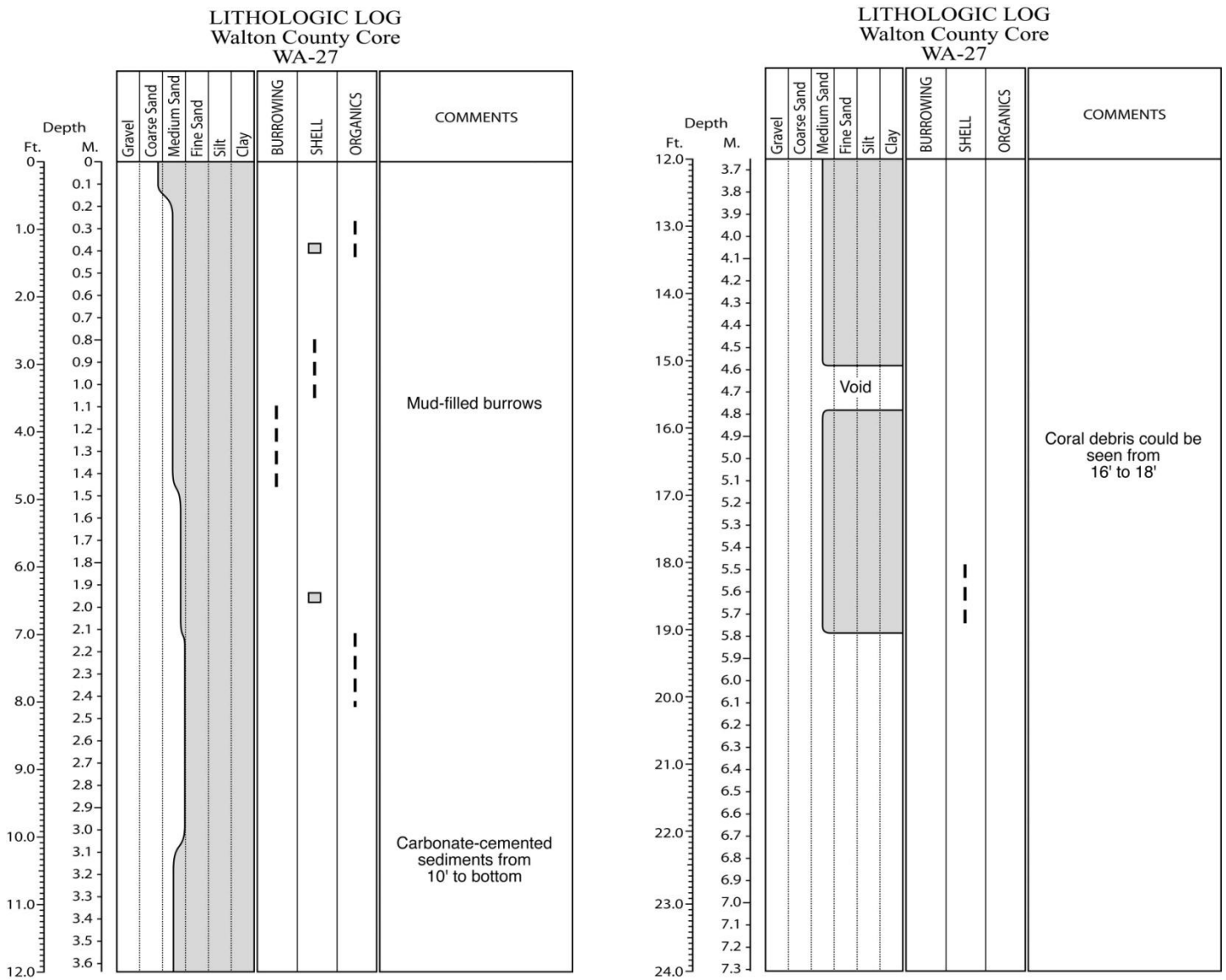

Figure E.100. Core WA-27 log.

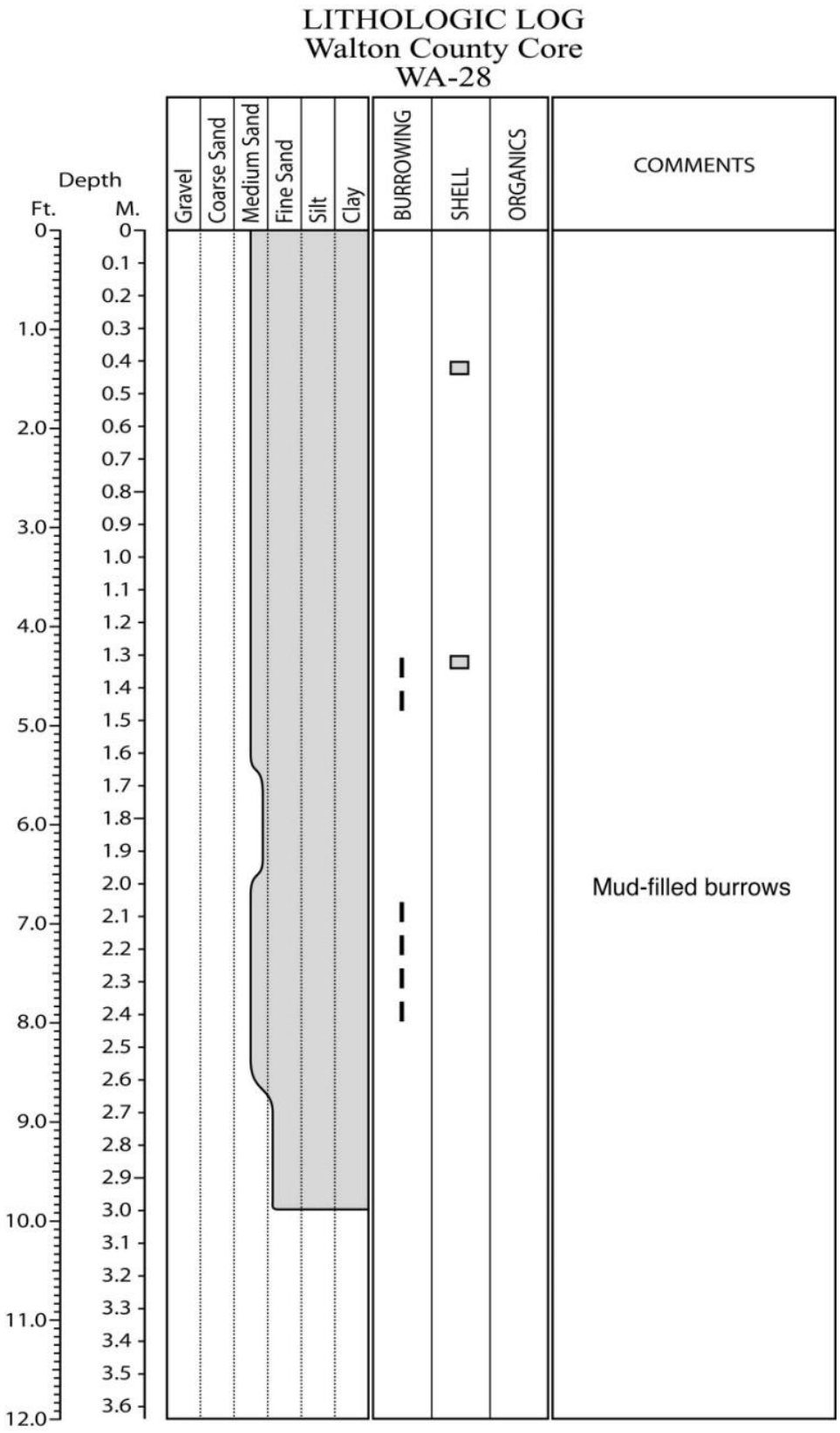

Figure E.101. Core WA-28 log.

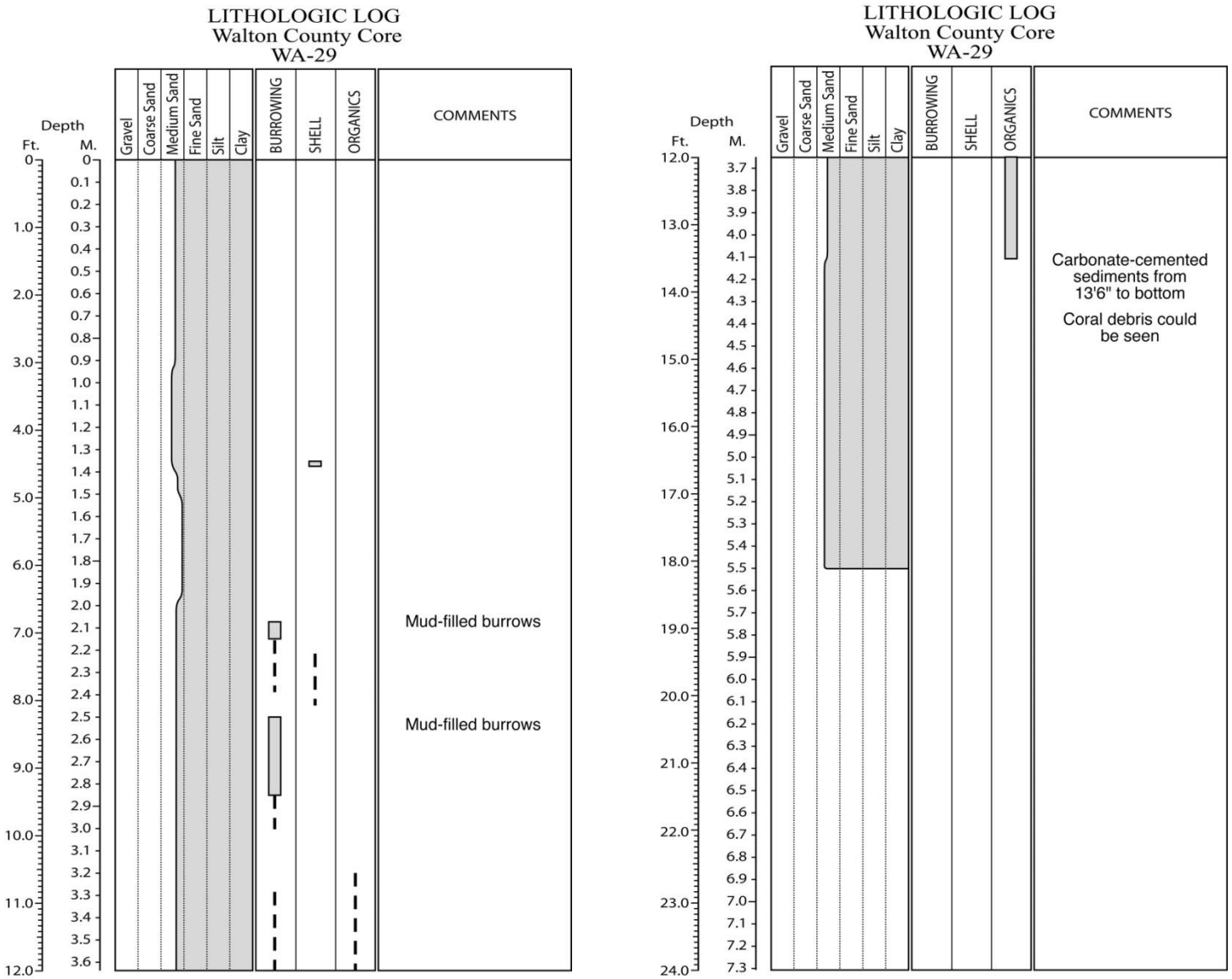

Figure E.102. Core WA-29 log.

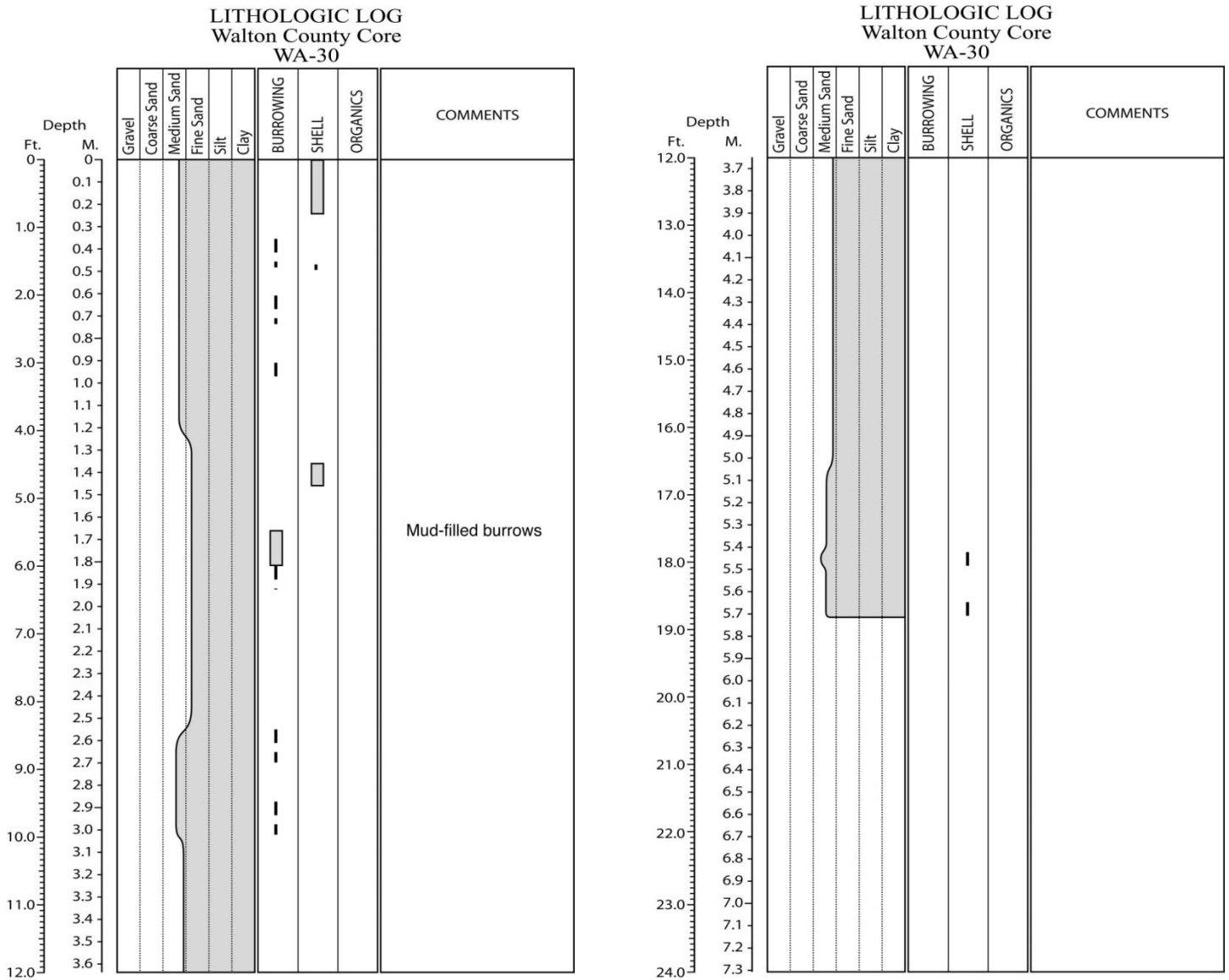

Figure E.103. Core WA-30 log.

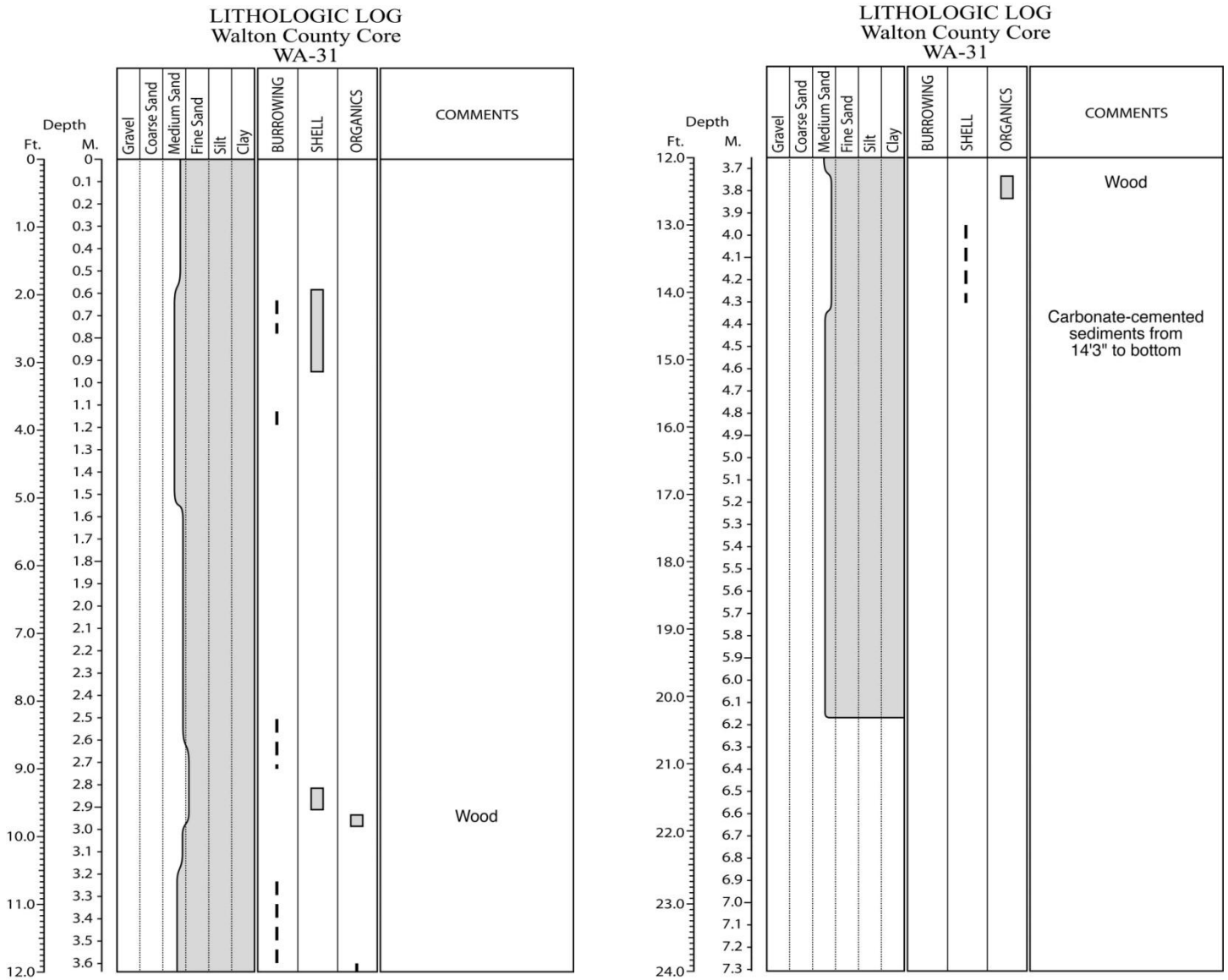

Figure E.104. Core WA-31 log.

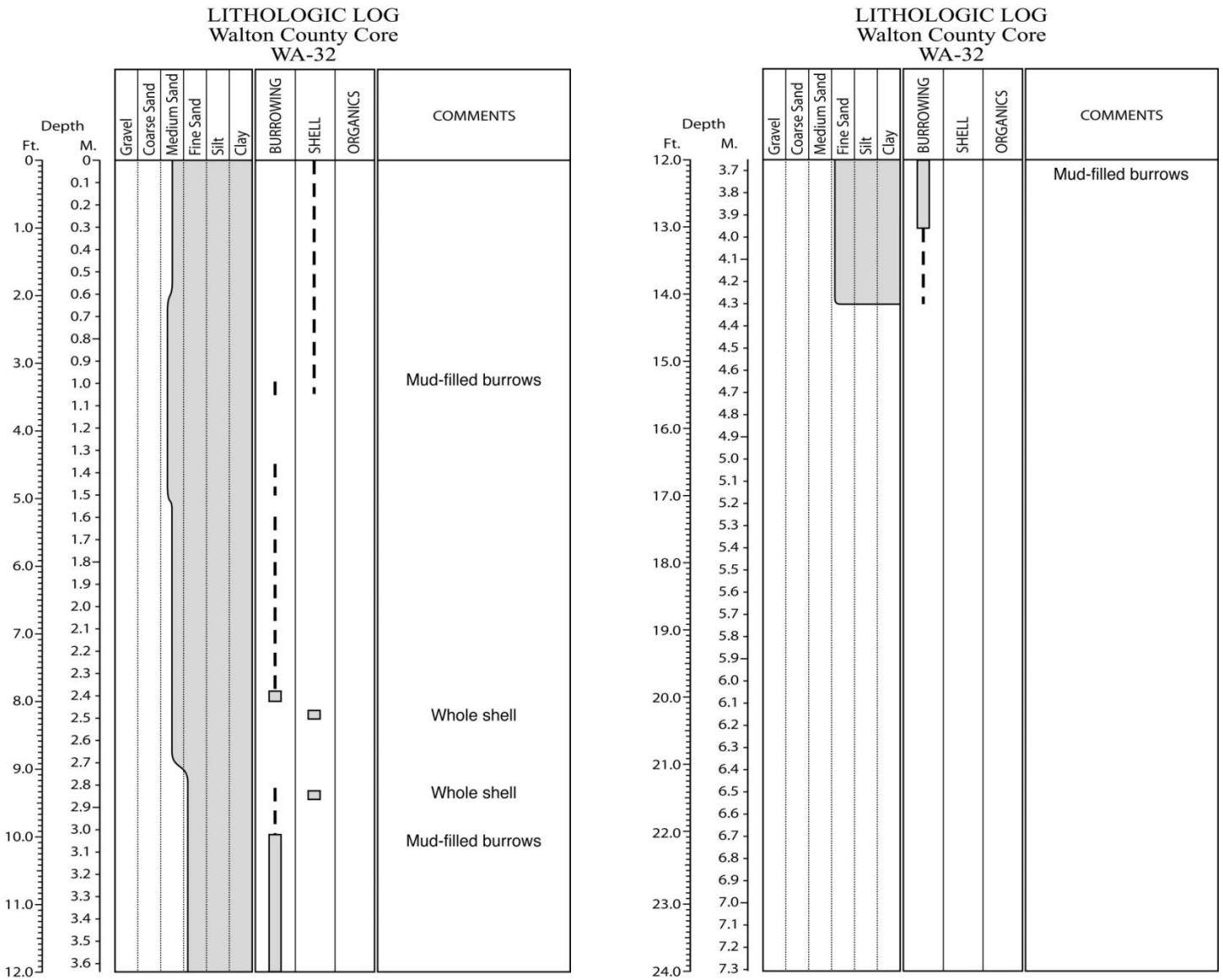

Figure E.105. Core WA-32 log.

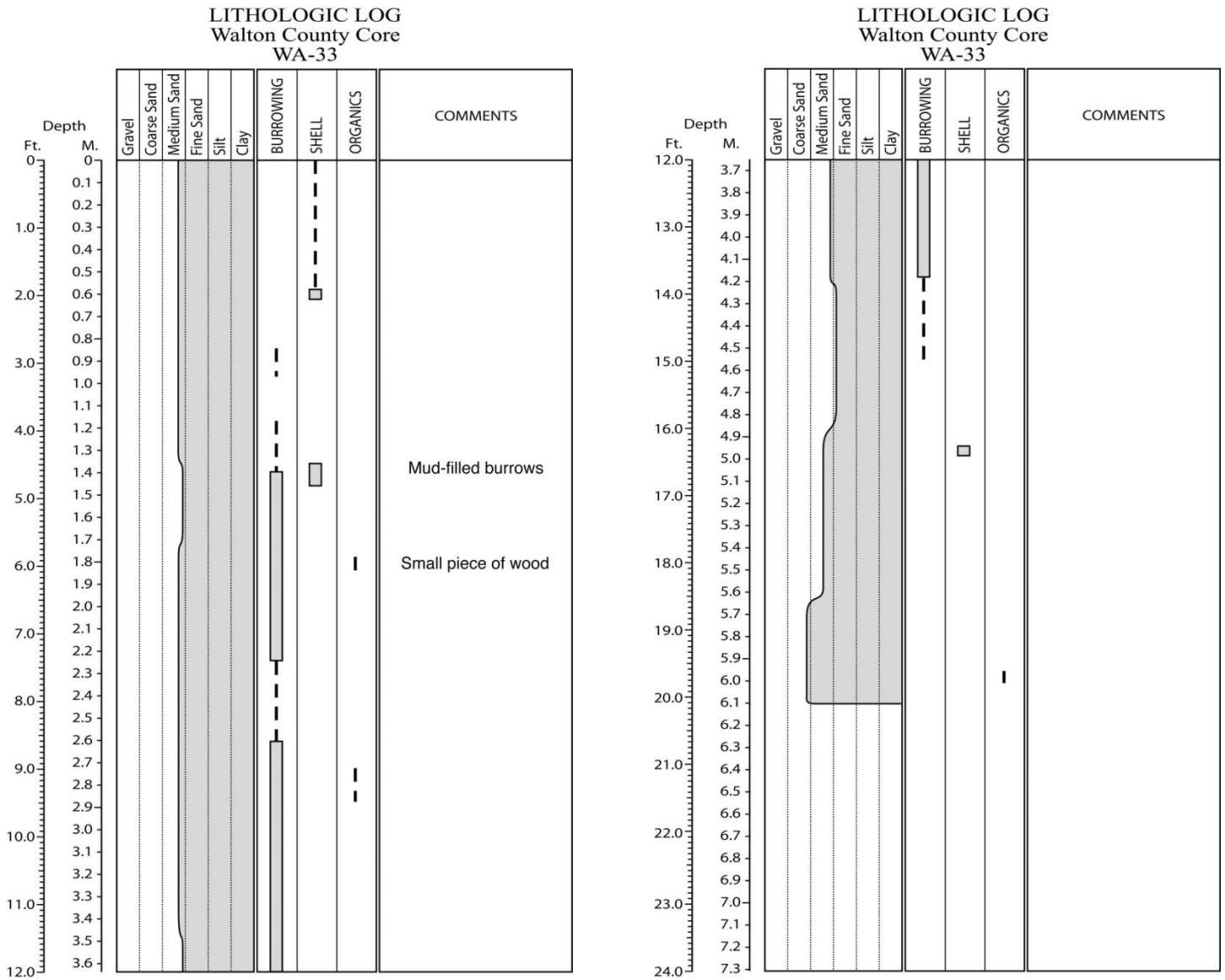

Figure E.106. Core WA-33 log.

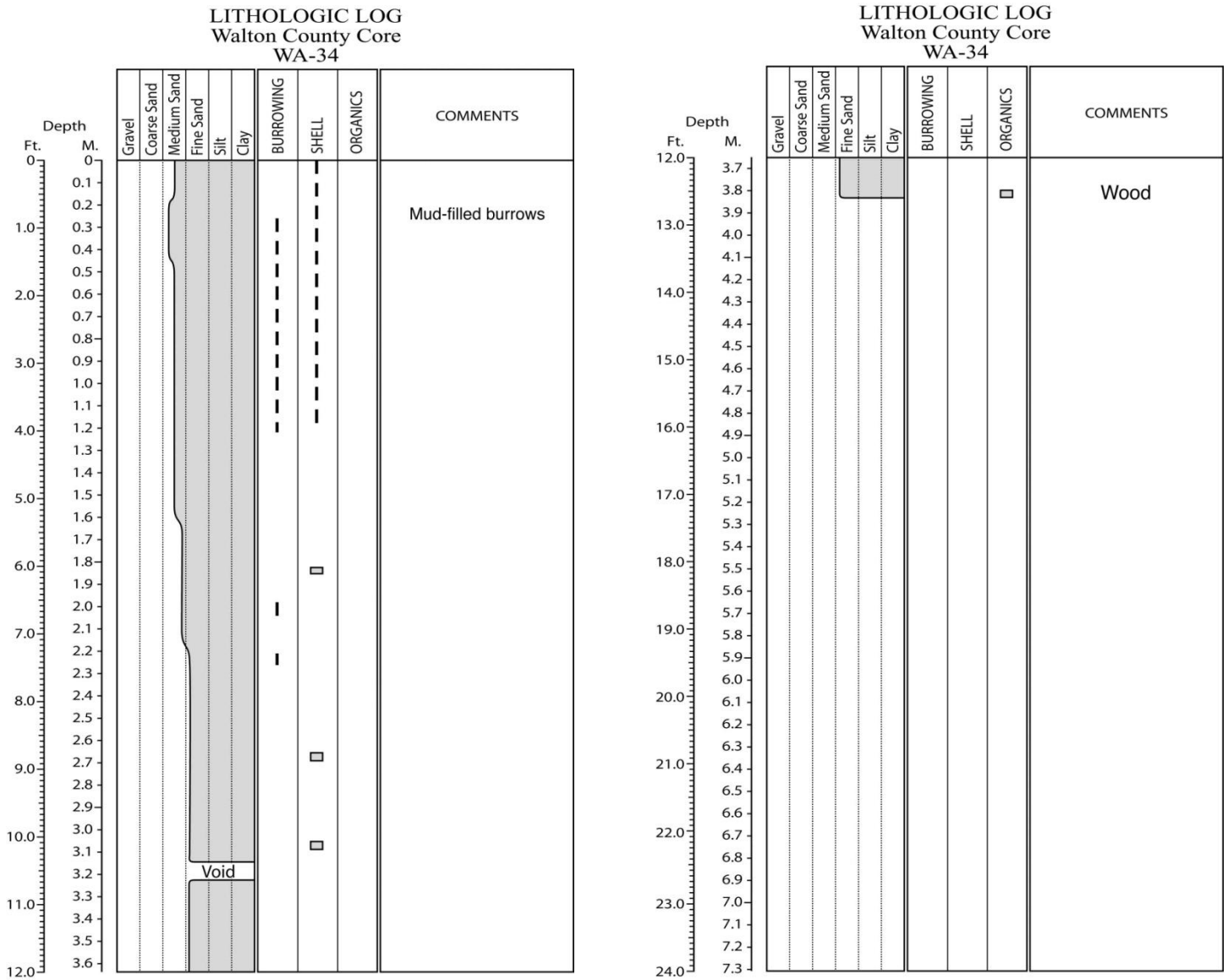

Figure E.107. Core WA-34 log.

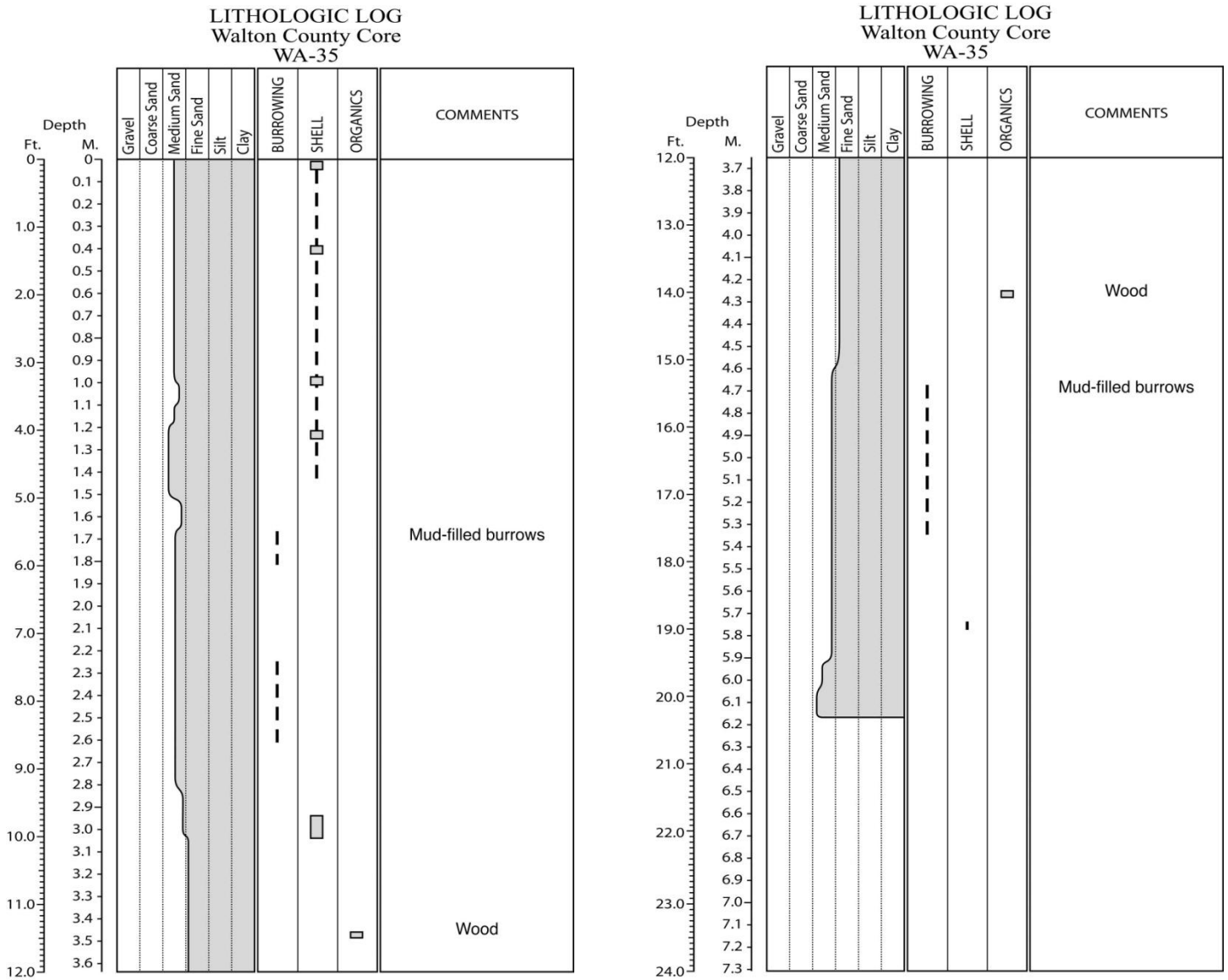

Figure E.108. Core WA-35 log.

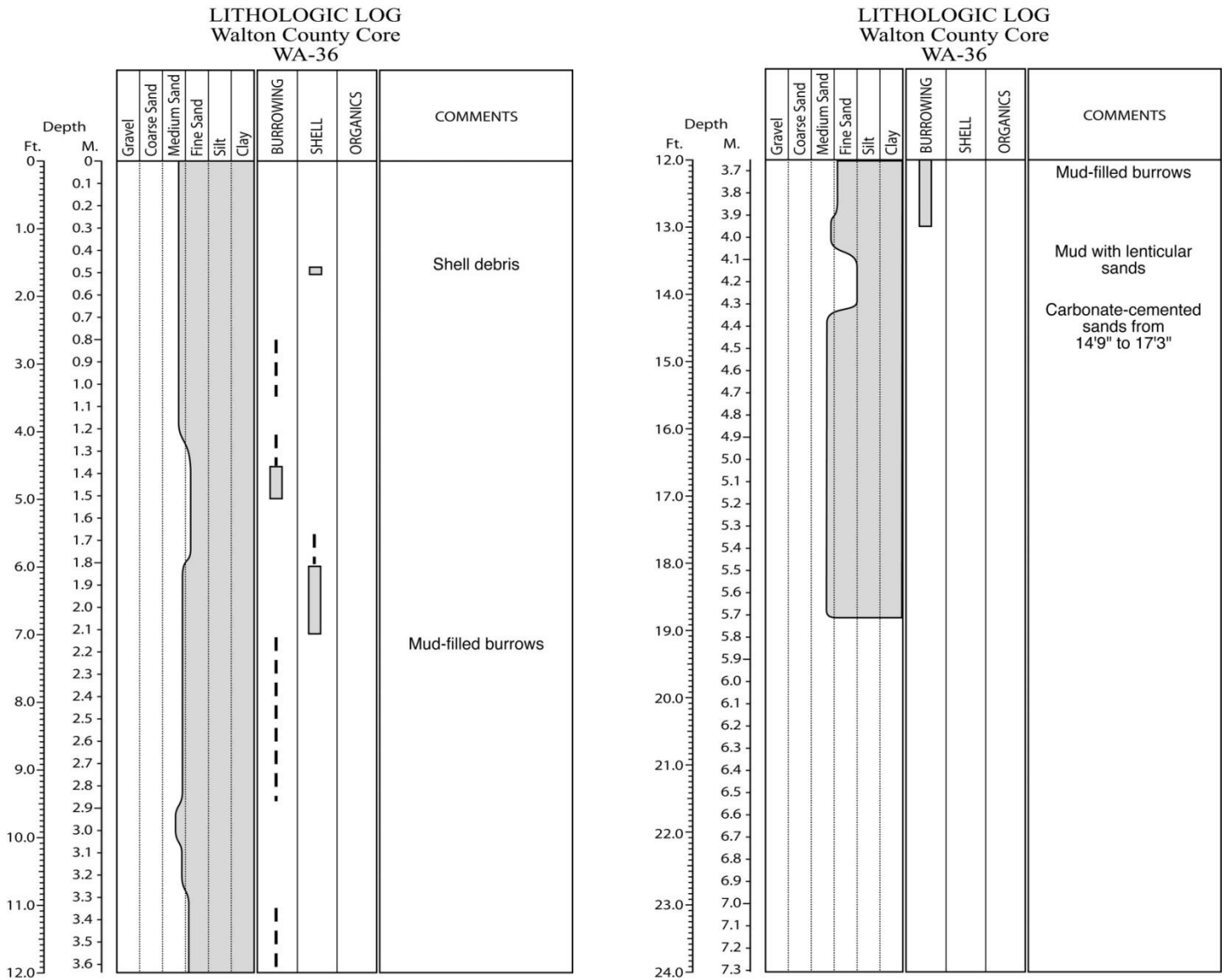

Figure E.109. Core WA-36 log.

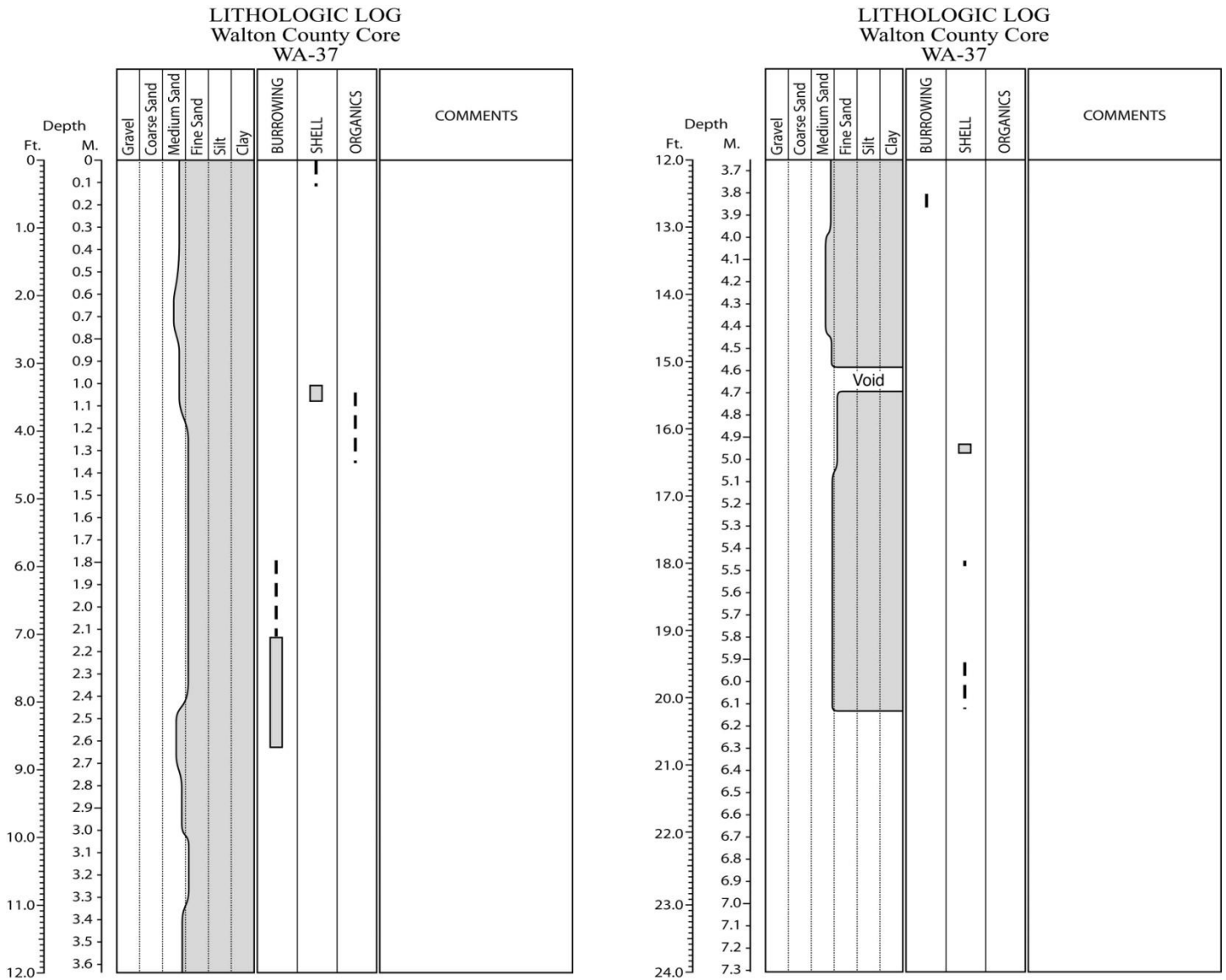

Figure E.110. Core WA-37 log.

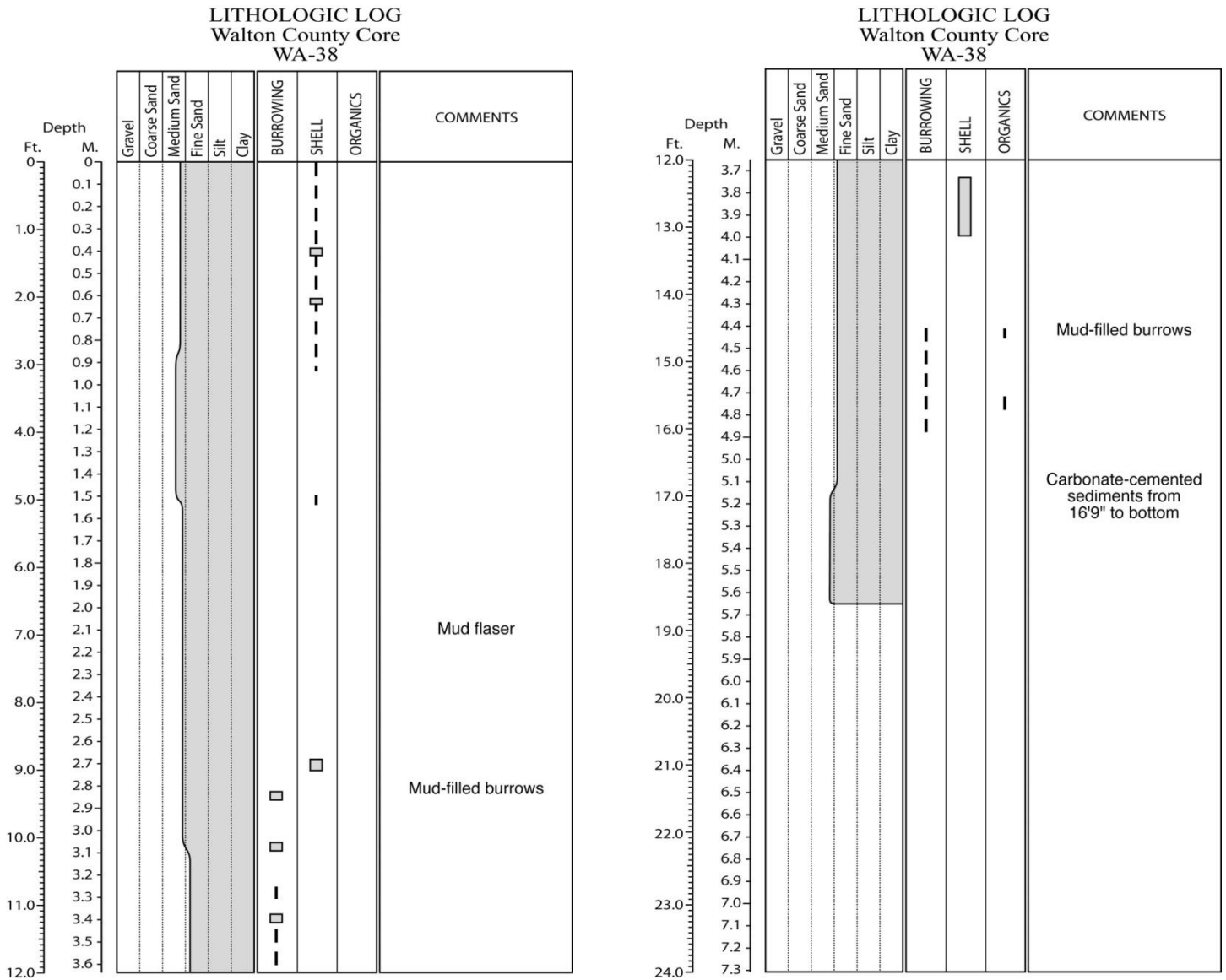

Figure E.111. Core WA-38 log.

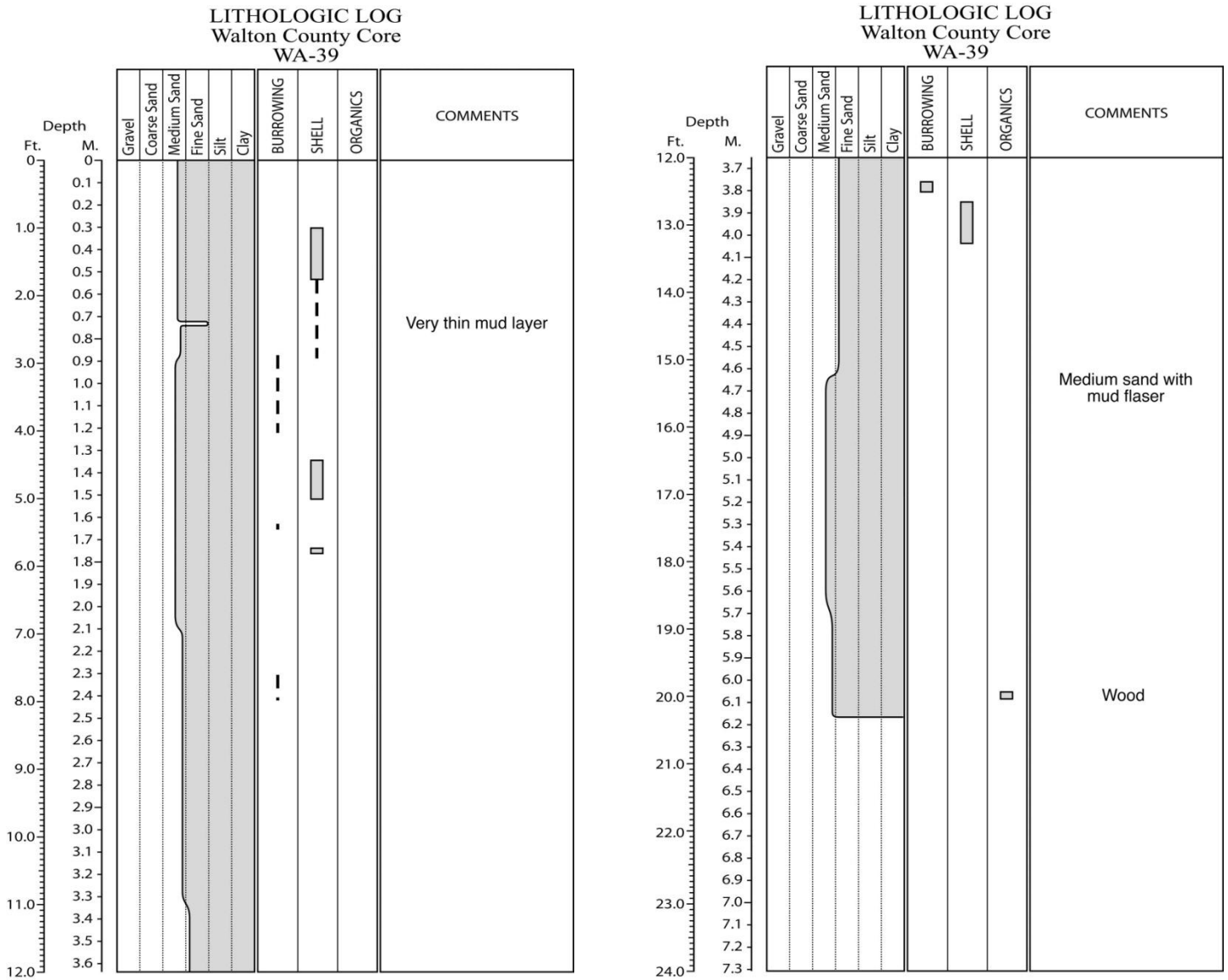

Figure E.112. Core WA-39 log.

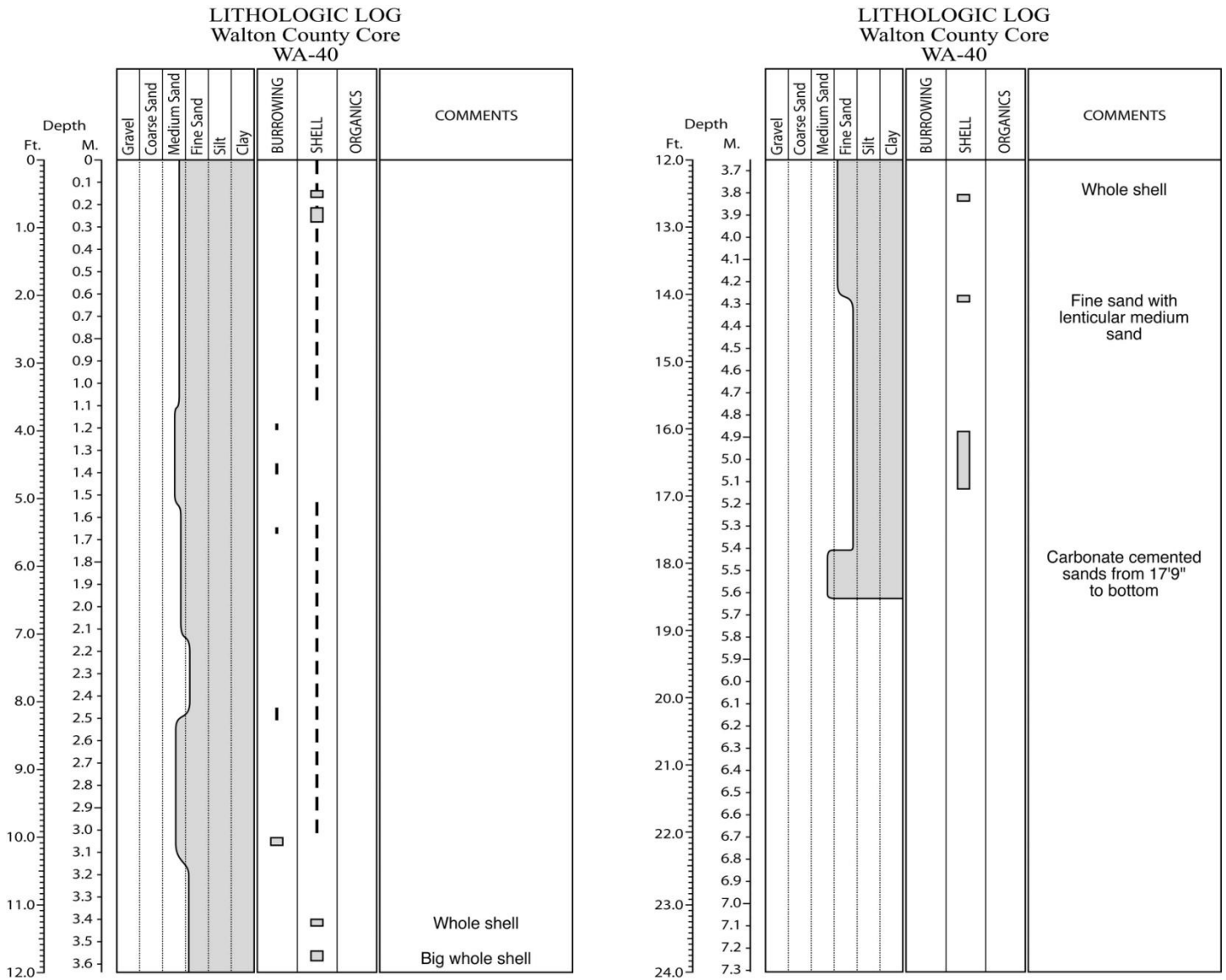

Figure E.113. Core WA-40 log.

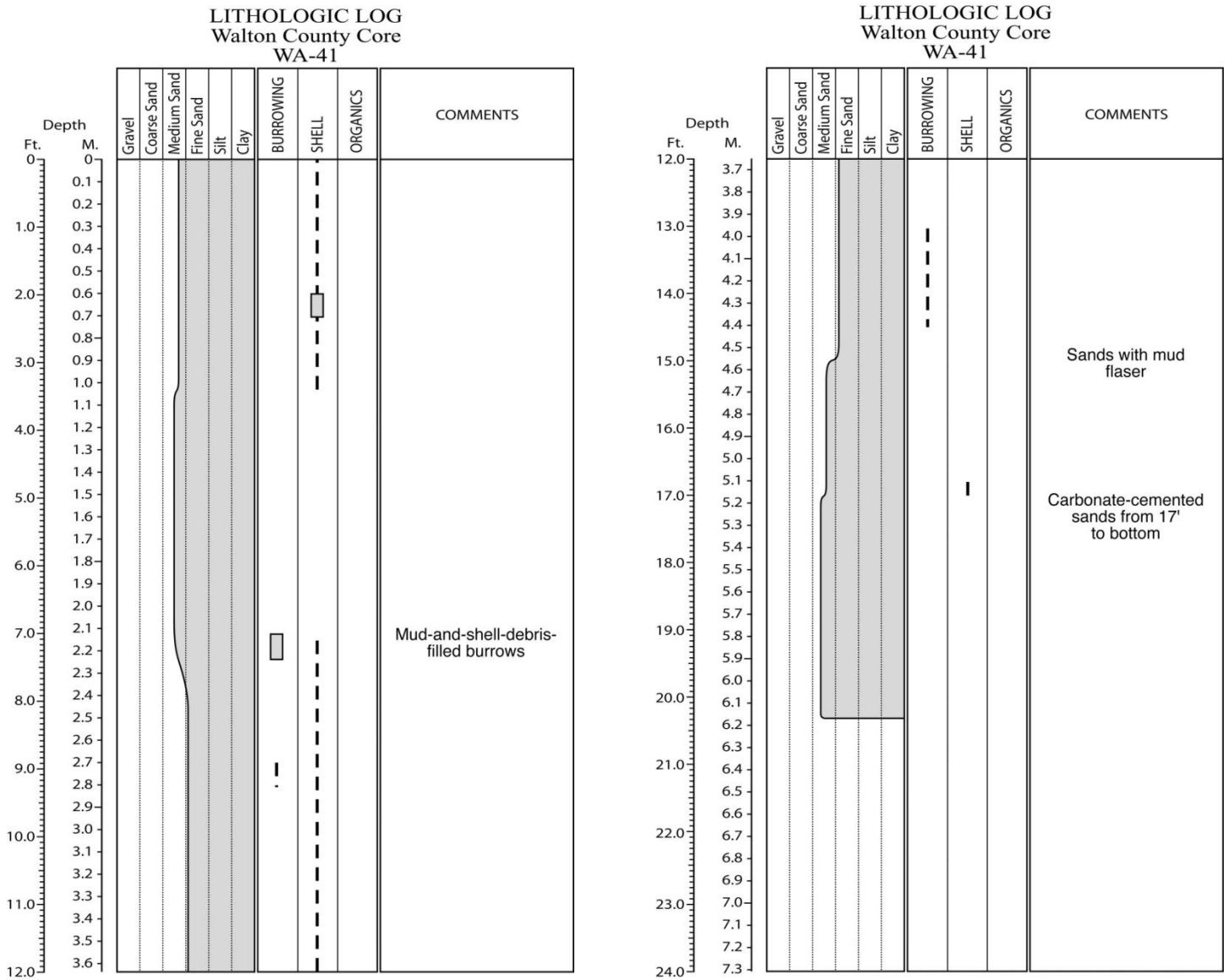

Figure E.114. Core WA-41 log.

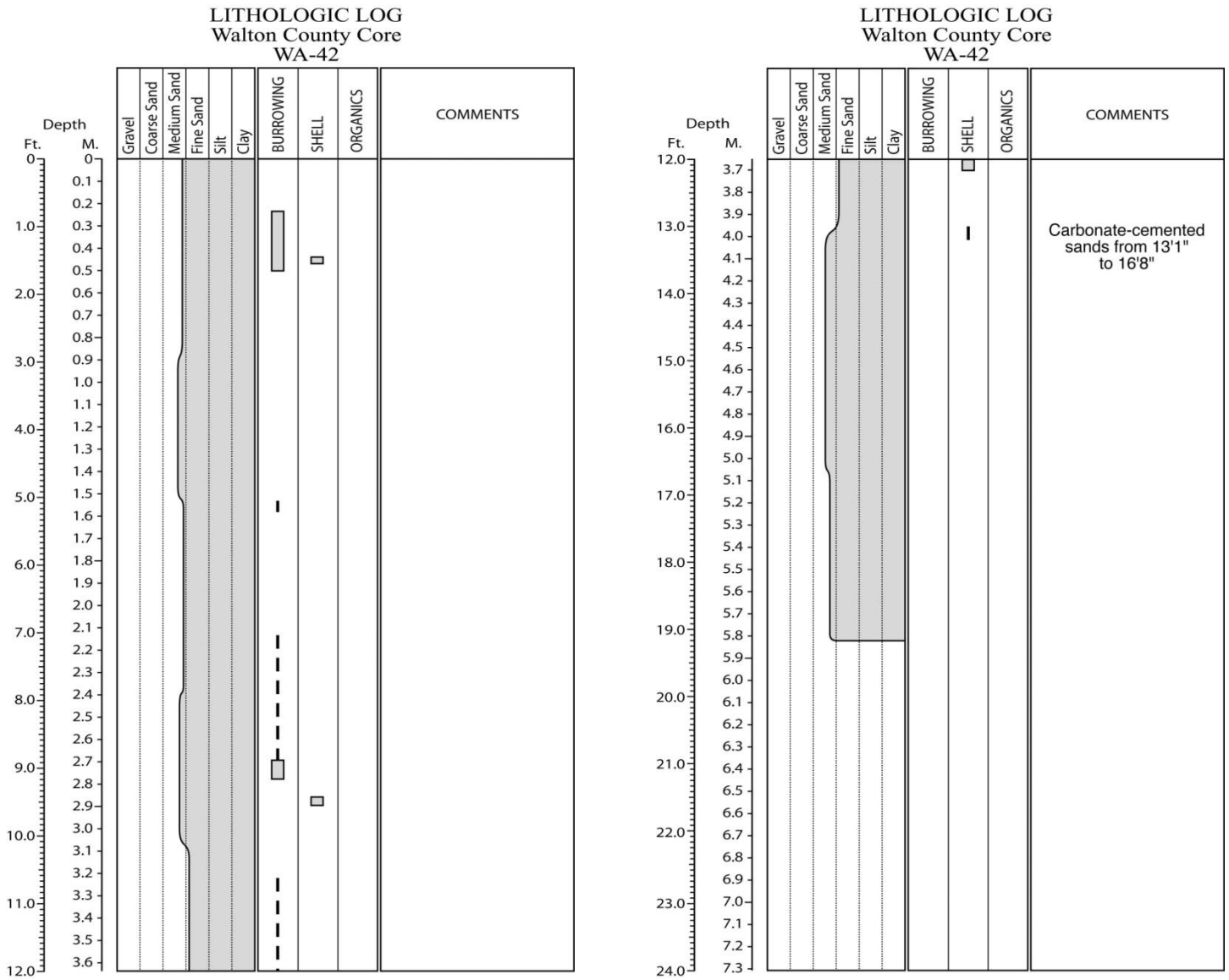

Figure E.115. Core WA-42 log.

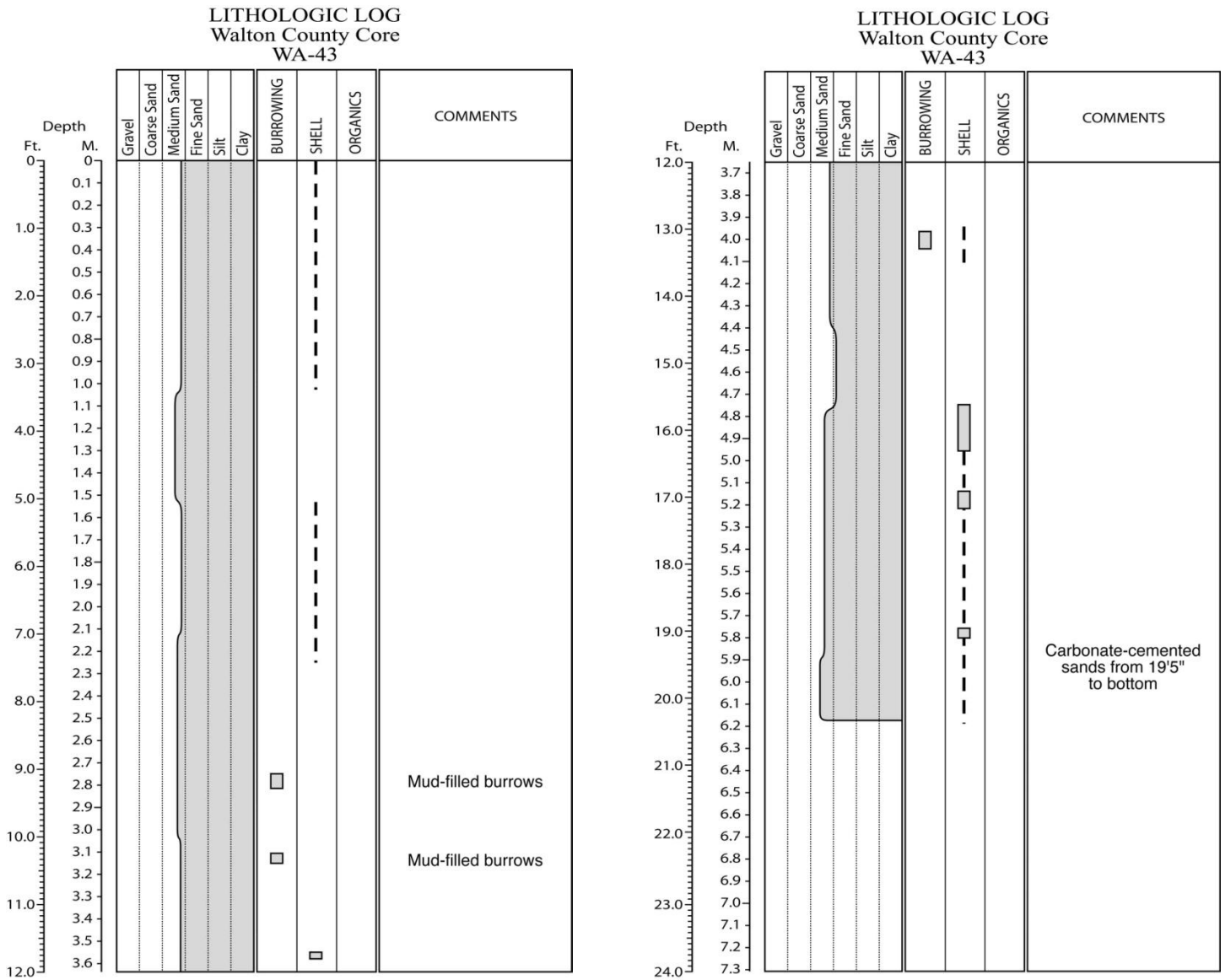

Figure E.116. Core WA-43 log.

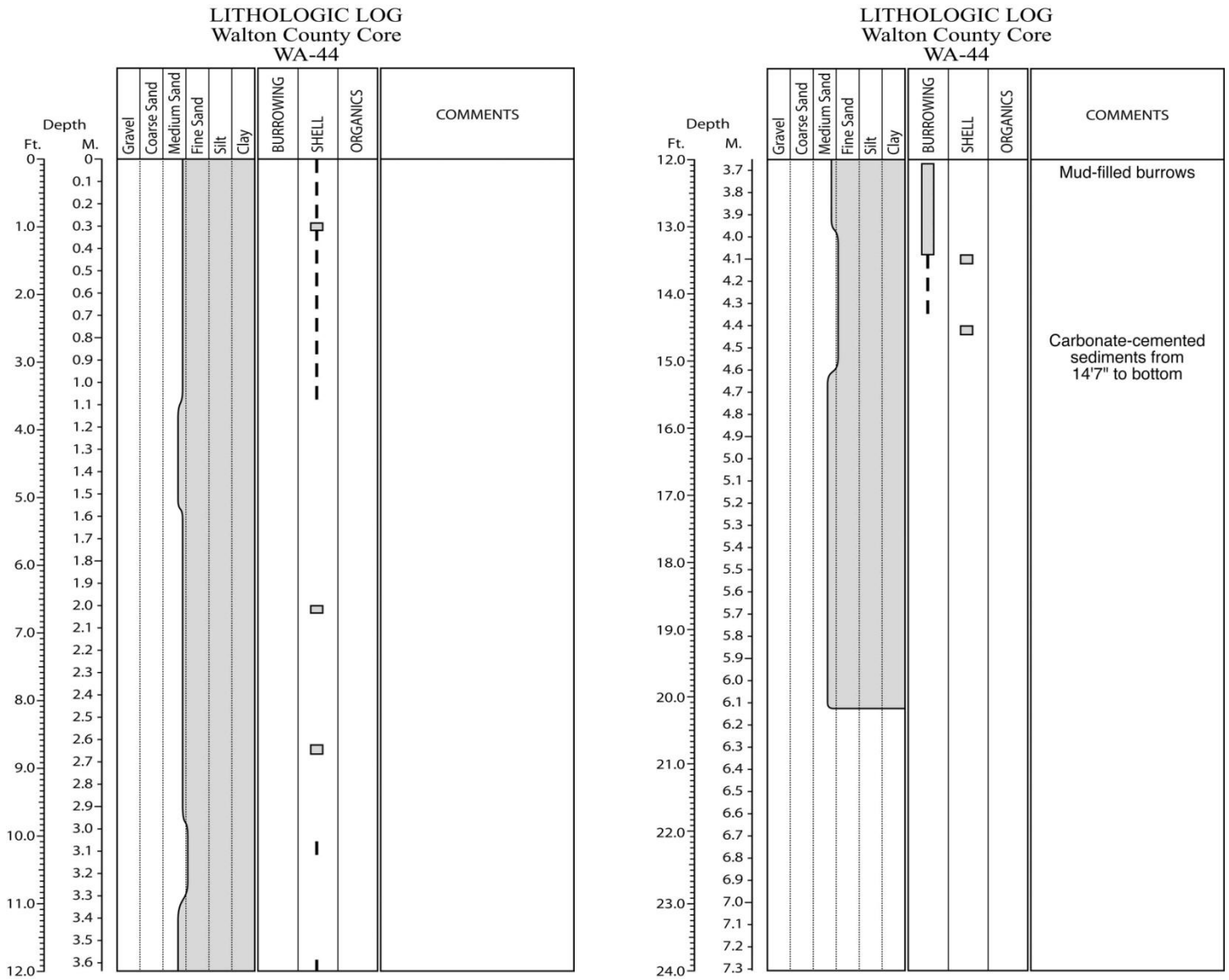

Figure E.117. Core WA-44 log.

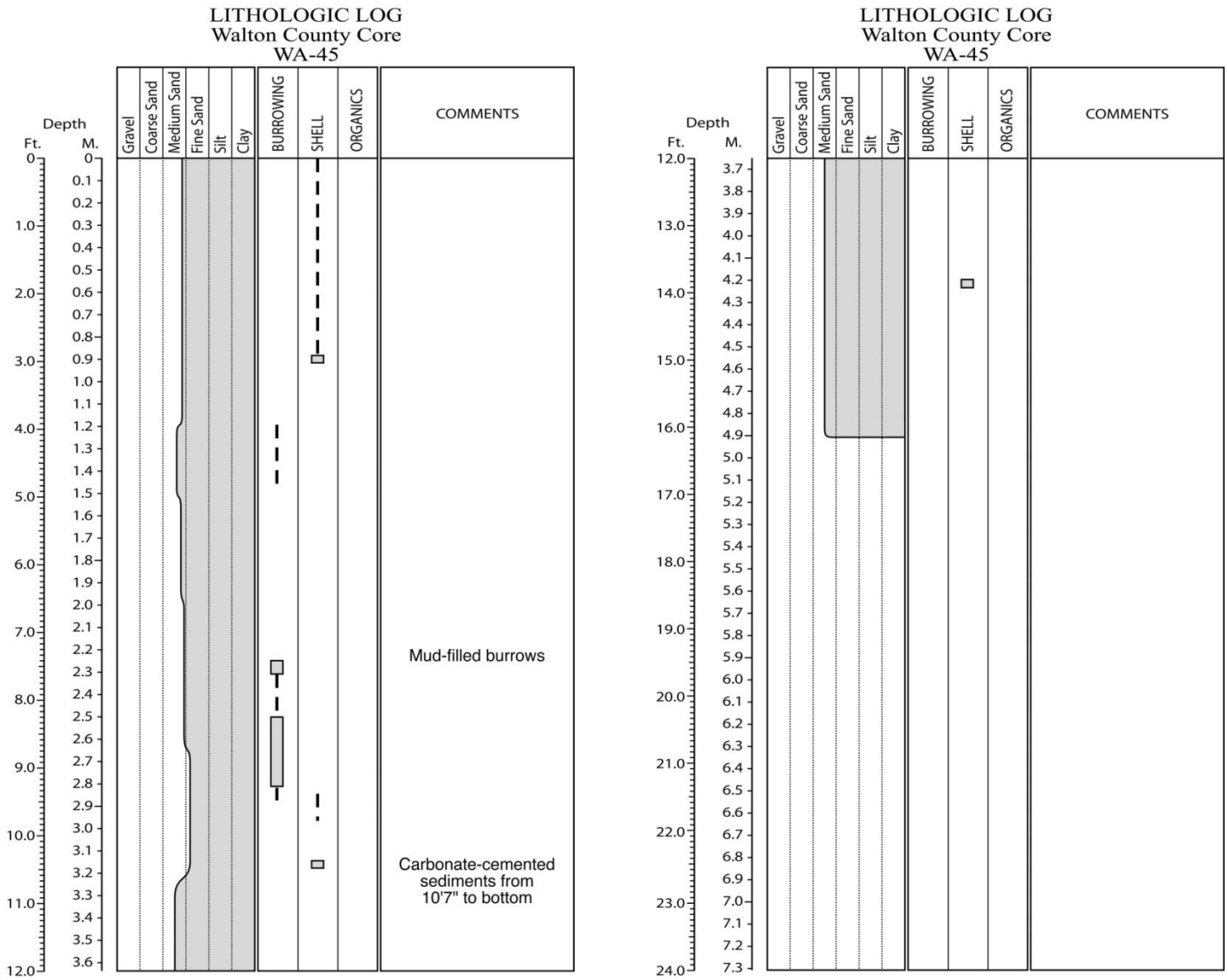

Figure E.118. Core WA-45 log.

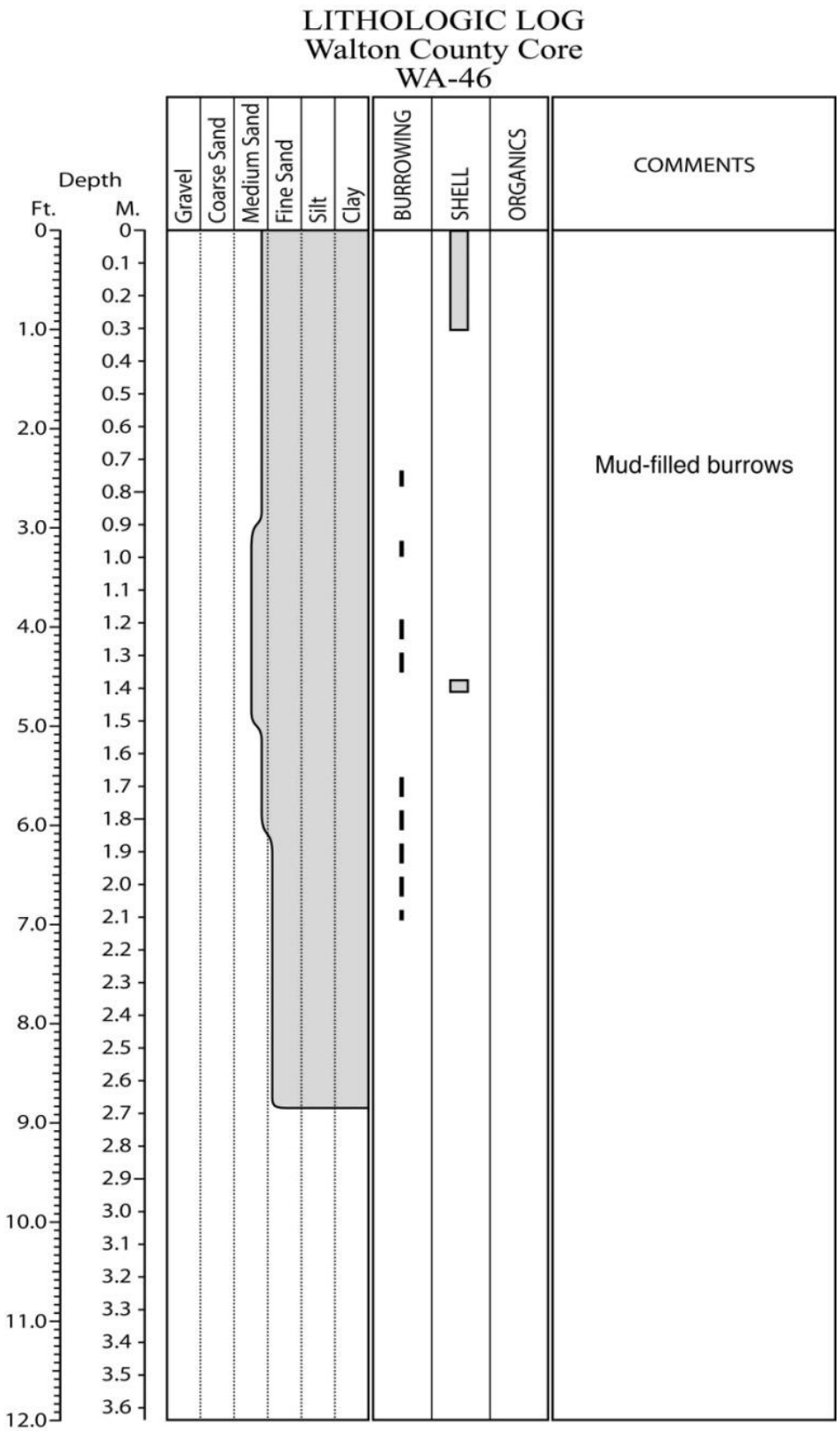

Figure E.119. Core WA-46 log.

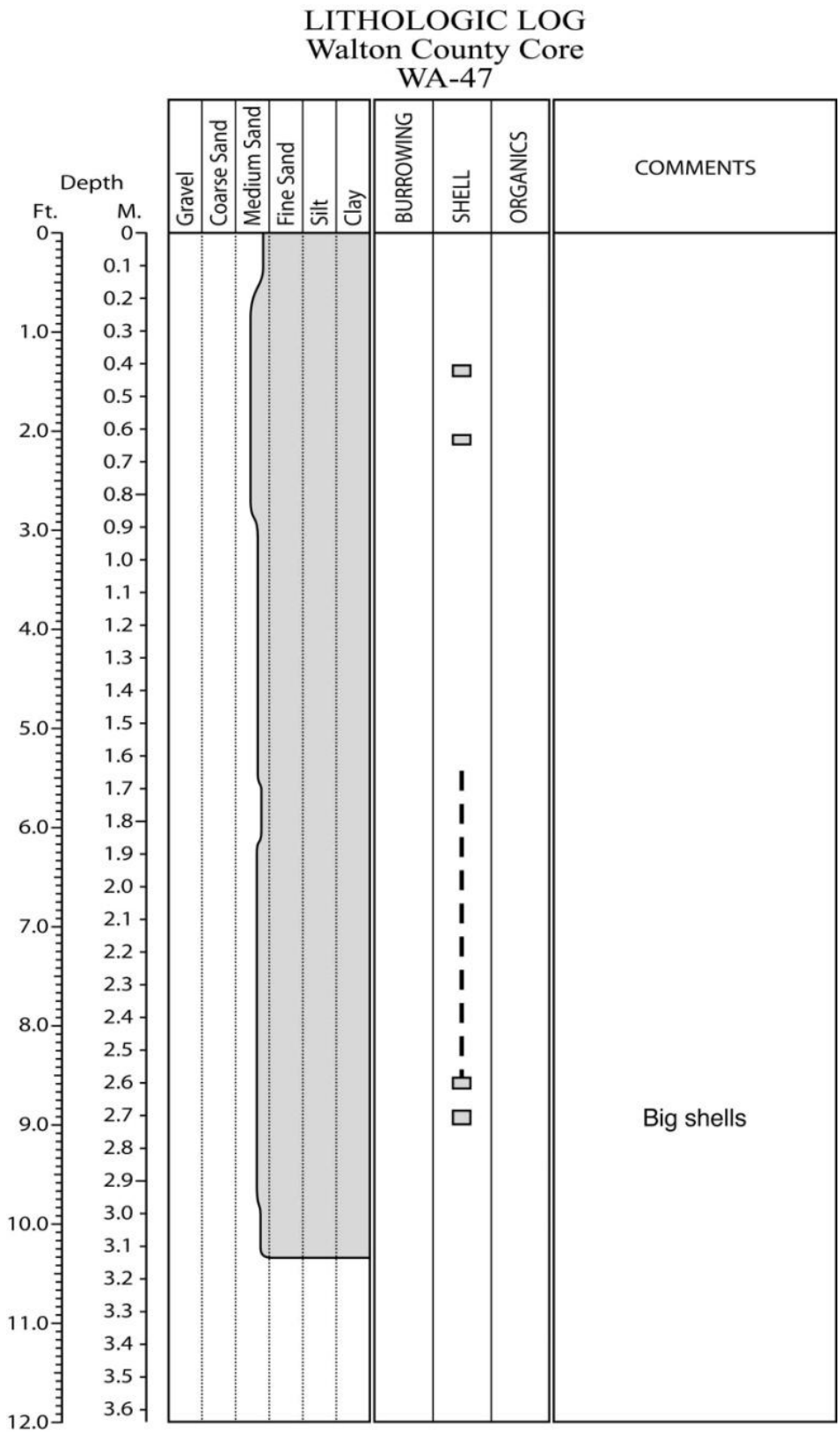

Figure E.120. Core WA-47 log.

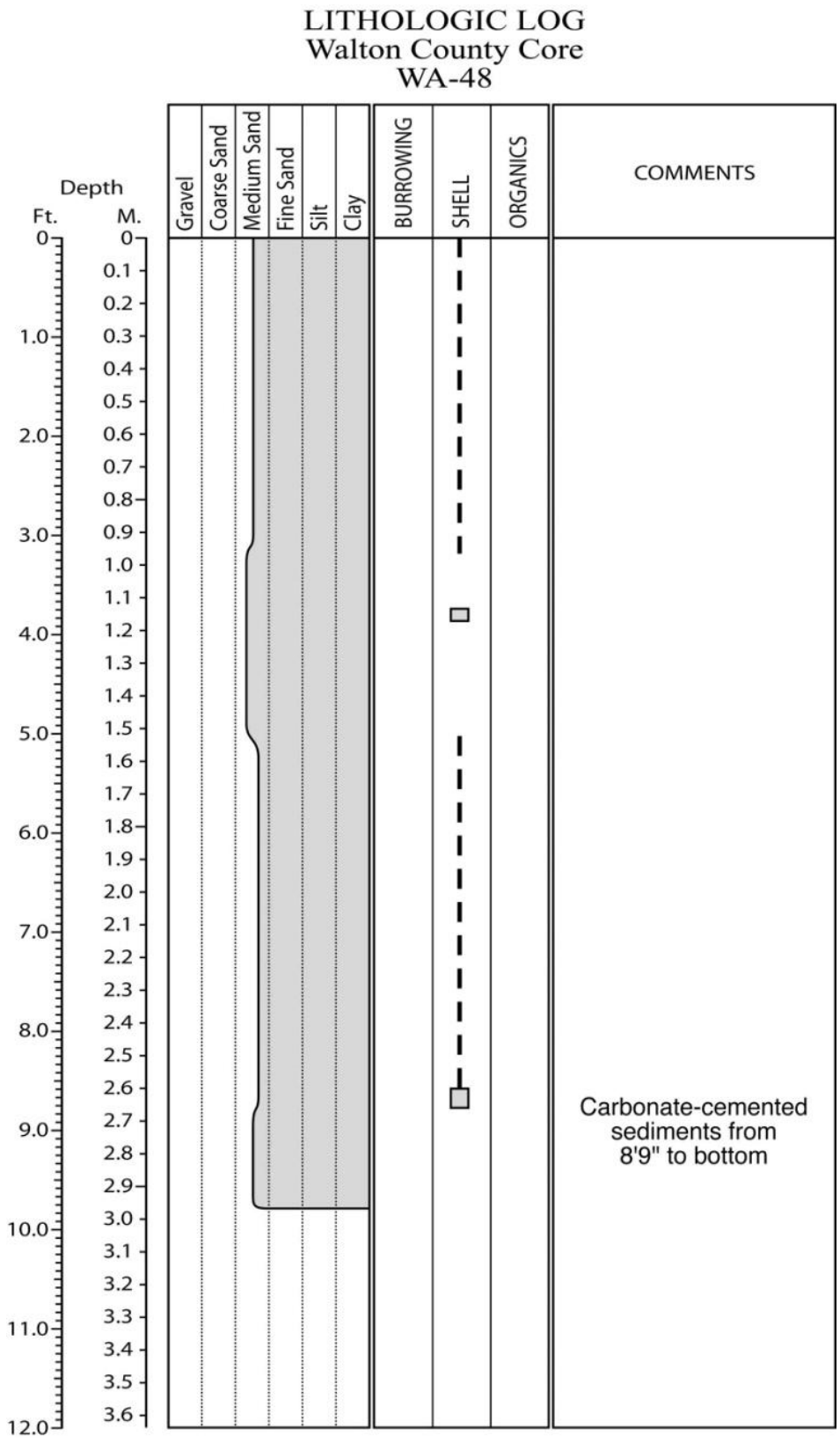

Figure E.121. Core WA-48 log.

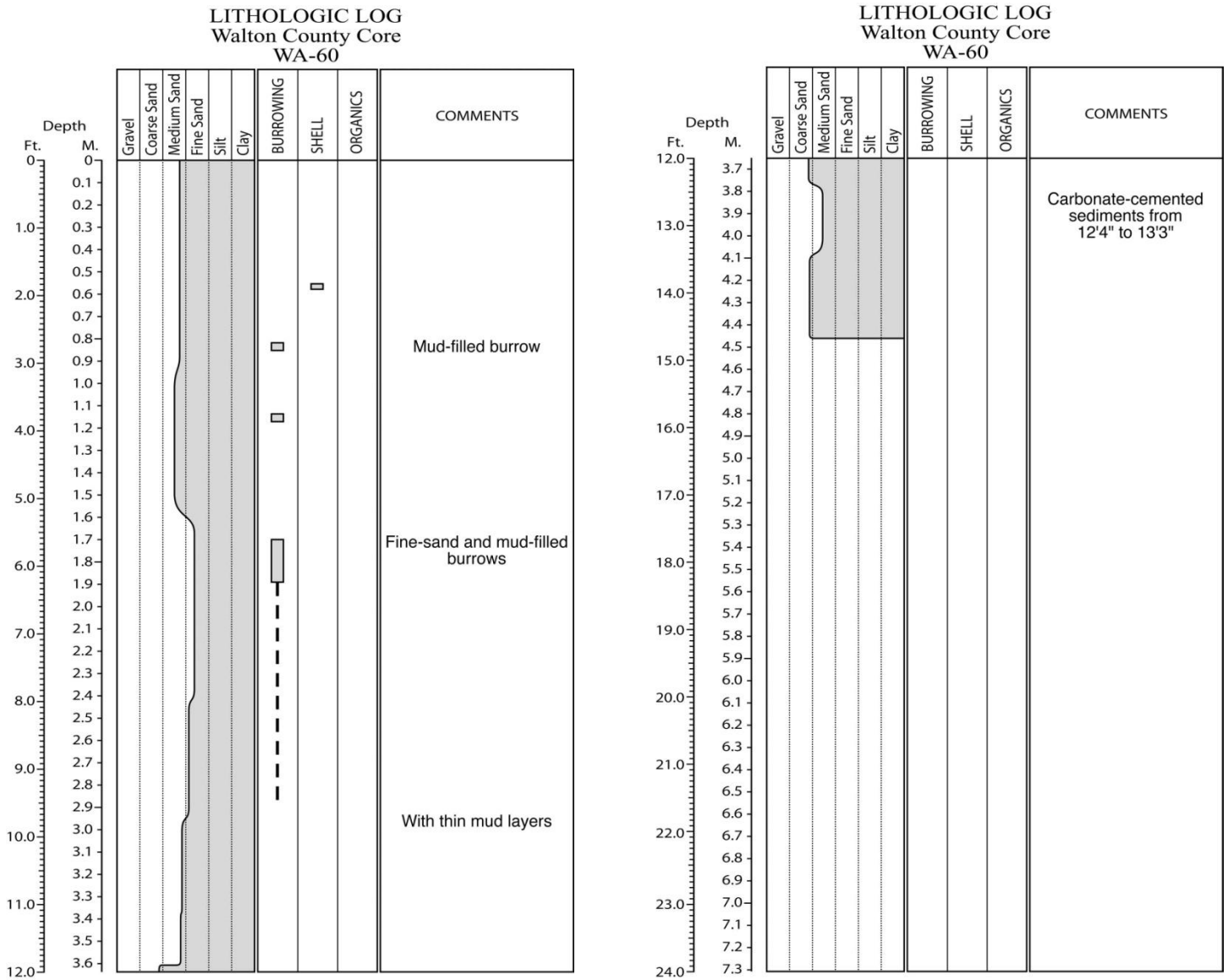

Figure E.122. Core WA-60 log.

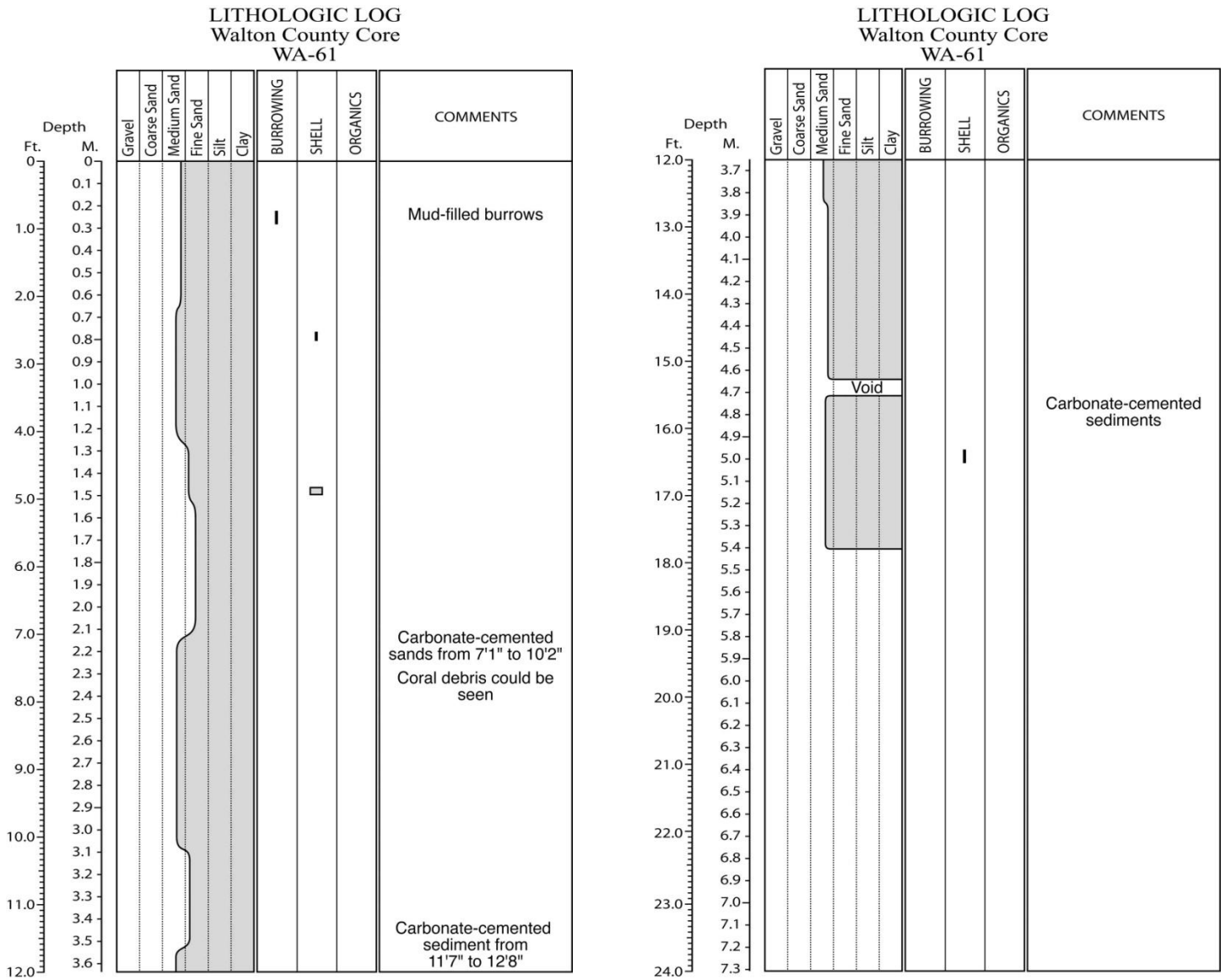

Figure E.123. Core WA-61 log.

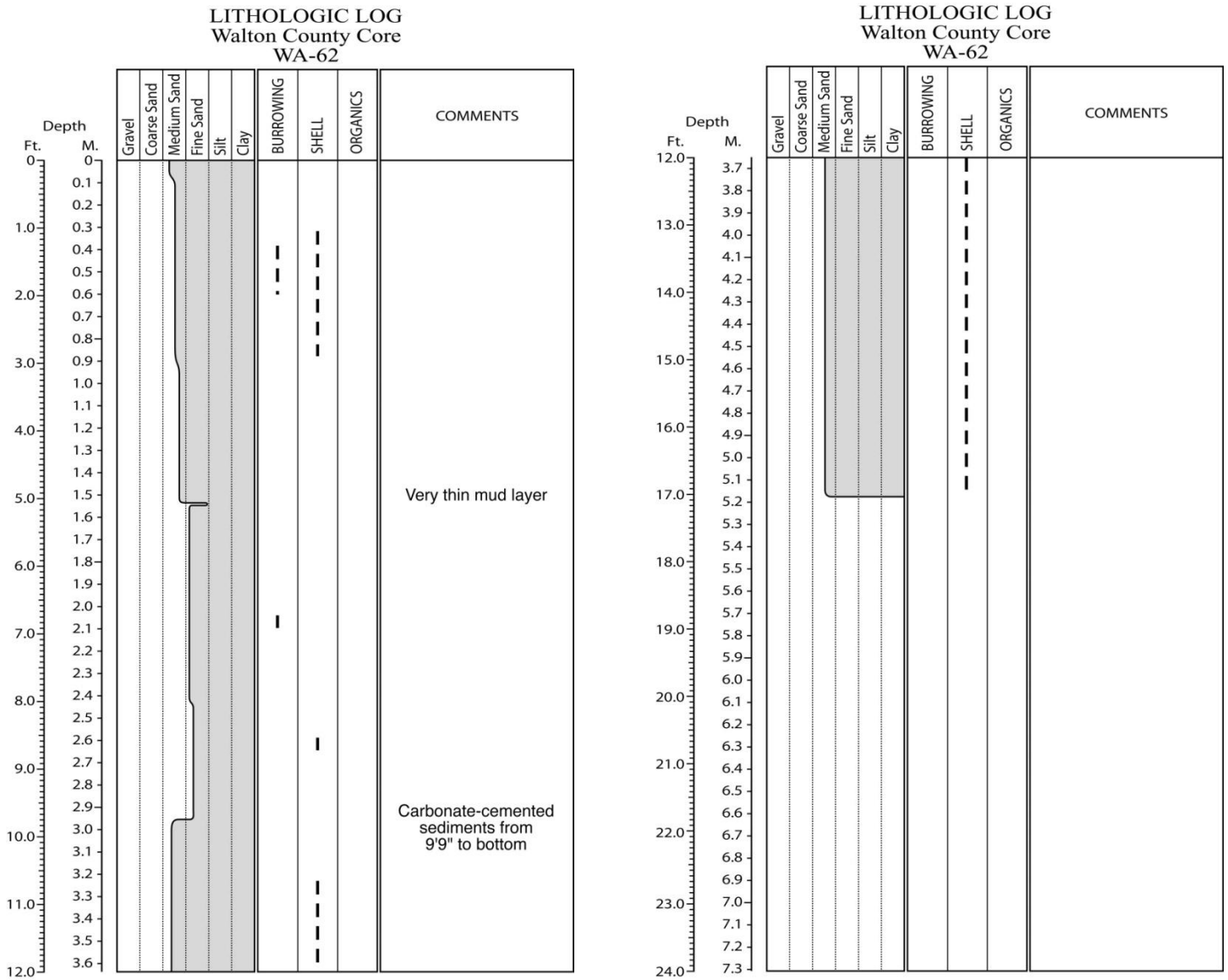

Figure E.124. Core WA-62 log.

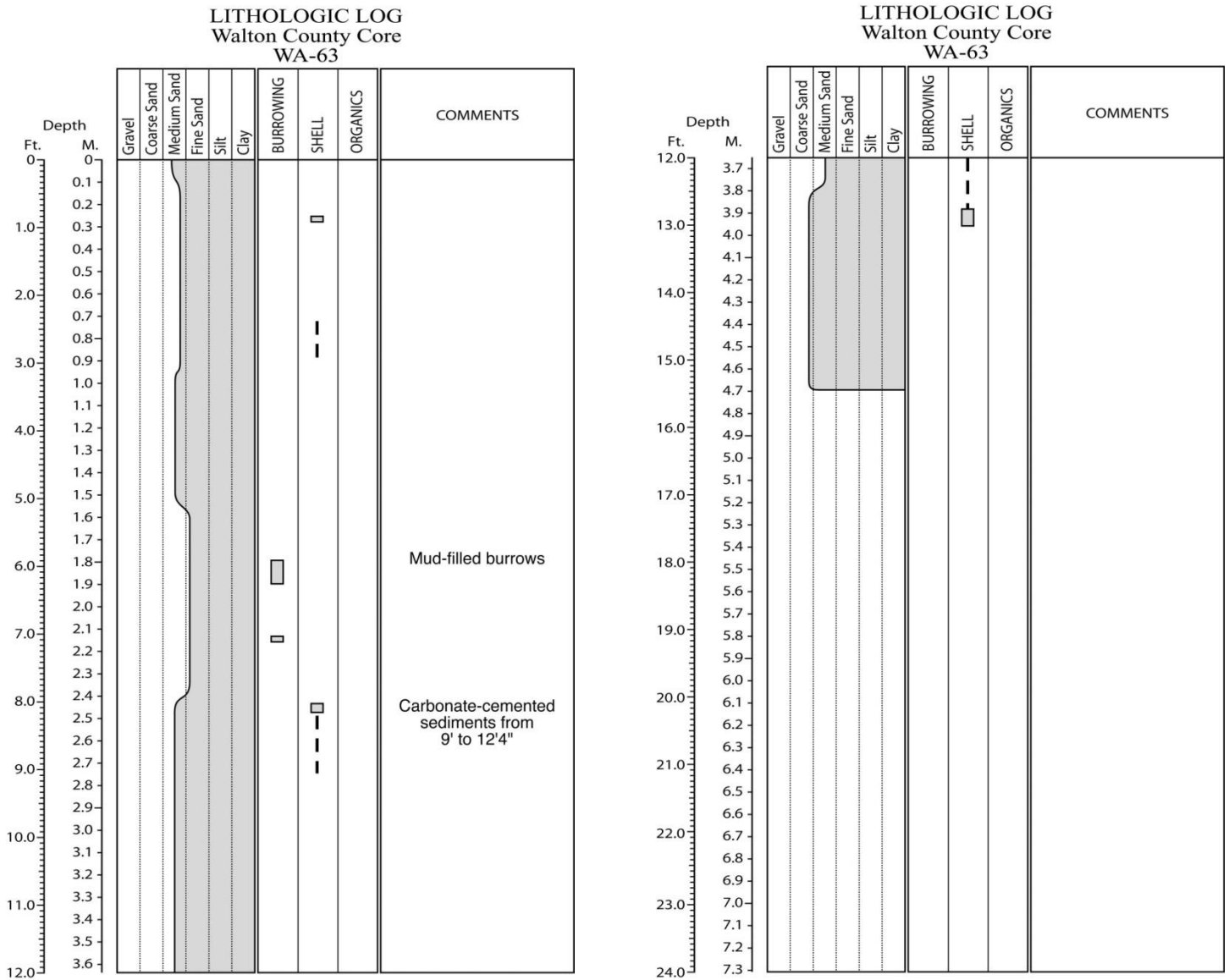

Figure E.125. Core WA-63 log.

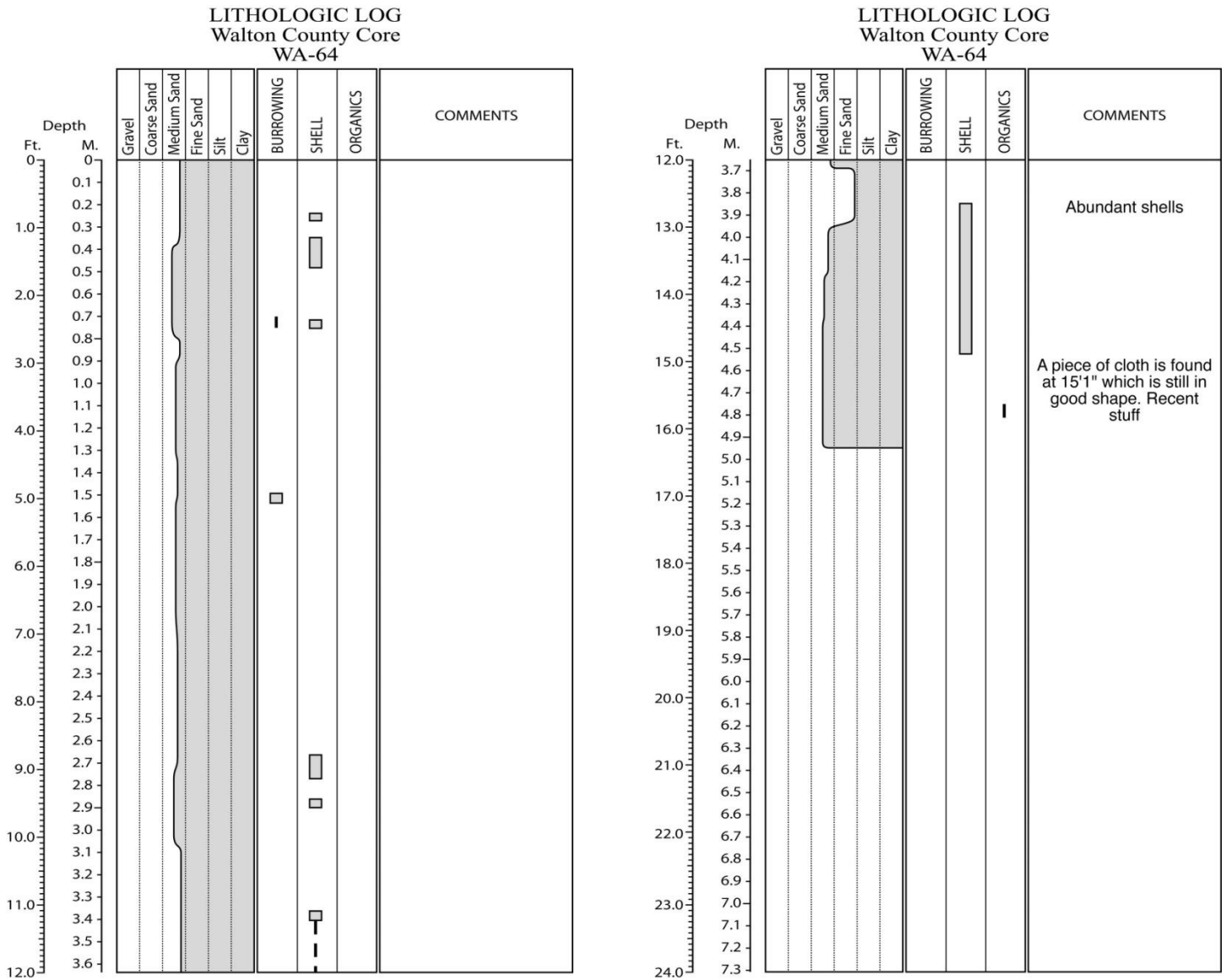

Figure E.126. Core WA-64 log.

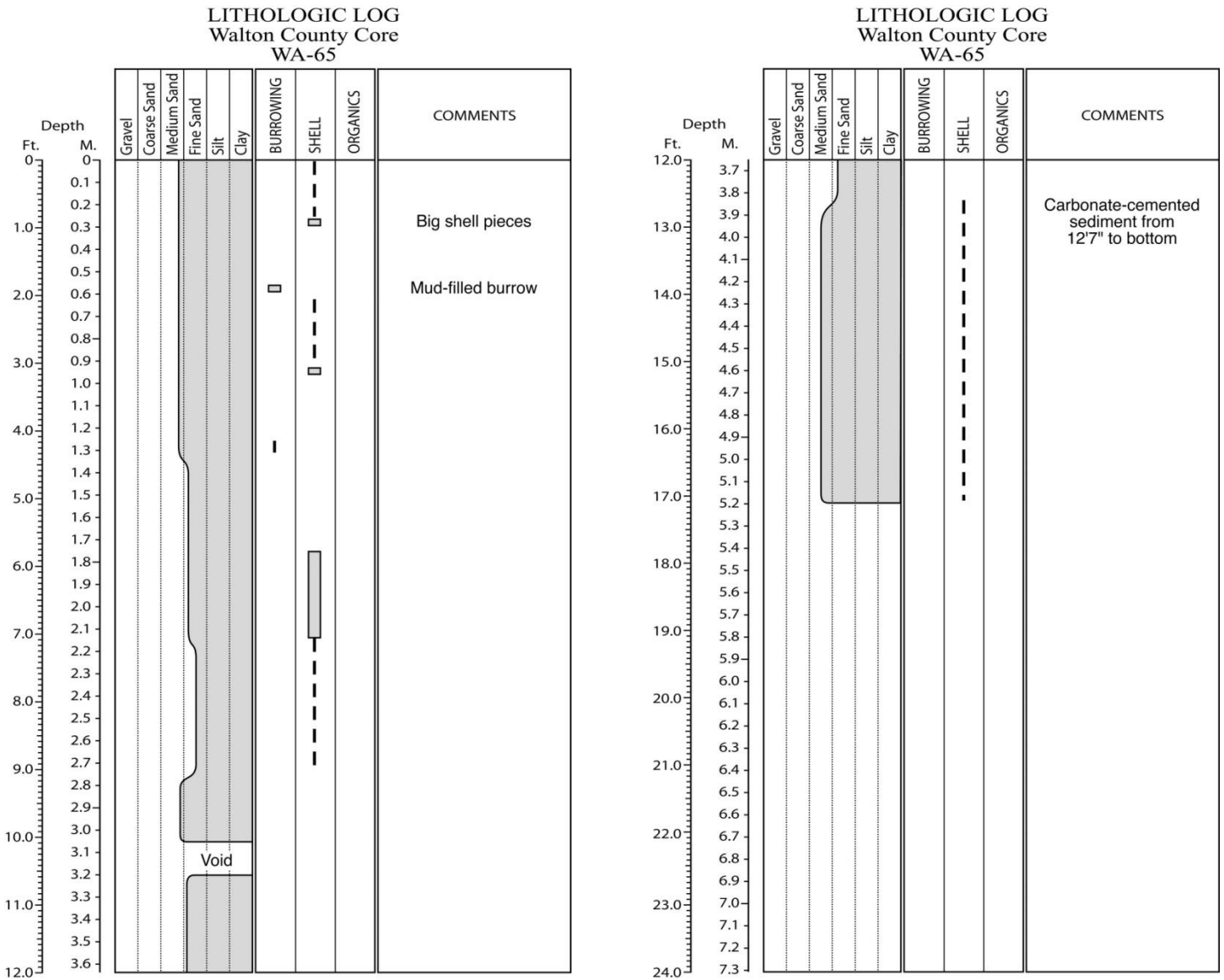

Figure E.127. Core WA-65 log.

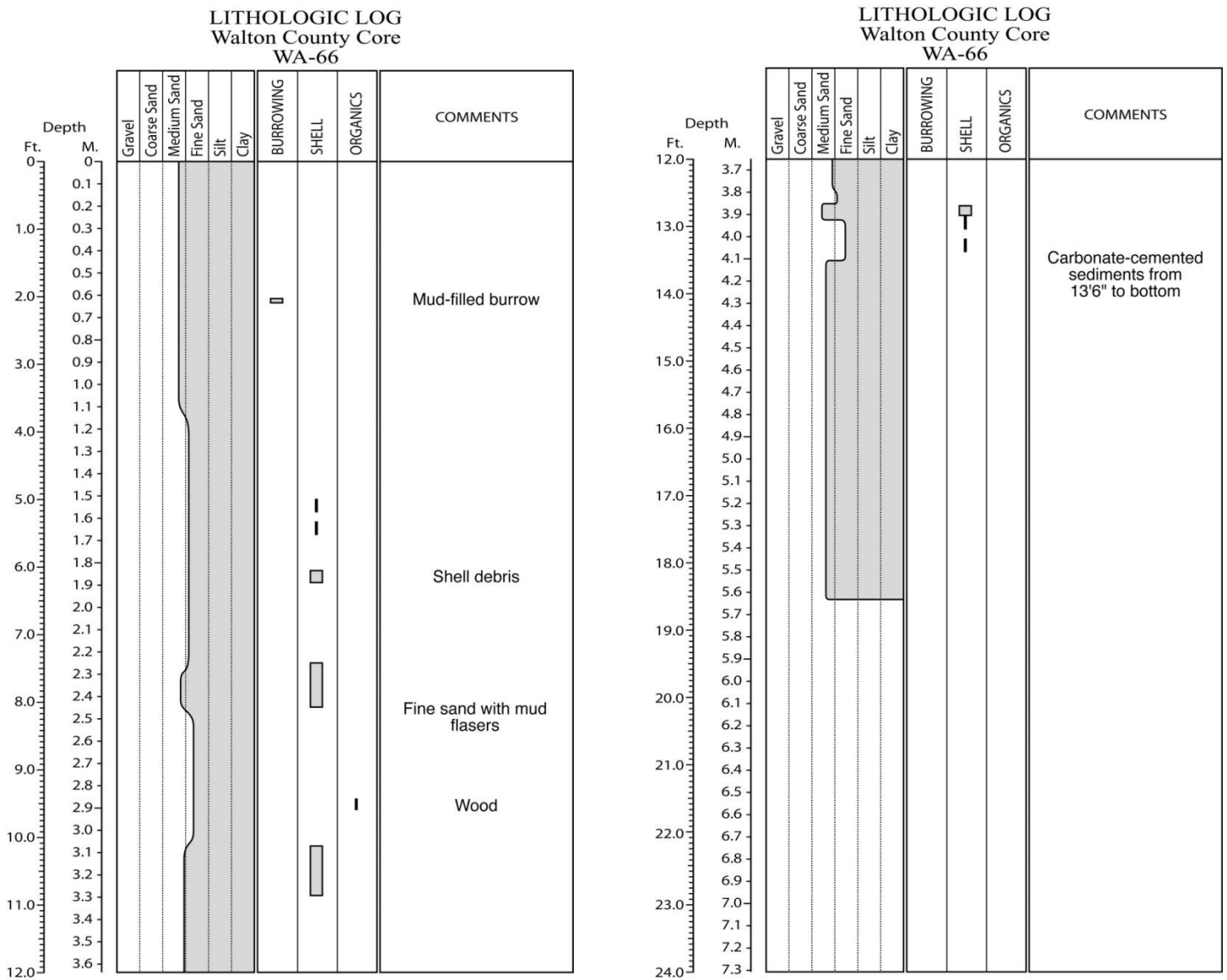

Figure E.128. Core WA-66 log.

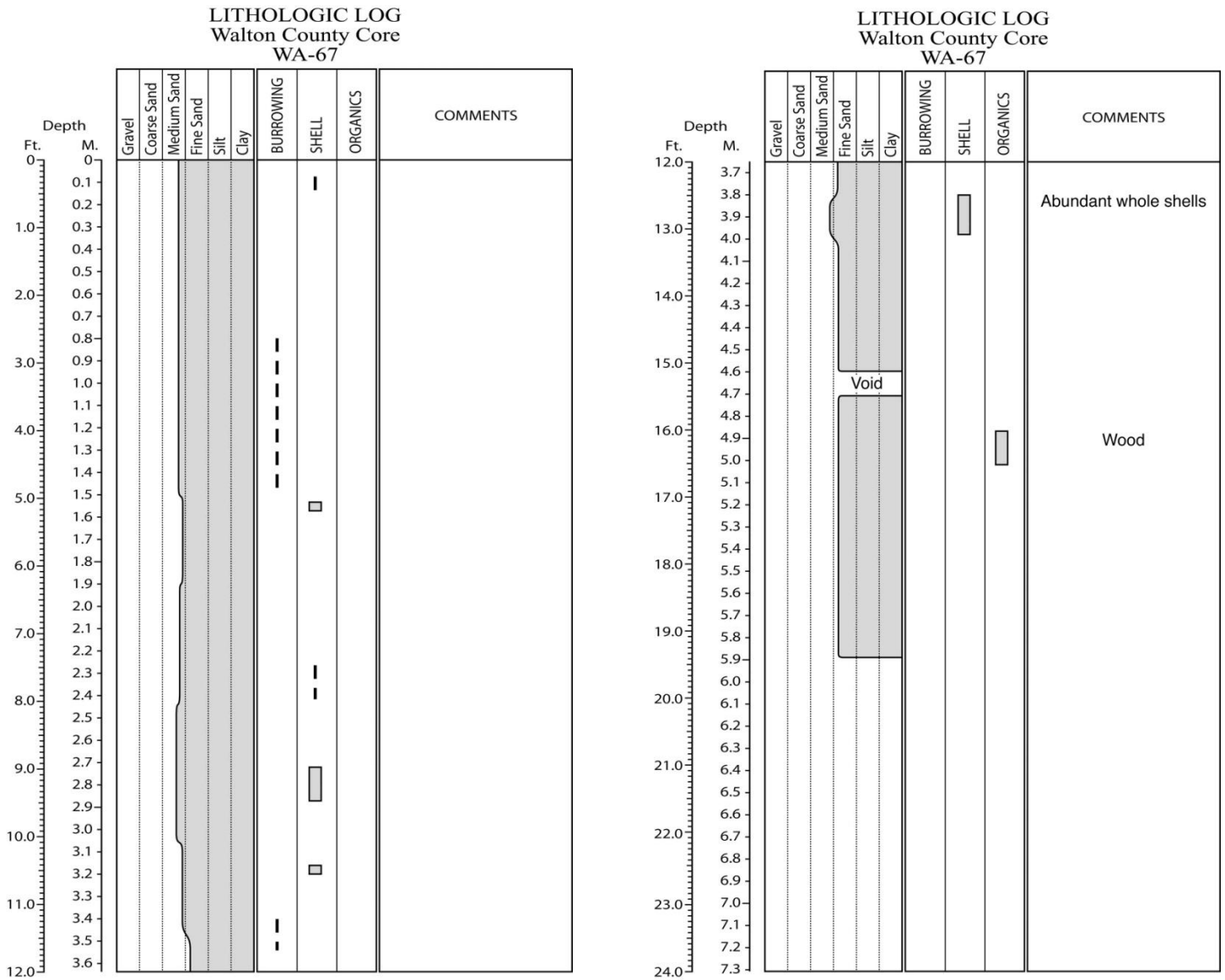

Figure E.129. Core WA-67 log.

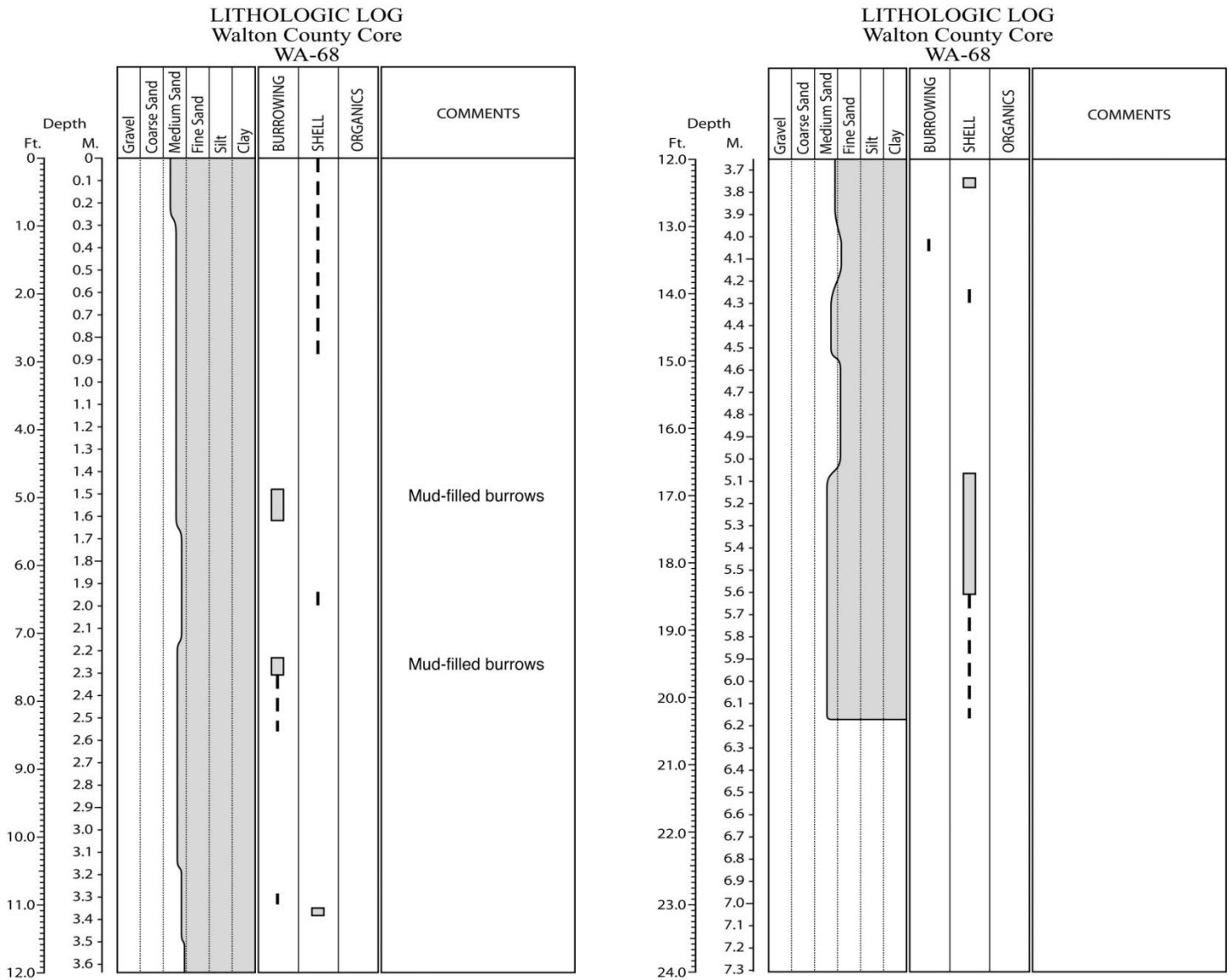

Figure E.130. Core WA-68 log.

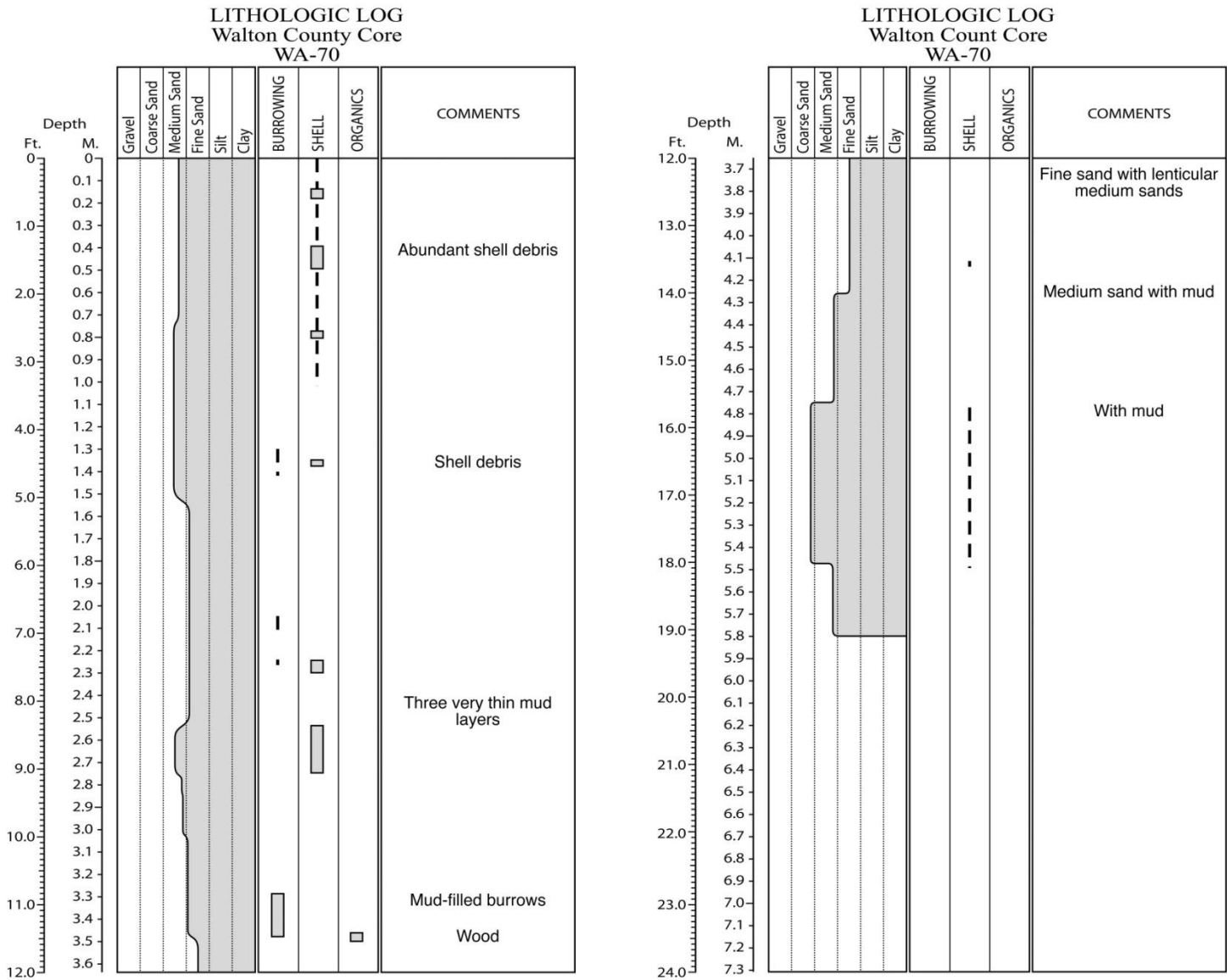

Figure E.131. Core WA-70 log.

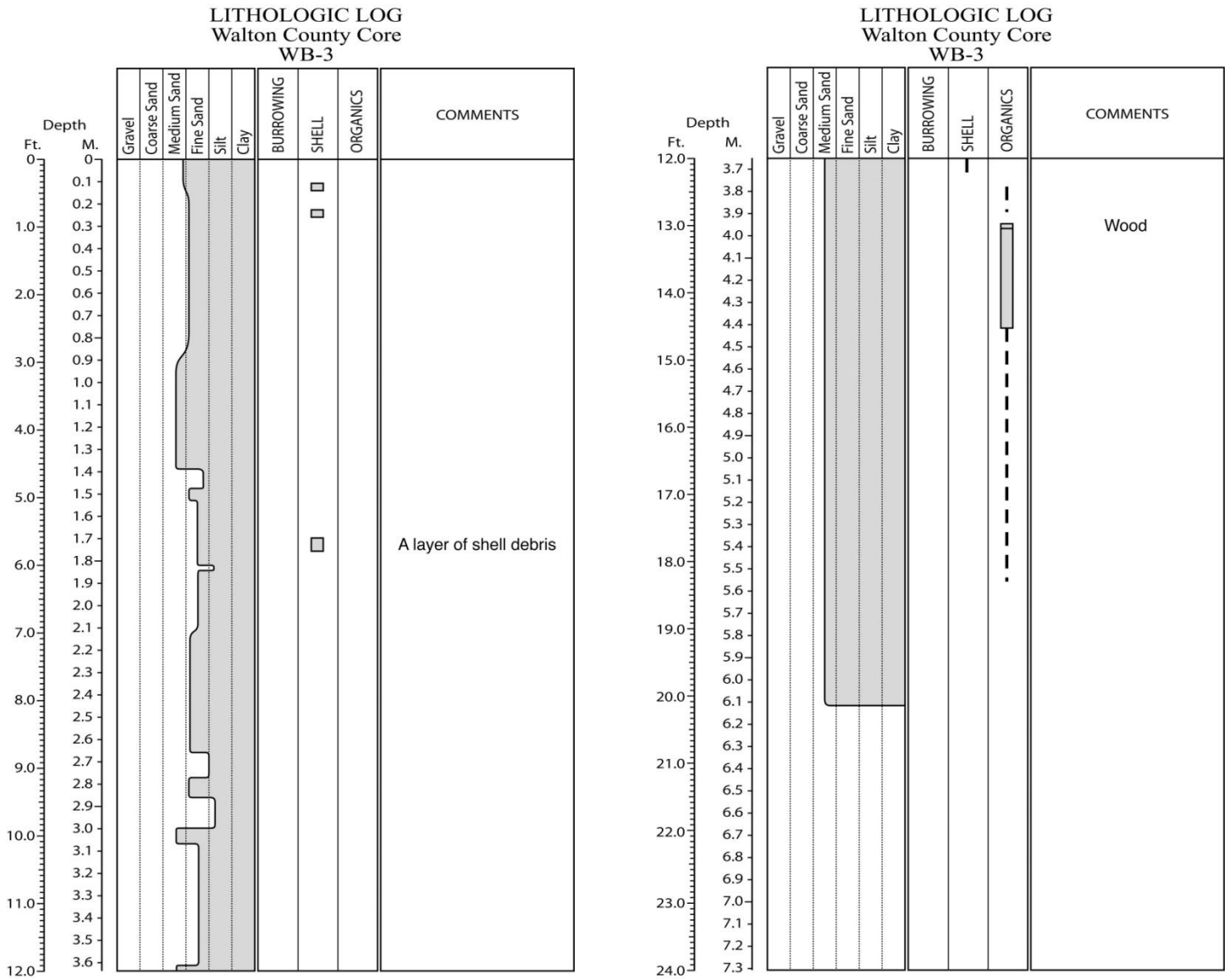

Figure E.132. Core WB-3 log.

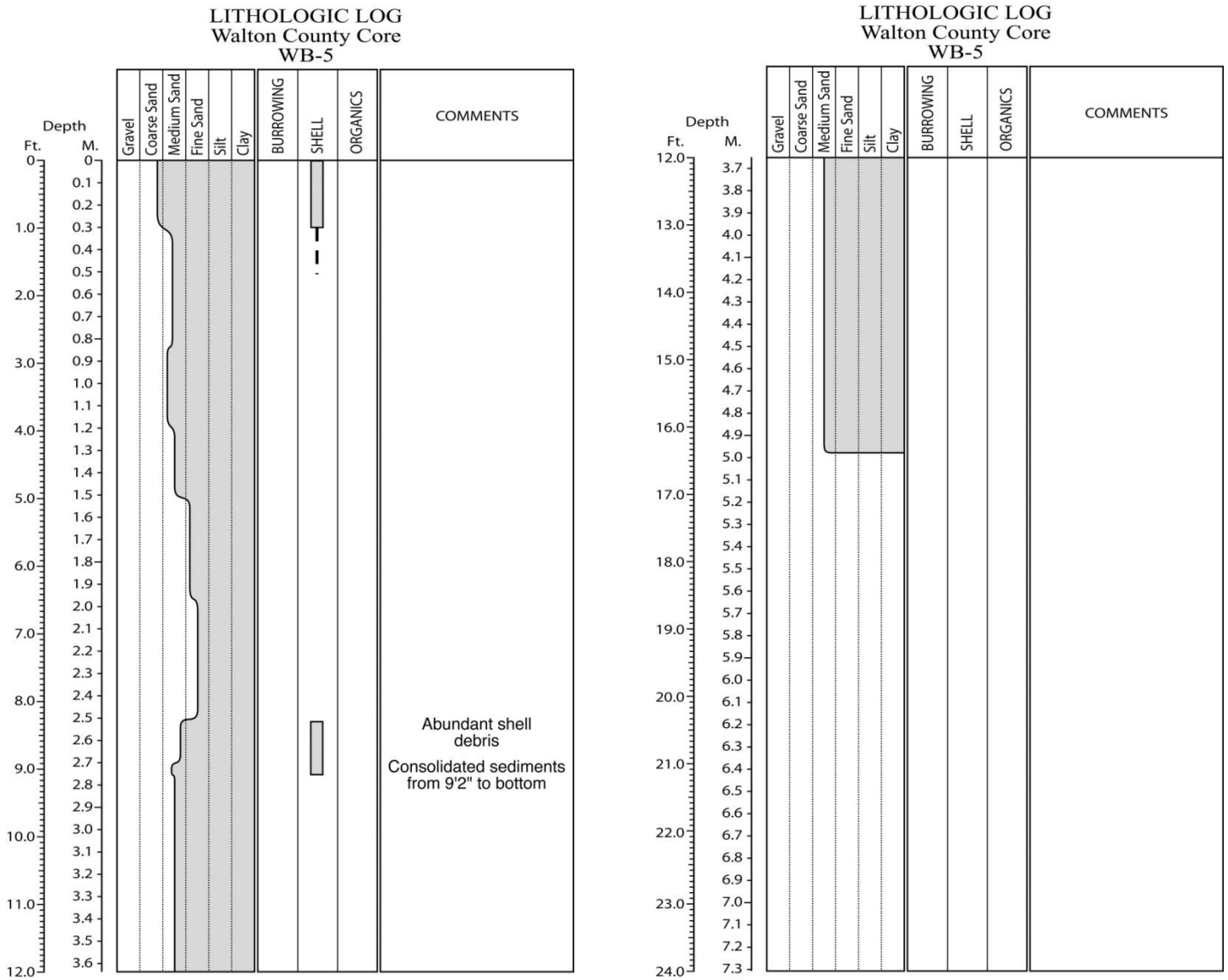

Figure E.133. Core WB-5 log.

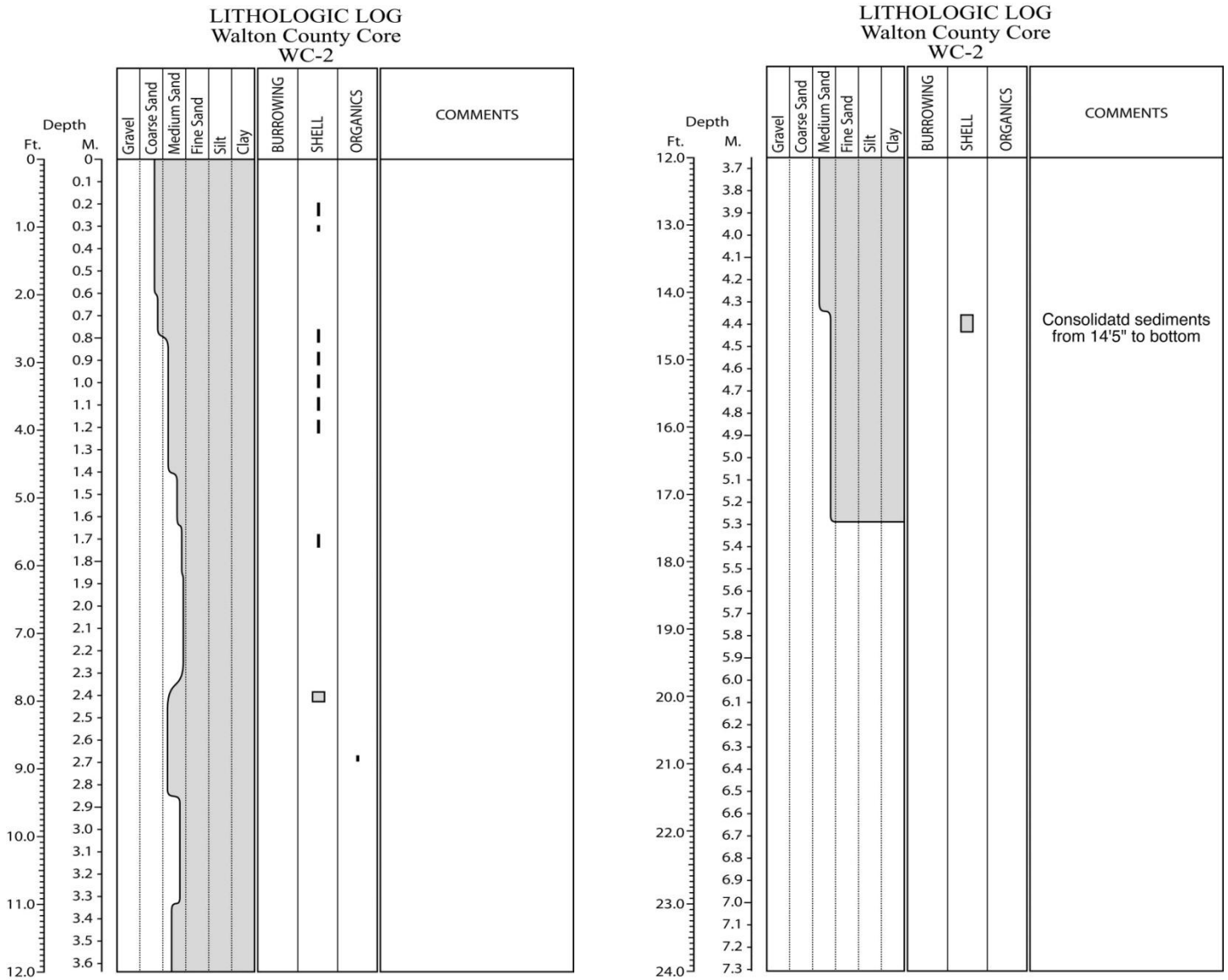

Figure E.134. Core WC-2 log.

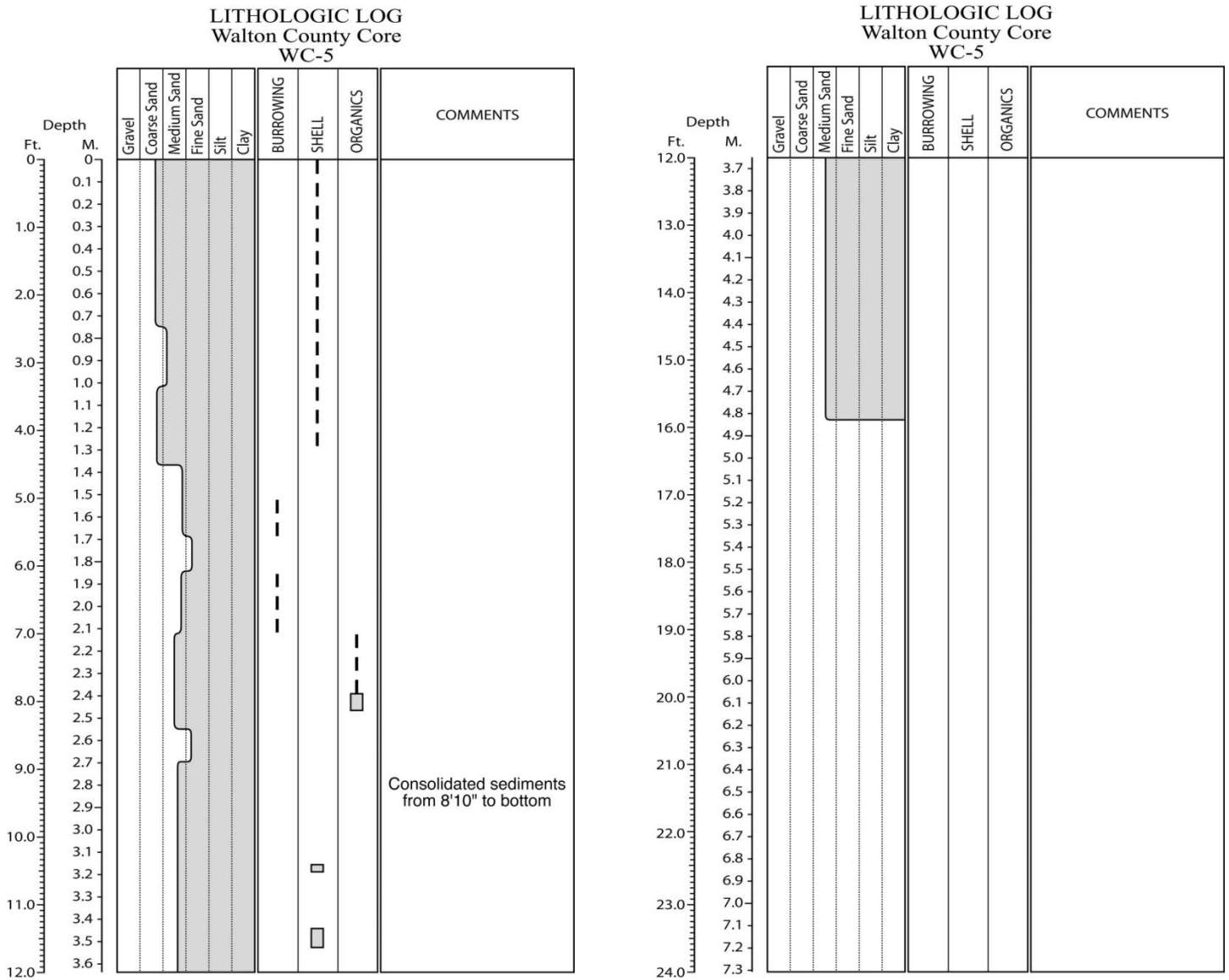

Figure E.135. Core WC-5 log.

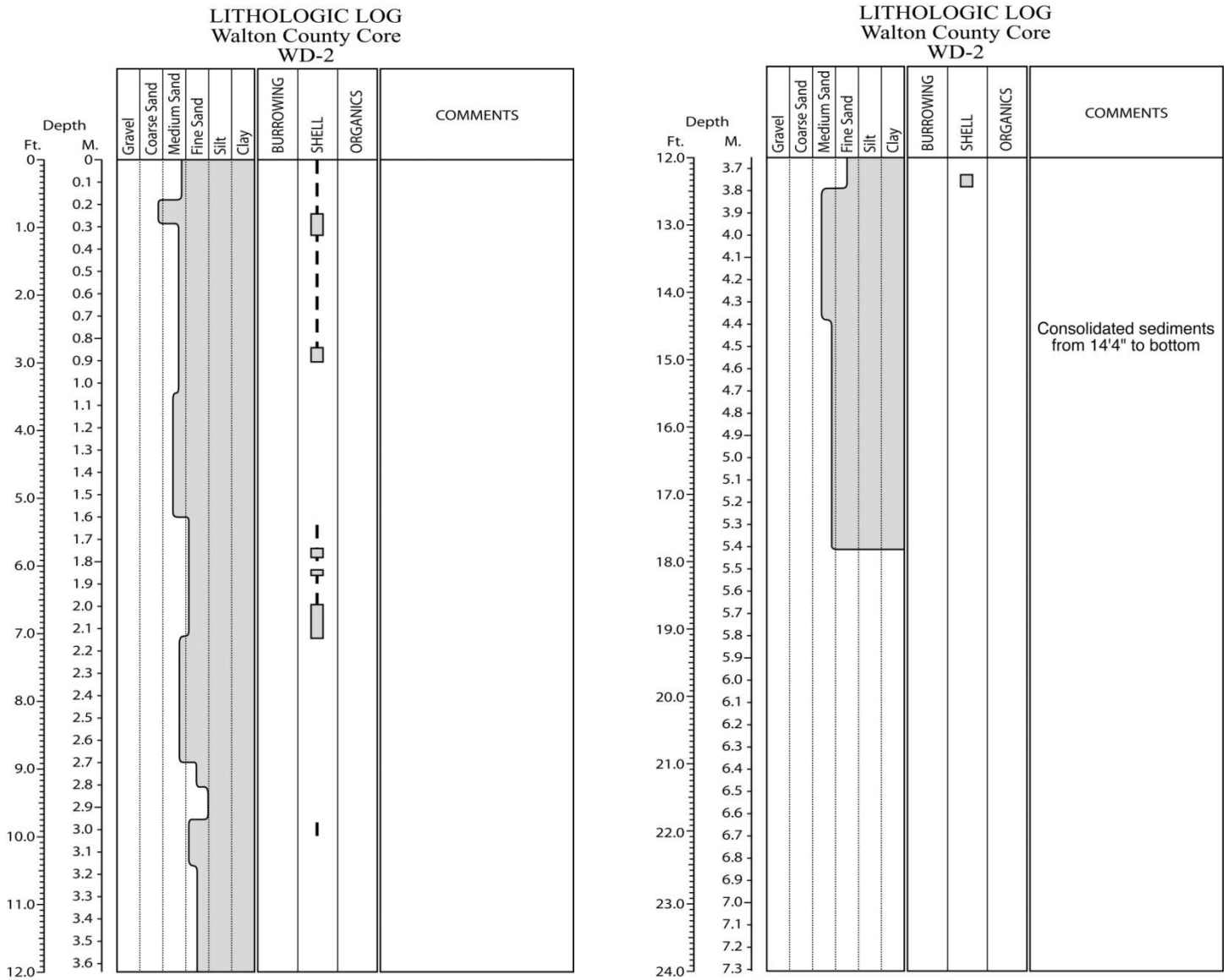

Figure E.136. Core WD-2 log.

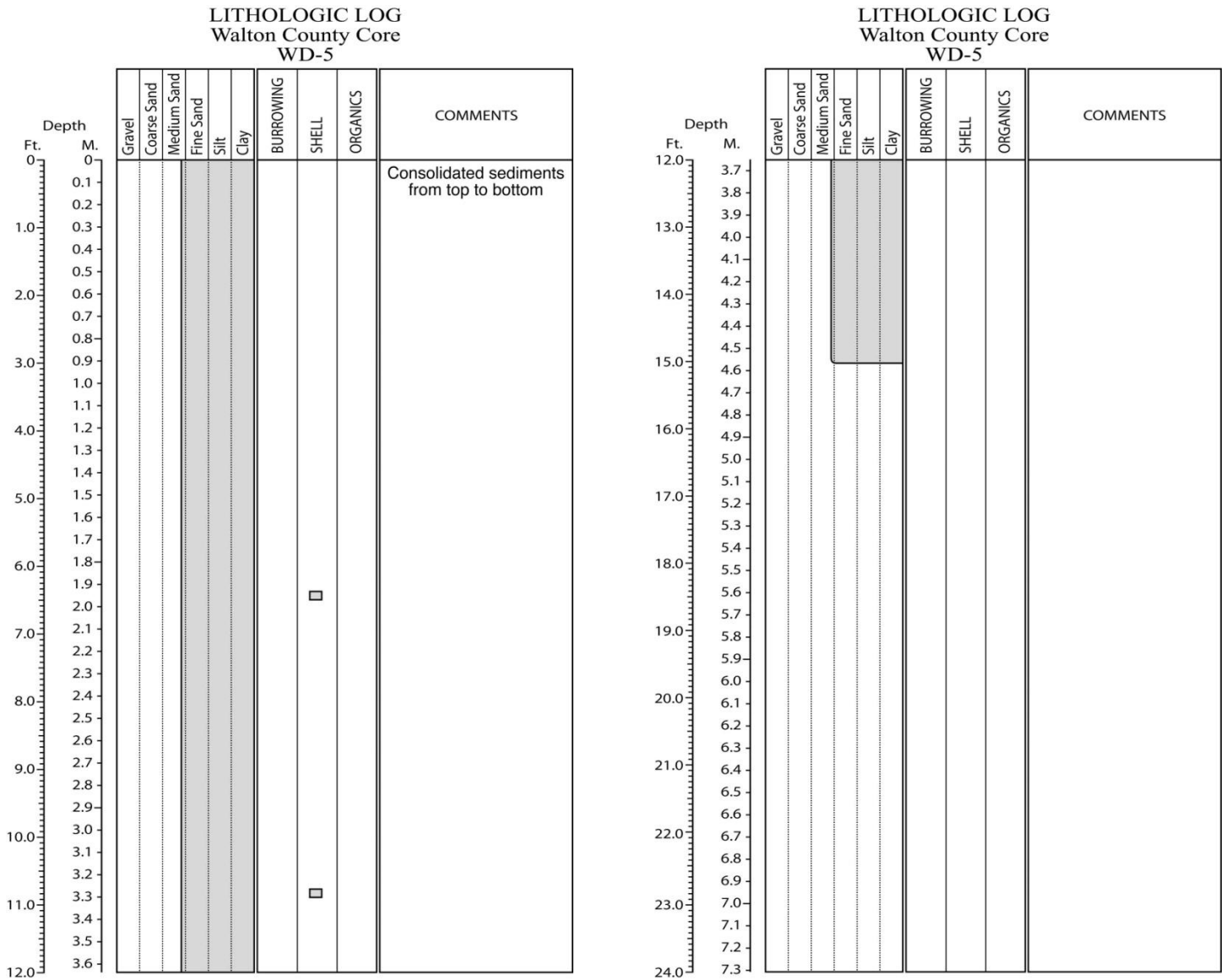

Figure E.137. Core WD-5 log.

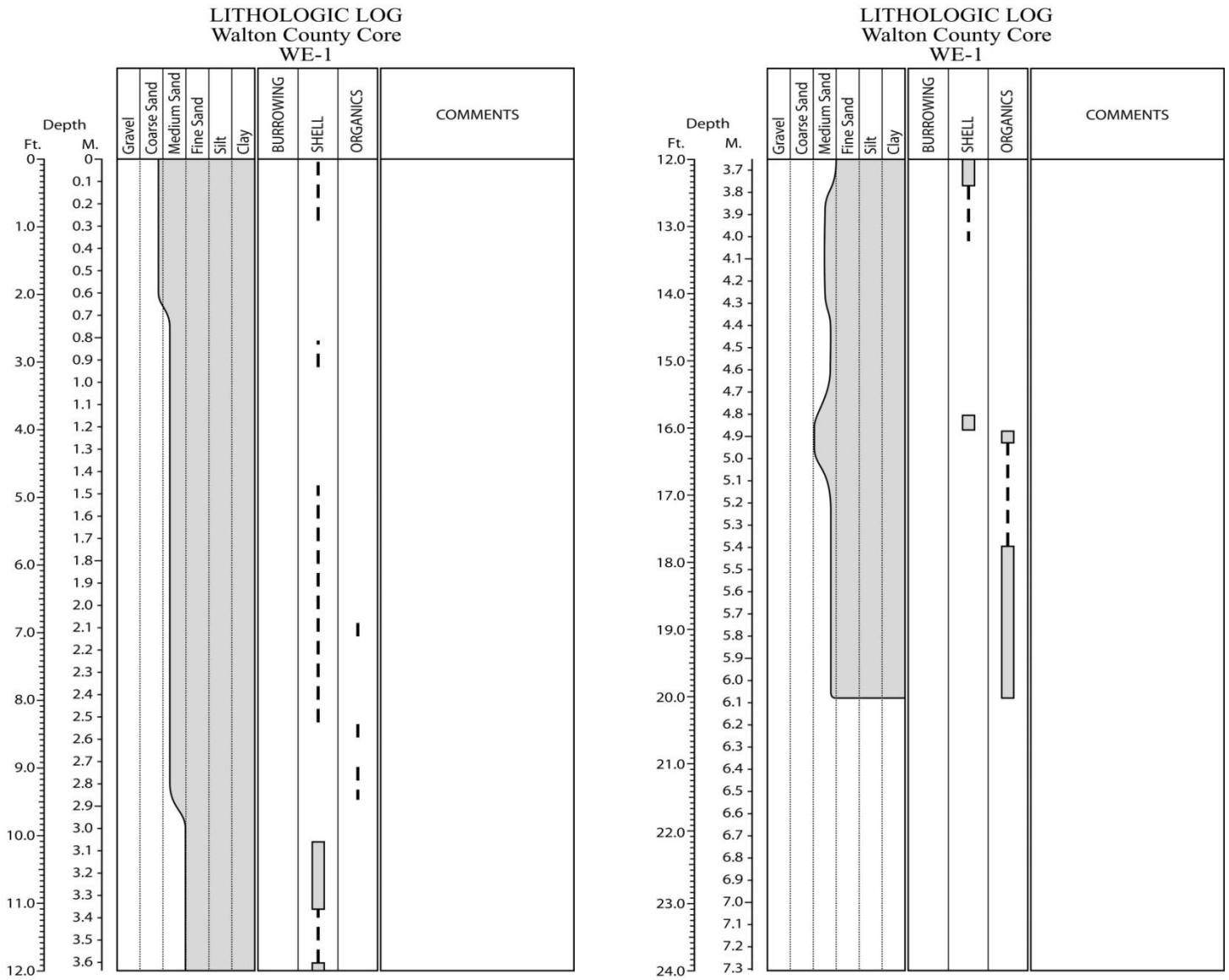

Figure E.138. Core WE-1 log.

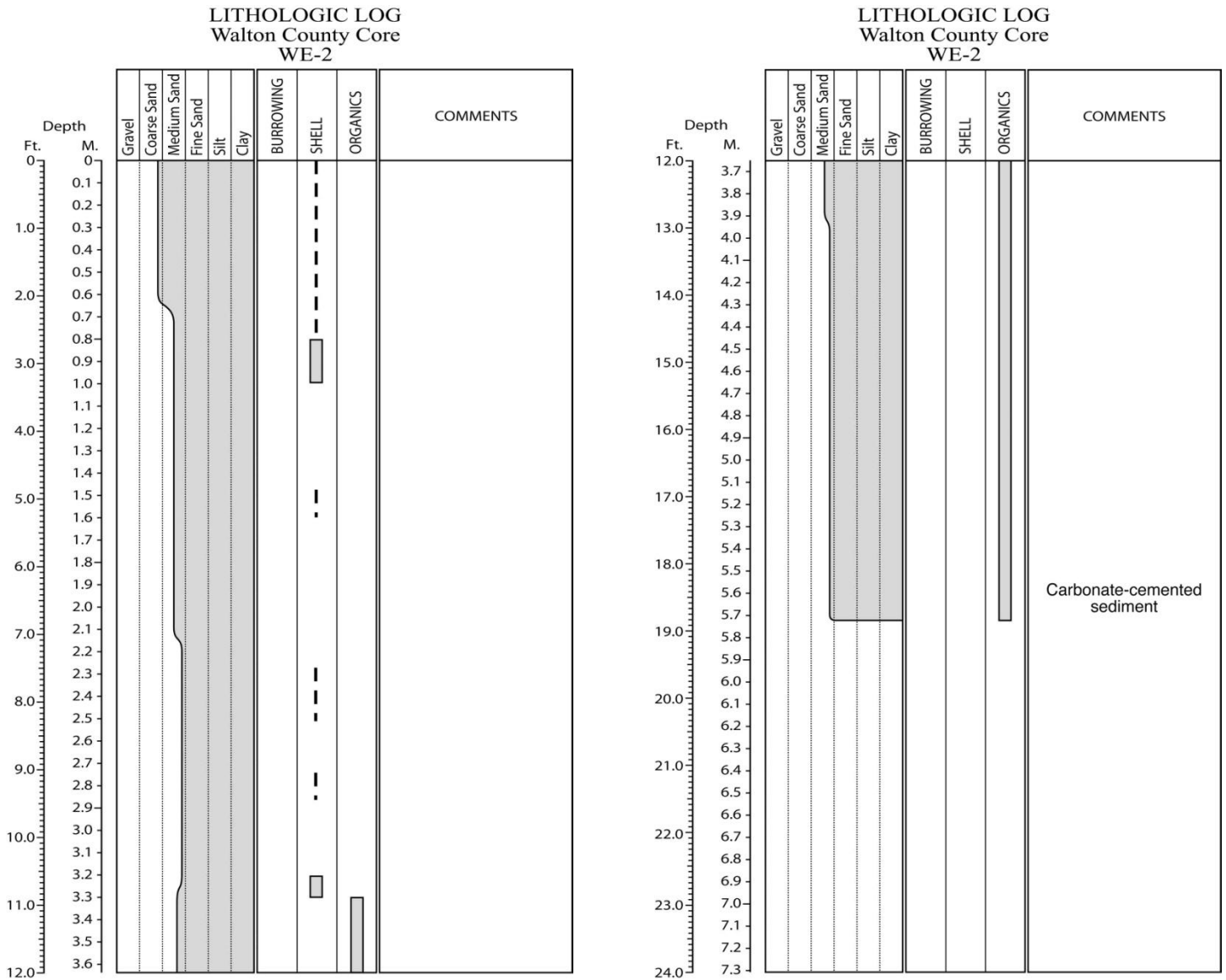

Figure E.139. Core WE-2 log.

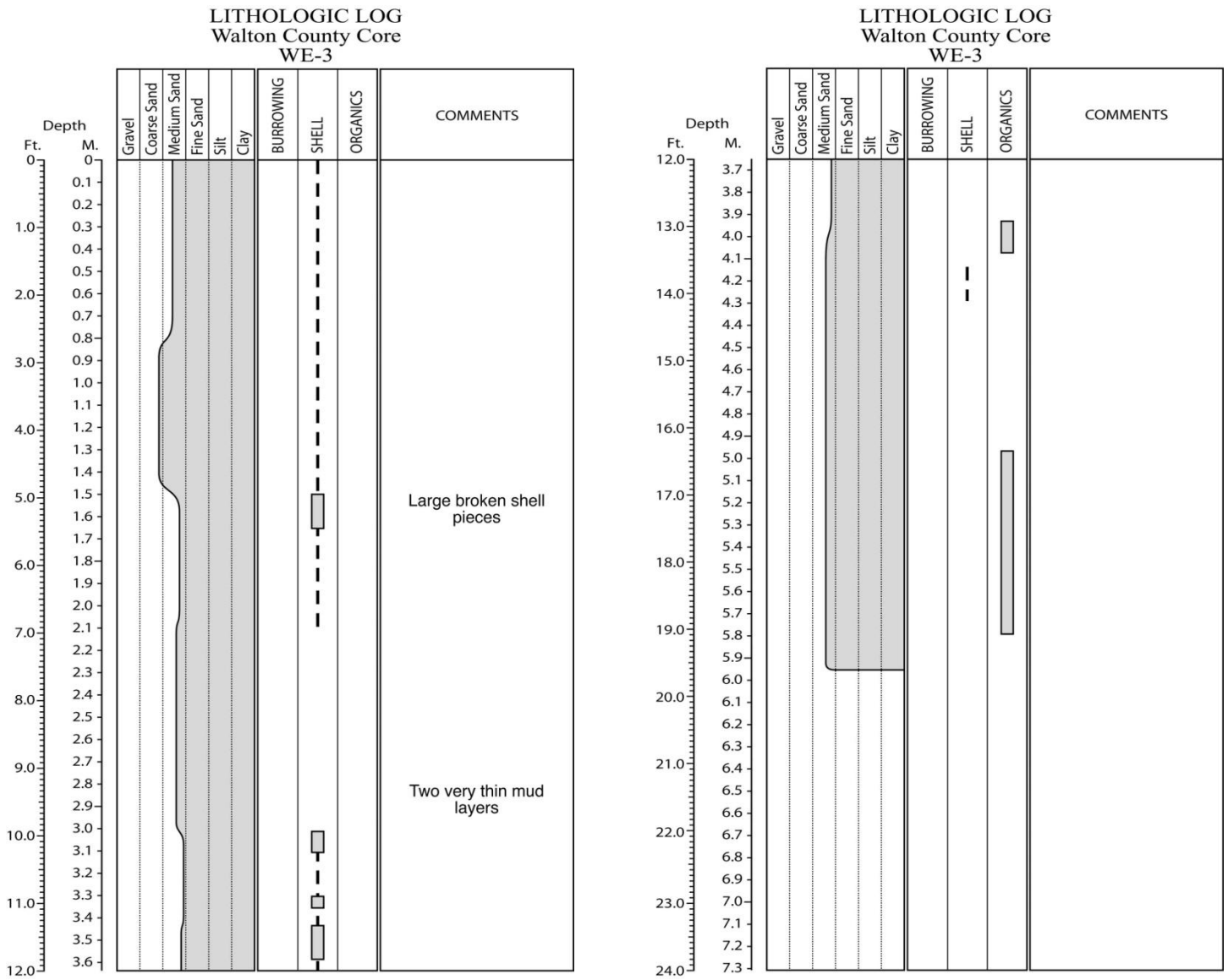

Figure E.140. Core WE-3 log.

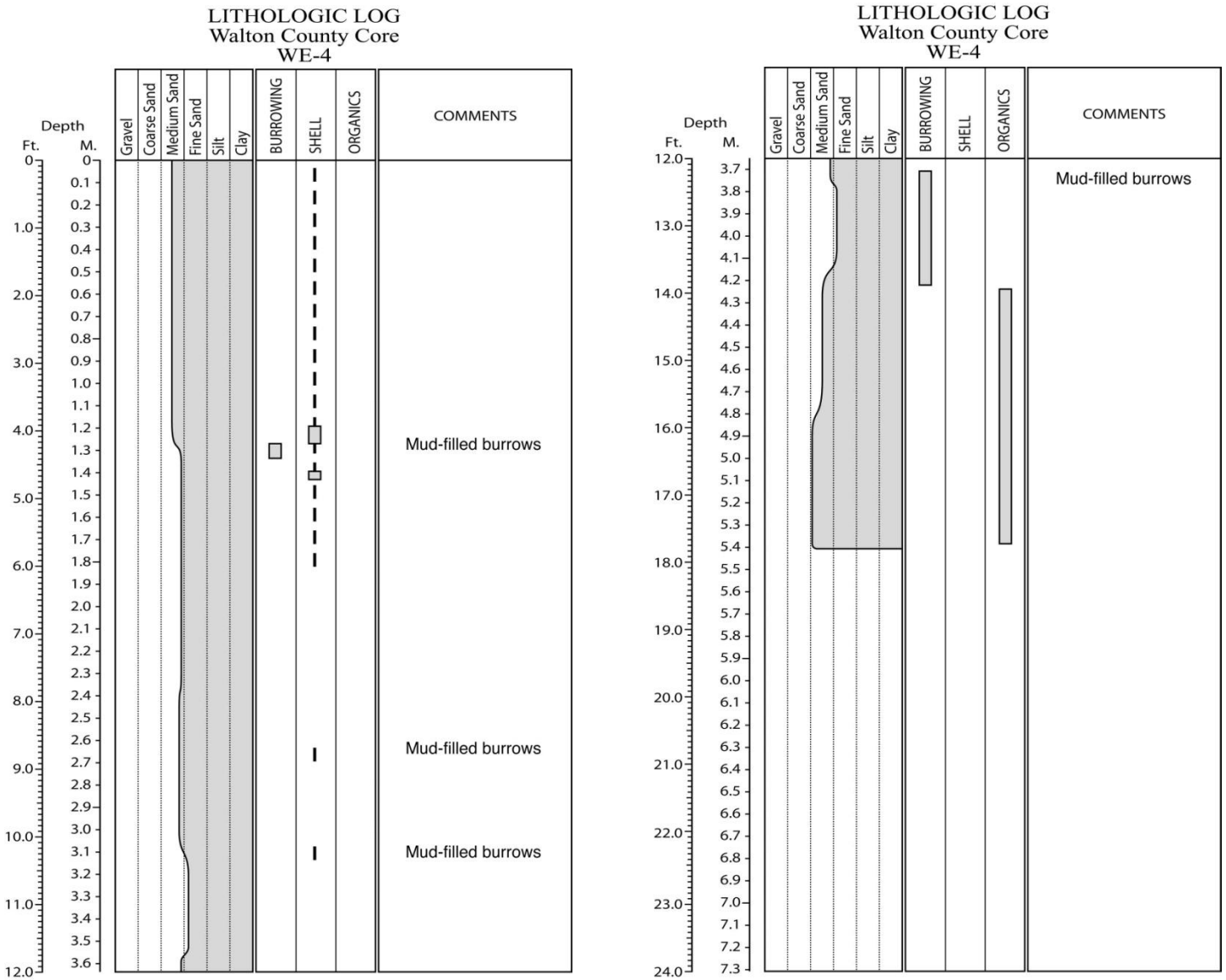

Figure E.141. Core WE-4 log.

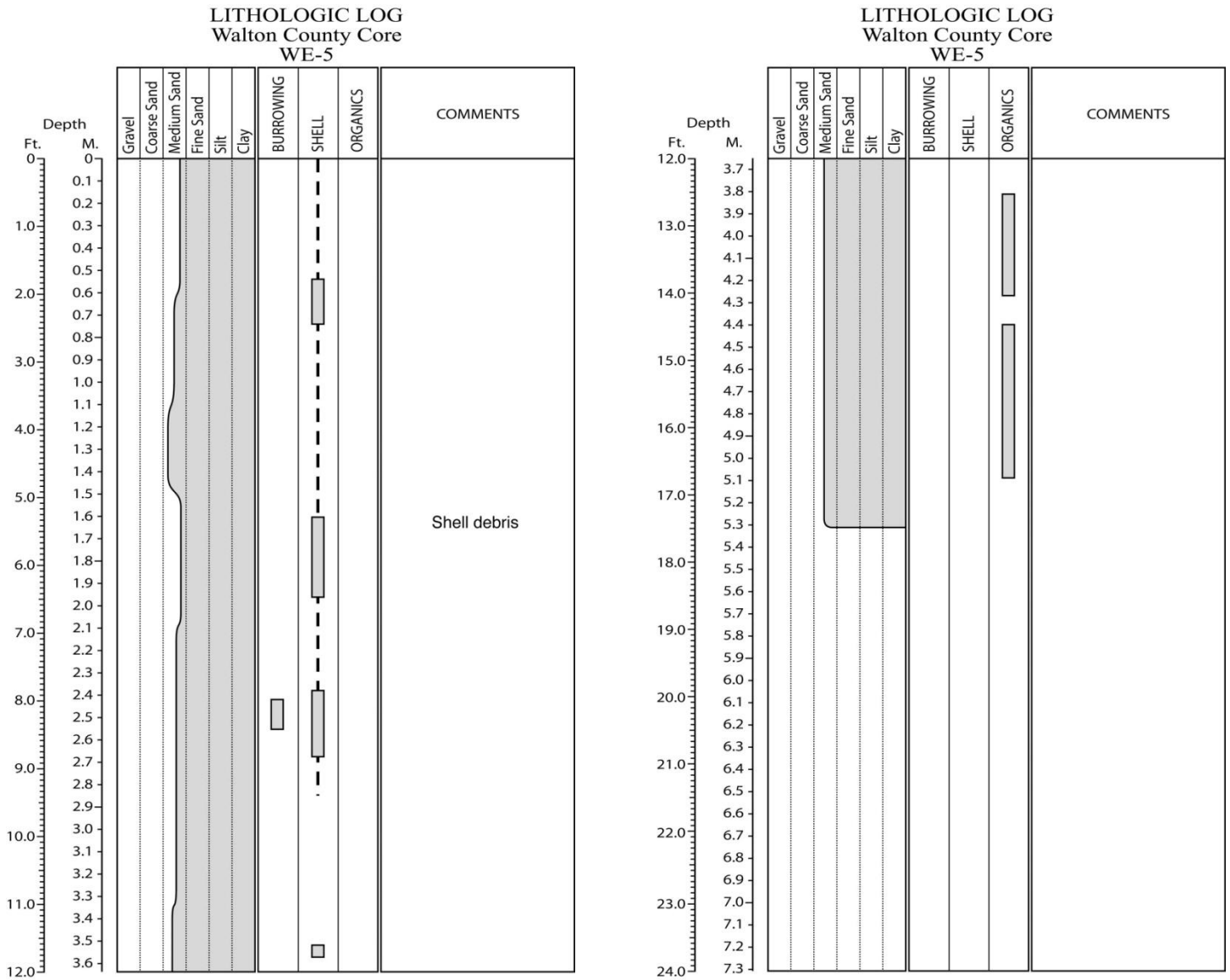

Figure E.142. Core WE-5 log.

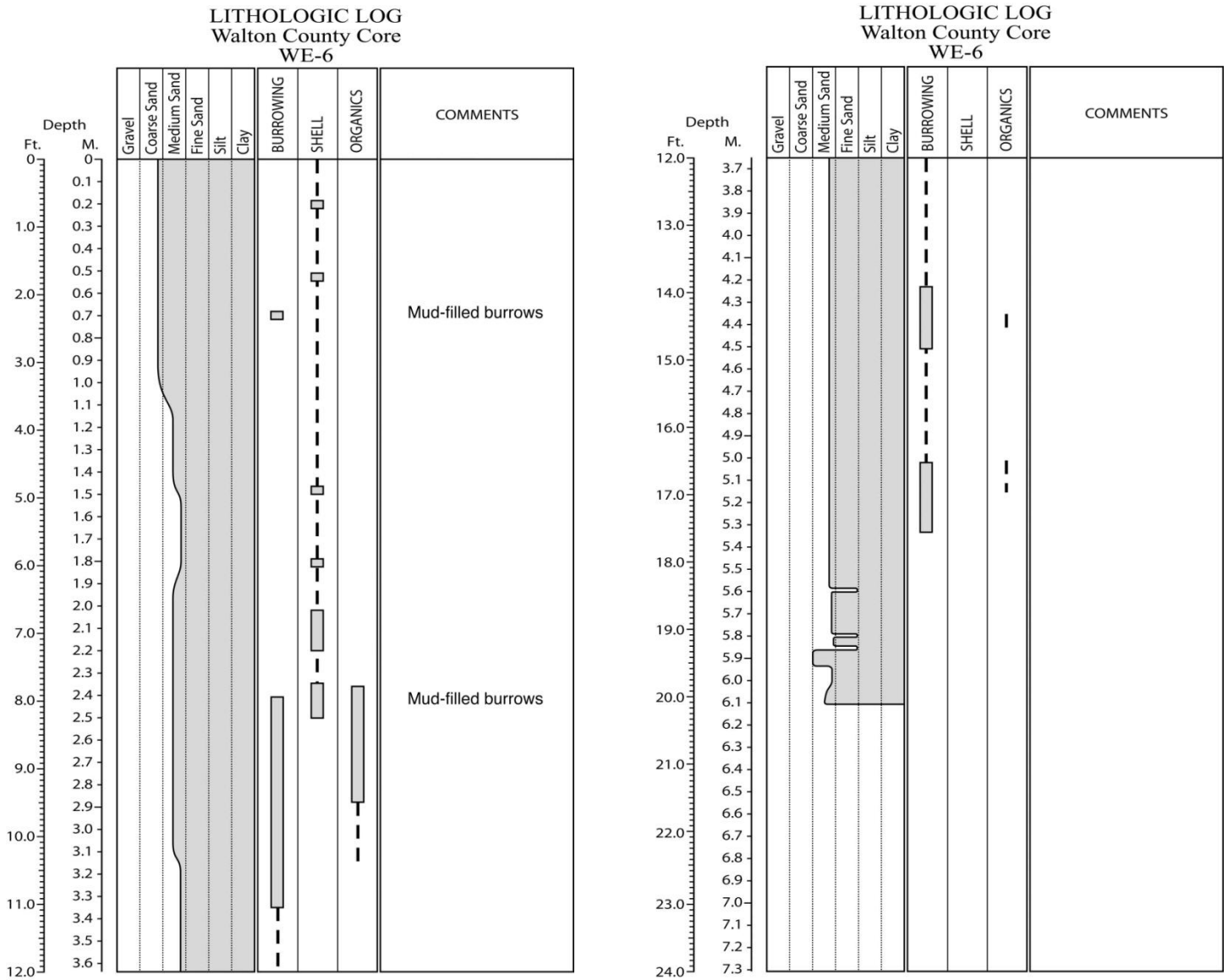

Figure E.143. Core WE-6 log.

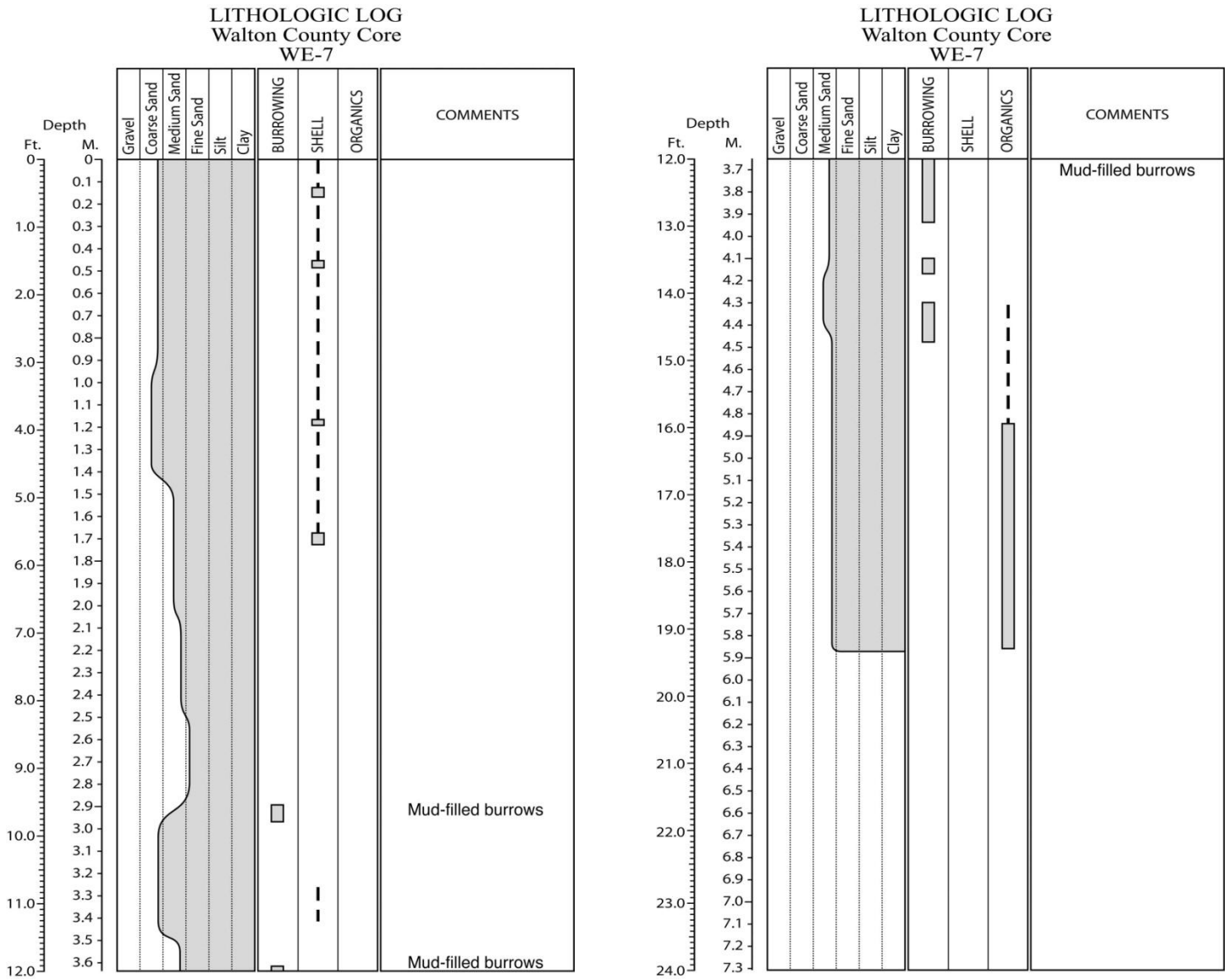

Figure E.144. Core WE-7 log.

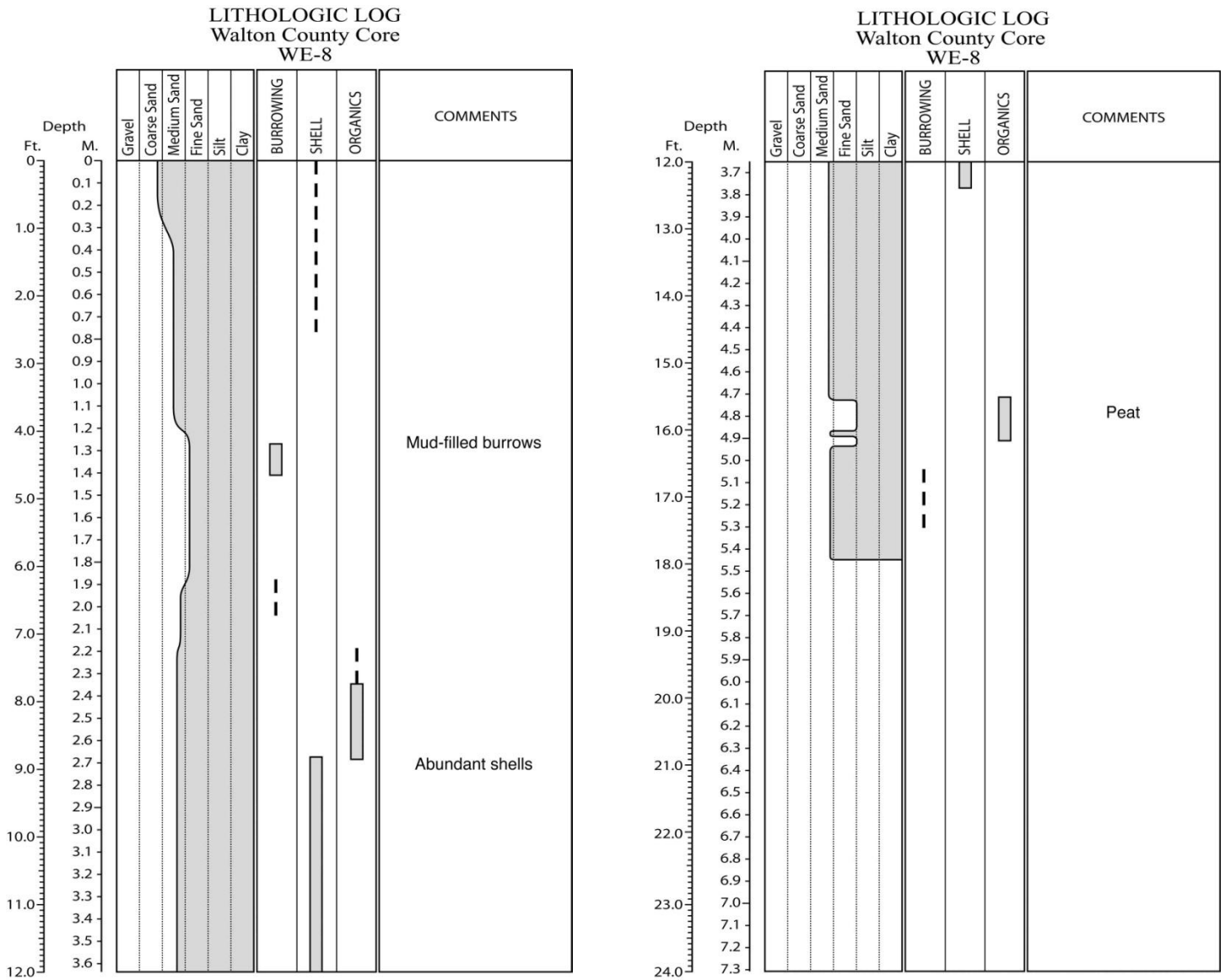

Figure E.145. Core WE-8 log.

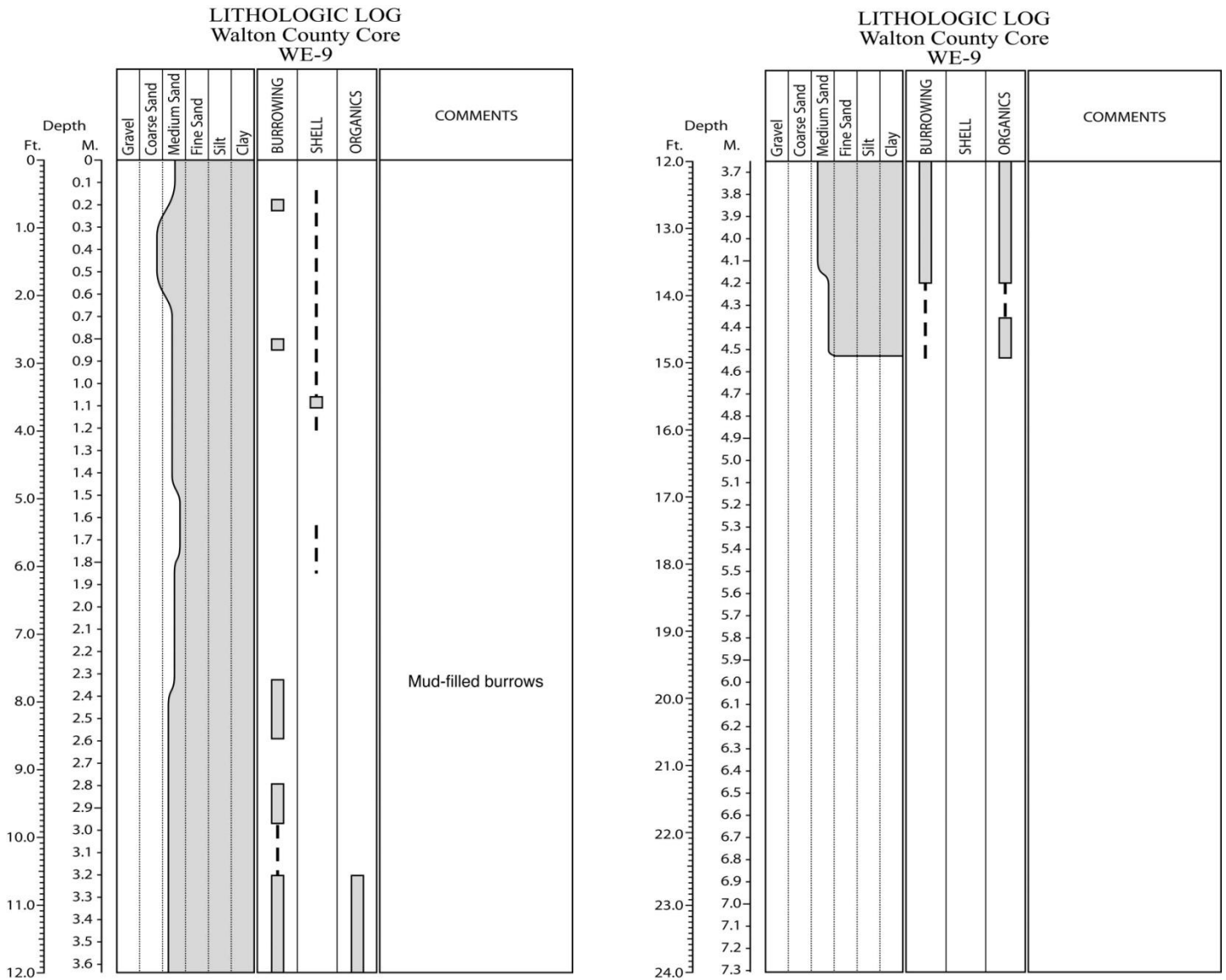

Figure E.146. Core WE-9 log.

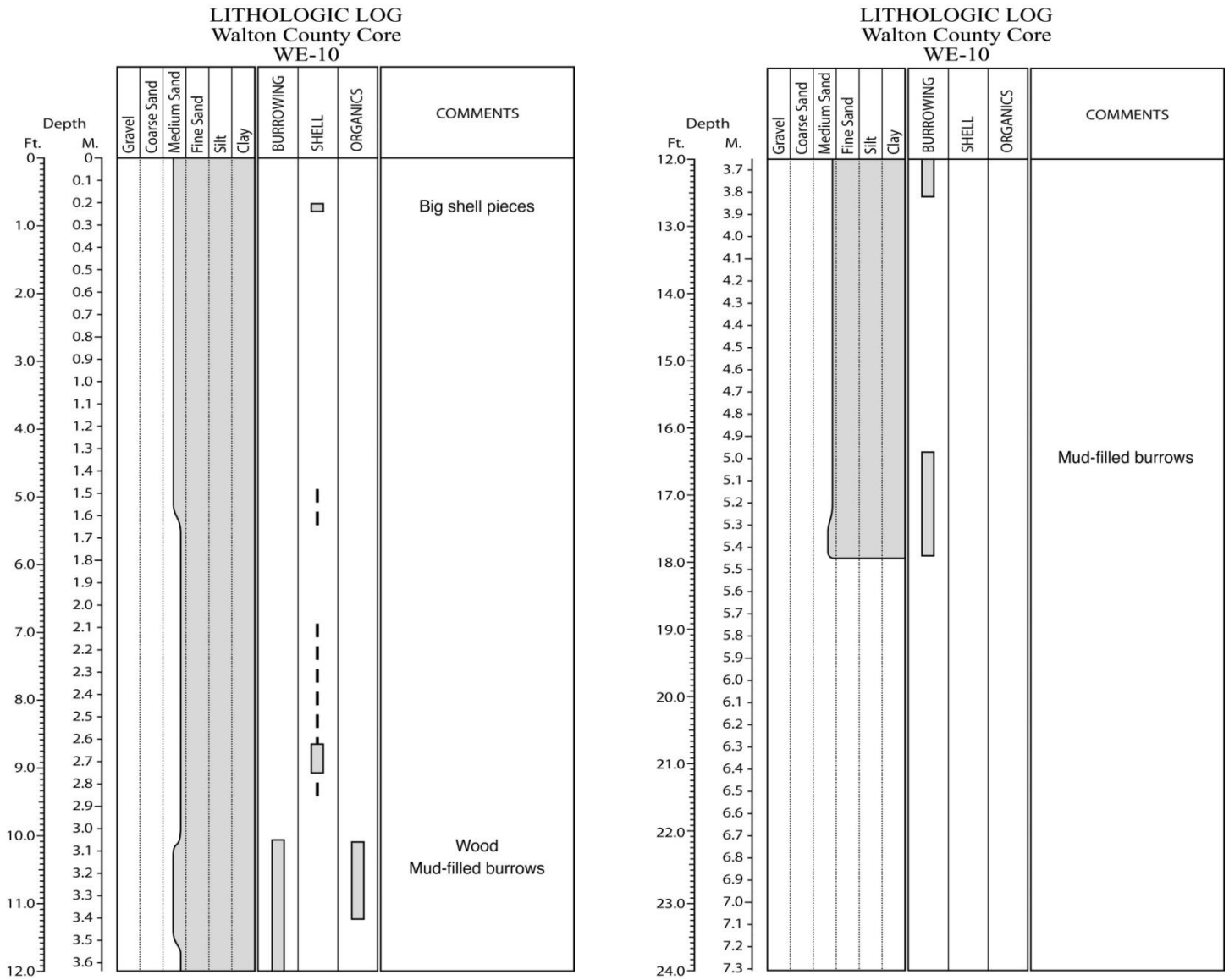

Figure E.147. Core WE-10 log.

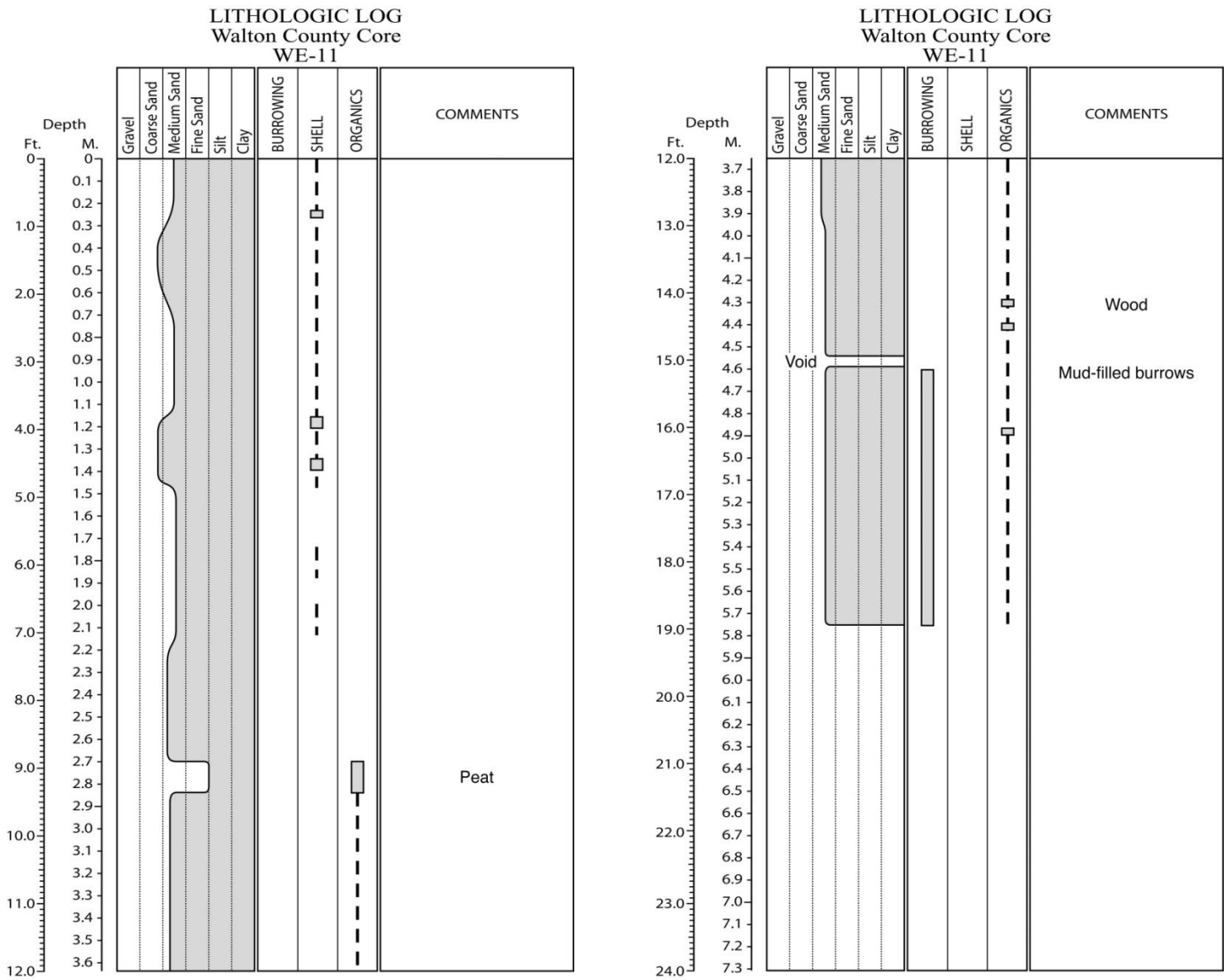

Figure E.148. Core WE-11 log.

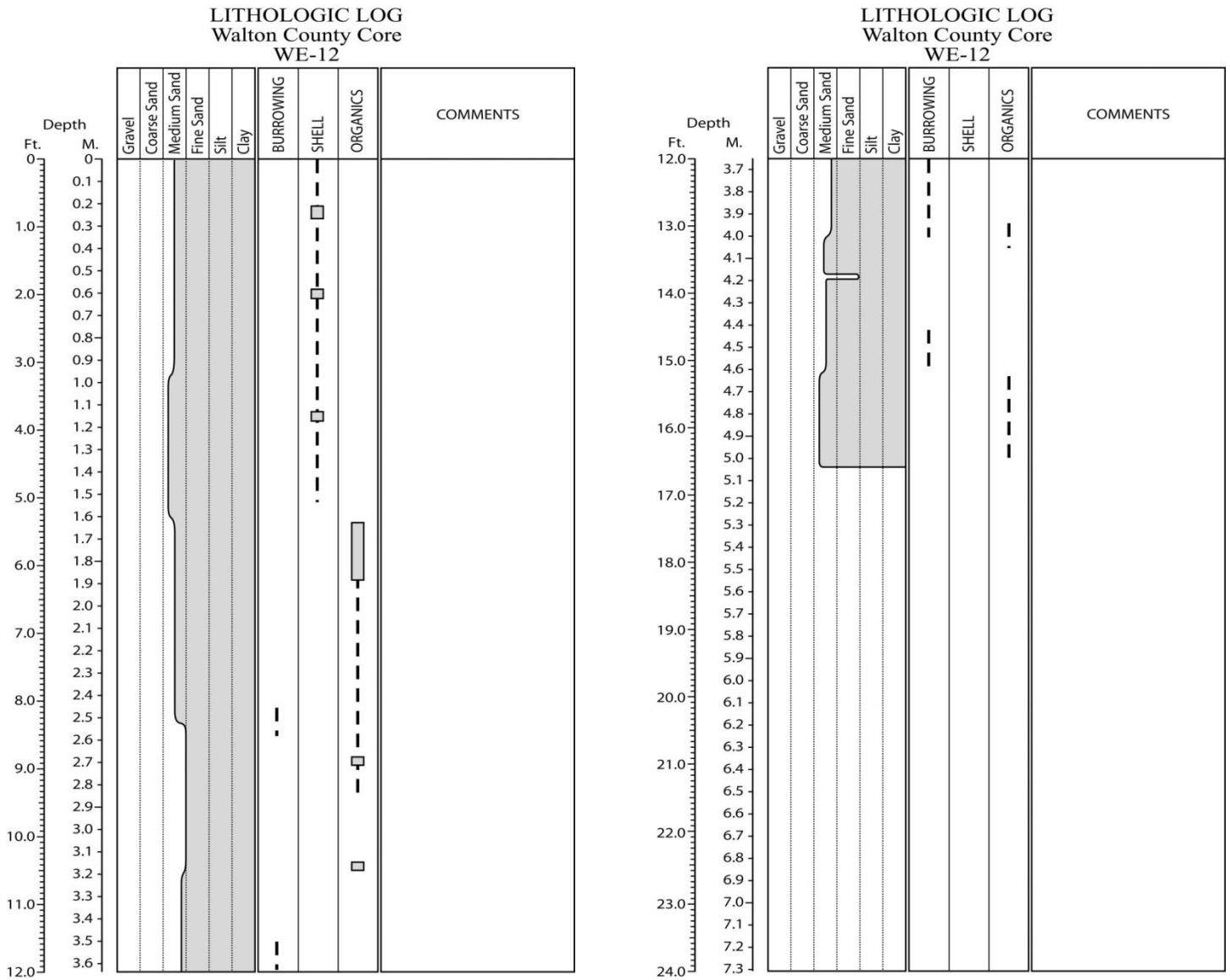

Figure E.149. Core WE-12 log.

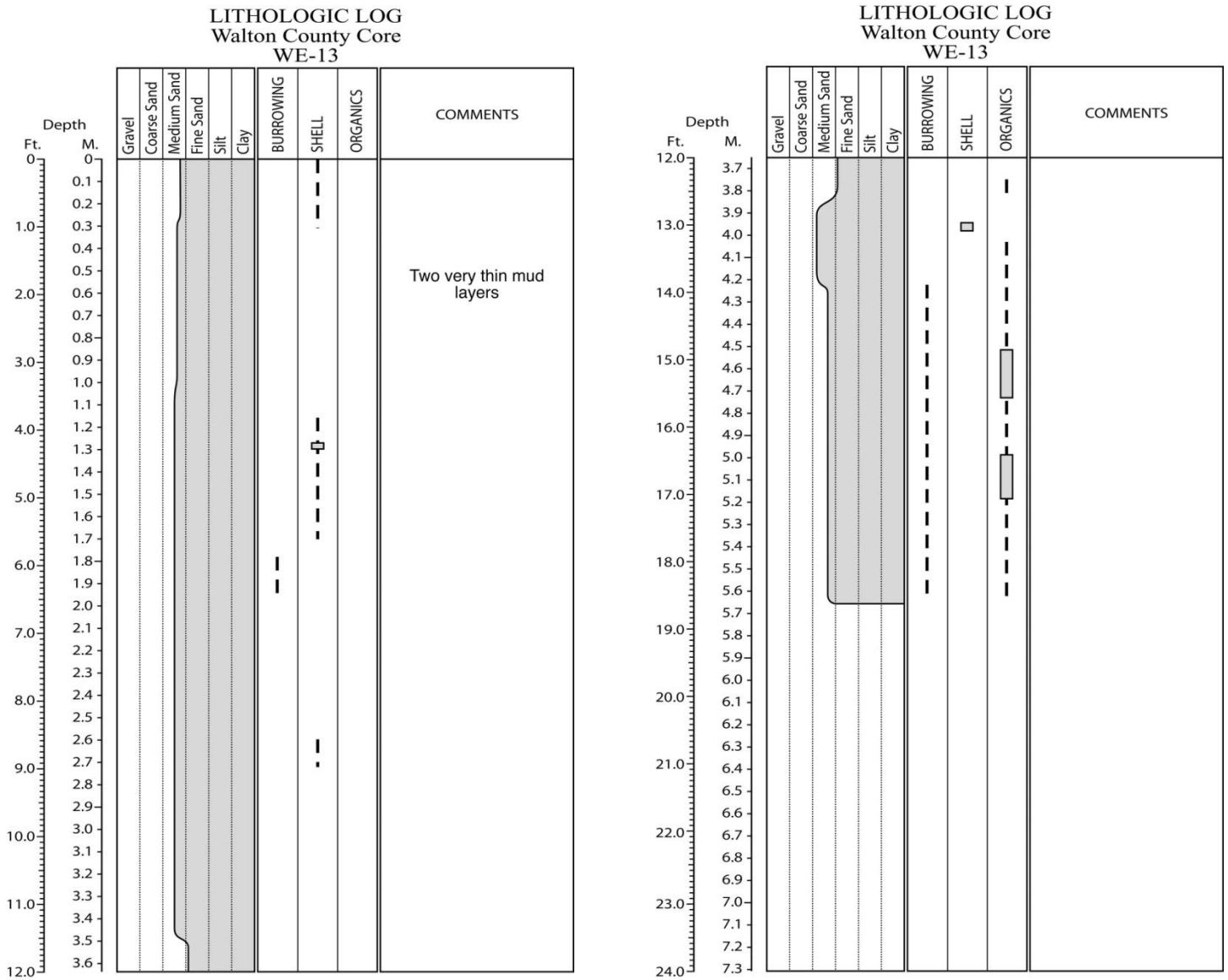

Figure E.150. Core WE-13 log.

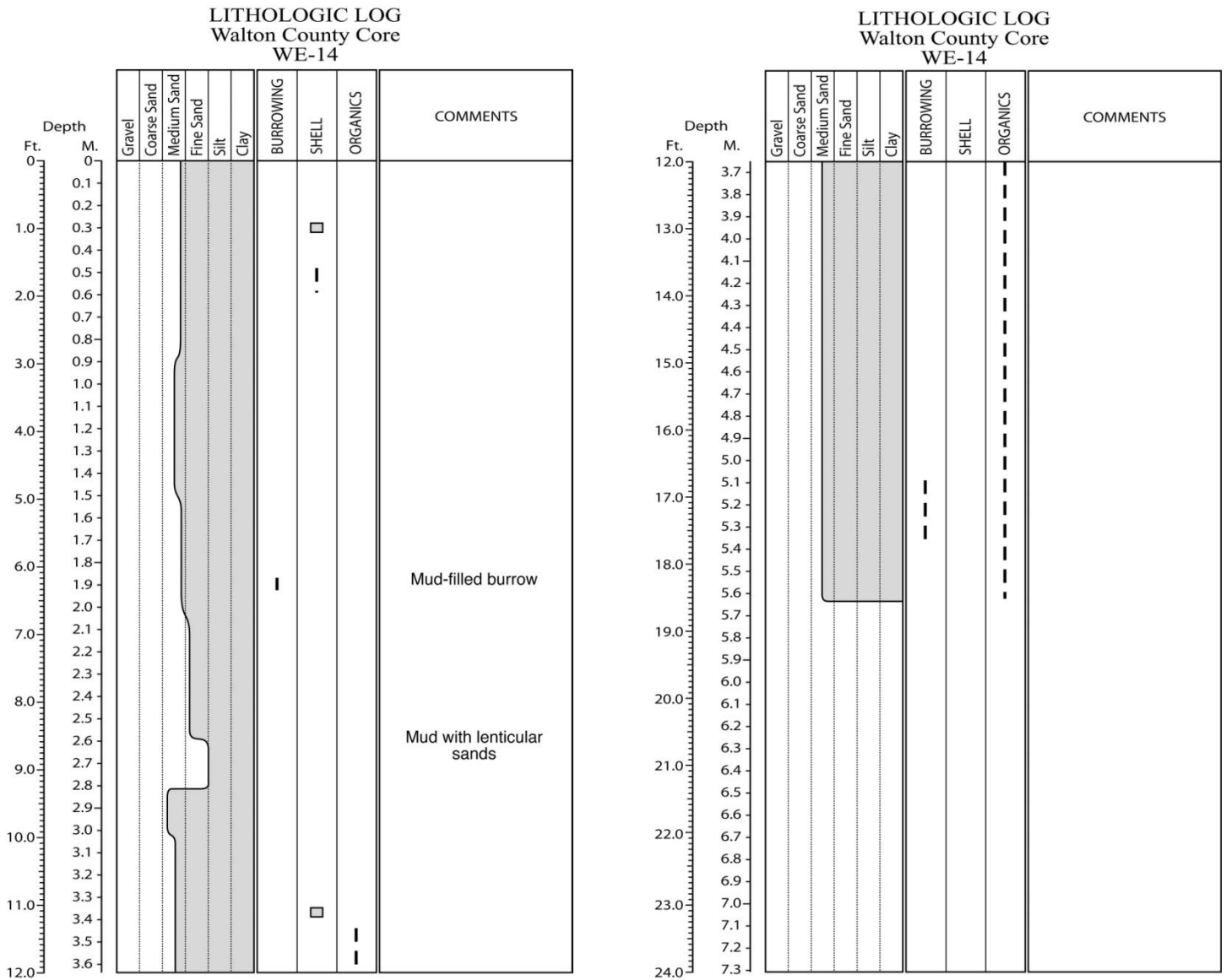

Figure E.151. Core WE-14 log.

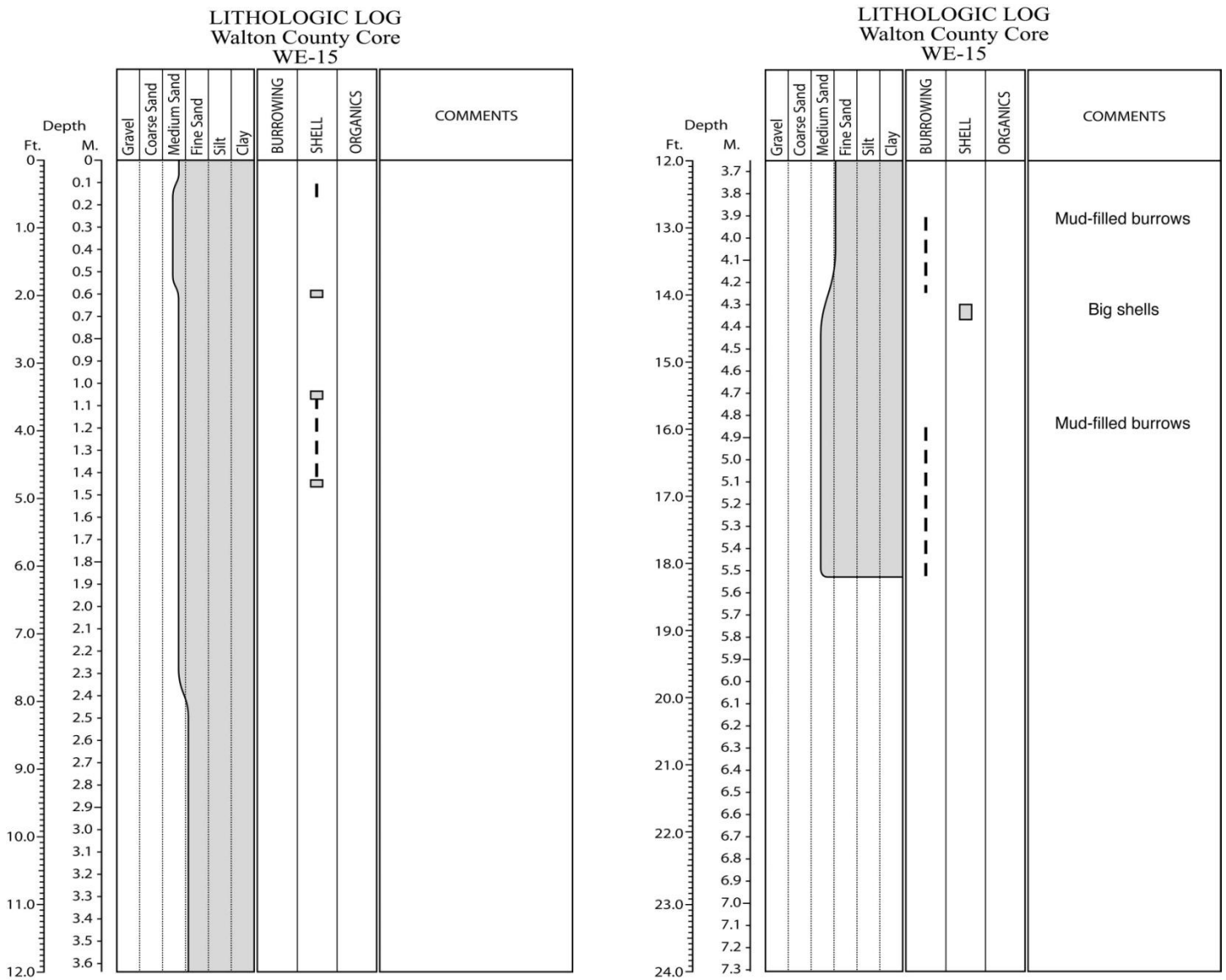

Figure E.152. Core WE-15 log.

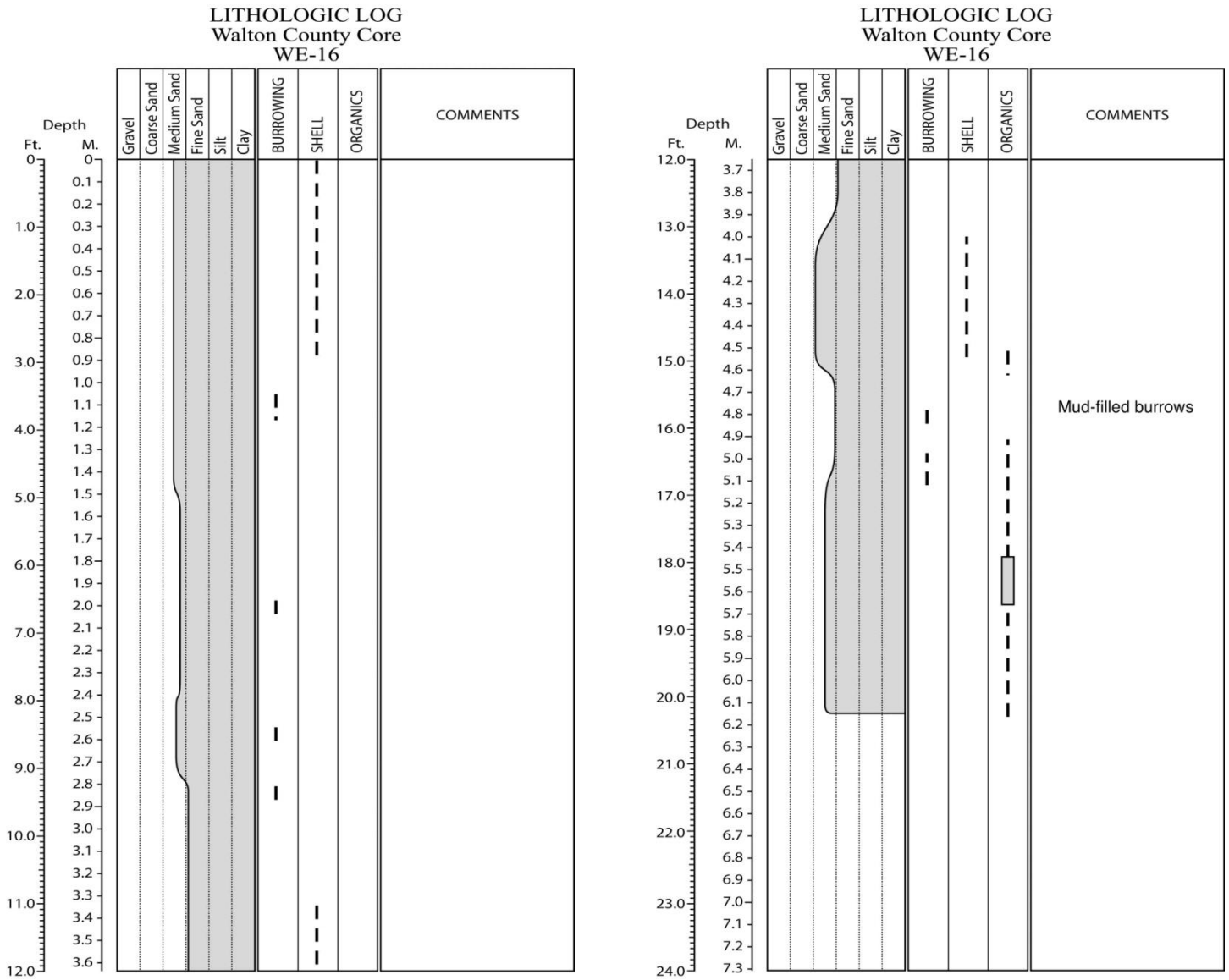

Figure E.153. Core WE-16 log.

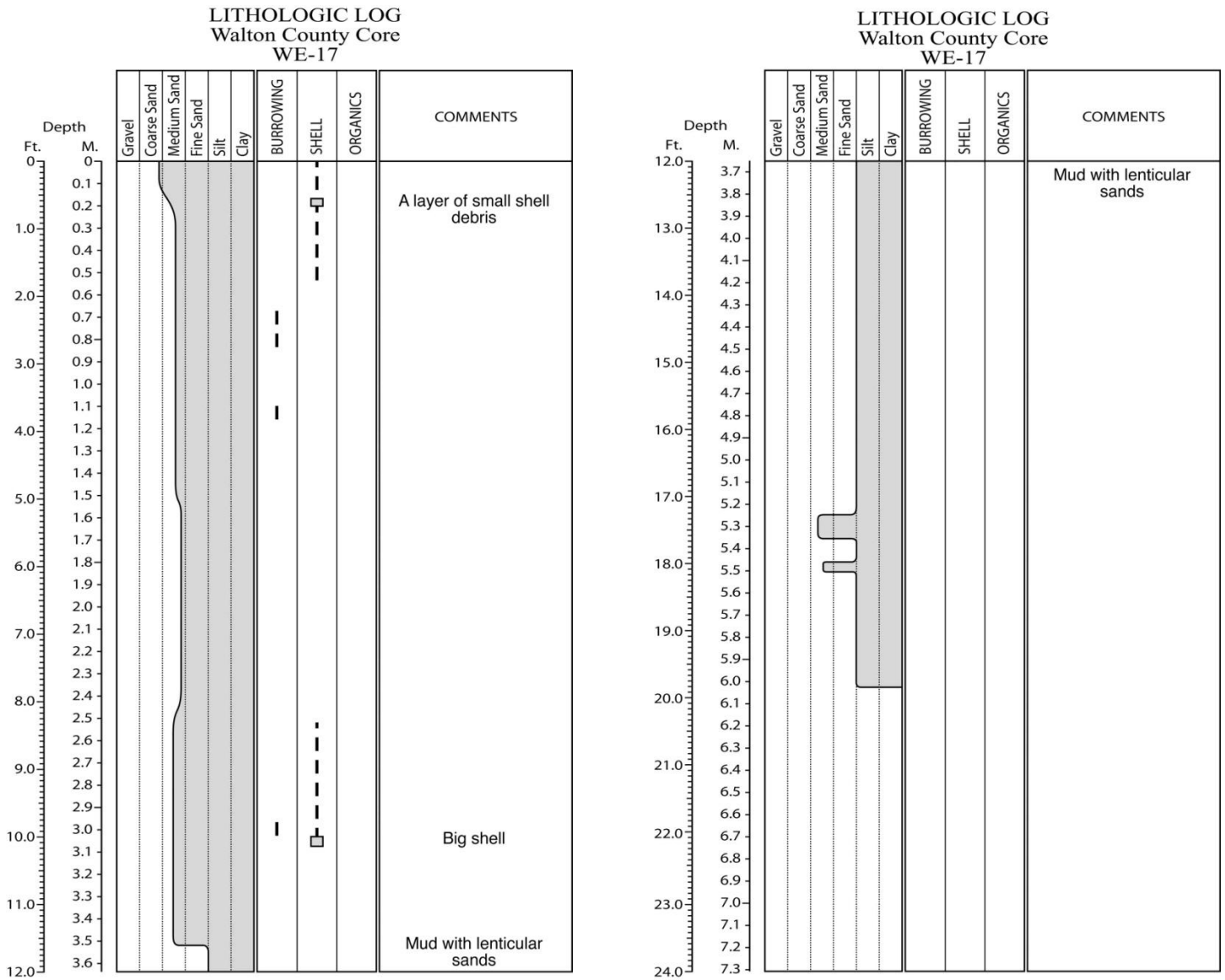

Figure E.154. Core WE-17 log.

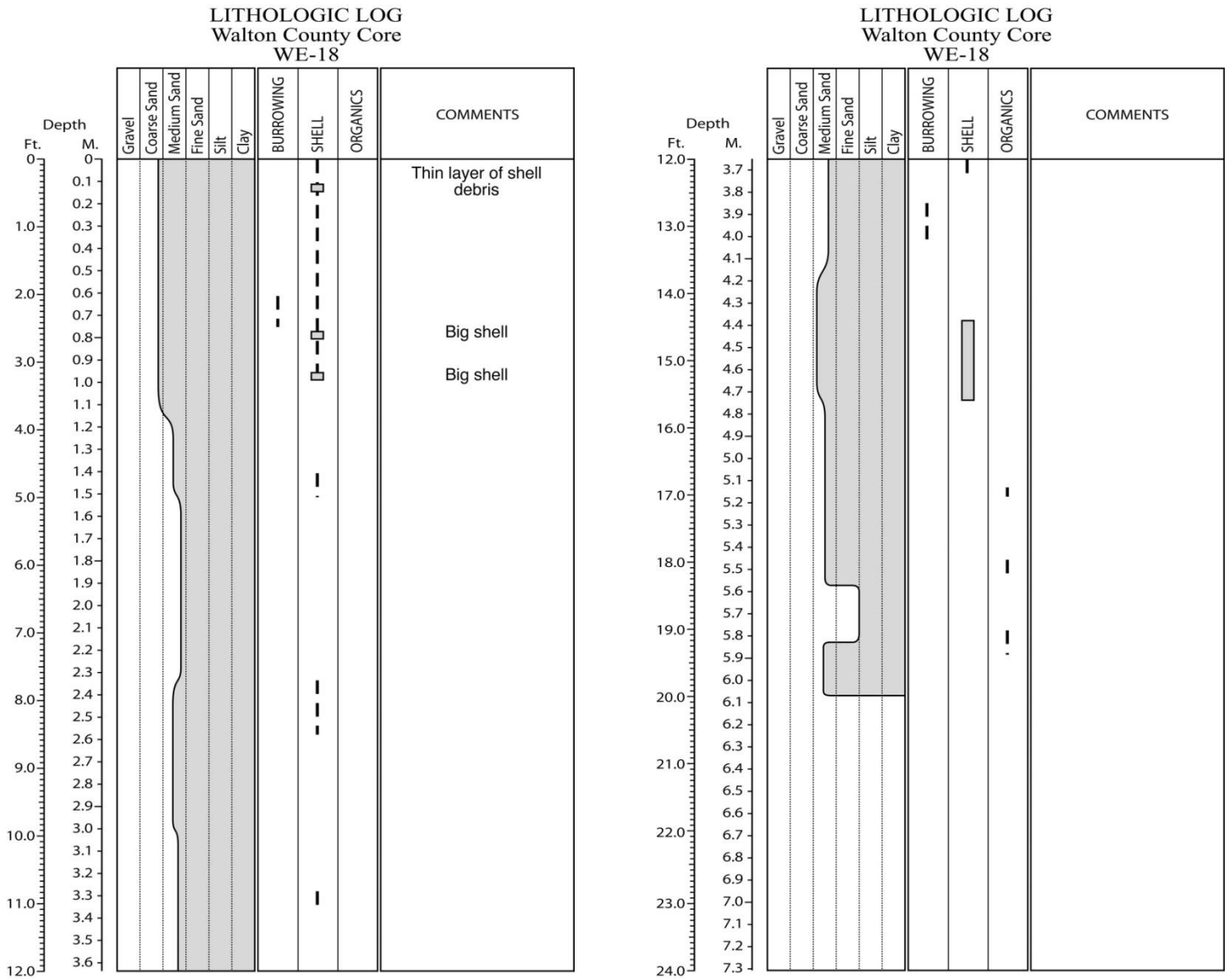

Figure E.155. Core WE-18 log.

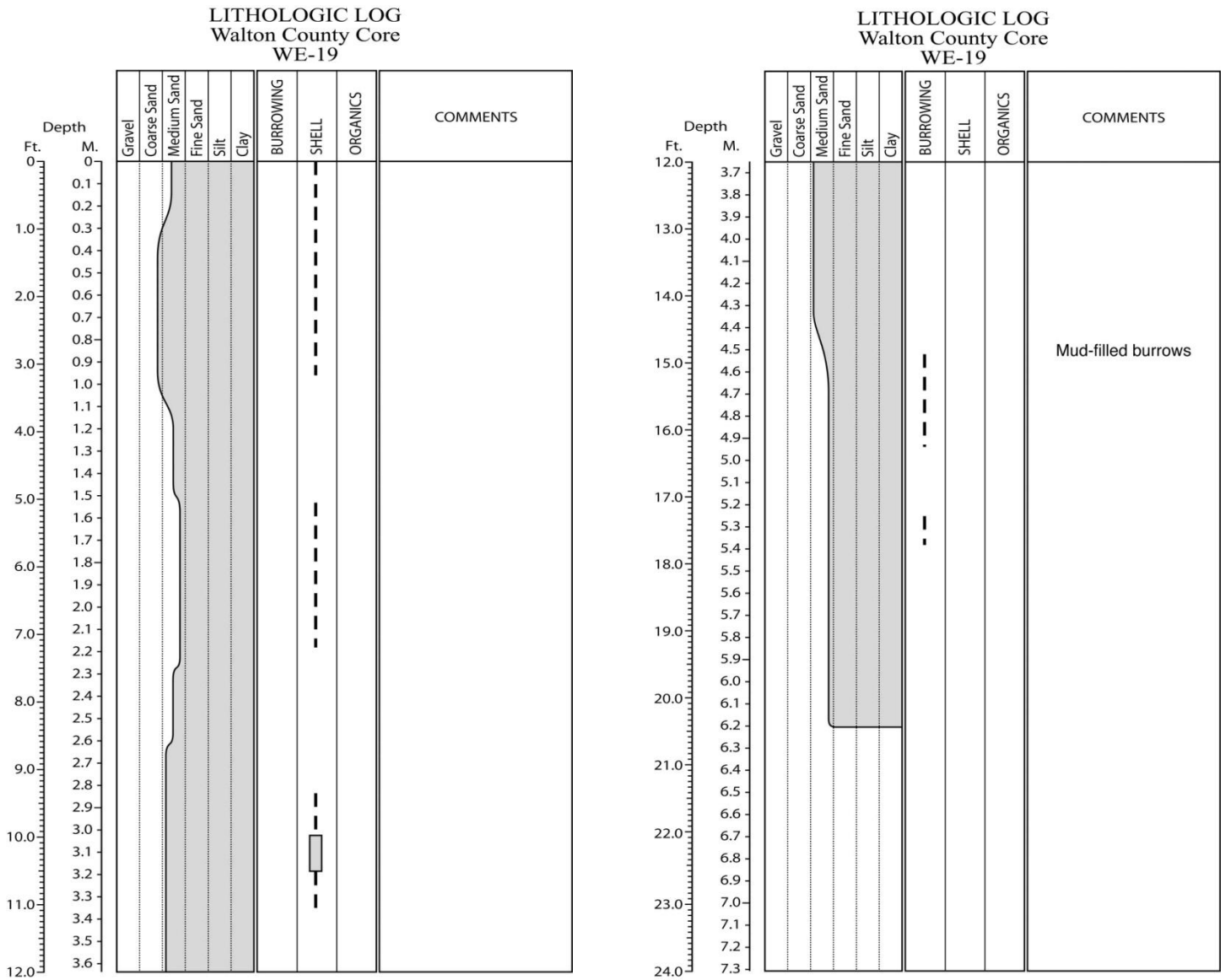

Figure E.156. Core WE-19 log.

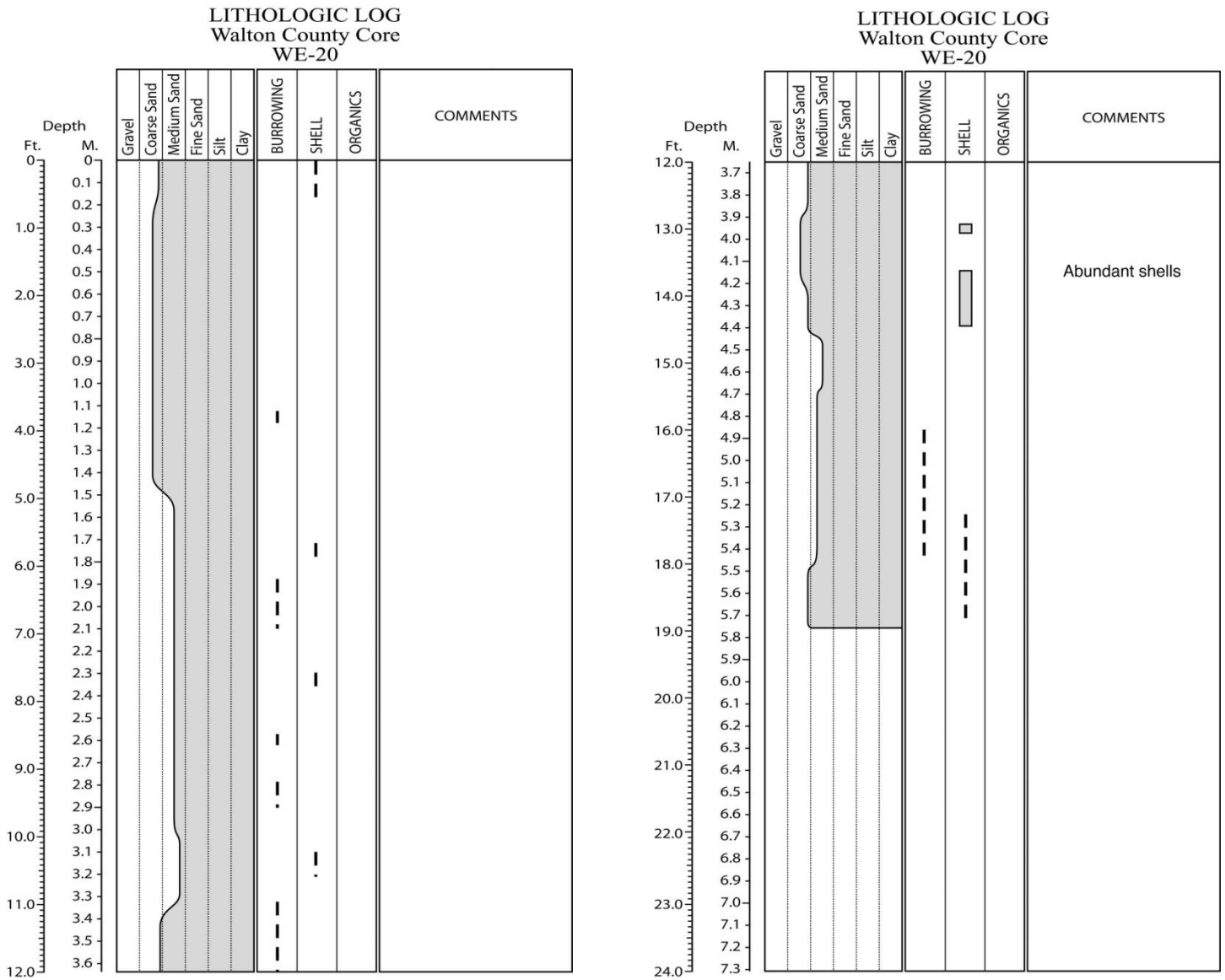

Figure E.157. Core WE-20 log.

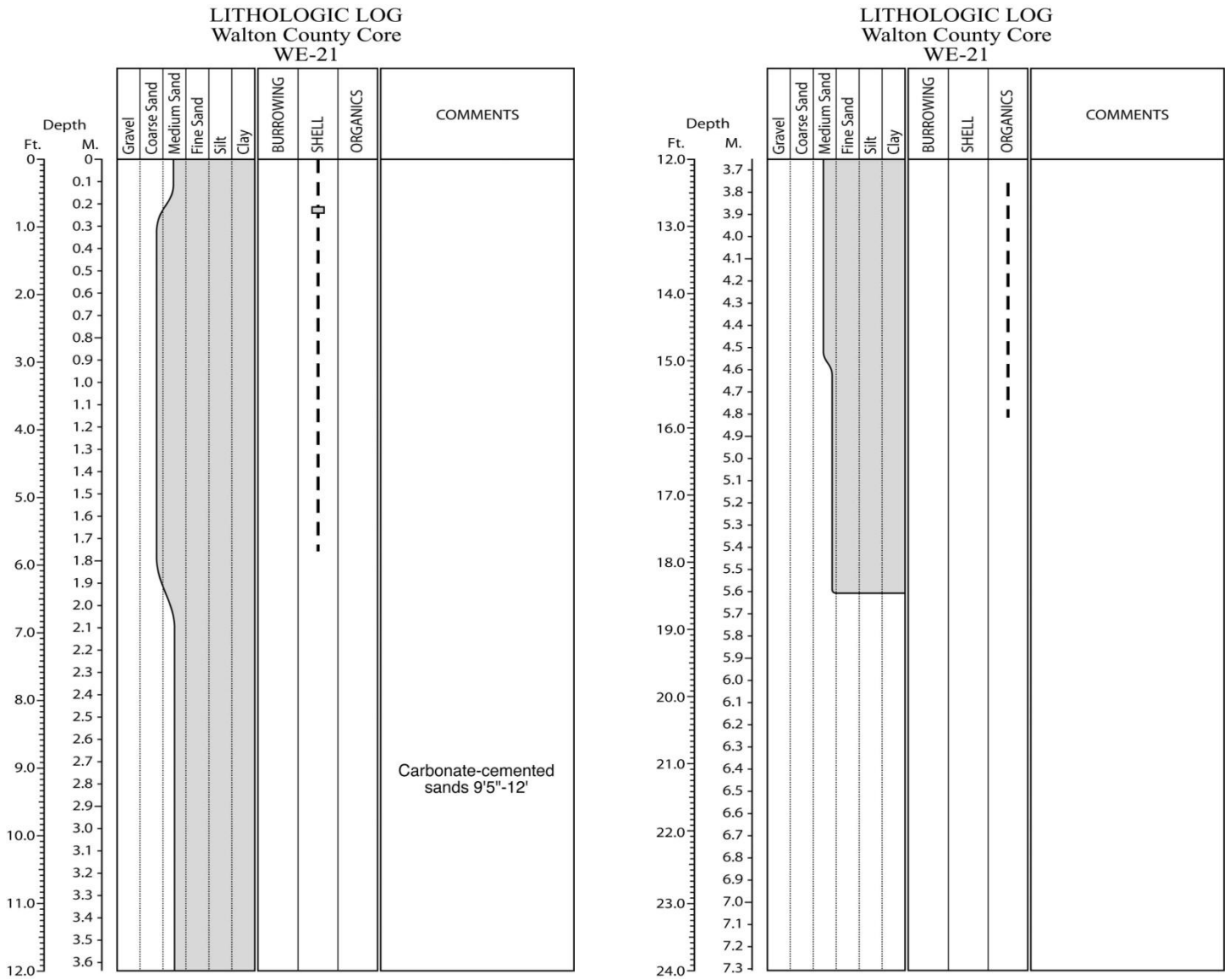

Figure E.158. Core WE-21 log.

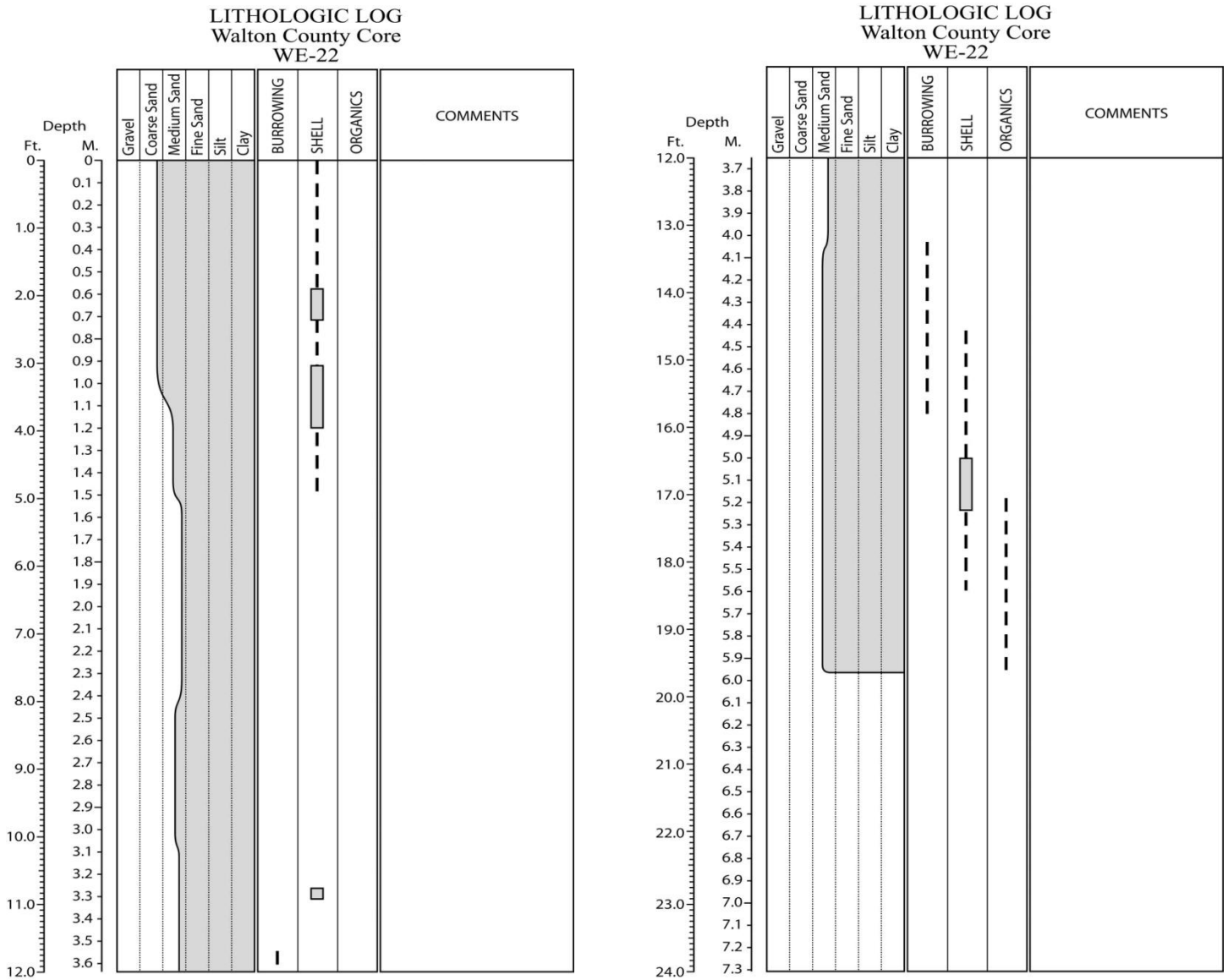

Figure E.159. Core WE-22 log.

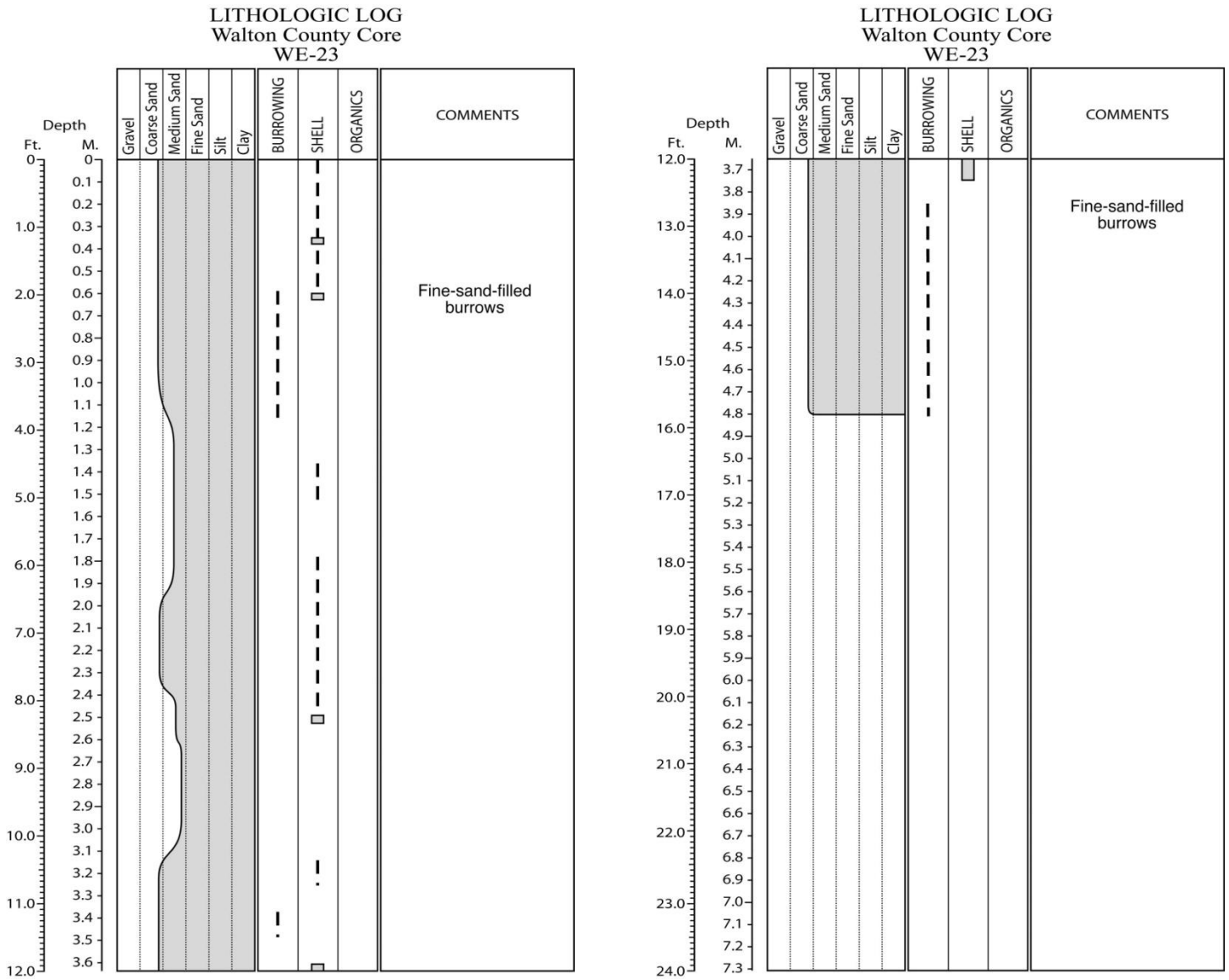

Figure E.160. Core WE-23 log.

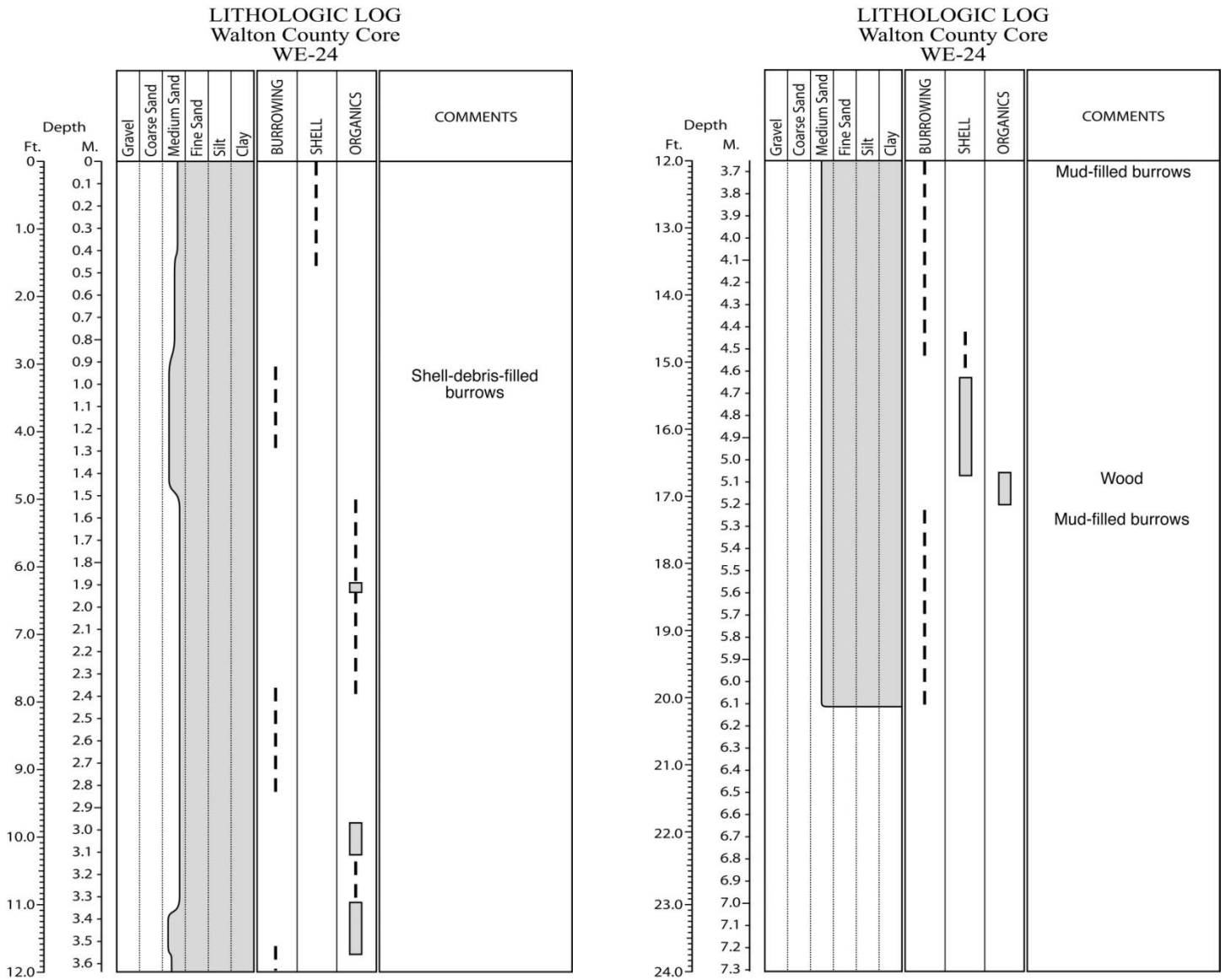

Figure E.161. Core WE-24 log.

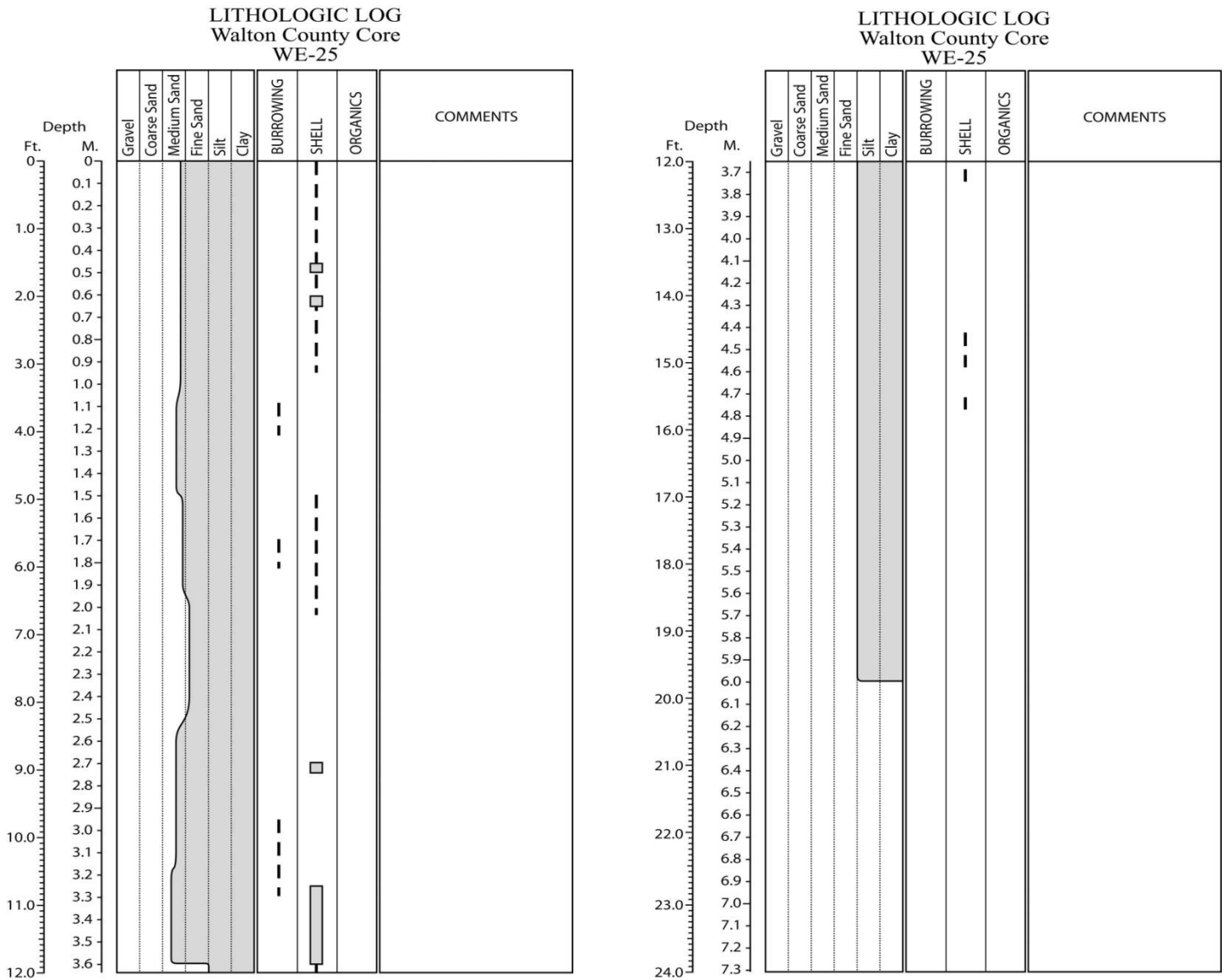

Figure E.162. Core WE-25 log.

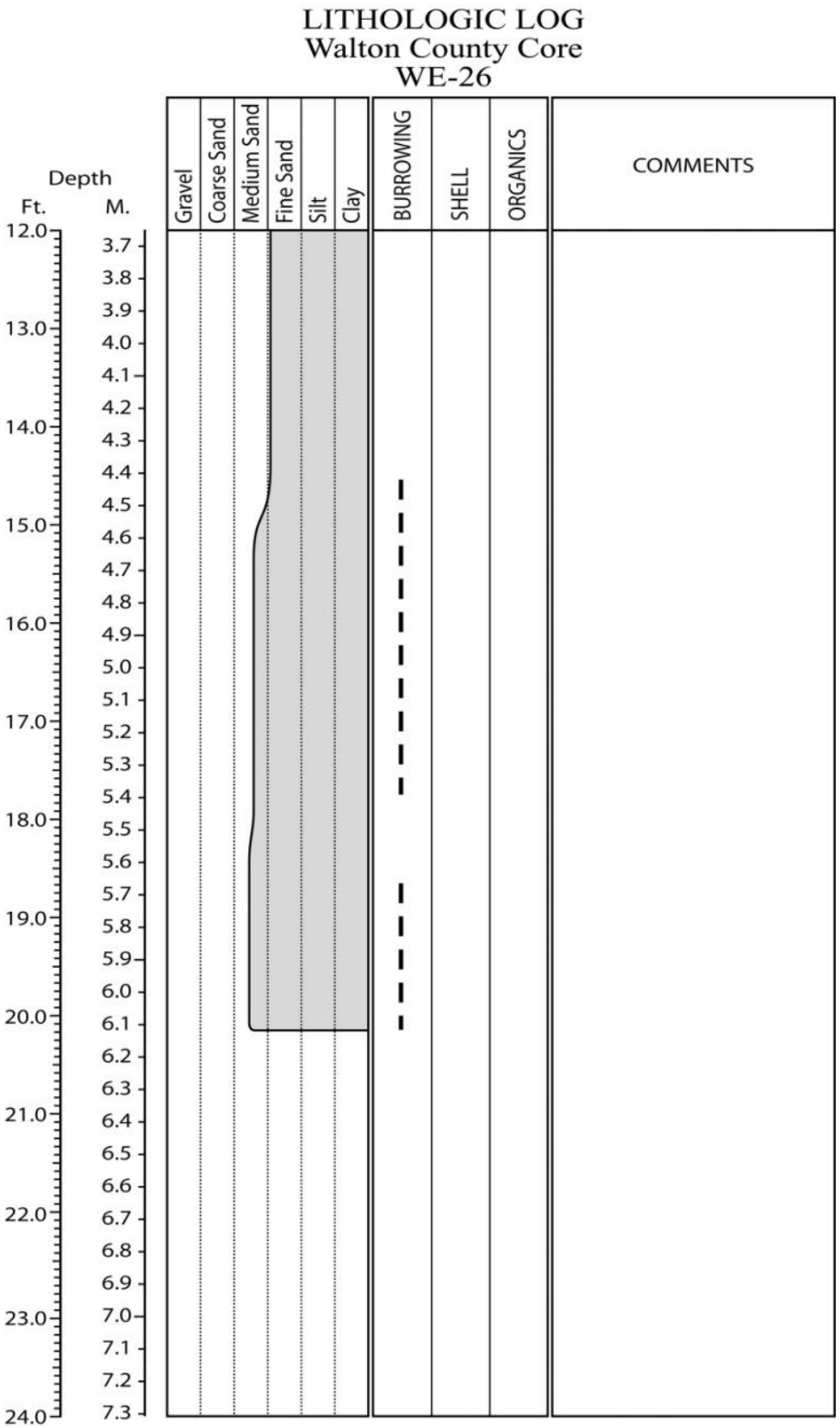

Figure E.163. Core WE-26 log.

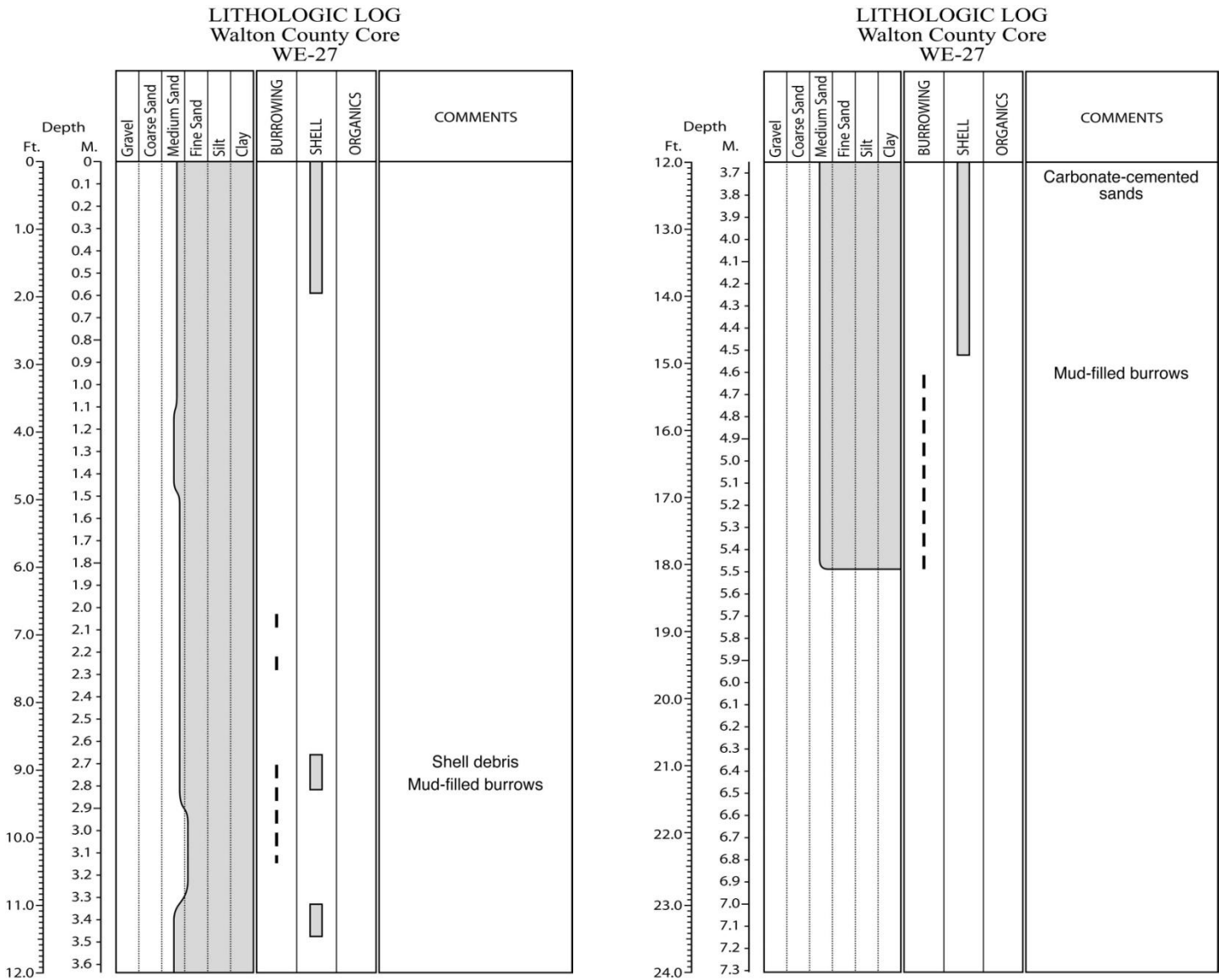

Figure E.164. Core WE-27 log.

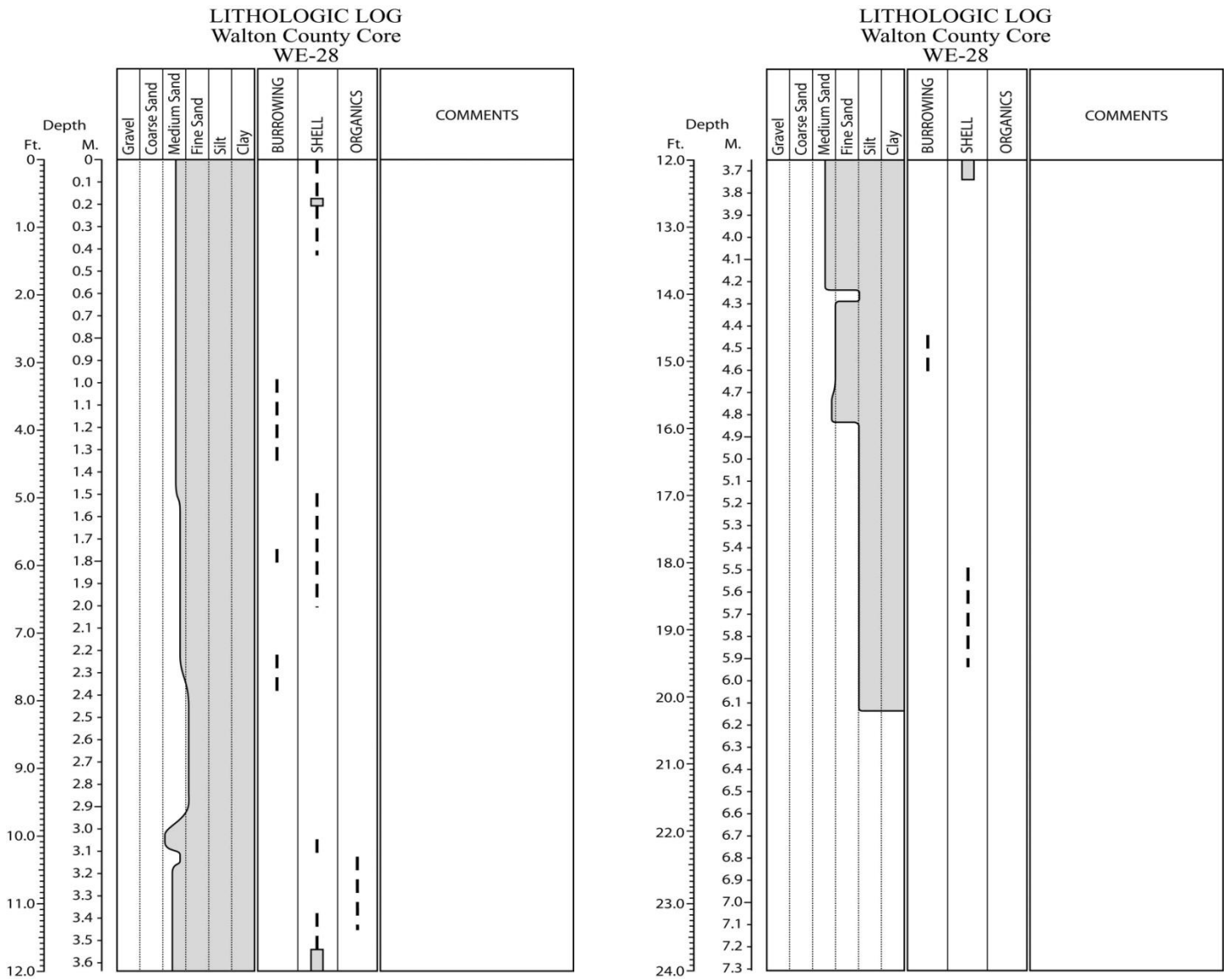

Figure E.165. Core WE-28 log.

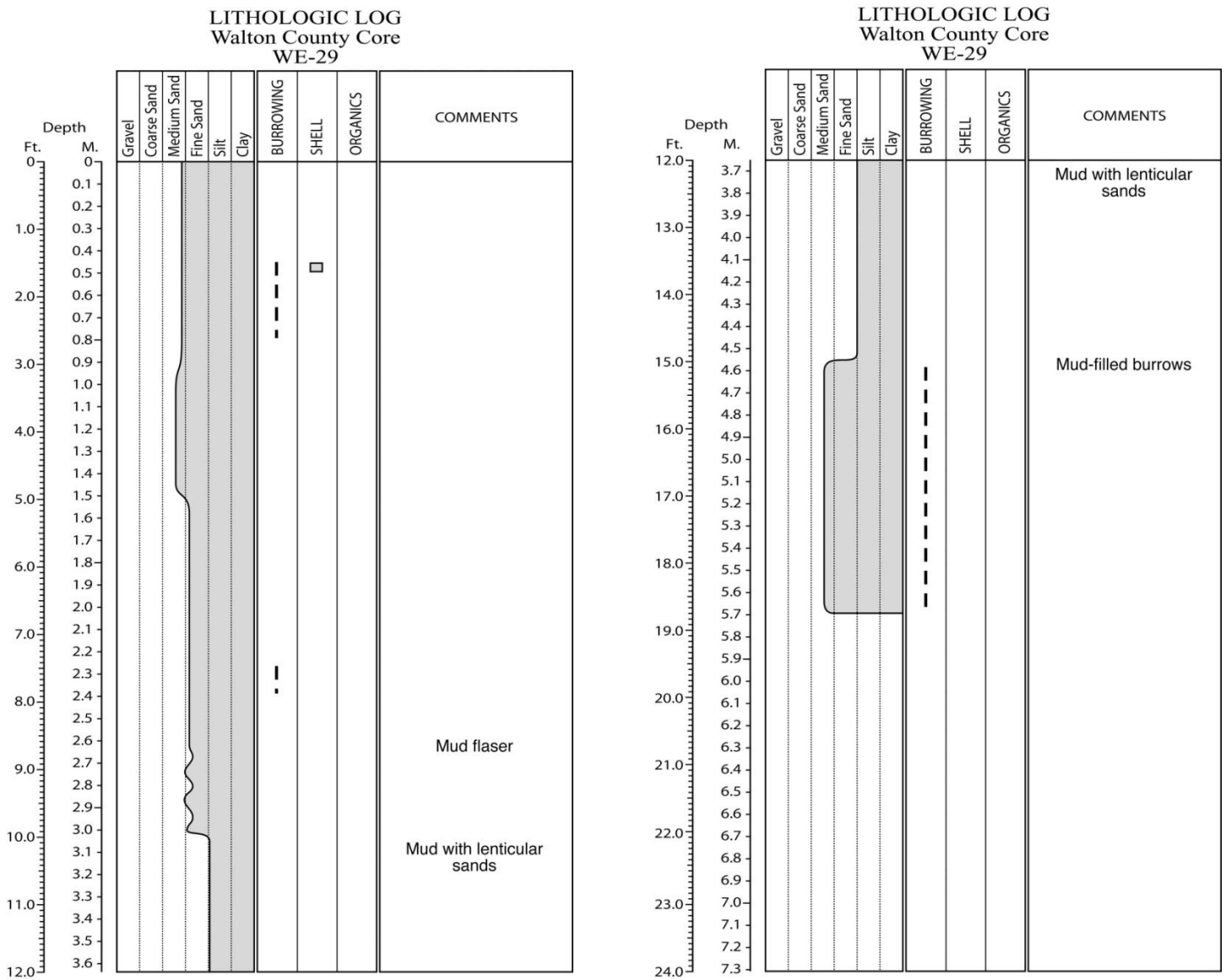

Figure E.166. Core WE-29 log.

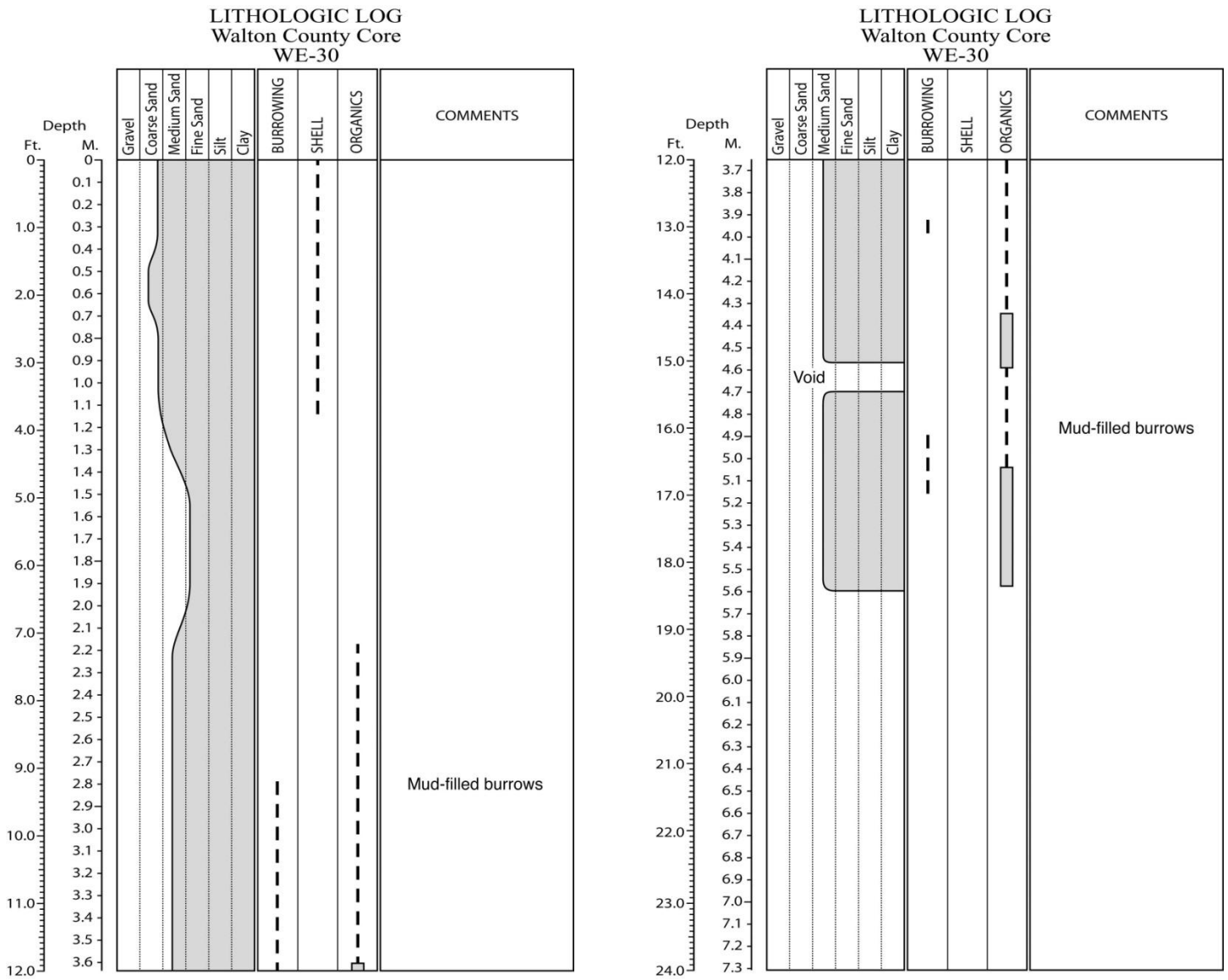

Figure E.167. Core WE-30 log.

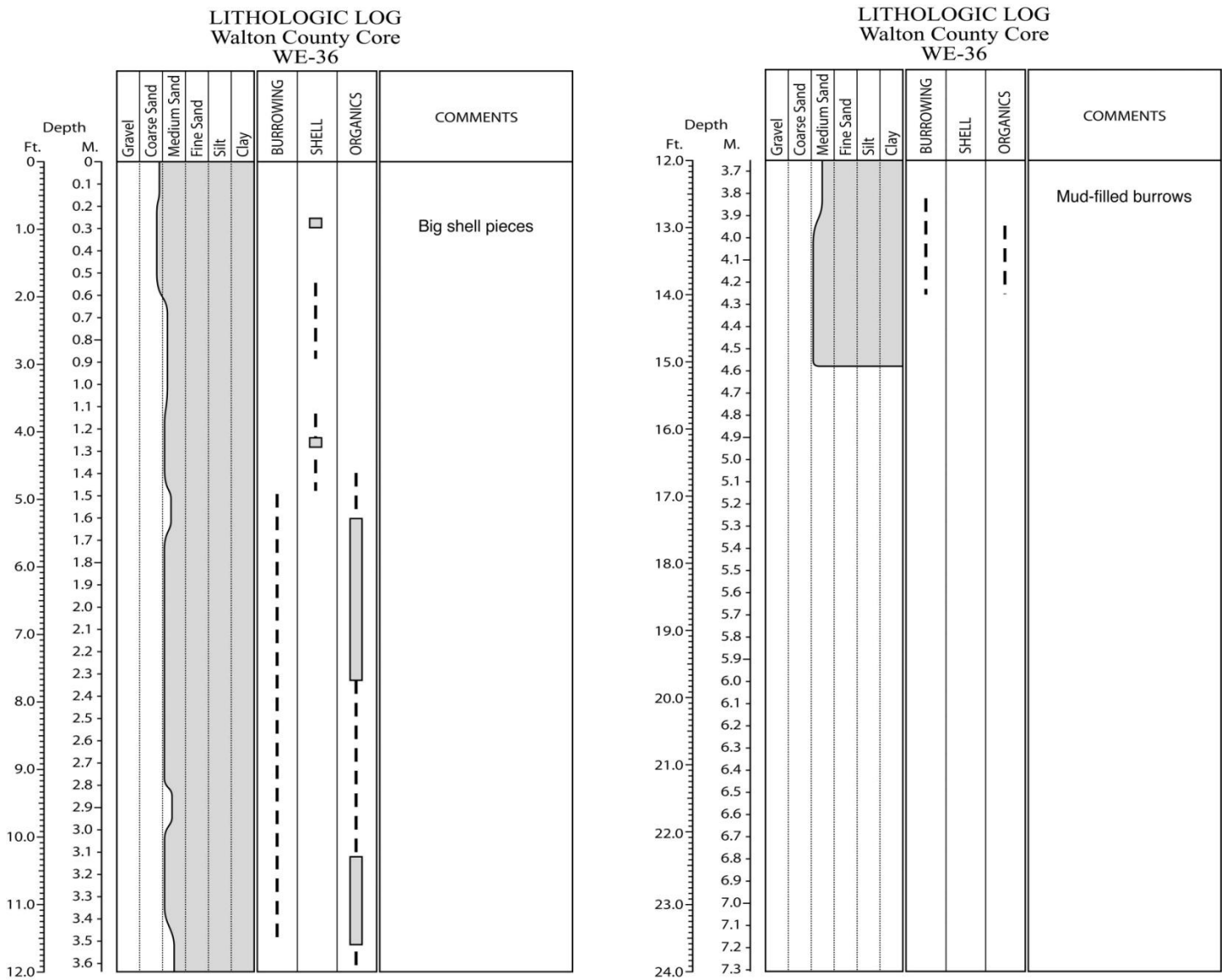

Figure E.168. Core WE-36 log.

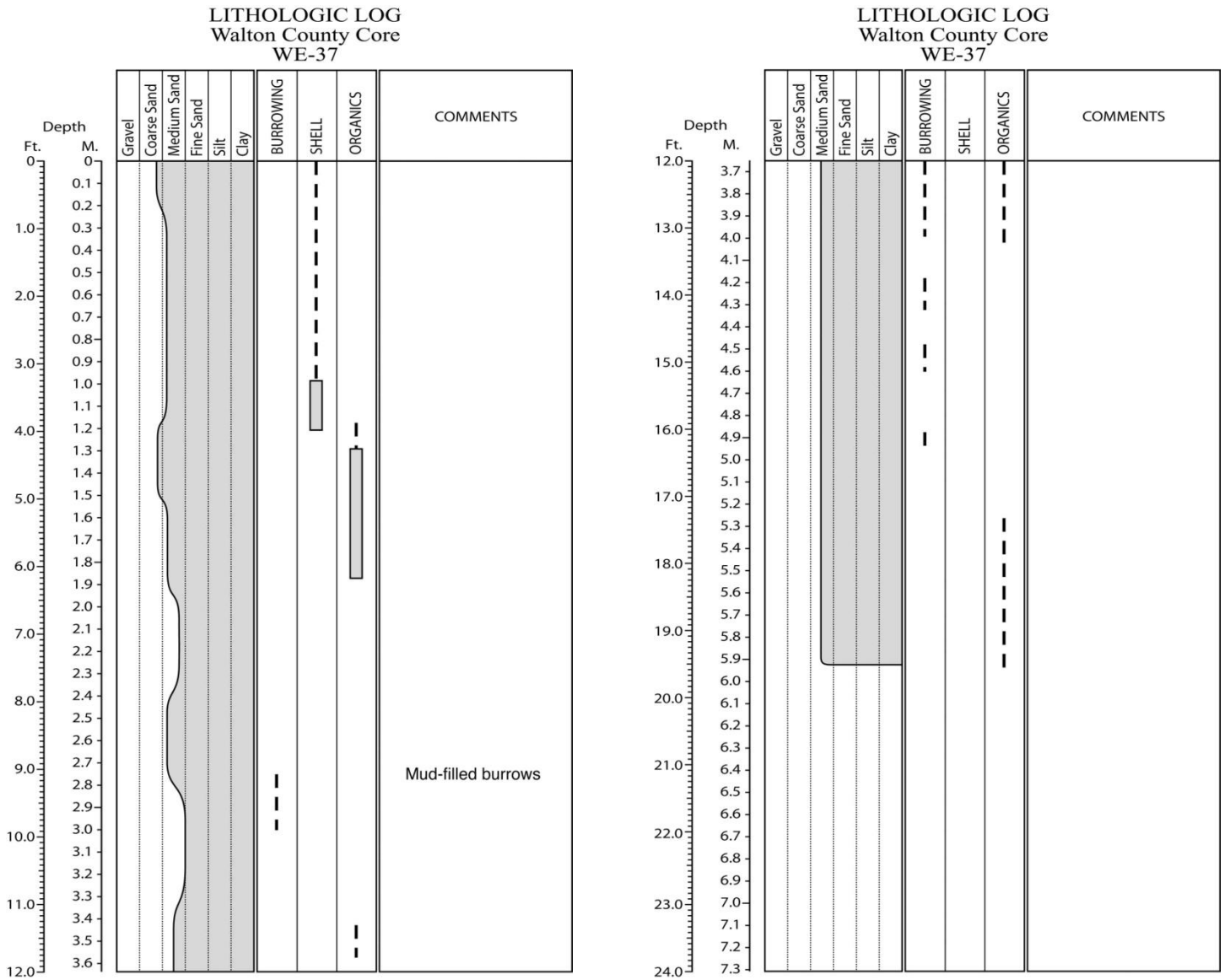

Figure E.169. Core WE-37 log.

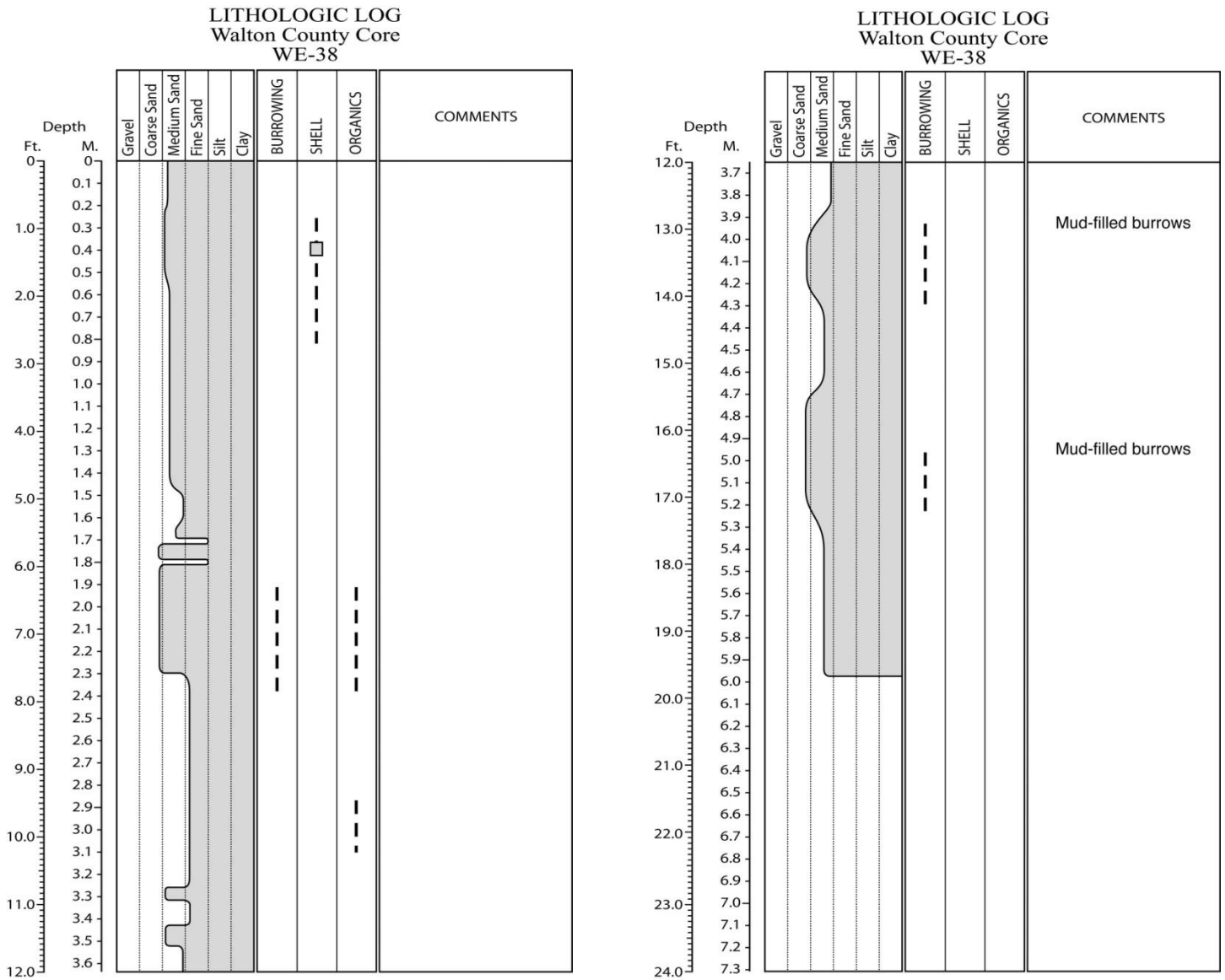

Figure E.170. Core WE-38 log.

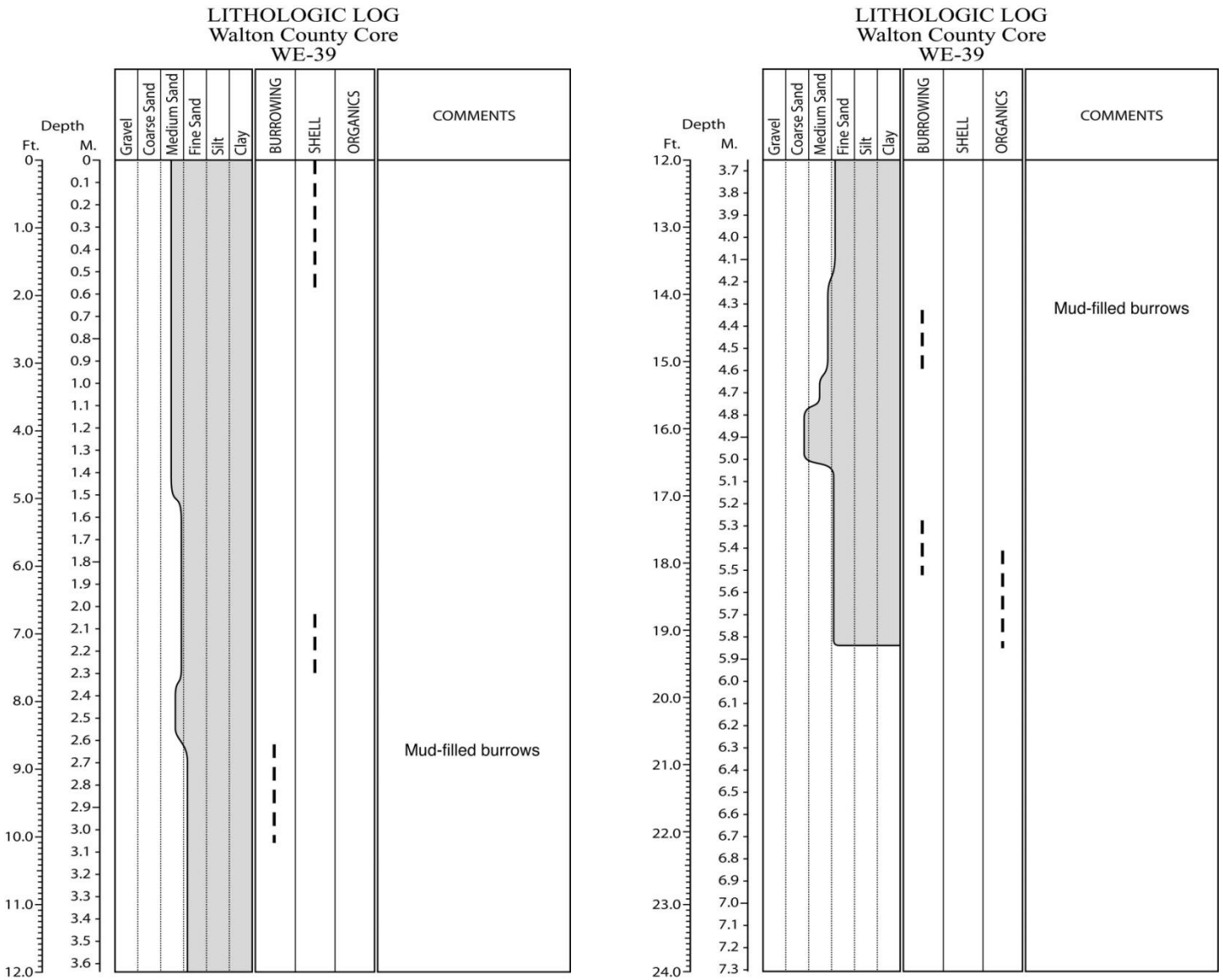

Figure E.171. Core WE-39 log.

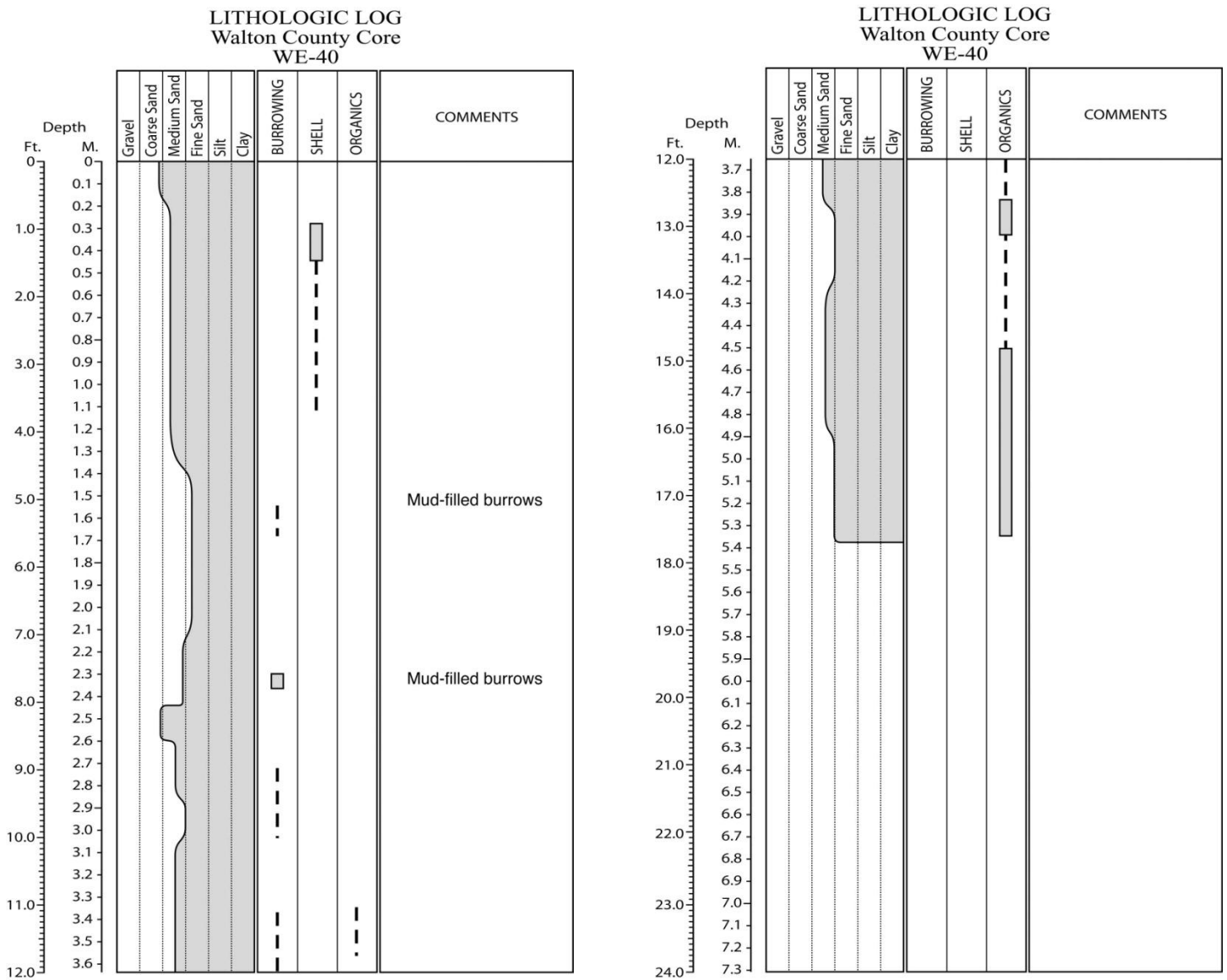

Figure E.172. Core WE-40 log.

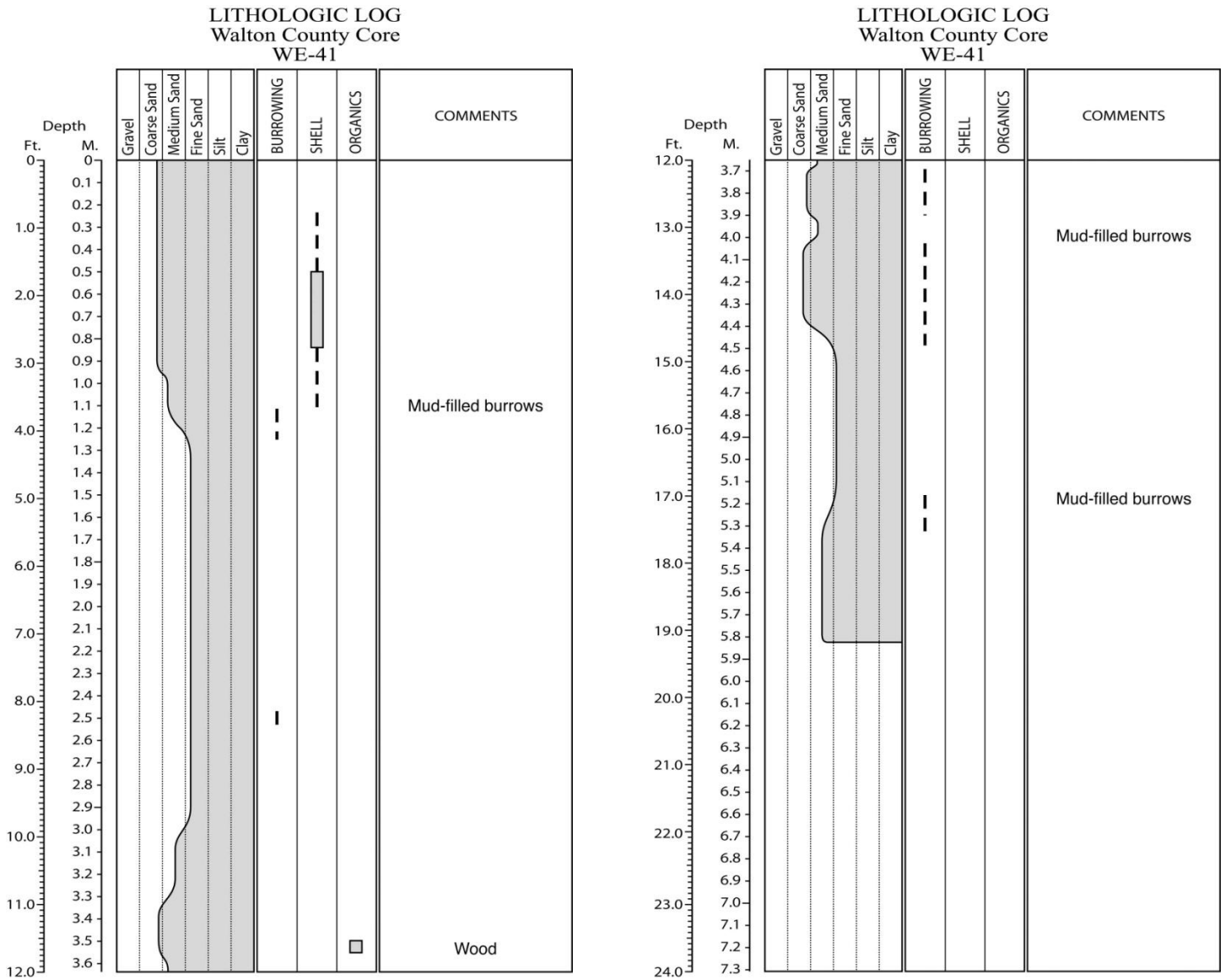

Figure E.173. Core WE-41 log.

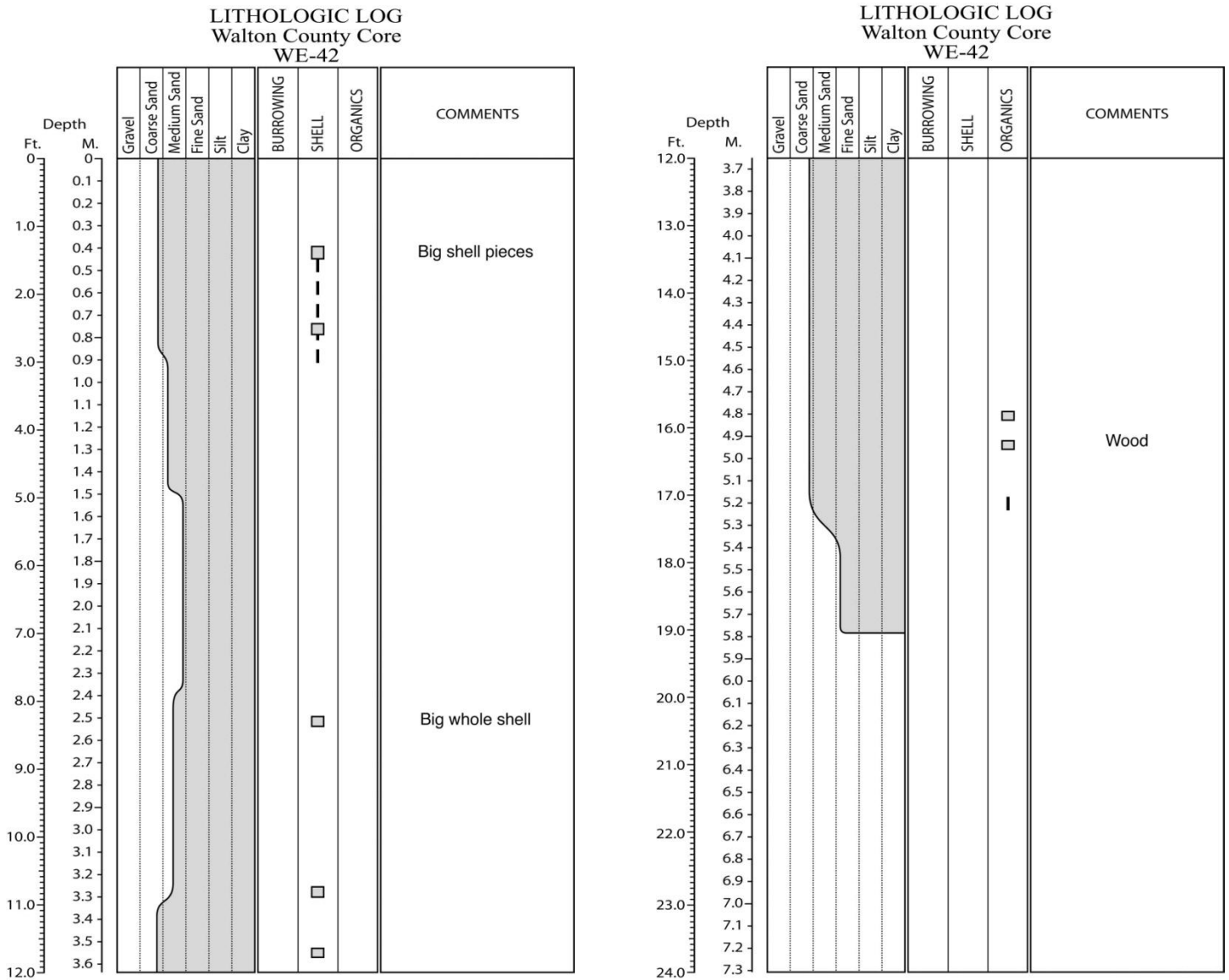

Figure E.174. Core WE-42 log.

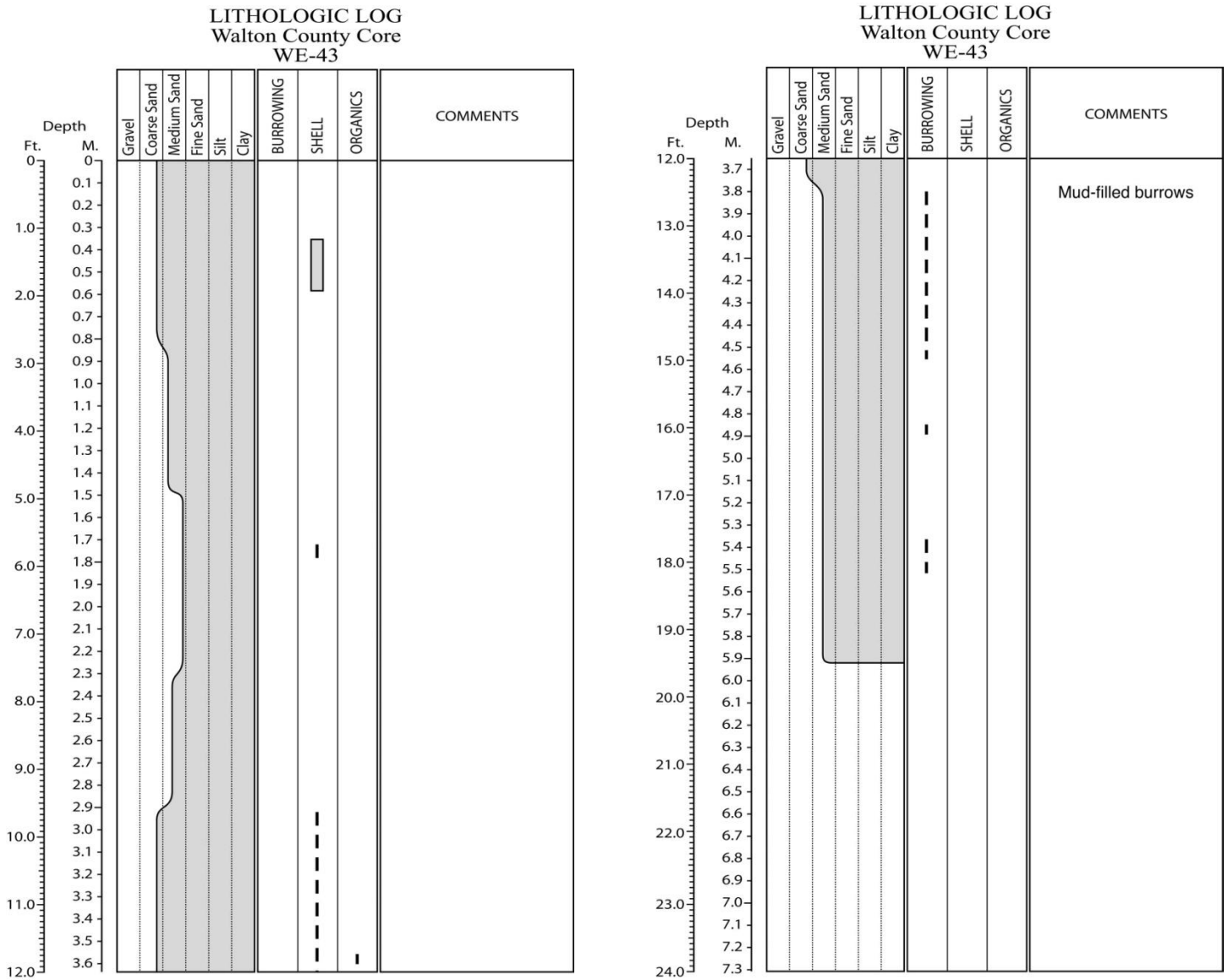

Figure E.175. Core WE-43 log.

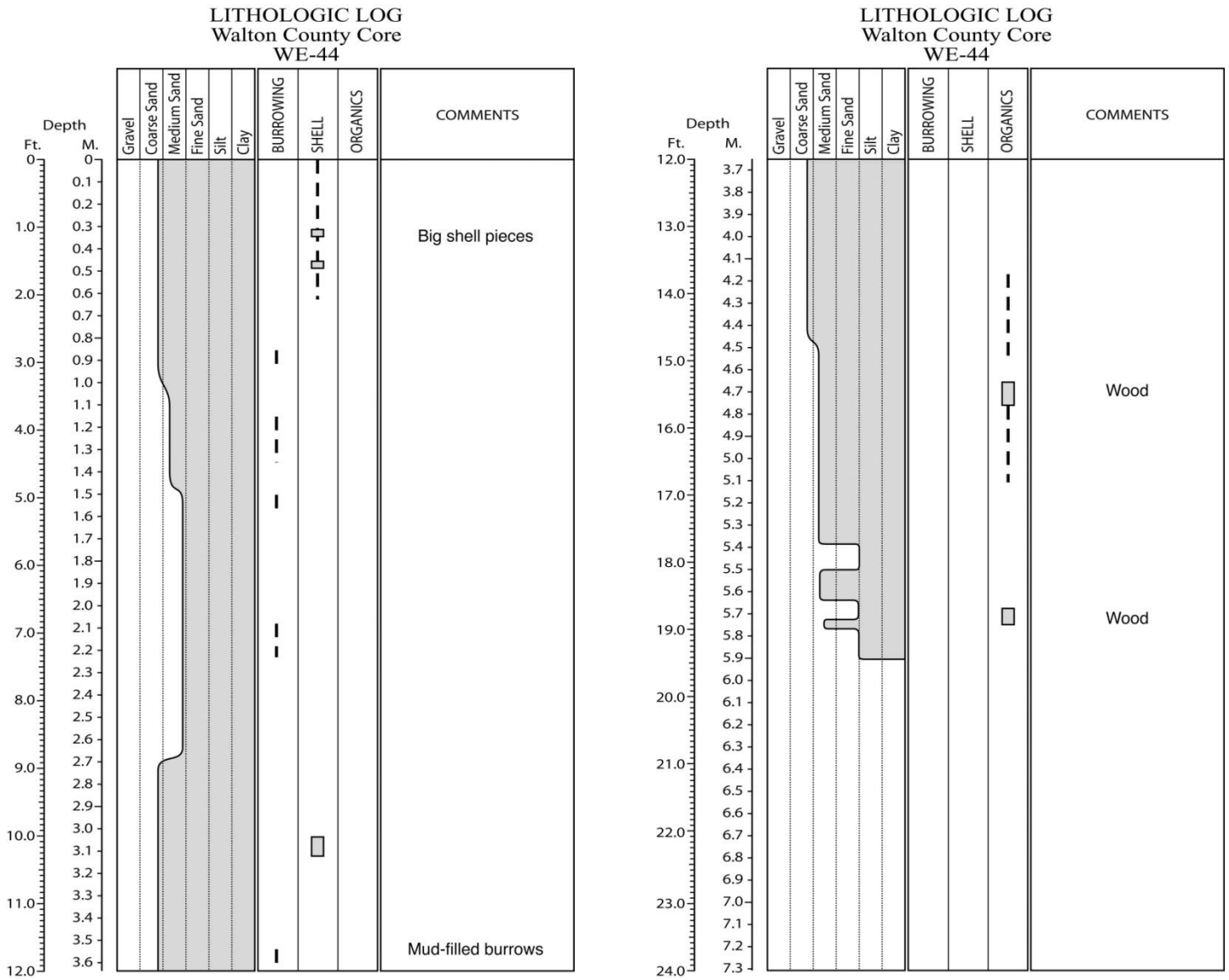

Figure E.176. Core WE-44 log.

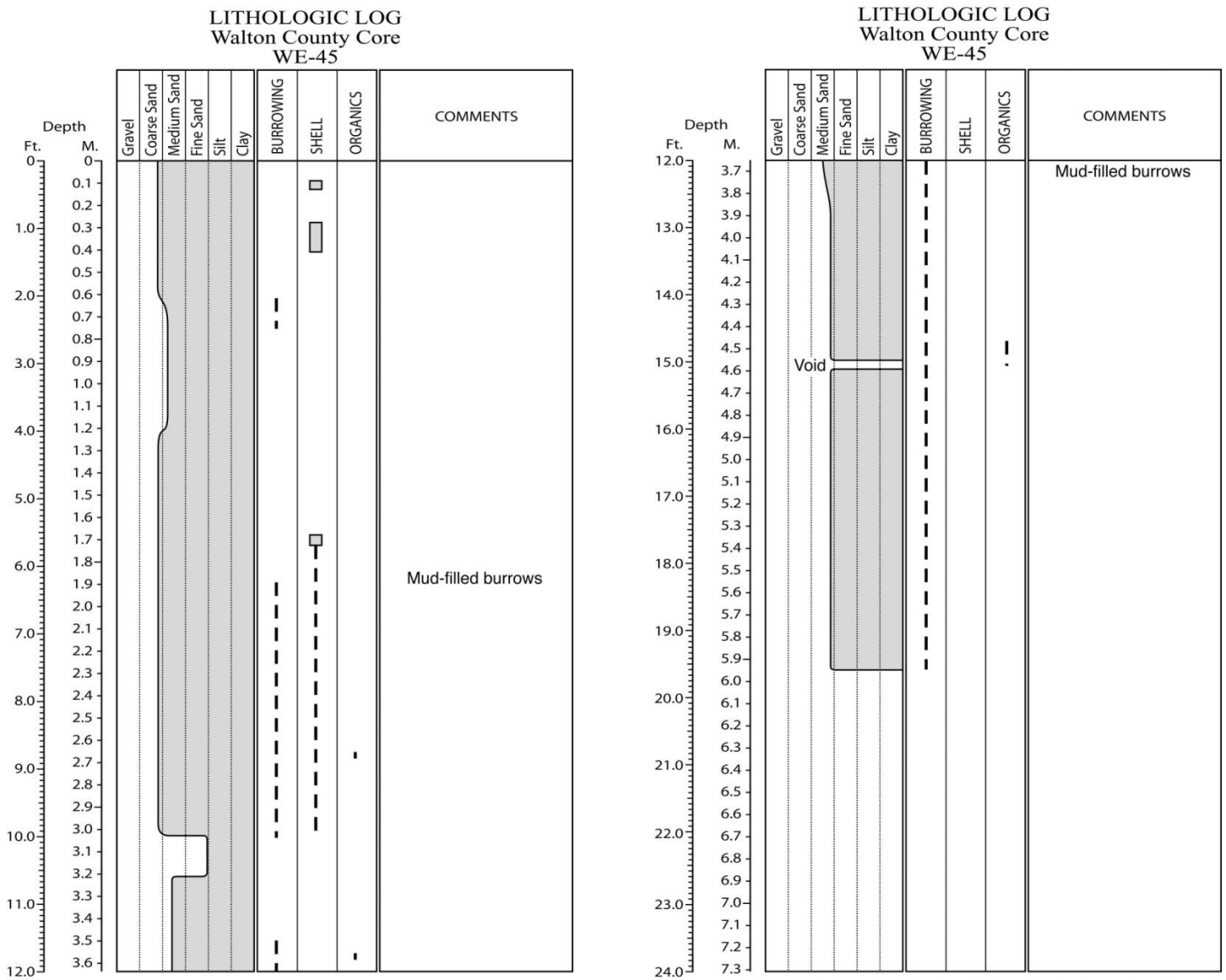

Figure E.177. Core WE-45 log.

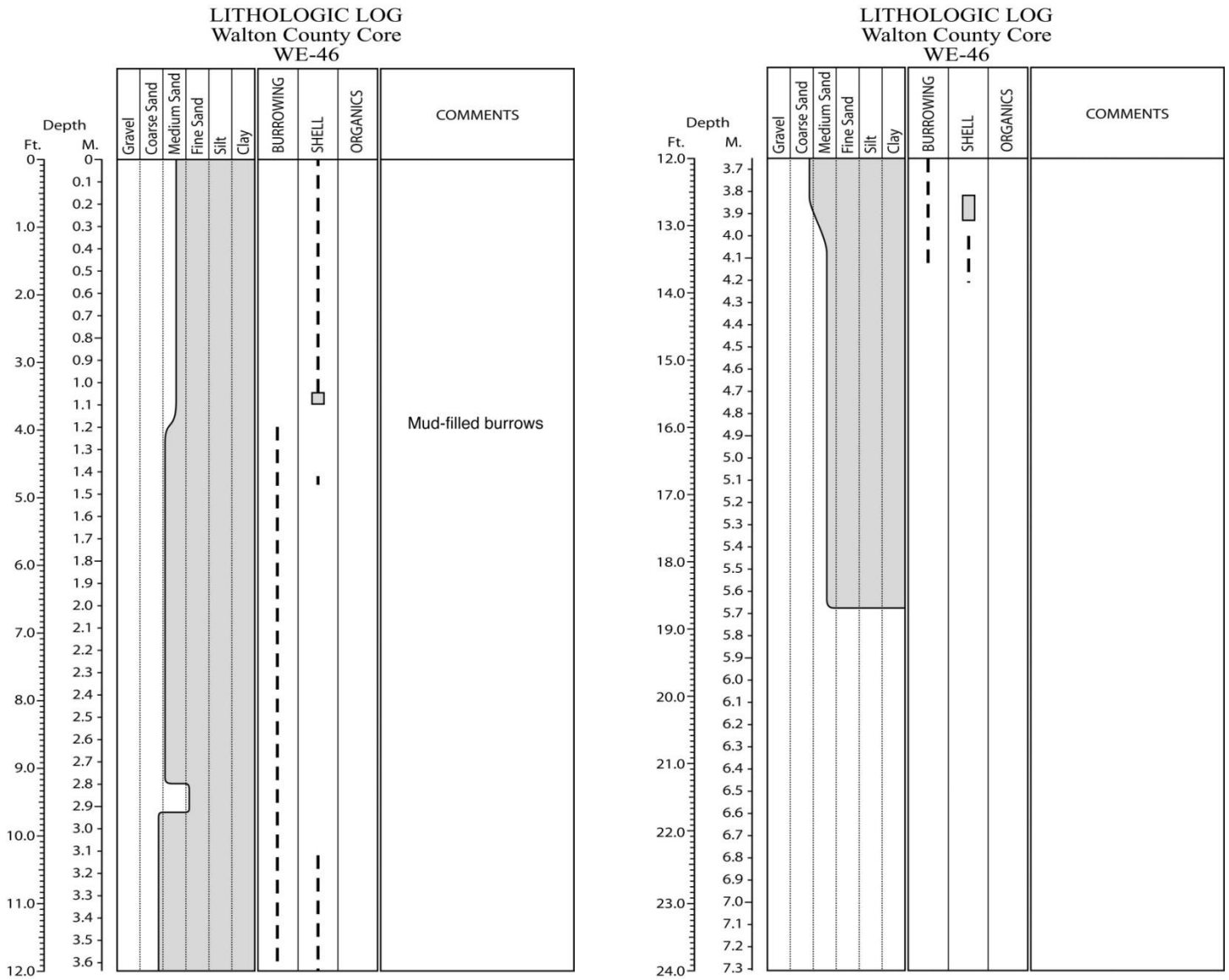

Figure E.178. Core WE-46 log.

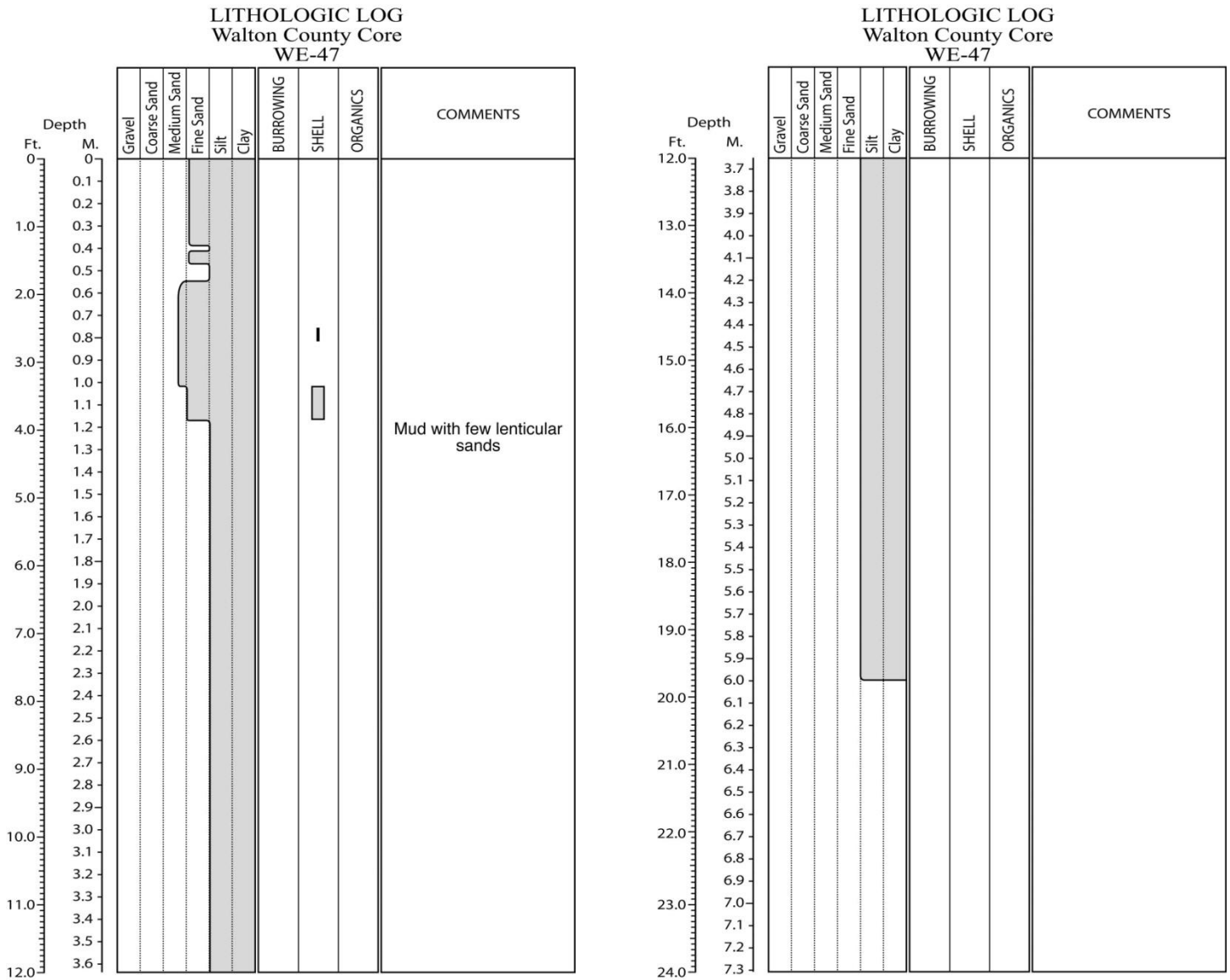

Figure E.179. Core WE-47 log.

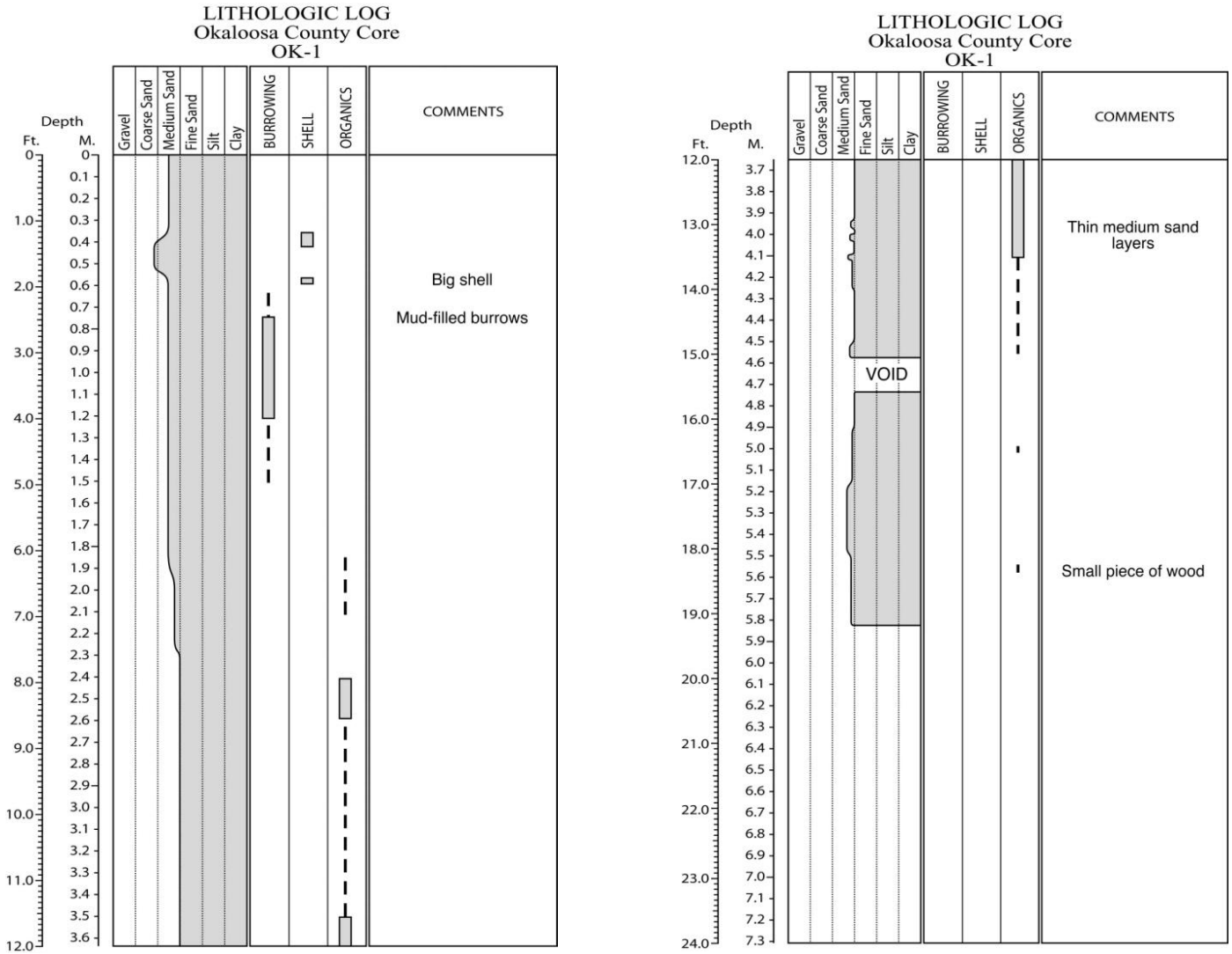

Figure E.180. Core OK-1 log.

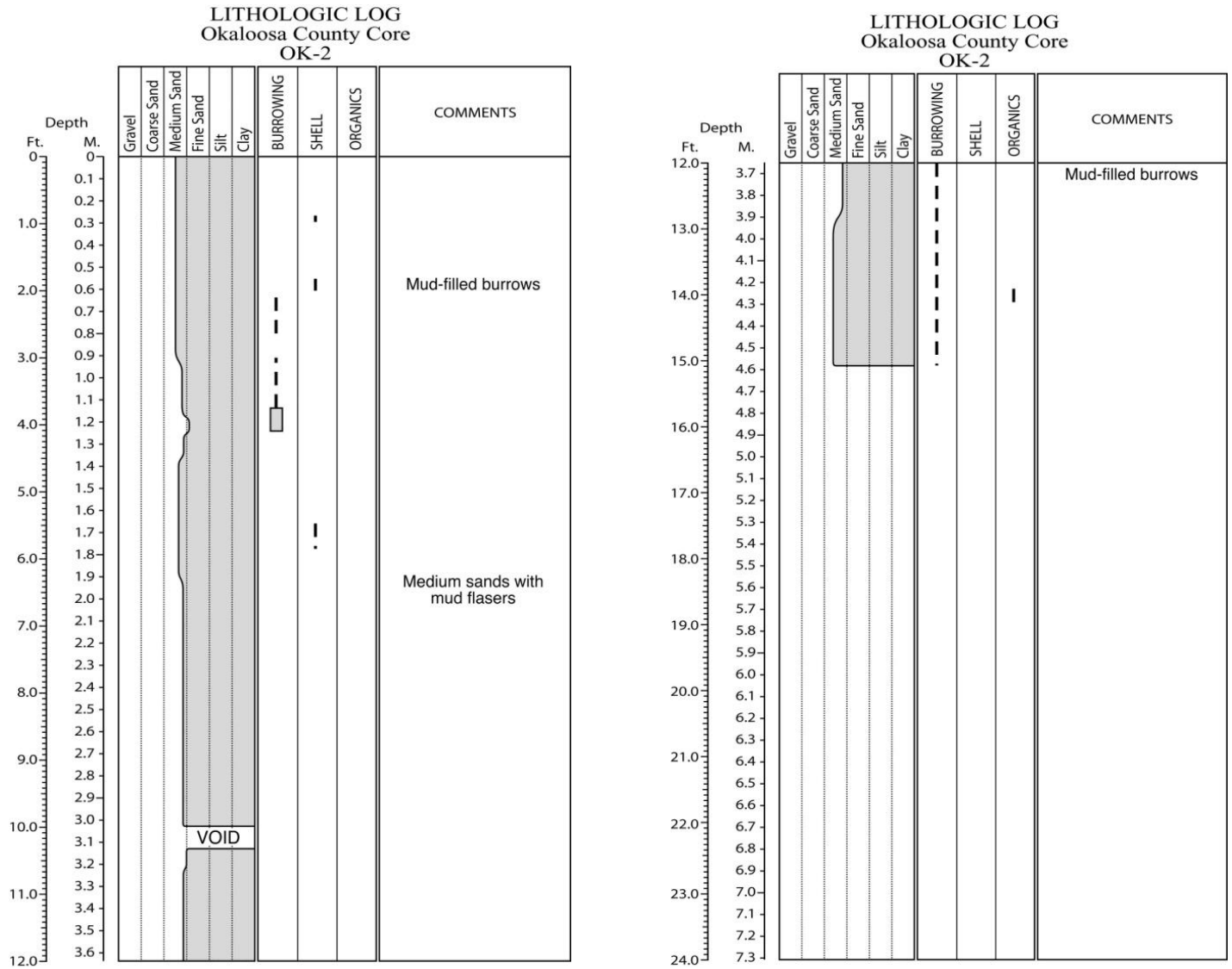

Figure E.181. Core OK-2 log.

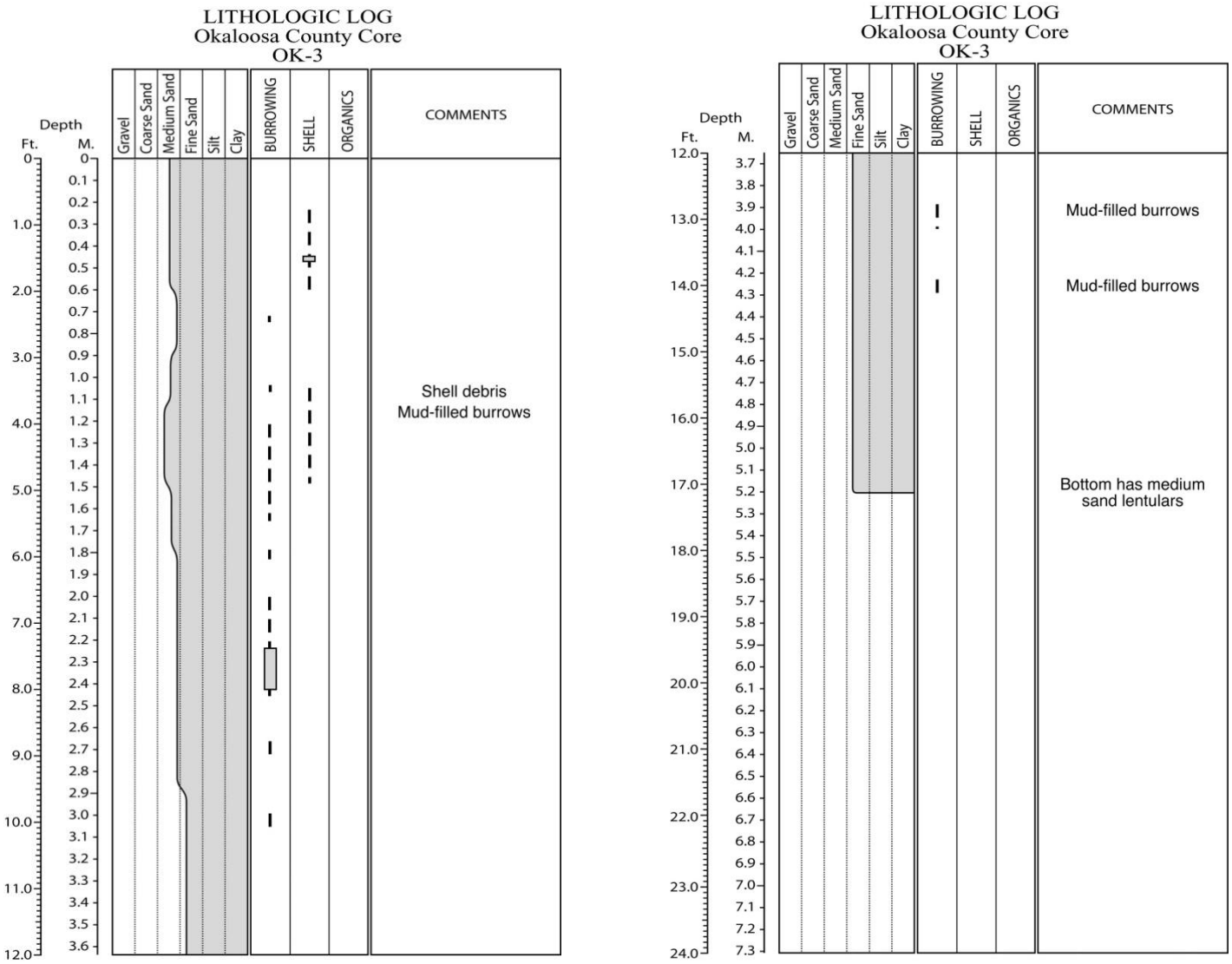

Figure E.182. Core OK-3 log.

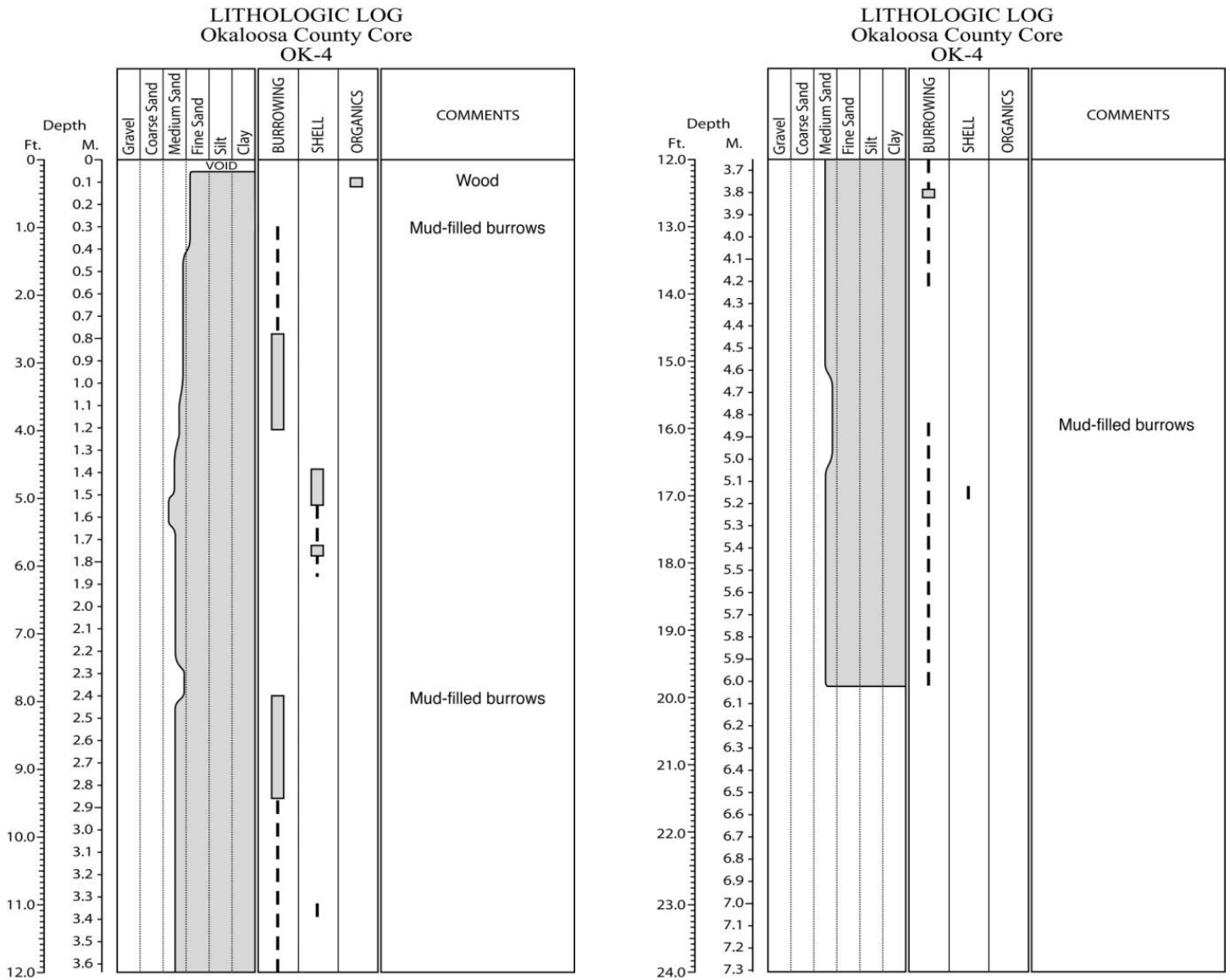

Figure E.183. Core OK-4 log.

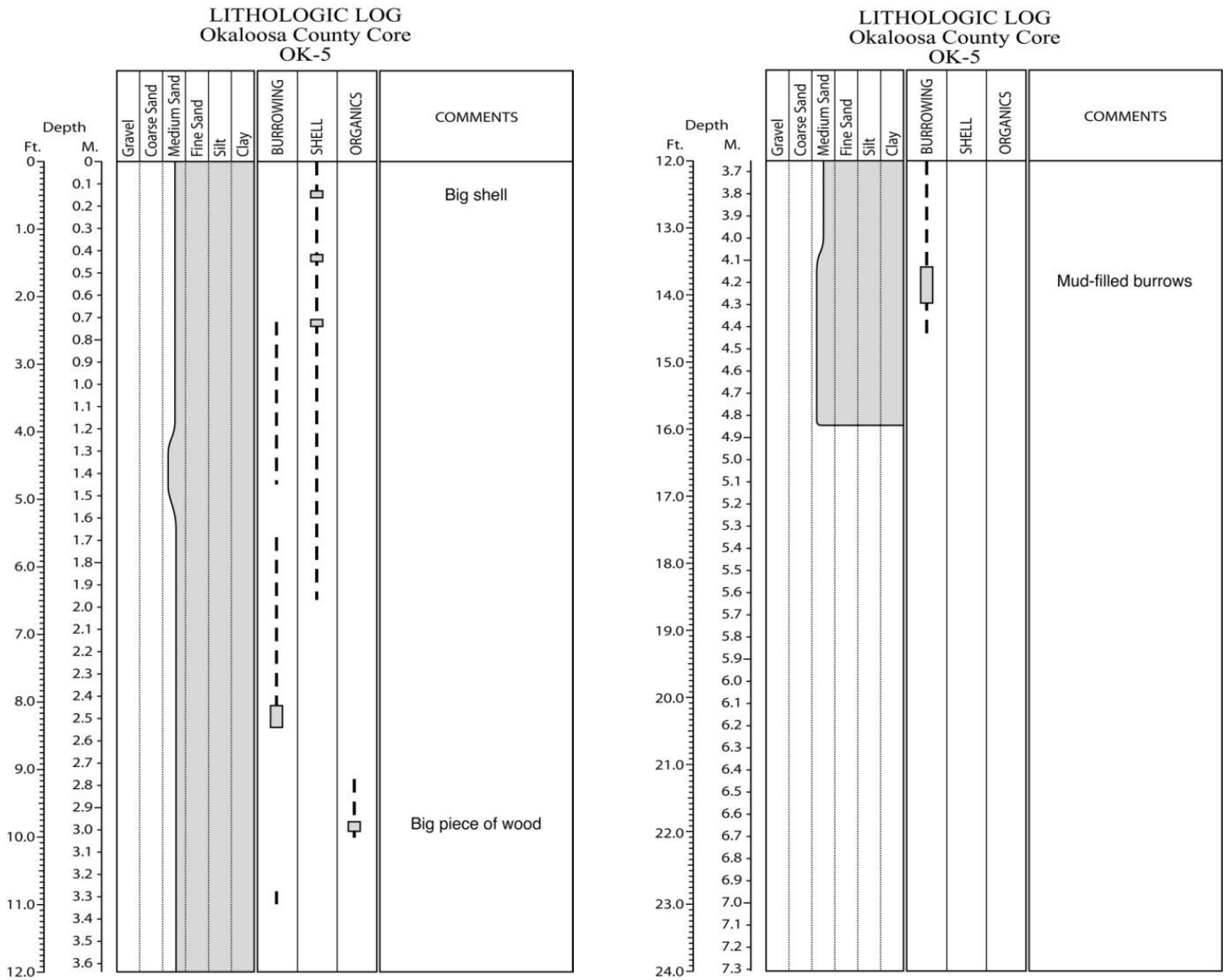

Figure E.184. Core OK-5 log.

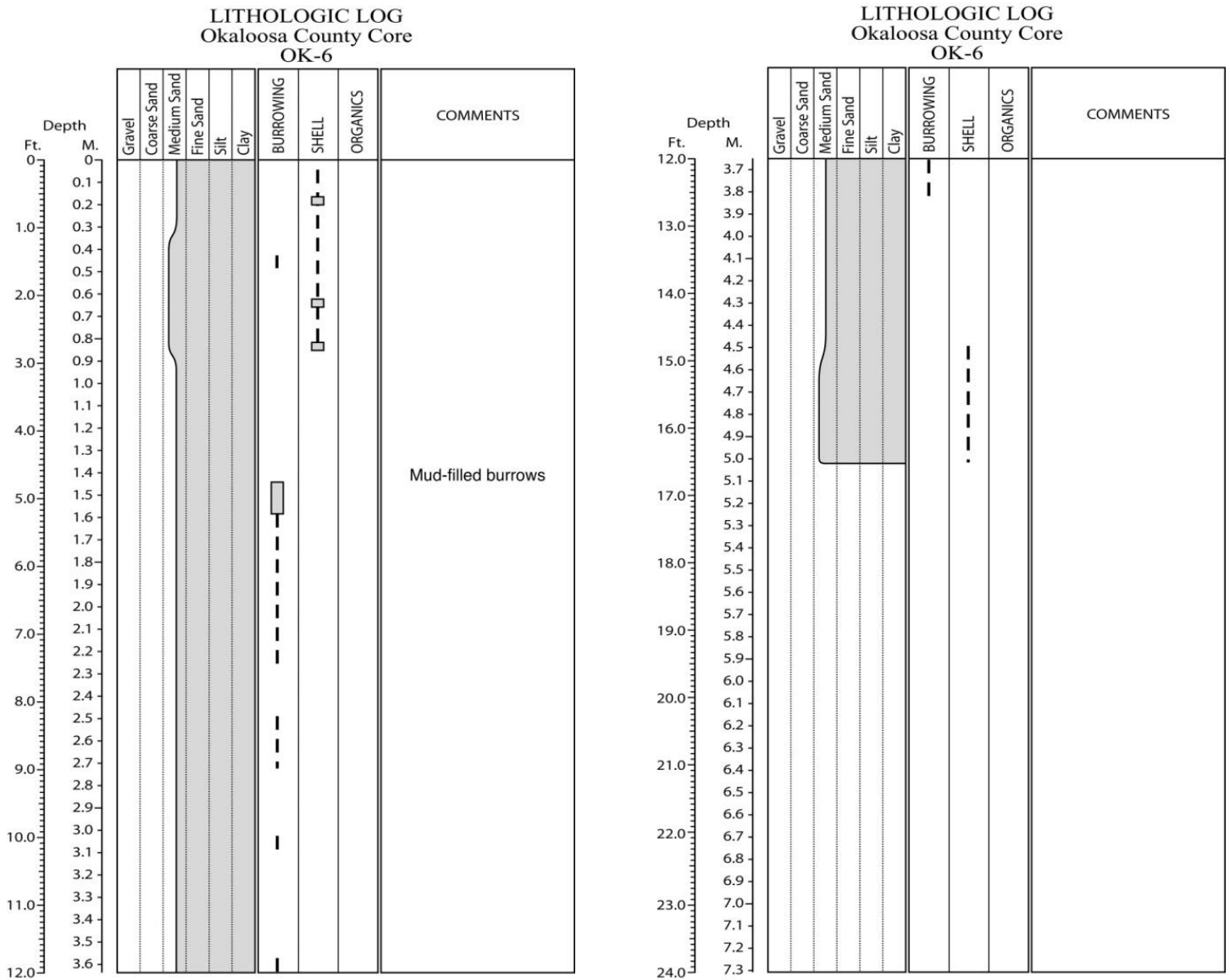

Figure E.185. Core OK-6 log.

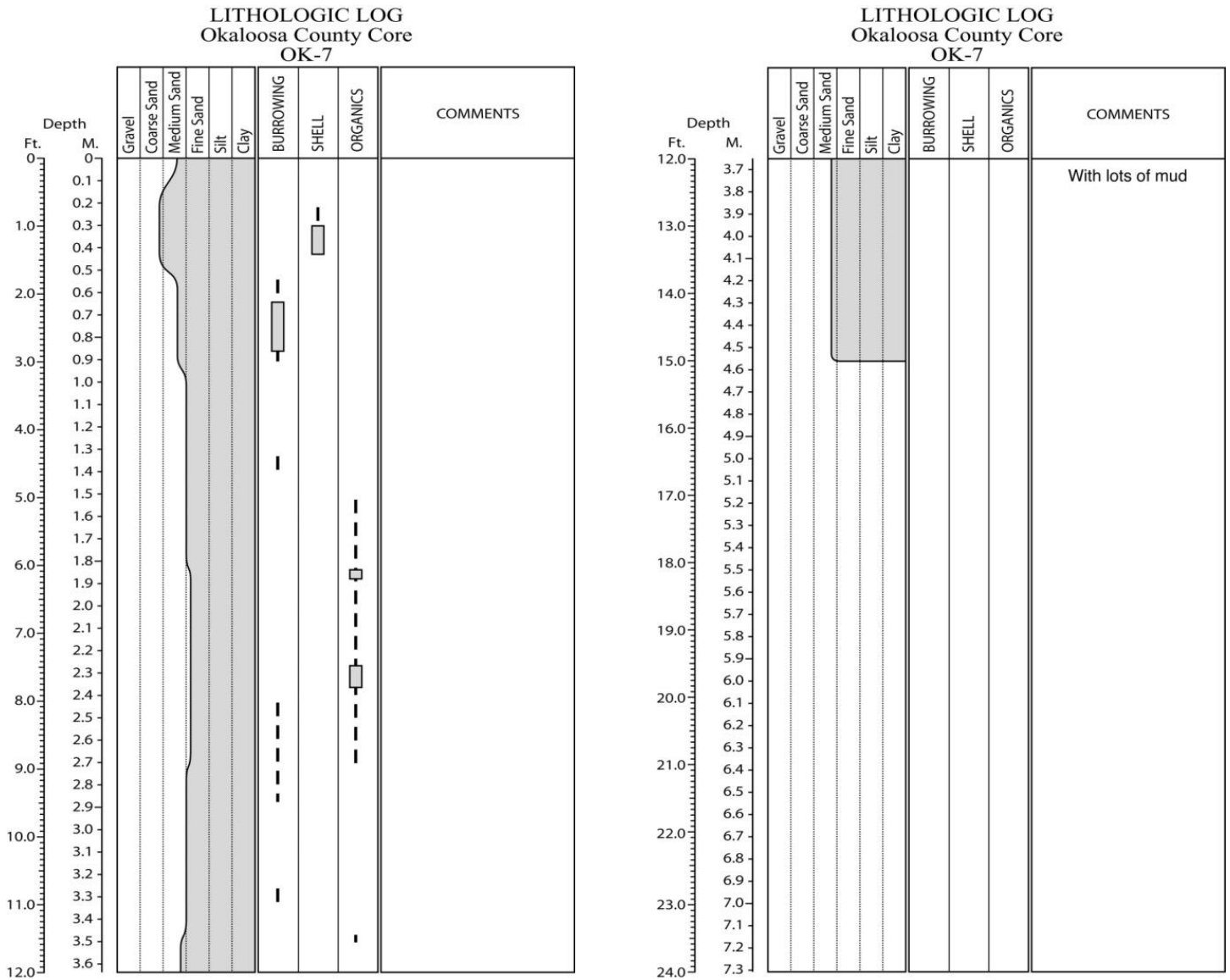

Figure E.186. Core OK-7 log.

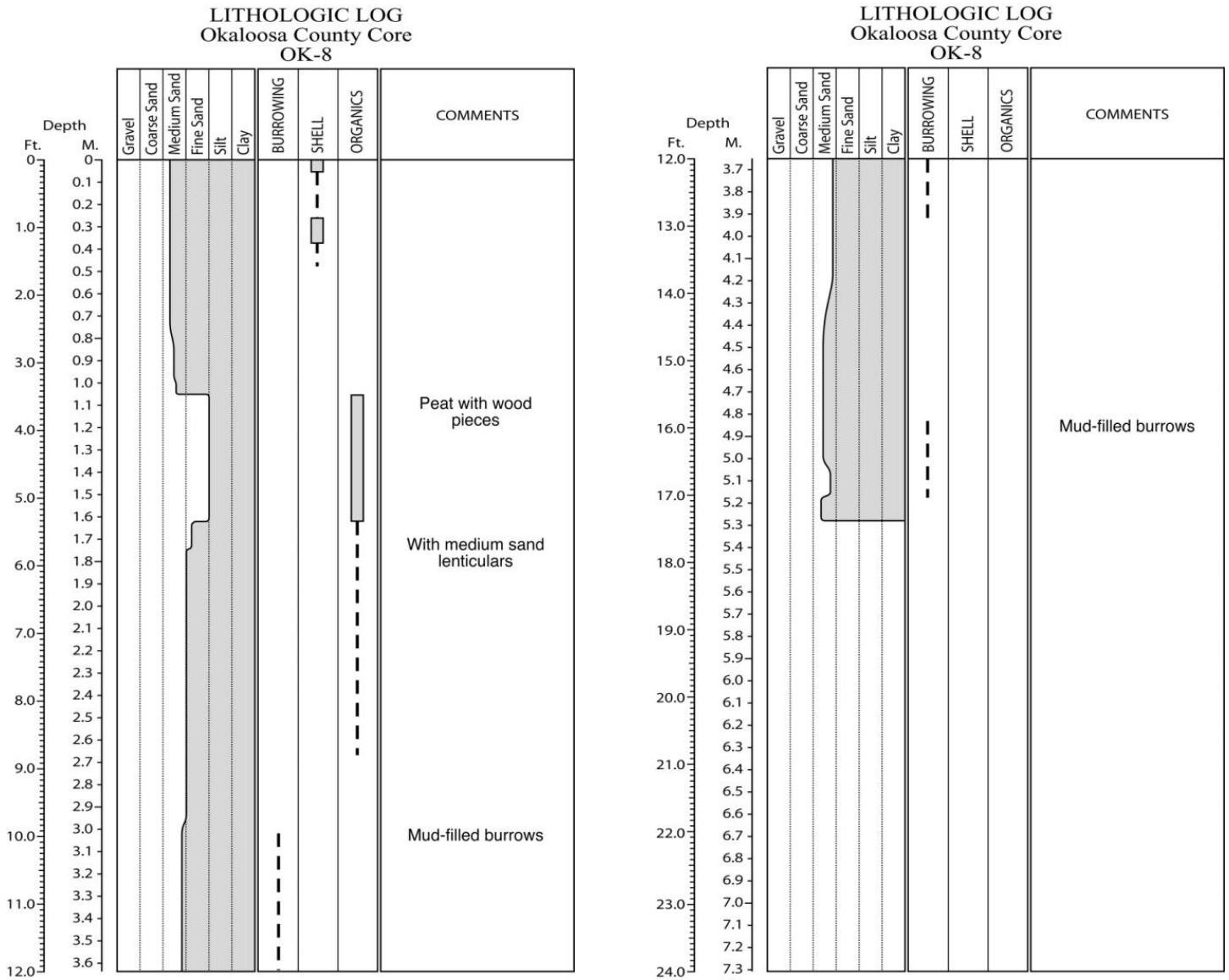

Figure E.187. Core OK-8 log.

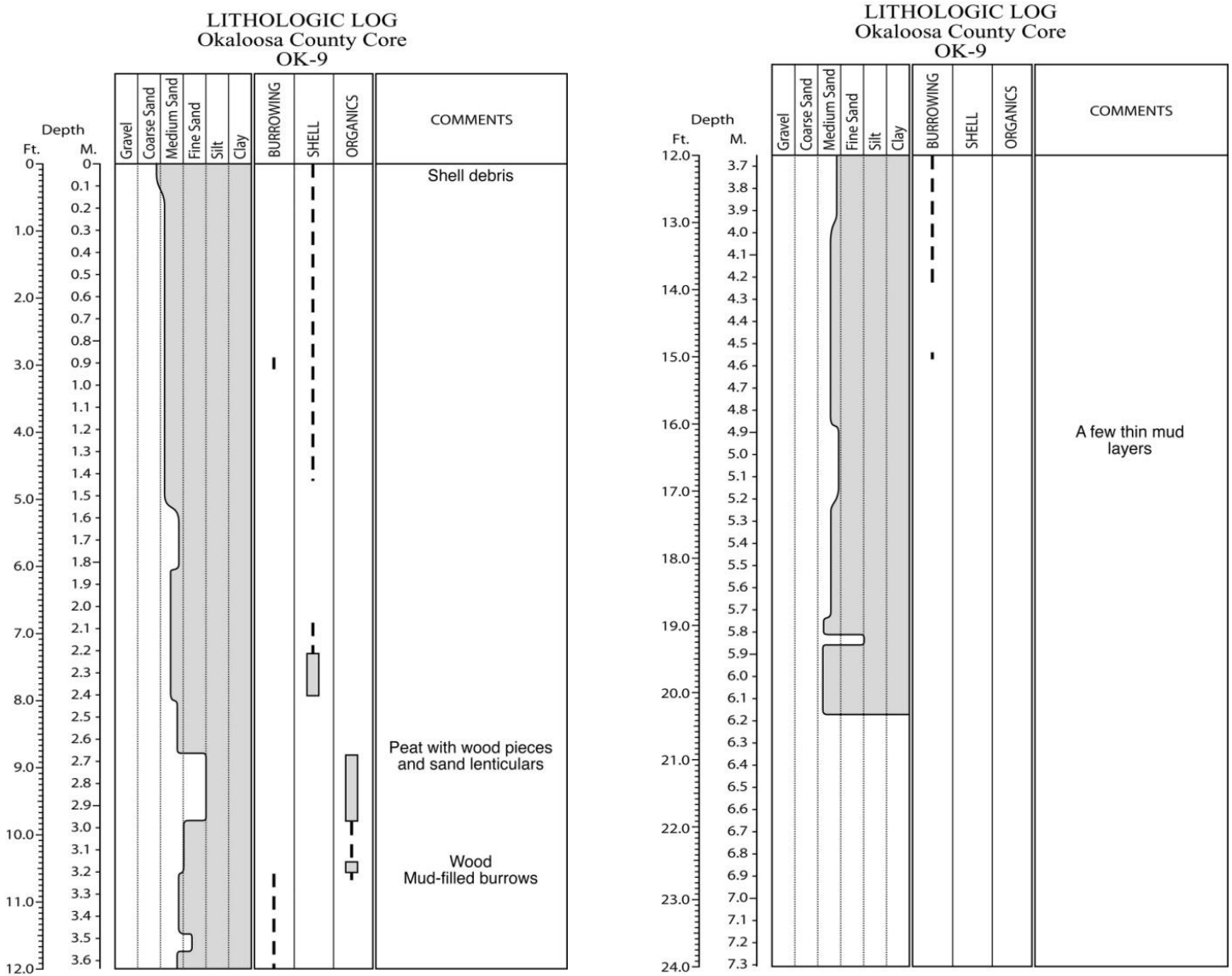

Figure E.188. Core OK-9 log.

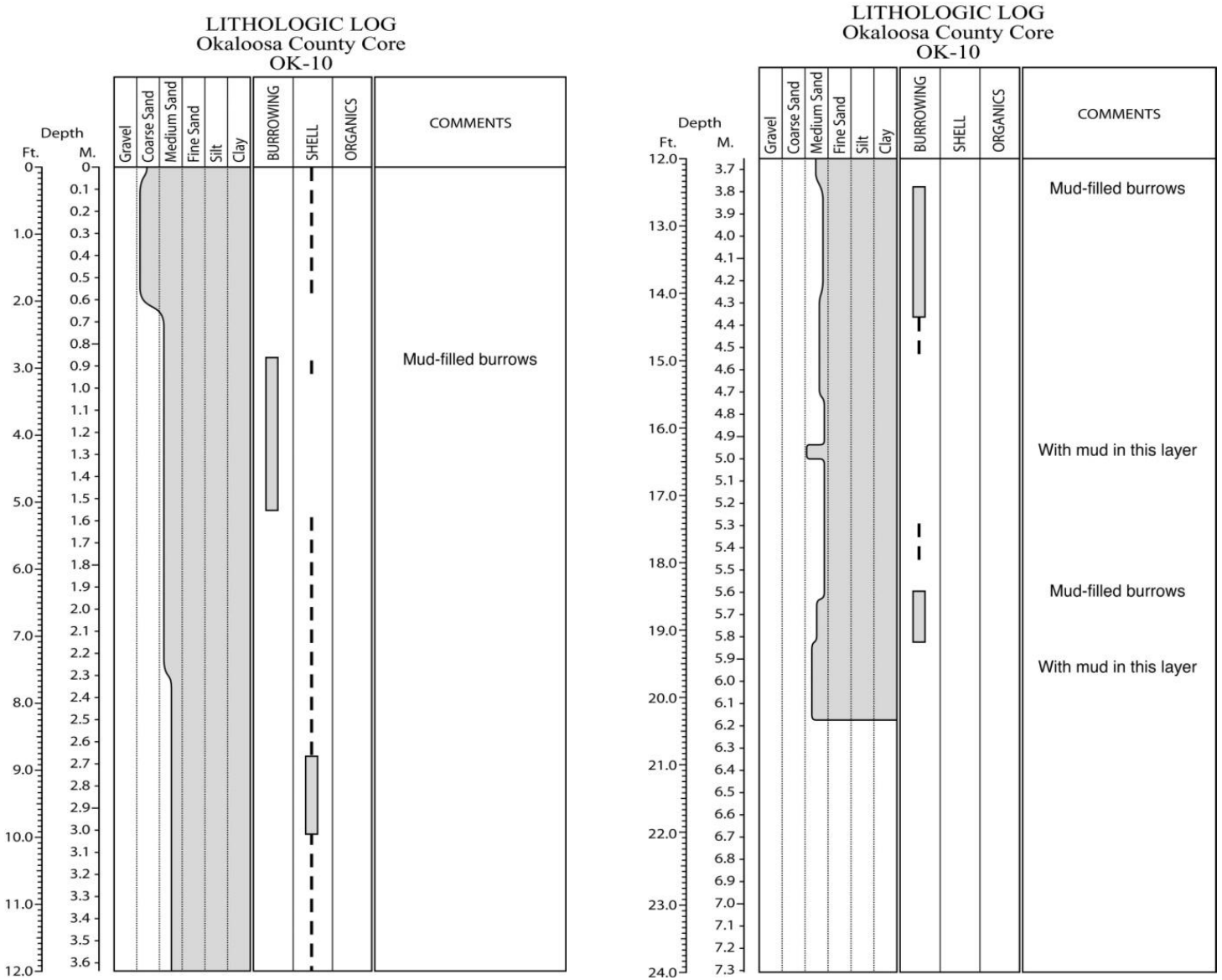

Figure E.189. Core OK-10 log.

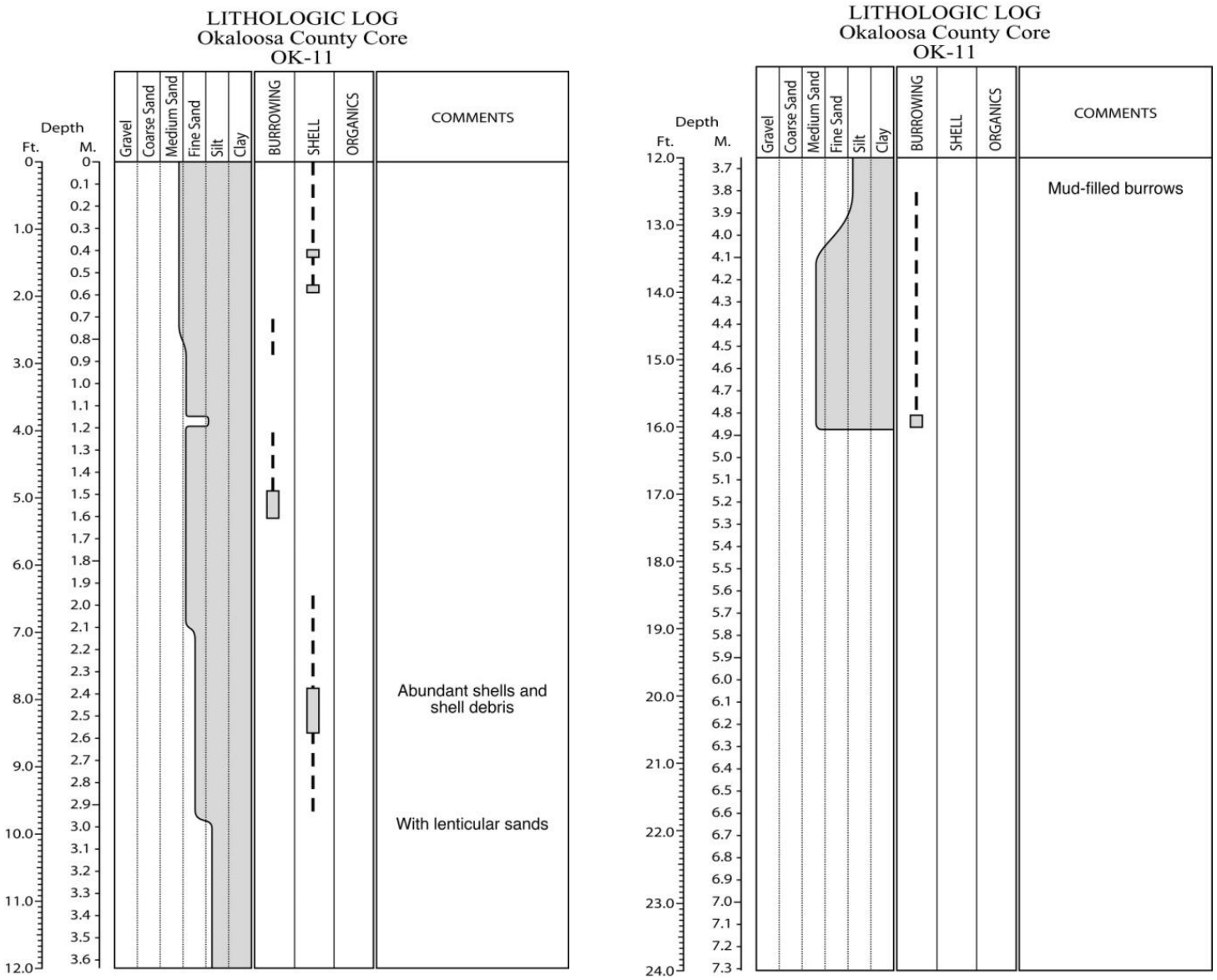

Figure E.190. Core OK-11 log.

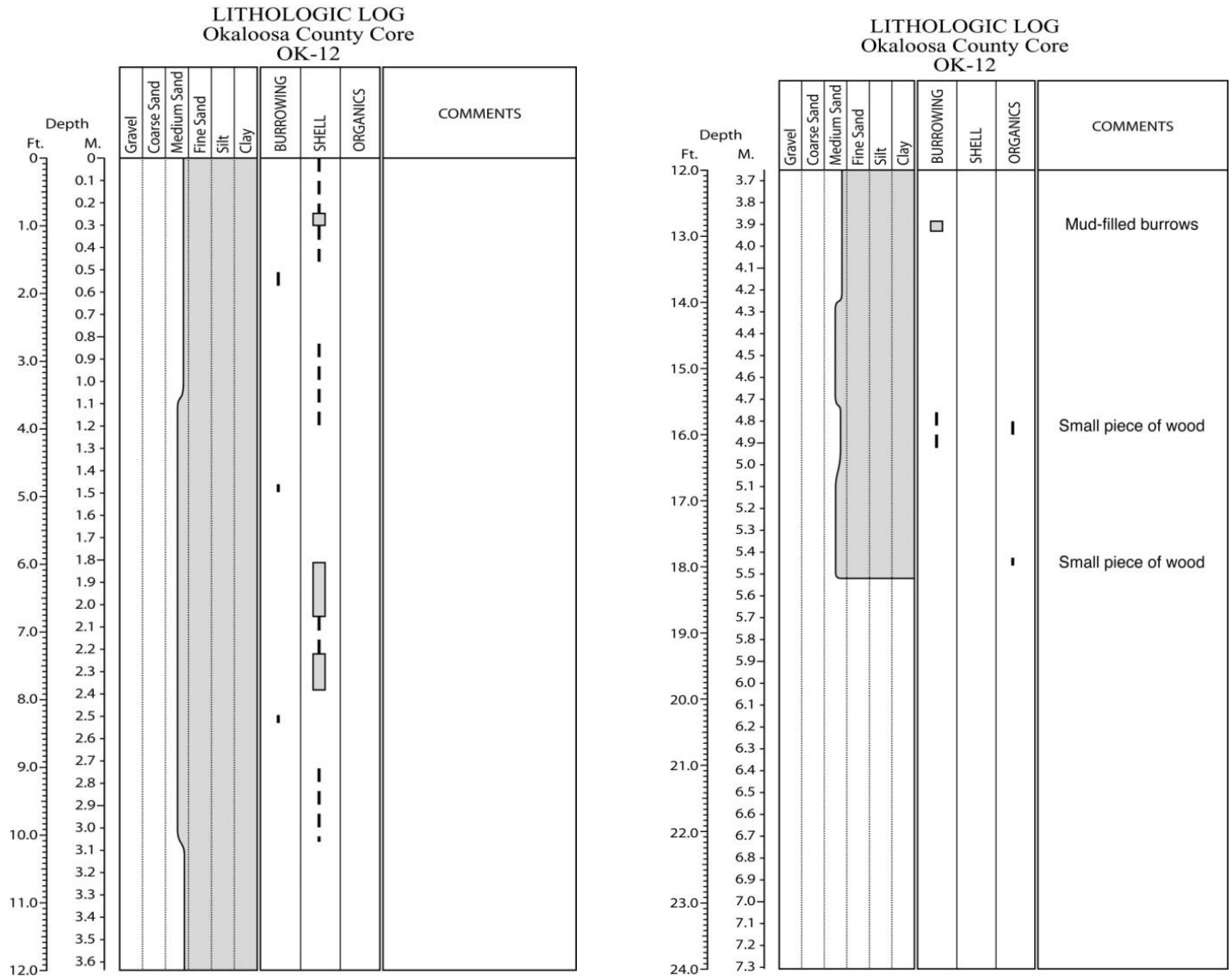

Figure E.191. Core OK-12 log.

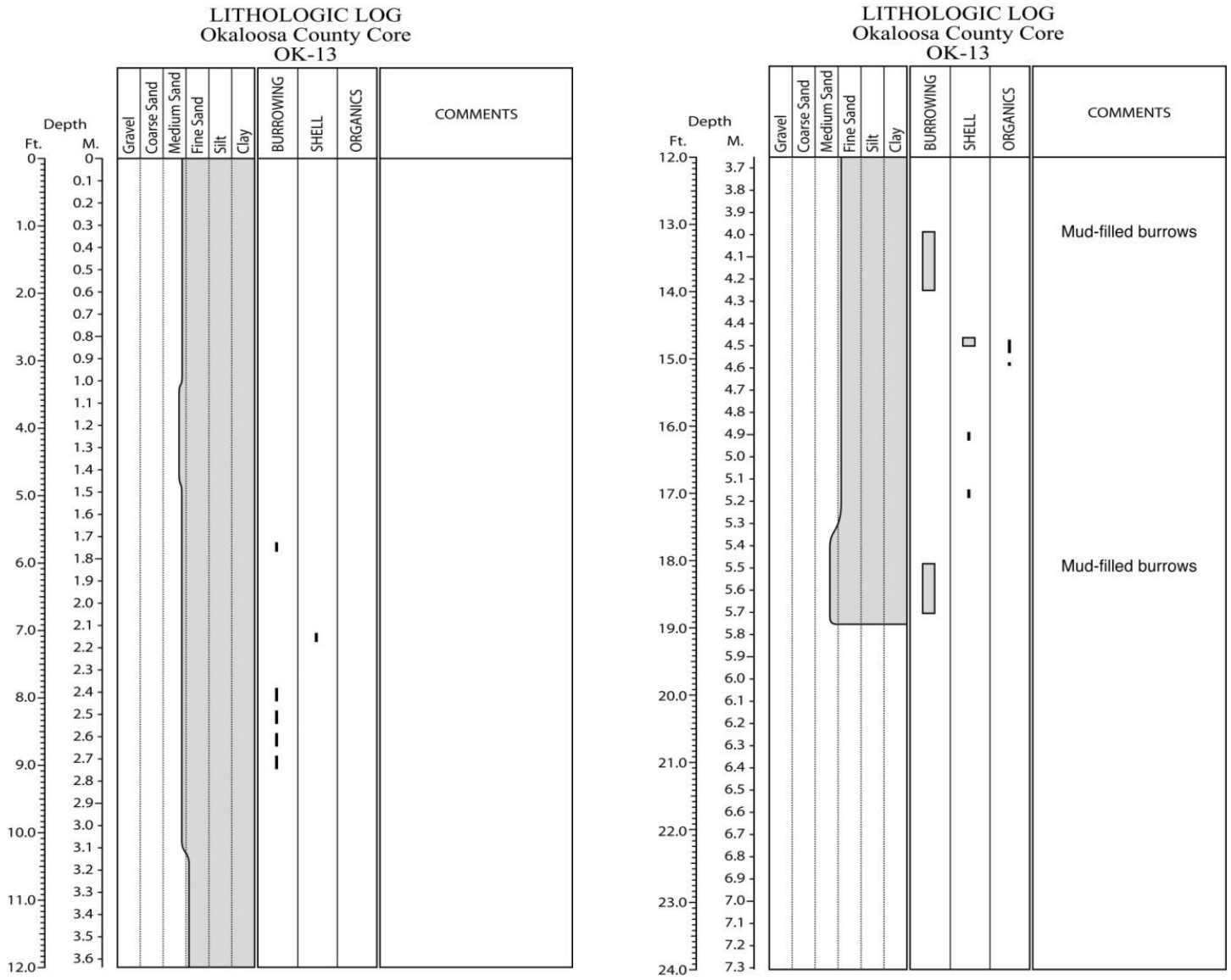

Figure E.192. Core OK-13 log.

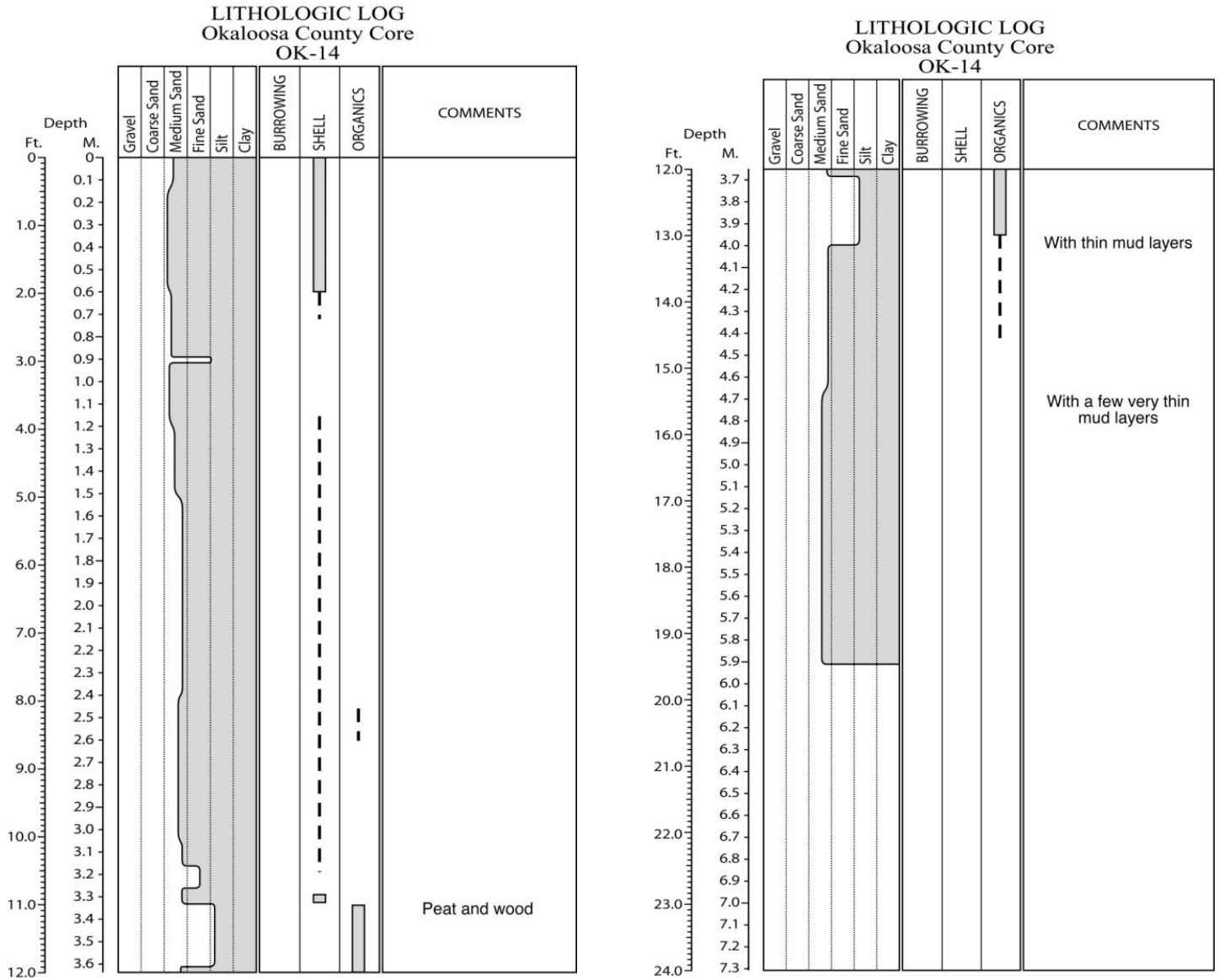

Figure E.193. Core OK-14 log.

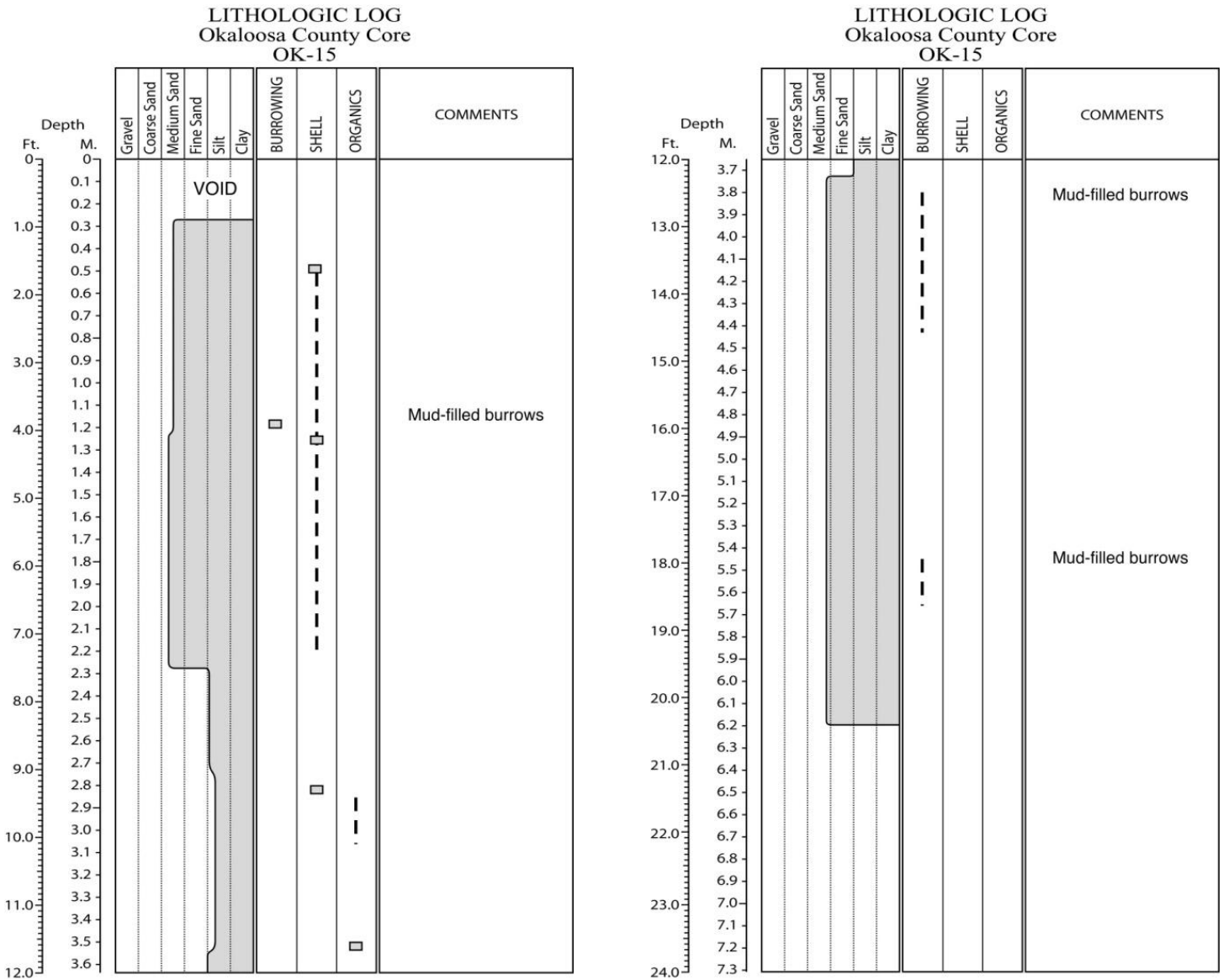

Figure E.194. Core OK-15 log.

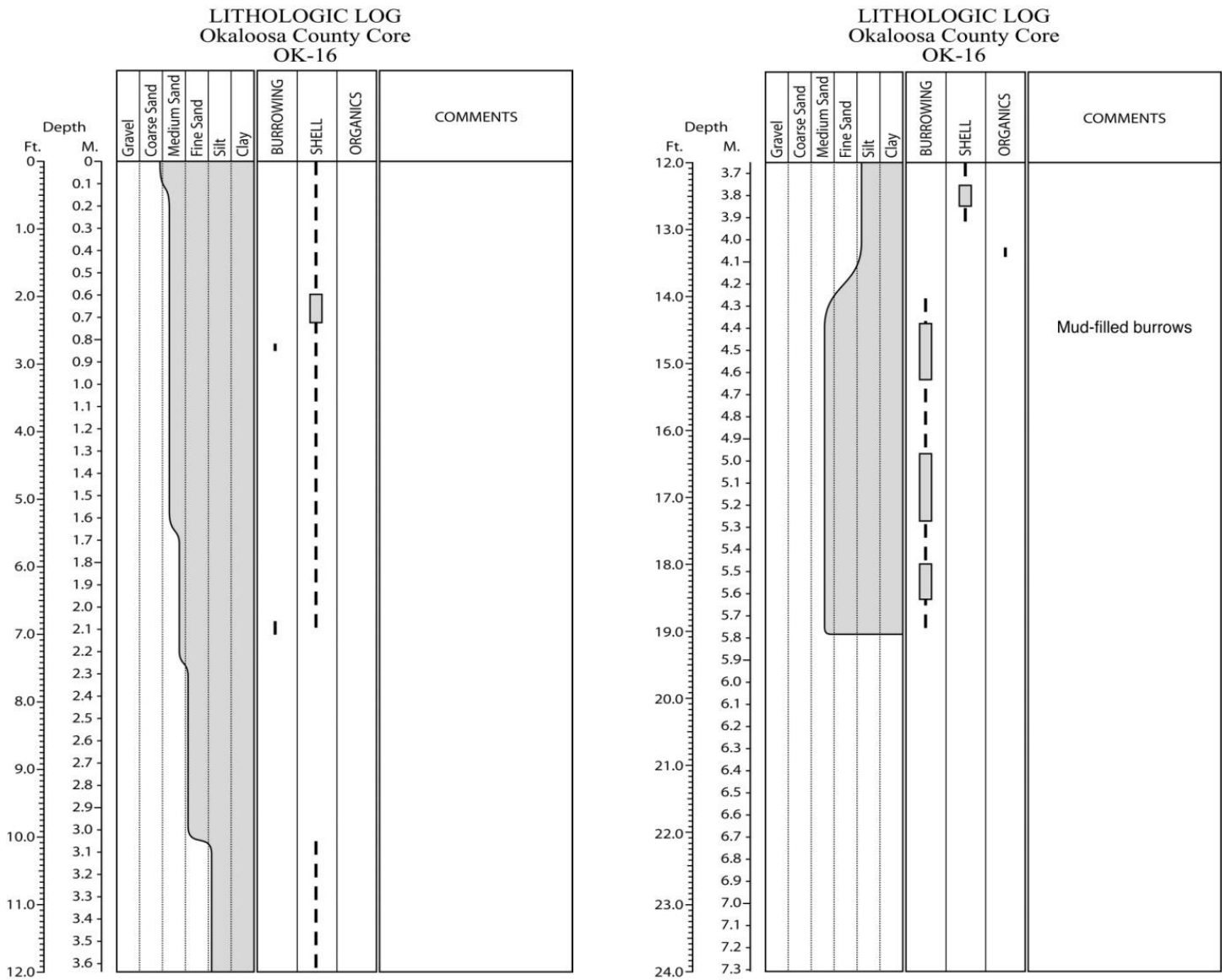

Figure E.195. Core OK-16 log.

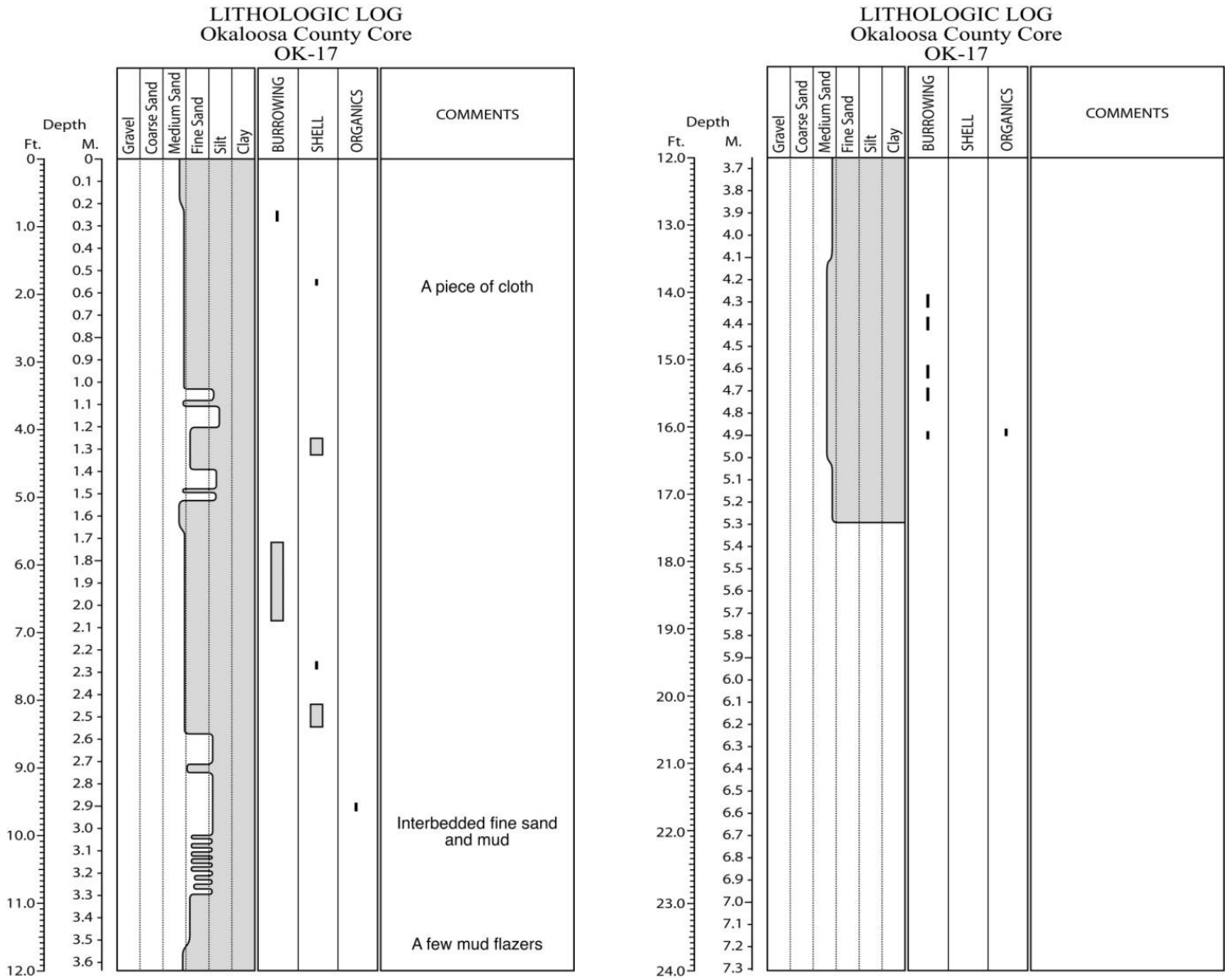

Figure E.196. Core OK-17 log.

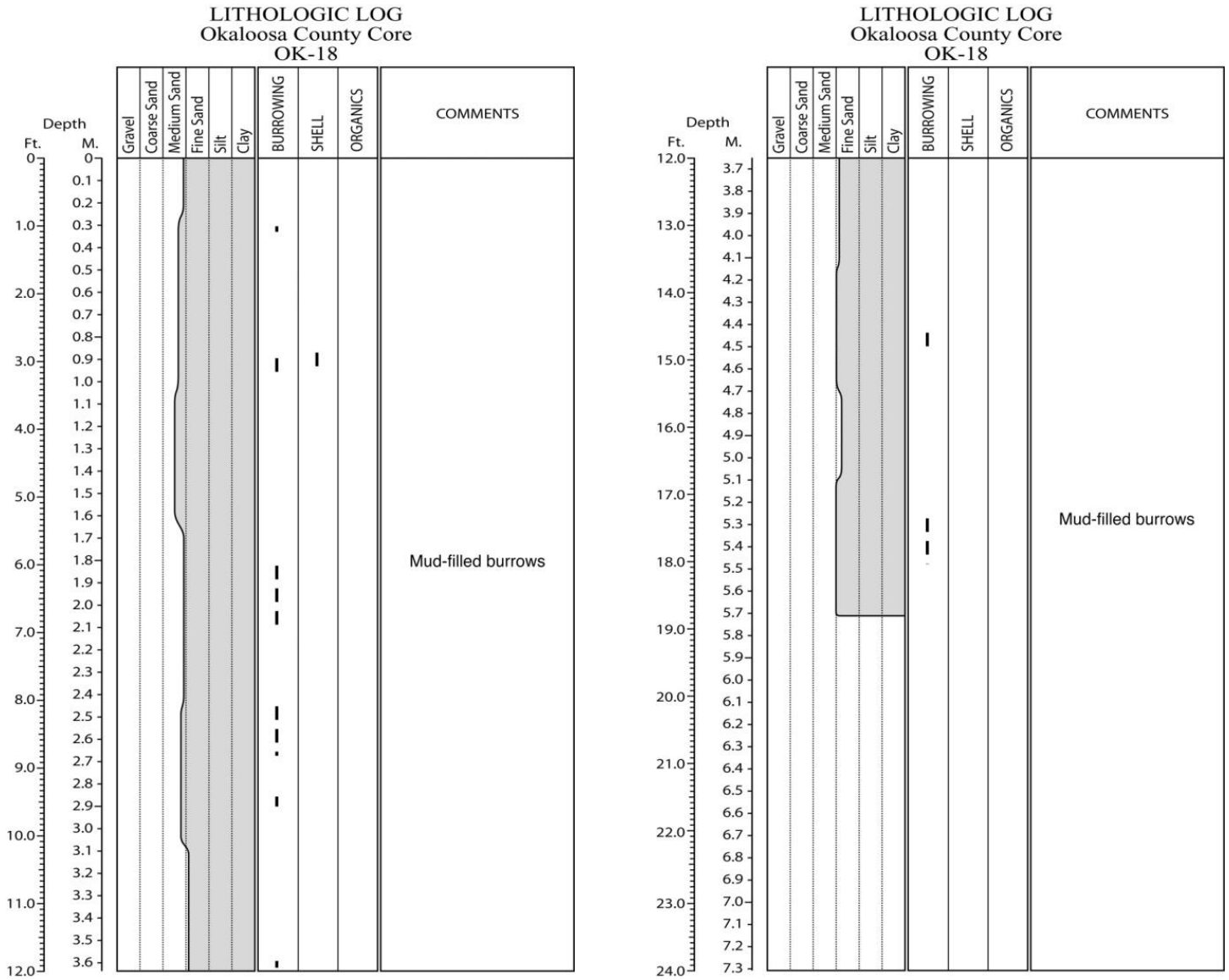

Figure E.197. Core OK-18 log.

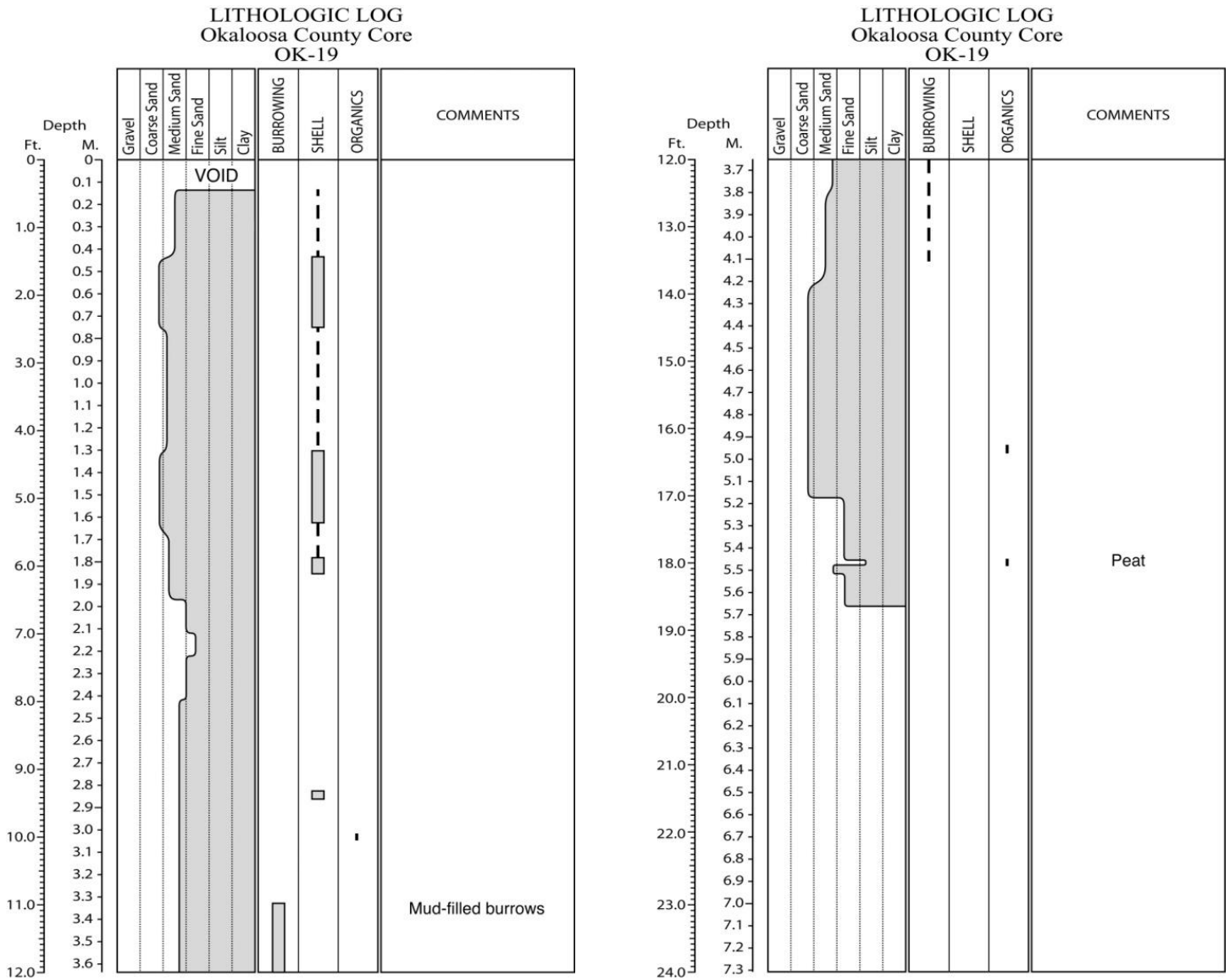

Figure E.198. Core OK-19 log.

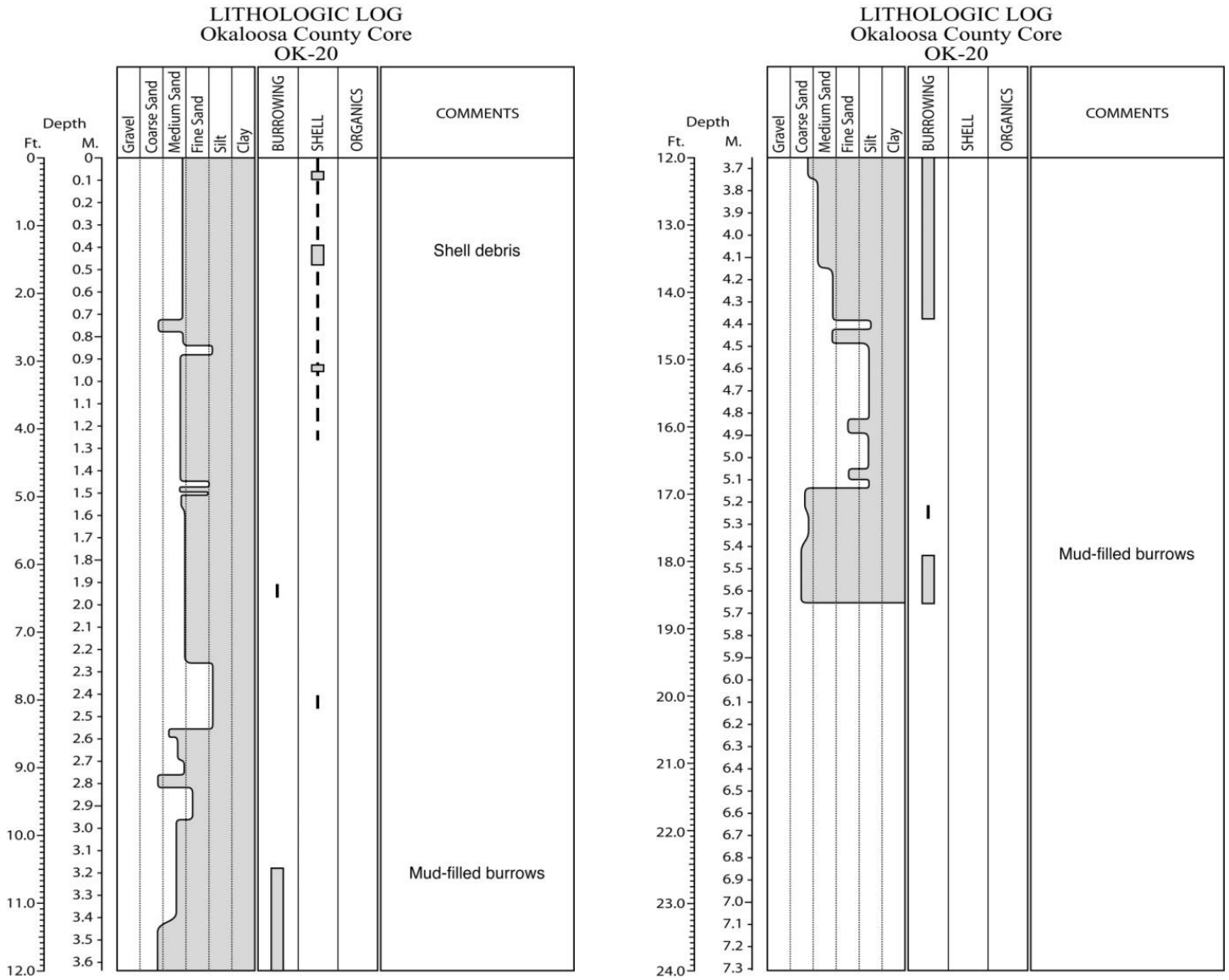

Figure E.199. Core OK-20 log.

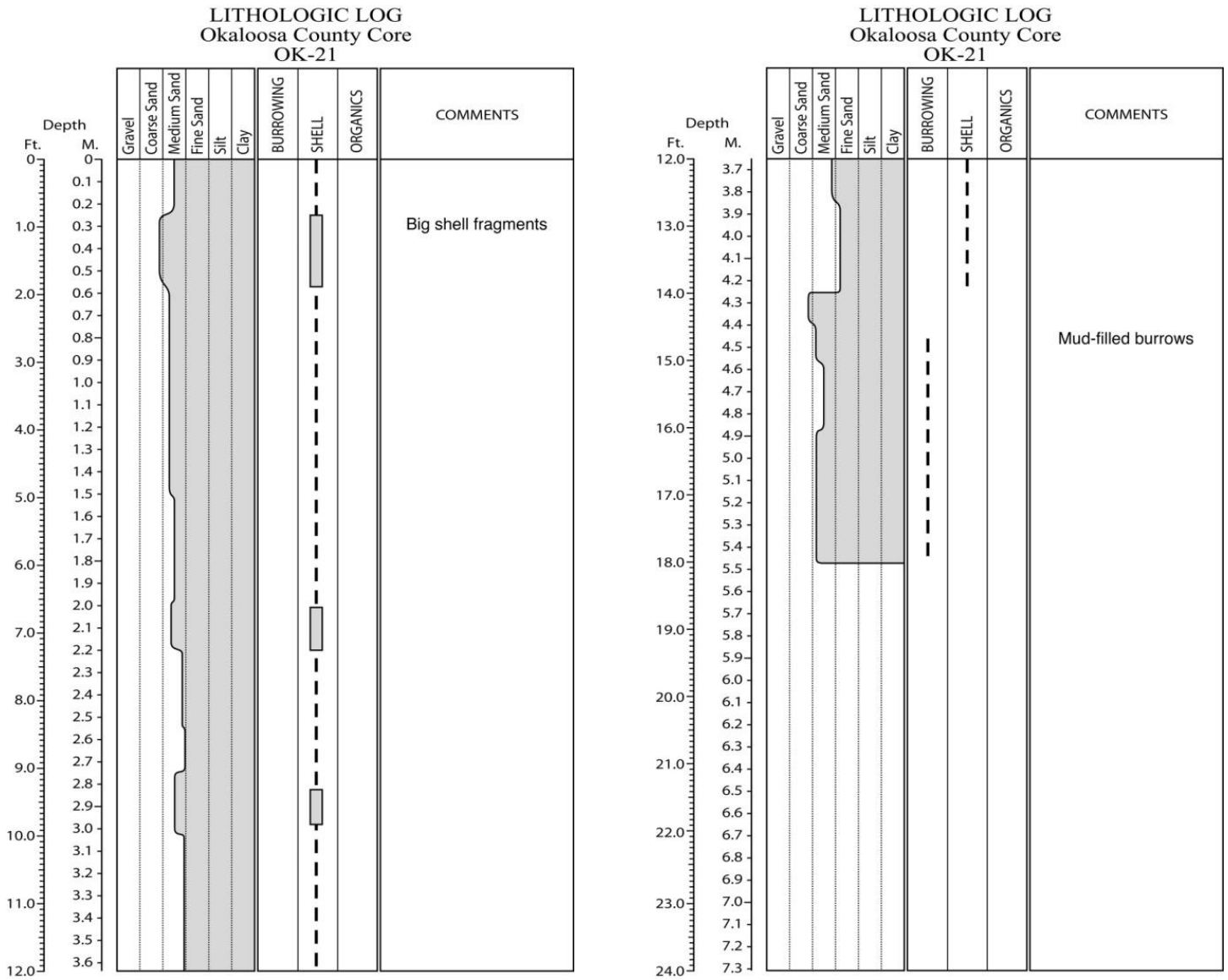

Figure E.200. Core OK-21 log.

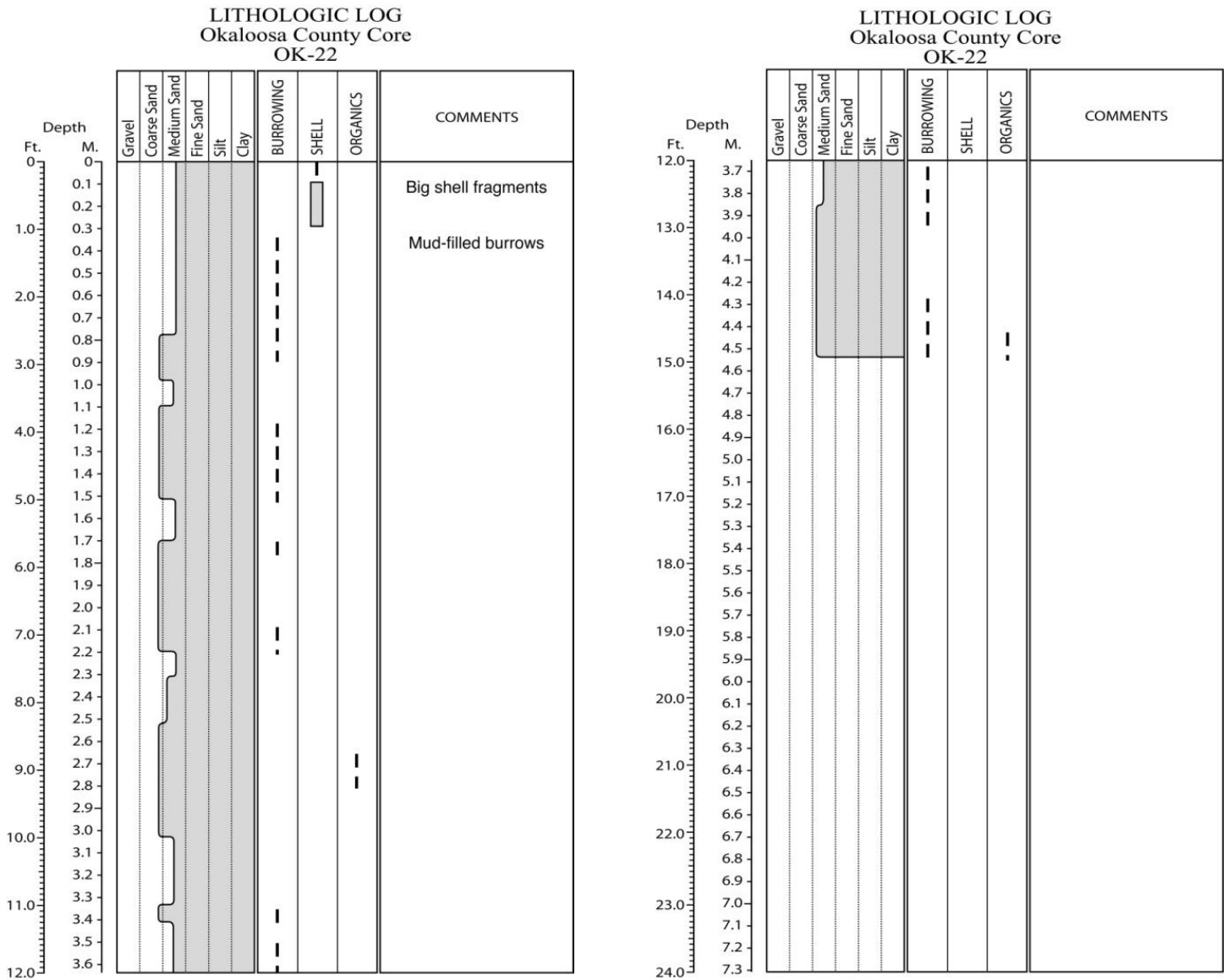

Figure E.201. Core OK-22 log.

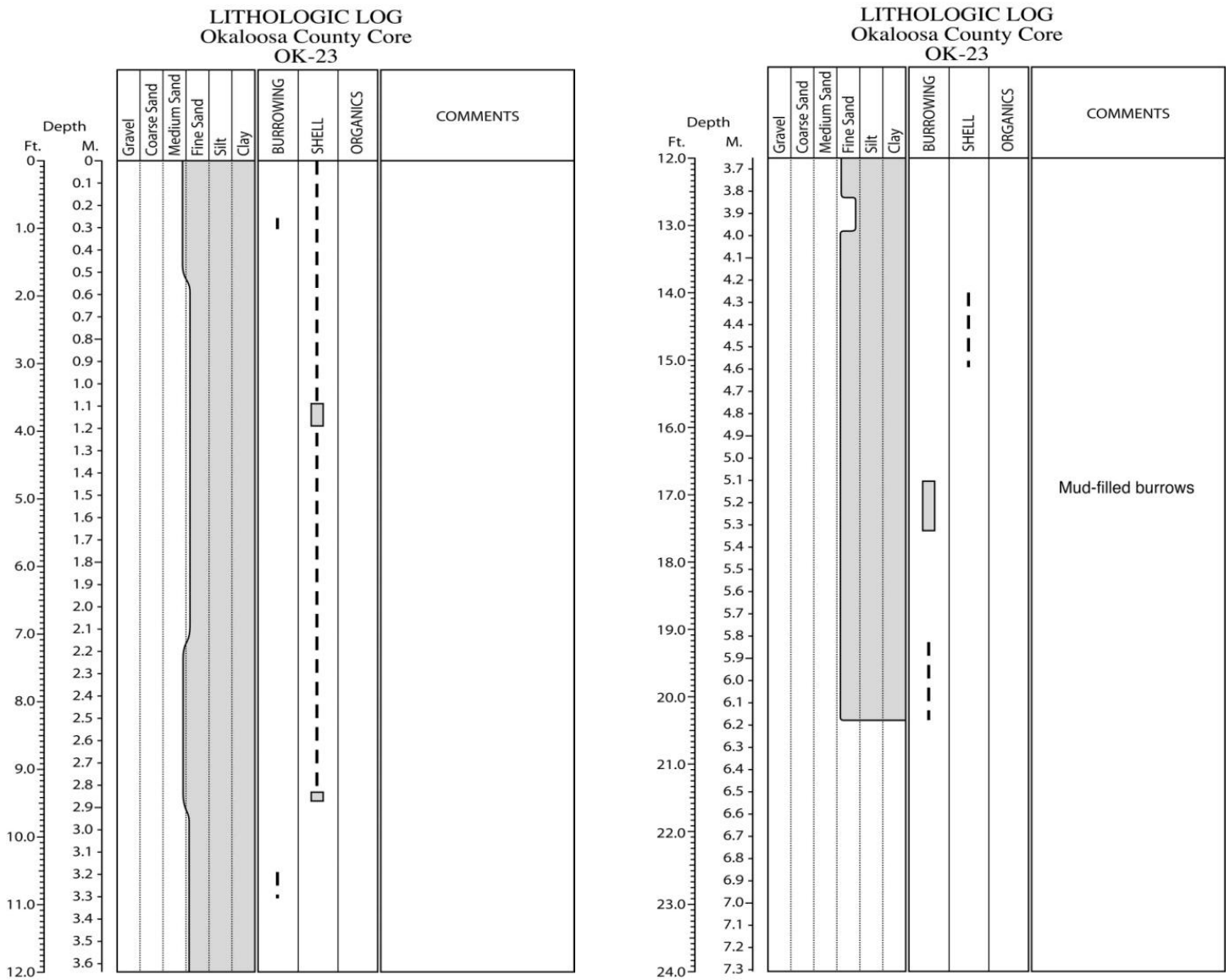

Figure E.202. Core OK-23 log.

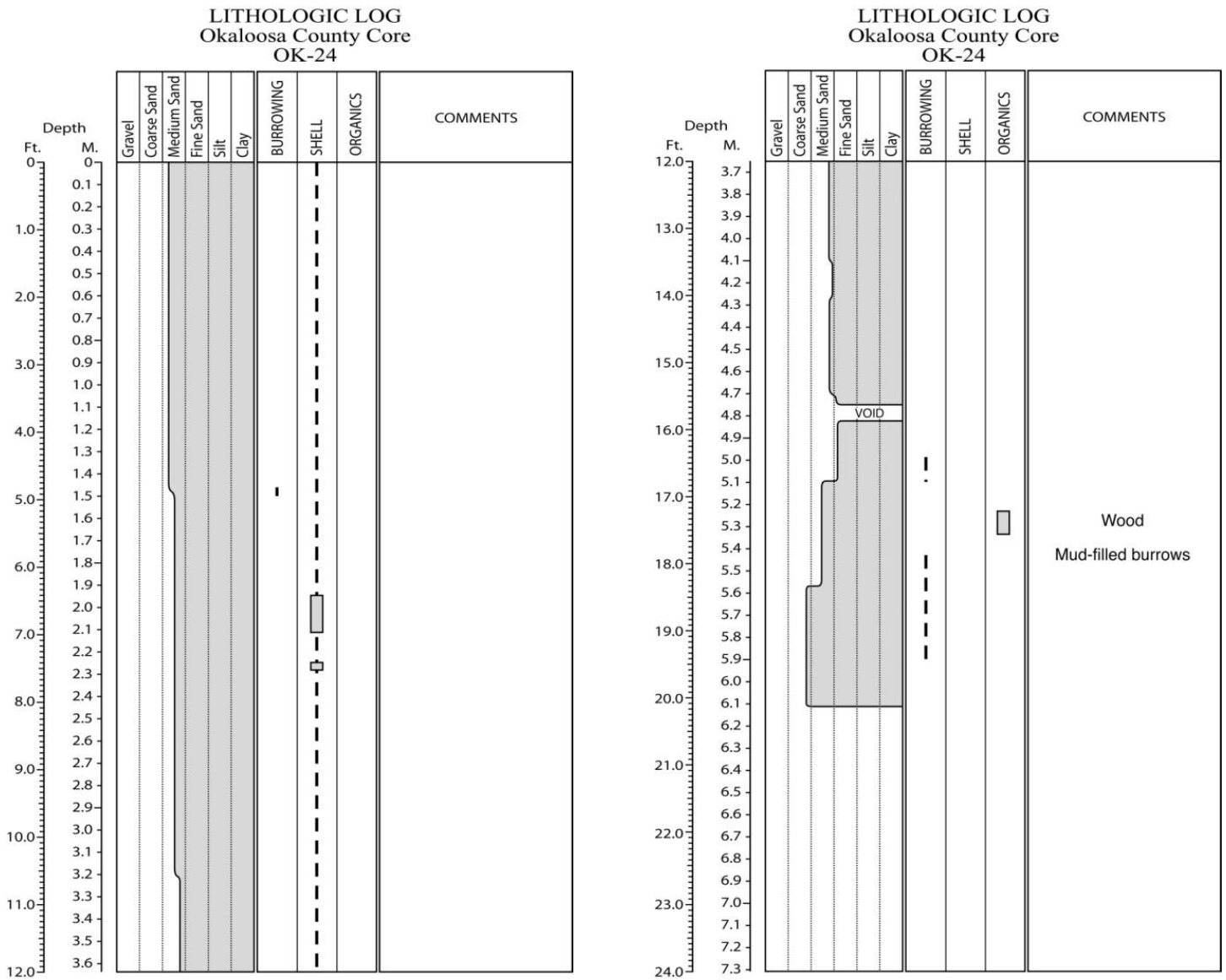

Figure E.203. Core OK-24 log.

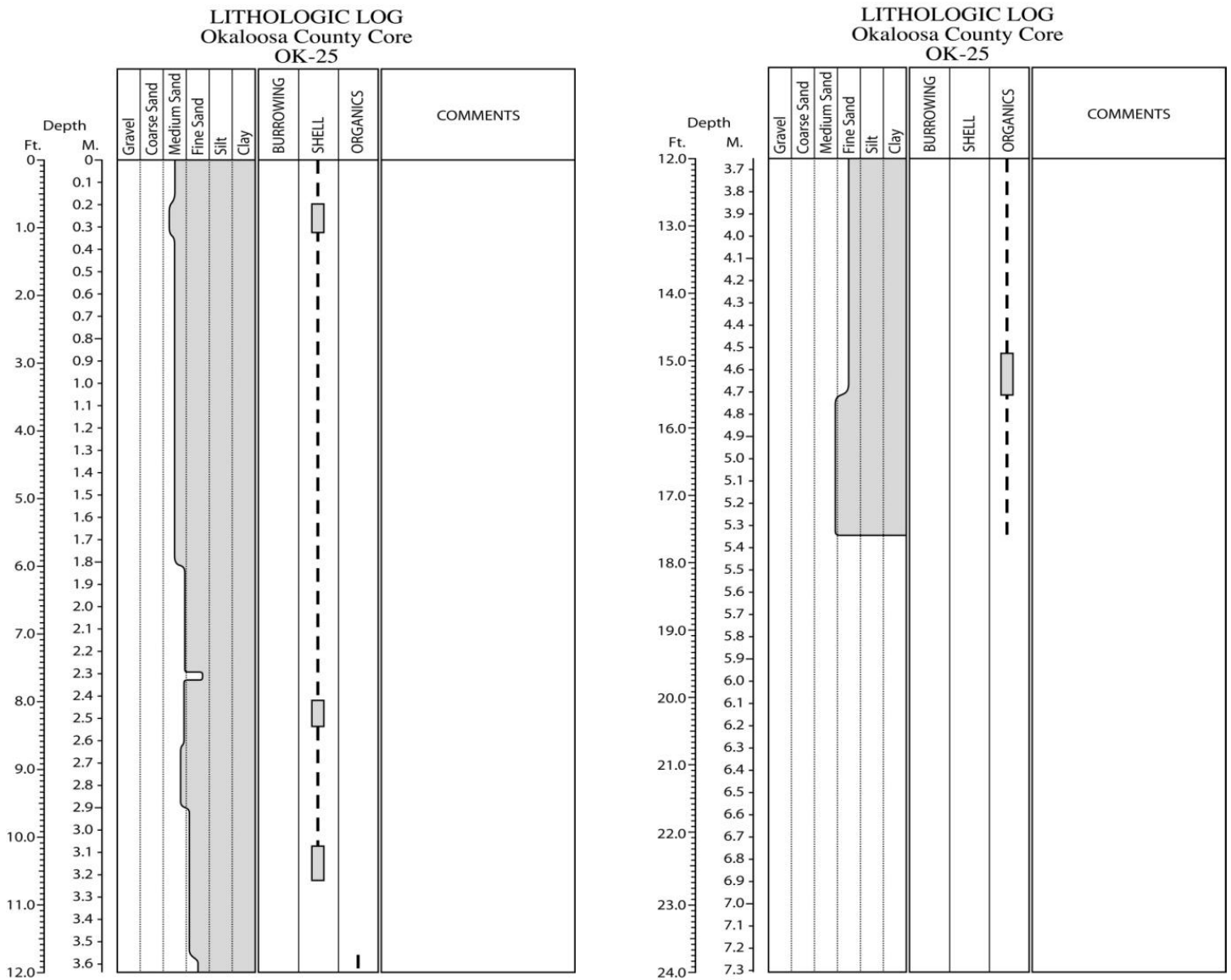

Figure E.204. Core OK-25 log.

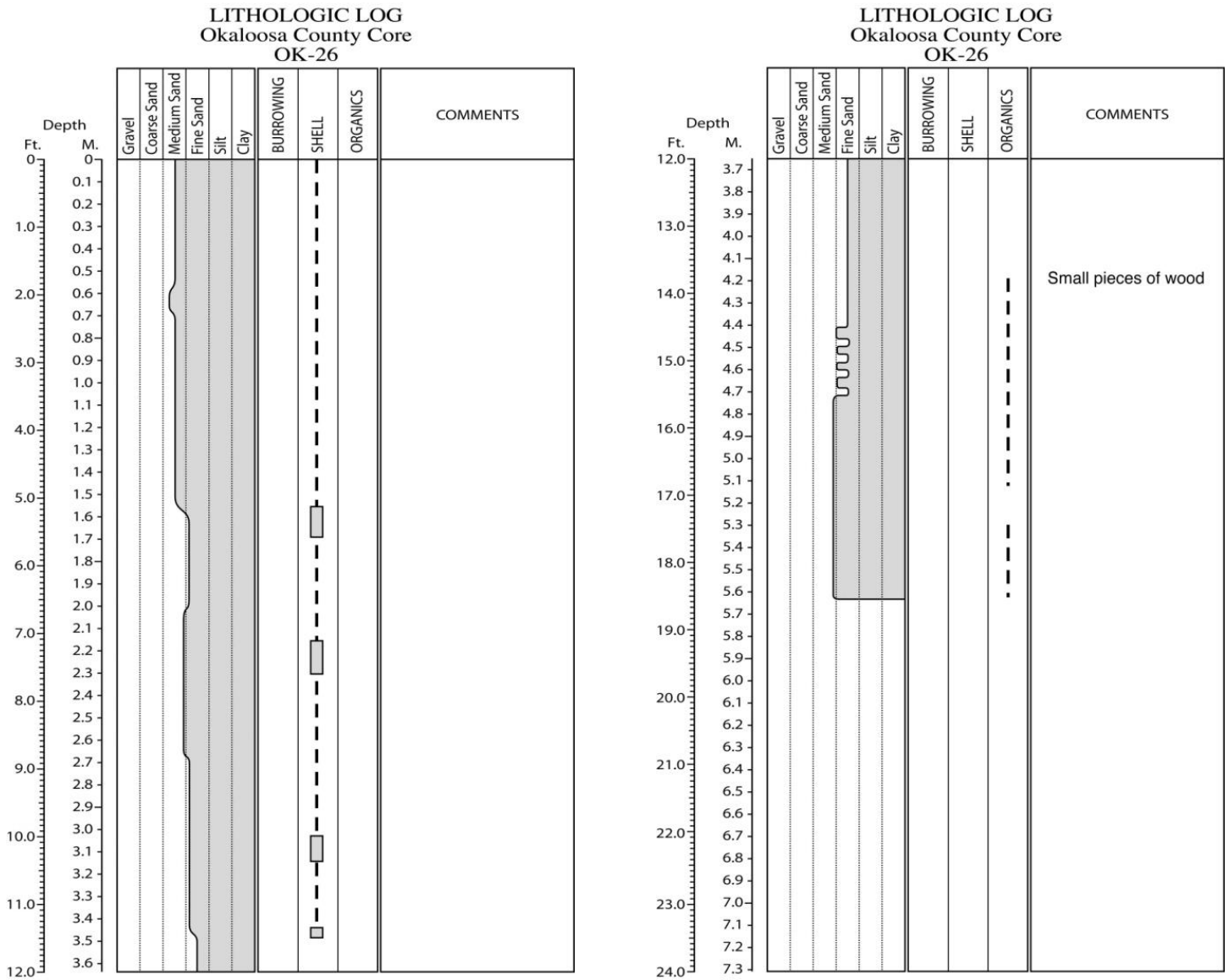

Figure E.205. Core OK-26 log.

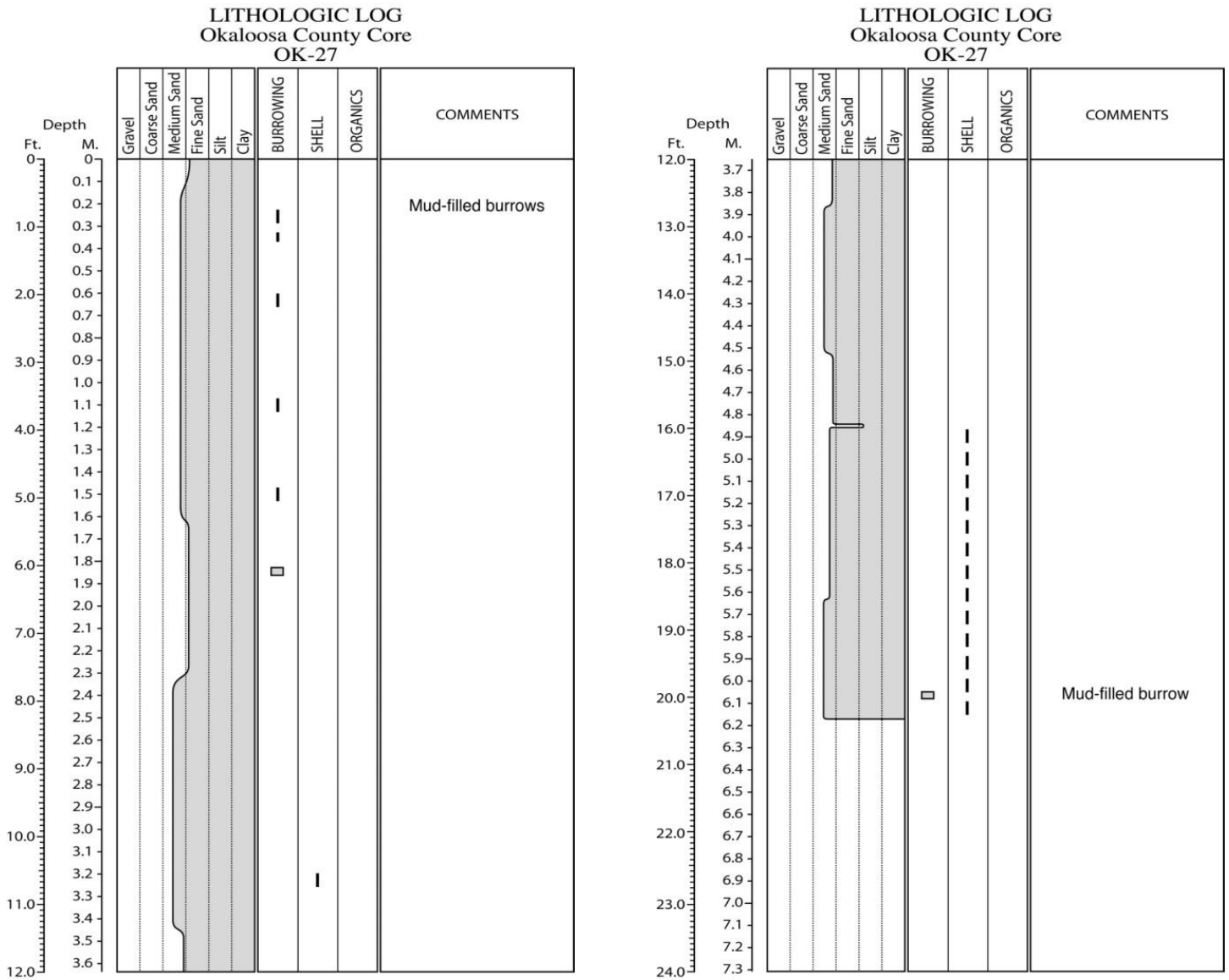

Figure E.206. Core OK-27 log.

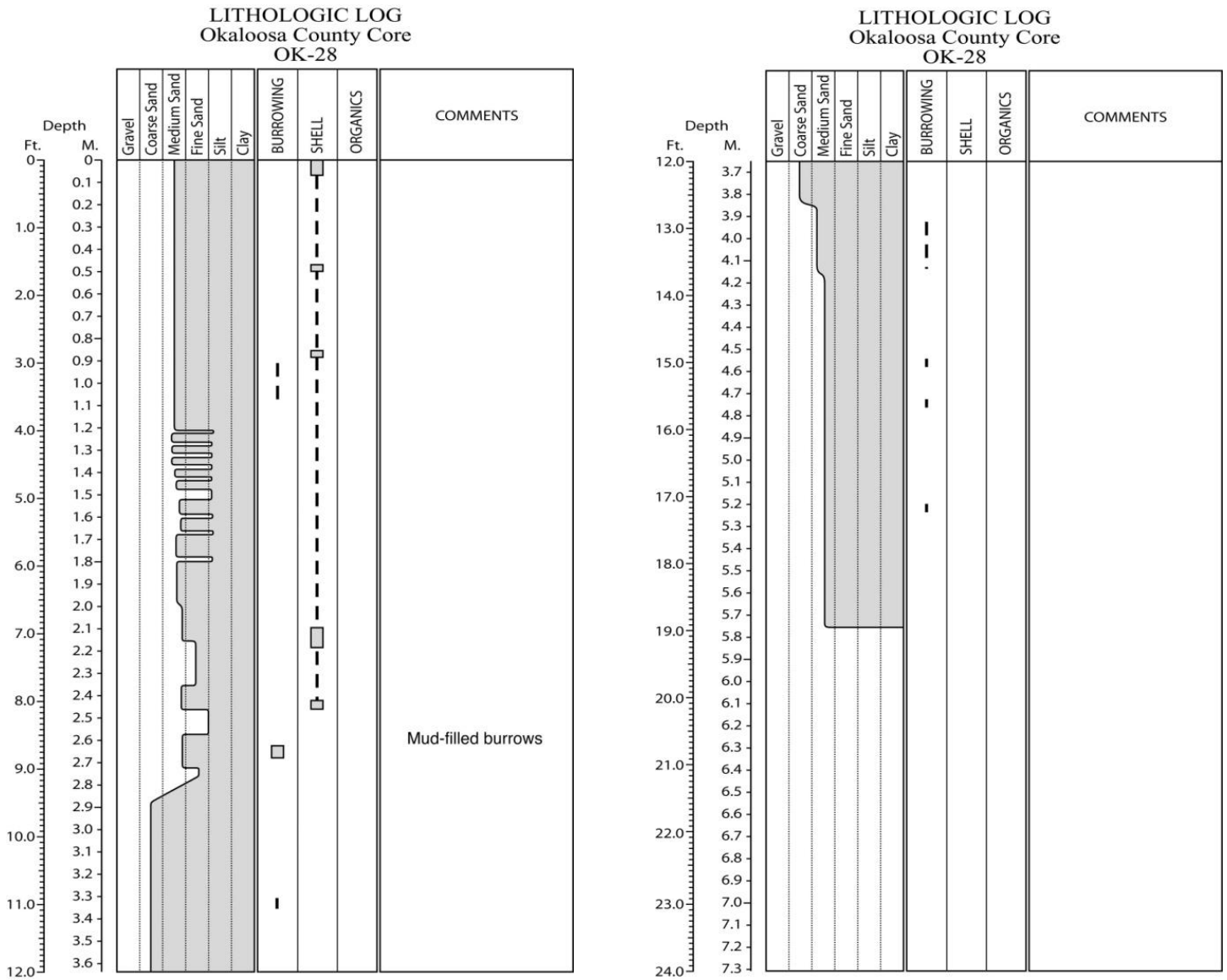

Figure E.207. Core OK-28 log.

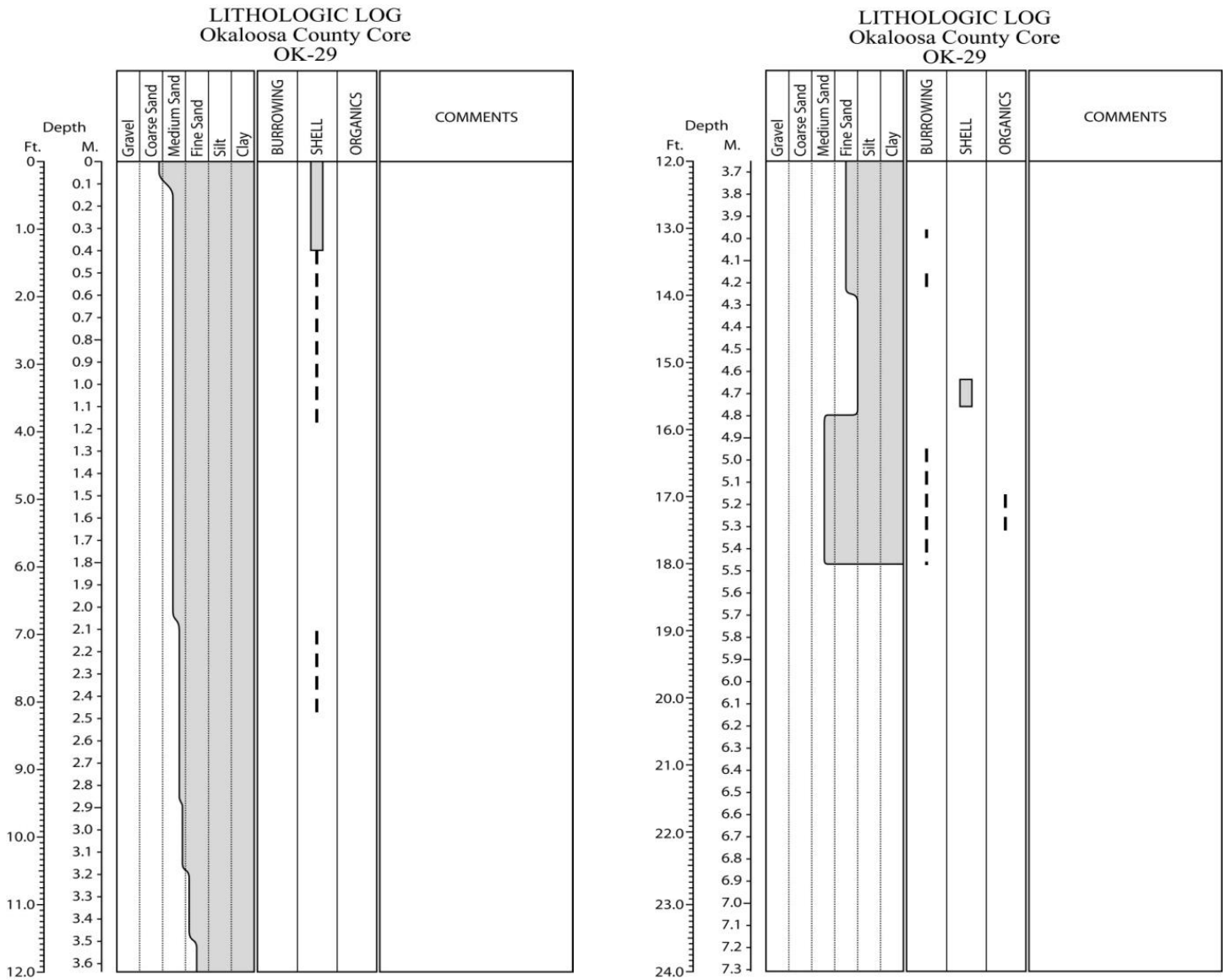

Figure E.208. Core OK-29 log.

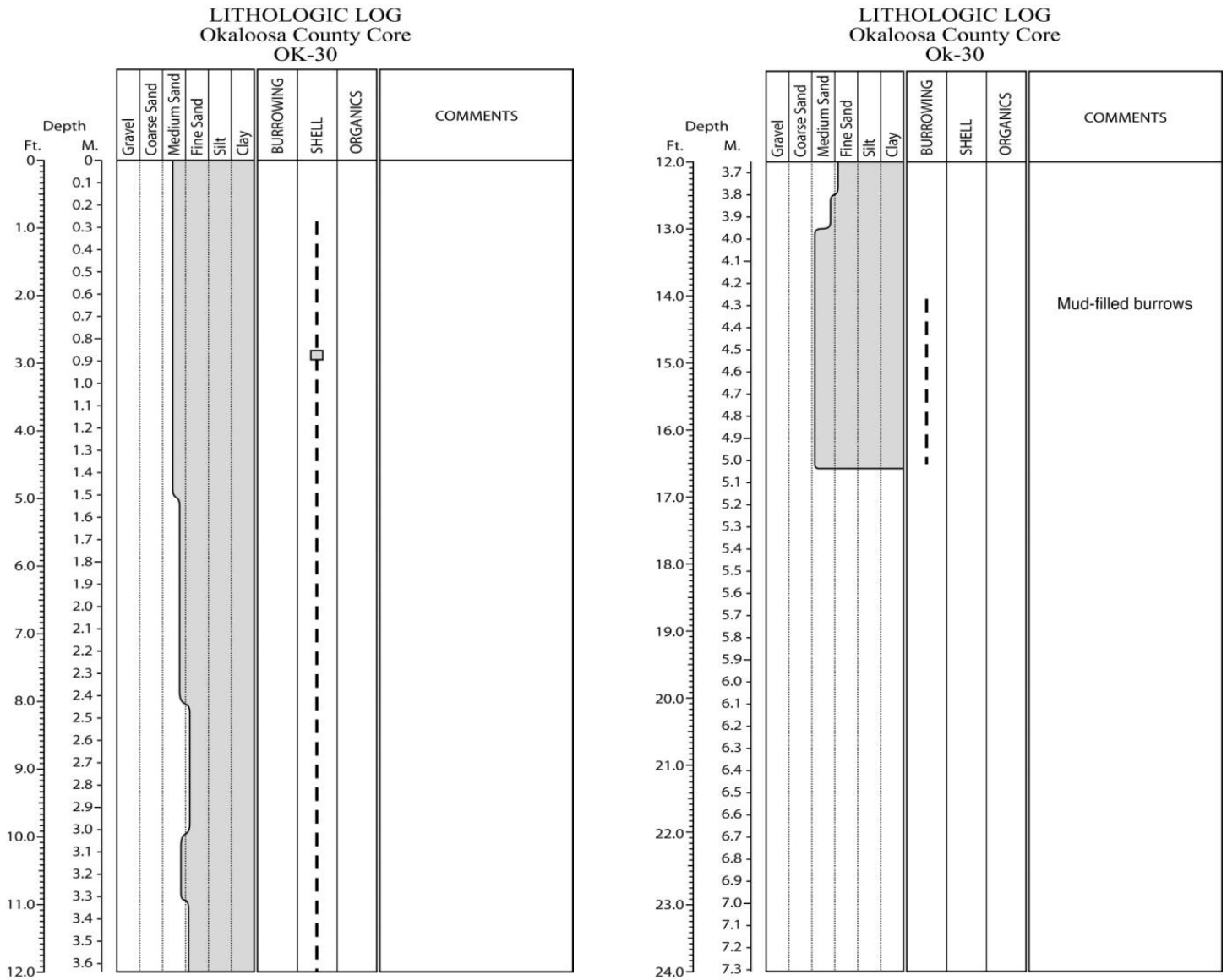

Figure E.209. Core OK-30 log.

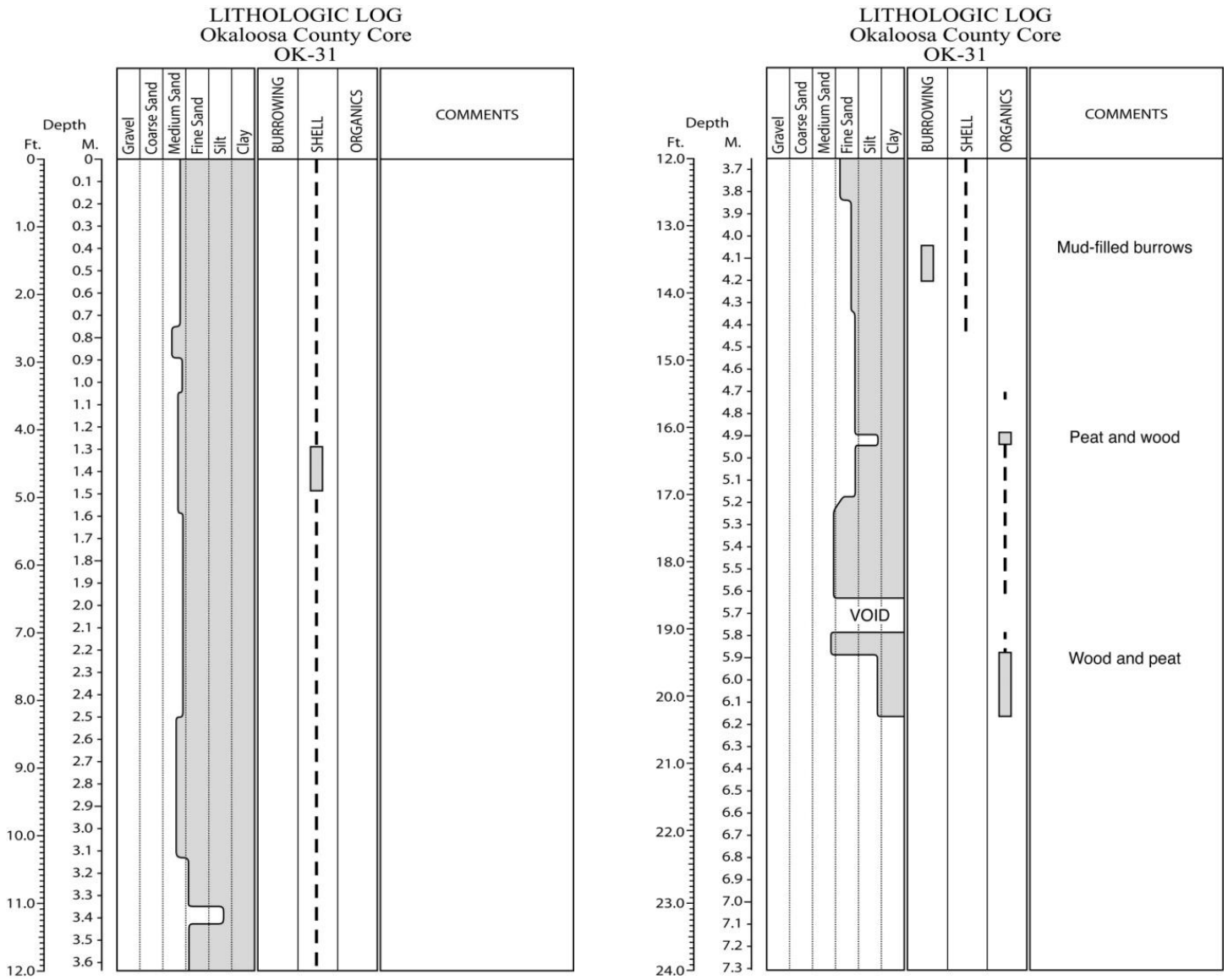

Figure E.210. Core OK-31 log.

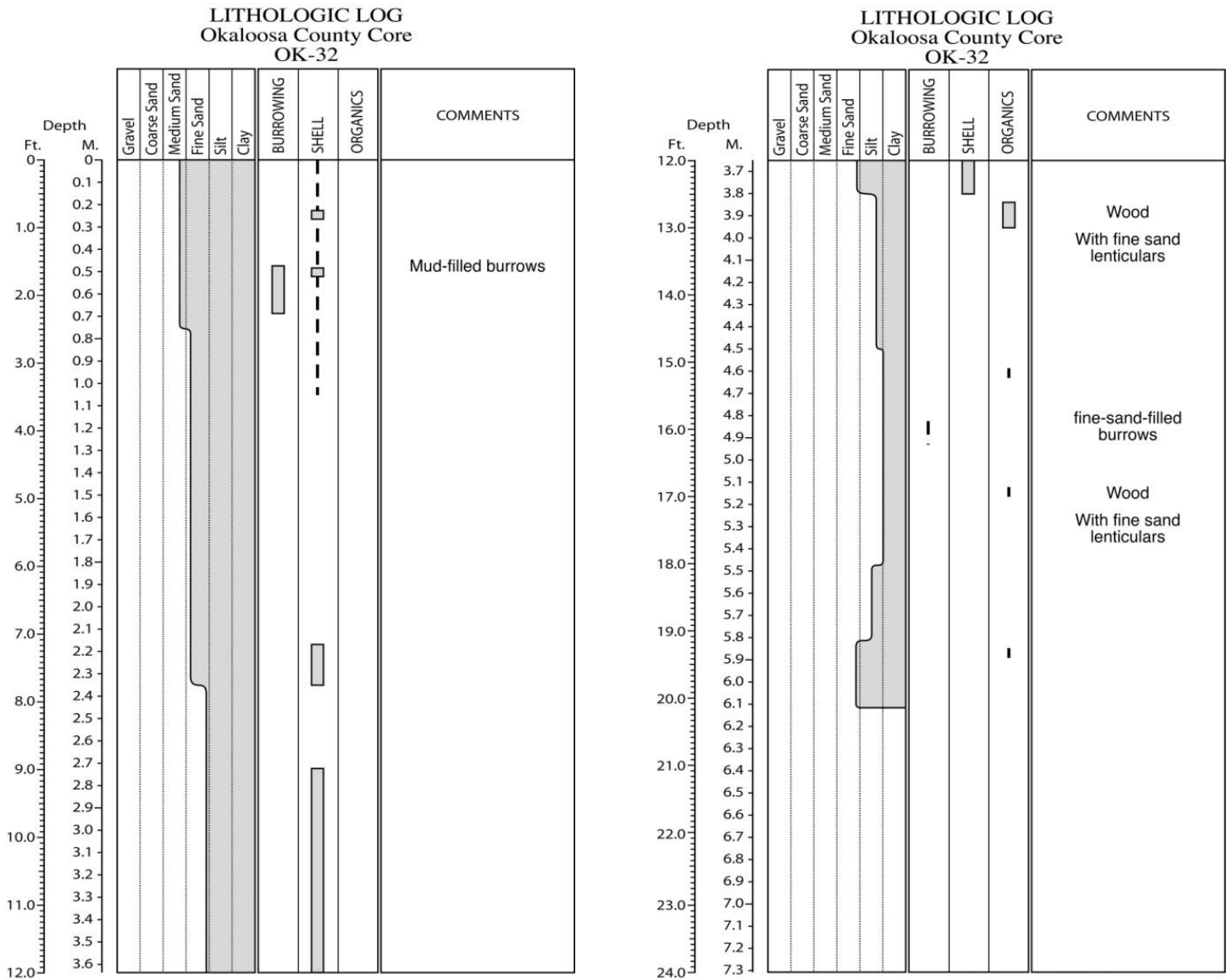

Figure E.211. Core OK-32 log.

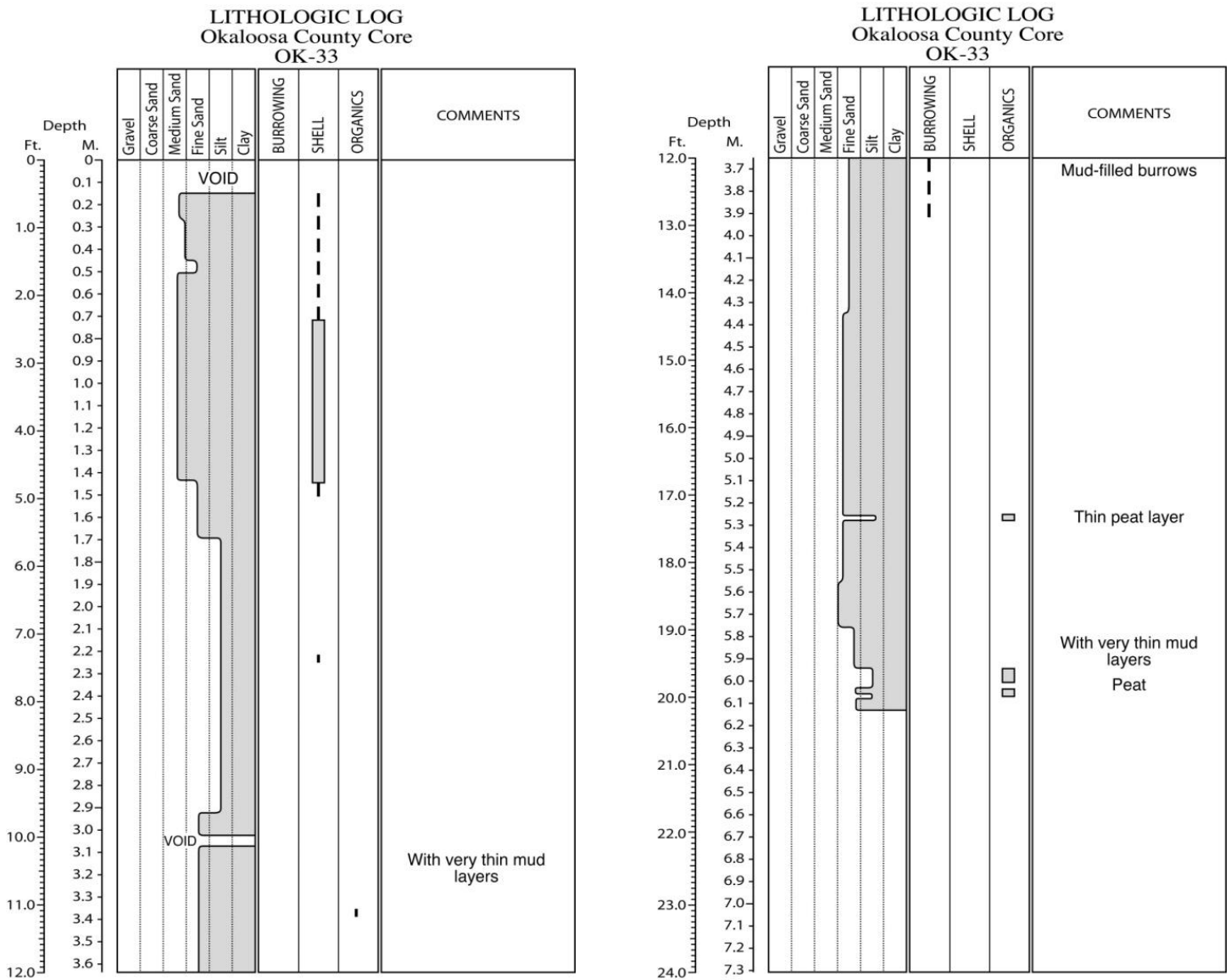

Figure E.212. Core OK-33 log.

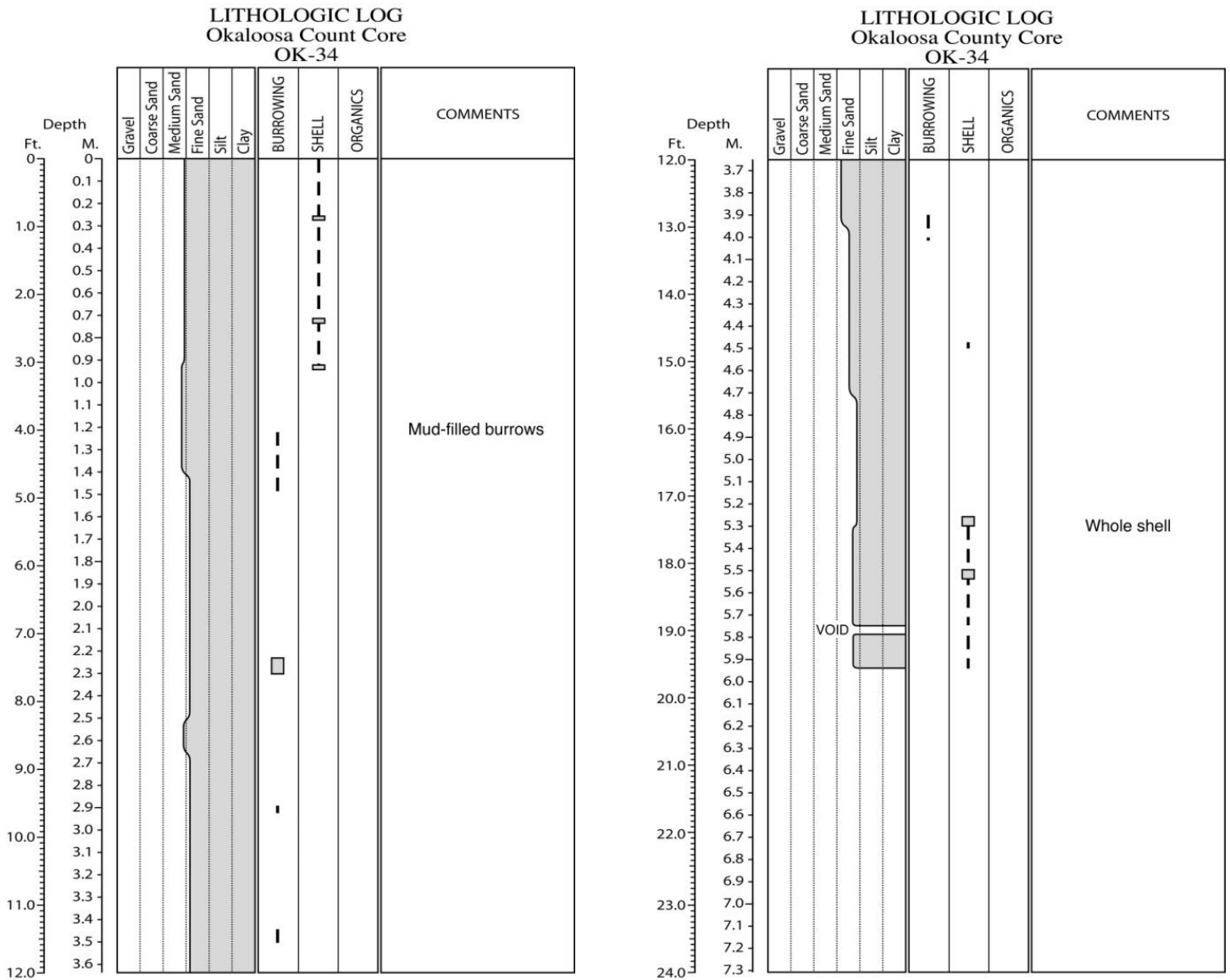

Figure E.213. Core OK-34 log.

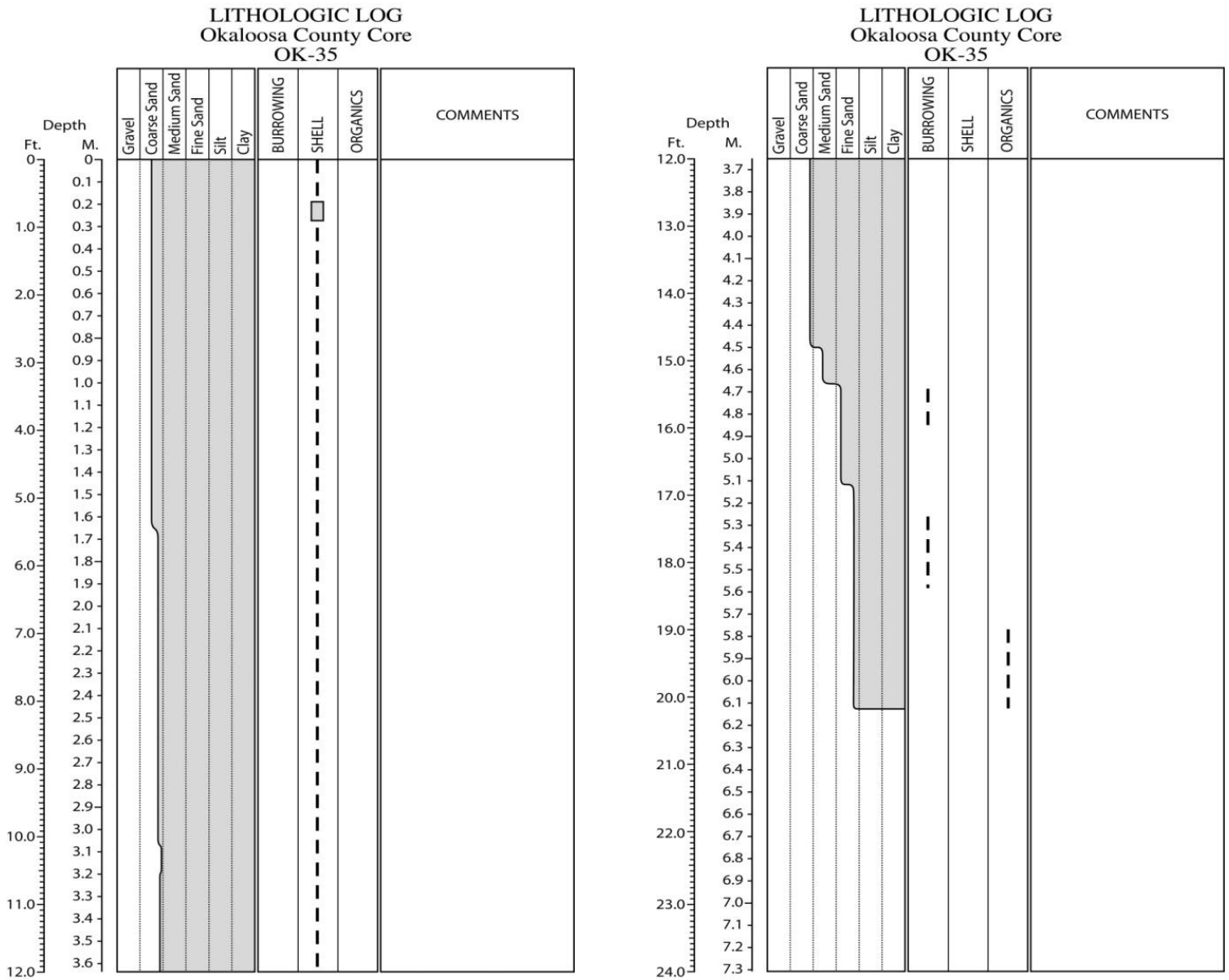

Figure E.214. Core OK-35 log.

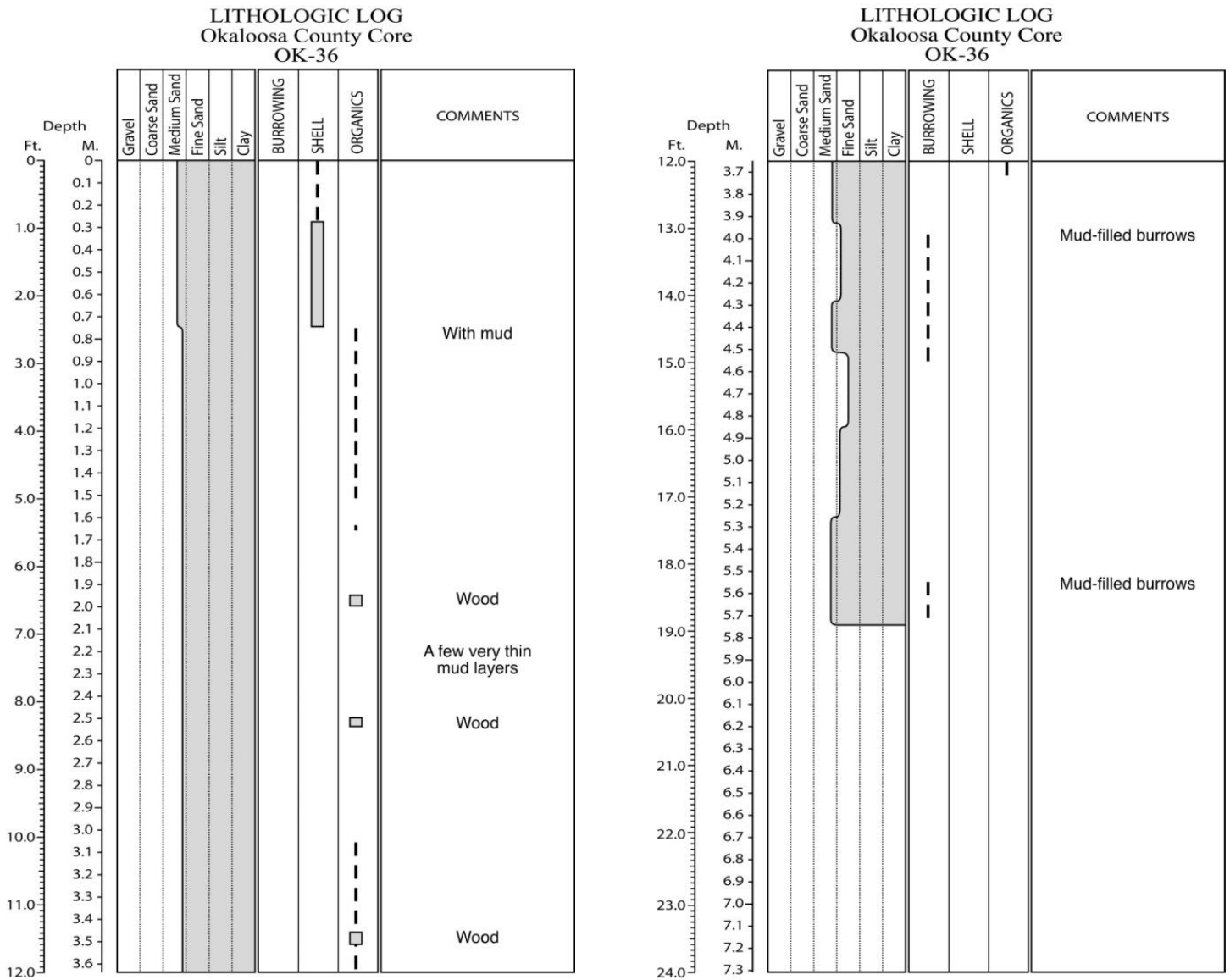

Figure E.215. Core OK-36 log.

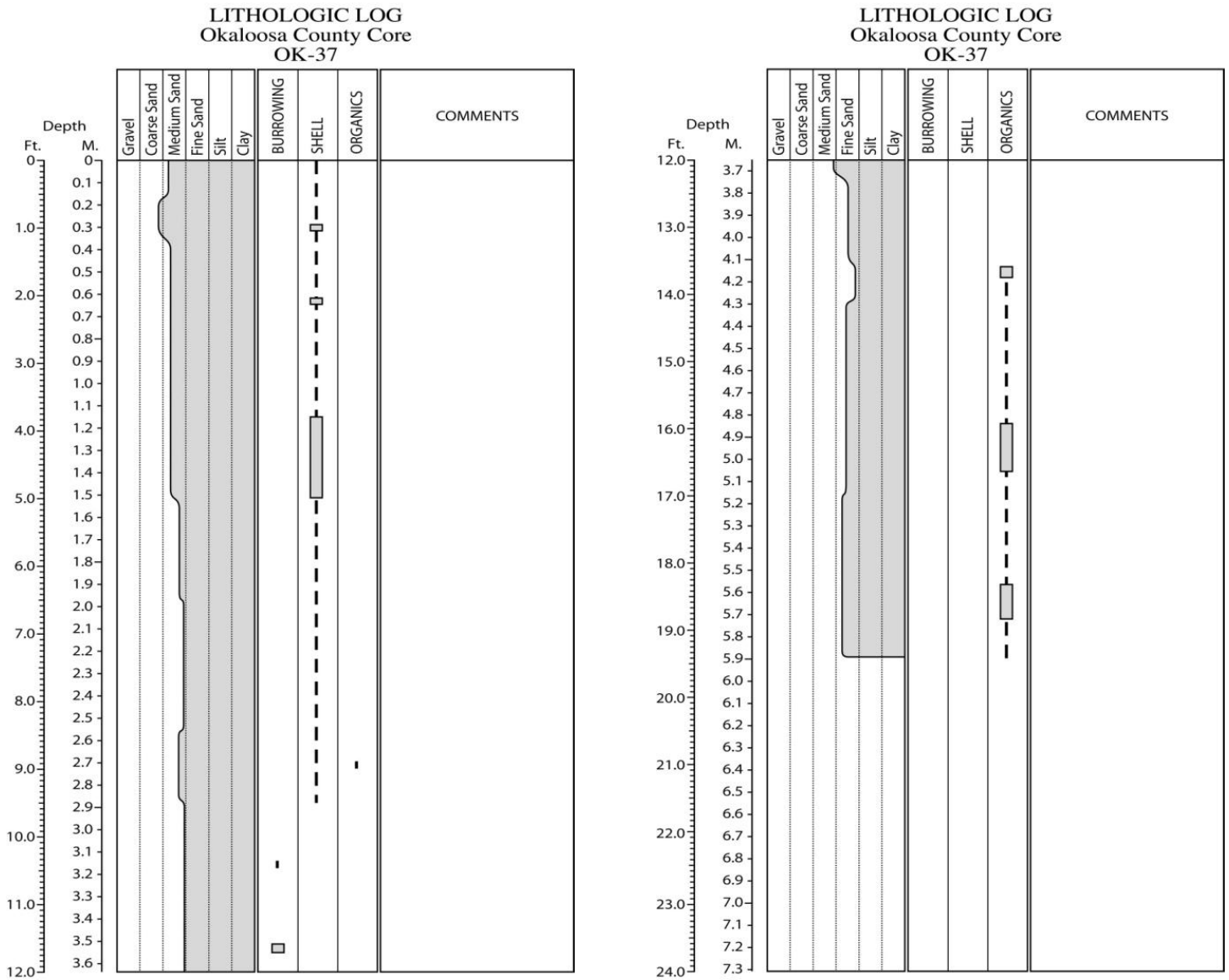

Figure E.216. Core OK-37 log.

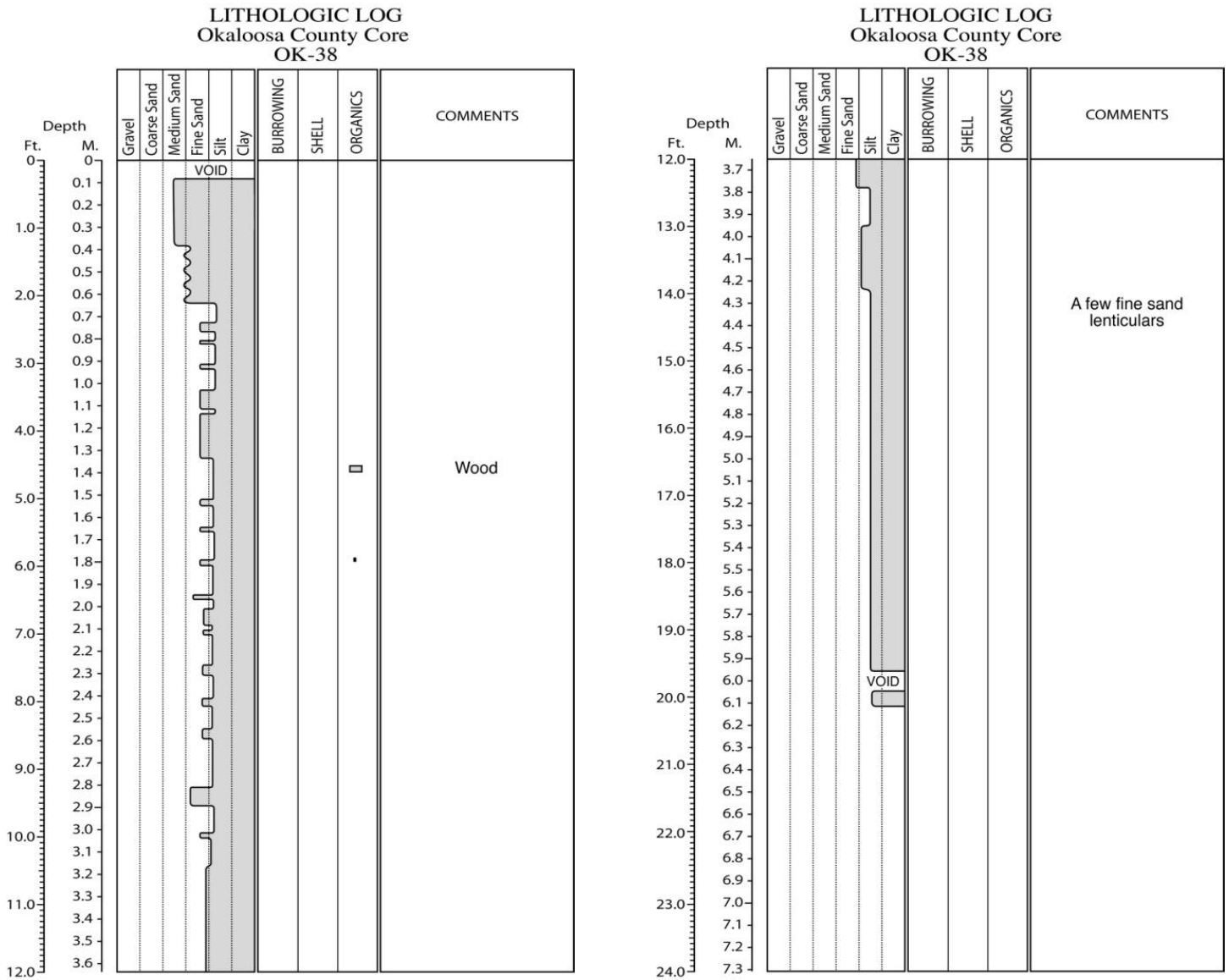

Figure E.217. Core OK-38 log.

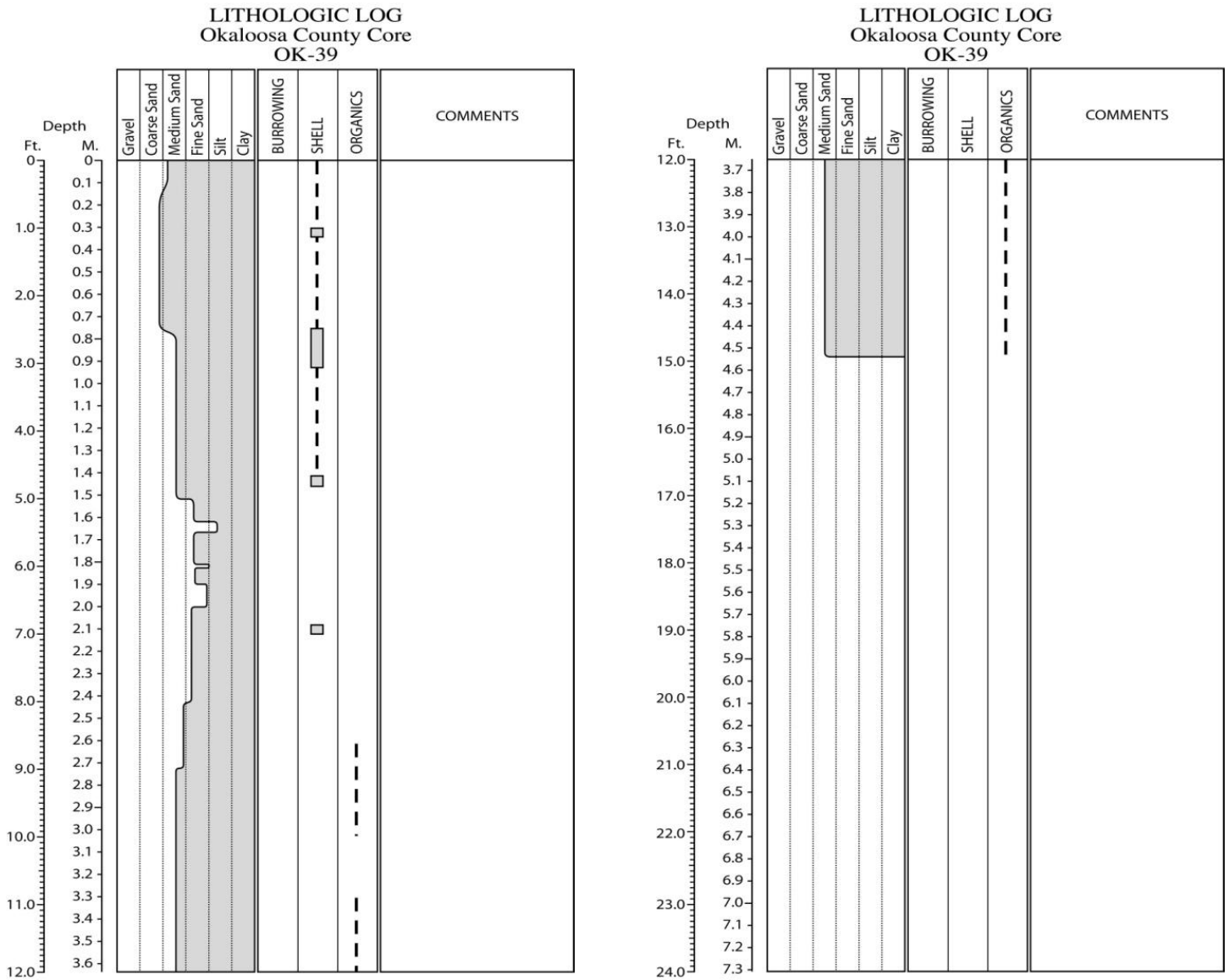

Figure E.218. Core OK-39 log.

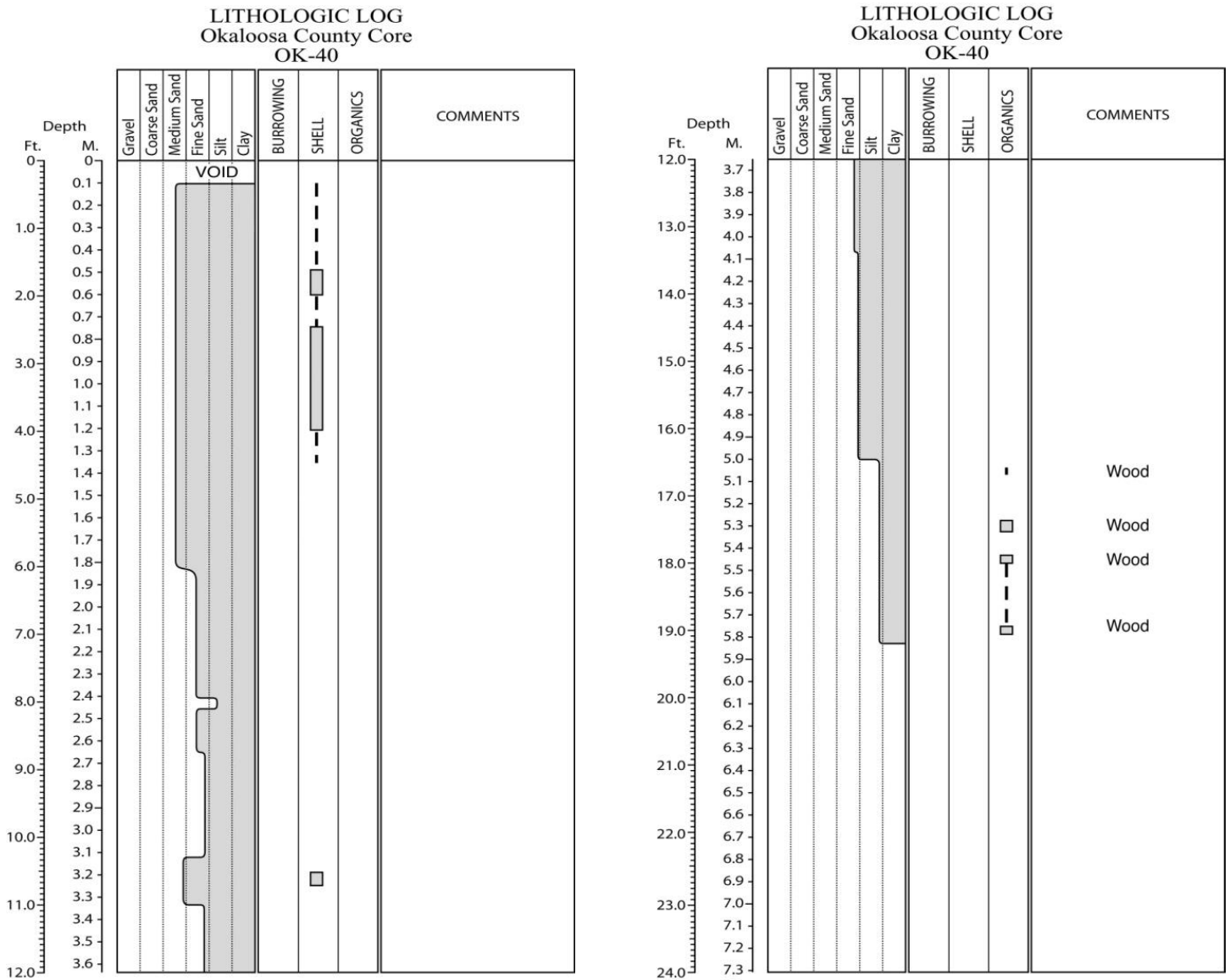

Figure E.219. Core OK-40 log.

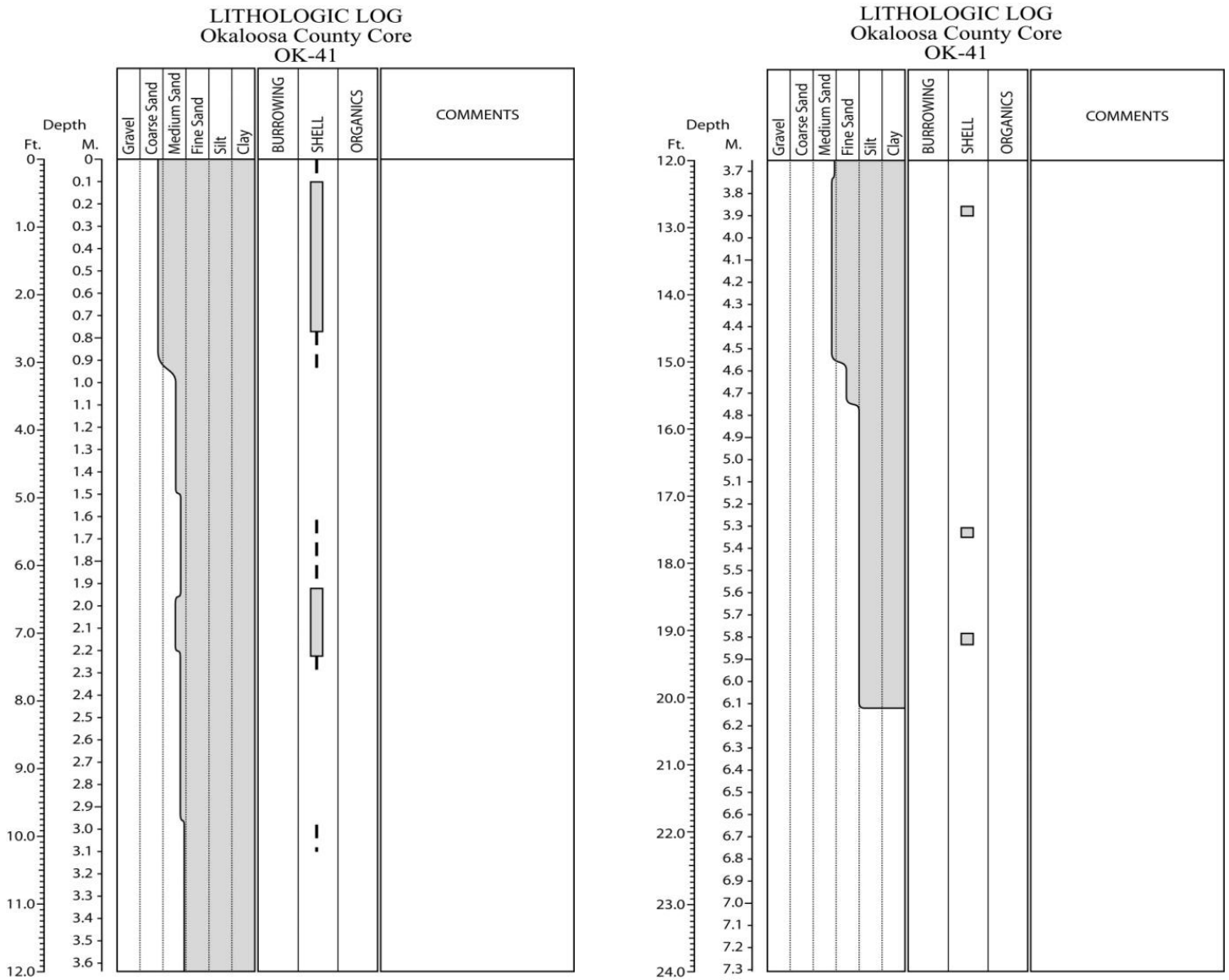

Figure E.220. Core OK-41 log.

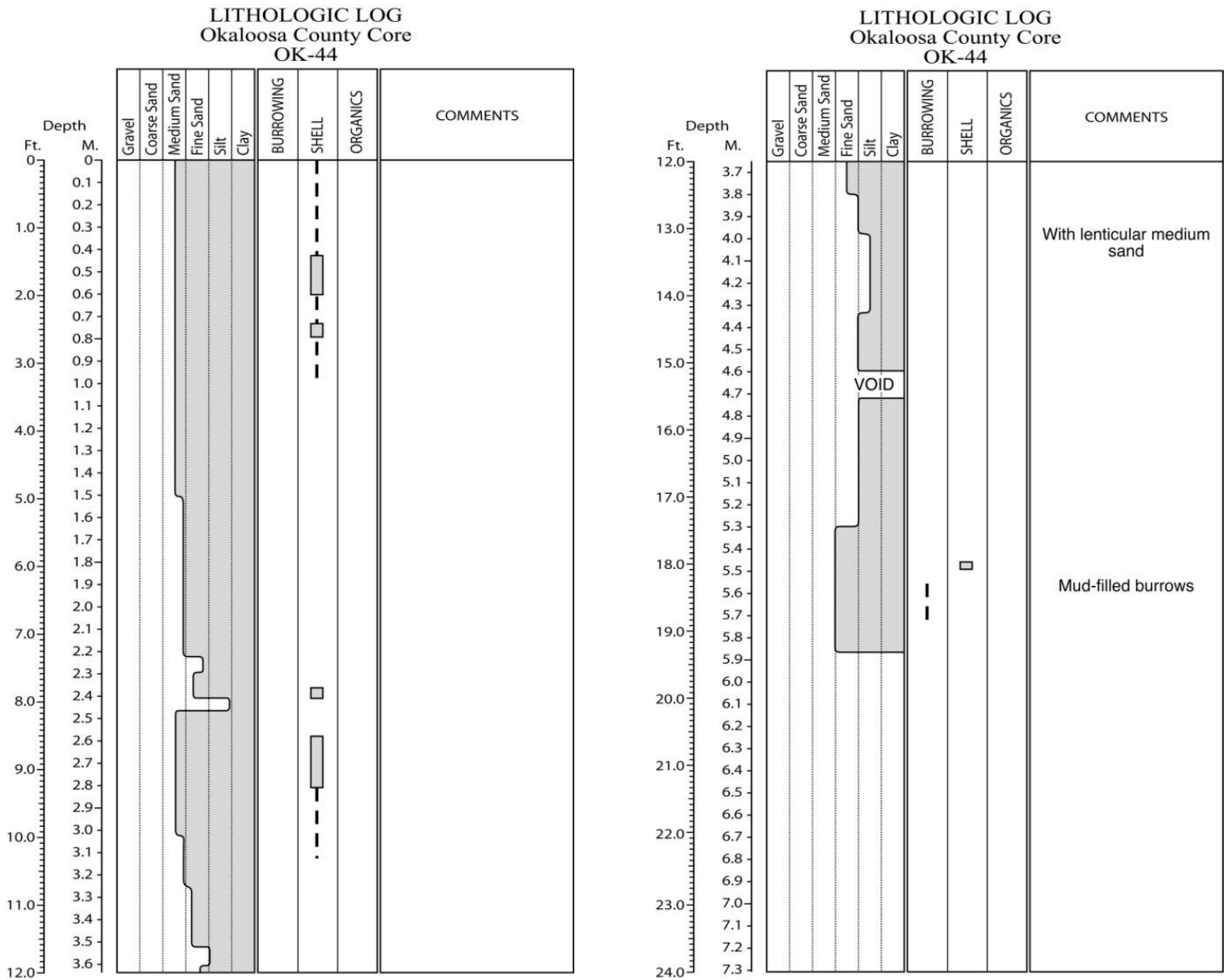

Figure E.221. Core OK-44 log.

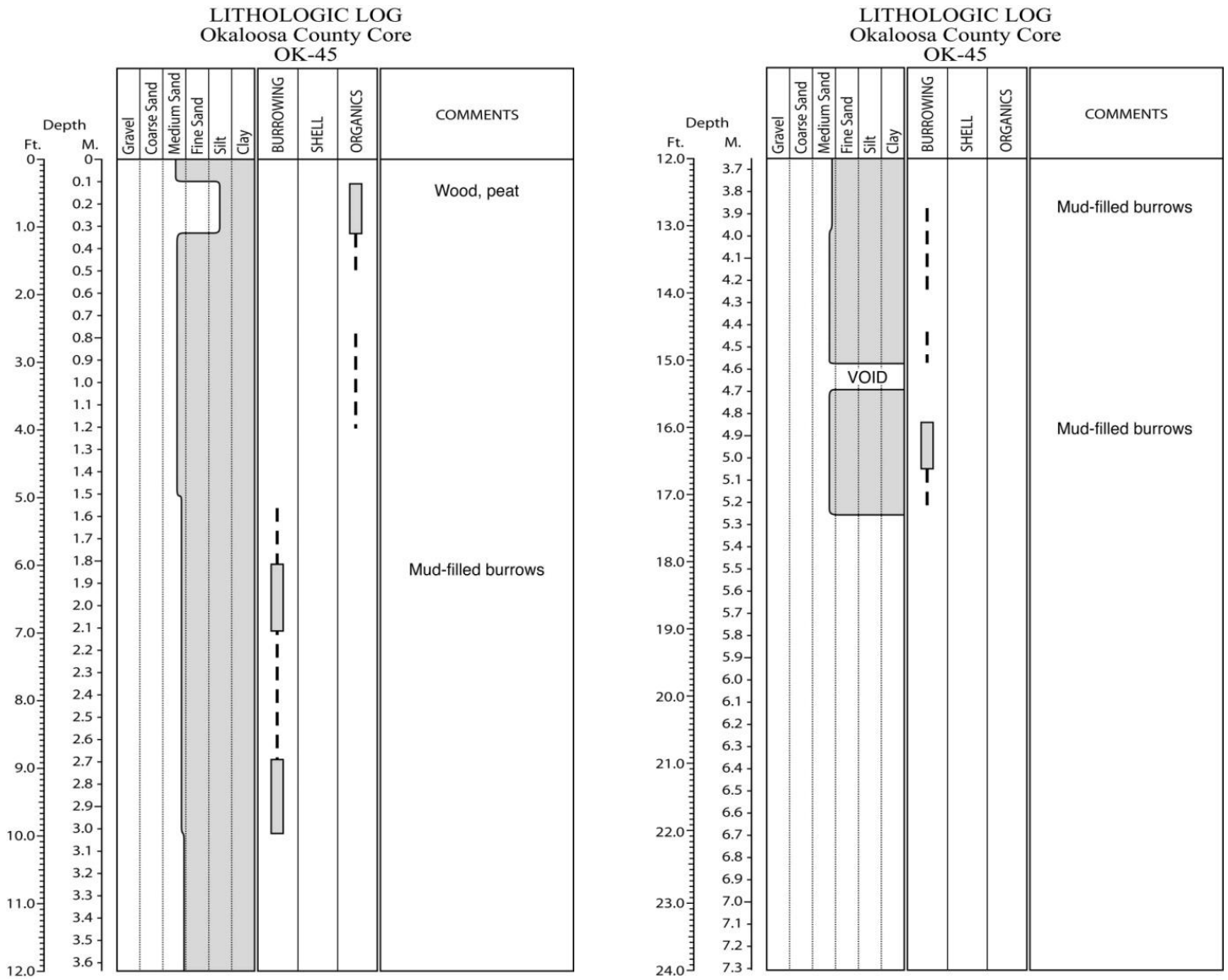

Figure E.222. Core OK-45 log.

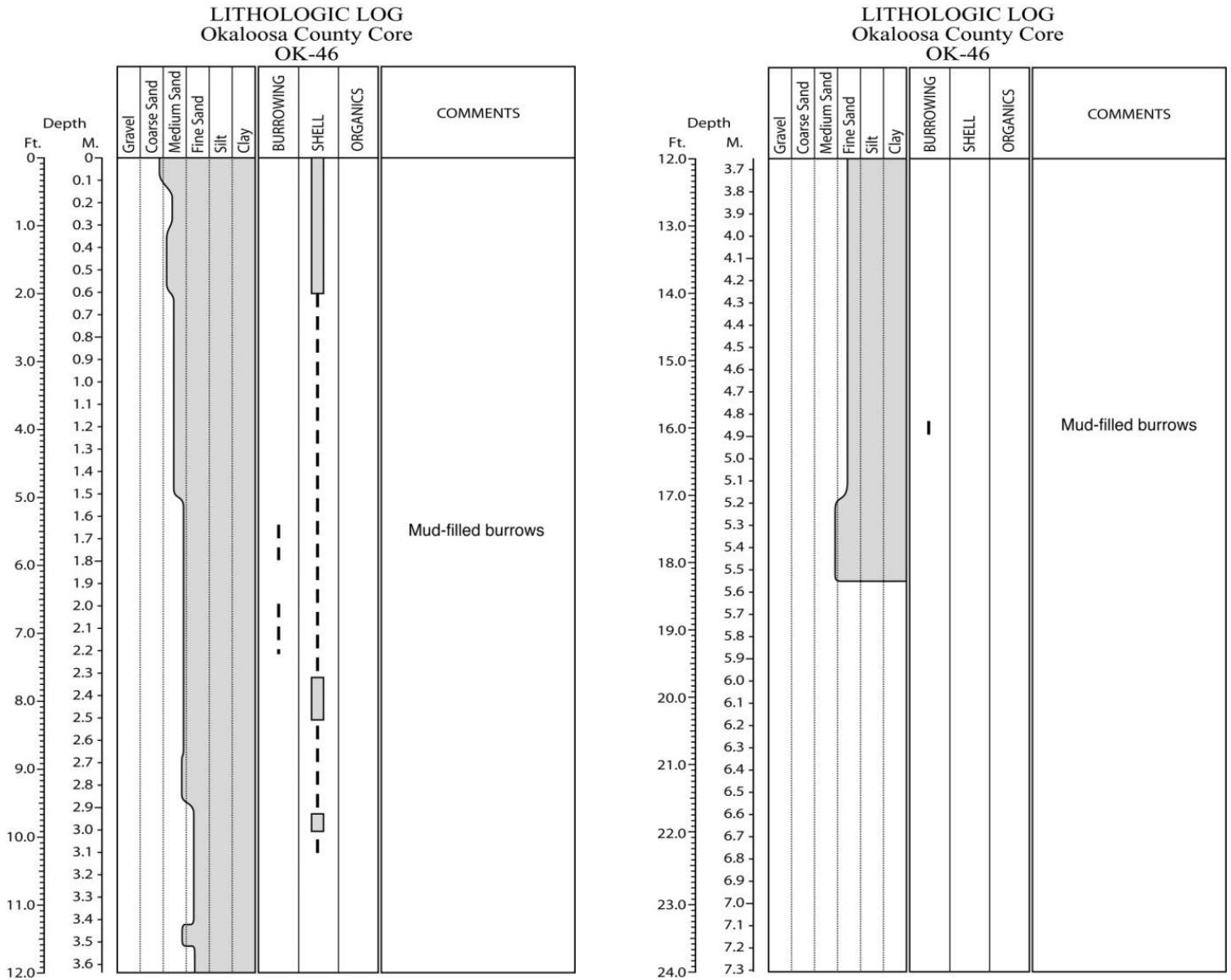

Figure E.223. Core OK-46 log.

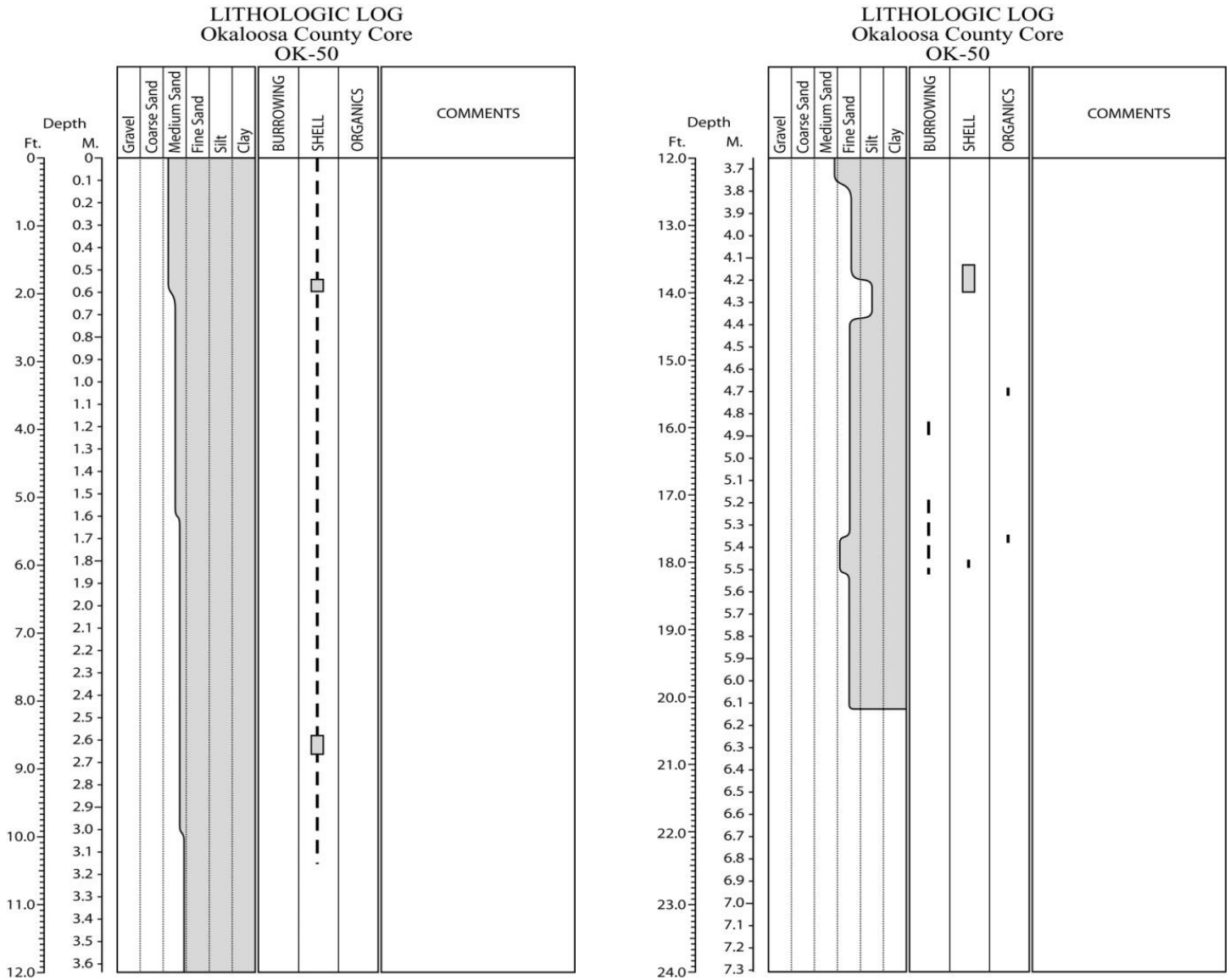

Figure E.224. Core OK-50 log.

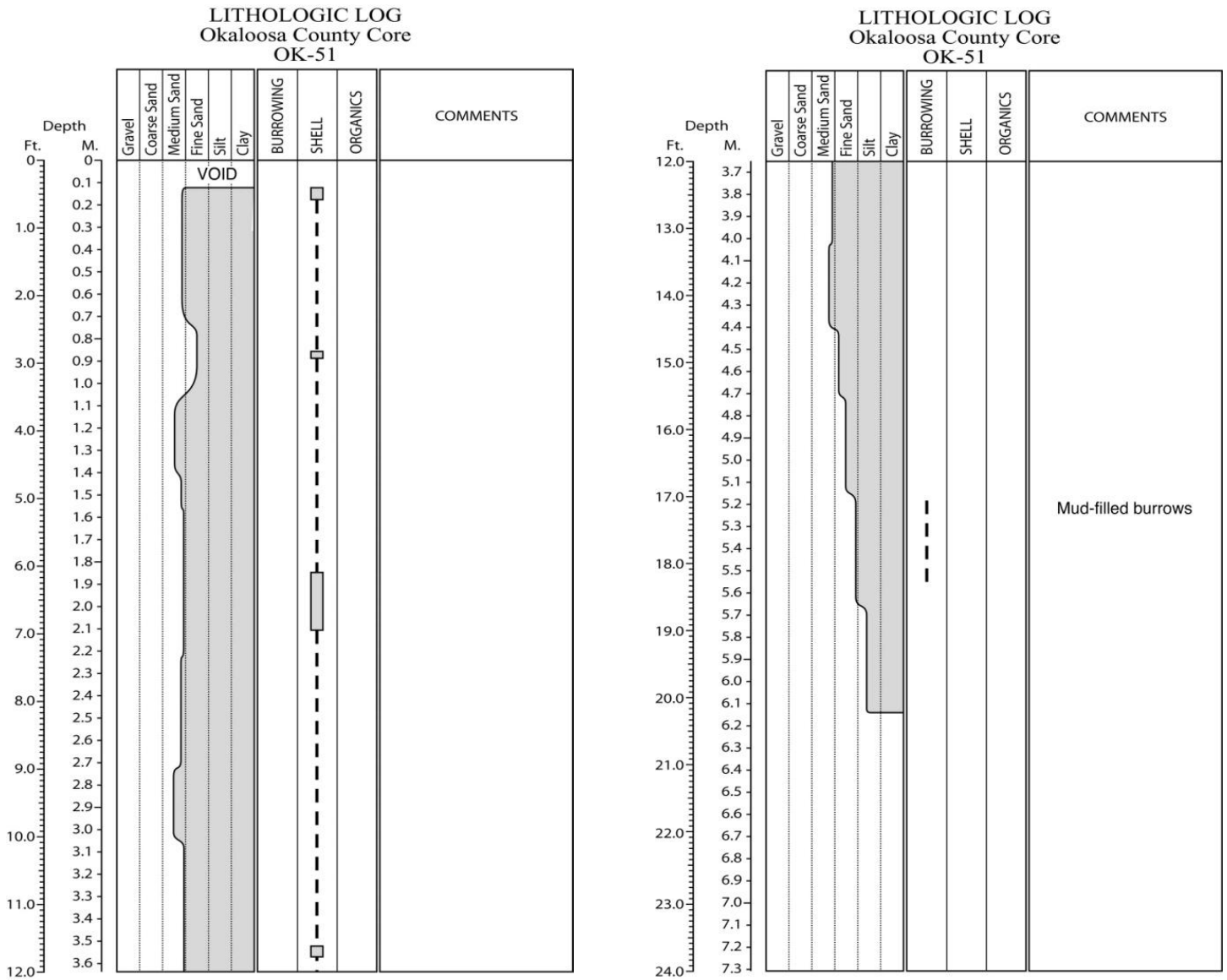

Figure E.225. Core OK-51 log.

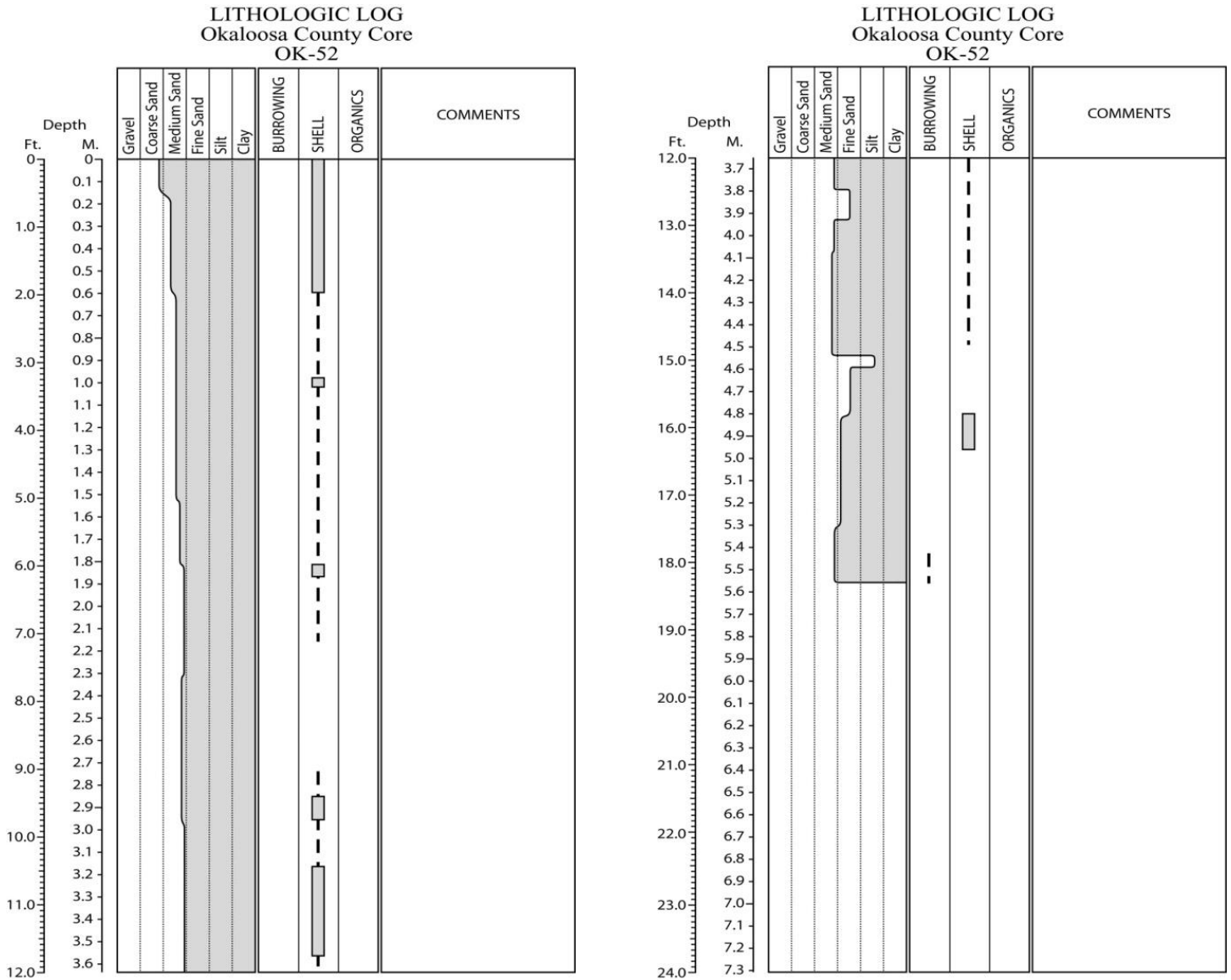

Figure E.226. Core OK-52 log.

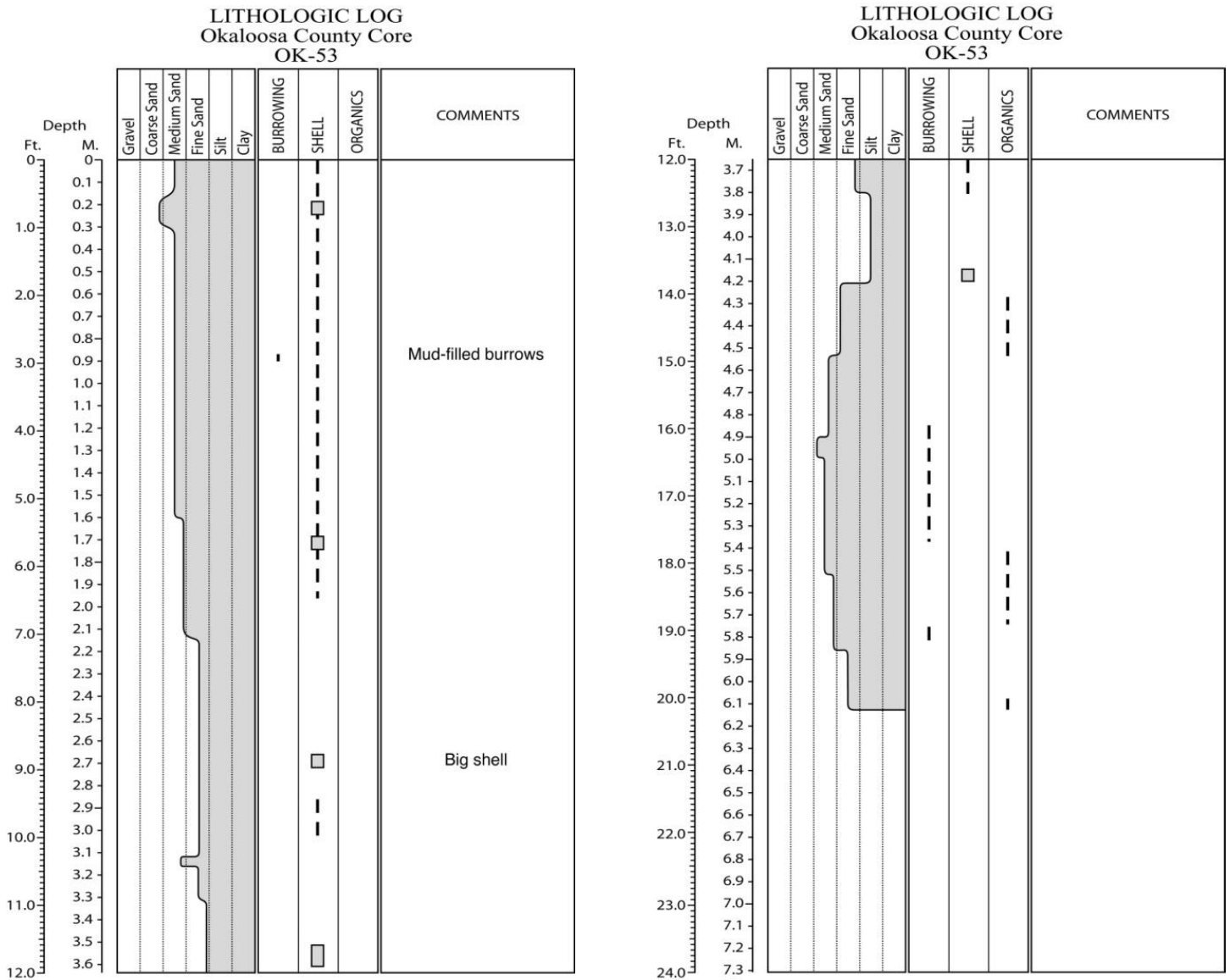

Figure E.227. Core OK-53 log.

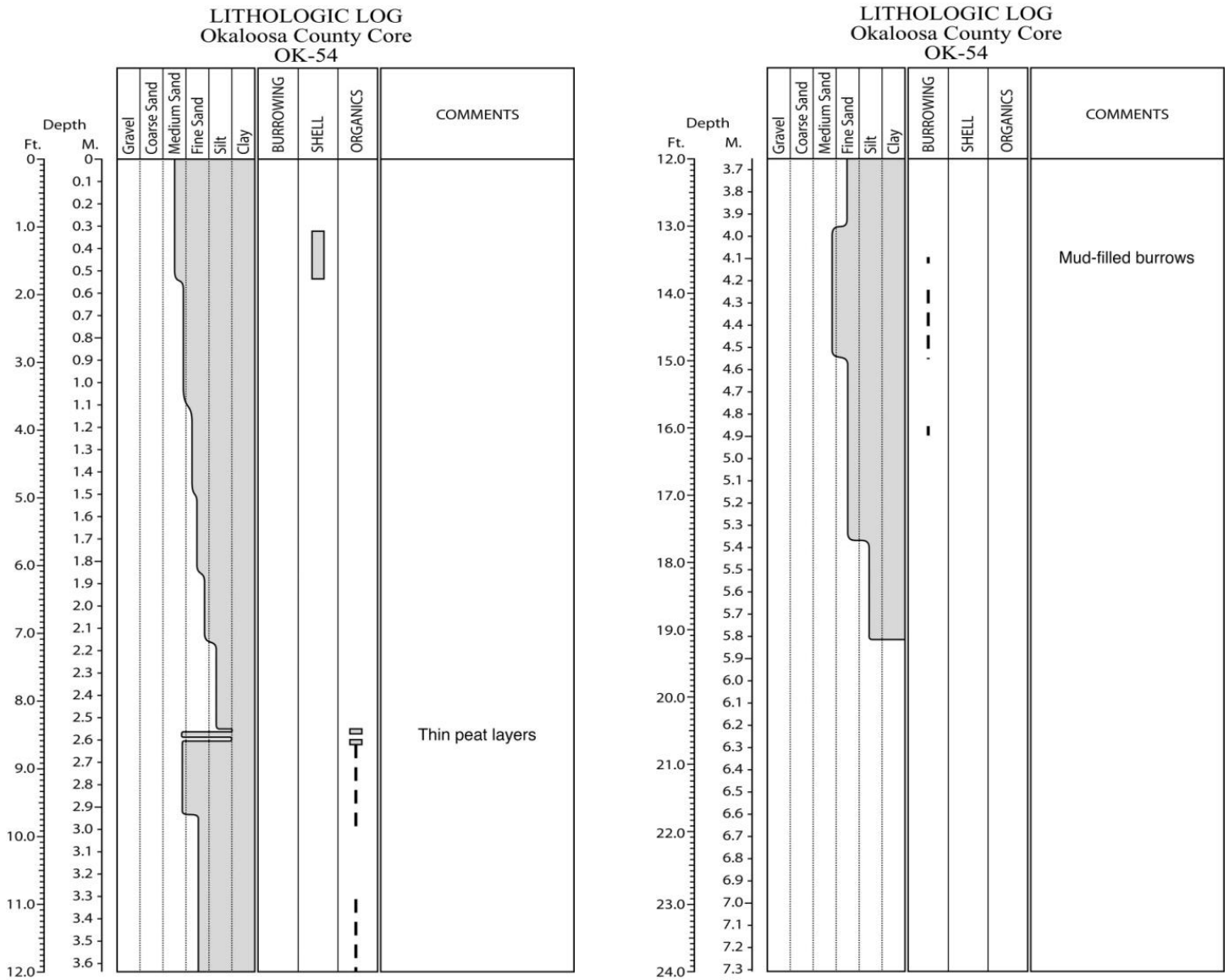

Figure E.228. Core OK-54 log.

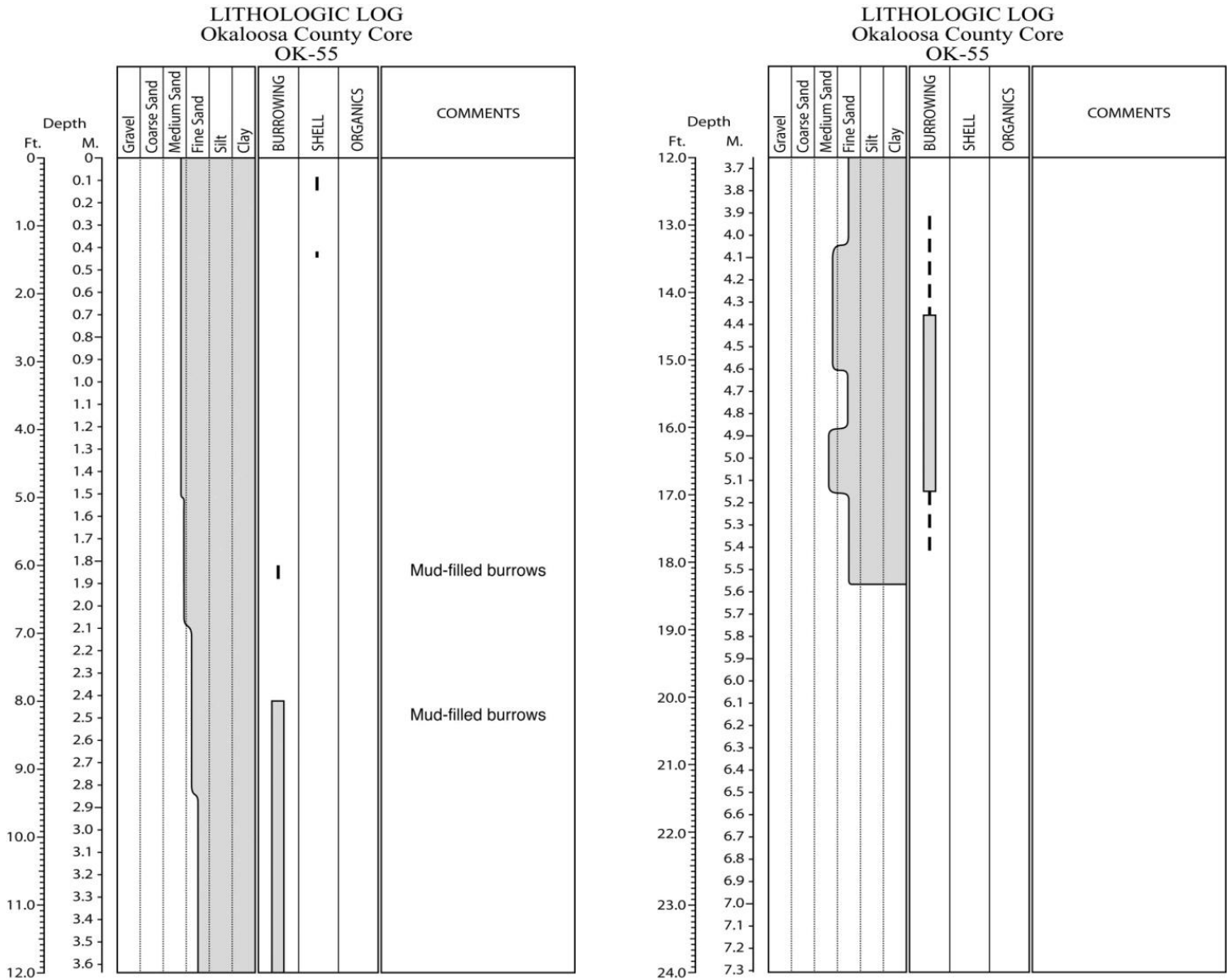

Figure E.229. Core OK-55 log.

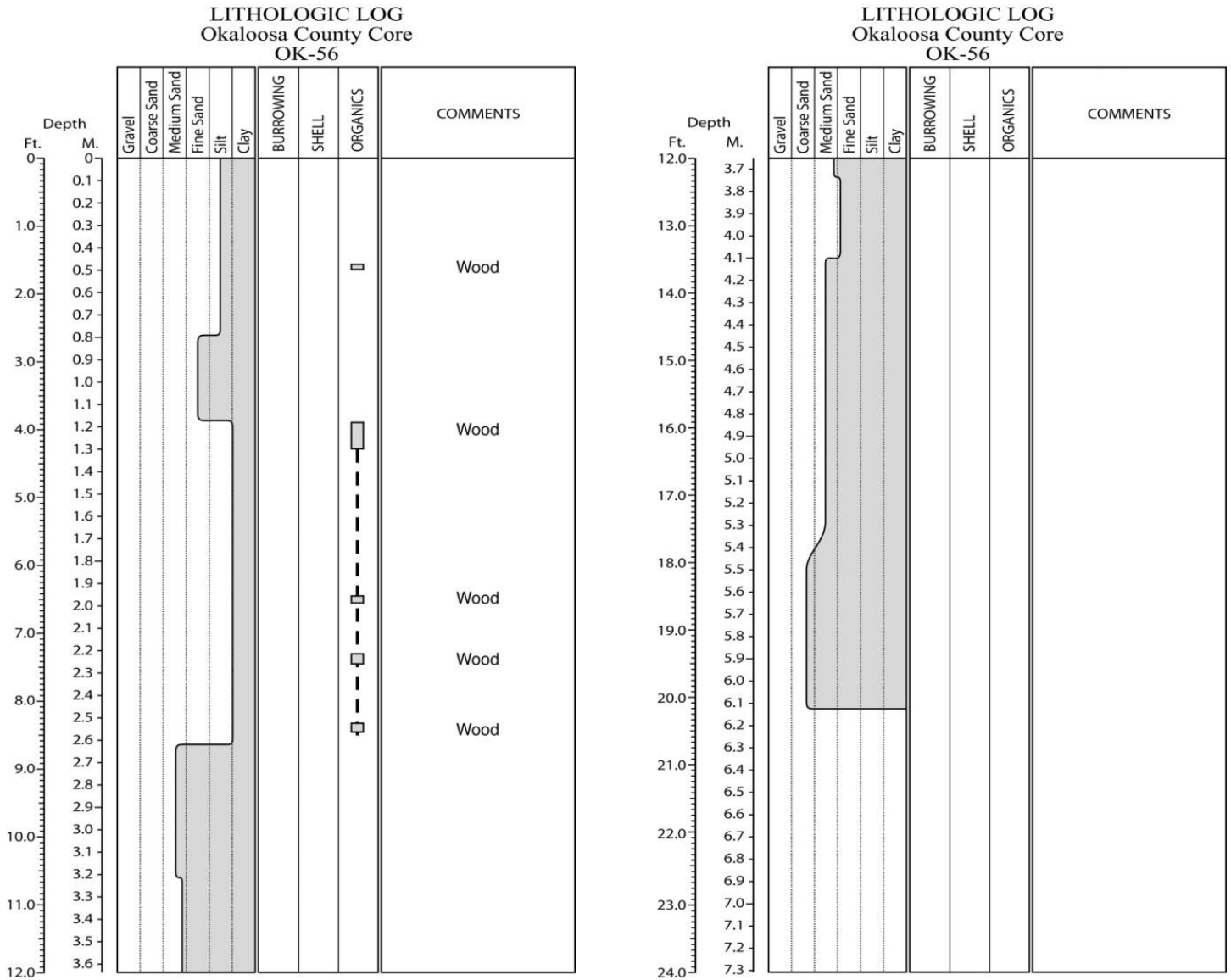

Figure E.230. Core OK-56 log.

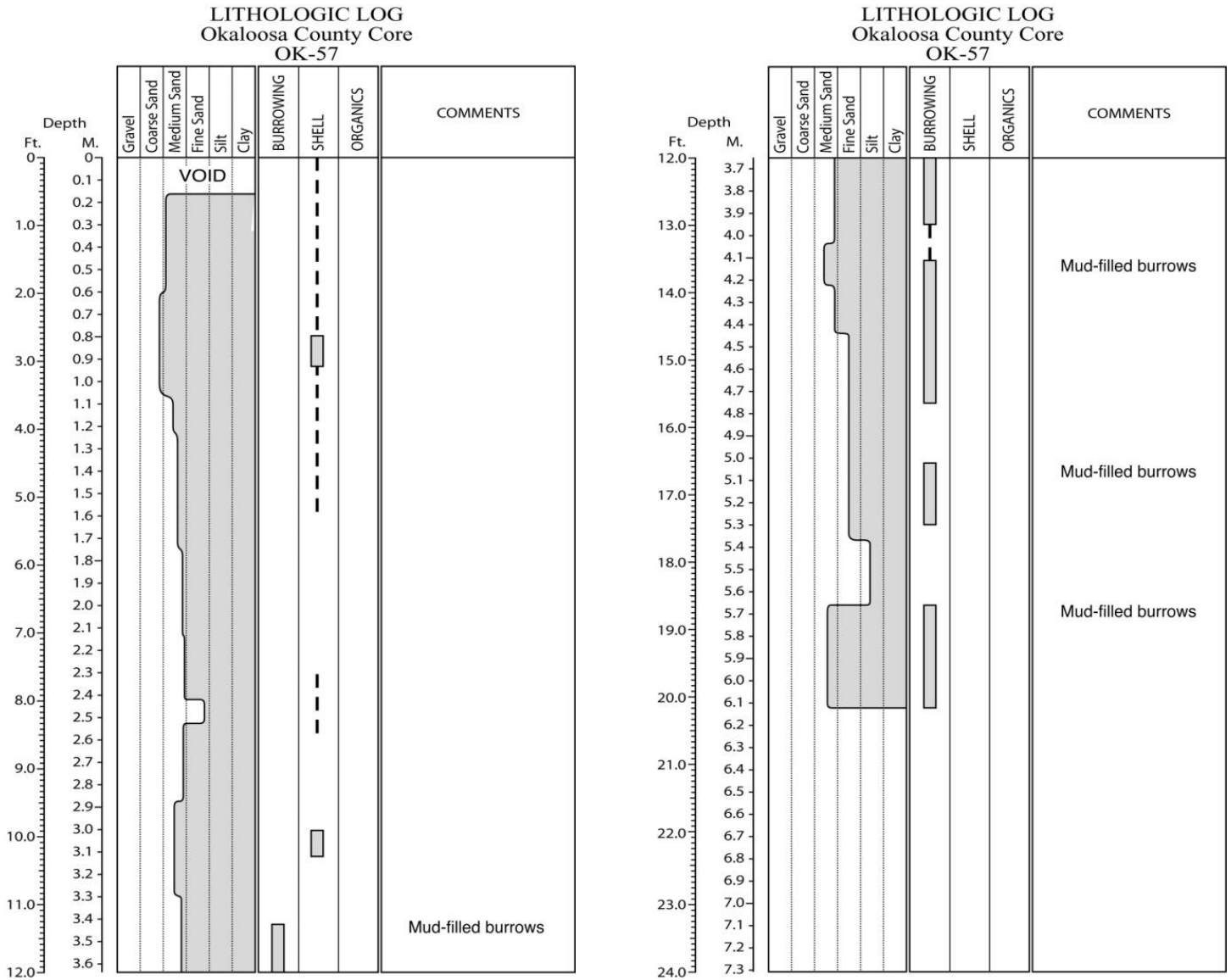

Figure E.231. Core OK-57 log.

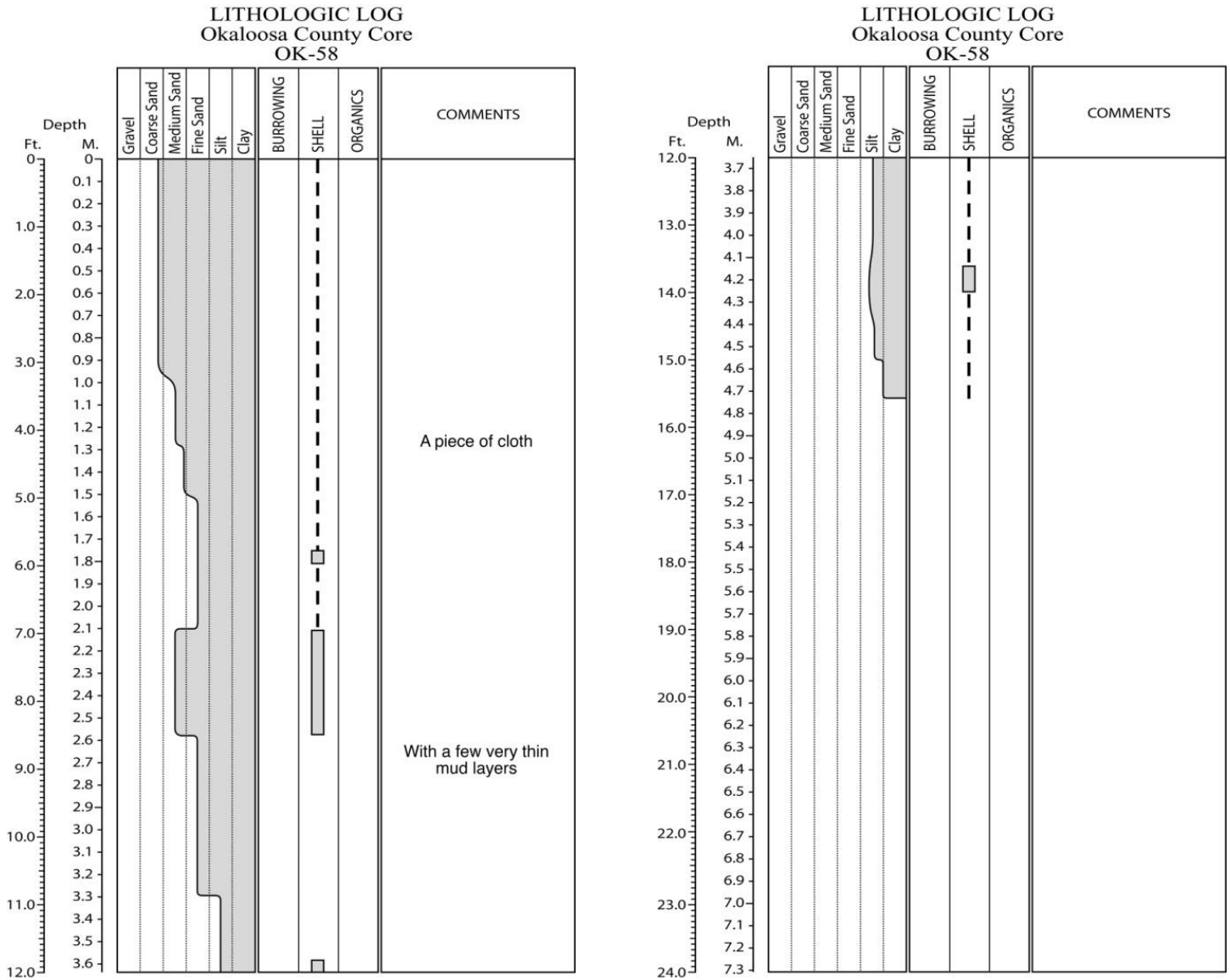

Figure E.232. Core OK-58 log.

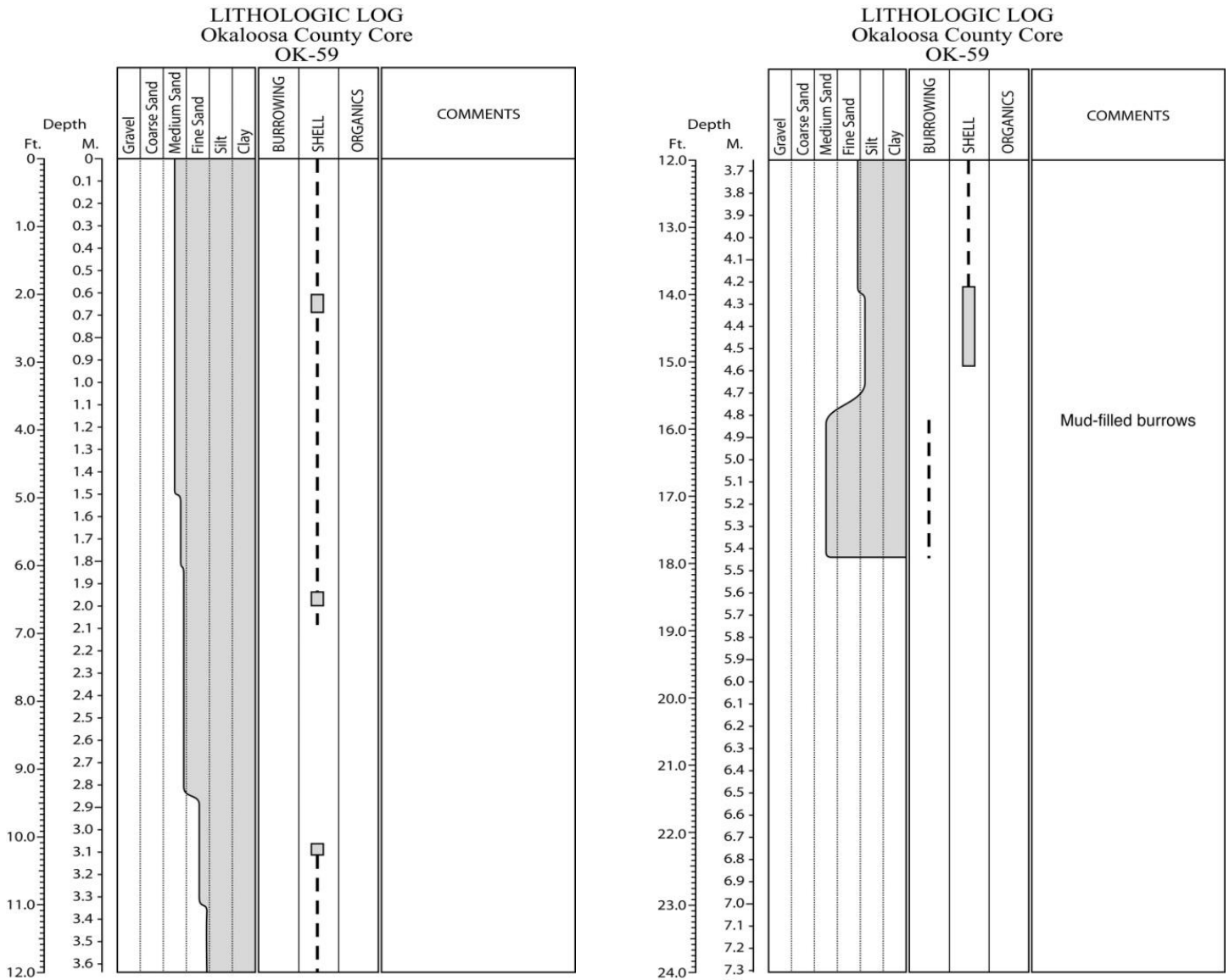

Figure E.233. Core OK-59 log.

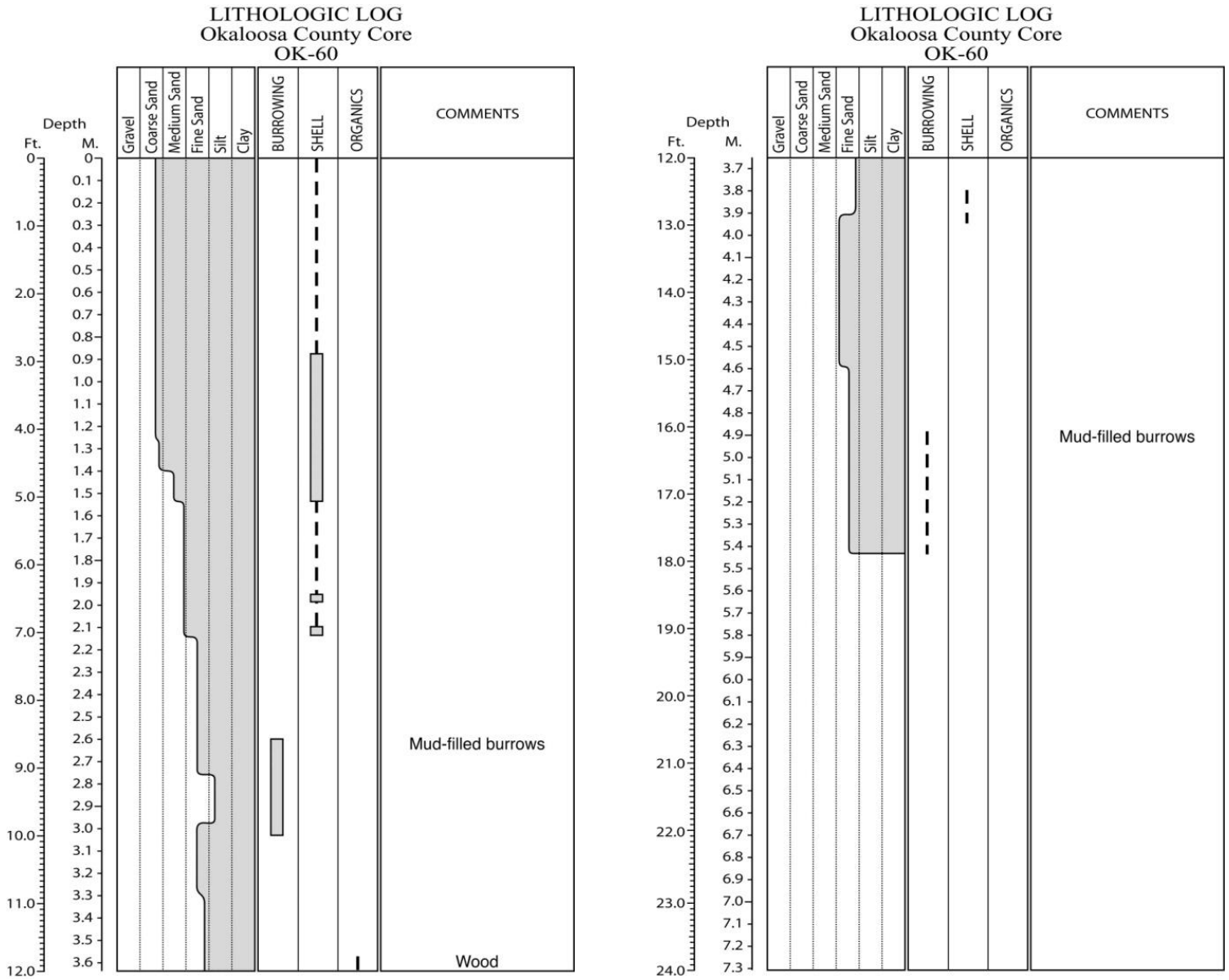

Figure E.234. Core OK-60 log.

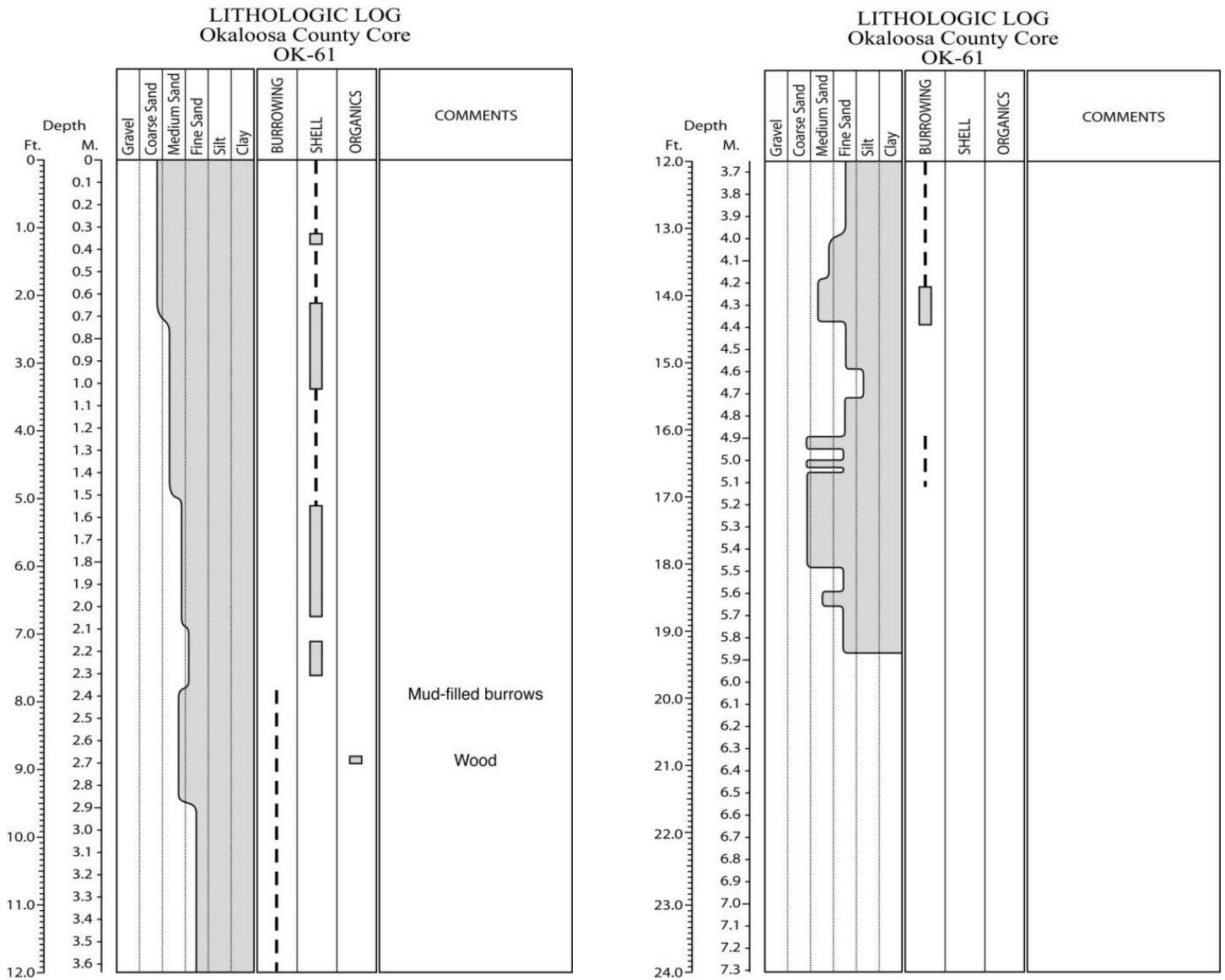

Figure E.235. Core OK-61 log.

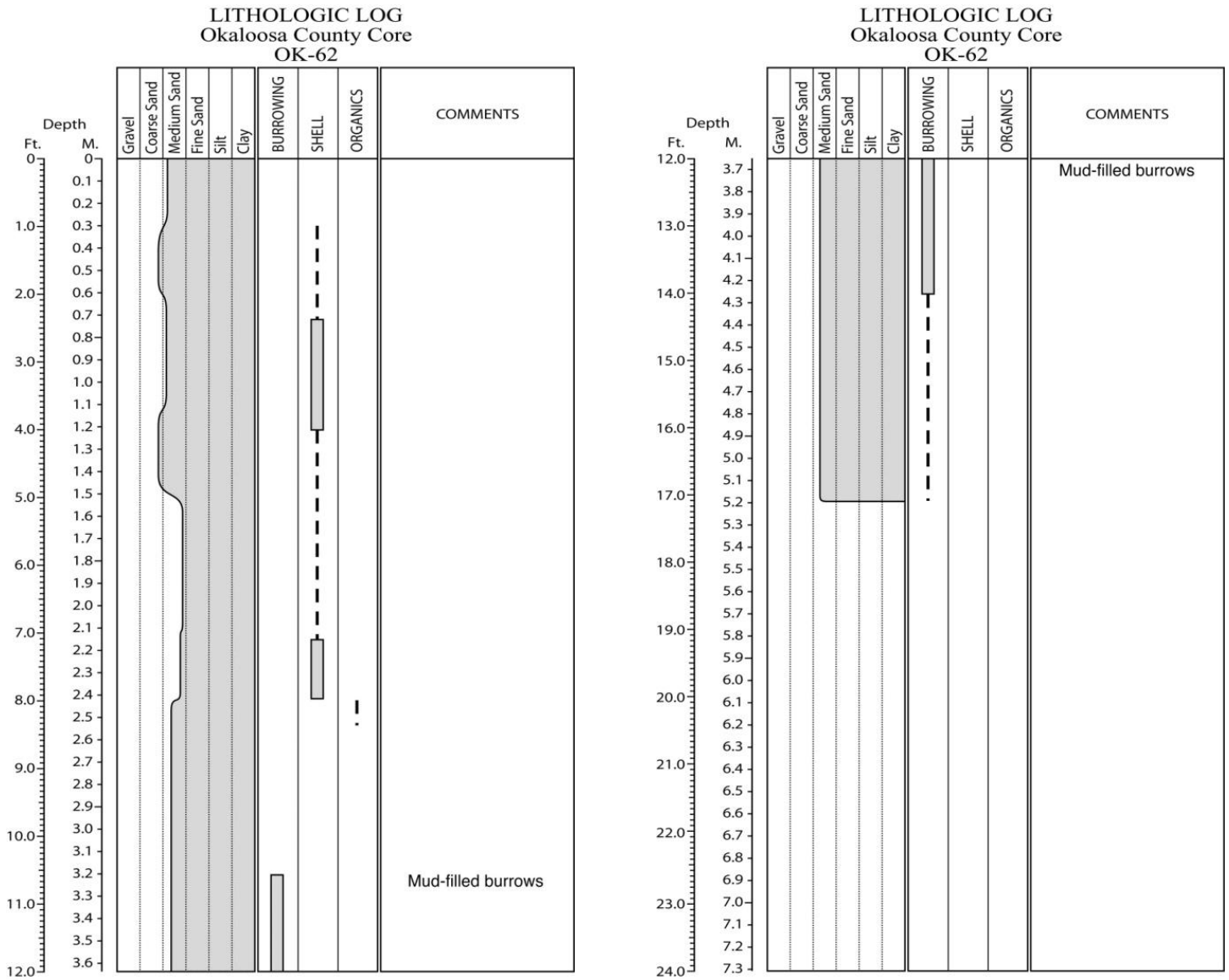

Figure E.236. Core OK-62 log.

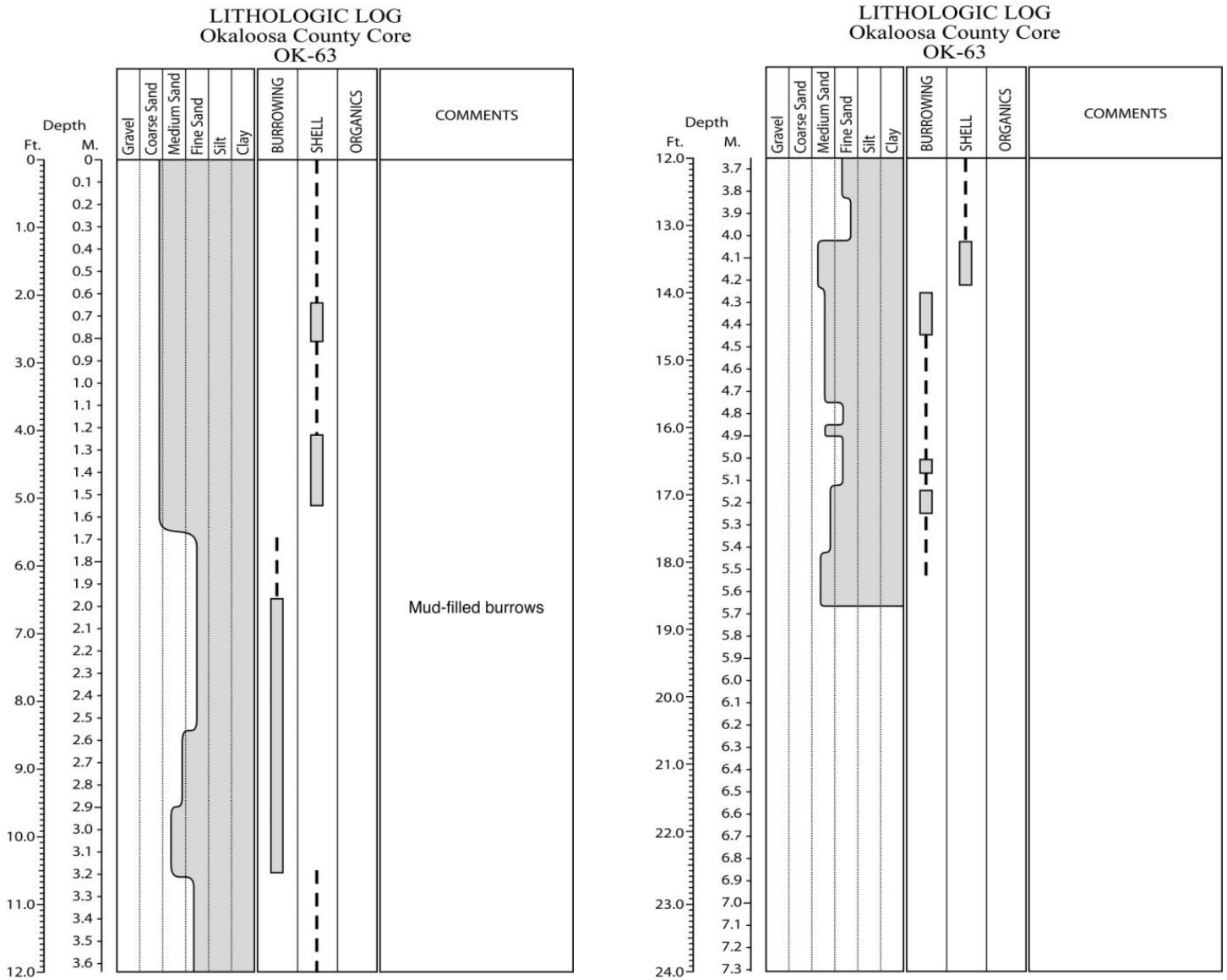

Figure E.237. Core OK-63 log.

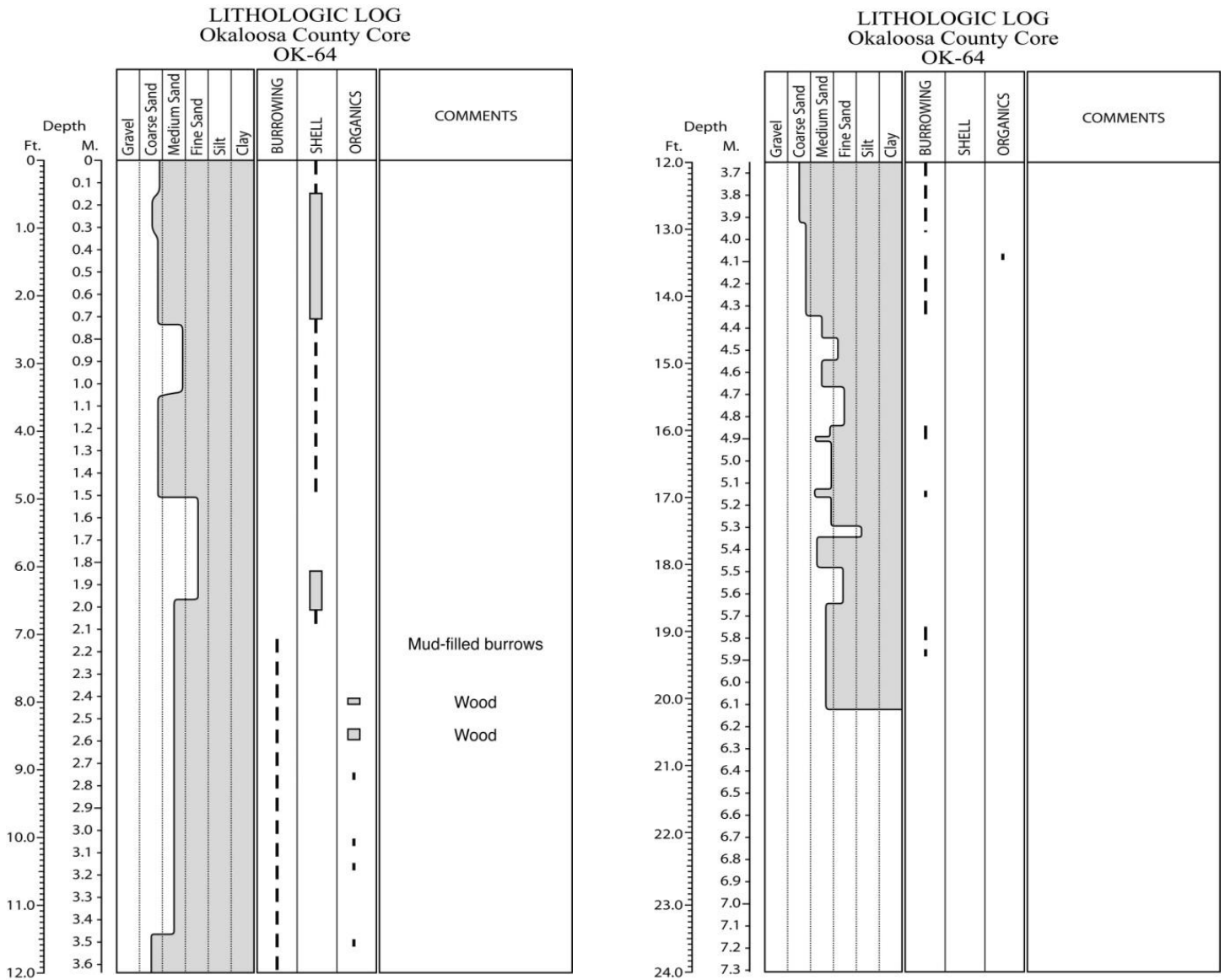

Figure E.238. Core OK-64 log.

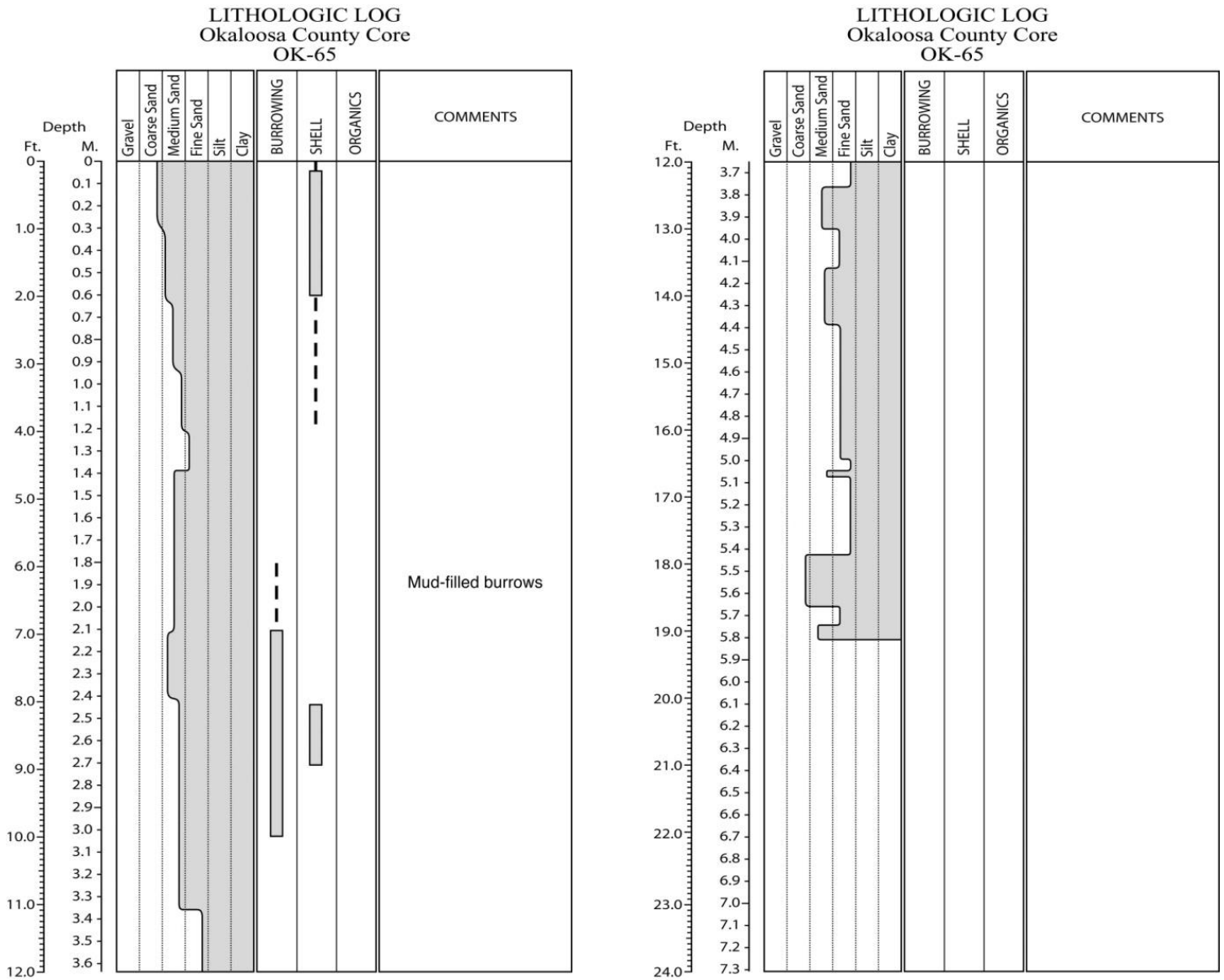

Figure E.239. Core OK-65 log.

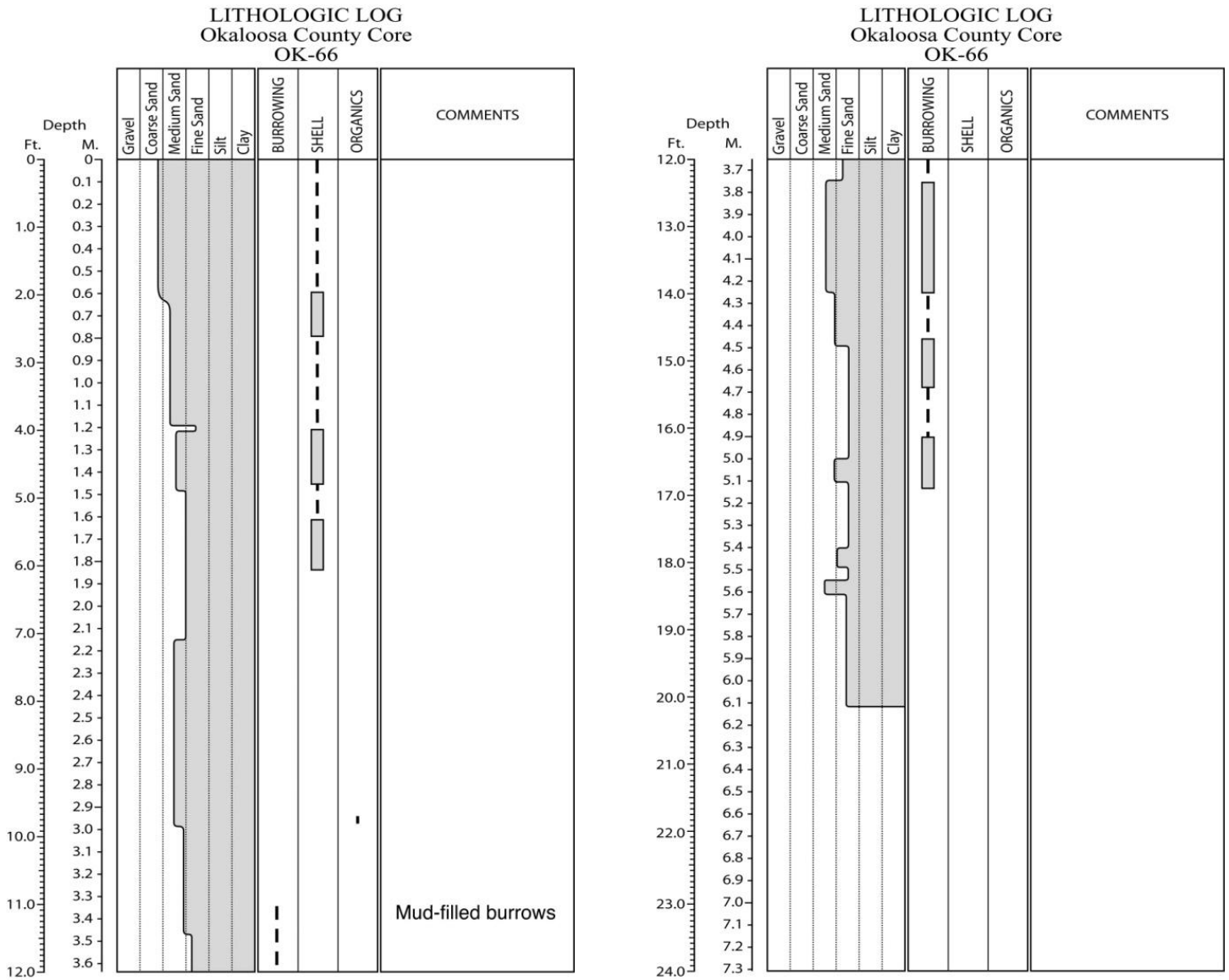

Figure E.240. Core OK-66 log.

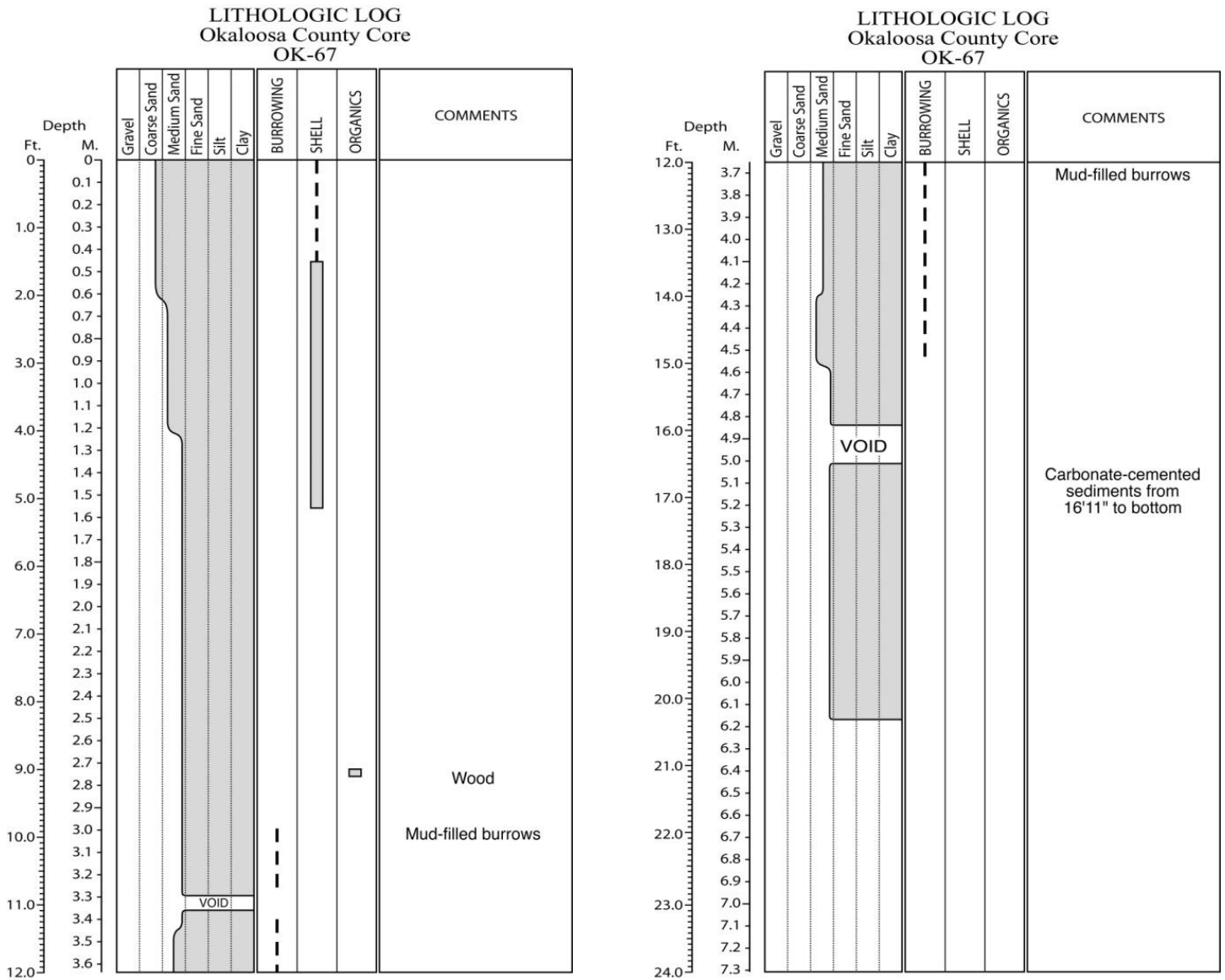

Figure E.241. Core OK-67 log.

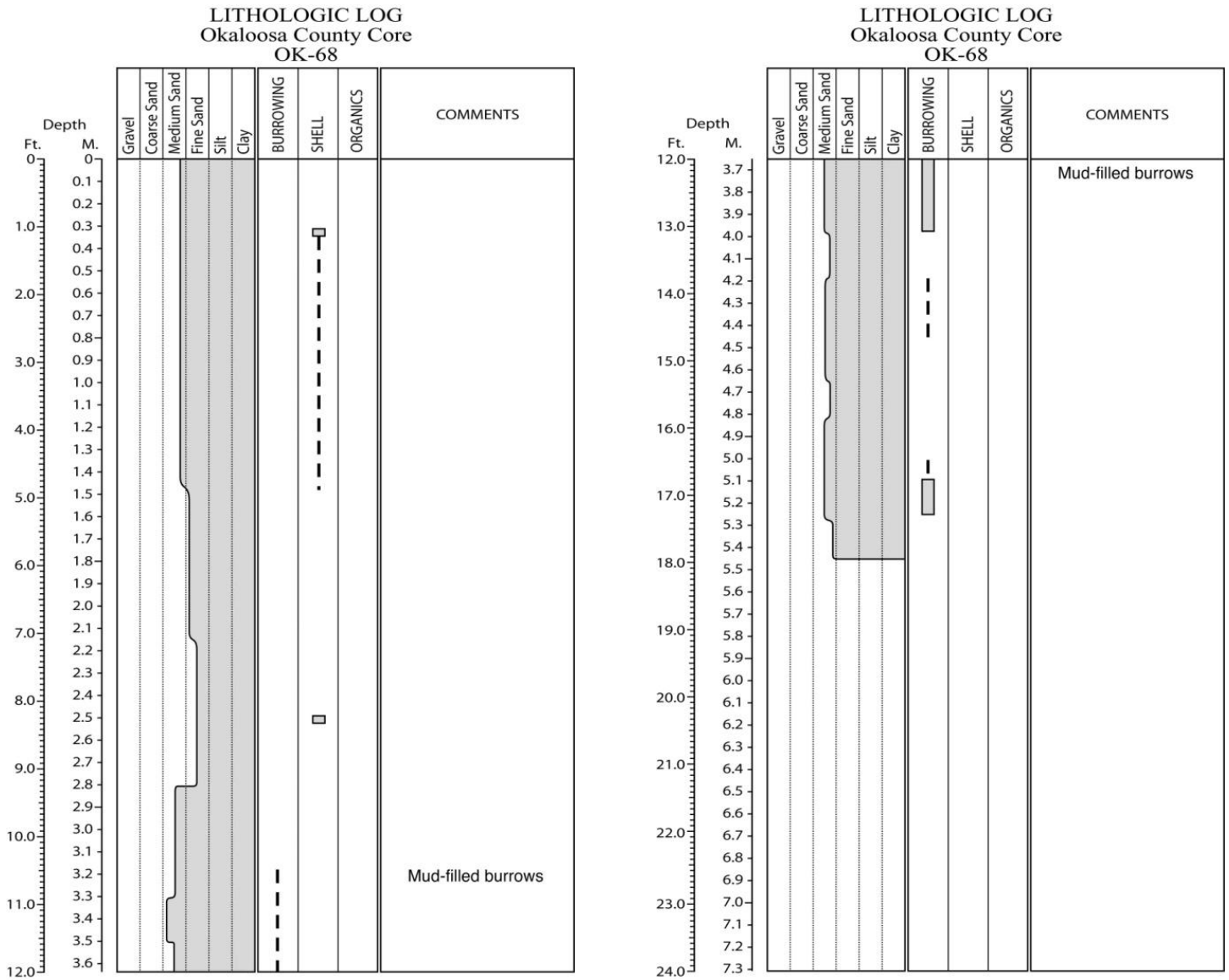

Figure E.242. Core OK-68 log.

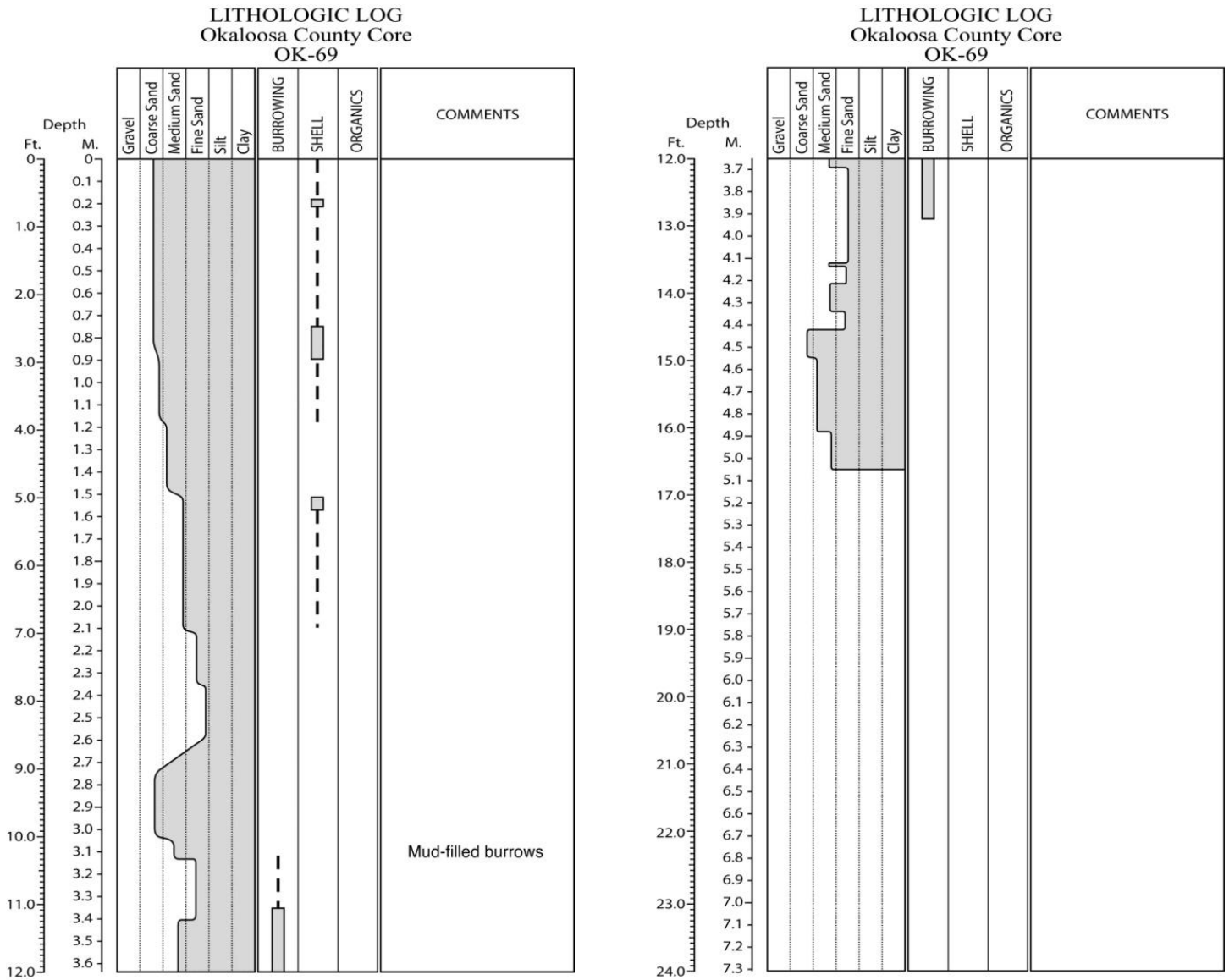

Figure E.243. Core OK-69 log.

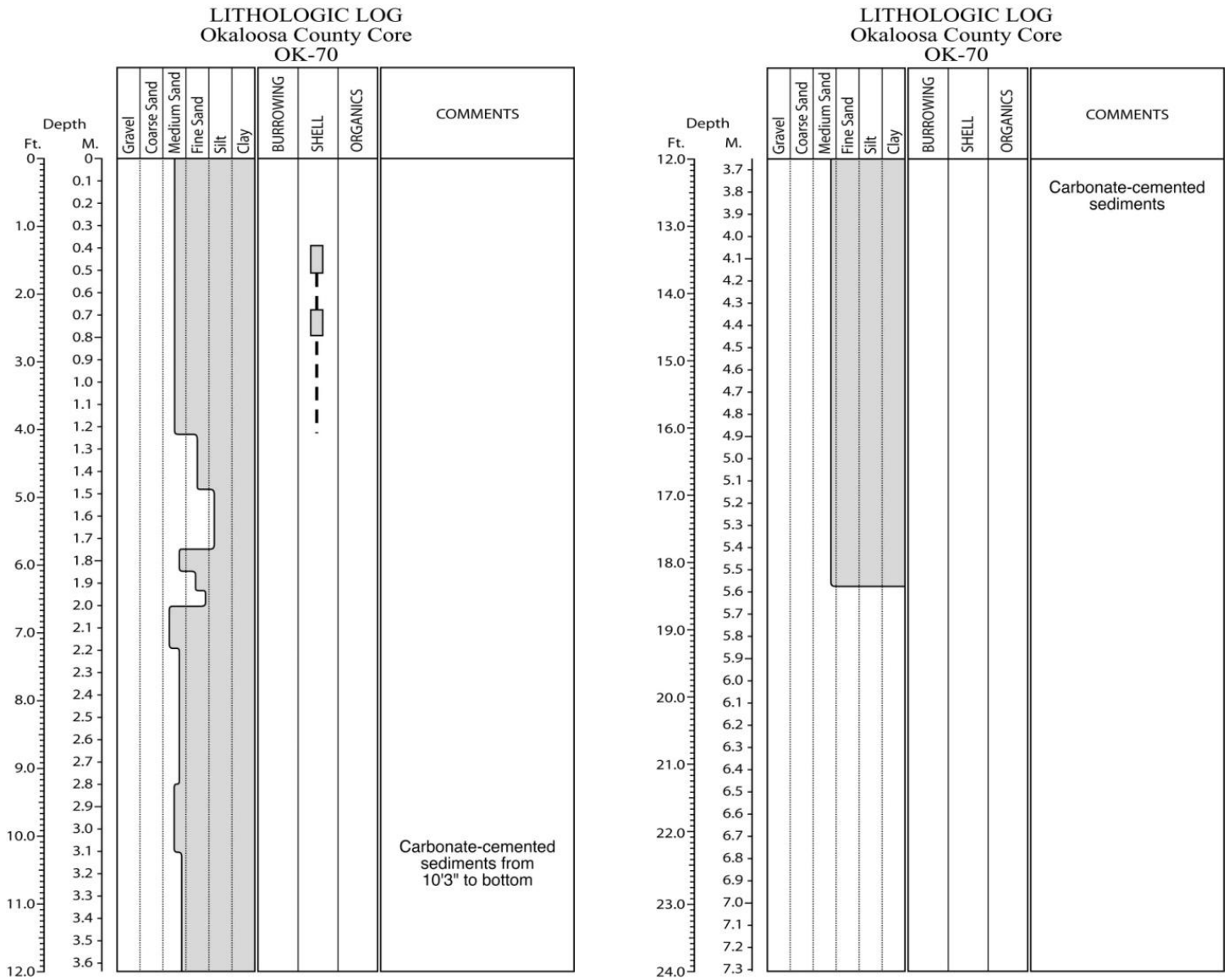

Figure E.244. Core OK-70 log.

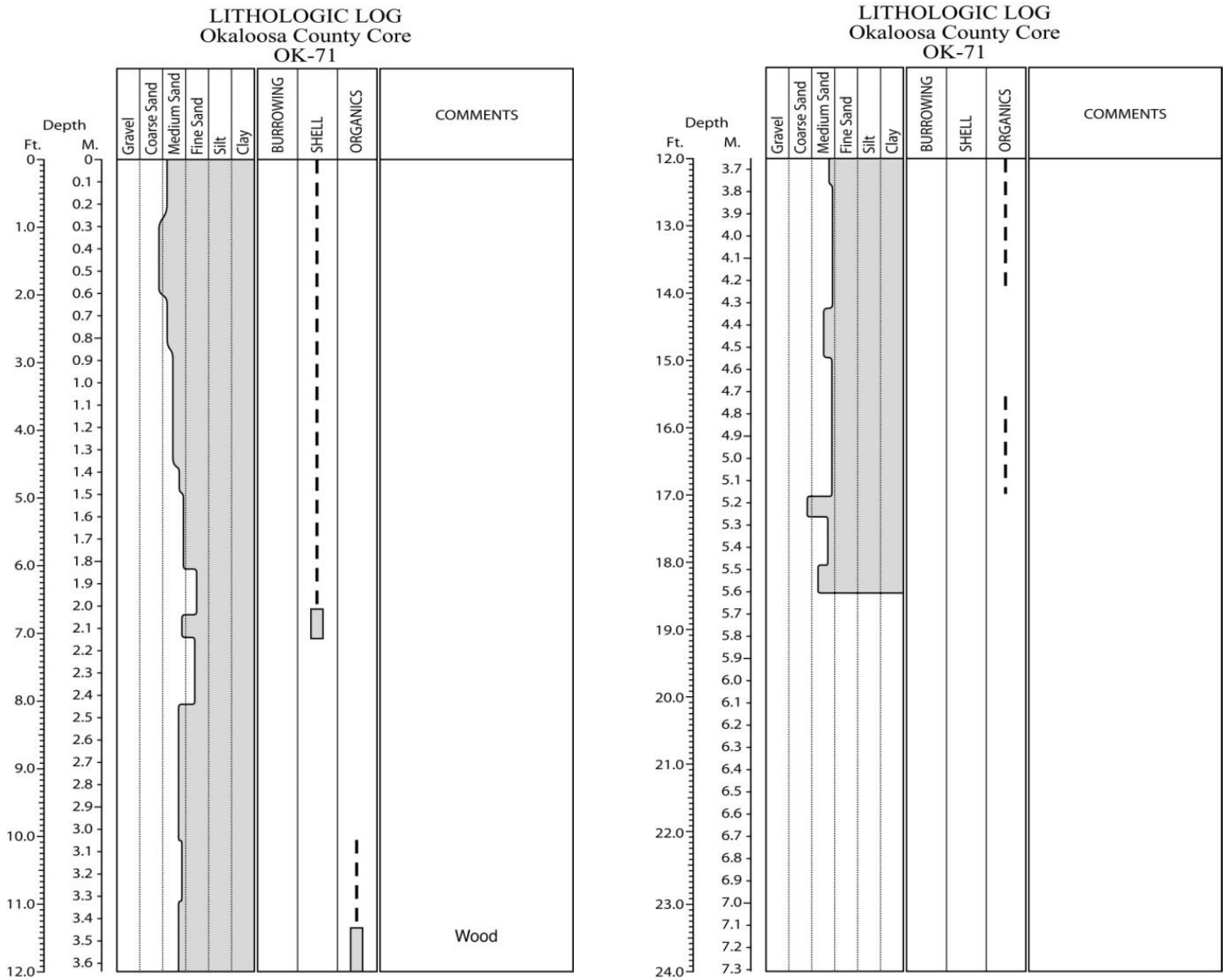

Figure E.245. Core OK-71 log.

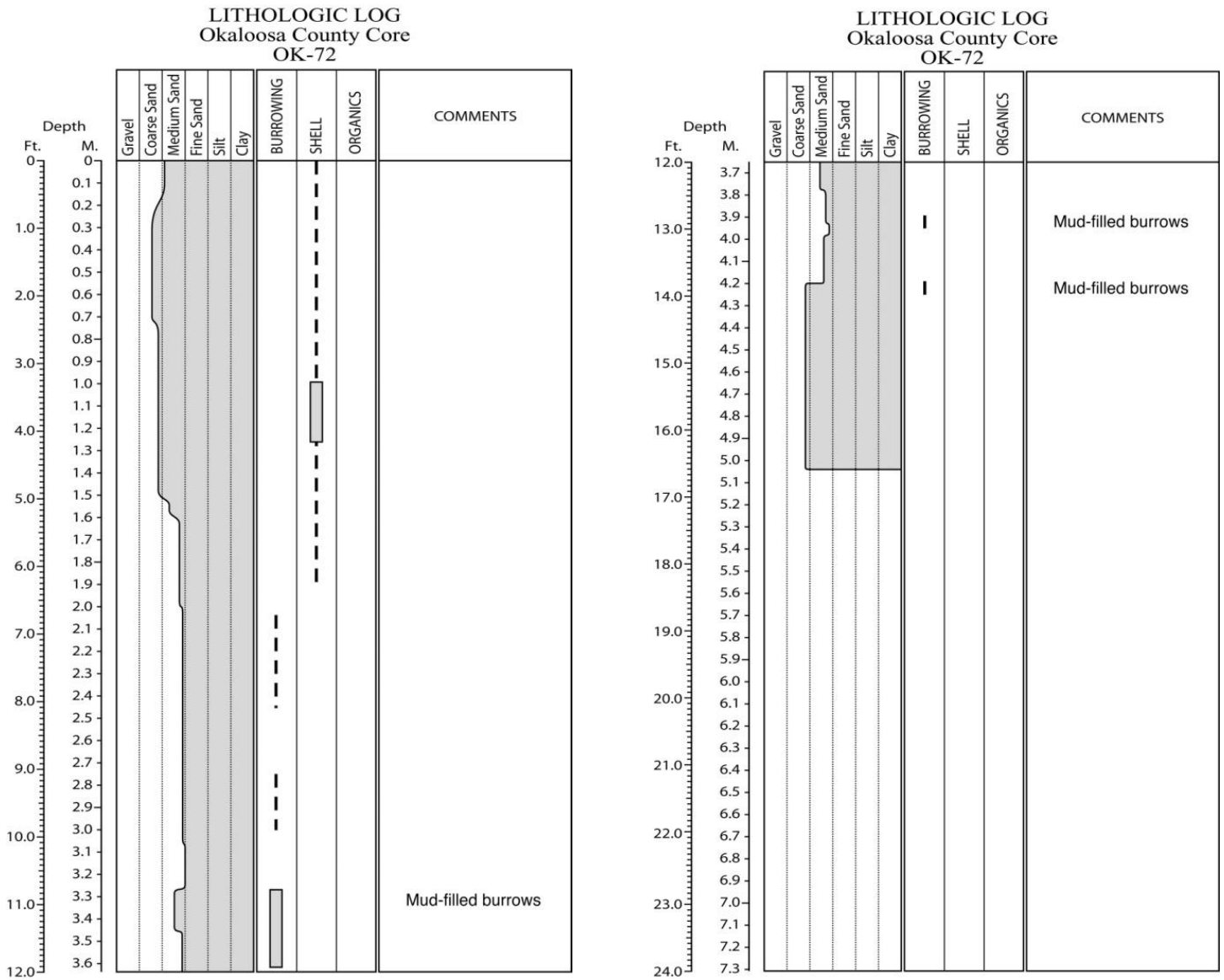

Figure E.246. Core OK-72 log.

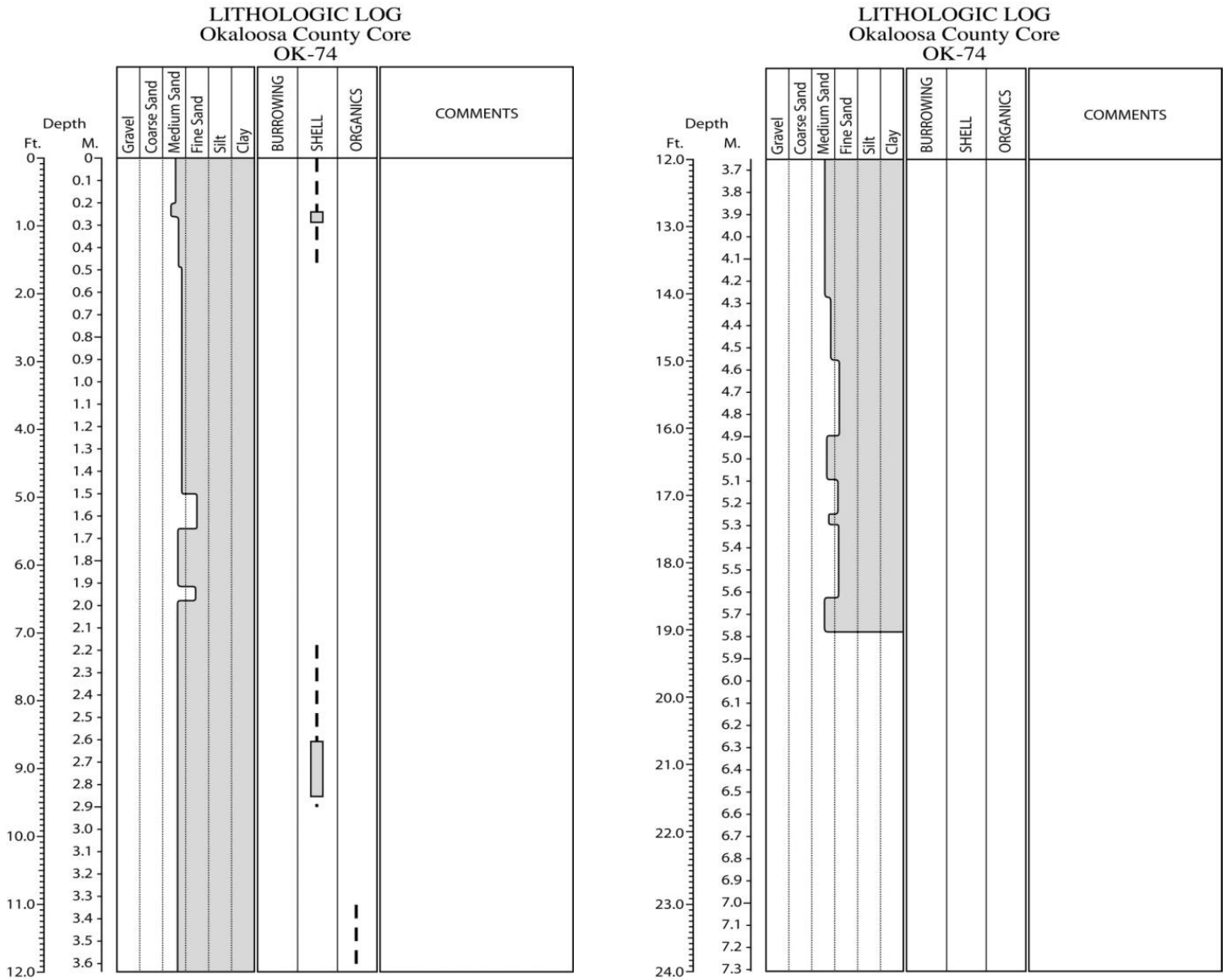

Figure E.247. Core OK-74 log.

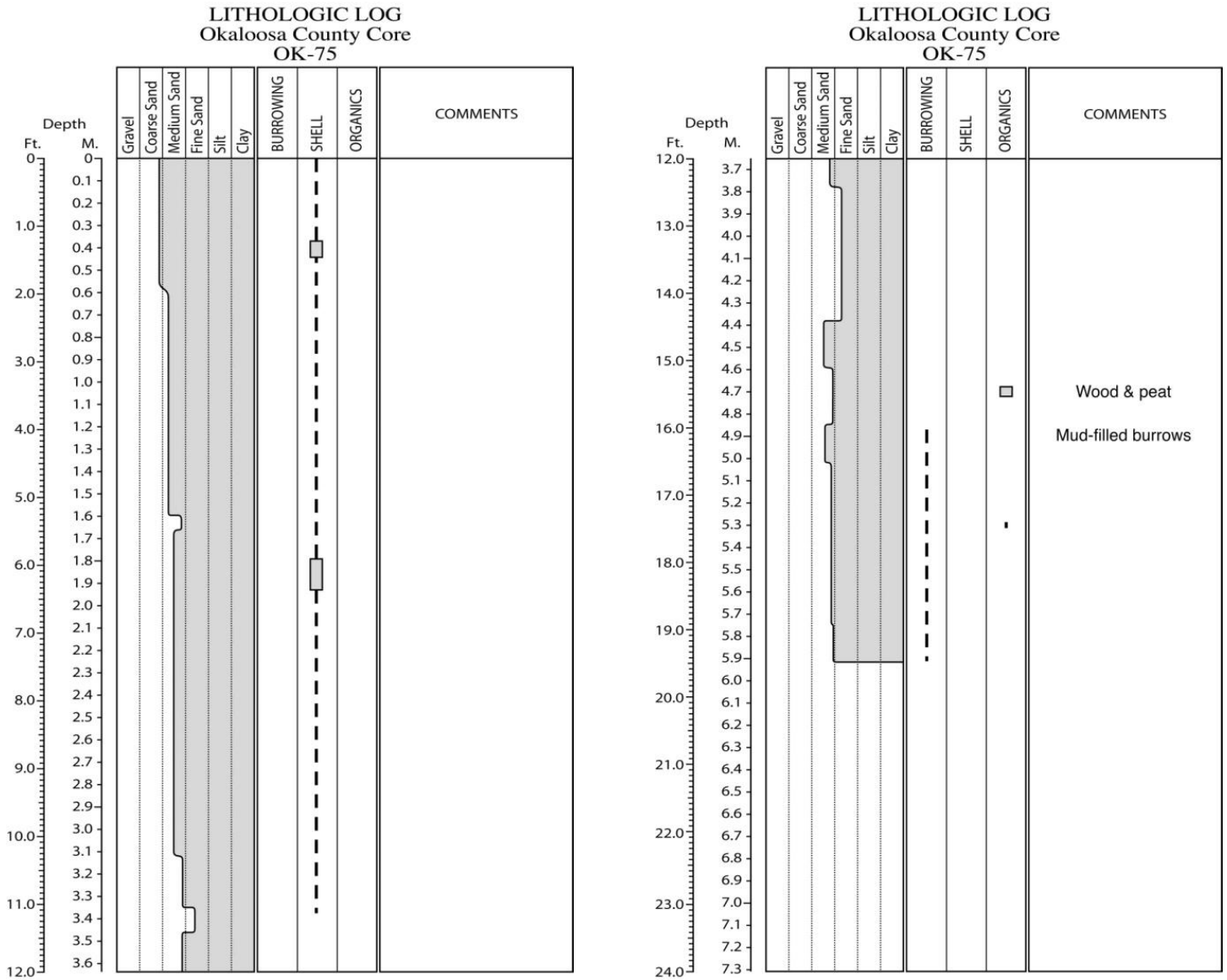

Figure E.248. Core OK-75 log.

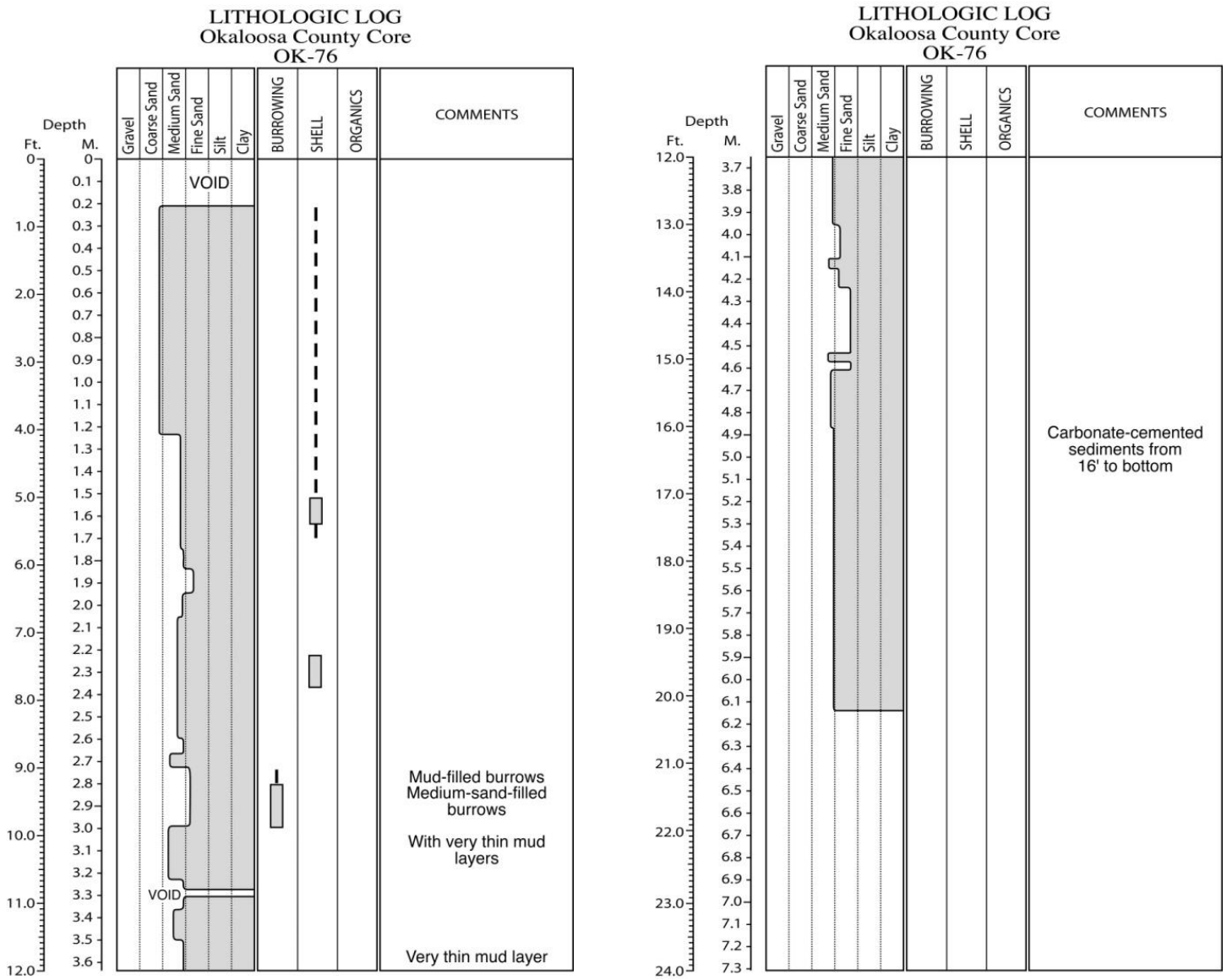

Figure E.249. Core OK-76 log.

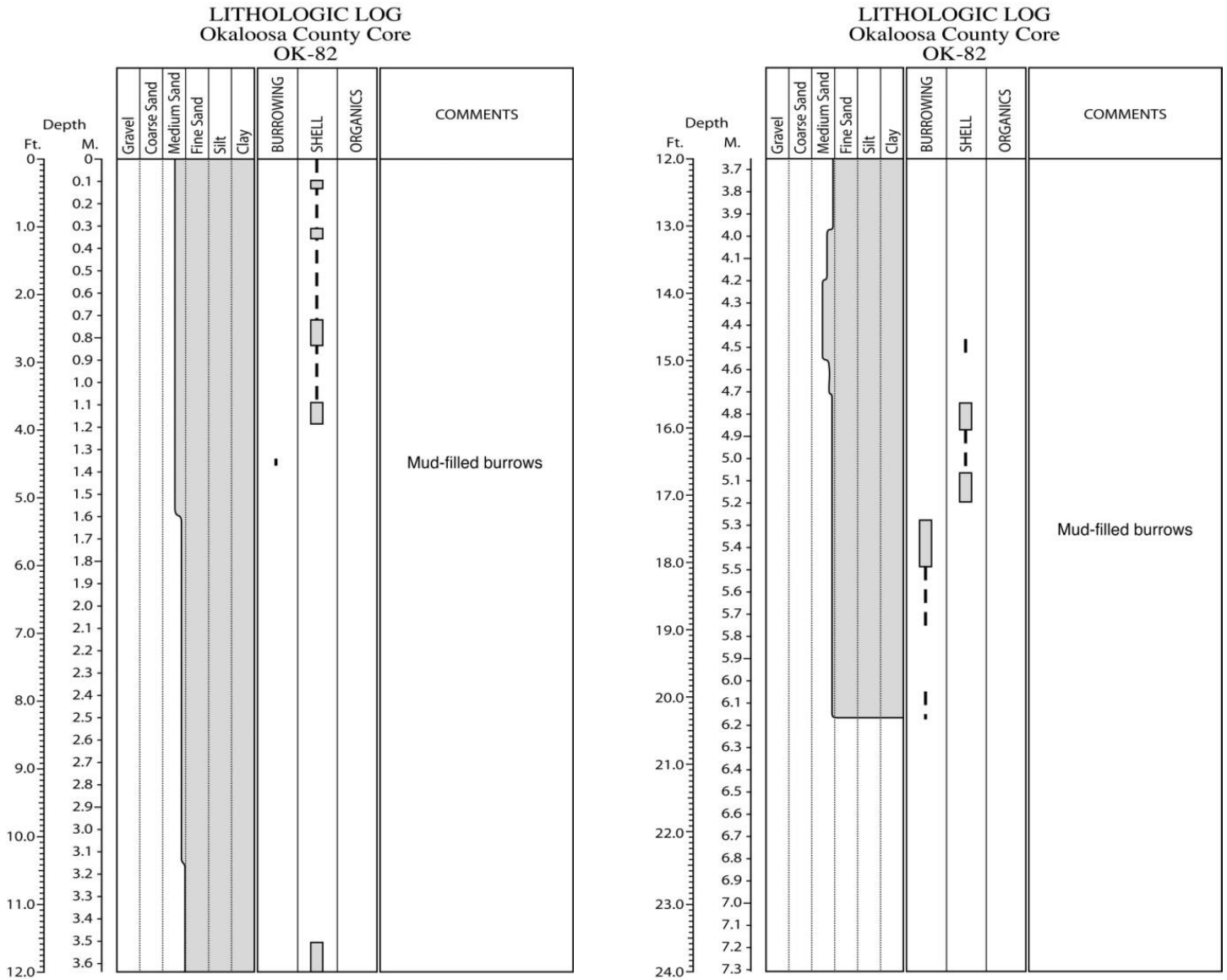

Figure E.250. Core OK-82 log.

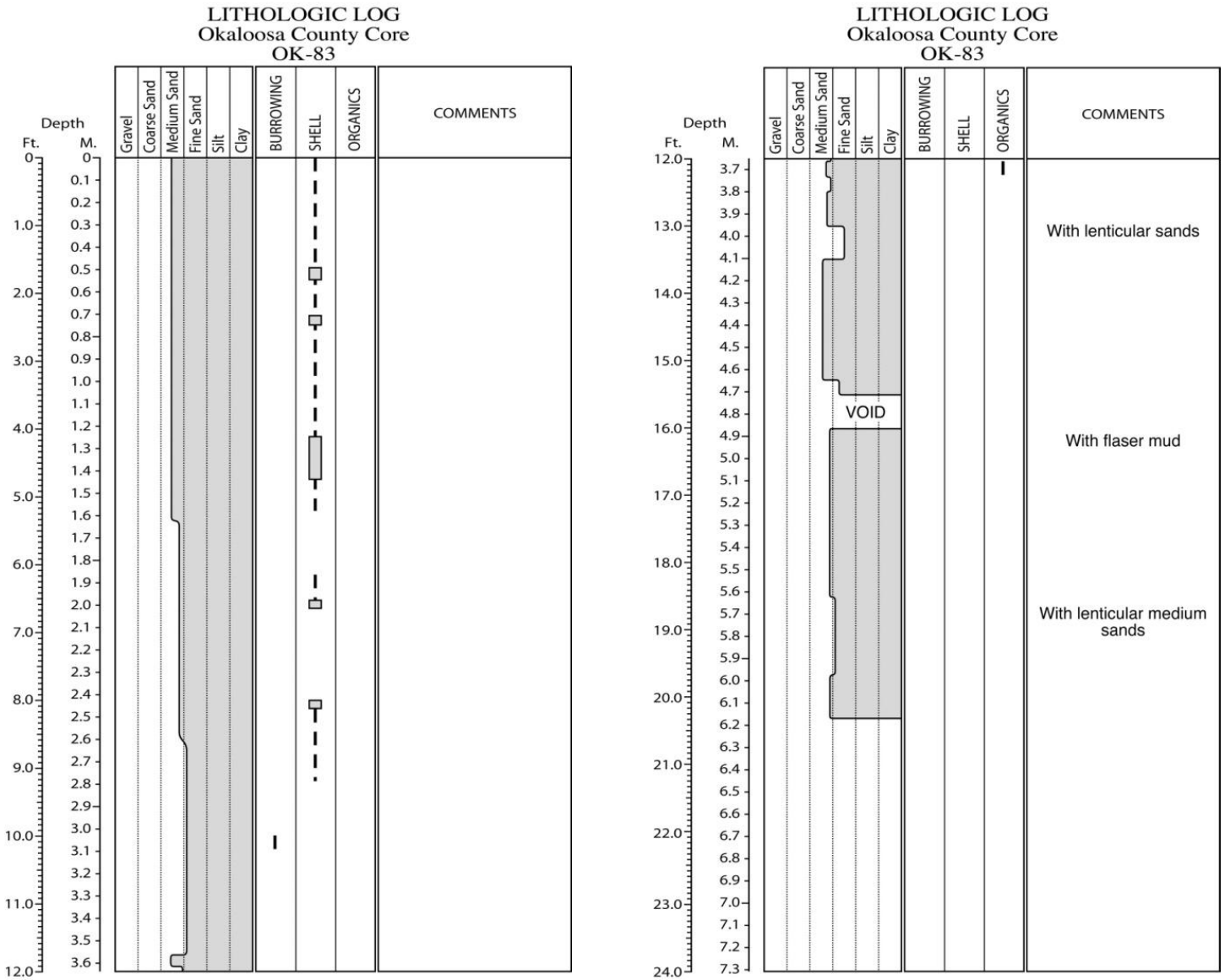

Figure E.251. Core OK-83 log.

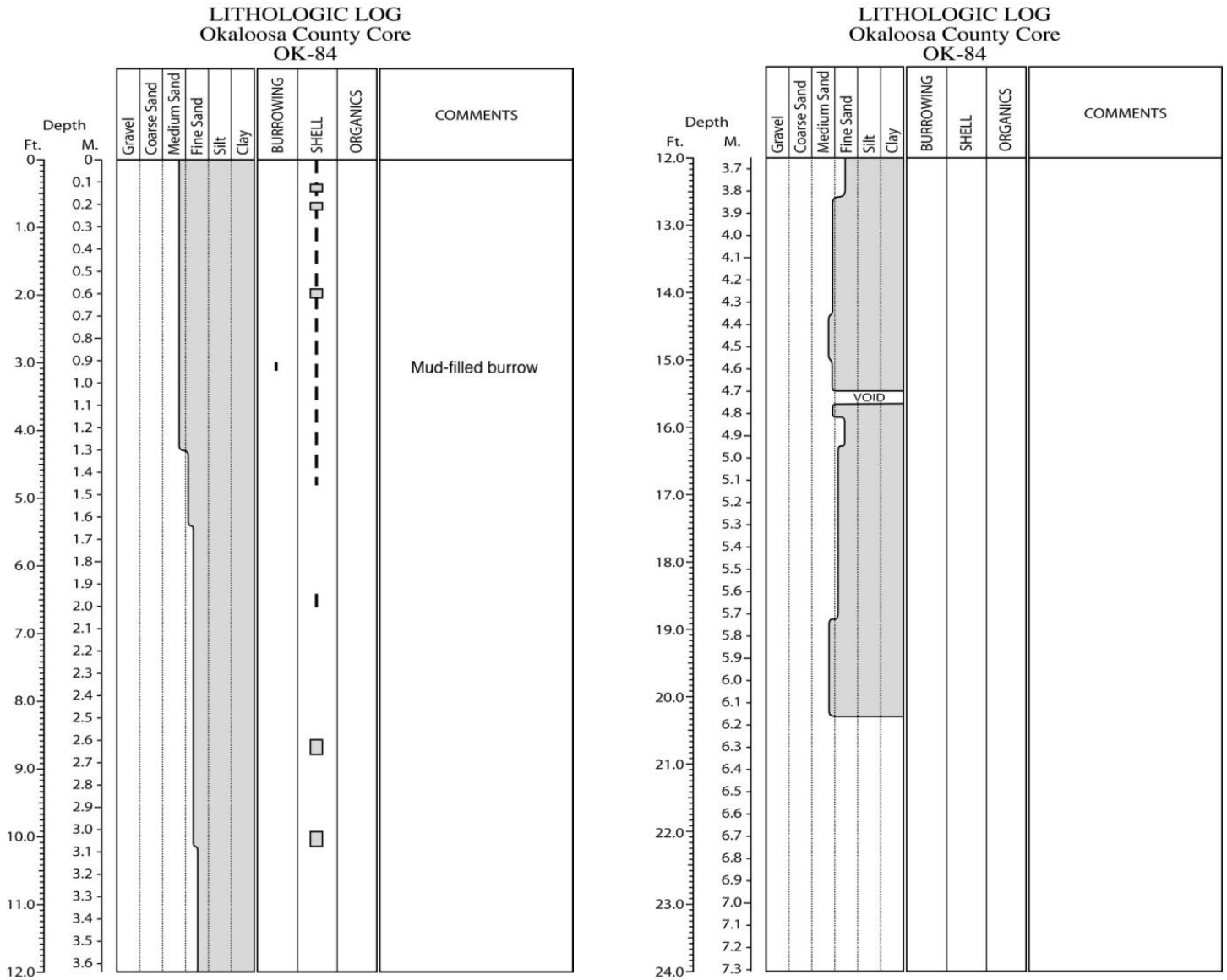

Figure E.252. Core OK-84 log.

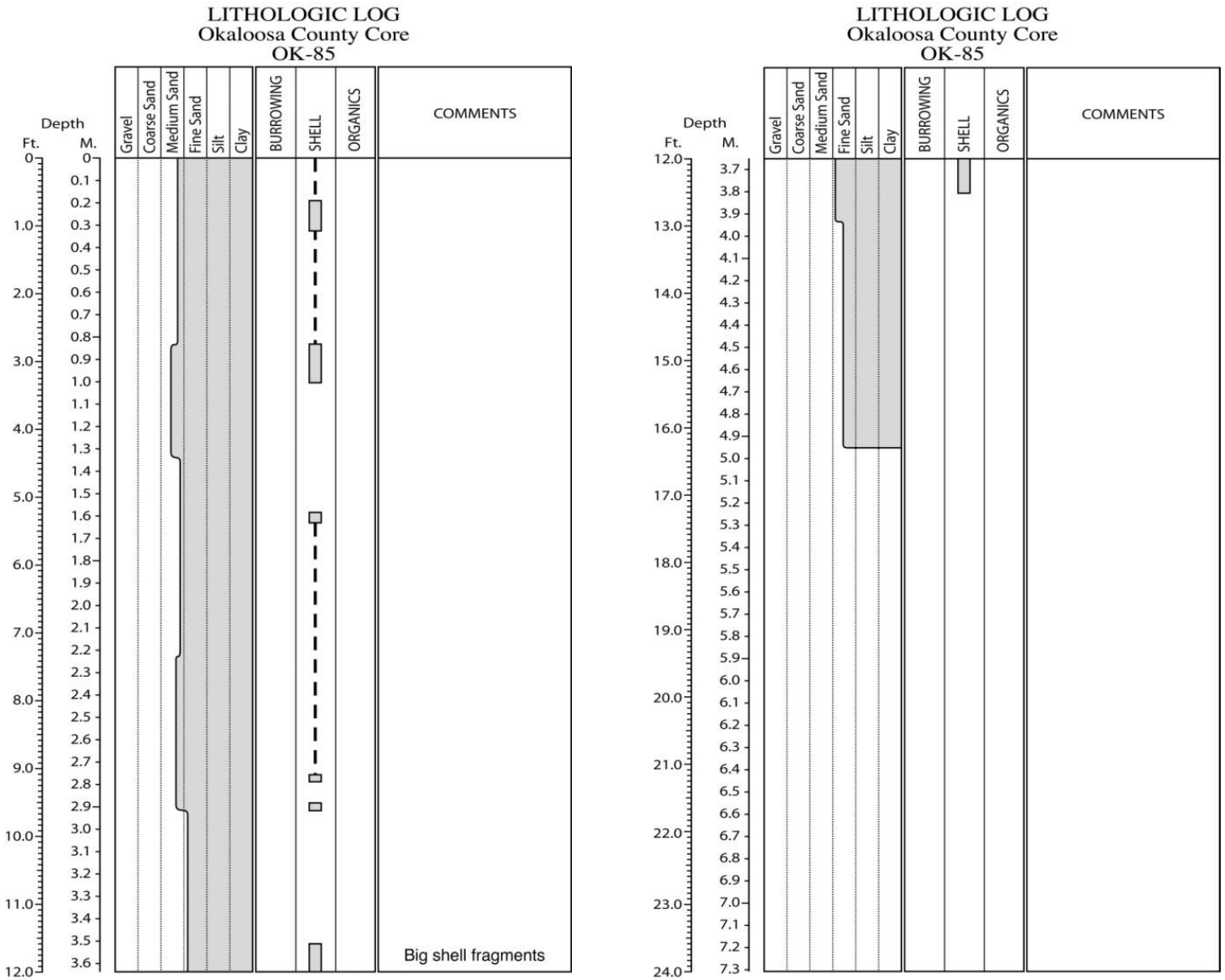

Figure E.253. Core OK-85 log.

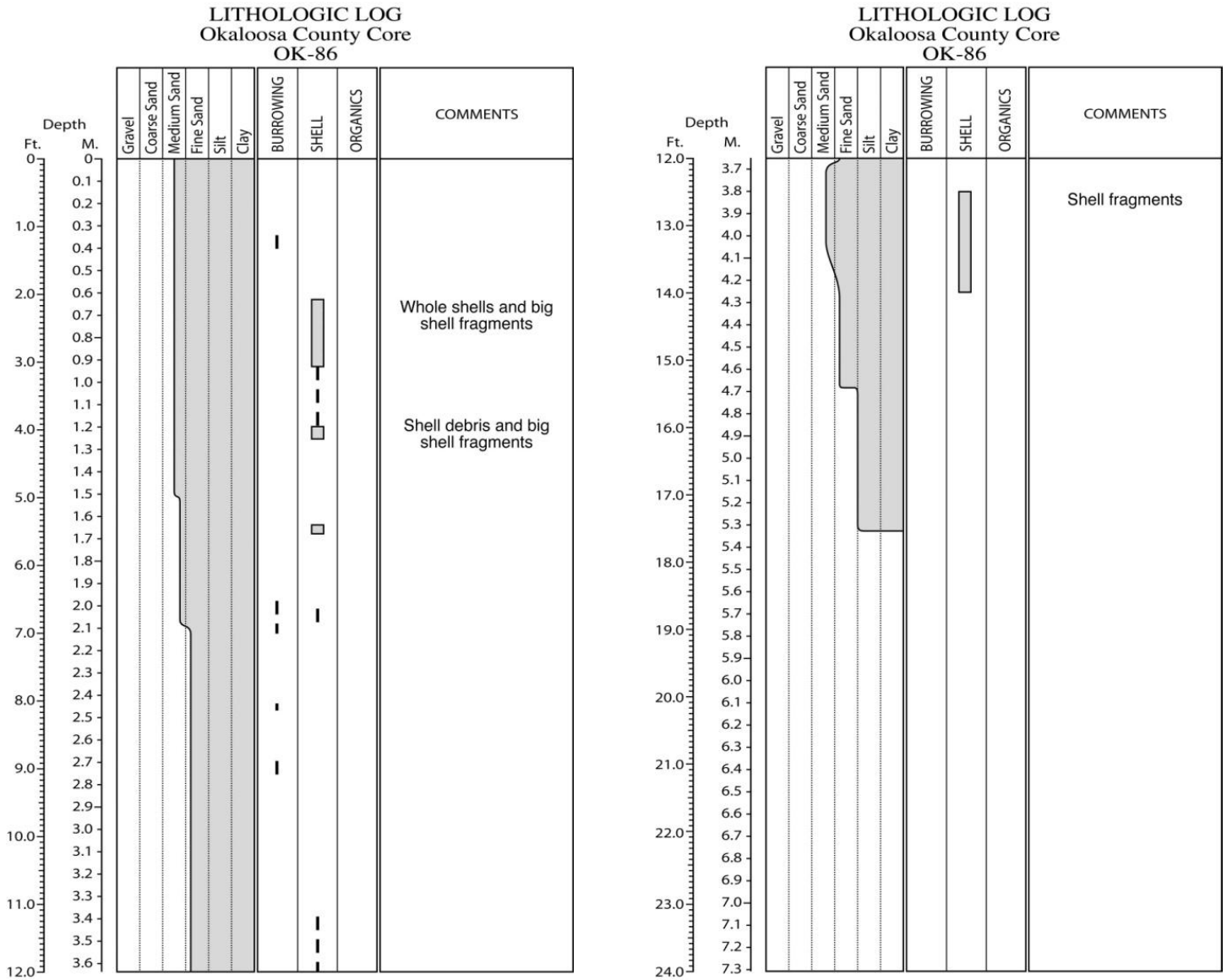

Figure E.254. Core OK-86 log.

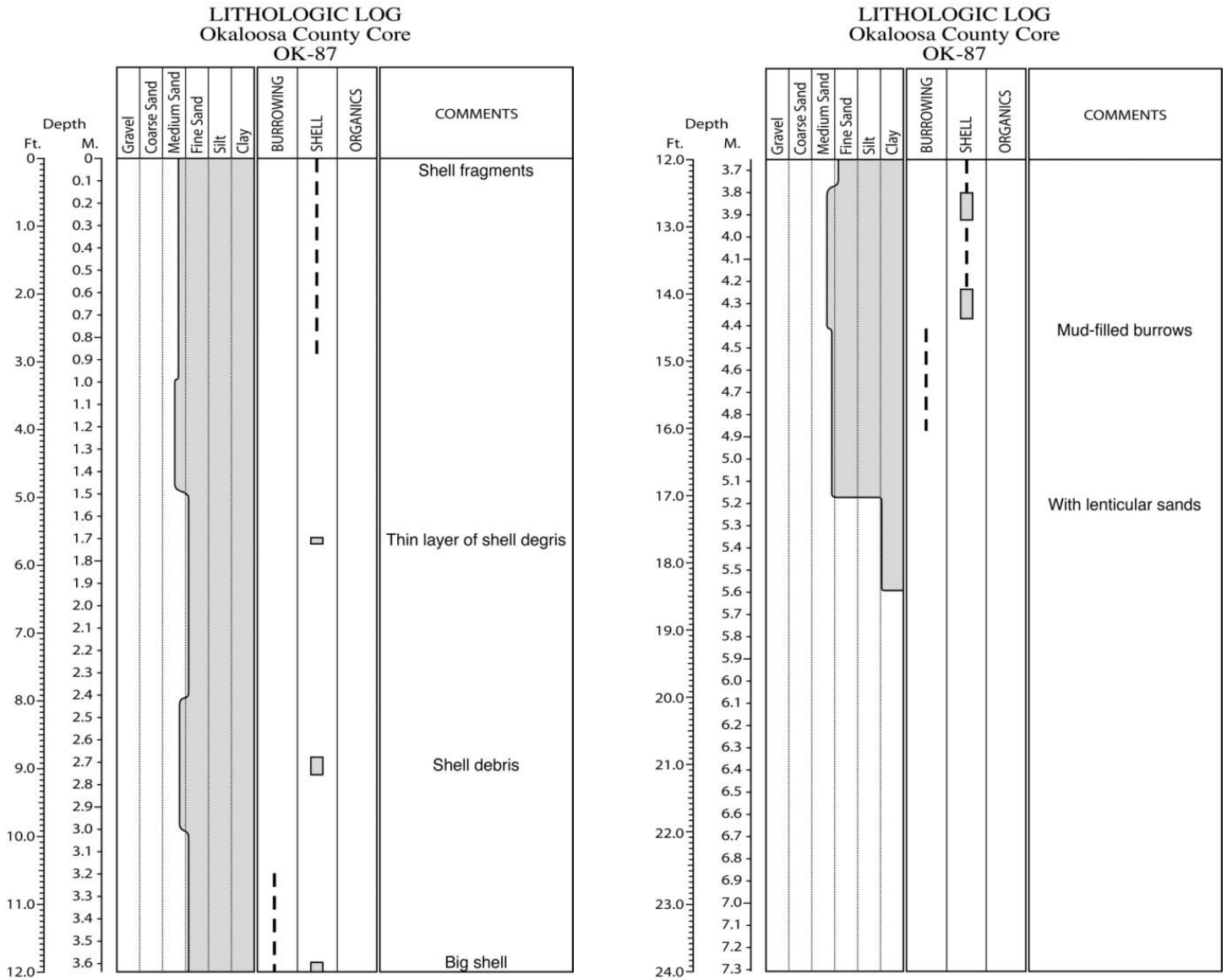

Figure E.255. Core OK-87 log.

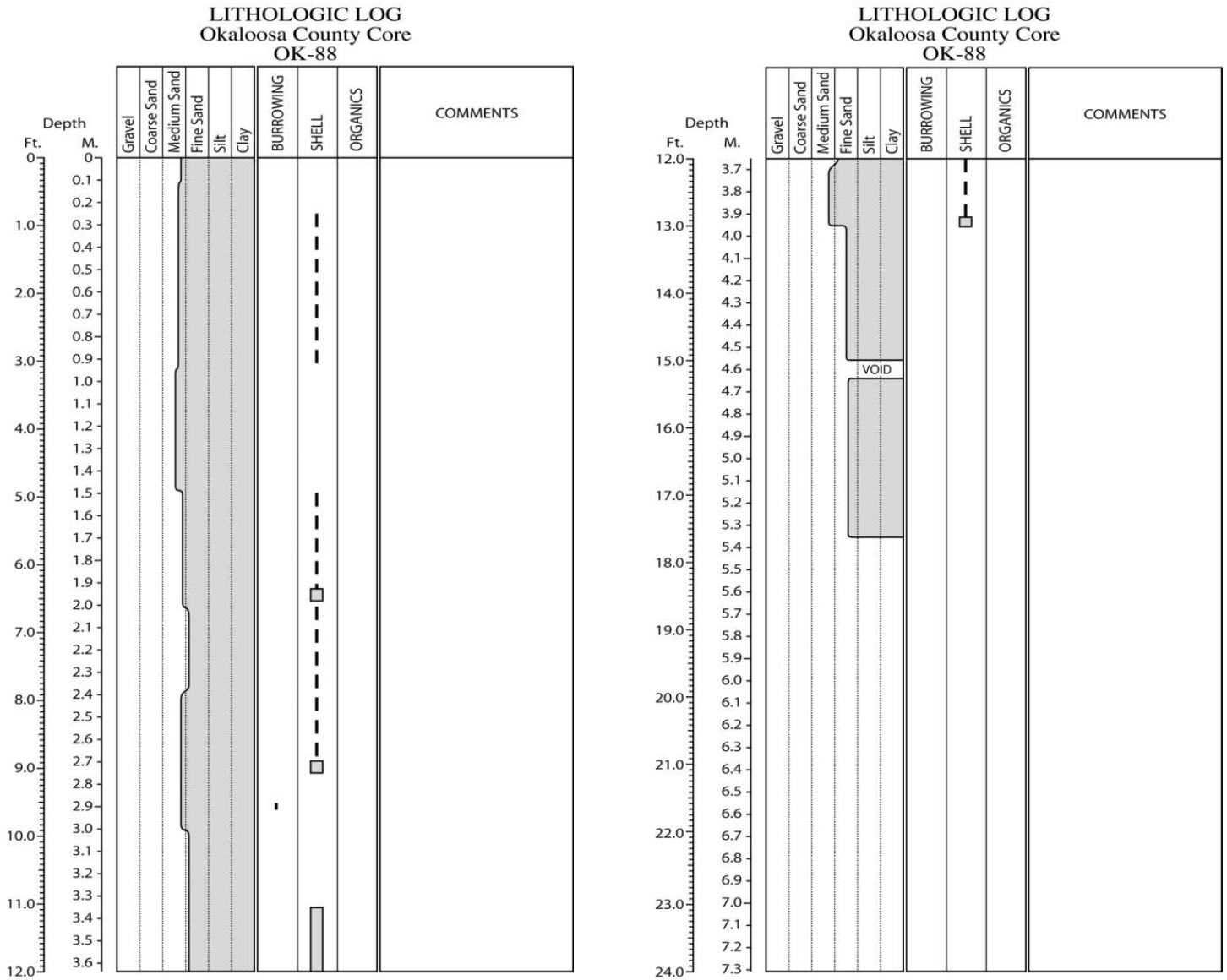

Figure E.256. Core OK-88 log.

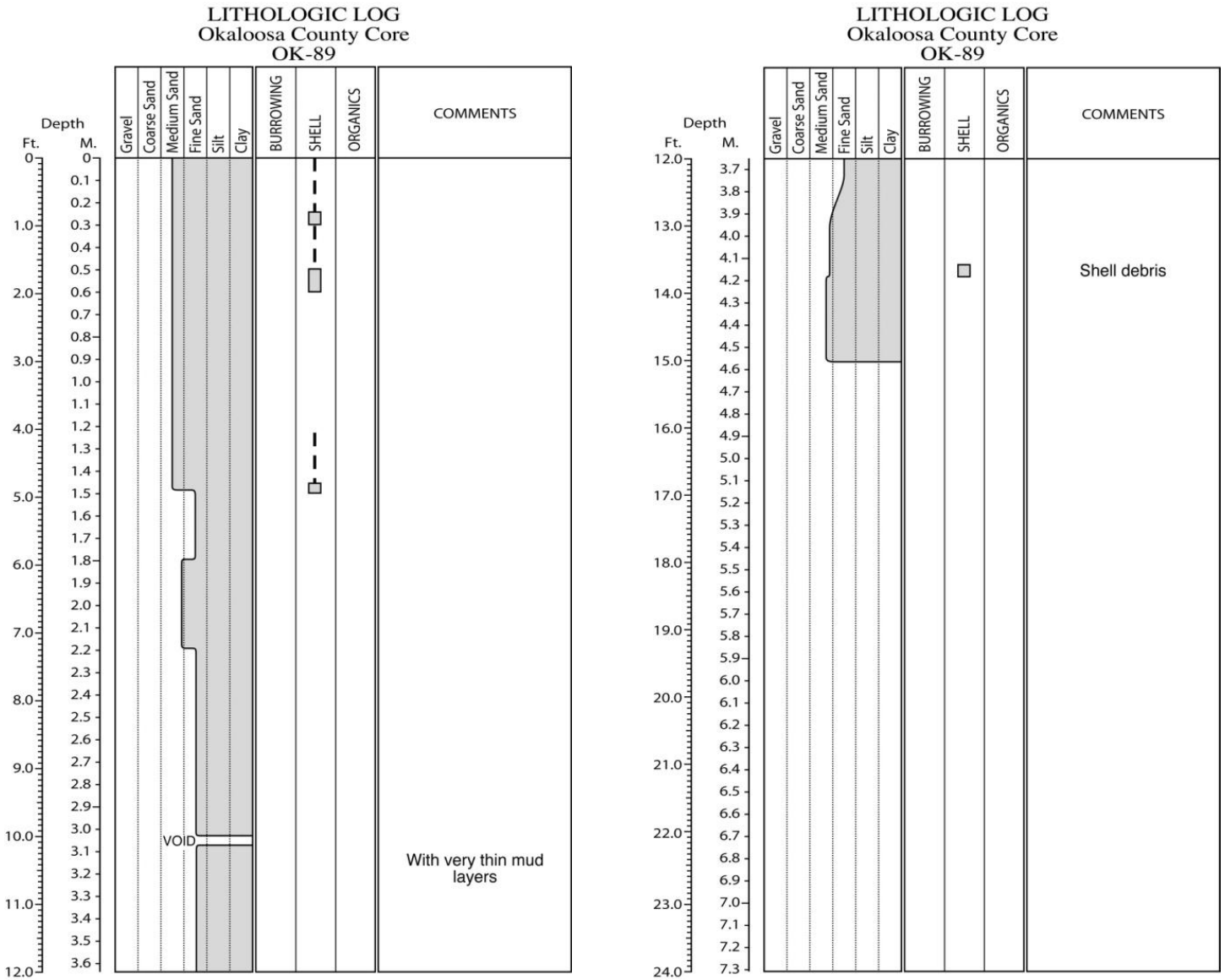

Figure E.257. Core OK-89 log.

APPENDIX F. MEAN GRAIN SIZE

Depth (ft)	0	0.3	0.5	0.6	0.8	1.5	1.6	2	2.5	3	3.3	4	4.3	4.5	4.9	5.3	6	6.3	6.5	6.6	7.3	7.5	8
Depth (m)	**0.00**	**0.09**	**0.15**	**0.18**	**0.24**	**0.46**	**0.49**	**0.61**	**0.76**	**0.91**	**1.01**	**1.22**	**1.31**	**1.37**	**1.49**	**1.62**	**1.83**	**1.92**	**1.98**	**2.01**	**2.23**	**2.29**	**2.44**
Core ID																							
DE-1	1.67					1.75				2.10				2.14			2.00						
DE-2	1.64					1.92				2.00				2.09			2.05						
DE-3	1.77					2.17				2.12				2.06			2.02						
DE-4	1.77					1.64				1.48				1.97			2.12						
DE-5	1.74					1.85				2.06				2.03			2.01						
DE-6	2.07					1.96				2.10				2.04			2.18						
DE-7	1.84					1.81				2.02				2.16			2.08						
DE-8																							
DE-9	2.14					2.04				2.03				1.98			2.10						
DE-10	1.88					1.86				2.01				1.90			1.76						
DE-11	1.88					2.02				2.07				1.90			1.99						
DE-12	1.91					1.95								1.51			1.96						
DE-13																							
DE-14	1.92					1.99				2.03				2.02			2.12						
DE-15																							
DE-16	1.88					1.97				2.12				2.04			2.13						
DE-17	1.89					1.96				2.22				2.11			2.28						
DE-18	1.91					2.02				1.97				2.18			2.19						
DE-19	1.94					2.08				1.83				1.99			1.93						
DE-20	1.88					2.00				2.12				1.97			2.14						
DE-21																							
DE-22	2.01					1.95				2.08				2.07			2.15						
DE-23	1.82					1.95				2.17				2.13			2.13						
DE-24	1.80					1.87				2.03				1.92			1.93						
DE-25	2.17					2.06				1.94				1.91			2.02						
DE-26	1.88					1.66				2.02				2.09			1.90						
DE-27																							
DE-28	1.95					1.99				2.10				2.18			2.19						
DE-29																							
DE-30	1.95					1.96				1.62				1.93			1.97						
DE-31	1.92					2.06				2.09				2.09			2.11						
DE-32	1.55					1.47				1.40				1.92			1.70						
DE-33	1.43					1.87				1.69				1.57			2.07						
DE-34	1.98					2.12				1.85				1.80			1.61						
DE-35	1.74					1.78				1.75				1.59			1.59						
DE-36	2.07					2.01				2.21				1.96			1.98						
DE-37	1.49					1.81				1.64				1.80			1.50						
WN-1	1.81					1.90				1.94				2.17			2.31						
WN-2	1.09					1.33				1.91				1.73			1.64					2.39	
WN-3	1.36					1.36				1.55				1.59			1.72					2.16	
WN-4	0.80					1.62				1.85				1.99			1.82					2.26	

WN-5	1.30					1.39				1.38				1.40			1.71					2.05	
WN-6	0.99					1.01				1.11				1.06			1.11					1.35	
WN-7	1.43					1.14				0.97				1.58			1.87					1.91	
WN-8	1.24					1.55				1.60				1.81			1.93					1.94	
WN-9	1.14					1.30				1.19				1.43			1.58					2.19	
WN-10	1.14					1.26				1.46				2.38			2.07					0.77	
WN-11	0.96					0.72				0.82				0.83			0.97					1.05	
WD-12	1.69											1.81							1.83				
WN-13	1.90									2.24				2.18		2.18							
WN-14	1.75								1.69				2.02					1.52					
WN-15	1.47									1.84							2.08						
WN-16	1.27							1.39						1.45			1.94						1.62
WD-17	1.73							1.83															
WN-18	0.85							1.04				1.15					2.09						1.28
WN-19	1.21					1.24				1.20				1.59			1.62					1.45	
WN-20	1.09					0.97				1.07				1.22			1.55					1.53	
WN-21	1.43					1.53				1.58				1.62			1.72					1.73	
WN-22	1.43					1.58				1.66				1.68			1.85						
WN-23	1.42					1.34				1.58				1.46			1.65					1.64	
WN-24	1.63					1.74				1.71				1.52			1.73					1.90	
WN-25	1.52					1.62				1.77				1.89									
W-26	1.78					1.87				1.88				1.95			2.12					1.92	
W-27	1.32					1.32				1.35				1.42			1.52					1.65	
W-28	1.30					1.64				1.72				1.74			1.87					1.93	
W-29	1.76					1.78				1.84				1.93			1.93					1.79	
W-30	1.71					1.78				1.78				1.88			1.95					1.97	
W-31	1.34					1.35				1.45				1.58			1.60					1.48	
W-32	1.75					1.77				1.80				1.77			1.63					1.78	
W-33	1.38					1.48				1.46				1.43			1.63					1.68	
W-34	1.47					1.46				1.63				1.57			1.75					1.77	
W-35	1.68					1.76				1.78				1.49			1.94					2.07	
W-36	1.94					2.03				2.03				2.02			2.10					2.01	
W-37	1.70					1.81				2.02				2.18			2.24					2.46	
W-38	1.49					1.72				1.76				2.08			2.19					2.18	
W-39	1.06					1.74				1.20				1.48			1.67					1.64	
W-40	1.54					1.73				1.46				1.88			2.20					2.22	
W-41	1.45					1.47				1.44				1.56			1.97					2.06	
W-42	1.22					1.32				1.42				1.54			1.82					2.00	
W-43	1.31					1.34				1.39				1.72			2.00				2.12		
W-44	0.82					1.11				1.50				1.69			1.29					1.57	
W-45	1.18					1.45				2.06				2.06			1.83					1.53	
W-46	1.55					1.30				1.44				1.57			2.14					2.06	
W-47	7.00					7.00				7.00				7.00			6.00					6.00	
W-48	0.84					1.34				1.62				1.73			1.86					1.79	
W-49	0.89					1.40				2.11				2.24			1.38					1.48	
W-50	0.81					0.96				1.48				1.12			1.97					2.29	
W-51	1.27					1.24				1.47				1.89			1.89					1.56	
W-52	1.06					1.04				1.58				2.02			2.20					2.24	
W-53	1.51					1.81				2.40				1.74			1.46					1.64	
W-54	2.02					2.22				1.99				1.64			1.50					1.45	
W-55	0.37						0.70				0.87				1.27					0.90			
W-56	1.28						0.98				1.12				1.05					0.97			

W-57	0.83						0.86				1.26				0.94					0.94			
W-58	0.97						1.97				1.46				1.63					1.26			
W-59	0.78					0.61				1.46				2.21			1.71					1.29	
W-60	0.95					1.00				1.24				1.53			1.84			1.54		1.54	
W-61	1.14					1.11				1.57				1.69			2.38						
W-62	0.49					1.48				2.34				3.31			3.58					2.02	
W-63	0.83					1.40				1.34												2.40	
W-64	0.62					1.10				1.05				1.51			1.52					1.40	
W-65	0.83					1.07				1.35				1.75			1.85					1.82	
W-66	1.67					1.34				1.29				2.10			2.27					1.84	
W-67	0.74					0.91				0.91				1.80								1.81	
W-68	1.52					2.03				2.11				2.33			1.90					0.89	
W-69	2.42					1.92				1.29				1.84									
W-70	0.63					0.63				1.41				1.54			2.51					2.60	
W-71	1.13					0.65				0.92													
W-72	1.97																						
W-73	1.82					1.97																	
W-74	1.88																						
W-75	1.46					1.69				1.95				1.89									
W-76	1.87					1.10																	
W-77	1.05					1.45				1.29				1.31			1.45						
W-78	2.12					1.49				1.87				1.79			1.69					2.12	
W-79	0.87					0.99				1.54				1.03			1.63					1.18	
W-80	0.97					0.98				1.10				1.51			1.78					1.99	
WA-1	1.82					1.56				1.39				1.33			1.83					1.48	
WA-2	1.34					1.36				1.72				1.83			1.92						
WA-4	1.46					1.38				1.42				1.42			1.71					1.91	
WA-5	1.28					1.56				1.99				2.05			2.11					2.08	
WA-6	1.60					1.73				1.80				1.76			1.87					1.95	
WA-7	1.58					1.54				1.63				1.92			2.09					2.11	
WA-8	1.59					1.57				1.64				1.97			2.08					2.10	
WA-9	1.39					1.48				1.58				1.83			1.99					2.14	
WA-10	1.54					1.52				1.51				1.50			1.64					1.85	
WA-11	1.49					1.50				1.66				1.90			2.10						
WA-12	1.68					1.55				1.58				1.67			1.91					1.96	
WA-13	1.66					1.54				1.59				1.72			1.80					1.90	
WA-14	1.37					1.51				1.59				1.68			1.74					1.74	
WA-15	1.61					1.59				1.65				1.89			1.96					1.95	
WA-16	1.45					1.52				1.50				1.65			1.76					1.80	
WA-17	1.53					1.54				1.67				1.83			1.97					2.05	
WA-18	1.41					1.35				1.37				1.46			1.56					1.77	
WA-19	1.06					1.37				1.41				1.50			1.70					1.79	
WA-26	1.20					1.06				1.42													
WA-27	0.69					1.19				1.43													
WA-28	1.24					1.23				1.29				1.55			1.84					1.87	
WA-29	1.36					1.44				1.55				1.37			1.83					1.56	
WA-30	1.49					1.76				1.89				2.07			2.05					2.18	
WA-31	1.50					1.56				1.62				1.80			1.94					1.89	
WA-32	1.37					1.45				1.51				1.52			1.82					1.84	
WA-33	1.60					1.68				1.97													
WA-34	1.43					1.50				1.70				1.90			1.99					2.08	
WA-35	1.51					1.58				1.72				1.53			1.68					1.74	
WA-36	1.67					1.82				1.98				2.02									

WA-37	1.82					1.80				1.78											
WA-38	1.51					1.47				1.50				1.70			1.67				1.71
WA-39	1.54					1.46				1.61				1.59			1.61				1.70
WA-40	1.67					1.54				1.65				1.68			1.96				2.02
WA-41	1.52					1.57				1.56				1.74			1.84				1.87
WA-42	1.72					1.65				1.52				1.79			1.83				1.92
WA-43	1.61					1.59				1.71				1.78			1.87				1.83
WA-44	1.50					1.56				1.57				1.62			1.80				1.78
WA-45	1.65					1.70				1.68				1.78			1.86				1.92
WA-46	1.42					1.59				1.58				1.92			1.87				2.03
WA-47	1.67					1.55				1.62				1.64			1.67				1.77
WA-48	1.50					1.56				1.62				1.69			1.80				1.83
WA-60	1.77					1.82				1.87				1.94			2.01				2.10
WA-61	1.80					1.94				1.97				2.35							
WA-62	1.69					1.71				1.79				1.91			1.90				2.04
WA-63	1.78					1.88				1.89				1.77			2.12				2.12
WA-64	1.57					1.56				1.61				1.97			1.94				1.79
WA-65	1.79					1.85				1.92				2.05			2.15				
WA-66	1.98					1.91				1.91				2.02			2.04				2.22
WA-67	1.63					1.71				1.75				1.79			1.85				1.78
WA-68	1.51					1.51				1.64				1.77			1.78				1.89
WA-70	1.65					1.55				1.77				1.81			2.01				2.08
WB-3	1.66					2.10				1.70											
WB-5																					
WC-2																					
WC-5																					
WD-2																					
WD-5																					
WE-1	0.92					0.99				0.97				1.12			1.18				1.29
WE-2	0.89					0.98				1.05				1.04			1.38				1.52
WE-3	1.00					1.00				0.93				0.98			1.28				1.64
WE-4	1.29					1.25				1.43				1.38			1.70				1.91
WE-5	1.21					1.15				1.04				1.47			1.64				1.76
WE-6	0.91					0.88				0.95				1.27			1.40				1.10
WE-7	0.86					0.95				0.96				0.82			1.25				1.71
WE-8	0.99					1.19				1.52				2.10			2.12				1.64
WE-9	1.04					0.87				1.02				1.09			1.30				1.51
WE-10	1.10					1.03				1.16				1.22			1.48				1.77
WE-11	1.13					0.91				1.02				0.81			1.29				1.29
WE-12	1.19					1.07				1.41											
WE-13	1.54					1.32				1.32				1.18			1.18				1.31
WE-14	1.47					1.48				1.43				1.72			1.98				2.20
WE-15	1.28					1.22				1.33				1.49			1.63				1.85
WE-16	1.02					1.13				1.15				1.53			1.67				1.90
WE-17	0.93					1.04				0.99				1.31			1.58				1.64
WE-18	0.86					0.85				0.98				1.14			1.37				1.41
WE-19	1.01					0.88				0.85				1.06			1.29				1.37
WE-20	0.91					0.84				0.82				0.89			1.00				1.14
WE-21	1.00					0.95				0.96				0.96			0.94				1.01
WE-22	0.78					0.95				1.00				1.01			1.26				1.15
WE-23	0.90					0.94				0.92				1.06			1.03				0.97
WE-24	1.11					1.05				1.06				1.09			1.36				1.36

WE-25	1.23					1.29				1.57				1.72			2.00				2.18	
WE-26	1.06					1.12				1.42				1.55			1.86				1.94	
WE-27	1.14					1.12				1.25				1.43			1.66				1.75	
WE-28	1.11					1.27				1.42				1.55			1.65				1.87	
WE-29	1.77					1.55				1.84				1.55			2.10				2.24	
WE-30	0.73					0.88				0.90				1.61			2.40					
WE-36	0.82					0.94				1.61				1.09								
WE-37	0.93					1.02				1.32												
WE-38	1.04					1.06				1.69				1.93			0.99				0.99	
WE-39	1.27					1.15				1.27				1.61			1.85				1.94	
WE-40	0.94					1.15				1.42				1.72			2.16				1.87	
WE-41	0.70					0.88				0.98				2.00			2.17				2.24	
WE-42	0.89					0.90				1.05				1.30			1.70				1.73	
WE-43	0.91					0.90				1.01				1.60			1.80				1.86	
WE-44	0.90					0.87				0.88				1.45			1.52				1.33	
WE-45	0.82					0.81				1.19				0.85								
WE-46	1.21					1.22				1.14												
WE-47	2.03																					
WE-60																						
WE-61																						
WE-62																						
WE-63																						
WE-64																						
WE-65																						
WE-66																						
WE-67																						
WE-68																						
OK-1	1.19					0.70				1.47				1.62			1.26				1.97	
OK-2	1.48					1.23				1.81				2.04								
OK-3	1.03					1.39				1.36				1.22			1.25				1.66	
OK-4	2.13					1.95				1.79				1.19			1.13				1.81	
OK-5	1.72					1.52				1.84				1.56			1.40				1.31	
OK-6	1.38					1.01				1.76				1.36			1.60				1.43	
OK-7	1.03					0.87				1.64												
OK-8	1.19					1.03				1.34												
OK-9	0.91					1.05				1.20				1.23								
OK-10	0.92					0.94				1.14				1.23			1.26				1.71	
OK-11	1.79					1.65				2.03				2.01								
OK-12	1.51					1.72				1.78				1.56			1.21				1.14	
OK-13	1.98					1.90				1.87				1.90			1.80				1.93	
OK-14	1.02					1.07				1.15				1.29			1.36				1.28	
OK-15	N/A					1.25				1.45				1.01			1.15					
OK-16	0.98					1.24				1.28				1.38			1.78				2.12	
OK-17	1.12					1.79				1.82				2.10			1.97				1.88	
OK-18	1.92					1.77				1.82				1.94			1.79				1.89	
OK-19	N/A		1.11			0.70				1.06				0.98			1.08					
OK-20	1.50					1.37				1.54				1.80			2.00					
OK-21	1.05					0.99				1.14				1.16			1.65				1.48	
OK-22	1.05					1.42				0.77				0.94			0.53					
OK-23	1.92					1.95				2.02				2.03			2.03				1.95	
OK-24	1.16					1.20				1.08				1.39			1.47				1.50	

OK-25	1.24					1.30				1.43				1.56			1.97					1.81	
OK-26	1.33					1.56				1.60				1.72			2.04					1.84	
OK-27	2.11					1.99				1.82				1.69			2.11					2.03	
OK-28	1.07					1.11				1.27													
OK-29	0.93					1.05				1.25				1.38			1.37					1.61	
OK-30	1.29					1.22				1.28				1.46			1.55					1.86	
OK-31	1.45					1.38				1.45				1.38			1.70					1.80	
OK-32	1.38					1.79				2.37													
OK-33	N/A																						
OK-34	2.00					1.99				1.91				1.77			2.18					2.10	
OK-35	0.76					0.76				0.83													
OK-36	1.28					1.18																	
OK-37	1.16					1.04				1.17				1.20			1.40					1.62	
OK-38	N/A																						
OK-39	1.04					0.98				1.07				1.24			2.24						
OK-40	N/A	1.31				1.09				1.24				1.44			1.84					2.02	
OK-41	0.80					0.72				0.83				1.62			1.76					1.56	
OK-44	1.20					1.18				1.40				1.55			1.93					2.01	
OK-45	1.18																						
OK-46	1.00					1.11				1.10				1.23			1.48					1.70	
OK-50	1.17					1.19				1.11				1.16			1.42					1.56	
OK-51	N/A		1.75			1.93				2.05				1.55			1.93					1.34	
OK-52	0.83					1.16				1.25				1.23			1.72					1.89	
OK-53	1.40					1.03				1.32				1.16			1.92						
OK-54	1.21					1.07				1.73				2.04			2.26						
OK-55	1.36					1.33				1.39				1.54			1.57					2.03	
OK-56	5.00					5.00				3.00				7.00			7.00					7.00	
OK-57	N/A			1.12		1.07				1.12				1.16			1.19					1.63	
OK-58	0.98					0.69				0.95													
OK-59	0.92					0.93				0.86				0.90			1.57					1.81	
OK-60	0.80					0.82				0.88				0.96			1.68					2.22	
OK-61	0.91					0.84				0.91				0.96			1.39						
OK-62	1.20					1.00				1.02				1.00			1.83						
OK-63	0.92					0.79				0.82													
OK-64	0.74					0.85				1.67				0.78									
OK-65	0.61					1.07				1.45				2.09									
OK-66	0.93					1.00				1.05				1.30									
OK-67	0.84					0.91				1.08													
OK-68	1.24					1.38				1.39				1.63			2.32						
OK-69	0.65					0.65				0.67				1.45			1.93						
OK-70	1.27					1.21				1.19													
OK-71	1.05					0.97				1.19				1.75			1.74						
OK-72	1.01					0.86				0.87				0.76			1.48					1.88	
OK-74	1.40					1.30				1.82				1.87			1.00						
OK-75	0.99					0.66				1.10				1.01			1.17					1.19	
OK-76	0.92				0.92	0.99				1.00													
OK-82	1.51					1.64				1.60				1.37			1.89					1.82	
OK-83	1.52					1.58				1.76				1.73			1.86					1.91	
OK-84	1.70					1.80				1.93				2.18			2.14					2.32	
OK-85	1.63					1.69				1.44				1.81			1.85					1.75	
OK-86	1.74					1.84				1.76				1.85			1.98					2.05	
OK-87	1.67					1.73				1.76				1.82			2.05					2.00	

OK-88	1.65					1.75				1.83				1.58			1.87						2.08	
OK-89	1.58					1.63				1.68				1.67										

Depth (ft)	8.2	8.5	9	9.3	9.8	10	10.5	10.8	11	11.5	12	12.8	13.1	13.5	14	15	16.4	16.5	16.7	18	19.2	19.5
Depth (m)	**2.50**	**2.59**	**2.74**		**2.99**	**3.05**	**3.20**	**3.29**	**3.35**	**3.51**	**3.66**	**3.90**	**3.99**	**4.12**	**4.27**	**4.57**	**5.00**	**5.03**	**5.09**	**5.49**	**5.85**	**5.94**
Core ID																						
DE-1			1.83								1.27											
DE-2			2.12								1.71											
DE-3			1.84								1.90											
DE-4			2.10								2.06											
DE-5			2.10								2.14											
DE-6			1.65								1.93											
DE-7			2.00						1.94													
DE-8																						
DE-9			2.07								2.22											
DE-10			2.06								2.20											
DE-11			2.14								2.10											
DE-12			1.86								1.99											
DE-13																						
DE-14			2.28								2.25											
DE-15																						
DE-16			1.94								2.07											
DE-17			1.98								2.23											
DE-18			1.70								2.16											
DE-19			2.00								2.12											
DE-20			2.08								2.12											
DE-21																						
DE-22			2.01								2.19											
DE-23			2.23								1.74											
DE-24			2.09								2.45											
DE-25			2.00								2.03											
DE-26			1.83								2.02											
DE-27																						
DE-28			2.03								2.24											
DE-29																						
DE-30			2.14								2.12											
DE-31			1.97								2.29											
DE-32				1.81							1.78											
DE-33			2.18								2.07											
DE-34			1.62								1.79											
DE-35			1.80								1.96											
DE-36			1.54								1.97											
DE-37			1.55								1.86											
WN-1																						
WN-2																						
WN-3			1.89				1.79				1.63			1.50		2.93						
WN-4			2.23				2.08				1.87											

WN-5																					
WN-6			1.33				1.28														
WN-7																					
WN-8			1.47				2.02				2.23										
WN-9			2.18				2.01				2.19										
WN-10			1.81				0.85				1.42			1.25							
WN-11			1.22				0.91														
WD-12			2.00							1.91					2.28						
WN-13			1.77					2.00				2.42							1.89		
WN-14		2.18							2.34				1.96							2.11	
WN-15			2.43						1.80						1.49		1.90				2.13
WN-16						1.68					2.32										
WD-17																					
WN-18																					
WN-19			1.79																		
WN-20																					
WN-21			1.78				1.89				1.84			1.94		2.14		2.16			
WN-22																					
WN-23			1.60				1.82				2.26			2.35		2.32					
WN-24			1.69				1.79				1.87										
WN-25																					
W-26			1.84				2.44				2.54			2.54		2.53		2.65		2.69		2.23
W-27			1.71				1.80				1.98			2.03		2.34		2.64		2.63	
W-28			2.07				2.03				1.82			1.64		1.93		2.18		2.84	
W-29			1.97				2.05				2.07			2.14		1.77		1.82		1.92	
W-30			2.13				2.16				2.22			2.13		2.15		2.36		2.32	
W-31			1.50				1.69				1.79			1.82		1.76		1.99			
W-32			1.47				1.99				2.05			2.36		2.15		2.31			
W-33			1.69				1.83				1.96			2.11		2.02		2.08			
W-34			1.79				1.79				1.87			2.12		2.07		2.10		2.02		1.76
W-35			1.96				2.60				2.79			2.58							
W-36			2.07				1.87				2.14			2.36		2.52		2.46		2.34		1.93
W-37			2.45				2.49														
W-38			2.21				1.75														
W-39			1.61				1.88														
W-40			2.24				2.10														
W-41			2.03				2.19														
W-42			2.15				2.16														
W-43																					
W-44			1.12				1.15														
W-45			1.53				1.89														
W-46			1.39				1.13														
W-47			6.00				6.00				6.00			6.00		6.00		6.00		6.00		6.00
W-48			0.87																		
W-49			1.36				0.81														
W-50			1.47				0.95														
W-51			0.70				1.27														
W-52			1.43				1.26														
W-53			2.58				2.20														
W-54			1.30				1.16														
W-55	1.31				1.13					1.36											
W-56	1.25				1.75					1.87											

W-57	1.72				1.73					1.86												
W-58	1.44				1.51					1.44												
W-59			1.30				2.15															
W-60			1.52				1.78															
W-61																						
W-62			1.74				1.59															
W-63			0.65				2.24															
W-64			2.01				1.84															
W-65			1.53				1.88															
W-66			2.09				1.50															
W-67			1.66				2.18															
W-68			0.92				1.40															
W-69																						
W-70			1.90				1.60															
W-71																						
W-72																						
W-73																						
W-74																						
W-75																						
W-76																						
W-77																						
W-78			2.06				2.06															
W-79			1.21				1.29															
W-80			1.99				1.77															
WA-1			1.75																			
WA-2																						
WA-4			1.84				2.35															
WA-5			1.35																			
WA-6			2.00				2.14				2.15											
WA-7			2.13																			
WA-8			2.17																			
WA-9			2.06				2.16				2.21			2.00								
WA-10			1.96				2.05				1.92			2.13		1.77						
WA-11																						
WA-12			1.98				2.05				1.87			1.98		2.23						
WA-13			2.00				1.97				1.91											
WA-14			1.85				1.92				1.88			1.90		1.97						
WA-15			1.99				2.06				2.08			1.92								
WA-16			1.94				2.05				2.14			2.03		2.13						
WA-17			2.06				1.97															
WA-18			1.65				1.86															
WA-19			1.88				1.97															
WA-26																						
WA-27																						
WA-28			2.19																			
WA-29			1.88																			
WA-30																						
WA-31			2.03																			
WA-32			2.09																			
WA-33																						
WA-34			2.21																			
WA-35			1.88																			
WA-36																						

WA-37																					
WA-38			1.70				2.02				2.05										
WA-39			1.78				1.91				2.05										
WA-40			1.95				2.09				2.19										
WA-41			2.08				2.05				2.06			2.23							
WA-42			2.00				2.18				2.18										
WA-43			1.92				1.86				1.84			1.93		2.07					
WA-44			1.83				2.08				1.87			2.10		2.28					
WA-45			2.17																		
WA-46																					
WA-47			1.92				1.98														
WA-48																					
WA-60			2.06				1.87														
WA-61																					
WA-62			2.13																		
WA-63																					
WA-64			1.92				1.97				1.97			1.79							
WA-65																					
WA-66																					
WA-67			1.83				2.00				2.12										
WA-68			1.72				1.91				1.98			2.05		2.22					
WA-70			1.88																		
WB-3																					
WB-5																					
WC-2																					
WC-5																					
WD-2																					
WD-5																					
WE-1			1.62				1.25				1.91			1.68		1.90					
WE-2			1.64				1.83														
WE-3			1.67				1.95				1.48			1.49		1.74					
WE-4			1.74				2.07				1.83			2.28							
WE-5			1.33				1.67														
WE-6			1.26				1.18														
WE-7			2.19				0.91														
WE-8																					
WE-9																					
WE-10			1.94																		
WE-11			1.30																		
WE-12																					
WE-13			1.32				1.51				2.09										
WE-14																					
WE-15			2.02				2.04				2.20			2.22		1.58					
WE-16			1.92				2.06				2.26										
WE-17			1.50				1.48														
WE-18			1.41				1.33				1.40			1.24							
WE-19			1.03																		
WE-20			1.22				1.19				0.99										
WE-21																					
WE-22			1.26				1.30				1.25			1.15		1.01					
WE-23			1.18				0.99														
WE-24			1.46				1.28														

WE-25			1.55				1.74															
WE-26			2.24				2.13				2.17			2.35		2.14						
WE-27			1.64				2.34				1.53											
WE-28			2.14				1.09															
WE-29																						
WE-30																						
WE-36																						
WE-37																						
WE-38			2.27				2.32				1.85			0.93		1.92						
WE-39			2.08				2.11				2.26			2.34								
WE-40			1.56																			
WE-41			2.10				1.72															
WE-42			1.88				1.96															
WE-43			1.83																			
WE-44			1.38																			
WE-45																						
WE-46																						
WE-47																						
WE-60																						
WE-61																						
WE-62																						
WE-63																						
WE-64																						
WE-65																						
WE-66																						
WE-67																						
WE-68																						
OK-1																						
OK-2																						
OK-3			1.76				2.50															
OK-4			1.30				1.09															
OK-5			1.77				1.48															
OK-6			1.32				1.47															
OK-7																						
OK-8																						
OK-9																						
OK-10																						
OK-11																						
OK-12			1.77				1.90															
OK-13			1.94				2.08															
OK-14																						
OK-15																						
OK-16																						
OK-17																						
OK-18			1.39				2.10															
OK-19																						
OK-20																						
OK-21			1.15				1.92															
OK-22																						
OK-23			1.88				2.06															
OK-24			1.37				1.48															

OK-25			1.88																		
OK-26																					
OK-27			1.35				1.29														
OK-28																					
OK-29			1.55				2.08														
OK-30			2.03				1.42														
OK-31			1.87				2.11														
OK-32																					
OK-33																					
OK-34			2.26				2.27														
OK-35																					
OK-36																					
OK-37			1.35				1.99														
OK-38																					
OK-39																					
OK-40			2.05				1.90														
OK-41			1.48				1.94														
OK-44			1.16				1.84														
OK-45																					
OK-46			1.32																		
OK-50			1.50				1.80														
OK-51			1.27				1.60														
OK-52			1.70				1.68														
OK-53																					
OK-54																					
OK-55																					
OK-56			1.50				1.50				2.00			2.00		1.50		1.50		0.50	0.50
OK-57			1.81																		
OK-58																					
OK-59			1.68				2.18														
OK-60			1.95																		
OK-61																					
OK-62																					
OK-63																					
OK-64																					
OK-65																					
OK-66																					
OK-67																					
OK-68																					
OK-69																					
OK-70																					
OK-71																					
OK-72			1.99				1.85														
OK-74																					
OK-75			1.07				1.29														
OK-76																					
OK-82			1.43				2.00														
OK-83			2.03				2.20														
OK-84			2.20																		
OK-85			1.52				2.04														
OK-86			2.06				2.12														
OK-87			1.68				2.07														

OK-88			1.97				2.14														
OK-89																					

VITA

Amy Lynn Spaziani was born in 1981, in Horseheads, New York, to parents David and Barbara Spaziani. She attended schools in Horseheads, New York, and graduated from Horseheads Senior High School in 1999. She attended Geneseo State University of New York (SUNY), where she earned a Bachelor of Arts in geological sciences and political science in May 2004, and was a member of the women's varsity lacrosse team. Her undergraduate thesis focused on scarp development along Irondequoit Bay, Lake Ontario, New York. Post-undergraduate, she worked at the United States Geological Survey (USGS) in Reston, Virginia, as an Environmental Careers Organization (ECO) Intern with the Eastern Earth Surface Processes Team. Following this position, Amy became the education assistant at the American Geological Institute (AGI). She enrolled at Louisiana State University in August 2006 to study coastal and marine geology under Dr. Gregory Stone. She will graduate with a Masters of Science in oceanography with a minor in geology in May 2010.